Impact of basin tectonics and climate change on the timing of sediment flux to the Ainsa Basin, Middle Eocene, Spanish Pyrenees

Blanca Cantalejo López

2014

University College London

Thesis submitted for examination for the award of
Doctor of Philosophy (Ph.D)

Declaration

I, Blanca Cantalejo López confirm that the work presented in this thesis is my own. Where information has been derived from other sources, I confirm that this has been indicated in the thesis.

Signed _____

Date _____

Abstract

This thesis integrates sedimentological, geochemical, magnetostratigraphic and spectral work from field and core data from the Middle Eocene, deep-marine siliciclastic sediments in the Ainsa Basin, Spanish Pyrenees.

The deep-marine sediments of the Ainsa Basin comprise an alternation of coarse-grained sandbodies (submarine fans) and fine-grained packages of fan lateral-margin and interfan deposits. Time-series analysis performed on spectral gamma-ray and sandstone turbidite intensity data from 10 fine-grained interfan stratigraphic sections covering ~ 1.5 km of stratigraphy, and using multiple geochemical proxies (including high-resolution elemental XRF scanning, total organic carbon and carbon stable isotopes), all show that the interfan sediments contain a strong Milankovitch cyclicity. Orbital parameters most likely paced the cyclic delivery of the finer-grained sediments mainly by river- and delta-derived hyperpycnal turbidity currents. Sediment accumulation rates determined from spectral analysis reveal an overall decrease throughout the deep-marine stratigraphy from ~ 50 to ~13cm/kyr. Orbital tuning of the fine-grained sections using polarity reversals as anchor points permits the conversion from a depth-stratigraphy to a chronostratigraphy and also allows the estimation of the timing of initiation of each sandy submarine fan. The pacing of these sandbodies appears to have occurred at irregular time intervals and to have been of variable duration. They are, therefore, most likely controlled by the tectonic pulsating activity of the Pyrenean thrust systems linked with episodic changes in relative base level (e.g., overall tilting of the graded profile from source to sink, changing relative sea level).Climate may still have been important but only as a contributory rather than principal driver of submarine-fan development.

Table of contents

List of figures

List of tables

List of plates

List of equations

List of acronyms

AF	Alternating field
AR1	1st order autoregressive process
ASM	Average spectral misfit
BEI	Backscattered electron images
BEIF	Bloomsbury Environmental Isotope Facility
BSE	backscattered electrons
CCD	calcite compensation depth
CL	Confidence levels
CPS	Counts per second
E	eccentricity
EA	Elemental analysis
EECO	Early Eocene Climatic Optimum
EECO	Early Eocene Climatic Optimum
EOT	Eocene-Oligocene Transition
ETM	Eocene Thermal Maximum
FFT	Fast Fourier Transform
Fm	Formation
FOV	Field of View
GAD	Geocentric Axial Dipole
GPS	Global Positioning System
GPTS	Geomagnetic Polarity Timescale
IAEA	International Atomic Energy Agency
IC	Inorganic carbon
ICDD	International Centre for diffraction Data
IRMS	Isotope Ratio Mass Spectrometry
kyr	Thousands of years
LSFT	Lomb-Scargle Fourier Transform
M	Number of lags
Ma	Million yars ago
MAD	mean angle of deviation
MEM	Maximum entropy method
MT	megaturbidites
MTC	Mass transport complex
MTCs	Mass transport complexes
MTD	Mass transport deposit
MTDs	Mass transport deposits
MTM	Multi-taper method
Myr	Million years
N	Number of data points
NPF	North Pyrenean Fault
NPFT	North Pyrenean Frontal Thrust
NRM	natural remanent magnetisation
Nsim	Number of simulations
O	obliquity

ODP	Ocean Drilling Program
OFAC	Oversampling factor
P	precession
PETM	Paleocene-Eocene Thermal Maximum
RM	remanent magnetisation
SAR	Sediment accumulation rate
SARs	Sediment accumulation rates
SCPU	South-Central Pyrenean Unit
SEM	Scanning electron microscopy
SGR	Spectral gamma-ray
SI	Sampling interval
SPFT	South Pyrenean Frontal Thrust
SPTS	South Pyrenean Thrust System
SQUID	Superconducting Quantum Interference Device
TC	Total carbon
TOC	Total organic carbon
UCL	University College London
WOSA	Welch-Overlapped-Segment-Averaging Procedure
XPL	cross-polarised light
XRD	X-ray powder diffraction
XRF	X-Ray Fluorescence

Acknowledgements

I would like to express my sincere appreciation to my supervisor Prof. Kevin T. Pickering for his advice, guidance and enthusiasm during my research. I would also like to express my gratitude to Prof. Gerald Roberts (Earth Sciences, Birkbeck University) who kindly funded the palaeomagnetic study. I also thank the UCL Graduate School that provided extra funding for the geochemical analyses.

I would like to thank the UCL staff at the department of Earth Sciences who provided great technical support and many discussions. I would specially like to thank Dr Stuart Robinson for assistance in the measurement of stable carbon isotopes, Prof. Jürgen Thurow for his supervision with the XRF analysis, Dr Ian Wood for support with the XRD analysis and Jim Davies for the SEM analysis and thin sections. I would also like to take the opportunity to thank Dr Dave Kemp (Opening University) and Dr James Scotchman for all the guidance and great ideas with the time-series analysis. I sincerely thank Dr Conall MacNiocaill (Earth Dep., Oxford University) for supervising the palaeomagnetic work and to MSc student Kyrre Johansen for getting involved in such a fantastic project. I also would like to thank my PhD colleague and friend Nikki Dakin, for the great company during the long isolated months we spent in the Pyrenees collecting data.

Finally, I would like to thank my family and friends for their unconditional support. A very special thanks goes to Nick Lynch. I am forever grateful for your continuous support, encouragement and for being by my side every step of the way.

I dedicate this thesis to my mum who taught me that everything is possible if you have the mindset and the will to do it.

Chapter 1

Introduction

1.1 Introduction

The stratigraphy of sedimentary basins is controlled by changes in the accommodation space and sediment supply (e.g., Nelson *et al.,* 2009; Bourget *et al.,* 2010; Toucanne *et al.,* 2012). These factors are mainly controlled by basin tectonics and climatic variability. In active tectonic areas, basin subsidence and tectonic uplift will have an effect on erosion (Raymo *et al*.,1988; Rea, 1992), weathering patterns (Riebe *et al*., 2001; Jacobson *et al*., 2003; Riebe *et al*., 2004; Carey *et al*., 2005; Dixon *et al*., 2012) and relative sea-level changes (Watts and Thorne, 1984; Vött, 2007). As a consequence, the nature, the amount and the path of the sediment being transported to deep-water basins play a critical role in determining depositional patterns. Climate exerts a major control on the nature and amount of sediment supply by affecting intensity and seasonality of precipitation (Kostaschuk et al., 2002; Bouraoui et al. 2004), riverine run-off (Brown and Barber, 1985; Coulthard and Macklin, 2001) and rock weathering patterns (White and Blum, 1995; Jacobson *et al*., 2003; Riebe *et al*., 2004). Differentiating climatic and tectonic forces from stratigraphic records can therefore be challenging.

Whilst many studies have demonstrated the importance of global climate change as a major driver for cyclic depositional patterns in pelagic and hemipelagic sediments in deep time (e.g., Herbert and Fischer, 1986; Fischer *et al.,* 1991; Claps and Masetti, 1994; D'Argenio *et al.,* 1998), there remains considerable controversy about the role of climate, tectonic and/or autocyclic processes for deep-marine

siliciclastic deposits. Deep-water siliciclastic turbidite successions have long been associated with tectonic forcings (e.g., Macdonald, 1993; Mutti *et al.*, 2003; Underwood *et al.*, 2003; Goldfinger *et al.*, 2003, 2007). However, the development of deep-marine turbidite successions depends on external forcings such as river run-off and eustatic sea-level changes which control the sediment supply to the deep-marine environment (e.g., Schlager, 1993; Carvajal *et al.*, 2009; Toucanne *et al.*, 2012). These parameters are at the same time, affected by climatic fluctuations such as storminess and the waning and waxing of polar ice sheets. Submarine fan records have been shown to reflect climatic fluctuations (Milliman and Syvitski, 1992; Weltje and De Boer, 1993; Mutti *et al.*, 2003; Sømme *et al.*, 2009) and in some cases, packaging of deep-marine turbidites on convergent margins have been shown to be orbitally controlled during the Quaternary (e.g., Pickering *et al.*, 1999; Marsset *et al.*, 2009; Bourget *et al.*, 2010) and in older successions (e.g., Payros and Martínez-Braceras, 2014).

Attempting to gain a better understanding of the controls which tectonic and climatic variability exert on actively growing mountain belts and their associated basins is fundamentally important to any understanding of how Earth surface processes create the stratigraphic record. Analysis of deep-marine fine-grained thin-bedded turbidite and hemipelagic deposits in an active tectonic setting provides an opportunity to interrogate sedimentation patterns and to try and understand the main controls on sediment supply to sedimentary basins.

1.2 Geological setting

1.2.1 The Pyrenean orogen

The Pyrenees are a ~ 2,000 km long orogenic belt which extends from the northwestern part of Spain to the southern part of the Alps. The Pyrenees form an asymmetrical, east-west trending, double-wedge Alpine fold-and-thrust belt (Choukroune *et al.*, 1989; Roure *et al.*, 1989; Muñoz, 1992; Beaumont *et al.*, 2000), which developed from Late Cretaceous to Early Miocene (Roest and Srivastava, 1991; Rosenbaum *et al.*, 2002). The structural evolution of the Pyrenees has been studied integrating a wide range of geophysical techniques (e.g., deep-reflection and refraction seismic profiles (Roure *et al.*, 1989, Choukroune *et al.*, 1989; Muñoz, 1992), gravity (Casas *et al.*, 1997; Jammes *et al.*, 2010), magnetotellurics (Campanyá *et al.*, 2012), paleomagnetic studies (Van der Voo and Zijderveld, 1971; Van der Voo and Boessenkool, 1973), geoelectrical (Ledo *et al.*, 2000) tomography (Amaru *et al.*, 2008; Souriau *et al.*, 2008; Koulakov *et al*, 2009) and thermal studies (Tesauro *et al.*, 2009).

1.2.2 Evolution of the Pyrenees

The Pyrenees have undergone several phases of tectonic evolution: from an Early Mesozoic rift margin, to a collisional margin during the Tertiary, followed by a large passive margin during most of the Miocene and Quaternary (Srivastava *et al.*, 1990a, 1990b; Vergés *et a*l., 1995; Srivastava *et al*., 2000; Wilson *et al*., 2001; Sibuet *et al*., 2004).

The Pyrenees developed over a previously thinned continental crust, caused by the development of an extensional to transtensional rift system during the

Triassic and Late Jurassic. Extensional forces continued throughout the Cretaceous resulting in the separation of Iberia from Eurasia (Srivastava *et al.*, 1990a). This extensional regime was associated with the break-up of Pangaea (Torsvik *et al.*, 2008) and the opening of the central Atlantic Ocean and the Bay of Biscay (Le Pichon *et al.*, 1988; Srivastava *et al.*, 1990b; Roest and Srivastava, 1991). Lower crustal and upper mantle rocks rose to upper and middle crustal depths during this rifting event (Jammes *et al.*, 2010). The rift system had an oblique slip motion and was characterised by the development of very steep normal faults which formed strongly compartmentalised and asymmetric rift basins (Savostin *et al.*, 1986; Jammes *et al.*, 2010) which were infilled by carbonates and shallowing successions (Puigdefábregas and Souquet, 1986).

Seafloor spreading and the eastward opening of the Bay of Biscay in the Late Cretaceous caused the drift and progressive rotation of the Iberian microplate ~ 35° anticlockwise and resulted in the collision between the Iberian and the Eurasian plates during the Turonian (Choukroune, 1992; Vergés *et al.*, 2002; Vissers and Meijer, 2012). The collision was diachronous and propagated westwards along the margins of both plates (Meigs *et al.*, 1996; Vergés *et al.*, 2002). Geological and geophysical data shows that the Iberian lower crust detached from the upper crust and subducted together with the lithospheric mantle into the mantle along a north-dipping plane (Roure *et al.*, 1989; Muñoz, 1992; Beaumont *et al.*, 2000) whilst the upper crust delaminated, resulting in the propagation of a major fold-and-thrust belt to the south (the South Pyrenean Zone) and a backthrust system to the north (the North Pyrenean Zone) (Bourrouilh, *et al.*, 2004).

Continental collision resulted in the inversion of the Cretaceous rift basins and the reversed oblique-slip extensional faults were incorporated into the thrust

system (Roure *et al.*, 1989; Muñoz, 1992; Beaumont *et al.*, 2000; Vergés and García-Senz, 2001). The geometry of this fault system is responsible for the significant along-strike differences which exist in the crustal structure of the Pyrenees. Fault activity in the zone occurred in distinct tectonic pulses with active periods of deformation being followed by periods of tectonic quiescence (Meigs, 1997; Meigs and Burbank, 1997). The thrust transport direction was mainly from north/NNE to the south/SSW and remained constant throughout most of the tectonic evolution of the orogen (Dinarés *et al.*, 1992). The end of deformation, determined by magnetostratigraphy studies on growth strata (Meigs *et al.*, 1996) and fission track cooling ages (Fitzgerald *et al.*, 1999) occurred during the Late Oligocene giving an estimated duration of convergence of about 60 Ma (Beaumont *et al.*, 2000). It has been estimated from balanced and restored cross-sections a total shortening of 165 km and a mean shortening rate of ~ 0.25 cm/yr (Vergés *et al.*, 1995; Beaumont *et al.*, 2000). Convergence rates have probably varied during the orogenic phase and the evolution of the orogen has been estimated by age-constraining the emplacement of thrust structures through the study of syn-orogenic strata (e.g., Puigdefábregas and Souquet, 1986; Fernández *et al.*, 2004; Fernández *et al.*, 2012).

1.2.3 Structural units

The Pyrenean orogen can be divided from east to west, into two main sections: the Aragonese-Catalan Pyrenees and the Basque-Cantabrian Pyrenees (also known as the Western Pyrenees) (e.g., Vergés *et al.*, 2002). These two main zones are divided by an inverted Early Cretaceous transfer zone known as the Pamplona Fault (e.g., Muñoz, 2002).

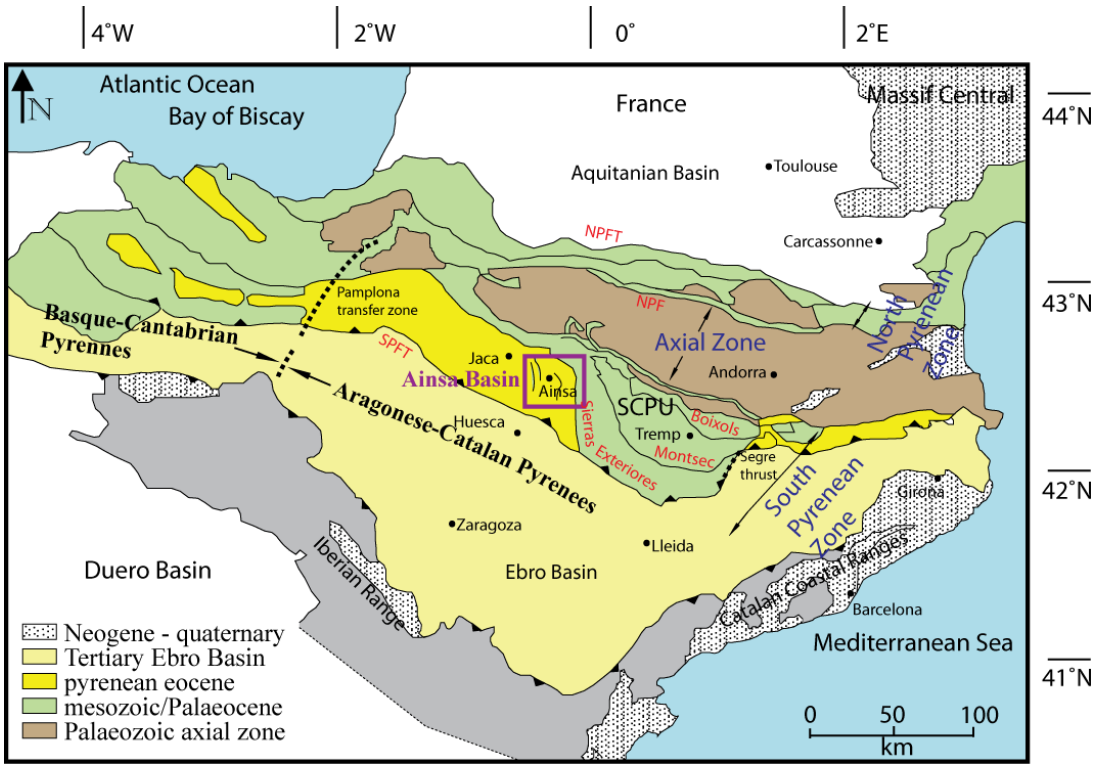

Figure 1.1 Schematic geological map of the Pyrenees showing the position of the study area (Ainsa Basin). NPFT = North Pyrenean Frontal Thrust; NPF = North Pyrenean Fault; SPFT = South Pyrenean Frontal Thrust; SCPU = South-Central Pyrenean Unit (modified after Vergés *et al.* (2002).

The Aragonese-Catalan Pyrenees form the main part of the orogen and can be subdivided into the Eastern Pyrenees, extending from the Mediterranean Sea to the Segre Thrust, and the Central Pyrenees, from the Segre Thrust to the Pamplona Fault (e.g., Vergés *et al.*, 2002) (Figure 1.1).

The Aragonese-Catalan Pyrenees were formed by an asymmetric, double wedge thrust system which divided the orogen into the Northern and the Southern Pyrenees. In between these two wedges, at the centre of the orogen, there is the Axial Zone of the chain formed by Palaeozoic rocks, intensely deformed and metamorphosed (e.g., Muñoz, 1992) (Figure 1.1). Deformation of the double wedge orogen primarily migrated outward in a piggyback manner (Puigdefábregas *et al.*, 1992; Déramond *et al.*, 1993), although localised breakback successions have also been recognised (Vergés and Muñoz, 1990). The Southern Pyrenees are wider and

have accumulated larger amounts of cumulative shortening and displacement, ~ 37 km for the northern edge and ~ 128 km for the southern orogen (Beaumont *et al.*, 2000). The South and North fold-and-thrust belts are flanked by two flexural foreland basins which developed by lithospheric compensation in response to crustal thickening in the Axial Zone: the Ebro Basin in the south and the Aquitanian Basin in the north.

The Pyrenees can be divided from north to south into five main structural units: the Aquitanian Basin, the North Pyrenean Zone, the Axial Zone, the South Pyrenean Zone and the Ebro Basin (Figure 1.2).

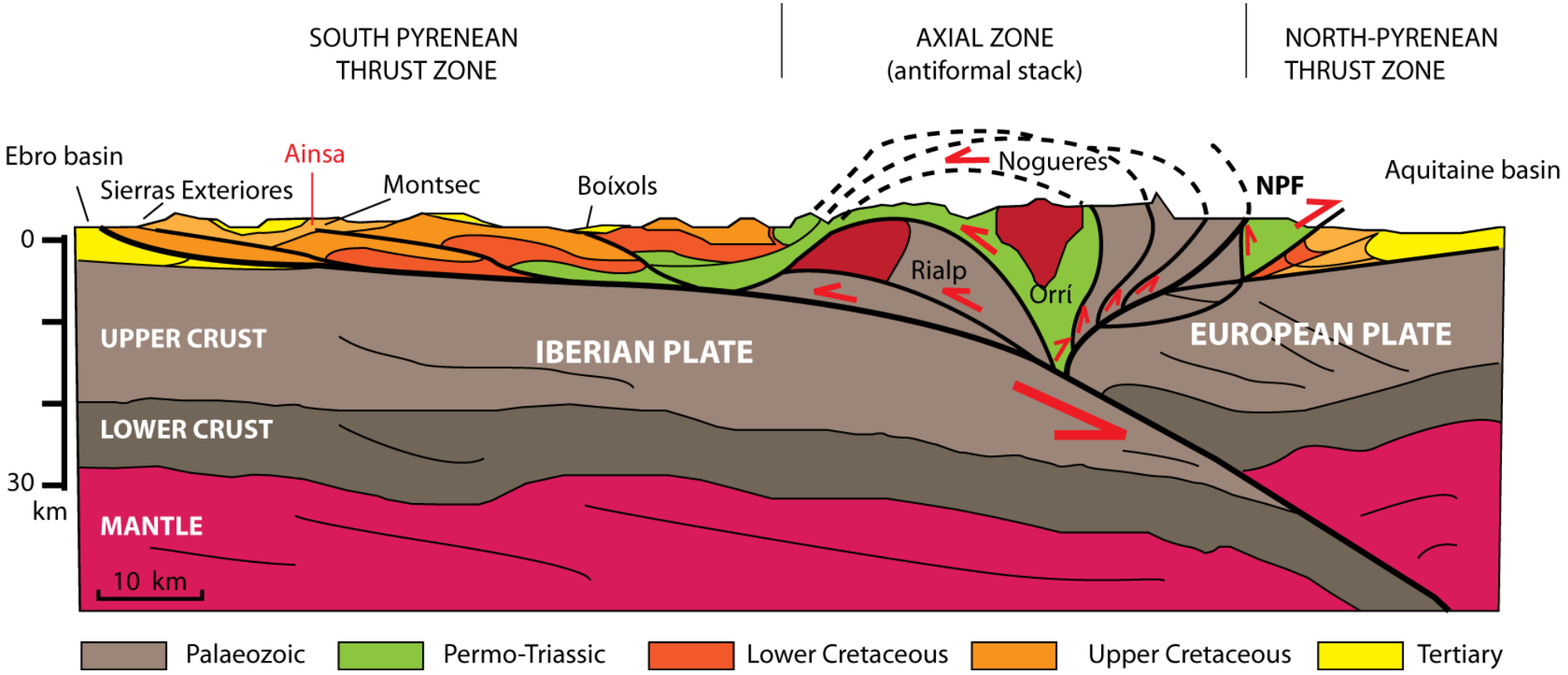

Figure 1.2 North-south cross-section across the Pyrenees. The cross-section shows the five main structural units: The Aquitanian Basin, the North Pyrenean Thrust Zone, the Axial Zone, the South Pyrenean Thrust Zone and the Ebro Basin. Modified after Muñoz (1992) and Beaumont *et al.* (2000).

1.2.3.1 The Aquitanian Basin

The Aquitanian Basin is a retro-foreland basin developed on the northern edge of the Iberian and over the European Plate (Bourrouilh *et al.*, 2004). The infill of this basin comprises of a thick (~ 5 km) succession of synorogenic Upper Cretaceous turbidites (Déramond *et al.*, 1993), overlain by a thick (~ 5 km) Palaeogene to Early Eocene alluvial and fluvial deposits (Buis and Rey, 1975). This foreland basin developed in the footwall of the North Pyrenean Frontal Thrust (NPFT) (Figure 1.1) and evolved by flexure in response to the load of the North Pyrenean Thrust (Brunet, 1986).

1.2.3.2 The North Pyrenean Zone

The North Pyrenean Thrust System, located to the north of the Axial Zone, developed on top of the European Plate and consists of a northward directed imbricate stack composed of folds and high-angle reverse faults involving a Hercynian basement and Mesozoic to Early Eocene cover rocks (Souquet, 1988; Déramond *et al.*, 1993). This fold-and-thrust belt is narrower than the fold-and-thrust system to the south and has undergone almost continuous deformation from the Late Cretaceous to the Late Eocene (Derámond *et al.*, 1993).

The North Pyrenean Thrust System is bordered to the north by the North Pyrenean Frontal Thrust (NPFT) and to the south by the North Pyrenean Fault System (NPF). The NPFT affects post-Triassic rocks which are thrusted over Eocene sediments of the Aquitanian Basin (Teixell, 1998). The NPF is a complex system of deep faults which probably affects the whole of the lithosphere (Casas *et al.*, 1997). Crustal granulitic rocks and ultrabasic mantle rocks (lherzolites) are found to the north associated with this fault system (Hall and Bennet, 1979; Vielzeuf

and Kornprobst, 1983; Montigny *et al.*, 1986) and many researchers believe that this fault marks the suture between the Iberian and the European plates (Choukroune, 1992; Muñoz, 1992; Casas *et al.*, 1997; Vergés and García-Senz, 2001). The emplacement of lherzolites appears to be associated with crustal thinning in a transtensional north-south setting, emplaced at shallow levels by thrusting during mountain building and is more recent in the east (90 Ma) than in the west (95-110 Ma), indicating an oblique collision and asynchronous evolution of the Pyrenees (Casas *et al.*, 1997).

1.2.3.3 The Pyrenean Axial Zone

The Pyrenean Axial Zone lies to the south of the North Pyrenean Fault and represents the ancient core of the mountain range (Muñoz, 1992). The Axial Zone is composed of ~ 10 km of Cambrian to Carboniferous rocks which have been affected by the Variscan Orogeny and are highly deformed, metamorphosed and intruded by crustal-derived granodioritic plutons (Vissers, 1992; Evans *et al.*, 1998). This deformed Palaeozoic rocks are overlain uncomformably by an Upper Carboniferous to Triassic cover, composed of sedimentary and volcanic rocks (Vergés *et al.*, 1995). The Pyrenean Axial Zone is characterised by the stacking of several southward-facing thrust and backthrusts that piled on top of each other forming an antiformal stack (Muñoz, 1992; Teixell, 1998; Muñoz, 2002). These overstacking slabs of Hercynian crust have resulted in a significant thickening of the Iberian crust in this region (Roure *et al.*, 1989; Teixell, 1998). The four main complex thrust sheets from top to bottom are: Nogueres, Erta, Orri and Rialp (Muñoz, 1992) (Figure 1.2). The transport direction of these thrusts is towards the SSW (Saura and Teixell, 2006) and parallel to the main shortening direction of the Pyrenees (Muñoz, 1992). As new

thrusts were emplaced, previous thrust sheets rotated towards the foreland (Muñoz, 1992). The Pyrenean Axial Zone has a very complex three dimensional (3D) structure with lateral ramps and sudden changes in structural relief. This complex structure is associated with the inversion of several small Stephanian-Permian extensional basins which controlled thrust geometries and kinematics causing lateral structural variation (Saura and Teixell, 2006).

1.2.3.4 The South Pyrenean Thrust System (SPTS)

The South Pyrenean Thrust System (SPTS) lies to the south of the axial zone and comprises of a southward directed imbricate stack developed on top of the subducted Iberian Plate (Cámara and Klimowitz, 1985; Muñoz, 1992; Capote *et al.*, 2002). The northern limit of the SPTS is the Axial Zone Nogueres nappe and the southern limit is marked by the frontal thrust of the Sierras Exteriores (Muñoz, 1992; Meigs and Burbank, 1997).

The South Central Pyrenean Unit (SCPU) is located in the central section of the South Pyrenean Thrust System and contains the study area in its western part. The SCPU has a trapezoidal shape and is bounded to the east by the Segre Thrust and to the west by a set of north-south trending folds and thrusts (such as the Mediano and Boltaña anticlines) (Séguret, 1972). These structures are transverse to the main Pyrenean trend (WNW-ESE). The SCPU is composed of three main imbricated thrust sheets detached over evaporates of the Triassic Keuper Formation, from top to bottom these are: the Bóixols-Cotiella thrust sheet, Montsec-Peña Montañesa thrust sheet and the Sierras Exteriores thrust sheet (Vergés and Muñoz, 1990; Muñoz, 1992; Puigdefábregas *et al.*, 1992; Fernández *et al.*, 2012). These thrust systems were generated by tectonic inversion of pre-existing Early Cretaceous

extensional faults which played a major role in controlling the geometry and configuration of oblique and lateral ramps and the lateral variation of facies across them (Farrell *et al.*, 1987; Puigdefábregas *et al.*, 1992; Fernández, *et al.*, 2004; Saura and Teixell, 2006).

The emplacement of the Bóixols Thrust occurred during the Late Cretaceous (Bond and McClay, 1995). Deep, narrow basins trending east-west were developed in the footwall of the inverted extensional faults (Puigdefábregas *et al.*, 1992) and were infilled with Upper Cretaceous turbiditic deposits of the Vallcarga Formation. During the Uppermost Maastrichtian to Palaeocene period, marine sedimentation gave way to a thick deposition (>1km) of fluvial and lacustrine red beds (Tremp Group) (Puigdefábregas *et al.*, 1992; Ardévol *et al.*, 2000). Lower Cretaceous extensional faults were completely inverted during Palaeocene times and the upper crust recovered its stretched nature (Puigdefábregas *et al.*, 1992).

The Montsec-Cotiella Thrust developed during the Early Eocene (Ypresian) (Farrell *et al.*, 1987; Muñoz, 1992, Vergés and Burbank, 1996) and involves Hercynian basement rocks. The thrust climbs up section southward from the basement into Triassic evaporates and emerges in the Sierras Exteriores at the Pyrenean thrust front (Teixell, 1996).

The Sierras Exteriores thrust sheet developed in the Middle Eocene and thrust activity continued until the Early Miocene (Puigdefábregas *et al.*, 1992; Meigs *et al.*, 1996). This thrust acted as an upper detachment thrust accumulating over 30 km of displacement (Cámara and Klimowitz, 1985; Fernández *et al.*, 2012). To the north of the Ainsa Basin, several basement thrusts branch into the Sierras Exteriores Thrust, with the Gavarnie and the Guarga thrusts being the two which show the greatest displacement (Fernández *et al.*, 2012).

1.2.3.5 The Ebro Basin

The Ebro Basin is a large intraplate pro-foreland basin developed over the Iberian Plate and limited to the north by the Pyrenees range and the Catalan and Iberian mountain ranges to the southeast and southwest, respectively. Basin formation began at the end of the Cretaceous as a response to lithospheric flexure due to loading in the Axial Zone and South Pyrenean Thrust System (Gaspar-Escribano *et al.*, 2001; Vergés *et al.*, 2002). The Ebro Basin is wider than the Aquitanian Basin and has a thicker syn-orogenic succession (Beaumont *et al.,* 2000). Rocks exhumed and eroded at the Axial Zone, were transported and deposited in piggyback basins in the south thrust-and-fold belt and in the foreland Ebro Basin (Muñoz, 1992). The first syn-orogenic deposits are Upper Cretaceous turbidites, which grade upwards to shallow-marine and continental deposits (deltaic, fluvial, alluvial and occasional lacustrine) by the Miocene (Puigdefáfregas *et al.*, 1992). There is a strong lateral variability of facies due to basin compartmentation (Puigdefábregas *et al.,* 1992). After the cessation of the compressional period, a period of quiescence followed in the Ebro Basin, where the basin slowly filled with continental clastics which progressively buried the synorogenic sediments and Pyrenean thrust structures (Coney *et al.,* 1996; Beaumont *et al.*, 2000). The final stage of the evolution of the basin was characterised by denudation and river incision where the Ebro Basin opened to the Mediterranean Sea (Vergés *et al.*, 2002).

1.2.4 The Ainsa Basin: study area

1.2.4.1 Tectonic setting

The Ainsa Basin is a small basin, ~ 25 km wide and 40 km long, located in the footwall of the Montsec-Cotiella Thrust, within the oblique thrust-and-fold system of the South Central Pyrenees (Segurét, 1972) (Figure 1.3). The thrust surface underlying the Ainsa Basin is the Gavarnie-Sierras Exteriores Thrust (Fernández *et al.*, 2012). The basin developed as a foredeep during the Cuisian-Lutetian, due to flexural subsidence caused by the advancement of the Montsec-Cotiella thrust sheet (Dreyer *et al.*, 1999).

In the middle Lutetian and Bartonian, thrust sheets propagated westwards towards the foreland and a number of north-south trending anticlines and synclines developed in the basin within and along the leading edge of the Sierras Exteriores thrust sheet (Muñoz *et al.*, 1998, Fernández *et al.*, 2004). These folds are oblique to the general WNE-ESE trend of the Pyrenean structures. The northeastern side of the basin appears more severely deformed with a stack of thrust-and-fold structures known as the Arro Thrust System (Fernández *et al.*, 2012). The development of the Mediano and the Boltaña anticlines marked the evolution from a transitional foredeep basin to a thrust-top basin which was incorporated into the hangingwall of the Gavarnie-Sierras Exteriores thrust sheet during the Middle Eocene (Muñoz *et al.*, 1998; Dreyer *et al.*, 1999; Fernández *et al.*, 2004; Fernández *et al.*, 2012). These folds developed synchronously with their dextral rotation in the footwall of the Cotiella thrust sheet (Fernández *et al.*, 2012).

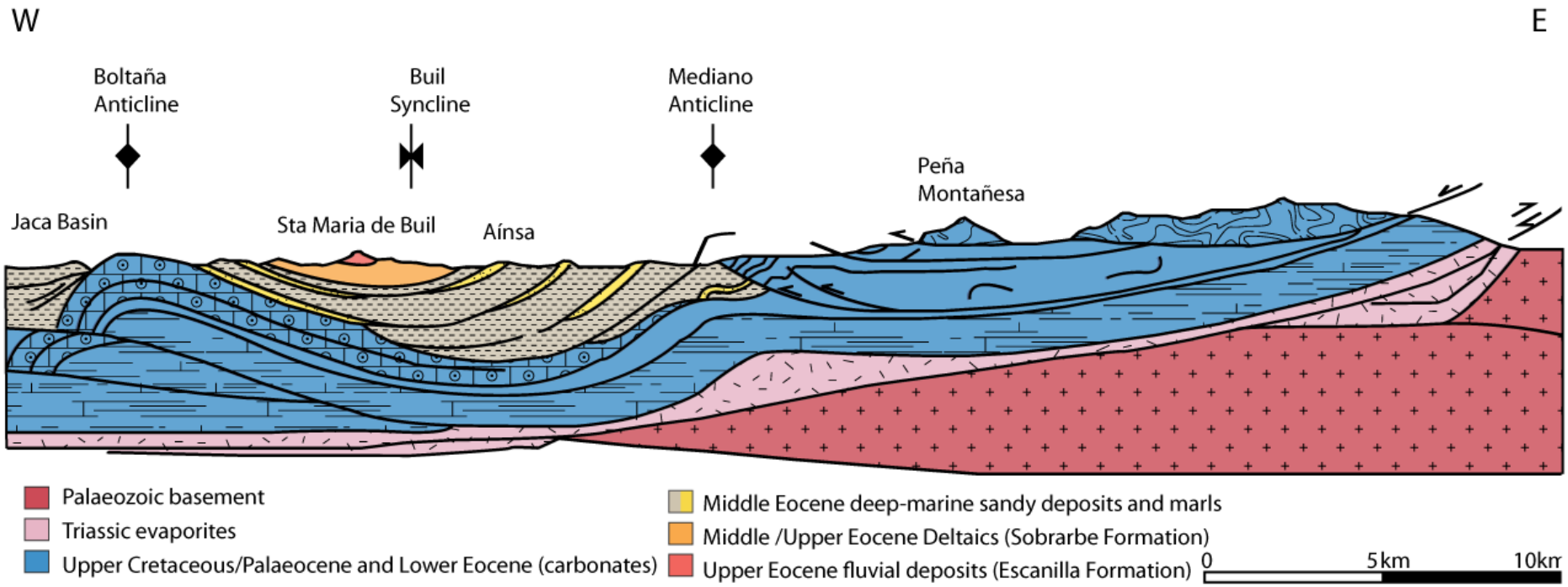

Figure 1.3 West-east structural section of the Ainsa Basin. Cross-section based on regional geological maps and seismic profiles. Modified from Dreyer *et al.* (1999).

The infill of the Ainsa Basin consists of 4 km of slope and base-of-slope turbidite complex. The basin was connected, at least during the Early Eocene, to the western more basinal part of the foredeep, the Jaca Basin (Mutti *et al.*, 1972) (Figure 1.3). The basin-floor complex in the Jaca Basin consists of 'outer-fan' sandstone lobes, typically tens of metres thick and more than 15 km wide, which are replaced downcurrent by basinal sandstone and mudstone interbeddings (Mutti *et al.*, 1972).

Turbidites of the Ainsa Basin were sourced from a large fluviodeltaic complex deposited in the Tremp-Ager Basin on top of the Montsec thrust sheet. Rivers and deltas entered this basin from the east forming the Montanyana Group (Mutti *et al.*, 1985; Marzo *et al.*, 1988) (Figure 1.4). The central and southern part of the Ager-Tremp Basin is dominated by a fluvial system that supplied sand and mud from the southeast, whilst in the northeastern part of the basin, a complex of alluvial fans and fan-deltas developed which supplied coarser-grained sediments (Nijman, 1998). Three fan-delta systems were active during the deposition of the Ainsa Basin turbidites: the Claramunt, the San Esteban and the Campanúe fans (Nijman, 1998). These fans are composed of coarse-grained sandstones and conglomerates (Puigdefábregas *et al.*, 1992; Nijman, 1998) derived from Mesozoic and Palaeozoic source rock (Weltje *et al.*, 1996), and related floodplain mudstones. These continental facies prograded stepwise across an oblique lateral ramp of the Cotiella-Montsec thrust sheet into the Ainsa Basin (Mutti *et al.*, 1988).

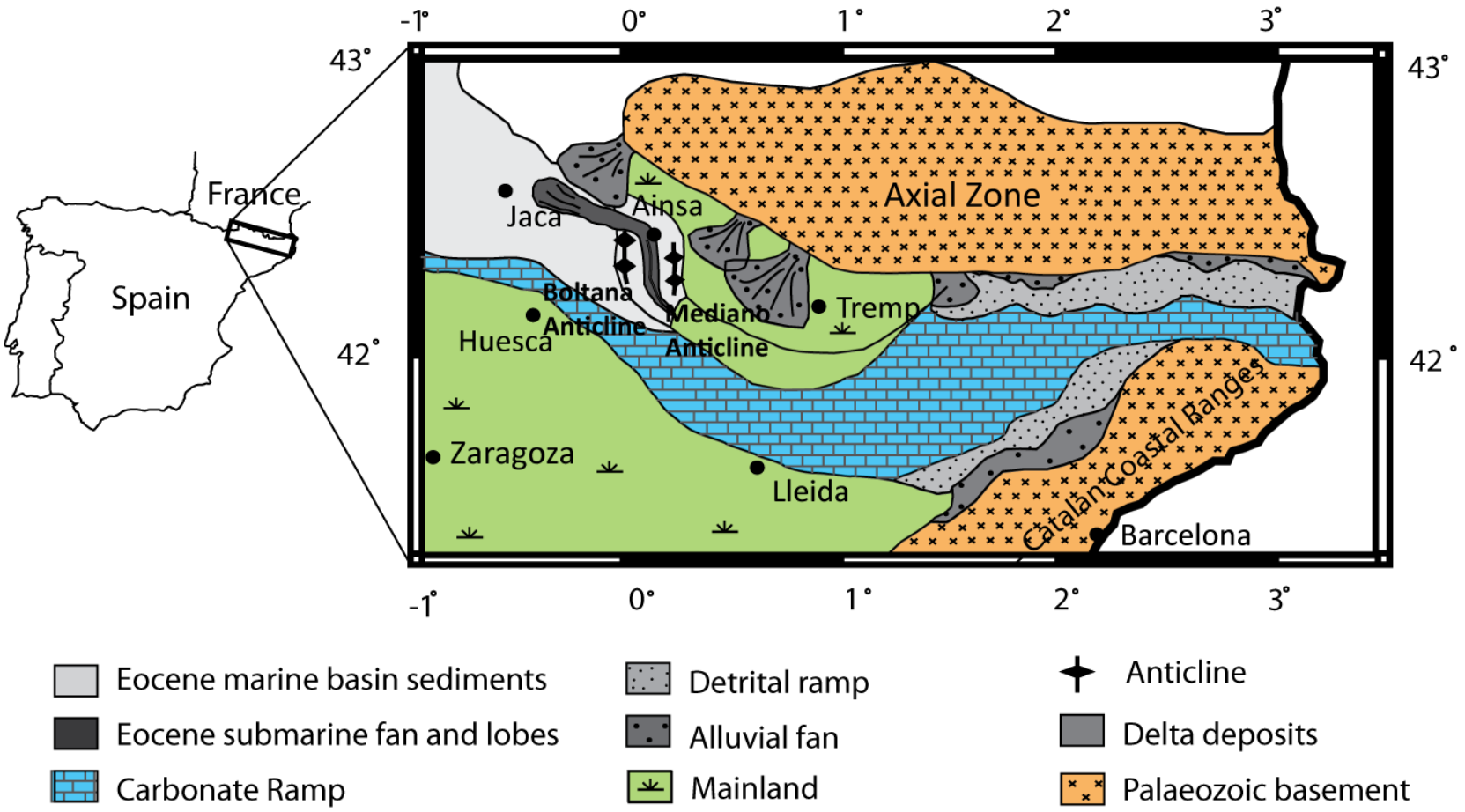

Figure 1.4 Palaeogeographic map of the South Central Pyrenees during the Middle Eocene. The study area (the Ainsa Basin) is located between the Boltaña and the Mediano anticlines and consists mainly on deep-marine channelised slope deposits. Modified after Puigdefábregas (1975) and Huyghe *et al.* (2012).

As a result of this overall transgressive facies pattern, fan progradation and aggradation resulted in coarsening-up trends separated by major stratigraphic boundaries and an increase of clastic supply towards the west (Nijman, 1998). The transition between the fluvial-deltaic deposits of the Montanyana Group and the sediment gravity flow deposits present in the Ainsa and further to the west, in the Jaca basins, occurred through a succession of oblique structures where incised canyons transferred clastics from the shallow platform to the deeper basin (e.g., the Charo Canyon) (Puigdefábregas *et al.*, 1992; Millington and Clark, 1995).

1.2.4.2 Structure of the Ainsa Basin

The structure of the Ainsa Basin is dominated by two main types of tectonic features: an oblique-lateral ramp thrust system that joins the Montsec-Peña Montañesa frontal ramp known as La Fueba or the Arro Thrust System (Casas *et al.*, 2002; Fernández *et al.*, 2012) and a set of N-S trending anticlines and synclines known as the Sobrarbe Fold System (Fernández *et al.*, 2012) (Figure 1.5).

The Arro Thrust System is present in the northeastern side of the Ainsa Basin and consists of a number of NW-SE trending thrusts and related fault-propagation-folds formed during the Cuisian to early Lutetian (Muñoz *et al.*, 1994). These thrusts typically show up to 2 km of displacement (Muñoz *et al.*, 1994; Fernández, *et al.*, 2012).

There are three major anticlines in the Ainsa Basin: Mediano, Boltaña and Añisclo (Figure 1.5). Fernández *et al.* (2012) identified a 4th anticline, the Cinca Anticline, running along the Cinca River, although this is considered a minor structure and will not be discussed further. The Mediano Anticline flanks the eastern side of the basin, the Boltaña Anticline flanks the west, and the Añisclo Anticline flanks the north

and northwest (Fernández *et al.*, 2004; Pickering and Corregidor, 2005). These north-south verging anticlines have been interpreted as transport-oblique lateral thrust ramps (Farrell, *et al.*, 1987), developed along the eastern margin of the Gavarnie thrust sheet (Tavani *et al.*, 2006). The Gavarnie Thrust and these anticlines are detached over the same Triassic evaporates of the Keuper Formation (Fernández *et al.*, 2004).

The Mediano Anticline is a 20 km long, north-plunging detachment anticline which plunges 10° towards the north (Holl and Anastasio, 1993; Poblet *et al.*, 1998). Palaeomagnetic and stratigraphic data indicates that the growth of the Mediano Anticline started in the early Lutetian and ended by 42 Ma (Holl and Anastasio, 1993; Poblet *et al.*, 1998). Holl and Anastasio (1993) found that the growth of Mediano was episodic with intervals of slow growth being superimposed by relatively fast and short lasting (< 1.5 Myr) growing episodes. This episodic growth associated with the pulsating activity of the Cotiella-Montsec thrust sheet caused the formation of angular and progressive unconformities as Lutetian turbidite deposits onlapped the flanks of the anticline (Holl and Anastasio, 1993). This anticline probably constituted a submarine topographic high during the infilling stages of the basin (Holl and Anastasio, 1993; Poblet *et al.*, 1998).

The Boltaña Anticline is a cylindrical 25 km long, north-south trending fault-propagation-fold developed above two-west-verging blind thrusts (Mutti *et al.*, 1988; Fernandez *et al.*, 2004; Fernandez *et al.*, 2012). This anticline is characterised by a sub-horizontal axis which extends to the north and south beyond the Ainsa Basin (Fernández *et al.*, 2004). The anticline started to grow during the last stages of the basin fill in the late Lutetian (Fernández *et al.*, 2012).

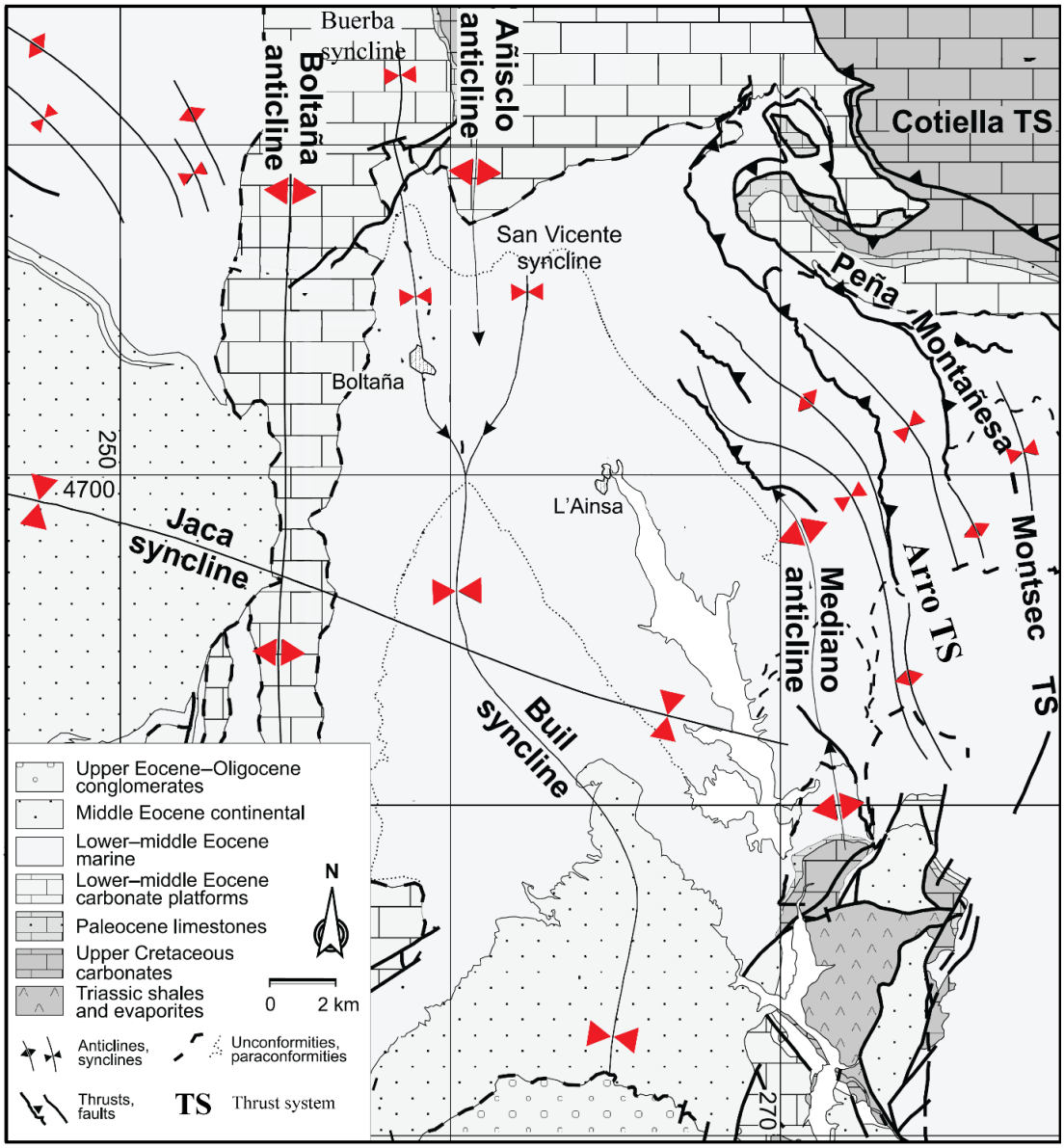

Figure 1.5 Structures of the Ainsa Basin. Map of the Ainsa Basin showing the main identified tectonic units. The Sobrarbe Fold System comprises the Boltaña, Mediano and the Añisclo anticlines and the Buil Syncline. The Buil Syncline is divided towards the north into the San Vicente and the Buerba synclines. The northwestern part of the basin is tectonically complicated by the Arro Thrust System (Arro TS). Modified after Fernandez *et al.* (2004).

The Añisclo Anticline is a west-verging fault-propagation-fold developed over a blind fault which plunges 10° towards the south in its northern sector, increasing to 25° in its southernmost termination underneath the Ainsa Basin (Fernández *et al.*, 2004; Tavani *et al.*, 2006). The growth of the Añisclo Anticline started more or less coeval with the Mediano Anticline but it is difficult to establish the end of the growing period due to erosion of the latest kinematic units (Fernández *et al.*, 2012).

These three anticlines acted as submarine topography highs which played a significant role in controlling the geometry of the basin and influenced sedimentation patterns (e.g., Sutcliffe and Pickering, 209; Bayliss and Pickering, 2014a, 2014b).

A major syncline, the Buil Syncline, crops out between the Boltaña and the Mediano anticlines, and occupies mainly the western part of the basin (Figure 1.5). This syncline is a north-south trending structure, ~ 10 km across, which plunges approximately 7° towards the south (Falivene *et al.*, 2006). To the north of the Ainsa Basin, the Buil Syncline splays around the Añisclo Anticline forming the Buerba Syncline on the west and the San Vicente Syncline on the east (Fernández *et al.*, 2004). Most of the syncline folding postdates the infill of the basin (Falivene *et al.*, 2006).

Superposed on these anticlines, there is the Jaca Syncline, a large east-west trending syncline structure in the Gavarnie-Sierras Exteriores thrust sheet that developed during the Late Eocene as a result of underthrusting of basement units (Muñoz, 1992; Teixell, 1996) (Figure 1.5). The development of this structure, transverse to the main folds of the Ainsa Basin, has caused the reduction of the plunge for the north plunging folds (e.g., Mediano and Boltaña anticlines) and the accentuation of the south plunging folds (e.g., Añisclo Anticline and Buil synclines) (Fernández *et al.*, 2004).

The rotation of these structures, from an originally west-east trend to a north-south direction has been determined by magnetostratigraphy. Palaeomagnetic data shows that these anticlines postdate the emplacement of the Montsec-Peña Montañesa Thrust and originated as east-west frontal structures, which were then rotated ~ 60-80° in a clockwise direction (Pueyo *et al.*, 2004; Mochales *et al.*, 2012). Most of the rotation occurred from the Ilerdian to the middle Lutetian where these structures were

actively growing and the axial rotation decreased during the late Lutetian to Bartonian, spanning the final stages of anticline growth (Mochales *et al.*, 2012).

1.2.4.3 Stratigraphy

The stratigraphy of the Ainsa Basin has been studied by multiple researchers (e.g., Garrido-Megías, 1968; Van Lunsen, 1970; Puigdefábregas, 1975; Mutti *et al.*, 1985, Pickering and Corregidor, 2005; Arbués *et al.*, 2007; Pickering and Bayliss, 2009) and can be divided into 4 tectonostratigraphic units.

The first and oldest unit extends from the Triassic to the base of the Early Eocene and comprises Keuper evaporites and shales which are overlain by a thick deposition (~ 1,500 m) of Cretaceous shelfal carbonates and marls. Above the Palaeocene sediments, a widespread transgressive episode during the Ypresian resulted in the deposition of the *Alveolina* Limestone which is present over most of the South and Central Pyrenees. These sediments were deposited prior to deformation or thrust motion (Fernández *et al.*, 2012).

The second tectonostratigraphic unit extends from the Lower Eocene (upper Ilerdian and middle Lutetian) to Late Ypresian and includes the Millaris, Metils, Yeba and Boltaña formations. These units consist on alternating shales, marls and platform limestones (Van Lunsen, 1970; Fernández *et al.*, 2012). The contact between the 2nd and 3rd unit is erosional, and locally the 3rd unit overlies directly the *Alveolina* Limestone of the 1st tectonostratigraphic unit (Fernández *et al*., 2012).

The third tectonostratigraphic unit includes sediments of Cuisian and Priabonian age. Within this unit there is a marked transition from shallow-marine limestones to syn-orogenic deep-marine slope and base-of-slope depositional systems in the Ainsa Basin (Mutti *et al.*, 1972; Dreyer *et al.*, 1999, Pickering and Corregidor,

2005). This sudden change towards deeper water lithologies reflects a northwestward plunge of the Pyrenees related to the advancement of the deformation front (Nijman *et al.*, 1998).

The fourth tectonostratigraphic unit comprises ~ 500 m of Bartonian shallow-marine and deltaic deposits of the Sobrarbe Formation (De Federico, 1981; Dreyer *et al.*, 1999) and the successive fluvial sediments of the Escanilla Formation (Garrido-Megías, 1968) which represents the final stages of basin infill (Puigdefábregas *et al.*, 1992; Dreyer *et al.*, 1999). These terrestrial sediments uncomformably overlie the slope deposits of the Ainsa Basin and postdate the growth of the oblique structures of the Ainsa Basin.

Internally, the Ypresian and Lutetian slope deposits of the third tectonostratigraphic unit can be subdivided into four major unconformity-bounded depositional cycles delineated by angular unconformities parallel to the elongation of the basin (Arbués *et al.*, 1998; Muñoz *et al.*, 1998) (Figure 1.6). These unconformities are submarine depressions or canyons, several hundred metres deep which step down towards the foreland and are caused by thrust activity in the northeastern margin of the basin (Muñoz *et al.*, 1994, 1998; Arbués *et al.*, 1998). Each of these unconformities have an incidence of several million years (Arbués *et al.*, 2007).

Approximately 4 km of syntectonic deep-marine deposits accumulated during the Ypresian and the Lutetian stages of the Eocene (Remacha and Fernandez, 2003; Fernandez *et al.*, 2004; Pickering and Corregidor, 2005). These deposits were defined by Mutti *et al.* (1972) as the 'Hecho Group' and consist of a succession of deep-marine mudstones (Van Lunsen, 1970) and several coarser-grained sandstone units (Mansurbeg *et al.*, 2009, Caja *et al.*, 2010). The mudstones are characterised by thick intervals (typically hundreds of metres thick) of thin bedded laminated siltstones and

marlstones which constitute both interfan and fan lateral-margin facies (Pickering and Corregidor, 2005) deposited from basinal background settling and low-density turbidity currents (Falivene *et al.*, 2010).

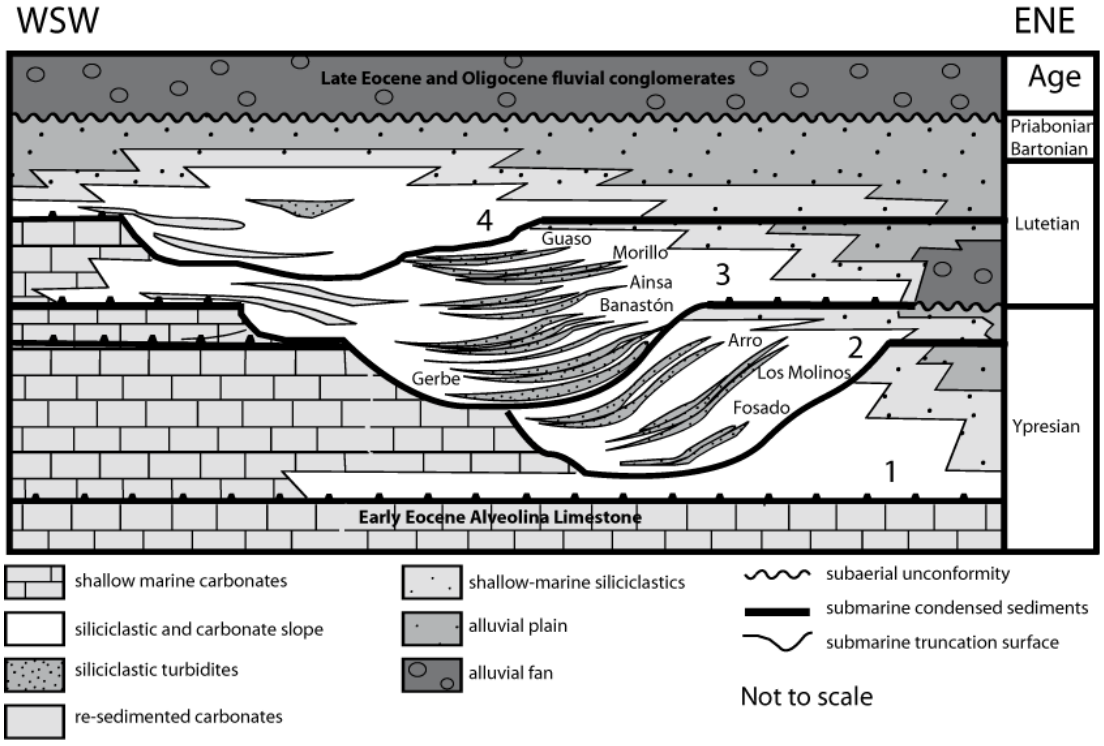

Figure 1.6 Stratigraphy of the Ainsa Basin. The figure shows the four unconformity-bounded units. Modified from Arbués *et al.* (1998); Fernández *et al.* (2004) and Fernández *et al.* (2012).

1.2.4.4 Sand-rich depositional systems

Eight sand-rich, deep-marine systems have been recognised, from the oldest: Fosado, Los Molinos, Arro, Gerbe, Banastón, Ainsa, Morillo and Guaso. Each of these systems contains 2-6 sandbodies interpreted as sand-prone channelised submarine fans (Pickering and Corregidor, 2005).

Sand-prone channels are typically 10-30 m thick and 0.5-2.5 km wide, but, typically reach 2.5-4 km if channel margin heterolithics, levées and overbank facies

are included (Pickering and Bayliss, 2009). Channel complexes have a low degree of sinuosity, are erosionally confined towards their bases and contain channel fills characterised by amalgamated erosional and mixed erosional-depositional sandstone turbidites (Pickering and Corregidor, 2005; Falivene *et al.*, 2010).

Different facies have been recognised in the coarser grained units (Pickering and Corregidor, 2005; Pickering and Bayliss, 2009; Favilene *et al.*, 2010):

- Channel infill facies composed of thickly bedded, coarse to medium-grained sandstone turbidites
- Channel-lobe transition or channel-margin represented by low net-to-gross ratio heterolithic facies
- Slumped facies consisting of soft-sediment deformation of fine-grained sediments
- Re-sedimented carbonates from destabilisation in the carbonate slope and platform developed in the southwestern section of the basin
- Debrites, including sandy and gravelly mudstones containing in occasions large and distorted sand rafts

Architectural elements from each of these systems can be related to specific environments of deposition. The Fosado System is 60 m thick and is composed of two successions (Fosado I and II) and represents lower-slope channels. Los Molinos System (~ 210 m thick) has three successions (Molinos I-III) and represents base-of-slope, slope apron with mid-slope channels. The Arro System contains two sandbodies (Arro I and Arro II) and has been interpreted as an upper/mid-slope canyon (Millington and Clark, 1995). The Gerbe System (up to 210 m thick), also contains two sandbodies (Gerbe I and II) and has been interpreted as lower-slope erosive channels. The Banastón System is the thickest of all the systems (~ 500-700 m thick) and contains six sandbodies (Banastón I-VI). Each of these sandbodies has been

interpreted as lower-slope and proximal basin-floor submarine fans (Pickering and Bayliss, 2009; Bayliss and Pickering, 2014b). The Ainsa System is up to ~ 250 m thick and contains three sandbodies (Ainsa I-III) interpreted as lower-slope and axial basin-floor channelised submarine fans (Pickering and Corregidor, 2005; Favilene *et al.*, 2010). The Morillo System is ~ 260 m thick and comprises three sandbodies (Morillo I-III) which were accumulated in a mid-slope canyon to the south and to a lower-slope confined channel system in the north (Pickering and Bayliss, 2009; Bayliss and Pickering, 2014a). Guaso is the youngest system, has a thickness of ~ 300 m and contains two sandbodies (Guaso I and II). These sandbodies have previously been interpreted as deep-erosional, canyon-like features (Stocchi, 1992; Stocchi *et al.*, 1992), but Sutcliffe and Pickering (2009) re-interpreted them as laterally extensive sheet-like sandbodies confined only by basin structure.

1.2.4.5 Submarine fans *versus* erosional channels

Previously, some researchers have referred to the deep-marine systems of the Ainsa Basin as a channelised slope system or slope complex (e.g., Cronin *et al.*, 1998). However, these sandbodies can be defined as submarine fans *sensu stricto*, because: (i) the proximal channelised parts can be correlated to the more distal lobe and related deposits in the Jaca Basin (Das Gupta and Pickering, 2008; Caja *et al.*, 2010). Typically, a submarine fan system will comprise: a sediment source area, a zone of sediment transfer, and a deposition zone (Allen, 1997) (Figure 1.7). In the study area, the source area comprises the fluvio-deltaic sediments of the Tremp-Ager Basin; the sediment-transfer zone contains submarine canyon-channel systems of the Ainsa Basin infilled with coarse-grained sediments that grade peripherally into overbank deposits containing finer-grained sediments. The more distal area where the sediment

accumulates, forming lobes and more distal deposits, is represented by the Jaca Basin (Mutti *et al.*, 1972).

(ii) the sandbodies in the Ainsa Basin have a high degree of architectural complexity and show a vertical change from initial non-channelised, sheet-like, lobe or mouth-bar deposits, through small and then larger channels, interpreted as fan progradation (Pickering and Corregidor, 2005; Pickering and Bayliss, 2009).

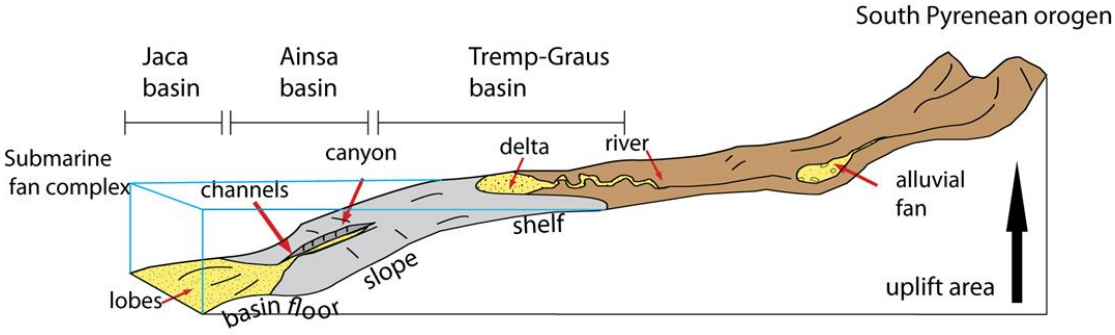

Figure 1.7 Generalised sediment-routing system for the Pyrenees during the Eocene. Modified from Graham *et al.* (2011) and Covault (2011).

1.2.4.6 Influence of tectonics on sedimentation patterns

The Arro Thrust System predates the growth of the Sobrarbe Fold System (Figure 1.8). This thrust system was active during the Cuisian and is synchronous with the motion of the Montsec-Peña Montañesa Thrust (Mutti *et al.*, 1988; Fernández *et al.*, 2012). The Sobrarbe Fold System developed from the Lutetian to the Bartonian. The Mediano Anticline started growing during the deposition of the Ainsa System (Poblet *et al.*, 1998; Fernández *et al.*, 2004). The general decrease in stratigraphic thickness of the Morillo System towards the southeast and the Guaso System towards the east gives evidence of the Mediano Anticline fold growth propagating from south to north (Fernández *et al.*, 2012). The increase of thickness between the Ainsa and Morillo systems in the San Vicente Syncline suggests that the Añisclo Anticline, associated

with the development of this synclinal structure, started growing during this time (Fernández *et al.*, 2004, Fernández *et al.*, 2012) (Figure 1.8). The growth of the Boltaña Anticline started at a later stage, during the Morillo and Guaso systems (Fernández et al, 2012). The growth of these anticlines, together with the presence of a carbonate platform in the southwest part of the basin, forced the sediments to enter from the southeast and to prograde towards the north-northwest within the Buil Syncline in a relatively confined environment (Puigdefábregas *et al.*, 1991; Muñoz *et al.*, 1994; Dreyer *et al.*, 1999). The Sobrarbe Fold System ceased to grow by the end of the Eocene (Bartonian to Priabonian) (Poblet *et al.*, 1998; Fernández *et al.*, 2012).

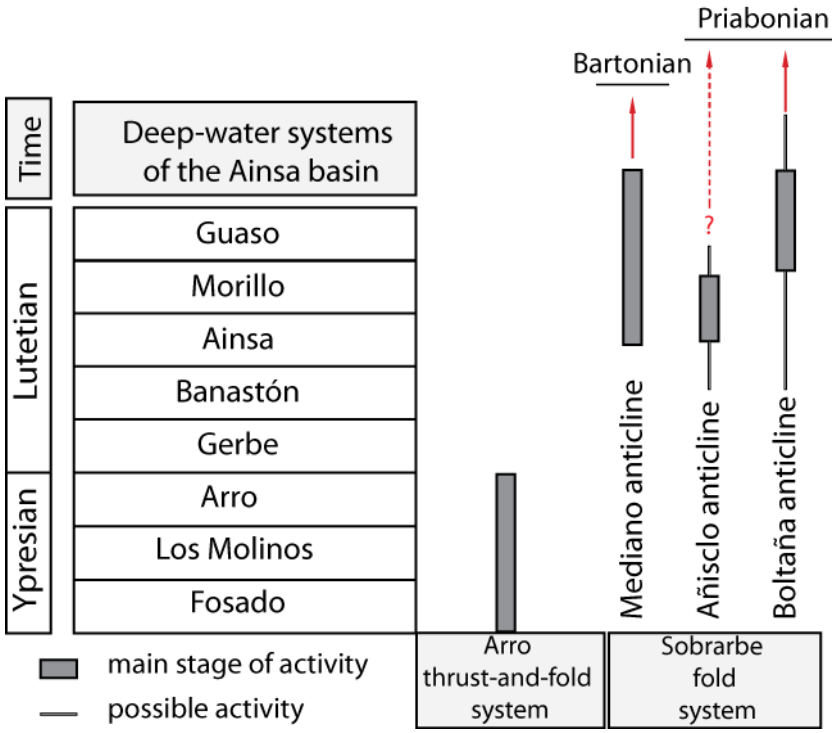

Figure 1.8 Timing of the structures in the Ainsa Basin in relation to the deposition of the mid-Eocene deep-marine fan systems. Modified after Fernandez *et al.* (2012).

These folds originated with a WNW-ESE orientation and then were progressively rotated to their present north-south orientation during growth, mainly during the Lutetian. This rotation was associated with the clockwise vertical axis rotation of the Gavarnie-Sierras Exteriores Thrust. Fernández *et al.* (2012) suggested

that the development of this rotation can be linked to the difference in shortening along strike in the Pyrenean orogen, which accounts for more than 80 km difference from the Central to the Western Pyrenees.

1.2.4.7 Age dating of the Ainsa Basin sediments

The determination of age dating for the Ainsa Basin fill succession has been undertaken by several studies. Foraminifera zonation studies by Pickering and Corregidor (2005) established the deposition of the Ainsa submarine fans within planktonic foraminifera zones P11-P12, an age slightly younger than the estimations of the Remacha *et al.* (2003) study which assigned the Ainsa System within zones P12-P13. The Sobrarbe Delta has been dated by magnetostratigraphy by Bentham and Burbank (1996) between 43.3 and 42.9 Ma, establishing the top of the deep-marine Hecho Group at 43.3 Ma. The overlying fluvial sediments of the Escanilla Formation have been dated as Bartonian in age (Dreyer *et al.*, 1999; Labourdette *et al.*, 2008). This age dating of the deep-marine sediments of the Ainsa Basin overlaps, but, is also slightly older than estimated dates for the more distal lobe deposits of the Hecho Group in the Jaca Basin using magnetostratigraphy by Oms *et al.* (2003).

Scotchman *et al.* (2014) developed a new age model for the Ainsa Basin based on larger benthic foraminifera and calcareous nannofossil age determination ranging from the Gerbe System to the top of the Sobrarbe deltaic complex (Figure 1.9). The Lower Hecho Group (Fosado, Los Molinos and Arro systems were not included in the study due to their structural complexity). The study by Scotchman *et al.* (2014) shows that the Upper Hecho Group accumulated over a period of 6.4 Myr, between 48.9 and 42.5 Ma.

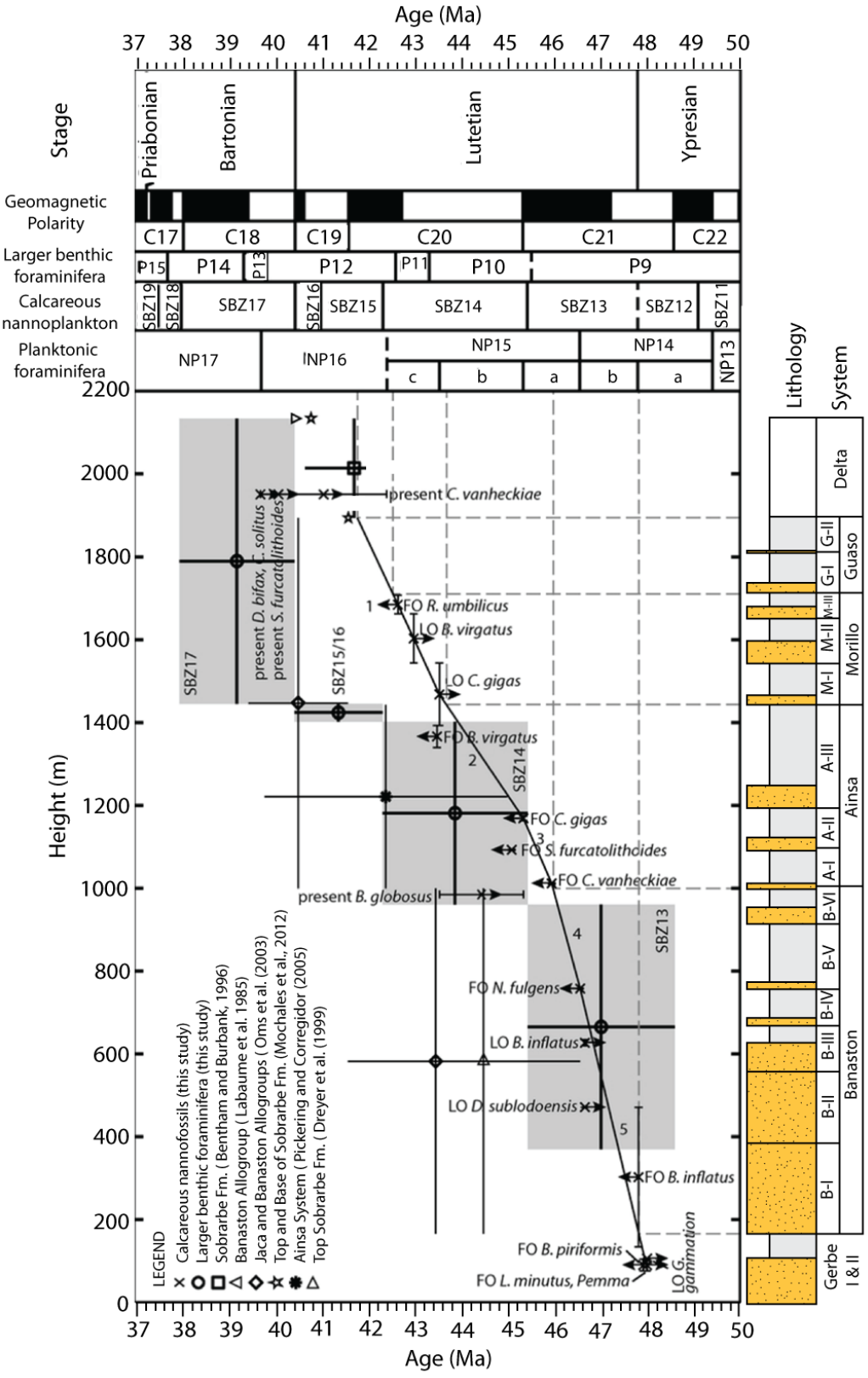

Figure 1.9 Age model of the Ainsa Basin. This age model, produced by Scotchman *et al.* (2014) is based on larger benthic foraminifera and calcareous nannofossils. This model is compared with other published age models. Modified after Scotchman *et al.* (2014).

1.2.4.8 Sediment accumulation rates (SARs) of the Ainsa Basin

SARs for the South Pyrenean Foreland Basin have been determined by Bentham and Burbank (1996) using magnetostratigraphy and structural data. The average rates of compacted deposition in the Ainsa Basin were calculated at ~ 15 cm/kyr prior to the main deformation area (middle Lutetian, ~ 44.5 Ma). These SARs increased to ~ 40 cm/kyr during the main deformation phase in the Pyrenees (middle Lutetian, ~ 44.5-43 Ma). The increase in sediment accumulation rate (SAR) was attributed to variations in basin subsidence caused by thrust advancement along the lateral ramp zone of the SCPU. Despite this rapid subsidence, these authors argue that the sediment supply was able to keep pace with subsidence and deltaic deposition was limited only along the axis of the basin. As uplift of the Mediano Anticline decreased towards the latest phases of basin infill, deltas and rivers of the Sobrarbe and Escanilla formations progradated and entered the basin across the structurally lower frontal ramp area to the south and spreaded across the entire region in a north/northwestern direction (Bentham and Burbank, 1996; Dreyer *et al.*, 1999). The SAR for this deltaic system has been calculated by Dreyer *et al.* (1999) at ~ 32 cm/kyr.

The recognition of short eccentricity and obliquity cycles in the fine-grained sediments of the Ainsa System, after applying spectral analysis on bioturbation intensity, has permitted the calculation of SARs based on the known periodicities of these Milankovitch parameters (Heard *et al.*, 2008). A SAR of ~ 30 cm/kyr has been estimated by Heard *et al.* (2008) for these fine-grained interfan successions. This result is consistent with an independent age model by Pickering and Corregidor (2005) who estimated 4 km of stratigraphy in ~ 10 Myr, giving a mean SAR of ~ 40 cm/kyr, not corrected for compaction.

Scotchman (2012) used the age model from Figure 1.9 to calculate SARs for different time intervals during the deposition of the Upper Hecho Group (Table 1.1). This table shows that SARs have greatly varied during the deposition of the Upper Hecho Group, spanning from 9 to 139 cm/kyr. Faster SARs appear to have occurred during the lower part of the Upper Hecho Group during the deposition of the Gerbe and Banastón systems, whilst SARs decreased during the Morillo and overlying systems. The average SAR for the entire Upper Hecho Group (~ 43 cm/kyr) is in agreement with the estimations of Pickering and Corregidor (2005). Heard *et al.* (2008) have argued that coarse-grained sandy packages and mass transport deposits (MTDs) are expected to have been deposited at much greater rates than the fine-grained interfan sediments and this can explain the large variations in the SARs estimated by Scotchman et al. (2012).

Table 1.1. SARs of the Upper Hecho Group.

System	Scotchman (2012)	Other studies
Sobrarbe Delta	33.4 ± 12.7 cm/kyr	32 cm/kyr (Dreyer *et al.*, 1999)
Guaso	33.4 ± 12.7 cm/kyr	
Morillo	9.5 ± 4.5 cm/kyr	
Ainsa	Ainsa III 47.4 ± 17.9 cm/kyr Ainsa I-II 35.2 ± 0.56 cm/kyr	Ainsa III 30 cm/kyr (Heard *et al.*, 2008)
Banastón	Banastón V-VI 35.2 ± 0.56 cm/kyr Banastón IV 139.5 ± 16.5 cm/kyr Banastón I-III 43.2 ± 10.5 cm/kyr	
Average Upper Hecho Group	43.2±10.5 cm/kyr	40 cm/kyr (Pickering and Bayliss, 2009)

The table shows SARs based on biostratigraphic studies by Scotchman (2012), time-series analysis data and stratigraphic correlation studies (Dreyer *et al.*, 1999; Heard *et al.*, 2008; Pickering and Bayliss, 2009). Modified after Scotchman (2012).

1.2.4.9 Water depths

Micropalaentological and palynological analysis in the Ainsa Basin (Pickering and Corregidor, 2005) indicates that the majority of the recognised foraminifera species are

typical of mid-bathyal water depths (~ 500 m) with some lower bathyal species (500-1,000 m) present such as *Nuttalides* which are known to have expanded their bathymetric range from abyssal depths to mid bathyal depths during the Eocene (Tjalsma and Lohmann, 1983). Analysis of benthic and planktonic foraminifera from the youngest submarine fan system, the Guaso System, shows that the majority of the species are typical of upper to mid bathyal water depths (e.g., *Anomalinoides* and *Nutallides*) with some (i.e., *Globobulimina, spp*) characteristic of off-shelf/upper bathyal zone. These analyses indicate that the entire stratigraphy of the Ainsa Basin had fully marine conditions prevailed with upper bathyal water depths (Pickering and Corregidor, 2005). Using these foraminifera studies in conjunction with realistic estimations of basin slope gradients, the bathyal depths during the deposition of the deep-marine Eocene clastic systems of the Ainsa Basin is estimated to be between 400 and 600 m (Pickering and Corregidor, 2005). The position of the slope right above the lateral ramp of the Cotiella-Montsec ramp may have caused, however, changes in water depth during pulsating tectonic activity (Dreyers *et al.*, 1999).

Epifaunal morphotypes are the predominant foraminifera, suggesting either anaerobic interstitial waters and/or low oxygen availability (Pickering and Corregidor, 2005). These authors also suggest that the laminated nature of the fine-grained sediments in the basin favours low-oxygen levels. However, studies on bioturbation (Heard *et al.*, 2008) indicate that the high degree of bioturbation in the fine-grained sediments is indicative of highly oxygenated waters with good food content. Heard *et al.* (2008) have suggested that orbitally-induced changes in basin oxygen levels may have caused stratification of the basin waters at Milankovitch scales.

1.2.4.10 Palaeocurrents within the Ainsa Basin

Palaeocurrents show a generally consistent palaeoflow throughout the stratigraphy towards approximately 320° (Mutti *et al.*, 1985, Millington and Clark, 1995, Pickering and Corregidor, 2005; Pickering and Bayliss, 2009). Although Pickering and Bayliss (2009) recognised that in the southeastern lower-slope erosional channels, palaeoflow has a more westerly direction towards 290°. Palaeocurrents directions show that sand supply for all the systems was essentially point sourced *via* lateral supply in submarine canyons and erosional slope channels to the east, across the growing Mediano Anticline. Upon meeting the basin floor, the flows turned axially towards the NNW (Pickering and Bayliss, 2009). The abandonment of the channelised parts of the submarine fans resulted in the switch-off of coarse clastic delivery to the basin and the accumulation of thick intervals of fine-grained laminated siltstones and marlstones which constitute both interfan and fan lateral-margin deposits (Pickering and Corregidor, 2005; Pickering and Bayliss, 2009).

1.2.4.11 Growth stages in submarine fan formation

The initiation and sedimentary evolution of a typical sandy submarine fan has been described by Pickering and Corregidor (2005) based on the architectural elements present in the submarine fans of the Ainsa Basin. These authors have recognised 4 major stages of fan growth (Figure 1.10).

Stage I

The initiation of a typical submarine fan succession commences with a large-scale collapse of the submarine fine-grained slope forming intraformational sediment slides, slumps and small debris flows which result in the deposition of Type Ia Mass

transport complexes (MTCs) at the base of the slope and on the basin floor, typically metre to tens of metres thick. These Type Ia MTCs are mainly composed of fine-grained marls and very thin-bedded sandy turbidites with layers of redeposited nummulites and other shallow-marine material such as corals and echinoids in a marl matrix. These deposits lack any extrabasinal material such as fluvial pebbles or sand.

Stage II

The deposition of Type Ia MTCs are followed by the deposition of Type II MTCs which result from the collapse of the upper slope and outer shelf to lateral zone. Extrabasinal material such as shelfal and coastal sands, rounded pebbles and shallow-marine shells and nummulites are redeposited as sediment slides, debris flows and complex granular flows, gravel lags, pebbly sandstones and pebbly mudstones. These deposits typically range from a few metres to tens of metres and show a wide range of internal complexity. Bases are typically erosive with scours of up to tens of metres causing large-scale truncation surfaces at the base of the fan. Tops are irregular, creating seafloor topography of at least several metres which are typically infilled by less-confined, sheet-like, clean and well-sorted sands with shallow-marine faunas from a littoral environment, followed by coarse fluvial sediments directly fed from deltas and river mouths as hyperpycnal flows.

Stage III

This stage represents the deposition of the main sand-rich fan, typically up to tens of metres thick, comprising of coarse-grained, thick-bedded sandy turbidites and other sediment gravity-flow deposits. Submarine fans show the development of several cycles of low sinuosity erosional channels, sediment bypass and channel infill. The

abundance of woody material and land-derived palynomorphs in the channel infill indicates a dominant fluvio-delatic source rather than shallow-marine.

Stage IV

This stage represents a decrease in sediment supply to the fan and comprises tens of metres of medium to very thin-bedded, coarse to fine-grained tabular sandstones. Towards the top, this succession is capped by a few-metres thick, thinning and fining upwards trends representing fan abandonment.

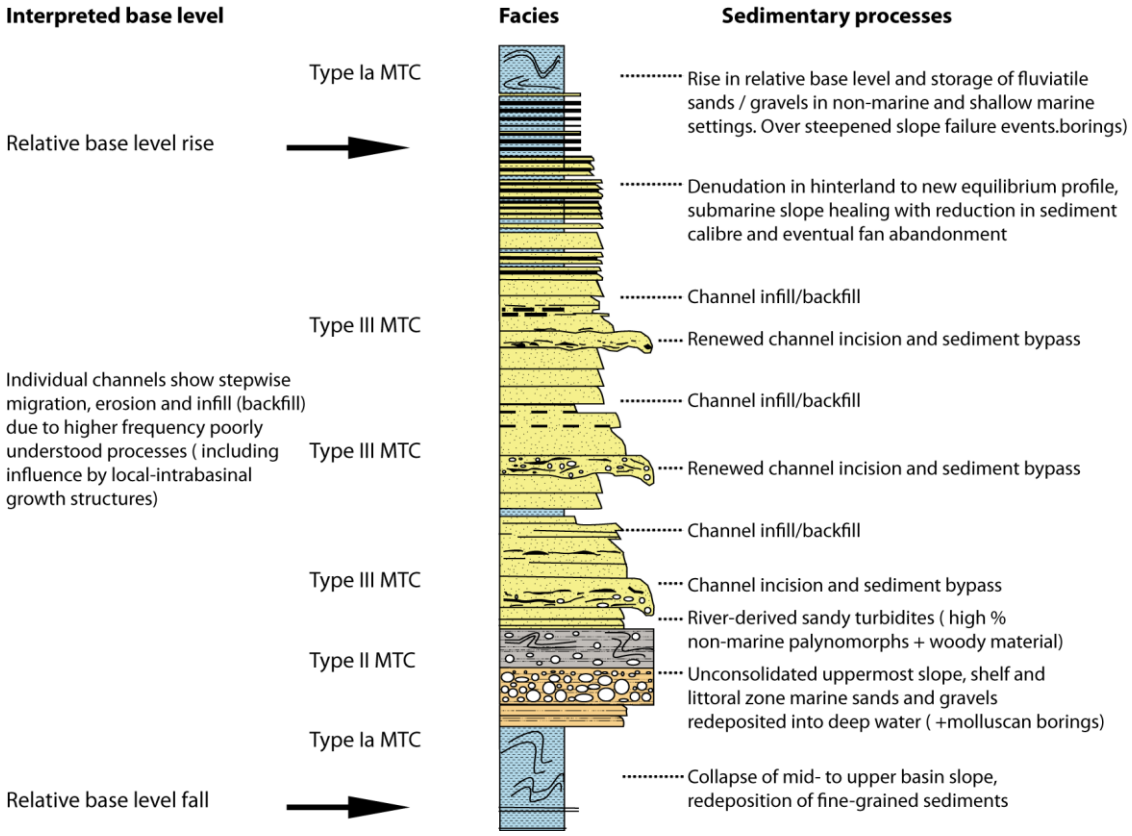

Figure 1.10 Idealised vertical complete succession of a submarine fan in the Ainsa Basin. There is a general fining-upwards profile. Typical fan thickness is ~ 10-70 m. Non-deposition, erosional processes and the location of the submarine fan within the basin (e.g., lateral, axial) can result in incomplete successions where bases and tops may be absent. Modified after Pickering and Corregidor (2005) and Pickering and Bayliss (2009).

1.3 Milankovitch cyclicity

1.3.1 Milankovitch theory

The Milankovitch theory or the astronomical theory of palaeoclimates tries to explain the recurrence of Ice Ages throughout the Earth's history from an astronomical perspective (Berger, 1978a, 1978b). These Ice Ages are short-lasting cold periods that can be reconstructed by analysis of proxy data taken from deep-sea cores, ice cores and land records (Berger and Loutre, 2007). Some well-known Ice Ages are the Pre-Cambrian Ice Ages, the Late Ordovician Ice Age, the Permo-Carboniferous Ice Age and the Quaternary Ice Age (Berger and Loutre, 2007). The study of records for the past million years show that glaciation and deglaciation intervals have occurred with a dominant quasi-periodicity of 100 kyr with overimposed cycles of 41 and 21 kyr (Berger and Loutre, 2007). The Milankovitch theory claims that these periodicities can be related to astronomical changes in the configuration of the Earth's orbit around the Sun and the Earth's rotational axis. The result of these orbital variations affects the amount and distribution of radiation that the Earth receives from the Sun (insolation). The Milankovitch theory states that there is a linear relationship between insolation and total ice volume and therefore the cyclical changes in astronomical parameters can be linked to the occurrence of glacial and interglacial cycles (Hays *et al.*, 1976; Imbrie *et al.*, 1984; Imbrie *et al.*, 1992).

The Milankovitch theory is based on previous work done by J.A. Adhemar and James Croll (Imbrie and Imbrie, 1979). In 1842, Adhemar explained the origin of glaciations using precession cycles. In 1864, Croll explained the Ice Ages using a combination of both the eccentricity cycle and the precession cycle. In 1875, Croll included the obliquity cycle (Imbrie and Imbrie, 1979). In 1941, Milutin Milankovitch,

using Croll's work, developed a mathematical model which calculated latitudinal differences in insolation and the corresponding surface temperature for the last 600,000 years (Berger and Loutre, 2007). Milankovitch recognised that the climatic fluctuations of the Late Quaternary characterised by an alternation between glacials and interglacials occurred through changes of insolation at high latitudes during the northern hemisphere summer. This theory, known as the Milankovitch theory, was however, widely disputed since it showed that the Quaternary Era had many more glacials than what it was recognised at the time. This was partially due to the use of incomplete and fragmented sedimentary records and to the use of inaccurate time-scales (Berger and Loutre, 2007). The interest in the Milankovitch theory revived after the work of Hays *et al.* (1976) and Berger (1978a, 1978b). Hays *et al.* (1976) used spectral analysis of deep-marine cores and found that cyclic successions with periodicities of 100, 41, 23 and 19 kyr were present in these successions. Berger (1978a) independently found these same periods associated with the variations of eccentricity, obliquity and precession using a new model of orbital forcing.

Since then, there has been a large volume of publications from Quaternary and older records identifying similar periodicities in cyclic successions all over the world and in all type of sediments and environments of deposition (e.g., aeolian, fluvial, shallow-marine and deep-marine) (e.g., reviews by De Boer and Smith, 1994). The orbital periodicities found in these cyclic sedimentary successions have been linked to climatic variations associated with changes in ice volume, precipitation and riverine run-off, ocean productivity, ocean circulation and sea-level temperatures (see sections 1.3.3-1.3.5). However, the mechanisms of how insolation variations can control the climate and the feedback mechanisms within the climate system are still not clearly understood (e.g., Raymo, 1997; Wolff *et al.*, 2009).

1.3.2 Orbital cycles

The three orbital cycles which are known to cause climate changes in the order of tens of thousands of years are precession, obliquity and eccentricity (Figure 1.11). These cycles occur associated with changes in the gravitational interaction between the Earth and other stellar bodies such as the Sun, the Moon, Venus and Jupiter. Changes in the configuration of the Earth's orbit around the Sun and the Earth's rotational axis affect the amount and distribution of insolation that the Earth receives from the Sun.

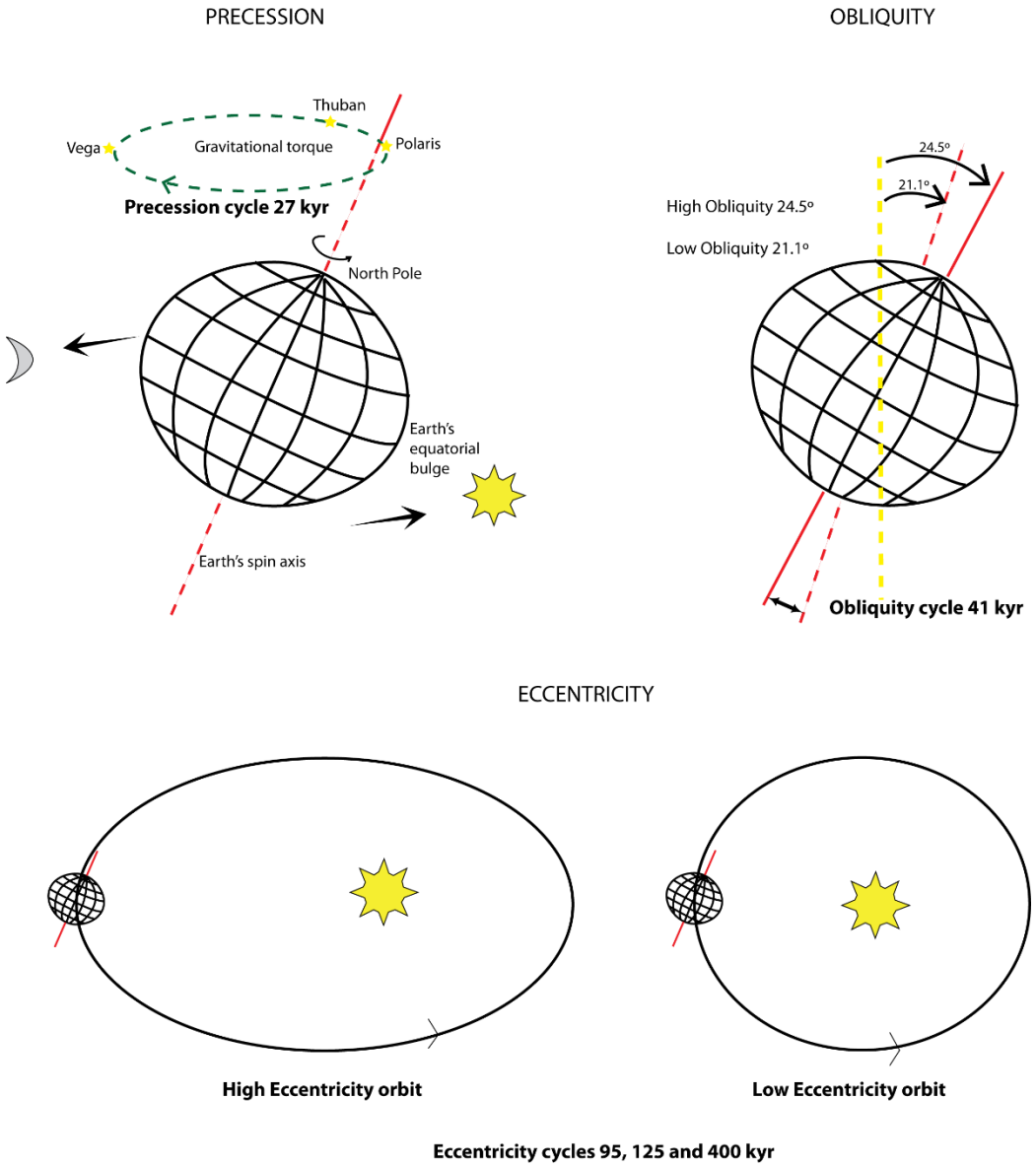

Figure 1.11 Main orbital parameters: eccentricity, obliquity and precession. Objects are not to scale. Orbits are exaggerated. Modified from Weedon (2005).

The total amount of insolation received by the Earth depends only on eccentricity whilst obliquity and precession determine the latitudinal distribution (Berger, 1978a, 1978b).

1.3.3 Eccentricity

Eccentricity is a term used to describe the shape of the Earth's orbit around the Sun. The Earth's orbit changes slowly with time from an almost exact circle (eccentricity = 0.0005) to a slightly elongated shape (eccentricity = 0.0607) (Figure 1.11). The gravitational pull of two planets, Jupiter (due to its big size) and Venus (due to the proximity to the Earth) are responsible for causing the eccentricity of the Earth's orbit to change. The torque that these planets cause in the Earth-Sun system changes in a cyclical manner. There are three main frequencies 0.0105, 0.0080 and 0.0025 cycles/kyr which correspond to periods of 95, 125 and 400 kyr, respectively. Of these periods, the ~ 100 kyr eccentricity cycle is more commonly found in palaeoclimatic records. Milankovitch argued that ice sheets were most likely to melt when summer occurs at perihelion (closest distance from the Sun) whilst ice will build-up when northern winter occurs in perihelion in the northern hemisphere. Many authors have found support for this theory and have associated the 100 kyr cycle to glaciation/deglaciation and contraction and expansion of climatic belts (Hays *et al.*, 1976; Berger *et al.*, 1990a, 1990b; Pillans *et al.*, 1998; Abreu and Anderson, 1998; Berger *et al.*, 2005; Lisiecki, 2010). However, the amount of insolation variance caused by changes in the eccentricity of the Earth's orbit seems to be too small (less than 1%) to cause any major climatic disturbances (e.g., Imbrie *et al.*, 1993) and this has caused and still is causing at present a lot of divided opinions about the origin of

the 100 kyr observed in the sedimentary and ice record, to the point that is now known as the '100 kyr problem' (see Section 1.3.6).

Despite this, eccentricity can have a significant impact in the length of the seasons. Increasing the eccentricity lengthens the time spent near aphelion (furthest distance from the Sun) and shortens the time near perihelion. At the current orbital eccentricity (0.016722), the increase in solar irradiation at perihelion (351 W/m^2) compared to the insolation at aphelion (329 W/m^2) is ~ 6.8%, although the current difference between perihelion and aphelion is only 3.4% (5.1 million km). Periods of higher eccentricity increase the difference between the distance of the periphelion and aphelion and the change in the amount of received solar radiation can be as high as ~ 23% causing a large seasonal variability.

1.3.4 Obliquity

Obliquity is the variation of the tilt of the Earth's axis away from the orbital plane. The tilt varies between 22.1^o and 24.5^o with the average being 23.5^o (Figure 1.11). The obliquity is not a purely periodic function. Dominant cycles have a periodicity of ~ 41 kyr but there is an additional lesser cycle at ~ 53 kyr (Berger, 1977; Berger *et al*., 1992; Levrard and Laskar, 2000; Berger *et al.*, 2006). Changes in obliquity cause variations in the degree of seasonality equally in both hemispheres. As this tilt increases, the seasons become more exaggerated with warmer summers and colder winters. A reduction in the tilt decreases the seasonal contrast with less severe seasons, the summer hemisphere insolation decreases and the winter hemisphere insolation increases resulting in cooler summers and milder winters (Mantsis *et al.*, 2010). During times of low obliquity (less tilt), more radiation reaches the meridional

latitudes and less reaches the poles (Phillips and Held, 1994) without causing a change in the global mean insolation (Lee and Poulsen, 2005). Mantsis *et al.* (2010) show that a reduction in obliquity of 2° increases the insolation at the Equator by ~ 1%, whilst the insolation is reduced at the poles by ~ 9%. As a result, the insolation gradient between the Equator and the poles increases, and this have significant effects on climate. An increase in insolation contrast between meridional and high latitudes driving the atmospheric general circulation and strengthening the heat and moisture transport polewards (Vimeux *et al.*, 1999; Trenberth and Caron, 2001; Mantsis *et al.*, 2010) is important for ice sheet growth (Vimeux *et al.*, 1999, Raymo and Nisancioglu, 2003). Some authors have recognised different climatic effects associated with periods of low obliquity. Lawrence *et al.* (2010) have shown that North Atlantic sea surface temperatures decreased 2°-4°C during low obliquity periods. Lower surface conditions in the North Atlantic favoured North Atlantic deepwater formation based on Mg/Ca ratios from ostracods (Dwyer *et al.*, 1995) and benthic foraminifera (Sosdian and Rosenthal, 2009). Low obliquity has also been associated with an increase in global ice volume as suggested by benthic $\delta^{18}O$ records (Raymo and Nisancioglu, 2003) and by records of ostracods Mg/Ca indicating lowering of sea levels (Dwyer *et al.*, 1995).

Obliquity is the dominant astronomical factor that affects the annual amount of insolation received in the Earth at high latitudes (Berger, 1978a). An increase of 1^{o} in obliquity causes an increase of insolation of ~ 1% in the northern hemisphere (Berger, 2001). The cool summers are thought to allow for the yearly build-up of snow and ice at high latitudes, possibly leading to the development of an ice sheet. Obliquity change also causes equatorward motion of the tropical circles and the poleward motion of the polar circles (Berger, 2001).

1.3.5 Precession

Precession involves two factors: a wobble of the Earth's rotational axis and the orientation of the long axis of the Earth's orbit. The Earth wobbles under the torque that the Moon and the Sun exert on its equatorial bulge. The Earth is an ellipsoid with the radius at the equator 0.34% larger than the radius at the poles. Because of this ellipticity the Moon and the Sun cause a gravitational pull which makes the Earth spin as a gyroscope. The Earth's axis precesses with a period of 27 kyr in a clockwise direction as viewed looking down from the North Pole resulting in a shift in the celestial poles. Currently the Earth's axis points towards the Polaris in the constellation Ursa Minor, but, 5,000 years ago the North Star was Thuban in the constellation Draco and half a precession period ago the axis was pointing at Vega (Figure 1.11). The precession of the Earth's rotational axis causes the dates of the equinoxes to rotate around the Sun changing the Earth-Sun distance for a particular date. Simultaneous to the change in the orientation of the Earth's axis, the long axis of the Earth's orbit rotates anticlockwise relative to the stars, with a periodicity of 105 kyr and controls the time of year when the Earth is at perihelion. The combined effect of these two orbital factors results in two main precessional periodicities, 19 and 23 kyr. The 19 kyr cycle results from combining the eccentricity of the orbit and the precession of the axis of rotation. The 23 kyr cycle is the result of coupling the precession of the axis of rotation and the precessional changes in the Earth's orbit. The combined effect of these two periodicities causes for each hemisphere that after summer occurs in perihelion, summer will be during aphelion at a period of ~21 kyr (Figure 1.12).

The total insolation during a year is not affected by the precession of the Earth (Berger and Loutre, 1994; Muller and MacDonald, 2000). The main reason for this is that the Earth moves faster in its orbit when is closer to the sun. If summer occurs in

the northern hemisphere during perihelion, the increase in insolation during a short amount of summer days will be balanced by a decrease in insolation during a larger number of winter days. This net amount of insolation received in the northern hemisphere is not affected greatly if the summer occurs instead in aphelion where medium length summers are balanced with medium length winters. The seasonal change however, is greater affected and can be more abrupt or milder depending on where in the orbit the summer occurs.

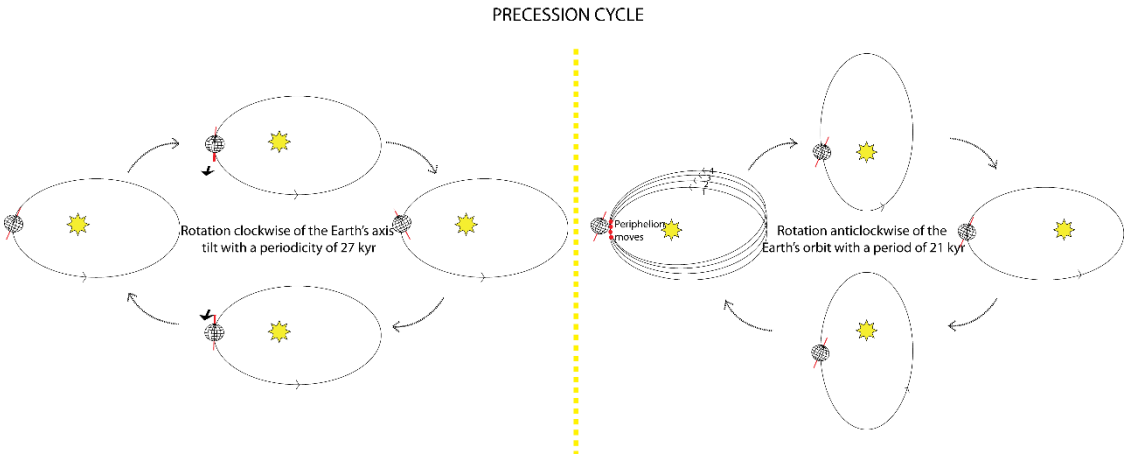

Figure 1.12 The precession cycle. The figure shows the rotation clockwise of the Earth's axis tilt with a periodicity of 27 kyr and the rotation of the long axis of the Earth's orbit with a periodicity of ~ 21 kyr. Modified after Weedon (2005).

The effect of precession on the intensity and length of seasons is influenced by the change in the Earth-to-Sun distance and in the change of speed of the Earth along its orbit (Weedon, 2005). The amplitude of the precession is therefore modulated by eccentricity and the combination of these two parameters is known as the precession parameter.

Time-series analysis of sedimentary successions often shows a stronger signal for eccentricity than for precession. Differences in the amplitude of these two parameters do not reflect a stronger influence of eccentricity on climate but can be

explained by the lower degree of variation of the eccentricity cycles compared with precessional cycles which may vary by a factor of two (de Boer and Smith, 1994).

Insolation is dominated by precessional cycles in equatorial latitudes (Berger, 1978b) and precession has been shown to have an effect on monsoon intensity (Tiedemann and Franz, 1997; Wang et al, 2001; Braconnot and Marti, 2003; Cruz *et al.*, 2005, Thompson *et al.*, 2005; Braconnot *et al.*, 2008). Other studies have also shown that precession cycles may have an important control on precipitation and river run-off (e.g., Kutzbach, 1981; Olsen, 1994; Mallison *et al.*, 2003; Tachikawa *et al.*, 2011).

1.3.6 The 100 kyr problem

The 100 kyr glacial-interglacial climatic cycles observed in the last ~1 Ma have often been directly associated with the 100 kyr eccentricity cycle (e.g., Clemens and Tiedemann, 1997; Lisiecki, 2010: Ganopolski and Calov, 2011). However, the small net insolation change caused by the 100 kyr eccentricity cycle (e.g., Imbrie *et al.*, 1993) has created a lot of opposition from palaeoclimatologists to directly associate the 100 kyr glacial-interglacial climatic cycles to eccentricity. Other problems include, the absence of the 400 kyr eccentricity frequency in the reconstructions of ice volume using benthic foraminifera oxygen isotopes (Muller and McDonald, 1997) and the mismatch between the amplitude of sea-level changes and the amplitude of insolation variations caused by eccentricity (Parrenin and Paillard, 2003). In fact, for the last ~ 800 kyr, the timing between glaciations is only quasiperiodic and vary between 87 and 119 kyr, and the dominant 100 kyr peak observed in the spectral results has been considered as an artifact of the spectral analysis (Maslin and Ridgwell, 2005). This has

been named as the ‘100 kyr eccentricity myth’ (Maslin and Ridgwell, 2005). Several researchers have tried to develop a number of conceptual models based on different assumptions to explain the origin of these glacial-interglacial 100 kyr cycles. Many of these conceptual models relate glacial variability to changes of the Earth’s other orbital parameters; obliquity and precession, which both have a more significant influence in insolation variability at the Earth’s surface than the eccentricity parameter. However, as various authors have discussed, orbital forcing on its own is insufficient to directly drive the glacial-interglacial cycles, but, can contribute to amplify and transform changes in insolation through various complex internal feedback mechanisms of the Earth’s climate-cryosphere system (Saltzman and Maasch, 1988; Gildor and Tziperman, 2001; Ashkenazy and Tziperman, 2004; Paillard and Parrenin, 2004; Maslin and Ridgwell, 2005).

Some researchers have argued that the glacial-interglacial cycles are paced by obliquity and occur each second or third cycle, triggered at times of increased orbital obliquity (Huybers and Wunsch, 2005; Huybers, 2007; Liu *et al.*, 2008). Obliquity causes an insolation gradient between the polar and tropical regions which has a major influence in the general circulation of the oceans and also of the atmosphere and is a link to ice sheet development (Raymo and Nisancioglu, 2003; Berger et al., 2006). Other authors have concluded that the key to explain the glacial and interglacial cycles lies in the seasonal redistribution of insolation associated with precession (e.g., Ridwell *et al.*, 1999; Maslin and Ridwell, 2005). These authors suggest that the glacial-interglacial cycles occur each fourth or fifth precession cycle and are paced by eccentricity. The episodic occurrence of unusually low maxima in the Northern hemisphere summer insolation, pushes the glacial climate system to a critical maximum degree of glaciation, which results in catastrophic ice sheet collapse, retreat

and finally deglaciation (Raymo, 1997). There are other authors who advocate for a combination of both obliquity and precession factors (e.g., Huybers *et al.*, 2011).

1.3.7 Periodicities through geological time

Present day orbital periodicities have not remained the same through geological time. Obliquity and precession cycles are affected by mechanisms such as lunar and solar tidal motion which slows down the Earth rotation's rate (Berger *et al.*, 1990a, 1990b). Eccentricity, on the contrary, does not appear to be affected by this mechanism and therefore, the ratios between the different orbital parameters (obliquity/eccentricity and precession/eccentricity) have changed through geological time.

There are different orbital configurations and insolation computations available. Berger and Loutre (1991) used trigonometric equations to quantify insolation from the effect of planetary masses and the Earth-Moon gravitational pull. These calculations recognise the 19, 23, 41, 100 and 400 kyr periodicities observed in many palaeoclimatic records. However, these solutions are only accurate back to 1.5 Ma and are considered reliable back to 5 Ma (Cronin, 2010). Laskar *et al.* (1993) computed insolation using a numerical solution where they included certain planetary elements using integrated secular equations. A later version of this solution was Laskar *et al.* (2004) which extended the numerical solutions for the past 65 Ma using improved computer and integration methods of gravitational equations. This orbital solution has now been updated and extended to the last 250 Myr in the version La2010 although the authors warn of the precision of these curves for records older than 60 Myr (Laskar *et al*., 2011). This updated version contain 4 different solutions (La2010a, b, c and d) which are all compatible with the position and motions of the astronomical

bodies. Of all these solutions, the La2010a is the nominal solution with higher numerical accuracy and the orbital solution chosen in this study.

Although these algorithms calculate the energy received at the top of the Earth's atmosphere, they are unable to predict how the ocean and the atmosphere will respond to these changes (de Boer and Smith, 1994). In fact, sedimentation processes will depend on more variables than just insolation. Berger (2012) have summarised some of the difficulties faced by palaeoclimatologists when trying to determine Milankovitch cycles in past records including the effects that non-orbital factors such as tectonic uplift, continental drifting, changes in the configuration of ocean gateways, in the carbon dioxide content of the atmosphere, and in the availability of methane ice on the sea-floor can have to influence the Earth's climatic system and obscure the orbital signal.

1.3.8 Possible effects of Milankovitch cycles in the Ainsa Basin during the Eocene

Palaeogeographic reconstructions place the Pyrenees at ~ 35°N during the Eocene (Hay *et al.*, 1999), a latitude that is known to be sensitive to astronomically-induced climatic changes. Figure 1.13 shows the Milankovitch orbital curves for the time period between 50 and 40 Ma where the sediments of the Ainsa Basin are thought to have been deposited (Pickering and Corregidor, 2005). Annual insolation changes, obliquity and precession cycles have been calculated using Laskar *et al.* (2004) computations and eccentricity curves have used the updated La2010a computation of Laskar *et al.* (2011). The length of the orbital periods for the Eocene (~ 40 and ~ 50 Ma) are calculated using Berger *et al.* (1992) equations and can be seen in Table 1.2.

Table 1.2 Orbital periodicities for the Middle Eocene.

Orbital period	40 Ma			50 Ma		
Eccentricity	94.78	123.82	404.18	94.78	123.82	404.18
Obliquity	40.12	52.48		39.9	52.1	
Precession	18.84	22.68		18.80	22.60	

Orbital periodicities calculated using the equations from Berger *et al.* (1992) at 40 Ma and 50 Ma.

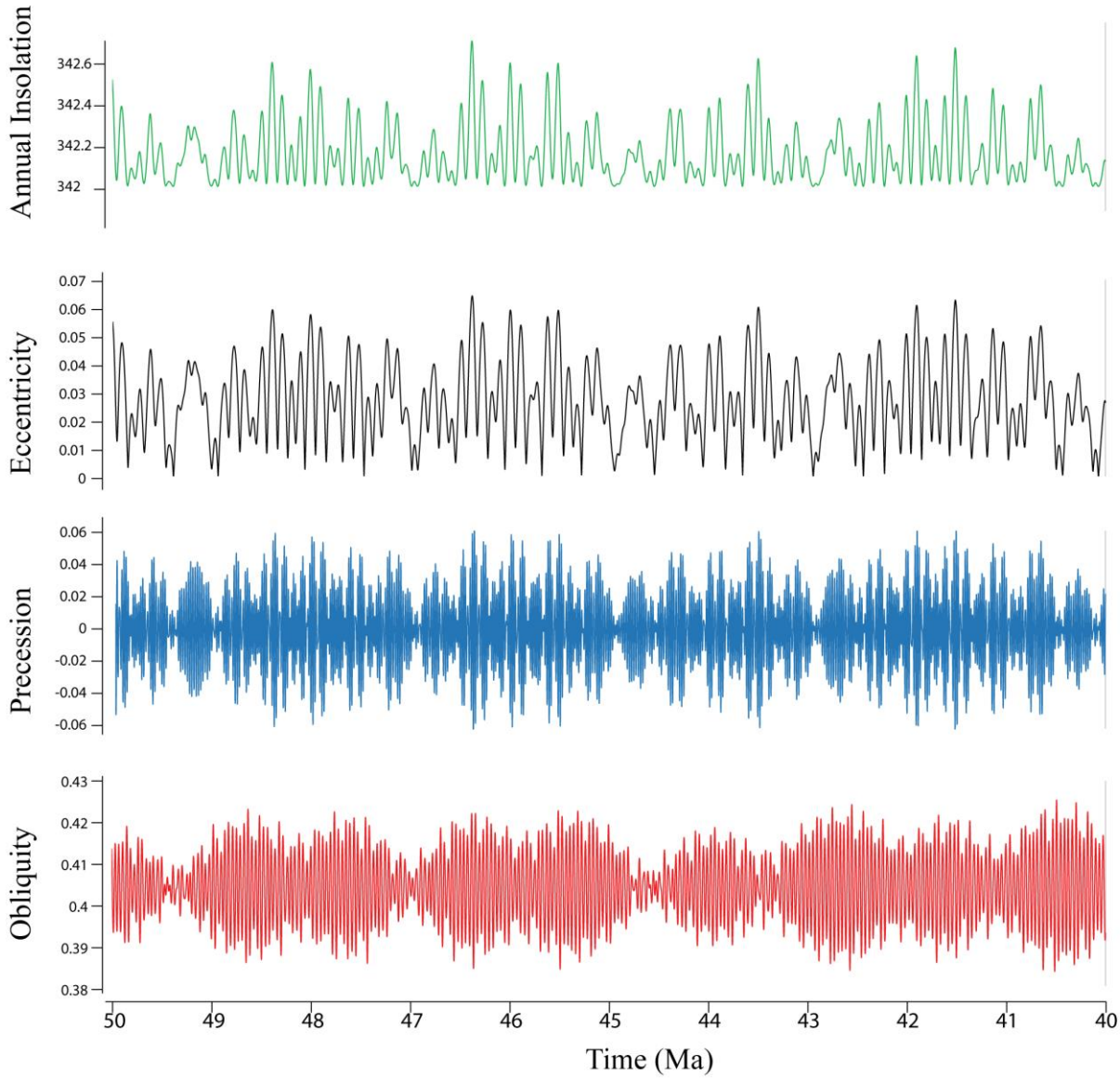

Figure 1.13 Annual insolation, eccentricity, precession and obliquity curves from 50 to 40 Ma. Computations from Laskar *et al.* (2004) with the exception of eccentricity which has used the La2010a orbital solution (Laskar *et al.*, 2011).

Sloan and Huber (2001) and Lawrence *et al.* (2003) have used realistic combinations of orbital parameters to model climate variability during the Eocene. These models compare the effect of orbital variability between two end members (MINSEAS and MAXSEAS). The orbital parameters used in the MINSEAS model damper the seasonal variation in the northern hemisphere and amplify it in the southern hemisphere whilst the MAXSEAS model, which occurs 11 kyr after MINSEAS (half a precessional cycle) amplifies the seasonal variability in the northern hemisphere and dampens it in the southern hemisphere.

These models show that greater seasonality in the northern hemisphere (MAXSEAS model) is associated with higher precipitation in all drainage basins in this hemisphere (mean annual precipitation and seasonal precipitation) (Lawrence *et al.*, 2003). The effect of changes in orbital precession has however, little effect on the mean annual temperature, but affects the seasonal mean temperature range (Lawrence *et al.*, 2003).

Sloan and Huber (2001) showed that changes in insolation over precession cycles can account for the changes in surface temperature, upwelling intensity and location and amount of continental run-off. For continental run-off, these authors calculated a 12% variance in the Pyrenees. Periods of enhanced storminess and precipitation may be linked to increase riverine run-off and higher detrital mixed and suspended river load.

1.4 Eocene climate

The deep-marine sedimentation of the Ainsa Basin covers a ~ 10 Myr period during the Middle Eocene (~ middle to late Ypresian and Lutetian, ~ 50 to 40 Ma) (Pickering and Corregidor, 2005). This time period witnessed a progressive cooling and

deterioration of global climate and marks the transition from the warm and ice-free world of the Early Eocene (~ 55 Ma) to the icehouse conditions of the Oligocene (~ 34 Ma) (e.g., Miller *et al.*, 1987; Zachos *et al.*, 2001, 2008; Coxall *et al.*, 2005; Liu *et al.*, 2009).

1.4.1 Global Eocene climate

1.4.1.1 The Early Eocene

The Early Eocene Epoch (~ 55-49 Ma) is recognised as the warmest climate of the past 65 Myr. This period was characterised by either small or absent polar ice-sheets (Miller *et al.*, 1987; Zachos *et al.*,1993, 1994; Crowley and Zachos, 2000), high latitude sea surface temperatures (up to 15°C warmer than modern) (Zachos *et al.*, 1993), diminished Equator-to-pole temperature gradients, with hotter sea surface temperatures relative to present, near the poles and least dramatic differences at the tropics (Pagani *et al.*, 2006; Zachos *et al.*, 1994; Greenwood and Wing, 1995; Bijl *et al.*, 2009), and atmospheric CO_2 in excess of 1000ppm (Yapp, 2004; Beerling and Royer, 2011). During this Early Eocene hothouse period, the climate warmed steadily until concentrations of greenhouse gases and global temperatures reached a maximum in a strong global warming event that lasted approximately 2 Myr known as the Early Eocene Climatic Optimum (EECO) (Zachos *et al.*, 2008).

The EECO was not the only strong global warming event which occurred during the Early Eocene, high-resolution studies of carbon and oxygen isotopes show that numerous short-lasting events (< 200 kyr), known as hyperthermals occurred during this time interval (e.g., Thomas *et al.*, 2001; Lourens *et al.*, 2005; Zachos *et al.*, 2006; Zachos *et al.*, 2008; Bohaty *et al.*, 2009). These hyperthermals were

characterised by large incursions of ^{13}C-depleted carbon into the ocean and atmosphere and were generally accompanied by an increase in Earth surface temperature and marked shifts in the distribution and intensity of precipitation and weathering rates (Thomas *et al.*, 2001; Zachos *et al.*, 2008). The fossil record shows that these extreme climatic warming events during the Early Eocene were also accompanied by biotic changes where species diversification, migrations, radiations and extinction rates affected both terrestrial and marine communities (Wing *et al.*, 1995; Slujis *et al.*, 2007).

The most dramatic and best-studied hyperthermal is the Paleocene-Eocene Thermal Maximum (PETM or Eocene Thermal Maximum 1 (ETM-1) which occurred at 55.5 Ma and lasted less than 170 kyr. This event signalled the onset of the Eocene hothouse and showed a global surface temperature increase of 5-9°C in less than 10,000 years (Dickens *et al.*, 1995; Thomas *et al.*, 2002; Wing *et al.*, 2005; Zachos *et al.*, 2005).

The PETM event was followed by other transient warming events identified by short increases of the deep-sea benthic foraminiferal oxygen-isotope incursions and deep-sea carbonate dissolution horizons but of a lower magnitude and duration than the PETM (Zachos *et al.*, 2008): the Eocene Thermal Maximum 2 (ETM-2) which occurred approximately at 53.7 Ma (Lourens *et al.*, 2005; Sluijs *et al.*, 2009; Stap *et al.*, 2010) and the Early Eocene Climatic Optimum (EECO) (51-53 Ma) (Lowenstein and Demicco, 2006; Zachos *et al.*, 2001). Other minor hyperthermals less known have also been recognised: H-2 at 53.6 Ma (Stap *et al.*, 2010; Abels *et al.*, 2013), I-1 at 53.3 Ma (Nicolo *et al.*, 2007, Samanta *et al.*, 2013), I-2 at 53.2 Ma (Nicolo *et al.*, 2007, Samanta *et al.*, 2013) and K, X or ETM-3 at 52.8 Ma (Röhl *et al.*, 2005; Agnini *et al.*, 2009; Galeotti *et al.*, 2010).

Numerous studies have tried to find the causal factors which led to the extremely warm climatic conditions of the Early Eocene. In 1896, Arrhenius suggested that the high levels of carbon dioxide in the atmosphere were responsible for the warm climate observed in the chemical records. Since then, many authors have tried to recognise which mechanisms are responsible for causing the build-up of high concentrations of greenhouse gases in the atmosphere during the Eocene. For many, high CO_2 concentrations were caused by an increase of volcanic emissions and hydrothermal degassing during the Palaeocene and Eocene epochs (Owen and Rea, 1985; Berner *et al.*, 1993). High CO_2 emissions have also been attributed to metamorphic CO_2 degassing from orogenic belts (Kerrick and Caldeira, 1998). Other authors have proposed that changes in the chemical weathering of silicate rocks (Walker *et al.*, 1981; Brady, 1991), and methane released from storage in wetlands (Sloan, 1992) or from large oceanic gas hydrate reservoirs (Dickens *et al.*, 1995) have resulted in the high atmospheric CO_2 levels during the Eocene.

Some authors have tried to explain the warm climate of the Eocene from the changes in continental configuration, orographic relief (e.g., uplift of the Himalayas and the Alpine region) and ocean circulation which occurred during the Eocene (e.g., Kennet, 1977; Sloan, 1994). It has also been proposed that external processes such as evolution of the Sun and solar variability and the position of the solar system relative to the galactic centre (Wigley, 1981) and changes in the orbit of the Earth (Cramer *et al.*, 2003; Galeotti *et al.*, 2010) caused the destabilisation of the Earth's radiation budget and modified the Earth's global climate.

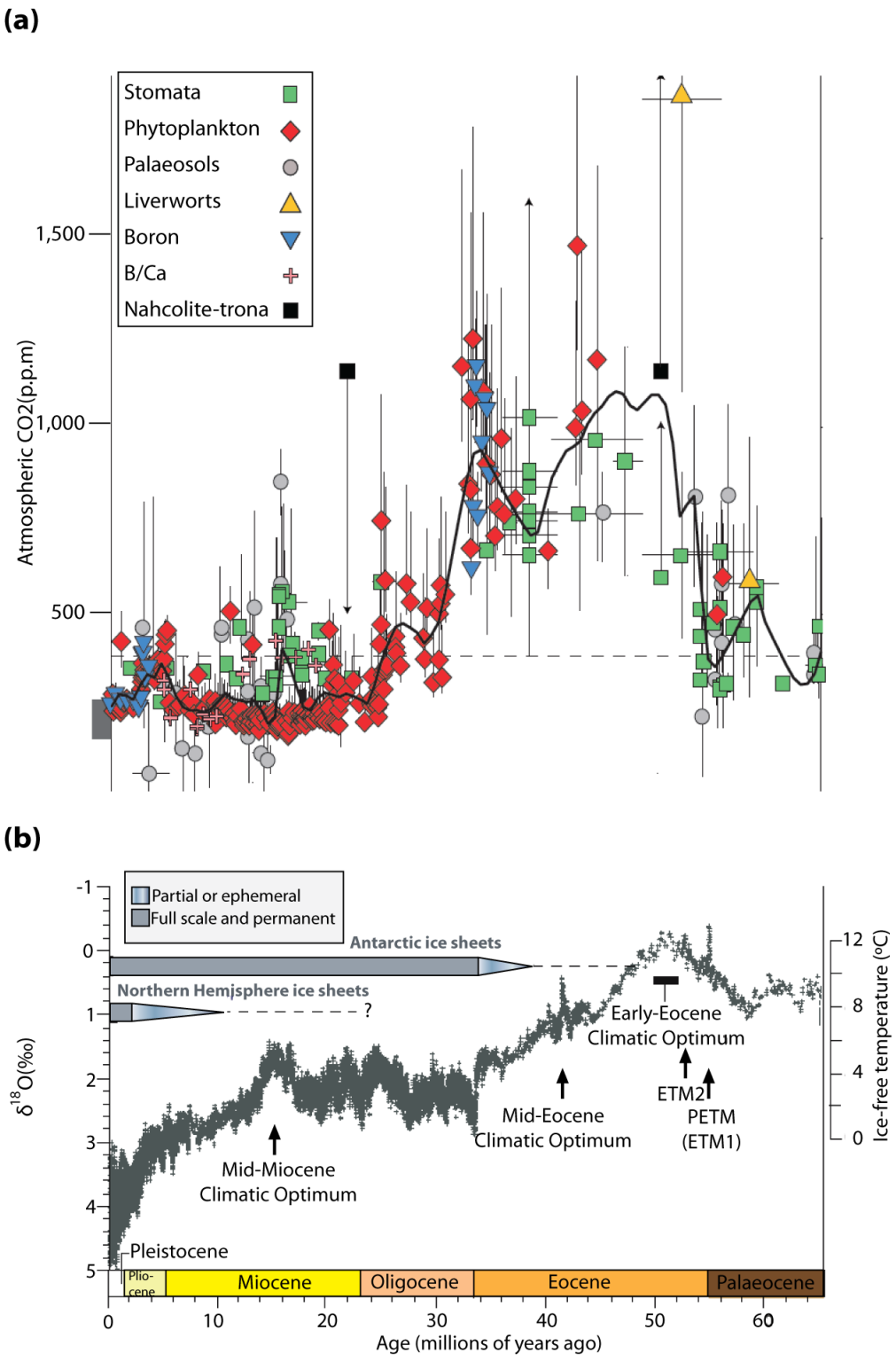

Figure 1.14 Atmospheric CO_2 concentration, deep-sea benthic foraminiferal oxygen isotope and temperature reconstruction over the past 65 Myr. (a) Earth's atmospheric CO_2 for the period 0 to 65 Ma. The dashed line represents present day atmospheric CO2 concentration (390 ppm). Figure modified after Beerling and Royer (2011). **(b)** Deep-sea benthic foraminiferal oxygen isotope curved based on records from Deep Sea Drilling Project and Ocean Drilling Program sites. The Middle Eocene to Middle Miocene period includes high-resolution records from Billups *et al.* (2002), Bohaty and Zachos (2003) and Pälike *et al.* (2006). Figure modified after Zachos *et al.* (2008).

1.4.1.2 The Middle and Late Eocene

The succession of these warm episodes of the Early Eocene was interrupted by a prolonged interval of global climatic deterioration in the Middle to Late Eocene (~ 49 to 34 Ma), which resulted in the initiation of major permanent ice-sheets in Antarctica at the Eocene-Oligocene boundary (~ 33.5 Ma) (Lear *et al.*, 2000; Zachos *et al.*, 2001; DeConto and Pollard, 2003; Coxall *et al.*, 2005). This Middle and Late Eocene global cooling trend was not linear and occurred through a series of prominent cooling steps and by several transient warming and cooling phases (Zachos *et al.*, 2008) (Figure 1.14).

The Paleogene cooling has its major expression during the Eocene-Oligocene Transition (EOT) (33.5 Ma) (Coxall and Pearson, 2007; Lear *et al.*, 2008), which includes the Early Oligocene isotopic Oi-1 event (Miller *et al.*, 1991; Zachos *et al.*, 2001).The EOT is evidenced by a large positive excursion in the mean $\delta^{18}O$ composition of benthic and planktonic foraminifera (throughout the Atlantic, Pacific, Indian and Southern Oceans (Miller *et al.*, 1987; Shackleton and Kennett, 1975; Zachos *et al.*, 2001; Coxall *et al.*, 2005; Katz *et al.*, 2008). This period also shows a deepening of the global calcite compensation depth (CCD) by 1 km (Van Andel, 1975; Coxall *et al.*, 2005; Rea and Lyle, 2005), an increase in thermohaline circulation (Kennett, 1977; Davies *et al.*, 2001), a decrease in sea surface temperatures associated with ice growth by 2.5°C-5°C (Zachos *et al.*, 2001; Lear *et al.*, 2008; Liu *et al.*, 2009; Miller *et al.*, 2009), a reorganisation of the carbon cycle (Shackleton and Kennett, 1975; Diester-Haass and Zahn, 1996; Zachos *et al.*, 2001; Coxall *et al.*, 2005; Merico *et al.*, 2008), an increase in ocean productivity (Diester-Haass and Zahn, 1996; Salamy and Zachos, 1999; Diester-Haass and Zachos, 2003) and sea-level fall (e.g., Miller *et al.*, 1991; Pekar *et al.*, 2002; Miller *et al.*, 2008). The cooling trend during this period

also affected many marine faunas with extinctions in tropical planktonic and larger foraminifera (Keller *et al.*, 1992; Pearson *et al.*, 2008; Wade and Pearson, 2008), molluscan extinctions (Hansen *et al.*, 2004) and the global diversity decline of calcareous nannoplankton (Aubry, 1992; Bown *et al.*, 2004; Dunkley Jones *et al.*, 2008). Floral changes and terrestrial fauna turnover occurred during this interval associated with the cold weather and an increase in regional arification (Francis, 1999; Hooker *et al.*, 2004; Jaramillo *et al.*, 2006; Zanazzi *et al.*, 2007).

Different mechanisms have been proposed to explain this significant climatic change which caused the transition from the greenhouse conditions of the Early Eocene to the icehouse world of the Oligocene and at present they are still being debated. Re-distribution of land-sea masses during the Cenozoic with an increase in high latitude land masses (causing ice-albedo feedbacks) and a decrease in continentality (causing changes in seasonality and summer temperatures) failed to explain the temperature ranges of this period inferred by modelling studies (Barron, 1985). The most predominant hypothesis to explain Cenozoic cooling involves the opening of the circumpolar passages. During the Late Eocene and Oligocene, South America separated from Antarctica, resulting in the formation of the Drake Passage, and Antarctica separated from Australia causing the opening of the Tasmanian Gateway. These tectonic events resulted in the formation of the Antarctic Circumpolar current which is believed to have caused the thermal isolation of the Antarctic continent and have resulted in the build-up of an ice sheet in Antarctica (Kennett, 1977; Exon *et al.*, 2004; Diekmann *et al.*, 2004; Lawver and Gahagan, 2003; Sijp and England, 2004; Scher and Martin, 2006). One of the main setbacks of this theory is the lack of precise dating of these tectonic events which complicate interpretation on the causal relationship between ocean circulation and global cooling. The age of the Drake

Passage ranges from the Middle Eocene (~ 49 Ma) (Livermore *et al.*, 2005; Livermore *et al.*, 2007) to the Early Miocene (~ 17 Ma) (Barker, 2001), whereas the Tasmanian Gateway is dated more consistently at ~ 35.5 Ma (e.g., Kennett and Exon, 2004; Stickley *et al.*, 2004). In addition to the difficulty in establishing an exact timing of these events, this theory has been challenged by some authors, who argue that the range in temperature reproduced by ocean-atmosphere modelling is very small to explain major Cenozoic cooling (Mikolajewicz *et al.*, 1993; Huber *et al.*, 2004; Zhang *et al.*, 2010).

Another mechanism proposed as the cause of Cenozoic cooling is a decrease in atmospheric CO_2 (DeConto and Pollard, 2003; Pagani *et al.*, 2005; Huber and Nof, 2006; Pearson *et al.*, 2009; Liu *et al.*, 2009; Peters *et al.*, 2010). The main support for this mechanism is shown by the parallel trend of atmospheric CO_2 records with other palaeoclimatic proxies such as long-term $\delta^{18}O$ records. Other mechanisms proposed to decrease global atmospheric CO_2 include an increase in silicate weathering (Raymo *et al.*, 1988) or an increased in organic carbon burial (Diester-Haass and Zachos, 2003; Zachos and Kump, 2005).

Some authors have proposed other mechanisms to explain Cenozoic cooling which are not related to changes in atmospheric CO_2 levels or to the opening of oceanic passages. Among these mechanisms are: a decrease in solar insolation that favoured cool summers and triggered ice build-up (Coxall *et al.*, 2005), the suppression of the Iceland mantle plume and its effect on the initiation of the North Atlantic deep-water circulation (Abelson *et al.*, 2008); terrestrial or marine volcanism (Jicha *et al.*, 2009) and even extraterrestrial impacts (Vonhof *et al.*, 2000).

1.4.1.3 Land ice development prior to the Eocene-Oligocene boundary

Although, there is compelling evidence and a general consensus that Antarctic ice sheets were stable and permanent at the Eocene-Oligocene boundary (e.g., Zachos *et al.*, 2001, 2008; Coxall *et al*., 2005), the extent and stability of land ice during the Middle and Late Eocene remains controversial. Some studies have suggested that there was little or no significant ice storage occurring prior to the earliest Oligocene (Miller *et al.*, 1991; Zachos *et al.*, 1994, 1996, 2001), although some authors do not disregard the presence of ephemeral ice sheets (De Conto and Pollard, 2003; Burgess *et al*., 2008). Other studies have used stratigraphic and geochemical proxies to suggest high-frequency sea-level variations in the order of tens of metres driven by glaciation in the Middle-Late Eocene in Antarctica (Browning *et al.*, 1996; Miller *et al.*, 2005; Pekar *et al.*, 2005; Tripati *et al.*, 2005; Edgar *et al.*, 2007; Kominz *et al.*, 2008; Payros *et al.*, 2009; Dawber *et al.*, 2011; Dawber and Tripati, 2011). There is also some evidence, mainly from ice-raft debris, to suggest that ice sheets developed at the same time in the Northern hemisphere (Moran *et al.*, 2006; Eldrett *et al.*, 2007; St John, 2008; Tripati *et al.*, 2008; Stickley *et al.*, 2009).

1.4.2 Palaeoclimatic conditions in the Pyrenees during the Eocene

Geochemical, paleontological and sedimentological data from the Palaeocene of the Central Pyrenees indicates that this period was characterised by a warm arid climate with little cover vegetation (Schmitz *et al.*, 2001; Schmitz and Pujalte, 2003, 2007; Arostegui *et al.*, 2011; Minelli *et al.*, 2013). Also, terrestrial palynoflora from Austria and the Eastern Alps suggests a warm and humid climate during the Late Thanetian and early Ypresian (Hofmann *et al.*, 2011). The carbon isotope excursion of the PETM is preserved in the continental Tremp Formation of the Tremp-Graus Basin (Schmitz

and Pujalte, 2003, 2007; Domingo *et al.*, 2009; Manners *et al.*, 2013) and fluvial deposits of the Ager Basin (Minelli *et al.*, 2013) and can be correlated to the west to the basin plain deposits in the Basque-Cantabrian Pyrenees (Schmitz and Pujalte, 2003, 2007; Minelli *et al.*, 2013). The PETM in the Pyrenees was characterised by a short-lasting abrupt increase in seasonal precipitation causing severe floods and rainstorms which resulted in an increase in land erosion and continental runoff (Schmitz *et al.*, 2001; Schmitz and Pujalte, 2003, 2007; Minelli *et al.*, 2013).

Tropical to subtropical, warm and humid conditions were maintained during the Middle Eocene in the Ebro Basin as evidenced from pollen taxa and floral diversity studies (Cavagnetto and Anadón, 1996). Similarly, clay mineral analysis from deep-marine pelagic and hemipelagic marlstones of the Lower Eocene in Zumaia, Western Pyrenees, are characterised by a widespread production of kaolinite which suggests that warm/perennially humid and seasonally wet climatic periods enhanced weathering (Winkler and Gawenda, 1999). Palynological data from Haseldonckx (1972, 1973) shows that tropical humid conditions were present during the deposition of the Lower Montanyana Group (Ypresian) in the Tremp Basin, changing towards a more seasonal subtropical climatic conditions during the Upper Montanyana Group deposition (Lutetian). These studies are consistent with most vegetation reconstructions for the Early to Middle Eocene which argue that the dominant vegetation at mid-latitudes was paratropical (e.g., Wolfe, 1985; Sewall *et al.*, 2000; Collinson and Hooker, 2003; Utescher and Mosbrugger, 2007). Vegetation cover at mid-latitudes in Eurasia was dominated by warm temperate vegetation with a high-diversity of evergreen woods and extra-tropical deciduous forests most probably growing under perhumid conditions (Collinson and Hooker, 2003; Utescher and Mosbrugger, 2007). Mean annual temperatures for mid-latitudes of Europe during the Middle Eocene were very high

between 23-25°C and cold month mean temperatures were between 17 and 21°C (Mosbrugger *et al.*, 2005). Towards the end of the Eocene, there is some evidence from pollen and floristic analysis in the Ebro Basin to suggest that climatic conditions changed to drier and cooler climatic conditions (Cavagnetto and Anadón, 1996). Data from other regions further north also shows from the Late Eocene onwards, the existence of a cooler and drier climate (Collinson, 1992; Knobloch *et al.*, 1993).

Palaeoclimatic conditions in the Ainsa Basin area during the Eocene are determined by palynofloral and microfaunal records from unpublished Robertson Research and are summarised in Pickering and Corregidor (2005). These records suggest a tropical to subtropical climate with moderately high rainfall patterns. Flora in the hinterland was dominated by coniferous vegetation in areas at higher altitudes whilst the lowlands were in general, well-drained. Based on the relative scarcity of pteridophyte and associated spores, the development of swamps with mangrove vegetation belts was limited.

1.5 Sea level

1.5.1 Estimation of sea-level changes

There are different methodologies employed to estimate sea-level changes. Published sea-level curves from the 1970's and 80's were made from the study of sedimentary strata deposited on passive continental margins and epicontinental seas (e.g., Vail *et al.*, 1977; Haq *et al.*, 1987). This methodology has been subjected to considerable controversy, mainly from the difficulty to obtain quantitative amplitude estimates of eustasy from inferred changes in coastal onlap (e.g., Christie-Blick *et al.*, 1990). Despite this limitation, sea-level curves created using this method are still in use nowadays since they tend to be quite consistent with calculations derived from other

methods, and are still reasonable at timing eustatic lowerings within an accuracy of ±1 Myr (Miller *et al.,* 2011).

Oxygen isotopic data obtained from the tests of marine fossils can be used to construct sea-level curves. Marine organisms form their skeletons using calcium, carbon and oxygen available from the oceans. The $^{18}O/^{16}O$ ratio ($\delta^{18}O$) from the oceans differs from the atmosphere and from continental glaciers due to selective isotope evaporation. As a consequence, variations in the oxygen isotopic ratio of the oceans is affected by the amount of continental ice and indirectly reflects sea-level change. Studying the $\delta^{18}O$ of marine organisms gives therefore an indication of global volume of ice and sea levels. One of the drawbacks of this method is that the amount of ^{18}O incorporated in the tests of organisms does not only reflect global glaciation but also depends on the temperature and salinity of the water (Miller *et al.,* 1991). In addition, this method cannot distinguish from eustatic changes of non-glacial origin (e.g., Miller *et al.*, 1991). The temperature component associated with these records can be evaluated by using Mg/Ca ratios in addition to deep-sea benthic foraminifera and $\delta^{18}C$ records to provide estimates of bottom-water temperatures (e.g., Lear *et al.*, 2000; Katz *et al.*, 2008; Sosdian and Rosenthal, 2009). However, errors in this approach are large and Mg/Ca records cannot be used with confidence for records older than Pliocene (Miller *et al.*, 2011).

More recently, global sea-level estimates have been produced using backstripping techniques. This methodology employs progressive decompaction and unloading of vertical successions of sedimentary layers to remove the effects of sediment compaction, loading and basin subsidence leaving a more accurate estimate of the amplitude of sea-level change (Steckler and Watts, 1978; Pekar *et al.*, 2002; Komintz *et al.,* 1998, 2008).

Sea-level curves produced using any of these methods, show that sea-levels can vary at different wavelengths and with different degrees of magnitude (Table 1.3). Long term (10^7-10^8 years) sea-level changes are slow and are mainly associated with tectonics, oceanic crust production and continent collision which can cause large variations in sea-level amplitude (e.g., Sloss, 1963; Miller *et al.*, 2011). Whereas, high-frequency sea-level cycles cause sea-level changes in the order of tens to hundreds of kyr, are caused by changes in the orbit of the Earth and result in much smaller amplitudes in sea-level change.

Table 1.3 Phanerozoic sea-level cycles.

Order	Time span	Magnitude	Dominant cause
1st order	100 Myr	Up to 500 m	Ocean-basin volume changes
2nd order	5-100 Myr	Up to 500 m	Thermotectonic subsidence
3rd order	1-5 Myr	Up to 200 m	Eustasy-tectonics
4th order	0.3-0.6 Myr	Up to 30 m	Eustasy-tectonics
5th order	~ 100 kyr	100–130 m	Glacio-eustasy (eccentricity)
6th order	~ 40 kyr	30–100 m	Glacio-eustasy (obliquity)
7th order	~ 20 kyr	Up to 50 m	Glacio-eustasy (precession)
Infra 7th order	< 20 kyr	Up to 50 m	Eustasy-sediment supply

Table after Fulthorpe (1991).

1.5.2 Sea-level changes in the Eocene

Numerous estimates of Eocene sea levels are available in the literature (e.g., Vail *et al.*, 1977; Haq *et al.*, 1987; Komintz *et al.*, 1998, 2008; Komintz, 2001; Miller *et al.*, 2005, 2011; Dawber *et al.*, 2011). Stratigraphically-based sea-level curves for the Eocene are mainly from the New Jersey Coastal Plain (Kominz *et al.*, 1998, 2008; Miller *et al.*, 2005). New Jersey records have been correlated to other successions such as the East Tasman Plateau (Röhl *et al.*, 2004) and the South Tasman Rise (Pekar *et al.*, 2005) indicating that these events are global. These sea-level curves have recognised

numerous Eocene succession boundaries associated with large (> 50 m) rapid (< 1 Myr) sea-level falls.

Figure 1.15 compares sea-level curves in the Eocene from $\delta^{18}O$ records (Cramer *et al.*, 2009), backstripping (Miller *et al.*, 2005; Kominz *et al.*, 2008) and sedimentary sequences (Haq *et al.*, 1987). These curves show a consistent general trend of sea-level change, although there is little agreement in terms of amplitude of sea levels. It has been claimed that amplitudes of the sedimentary records such as the Haq *et al.* (1987) sea-level curve are too high by a factor of 2-2.5 (Pekar *et al.*, 2002; Miller *et al.*, 2005). Despite these differences, the general consensus is that sea-levels during the Eocene were generally higher than today by 40-100 m. Sea-level curves from backstripping and benthic foraminifera oxygen isotope records show an abrupt increase in sea-level at the Early Eocene (~ 55 Ma) and then a long-term fall starting in the Late Middle Eocene that continued throughout the Oligocene. Higher frequency sea-level changes are also present in the records, although there is no evidence of sea-level fall higher than 100 m from the Palaeocene through the Oligocene in any of the sea-level curves estimates. Sea-level variability reaches as much as 40 m, but is generally less than 20 m. Many of the successions observed on the New Jersey Coastal Plain (Miller *et al.*, 2005; Kominz *et al.*, 2008) correspond to sequence boundaries of the global sea-level curve of Haq *et al.* (1987). For instance, there is a decrease in Eocene levels at 49.5 Ma that corresponds with a hiatus in the New Jersey sequences. Other estimates from $\delta^{18}O$ records in other parts of the world (e.g., Hampshire Basin and the Southern Ocean) also show moderate amplitude (40-60 m) relative sea-level variations during the Palaeocene and Eocene (Bohaty *et al.*, 2009; Dawber *et al.*, 2011).

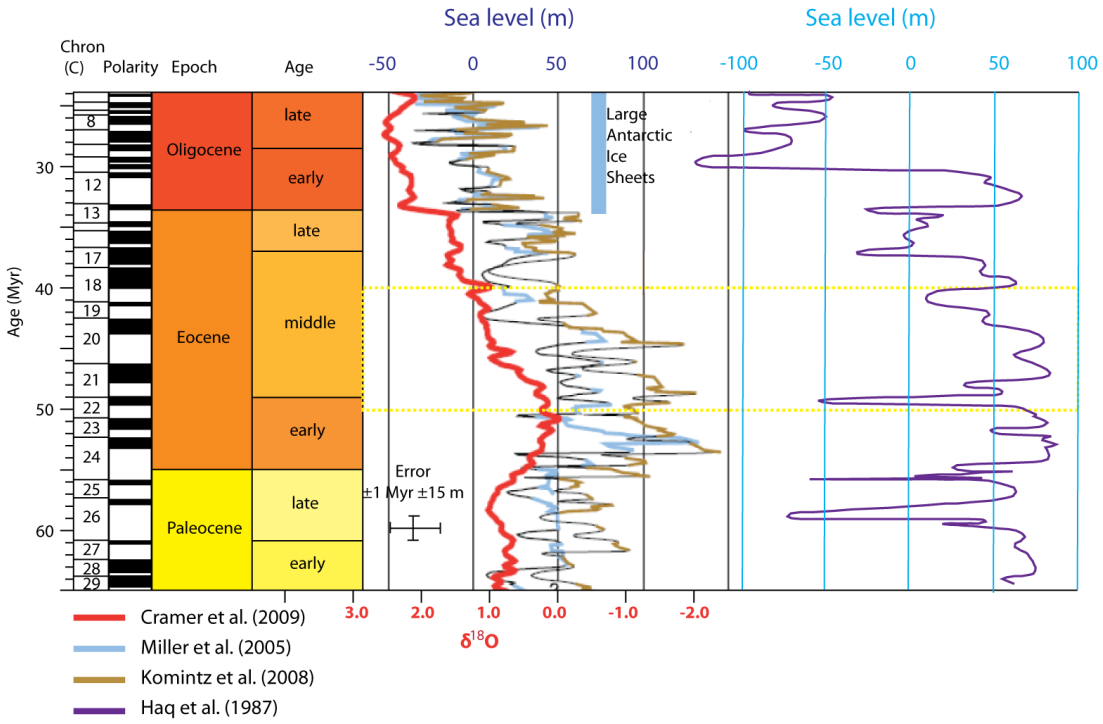

Figure 1.15 Sea-levels during the Eocene. The figure shows sea-level estimates from backstripping, New Jersey (Miller *et al.*, 2005; Kominz *et al.*, 2008); from seismic sequence analysis (Haq *et al.*, 1987) and from oxygen isotopic synthesis (Cramer *et al.*, 2009) from 65 to 35 Ma. The yellow box indicates the estimated age of the Ainsa deep-marine sediments (Pickering and Corregidor, 2005). Modified after Miller *et al.* (2011) and Haq *et al.* (1987).

1.6 Main research aim

The principal aim of this PhD is to calibrate sediment flux to a tectonic active basin in order to identify temporal changes in sedimentation patterns and to improve our understanding of what controls the nature and distribution of sediments. The analysis of high-resolution geochemical and mineralogical proxy data can help to evaluate climatic conditions in the hinterland and the resulting response that tectonics, climate and eustacy-driven changes can have on the depositional architecture of the Ainsa Basin. The comparison of these geochemical proxies against the frequency, thickness and SARs of turbidite deposits with a new developed age model can help to understand what controls sedimentation in this basin. Results from this research can have implications to our understanding of possible drivers of cyclic sedimentation in other

tectonic active basins in general and help to infer paleoclimatic changes which can serve as a model for other studies in modern and ancient deep-marine basins worldwide.

The Ainsa Basin was chosen as the study area because is one of the best world examples of confined turbidite deep-marine sedimentation, with superb three-dimensional outcrop exposure. The architectural simplicity of the basin is illustrated by clastic sediments mainly feeding from a unique southeast point source (Pickering and Corregidor, 2005) and by the development of only one major submarine channel at a time. This makes the Ainsa Basin a natural laboratory to study the evolution of the deep-marine systems through time. This PhD also focuses on a significant time period characterised by global climate which eventually led to the onset of Antarctic ice development and a switch from greenhouse to icehouse global climatic conditions.

1.7 PhD research objectives

(a) Refine the published Ainsa geological map and link it to topography

The calibration of the sediment influx to the basin requires a detailed geological map where stratigraphic thicknesses can be calculated with confidence. The published map of the Ainsa Basin (Pickering and Bayliss, 2009) was the product of a joined collaboration between Pickering and Corregidor (2000) and several later University College London (UCL) PhD students who mapped the different systems of the Ainsa Basin as part of their research degree. However, the use of different mapping techniques such as mapping on aerial photographs at different scales has caused that the published map appears ‘stretched’ in some areas, thus making thickness estimates difficult. One of the main objectives of this research project is to refine this map to show the geology linked to topography, in order to better calculate interfan sediment

thicknesses (i.e., determine thicknesses between the sandbodies). Estimation of stratigraphic thicknesses can be used in conjunction with the development of a new age model for the Ainsa Basin based on magnetostratigraphy data to better constrain timing of the deep-marine sedimentation in the basin.

(b) Gamma-ray logging of fine-grained interfan successions and cyclostratigraphy study of these successions

The duration of fan and interfan deposition can be established by identifying Milankovitch cycles in the finely-laminated deep-marine sediments of the Ainsa Basin using a portable gamma-ray spectrometer. Sections suitable for high-resolution gamma-ray logging should be undeformed, continuous and located between sandbodies (submarine fans) so that the timing of coarse sand flux into the basin can be established. Applying cyclostratigraphic techniques to high-resolution gamma-ray data can help to understand how these orbital cycles have had an effect on climate and ultimately in the sediment flux to the deep-marine environment.

(c) Magnetostratigraphy study across the Ainsa Basin

Rock sampling for magnetostratigraphy will be undertaken over ~ 1 km of stratigraphy in the Ainsa Basin. Sampling would occur mainly in the Upper Hecho Group (from the Gerbe to the Morillo systems) since the Lower Hecho Group is severely deformed with the emplacement of numerous thrust sheets and fault-propagation-folds, and these structurally-complex sediments would therefore not be included in these studies.

(d) Geochemical analysis of a fine-grained interfan core

The project also involves work on the Well A6 core which is one of the cores recovered from drilling in the Ainsa Basin. This core is located in the interfan deposits between the Ainsa and Morillo systems. The A6 core is ~ 230 m long and consists mainly of deep-marine marlstones and thin-bedded muddy siltstone turbidites. Work on the core involved the production of detailed sedimentary logs, chemical analysis of major and trace elements using the UCL multi-element XRF scanner (X-Ray Fluorescence), X-ray powder diffraction (XRD), total organic carbon (TOC), scanning electron microscopy (SEM) and stable carbon isotopic determination. All these analysis aim to determine the nature and provenance of the sediments in the basin and would contribute to our understanding of how climate variability has had an effect on the nature and distribution of deep-marine records. Previous work has been done on the A6 core by Heard *et al.* (2008) conducting bioturbation intensity studies and by Scotchman (2012) undertaking cyclostratigraphic studies from XRF data. Heard *et al.* (2008) described and interpreted the stratigraphy of the A6 core but sedimentary logs were not produced to support these interpretations. Time-series analysis on the A6 core by Scotchman (2012) was performed over a ~ 30 m section with the aim of identifying sub-Milankovitch cyclicity in the core. This interval is, however, insufficient to determine Milankovitch frequencies with confidence. As a result of these limitations, new work on the A6 core has been planned to include detailed sedimentary logs that can be interpreted together with geochemical analyses.

Chapter 2

Methods and mapping

2.1 Introduction

This project combines a variety of analytical approaches including field and laboratory-based techniques to help determine palaeo-environmental conditions and to reconstruct the depositional history of the Ainsa Basin. Figure 2.1 shows a work-flow diagram of the methodology adopted in this study.

This project involves a detailed sedimentological and geochemical study of an essentially fine-grained siliciclastic deep-marine sedimentary record, the Well A6 core, drilled in Middle Eocene deposits in the Spanish Pyrenees. Multiple geochemical techniques including XRF, SEM and XRD have been applied to infer variations in grain size, weathering and the geochemistry of the three main lithologies, sandstone, siltstone and mudstone. TOC and stable carbon isotope studies are also included as they provide a useful means for identifying the origin of organic matter and characterising the nature and provenance of the sediments in the basin.

Field-based techniques, including sedimentary logging, geological mapping and facies analysis have been applied to extensive areas of the Ainsa Basin. Detailed sedimentary logs were produced, including every bed thicker than 5 mm from mainly interfan and channel levée-overbank deposits covering ~ 1.5 km of stratigraphy. Geological maps have also been produced and cover an area of ~ 10 km^2. These maps are accompanied by geological cross-sections used to estimate stratigraphic thicknesses between sand-rich submarine fan sediments. High-resolution spectral gamma-ray logging of 10 undeformed fine-grained sections have also been undertaken

in over 1.5 km of the basin stratigraphy. Cyclostratigraphic techniques were then applied to the spectral data to determine the potential presence of orbital cycles in these deep-marine sediments. Time-series analyses include orbital tuning of selective sections using the results from palaeomagnetic studies undertaken over ~ 1 km of stratigraphy in collaboration with the palaeomagnetic laboratory in the Department of Earth Sciences, Oxford University.

The combination of all these techniques allows for the first time the robust establishment of the timing of coarse-grained delivery to the Ainsa Basin and to make tectono-climatic inferences on sediment supply and depositional architecture at a variety of temporal scales.

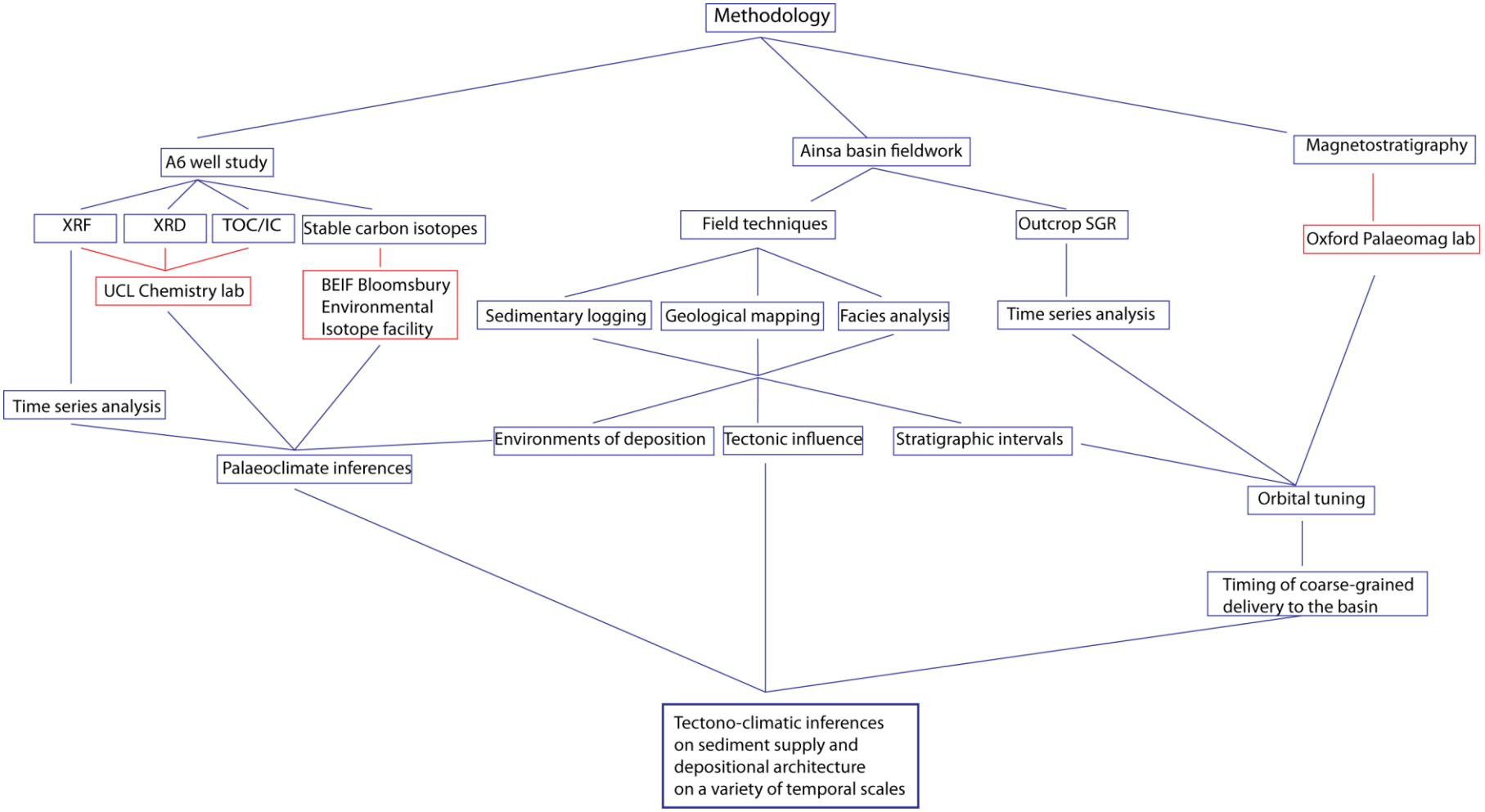

Figure 2.1 Work-flow of the methodology adopted in this study.

2.2 Geological mapping

Published geological maps of the Ainsa Basin include amongst others, work produced by Fernández *et al.* (2004), Pickering and Corregidor (2005), Pickering and Bayliss (2009), Sutfliffe and Pickering (2009), and Pohl and McCann (2013). These maps largely vary in terms of the extension of the area mapped and the detail of the geology included, with some of the maps produced restricted to only one deep-marine system. The most detailed map produced to date is from Pickering and Bayliss (2009). This map is a composite map which integrates previous work from Pickering and Corregidor (2005) in the Ainsa System, Sutcliffe and Pickering (2009) in the Guaso System and also Bayliss (2014a, 2014b) in the Banastón and Morillo systems. This map includes valuable information on the depositional history of the Ainsa Basin and mainly focuses on the depositional history of the basin during the upper part of the basin infill (from the Banastón to the Guaso systems), although it also includes some information on older deep-marine systems such as the Fosado, Los Molinos, Arro and Gerbe systems. The main problem associated with this work lies in the fact that the map has not been built on space and the use of different mapping techniques, including, mapping on aerial photographs at different scales has caused the map to appear distorted, thus making thickness estimates difficult. Geological mapping for this project has focused on those areas in the basin which contain long undeformed sections of fine-grained sediments located in between coarse-grained submarine fans. Geological maps of these areas have been produced with underlying topography to facilitate the calculation of stratigraphic thicknesses with accuracy.

2.2.1 Study area

The study area comprises ~ 20 km^2 and extends from the towns of Boltaña to the west to Los Molinos to the east. The limit to the north is just south of the town of Escalona and the southern limit being the town of Morillo-de-Tou.

2.2.2 Topography

The topography of the area is dominated by vegetated ridges which contain coarse-grained turbidite sandstones at the top and by V-shaped valleys (Figure 2.2). The elevation of this region varies between 500 m to 1,400 m above sea level. The area is crosscut by two main rivers, the Cinca and the Ara, which flow in a north to south direction and they join just pass the town of Ainsa in the centre of the study area, where the Mediano Reservoir is located. There are other smaller rivers present in the area, mainly tributaries of the Ara and the Cinca Rivers, such as the Eña River and the Forcaz stream. Various small villages have been located and built around these flat plains, including the Labuerda and Margudgued villages. However, most of the towns appear to have been constructed at the top of the sandstone ridges using the resistant local sandstone turbidites as their building blocks. Figure 2.2 is a panorama of the Ainsa Basin with an interpretative geology sketch. Each of the topographic ridges contains a package of coarse-grained sandstone turbidites represented on the sketch by yellow infilling. The rest of the stratigraphy comprises mainly of fine-gained sediments and MTCs which are represented on the sketch by a light grey colour. The particular limits of the basin to the east and west are marked by the Mediano and Boltaña anticlines, respectively.

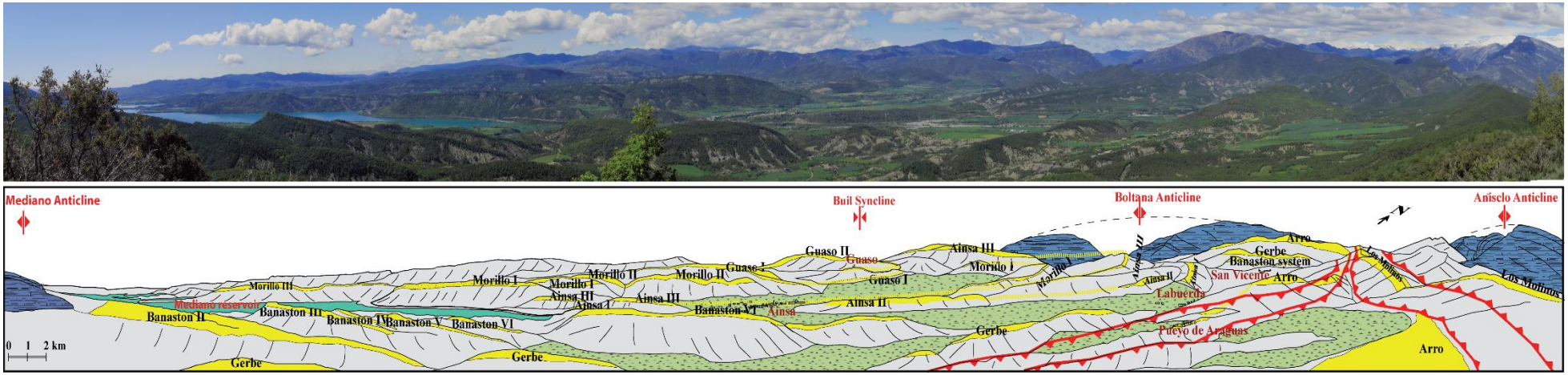

Figure 2.2 Panorama of the Ainsa Basin and geological interpretation. The Ainsa Basin is characterised by a number of topographic ridges separated by pastures and grasslands. Each of the topographic ridges contains a sandbody (coloured in yellow). Fine-grained sediments interpreted as interfan and overbank deposits are present in between the sandbodies (coloured in pale grey). The Mediano Anticline bounds the basin from the east and the Boltaña and the Añisclo anticlines bound the basin from the west and the northwest, respectively. These three anticlines are composed of carbonates and are coloured in dark blue. The Buil Syncline is clearly visible in this panorama view with the entire deep-water system folded around the Mediano Reservoir. An electronic version is provided in Appendix 2 to allow for a better visualisation of the geological interpretation of the respective areas.

2.2.3 Climate, vegetation and rock exposure

The climate in the field area is sub-arctic (severe winter, no dry season with a cool summer) and dry sub-humid. The landscape is primarily cold-deciduous pine forests with evergreens. A large proportion of the natural vegetation is still intact, although, along river valleys there are large areas of grassland, pasture landscapes and cultivated terrain. Northern hill sides are typically densely vegetated displaying poor outcrop exposure. However, at river valleys and road cuts, it is common to encounter continuous outcrop sections which allow for detailed mapping and sedimentary logging. Overall the rock exposure in the area is estimated to be ~ 35%.

2.2.4 Accessibility to the area

Access to the area is provided by two main roads. The national road, N-260, runs adjacent to the Cinca River and connects the towns of Boltaña-Ainsa-Gerbe and Arro. The A-138 road connects the towns of Ainsa and Labuerda and runs parallel to the Ara River (Figure 2.4). There are also numerous secondary roads and paths which connect small villages and form a complex infrastructure network allowing access to most of the outcrops.

Some areas are, however, impenetrable or have very limited accessibility. These areas are principally associated with sandstone ridges which are extensively vegetated, with limited rock exposure forming very steep slopes. The northwestern part of the study area also has limited access associated with the presence of numerous thrusts and fault-propagation-folds. Geological mapping across these areas is therefore limited and only possible along paths or streams.

2.2.5 Mapping technique

The area was mapped using Google Earth aerial photographs (version 6.0.3.2197, 2011). A total of 9 maps were produced at a scale of 1:8000 covering an approximate area of 1.5 km x 1 km for each of the sections selected for outcrop gamma-ray logging. The scale of the maps produced was adapted in certain locations where the geology was proven to be complicated. These areas were mapped at a scale of 1:6000. Since these 9 maps cover a significant area in the Ainsa Basin, a secondary objective to this project was to attempt to adapt the map of Pickering and Bayliss (2009) to the underlying topography to remove the stretching effect. For this purpose, aerial photographs at a scale of 1:17000 covering the complete study area were used. Due to time constraints, a broader mapping technique was employed consisting in traversing areas across the maps using predetermined routes, such as stream valleys, road cuts or hiking paths with the main objective of establishing the main geological contacts and defining the geometry of the main geological and structural features.

A Global Positioning System (GPS) receiver was used to increase location accuracy at different outcrops, especially in densely vegetated areas where reference points were difficult to identify. In bright clear days, GPS position accuracy was within a radius of 3 m. However, when mapping in adverse weather conditions or in deep narrow valleys the accuracy was reduced to a radius of 10-15 m. GPS locations were recorded in a field notebook together with geological sketches, outcrop descriptions and sedimentary and structural data.

Areas of outcrops have been recorded on transparent permatrace sheets that overlaid the aerial photographs. Outcrops are marked using a green line. In areas of poor accessibility and exposure, information on vegetation and topographic changes was used to infer lithological boundaries. Inferred contacts are represented with dash

lines and clear contacts in a solid black line. Lithologies are colour coded on the field slips. A simplified facies scheme was used and is summarised in Figure 2.3 together with the symbols used on the geological maps. Palaeocurrent directions were mainly measured from flutes and grooves at the base of sandstone turbidites or from ripples in well-exposed bedding planes to record direction of flows.

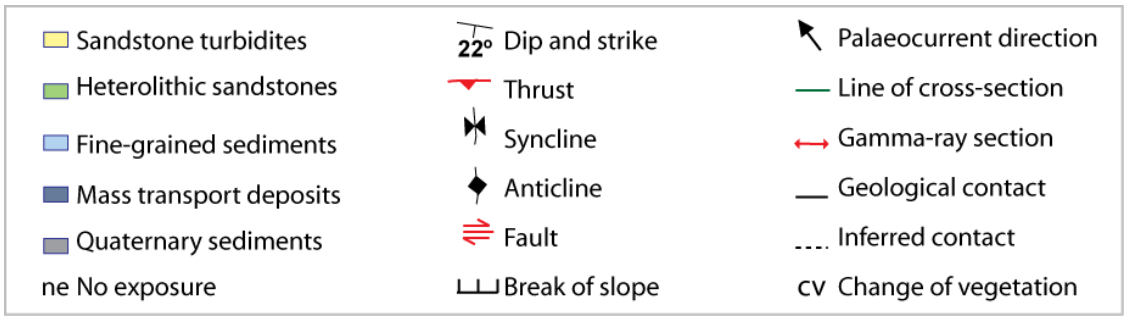

Figure 2.3 Legend used in the geological maps. A simplified facies scheme was used to describe the different lithological unis present in the field. Facies key is the same as used by Pickering and Bayliss (2009).

Structural data such as faults and folds were also recorded on the permatrace sheets together with any kinematic indicators that could provide information on thrust propagation and fold directions (e.g., crystal fibre, slickenside lineations on thrust planes, fault displacement and fold axis and plunges). Mapping these structural elements is important because it can help to identify the influence of intrabasinal tectonics on facies distribution and depositional patterns. Strike and slip bedding data are collected at numerous locations throughout the study area with the aim of understanding bedding geometries and tectonic effects in the area.

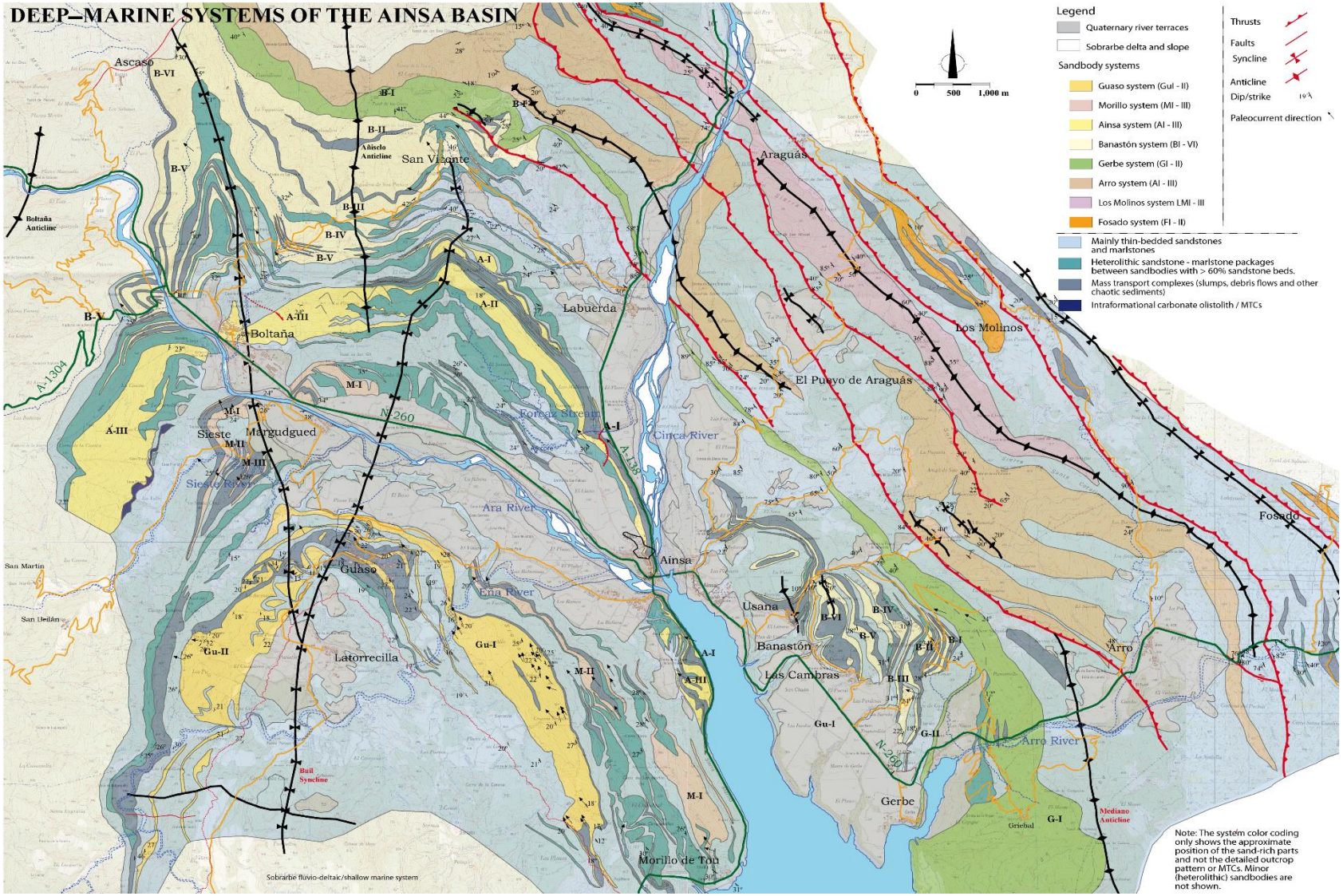

Figure 2.4 Ainsa Basin geology map adapted to underlying topography. Modified after Pickering and Bayliss (2009).

2.2.6 Revised geological map of the Ainsa Basin

Figure 2.4 shows the revised geological map of the Ainsa Basin which has been produced as part of this PhD study. This new map has the advantage of showing underlying topography which facilitates a better understanding of the geometry of the sandbodies and allows the creation of cross-sections to gain a better understanding of the subsurface geology. The revised map also shows more structural and geological detail in the northwestern part of the basin which is presented with a lesser degree of detail in the Pickering and Bayliss (2009) publication. This area is tectonically deformed with numerous thrusts and thrust-propagation-folds observed. Fold axis orientations are generally northwest-southeast and fault displacements are towards the west and south-west. The sediments of the Gerbe, Arro and Los Molinos are the main systems affected by this deformation front. Geological interpretations of this revised map are discussed in detail for each of the deep-marine systems in Chapter 5.

Geological maps produced on Google Earth aerial photograph maps for each of the gamma-ray sections are compiled on Appendix 1. Most of these maps are located in the central, western and southern part of the Ainsa Basin where most of the stratigraphy is undeformed and involves mainly the sediments of the Upper Hecho Group. Larger scaled maps produced to adapt the Ainsa Basin geological map to underlying topography are compiled in Appendix 2. Each of these maps have been digitalised using the drawing software Adobe Illustrator version CS4.

2.3 Sedimentary logging

Detailed bed-by-bed sedimentary logs have been constructed in the field for each of the gamma-ray logged sections. Sedimentary logs record vertical changes in lithology, bed thickness, colour, sedimentary structures and bioturbation at centimetre scale.

Chaotic sediments were graphically represented in the logs with detailed descriptions of textural characteristics. Grain-size was also recorded in the logs using the classification scheme by Wentworth (1922). The legend used in the sedimentary logs can be seen in Figure 2.5. A total of 1.5 km of measured sections were logged at a scale of 4 cm = 1 m. Every bed with a thickness of ≥ 5 mm has been included in the logs. All the sections were continuous and relatively well-exposed along river valleys and road cuts. The length of the logged sections varied between 40 m and 350 m, although the average length was typically ~ 140 m. Scree or very weathered surfaces were localised and rarely exceeded few metres in thickness. To prevent gaps in the sedimentary logs associated with poorly exposed areas, when possible, lateral sections were correlated to fill the missing gaps in the logs. In addition, to outcrop sedimentary logging, very detailed sedimentary logs were produced from a 230 m long core (the Well A6 core). These sedimentary core logs included all beds with a thickness ≥ 2 mm. The polished and unweathered working halves of the core allowed for a better observation of colour, ichnofacies and sedimentary structures. Locally, detailed observations of grain size distributions or of sedimentary structures were made using a light microscope.

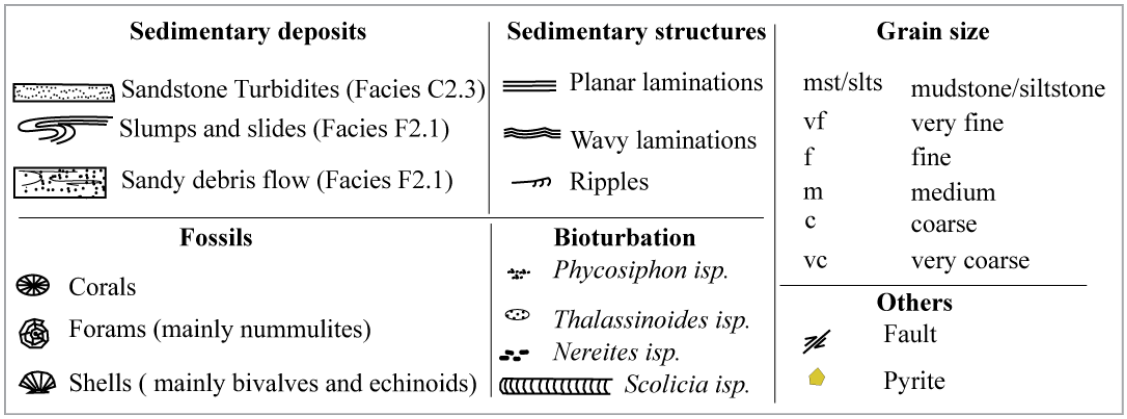

Figure 2.5 Legend used in the sedimentary logs. Sedimentary logs include information on grain size, type of sedimentary deposits and structures, sediment colour and presence of fossils and bioturbation.

2.4 Outcrop gamma-ray spectrometry

Radioactivity in sediments originates from the nuclear decay or disintegration of unstable isotopes which change to more stable nuclei of a different isotope by the emission of particles or energy. The three main types of radioactive decay are alpha, beta and gamma-rays. Alpha decay results in the release of an alpha particle consisting of 2 protons and 2 neutrons. Beta -ve decay emits a beta particle identical to a negatively charged electron and beta +ve decay, emits a positively charged positron. Alpha and beta particles have a low penetration range in matter and are absorbed more or less instantaneously. The emission of alpha and beta particles usually leaves the newly formed nucleus in an excited state and the energy excess is radiated as gamma-rays. Gamma-rays are photons of energy which travel at the speed of light and do not possess any charge or mass. These rays can penetrate up to 30 cm of rock and several hundred metres of air. The intensity of gamma radiation decreases with distance from the source. This is the result of gamma-rays being absorbed by material present between the source and the detector. As a consequence, the airborne gamma-ray spectrometric method is limited to approximately the top 35 cm of the Earth's surface, where over 98% of the radiation emanating from the Earth's surface originates (Gunn *et al.*, 1997).

Gamma-rays are part of the electromagnetic spectrum and have a discreet energy, frequency and wavelength. The discrete energy is characteristic of the source isotope emitting the gamma-rays. By measuring this energy with a detector, the source of the radiation can be recognised (Minty, 1997).

Potassium (K), uranium (U) and thorium (Th) are the only naturally occurring elements with radioisotopes that produce gamma-rays of sufficient energy and intensity to be measured. These elements have very long-lives (in the order of $5x10^9$

years) and although they have been decaying since creation, they are still relatively abundant in the Earth's crust. ^{40}K is the only radioactive isotope of K. Uranium occurs naturally as the radioisotopes ^{238}U and ^{235}U which give rises to decay series which terminate in the stable isotopes ^{206}Pb and ^{207}Pb. Thorium occurs naturally as the radioisotope ^{232}Th which gives rises to a cascading decay series that terminates in the stable isotope ^{208}Pb.

2.4.1 Gamma-ray spectrometer

Outcrop spectral gamma-ray detectors analyse the total gamma-ray radiation emanating from a formation. The gamma-ray detector is able to differentiate the likely source of the radiation and measures the individual contribution from the three major radioactivity sources: potassium, uranium and thorium.

The spectrometer used for field data collection is the portable RS-125 Super-Spec from Geomatrix. This instrument contains a large 0.35 l Sodium-Iodine (NaI) crystal detector which measures radiation from a ~ 0.9 m surface diameter. Large volume scintillation crystals give acceptable precision for quantitative analyses (IAEA, 2003). The total gamma-ray decays are measured in a 0-3 MeV energy range using a multichannel collector, resulting in high-sensitivity detection. The instrument has a fully automatic spectrum stabilisation and calibration system, to keep the discrimination threshold at a constant level and calibration constants are stored in the instrument memory. Gamma-ray spectrometers detect the energy from an incoming gamma-ray and convert the pulse amplitude into an energy spectrum of detected radiation (IAEA, 2003). Since individual radionuclides emit specific gamma-ray energies, spectrometers can differentiate the source of the radiation. Table 2.1 and

Figure 2.6 show the spectral windows for the detection of potassium, uranium and thorium.

The estimation of the K content in rocks is through the detection of 1.46 MeV gamma-rays emitted by ^{40}K. This nuclide occurs as 0.012% of natural K. This fixed proportion allows the direct estimation of the total amount of K present and the results are reported as % K. Since Th and U do not emit gamma-rays, their concentrations are estimated indirectly from the measurement of the gamma-ray emissions from their radioactive daughter products. U is detected by the emissions of 1.76 MeV gamma rays of ^{214}Bi, a daughter isotope in the ^{238}U decaying series. Th is estimated by the detection of 2.62 MeV gamma ray of ^{208}Tl, a daughter product of ^{232}Th decay series. Estimates of U and Th concentrations are based on the assumption of equilibrium conditions in the U and Th decay series. Th usually occurs in equilibrium in nature, but disequilibrium in the U series is common. Estimates of U and Th concentrations are therefore usually reported as ppm eU (parts per million of equivalent Uranium) and ppm eTh (parts per million of equivalent Thorium) as a reminder that they are based on the assumption of equilibrium conditions.

The conventional approach to the acquisition of gamma-ray spectrometric data consists in monitoring at least three energy windows which detect the gamma-rays emitted by ^{40}K, ^{214}Bi and ^{208}Tl. Suitable calibration and data processing of this data, can convert the total counts to concentrations of K, U and Th in the rocks. The portable RS-125 Super-Spec also includes a broader total-count energy window that measures the total radioactivity (Table 2.1).

Table 2.1 Spectral windows for the detection of K, U and Th.

Window	Nuclide	Energy range (MeV)
Total Count	-	0.4-2.81
Potassium	^{40}K (1.46 MeV)	1.37-1.57
Uranium	^{214}Bi (1.76 MeV)	1.66-1.86
Thorium	^{208}Tl (2.62 MeV)	2.41-2.81

Table showing the typical spectral windows for the detection and measurement of total radioactivity, K, U and Th compositions.

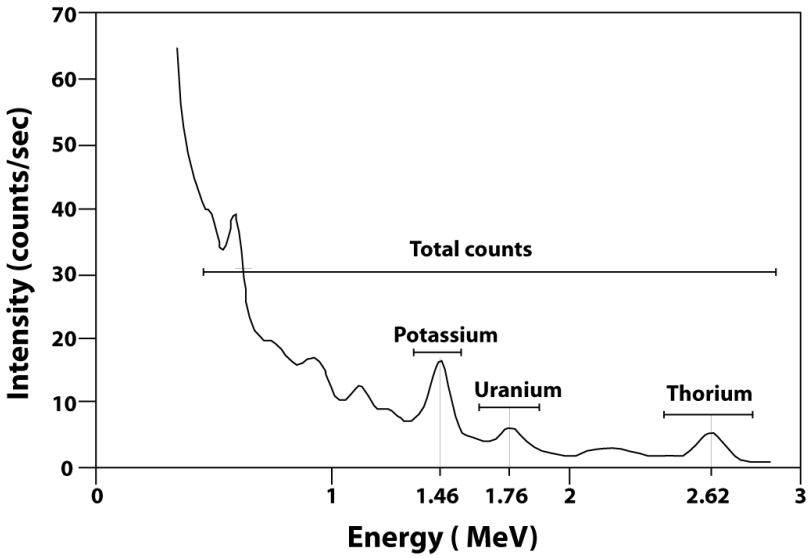

Figure 2.6 Gamma-ray spectrum window for the radioactive elements K, U and Th. The figure shows the photopeaks at 1.46, 1.76 and 2.62 characteristic of K, U and Th, respectively. Bars show the spectral windows for each of the radioactive elements. Modified after Minty (1997).

2.4.2 Sources of potassium, uranium and thorium in sedimentary rocks

Potassium is a volatile lithofile element, monovalent in natural conditions and abundant in the Earth's upper crust (2.33 wt% K). Potassium is abundant in sedimentary rocks and is contained principally in alkali-feldspars, micas and illite. Alkali-feldspars and micas are more common in sandstones and illite is commonly found in fine-grained rocks such as shales. Cowan and Myers (1988) argued that since alkali-feldspar has a greater K content than illite, the gamma-ray is only a measure of clay content in the absence of significant alkali-feldspars.

Uranium has an average abundance of about 2.5 ppm in the Earth's crust. Uranium is contained in accessory minerals such as zircon, monazite, apatite, allanite and sphene. Of these minerals, zircon and monazite are the most resistant to weathering. Uranium is also common in clays, feldspars, phosphates and organic matter. Rocks where uranium minerals tend to be present are pegmatites, syenites, carbonatites, granites and some shales. Svendsen and Hartley (2001) found that uranium was associated mainly with clay-rich sections and carbonate minerals in sedimentary rocks.

Thorium is much less abundant than K in the Earth's crust with a concentration of about 9 ppm. Thorium is a component of detrital minerals such as allanite, monazite, xenotime, zircon and thorite and also is present as trace amounts in other rock-forming minerals such as igneous rocks. Thorium can also be found adsorbed into natural colloidal-size materials, particularly clays (Langmuir and Herman, 1980).

In detrital sedimentary rocks the mean of the typical radioelement concentrations is 1.5% potassium , 4.8 ppm eU and 12.4 ppm eTh although the range of compositions is very broad (K ~ 0-10%, U ~ 0-80 ppm, Th ~ 0-362 ppm) (Killeen, 1979).

Potassium and uranium are considered relatively soluble in aqueous solution and can be leached from soils during weathering. Weathered rocks are depleted in K and the freed K is commonly incorporated into clay minerals. Uranium can be part of soluble minerals which leach during weathering, decreasing the U concentration of weathered material and the leached U can be adsorbed in clays and precipitate in iron oxides and carbonates. Thorium is commonly insoluble and major Th-bearing minerals such as monazite and zircon, are stable during weathering. As a result, Th compounds

tend to concentrate in sediments during weathering, mainly in clays and in iron or titanium oxides. As a result of this, weathering processes can cause specific radionuclides signatures. Mature sediments will tend to have elevated Th compositions whereas immature sediments will have radioelement concentrations which tend to correlate with the original concentrations of their source rocks. Parkinson (1996) suggested that variations during weathering may be preserved during subsequent erosion, transport, deposition of the weathered material and early diagenesis. The K, U and Th partitioning which occurred during soil weathering can therefore be detected in the sedimentary rocks that were subsequently deposited.

2.4.3 Outcrop spectral gamma-ray methodology

2.4.3.1 Sampling period

The sampling time required for a measurement depends on the radioactivity of the source and the precision of the measurement required. Løvborg and Mose (1987) derived equations giving the counting time for K, U, and Th assays with a 10% error in various K, U and Th ratios. The instrument specifications recommend a sampling period of at least 120 seconds, with higher counting times giving statistically more reliable data.

Prior to spectral gamma-ray logging, an estimation of the radiochemical composition of the rocks was obtained by undertaking some random measurements in a typical fine-grained lithology using a 10 min sampling period. Averaged values of the 5 measurements gave an estimation of (K ~ 3%, U ~ 3.5 ppm and Th ~ 12 ppm).

Using the equations derived by Løvborg and Mose (1987) to obtain a 10% precision, a 120 second period was satisfactory to obtain Th and K but was borderline

for the uranium determination limit. A sampling period of 180 seconds was considered adequate as a compromise between the economy of field measurement and precision of measured count rates.

2.4.3.2 Distance between measurements

Measurements were undertaken vertically through the stratigraphy at intervals of 20 cm. The sampling interval has been determined using the Nyquist critical frequency, which suggests a minimum of 2 samples per smallest oscillation to avoid aliasing in the time-series (Weedon, 2005), although most studies recommend a minimal of 8 samples per cycle in the period of the smallest oscillation (Herbert, 1994). Spectral studies of bioturbation intensity in the Ainsa Basin suggested SARs of ~ 30 cm/kyr (Heard *et al.*, 2008). A 20 cm sampling interval would, therefore, permit recognition of Milankovitch scale cycles with a minimum of 10 data points per shorter expected cycle (precession ~ 20 kyr). The gamma-ray logging strategy employed consisted of the identification of continuous exposed outcrops of long fine-grained laminated sediments in between the sandbodies. In order to successfully identify frequencies with confidence, at least 5 cycles should be present in a section (Weedon, 2005). Therefore, it is recommended that at the SARs of the basin, sections should be at least 150 m long in order to detect Milankovitch eccentricity cycles.

Surveying was discontinued during wet weather conditions and was not recommenced until the rocks were relatively dry. This is because rainfall can reduce the radiation flux and cause increases in U ground concentrations due to deposition of radioactive dust particles on rock surfaces (e.g., Myers and Wignall, 1987).

2.4.3.3 Geometry of the measurements

The effect of bed geometry on spectral gamma-ray logs has been well-documented by Svendsen and Hartley (2001). As these authors point out, the gamma-ray detector measures emission from the sediment body in front of the detector. Figure 2.7 shows the effects that the surface and bed geometry can have on the gamma-ray measurements. When available, the spectrometer was placed perpendicular to the rock face. Measurements close to cliff faces were avoided as this can cause an increase or a decrease in gamma-ray counts which are unrelated to lithology (Figure 2.7). Cleaned surfaces were exposed with the help of a hammer and a brush to remove accumulated weathered material.

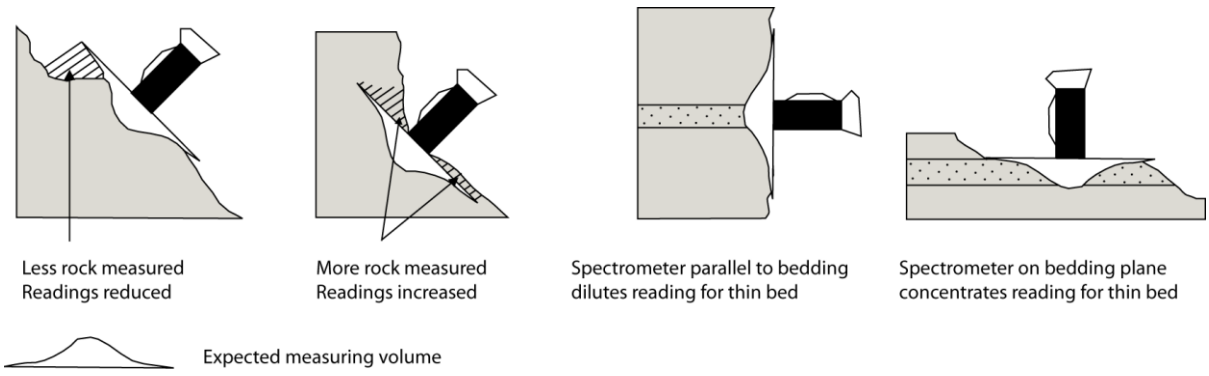

Figure 2.7 Effects of sampling surface and bed geometry upon outcrop gamma-ray measurements. Modified after Løvborg *et al.* (1971), Parkinson (1996) and Svendsen and Hartley (2001).

2.4.4 Application of gamma-ray detection in sedimentology

2.4.4.1 Facies recognition

Gamma-ray curve shapes and signatures have been used for facies recognition (Chamberlain, 1984; Myers and Bristow, 1989; Bristow and Williamson, 1998; North and Boering, 1999); for stratigraphic correlation and analysis (Myers and Bristow,

1989; Slatt *et al.*, 2000; Parkinson, 1996; Evans *et al.*, 2007); for the identification of parasequences and sequence stratigraphic interpretations (Aigner *et al.*, 1995; Davies and Elliot, 1996; George, 2000); for clay mineralogy and palaeoclimate studies (Myers and Wignall, 1987; Osmond and Ivanovich, 1992; Parkinson, 1996; Ruffell and Worden, 2000; Ruffell *et al.*, 2003; Schnyder *et al.*, 2006); for geochemical studies (Van Buchem *et al.*, 1992; Svendsen and Hartley, 2001; Deconinck *et al.*, 2003) and for sediment provenance (Šimíček *et al.*, 2012).

Some studies have shown, however, the limitations of this method. An example being Rider (1990), who argued that the application of gamma-ray logs to facies recognition can cause problems if the clay content and grain size is not consistent. North and Boering (1999) tried to apply gamma-ray signatures to distinguish between fluvial and aeolian sequences. Their research showed that gamma-ray signatures failed to differentiate between both depositional environments. However, other authors have been able to discriminate lithofacies. Bristow and Williamson (1998) showed that sandstones had low-values of K and Th, whilst finer grained lithologies such as silty sandstones, sandy siltstones and claystones were less well-differentiated and showed relatively high-levels of potassium and thorium. Svendsen and Hartley (2001) using whole-rock geochemistry with outcrop gamma-ray logs showed that the potassium distribution was controlled by illite and alkali-feldspars, the uranium distribution was enriched in clay-rich sections and carbonate minerals and thorium was linked to heavy mineral distribution, although not exclusively.

In siliciclastic sequences, higher gamma-ray counts are generally attributed to fine-grained facies whilst low gamma-ray counts are more typical of sandstones (Rider, 1990). The high gamma-ray counts in fine-grained facies such as silts and shales are related to the high contents of K, U and Th in clay minerals. K is common in

clay minerals including illite and U and Th tend to be adsorbed on the surface of clay minerals and organic matter. Low gamma-ray counts in sandstones are driven by the dilution effect of quartz, carbonate cement and pore space. However, these general assumptions are often complicated by the variable contents of the K-bearing grains (e.g., K-feldspars, albite and micas), by the distribution of Th- and U-bearing heavy minerals such as zircon, apatite, monazite and rutile, in sandstones (Rider, 1990; Svendsen and Hartley, 2001), and by the variability of clay mineral compositions (illite, kaolinite, glauconite and smectite) in mudstones. The content of TOC and diagenetic effects can also have an effect on the total gamma-ray counts (Bjørlykke and Egeberg, 1993; Fabricius *et al.*, 2003).

2.4.4.2 Weathering patterns

Various authors have tried to determine changes in climate and weathering patterns from spectral gamma-ray data comparing K/Th and U/Th ratios of sedimentary rocks (Rosholt, 1992; Osmond and Ivanovich, 1992, Parkinson, 1996; Ruffell and Worden, 2000). The U and Th content of sediments are undoubtedly also influenced by other minerals, especially by heavy minerals (Myers and Bristow, 1989; Hurst, 1990). Thus the Th/K ratio, whilst undeniably reflecting the detrital K content of sedimentary rocks, may occasionally be influenced by concentrations of thoriferous heavy minerals (for instance at transgressive surfaces). The clay mineral kaolinite is often associated with hot and humid areas, and its abundance in soils has been shown to display good correlation with high Th/K or Th/U ratios (Osmond and Ivanovich, 1992).

The clay mineral kaolinite forms in the soils of hot and humid areas and is usually associated with weathering. The mobility of potassium and uranium and the relative immobility and concentration of thorium during weathering has led some

authors (Rosholt, 1992; Osmond and Ivanovich, 1992; Parkinson, 1996) to suggest that weathering will result in elevated Th/K and Th/U ratios. Various authors have also shown a good correspondence of kaolinite with high Th/K or Th/U (Osmond and Ivanovich, 1992; Schnyden *et al.,* 2006), indicating that elevated Th contents can therefore be used as a proxy for humid palaeo-weathering. Although, Schnyden *et al.* (2006) suggest that Th/U ratios appear to have less sensitivity to changes in moisture conditions. Ruffell and Worden (2000) and Deconinck *et al.* (2003) have found a strong correlation between cross-plots of kaolinite/illite against Th/K. These authors argue that warm and humid conditions cause intense weathering, resulting in the kaolinitisation of feldspars and illites accompanied by leaching of K and U and relative concentration of Th. During arid climates, weathering decreased and the illite, U and K content of the rocks increased, causing a low Th/K ratio. Deconinck *et al.* (2003) pointed out that variation in the content of organic matter may affect the correlation between the kaolinite/illite and the Th/K ratios.

2.4.4.3 Storminess, oxygenation levels and change in sea-levels

High values of Th/K ratios have also been associated with an increased in the supply of detrital material, which may be associated with storminess and increased runoff (Pierini *et al.,* 2002; Grabowski *et al.,* 2013), and with sea-level lows or marine regressions (Ghasemi-Nejad *et al.,* 2010). Th/U ratios have been used as indicators of oxygenation level within the marine sediment (Wignall and Myers, 1988; Jones and Manning, 1994), with high Th/U ratios suggesting oxic conditions. Low Th/U ratios have also been associated with an increase in sea-levels and maximum flooding surfaces (Davies and Elliot, 1996).

2.5 X-ray fluorescence scanning

Well A6 core was scanned using a multi-element XRF Avaatech scanner located at UCL. A 170 m long, fundamentally continuous core length was scanned from 230 to 60 m depth below the surface using a core spacing interval of 4 cm between measurements. This section avoids the top 60 m of chaotic sediments of the A6 core (Type I MTCs, Pickering and Corregidor, 2005). A high-resolution sampling interval was selected to detect any high-frequency environmental changes using time-series analysis. A 31 m section, from 176 to 206 m depth, was scanned at a much higher resolution using a spacing interval of 3.5 mm. This spacing interval was selected to detect geochemical element associations and determine specific facies signatures of the cm-size sandstone turbidites, siltstones and structureless mudstones.

The resolution of the system was set with a 2 mm slit window and a 30 second sampling time. A two-run excitation mode was set in order to obtain a wide range of spectral data. The first run was set at 10 kV, 800 Ma with no filter being used. These settings were established to ensure reliable results for elements such as Al, Si, P, S, K, Ca, Ti, Fe and Mn. Elements such as Sr, Rb and Zr were effectively measured setting the scanner at 30 kV and 1000 Ma with a PD thick filter. These instrument settings are recommended to obtain reliable data (Richter *et al.*, 2006).

The A6 core was analysed on a polished and smooth horizontal surface to allow for the scanner prism to sit flat on the surface of the sediment, thereby reducing the presence of air which may cause interference on the spectral analysis. Where necessary, the sampling plan was adjusted to avoid fracture areas. Prior to analysis, the scanner was calibrated and optimized for data quality and noise reduction. Voltage (kV), current (mA) and filter settings were modified to obtain satisfactory X-ray excitation for a particular set of elements of interest.

XRF data obtained was processed using WinAxilBatch software. A processing model was selected to obtain counts for each element and WinAxilBatch calculated the element counts as peak integrals and applied background subtraction. Data quality was checked by examining the processed output data. Isolated high Chi-squared (X^2) values > 3 were deleted as they indicate a poor fitting between the scanner spectrum data and the mathematical model chosen for processing the data. Conversion of total counts per second (cps) values to absolute concentration was not attempted as the primary interest was the variation of element concentrations rather than absolute values. Elements such as Mo, V and Zn had very low cps close to the nominal sensitivity of the instrument and were, therefore, excluded from interpretation.

2.6 Total organic carbon (TOC)

Total carbon (TC) and TOC was determined using a Flash EA Analyser based at UCL. A total of 142 samples were obtained from the working halves of Well A6 core at a 1 m stratigraphic interval. Sampling took place from 230 to 88 m core depth. This section consists mainly of undeformed marlstones and thin to very-thin bedded turbidites and avoids the thrust situated at 71 m core depth. The interval between 88 and 71 m core depth was not sampled due to lack of available core material.

To obtain TC, approximately 30 mg of sample was weighed to obtain satisfactory CN chromatograph peaks. The analysis of TOC required 60 mg of sample which was treated with HCl 10% to remove inorganic carbonate content and then dried on a hot plate at 50°C for a minimum 12 hours prior to analysis. Standards were used at the beginning (to calibrate the equipment), during and at the end of the run to test for accuracy of the results. Total inorganic carbon (IC) was calculated from TOC and TC contents, and then converted to $\%CaCO_3$ following Equation 1.

$CaCO_3 = (TC-TOC) \times 8.333$ **Equation 1**

2.7 Stable carbon isotopes

Stable carbon isotopes of organic matter were measured in the UCL Bloomsbury Environmental Isotope Facility (BEIF) using a Flash EA 1112 mass spectrometer. The technique used for determination of $\delta^{13}C$ values is the EA-IRMS (Element Analysis - Isotope Ratio Mass Spectrometry). Preparation of the samples for stable carbon isotope analysis involved the treatment of the samples with HCl 10%. The high content of calcite cement in the samples required the use of at least three applications of HCl 10% to ensure digestion of all inorganic carbonate. The samples were centrifuged and the solution decanted. The samples were subsequently washed with de-ionised water (usually four to five times) and centrifuged until neutrality (pH = 7). The samples were then dried in a heater at 50°C for two days. Once dried, the samples were powdered with a mortar. Approximately 10mg of sample was required for analysis to obtain satisfactory peaks in the EA detector. Four separate sample runs were measured with five different standard samples covering a wide range of $\delta^{13}C$ values to monitor deviation, accuracy and reproducibility. This methodology allowed to determine carbon isotope ratios with a precision of 0.72%.

2.8 Scanning electron microscopy (SEM)

Only one polished thin section from the A6 core showing a 0.5 cm-thick, fine-grained sandstone turbidite surrounded by siltstone was carbon coated for examination in the scanning electron microscope. The instrument used was the Jeol JSM-6480 LV. This instrument uses a focused beam which emits high-energy electrons. When the beam hits the sample, it generates a variety of signals. The most common signals detected

are X-rays, secondary electrons and backscattered electrons (BSE). X-rays are produced by the inelastic collisions of the incident electrons with electrons in discrete orbitals of atoms in the sample. As the exited electrons return to lower energy states, they yield X-rays which are of a fixed wavelengths characteristic for each element in a mineral. Secondary electrons and BSE are used to generate images, SEM images and backscattered electron images (BEI), respectively. BEI are based on the differences in intensity of minerals reflecting their average atomic number. Thus, heavy minerals like pyrite will appear brighter than quartz and feldspar lighter than quartz in a greyscale. This technique was used to determine chemical compositions by performing analyses of selected point locations and to study textural relations on the sample. The BEI was used in combination with energy dispersive spectra where the peak position reflects a particular element and the peak intensity is proportional to the element concentration, allowing the identification of specific minerals. X-ray element mapping was also conducted to show the spatial distribution of elements in a sample. This technique was used to distinguish the elemental distribution between the siltstones and the sandstone turbidites.

2.9 X-ray power diffraction (XRD)

A total of 6 samples from the A6 core (two sandstone turbidites, two siltstones and two structureless mudstones) were analysed using X-Ray Diffraction (XRD). The instrument used was the PANalytical X'pert PRO MPD high-resolution powder diffractometer situated at UCL. The samples were powdered using a TEMA milling machine at 960 revolutions per minute for a period of 1 minute prior to analysis and then placed randomly in a holder. The diffractometer has a Cobalt anode X-ray tube and an incident beam which generates monochromatic X-rays. Scans were run at 40

kV and 30 Ma over a scanning range of 2° to 100°2θ, with a step time of 203 seconds and a step size of 0.01°2θ. Slits were 1 mm (divergence) and 0.1 mm (receiving). Digital data was processed using MacDiff software to smooth counts, determine background levels and calculate peak intensities and peak areas (total counts). Mineral identification was made by comparing measured diffraction peaks and intensities with standard reference patterns from the International Centre for diffraction Data (ICDD). As the intensity of the peaks can also be used to estimate the relative abundance of a mineral with accuracy which is generally $\leq$ 10% for major constituents (e.g., Johnson *et al.*, 1985; Fisher and Underwood, 1995), therefore, only the results from XRD were used to compare relative trends in the mineralogy of the A6 core rather than absolute values.

2.10 Thin section preparation

A total of eight 26 mm x 46 mm and 30 μm-thick thin sections from the A6 core were prepared at the UCL rock laboratory. Each core sample was first marked indicating the way-up direction and then sawn and trimmed down with a diamond saw to a chip size suitable for slice mounting, typically between 4 and 6 mm in thickness. The slices were trimmed so that when bonded to the glass slide a margin of at least 2 mm was maintained all around. The side of the chip from which the thin-section was cut was smoothed with a precision machine Lap to remove marks from the saw blade. The chip was then heated on a hot plate with the polished side upwards to avoid getting contaminated. A thin layer of low-viscosity epoxin resin was spread on the smoothed side of the warmed specimen with the frosted side of the slide then placed down on the epoxin. A slight pressure was exerted on the sample to expel any trapped bubbles and to ensure that the sample was well coated with epoxin. The slide and rock chip were

then placed in a bonding jig to ensure an even load. The sample was then left to cure for 30 minutes. The chip was then trimmed down to remove excess rock and to obtain a thickness of 30-50 µm using a diamond wafering motor saw. The specimens were then grinded to the correct 30 µm thickness using a precision machine Lap, ensuring smoothness and uniformity of thickness with all thin sections being studied using a reflected light microscope.

2.11 Magnetostratigraphy

Magnetostratigraphy is a geophysical technique which has been applied to sedimentology and stratigraphy to date sedimentary sequences.

The Earth's magnetic field is generated by the flowing of electrical currents created by convection of conductive molten iron in the outer core. The geomagnetic field created can be approximated to that of a magnetic dipole placed at the centre of the Earth with the dipole axis inclined at 11.5° to the Earth's rotational axis. This theoretical model is known as the Geocentric Axial Dipole (GAD) and can explain ~ 90% of the Earth's surface field. The remaining 10% is made of non-dipole magnetic components (Butler, 1992). The difference in the orientation axis of the magnetic dipole and the Earth's rotational axis results in the magnetic poles differing from the geographic poles (Figure 2.8).

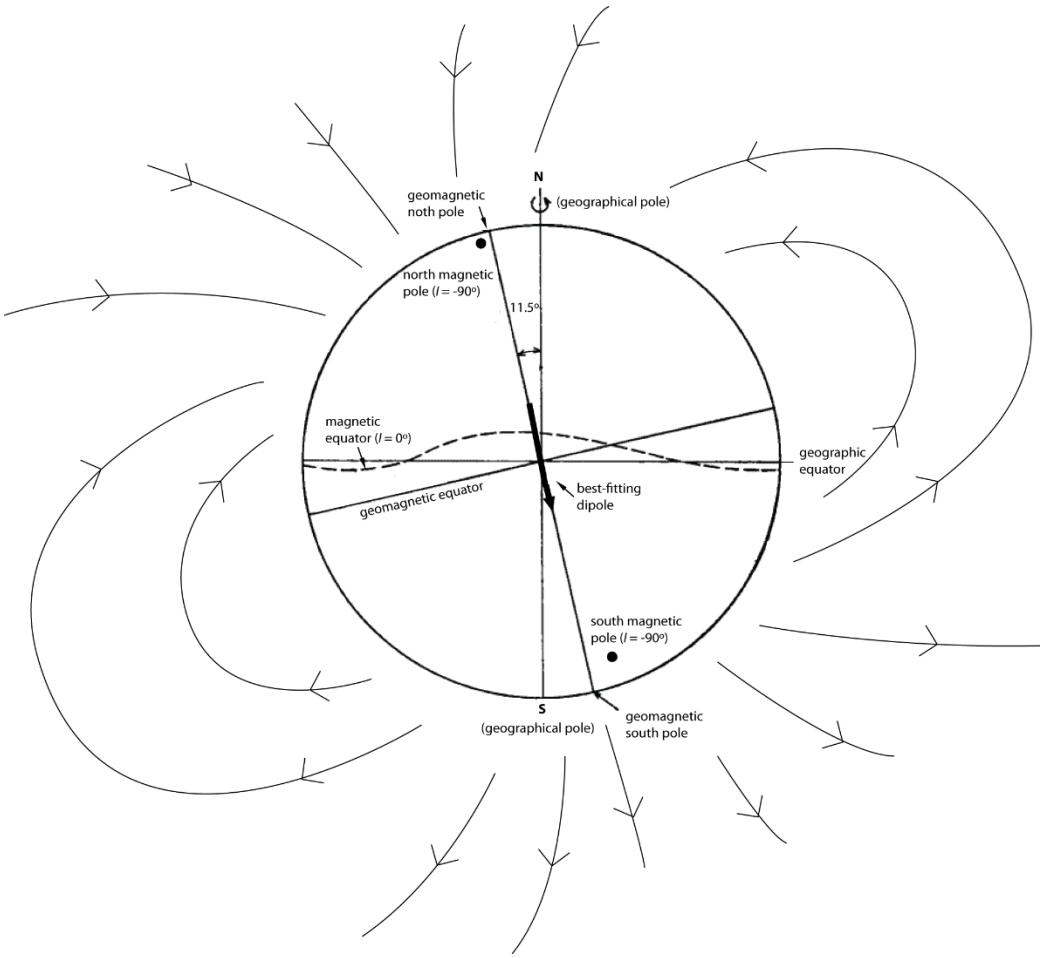

Figure 2.8 Geocentric Axial Dipole. The geocentric dipole is inclined and there is a difference of 11.5° between the geomagnetic and the geographical poles. Modified after Butler (1992).

The polarity of the Earth's magnetic field has reversed many times throughout geological history. These reversals happen simultaneously over the whole surface of the Earth. Polarity reversals occur at random intervals without a predictable pattern and each polarity interval can last from several thousand to millions of years. The causal mechanism of a magnetic reversal appears to be linked to flow instabilities in the outer core which can change the structure of the magnetic field. In order to reverse the magnetic field, the inner core must also reverse. For this to occur, the flow instabilities in the outer core must persist long enough (~ 3000 kyr) to cause the inner core to reverse by diffusion. Through geological time, there have been many aborted reversals with the geomagnetic pole moving towards the Equator (> 45°) for a short

period of time before moving backwards and aligning again with the Earth's spin axis. These transient changes in the geomagnetic pole direction are known as geomagnetic excursions and are believed to have resulted from the failure of the inner core to reverse (Gubbins, 1999). Magnetic reversals are well recorded across the entire globe but geomagnetic excursions are usually recorded at a more localised level.

The Geomagnetic Polarity Timescale (GPTS) records the history of reversals of the Earth's magnetic field and have been constructed from the analysis of magnetic anomalies measured in the ocean basins. This time scale consists of a series of black and white stripes which represent periods of time with normal and reverse polarities, respectively. The GPTS can be constructed back as far as ~ 200 Ma and have suffered many calibrations and updates over the years. The polarity observed in a stratigraphic sequence can be tied to the appropriate part of the GPTS. Often, this is achieved by including biostratigraphic work to have an estimation of the age of the rocks. If a polarity reversal is identified within a sedimentary sequence, a numerical age can be assigned to that stratigraphic interval. Figure 2.9 shows the GPTS scale during the Middle Eocene, between 40 and 48.5 Ma. Biostratigraphic studies suggest that the deep-marine sediments of the Ainsa Basin were deposited during this time interval (e.g., Pickering and Corregidor, 2005; Scotchman *et al.*, 2014). The time interval between polarity reversals is known as polarity chron. Each chron have assigned a letter, a number and a suffix. Sediments of the Cenozoic Era are preceded by the letter C, followed by the corresponding magnetic anomaly number (e.g., anomaly 22). This number is suffixed by the letter 'n' or 'r' to indicate normal or reverse polarity. The period between 40 and 48.5 Ma correspond to the chrons C18n to C21r and it records 7 polarity reversals (Figure 2.9).

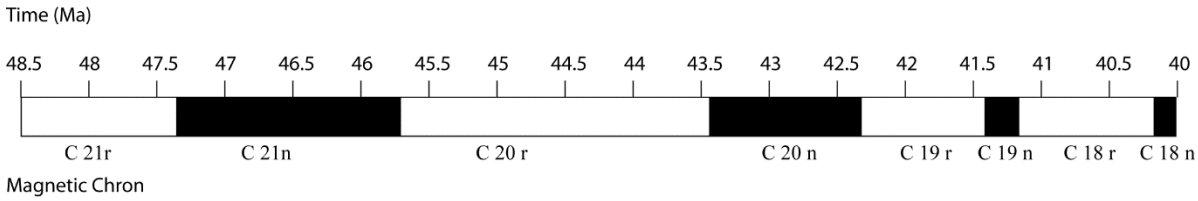

Figure 2.9 GPTS between 40 and 48.5 Myr. GPTS of Gradstein *et al.* (2012). This period corresponds to the chrons C18n to C21r. A total of 7 polarity reversals have been documented during this interval.

2.11.1 Primary and secondary remanent magnetisations

Rocks and sediments containing magnetic minerals acquire a natural remanent magnetisation (NRM) which reflects the direction of the Earth's magnetic polarity at the time of formation or deposition. At a later stage, these rocks can be subjected to other magnetisations known as secondary NRMs. These secondary NRMs can be misleading when trying to determine the original magnetisation of the rock and need to be stripped away from the rock samples by a stepwise process known as demagnetisation.

In sedimentary rocks, the most common types of NRM are detrital remanent magnetisation (detrital RM), viscous remanent magnetisation (viscous RM) and chemical remanent magnetisation (chemical RM).

Detrital RM is acquired when small grains of magnetic minerals settle through the water column and align themselves with the Earth's magnetic field during deposition. Verosub (1977) described how magnetisation can occur after deposition, as magnetic particles can still rotate within fluid-filled voids in the sediments. Once the water content in the sediment falls below a certain threshold, the grains are not able to rotate and the alignment of the particles is 'locked-in'. The magnetisation of the sample can be disturbed by processes such as those caused by burrowing organisms, which, may raise the water content of the sediment and cause further rotation of the magnetic particles, changing their original orientation (Bradley, 2013). These effects

usually occur at a localised level and the magnetic record of the rock should therefore be treated as an average directional value (Bradley, 2013).

Viscous RM is the change of the magnetisation vector in ferromagnetic minerals by being exposed to a magnetic field for a period of time. This type of magnetisation is considered a secondary NRM because it can obscure the record of the ancient geomagnetic field. The longer the exposure time, the stronger is the viscous RM. This type of magnetisation can also be developed unintentionally in the lab whilst measuring the NRM. In order to avoid this, measurements are made in magnetically shielded laboratories.

Chemical RM is acquired when new ferromagnetic minerals grow within the sediment in response to a changing chemical environment. These ferromagnetic minerals can result from the alteration of pre-existing minerals, or by precipitation of a ferromagnetic mineral from solution. As these newly-formed minerals grow, they can align to record the Earth's magnetic field. Depending on the timing of the mineral growth, chemical RM can act as a primary and/or secondary NRM.

2.11.2 Techniques of demagnetisation

Stepwise demagnetisation techniques are employed to isolate the primary NRM in a sample by selective removal of any secondary RM. The demagnetisation techniques used in this study include alternating field (AF) and thermal demagnetisation.

AF demagnetisation comprises the application of a decaying alternating magnetic field to a sample. The decaying AF results in a progressive reduction of the amplitude of each half-cycle. The resistance of a ferromagnetic mineral to become demagnetised is termed coercivity. The AF method results in the removal of any RM coercivity less than the peak intensity of the applied AF. Those magnetic particles with

coercivities lower than the applied field align themselves with the direction of the field, whilst the ones with greater coercivities will become fixed in direction. This process is repeated and will result in an equal number of grains being magnetised in the positive and in the negative direction resulting in a zero net remanent field in the sample. Secondary NRM is carried by grains that contain two or more magnetic domains (multi-domain grains) whereas primary RM is retained by single domain grains characterised by a stable magnetisation across the grain. Multi-domain grains have lower coercivities than single-domain grains and therefore are less resistant to demagnetisation. AF demagnetisation is an effective process to remove secondary RM, leaving the natural RM unaffected. Stepwise AF demagnetisation was undertaken using a 2-G Enterprises DC-SQUID (Superconducting Quantum Interference Device) cryogenic magnetometer based at Oxford University.

Thermal demagnetisation involves heating a sample to a high temperature until it reaches the grain blocking temperature and the sample demagnetises. Then, the sample is allowed to cool down to room temperature in a magnetically shielded environment to prevent the acquisition of secondary RM, especially chemical RM, as high temperatures may result in the chemical alteration of the sample and the growth of new ferromagnesian minerals.

The time it takes for a magnetic mineral to reach equilibrium with the surrounding magnetic field is called the relaxation time. The relaxation time depends on factors such as grain size and temperature. Grains with short relaxation times tend to have low blocking temperatures and are more prone to acquire secondary RM, whereas, grains with long relaxation times have higher blocking temperatures and are less likely to acquire secondary RM. Thermal demagnetisation can be an effective

process to remove secondary RM without affecting the primary RM carried by grains with longer relaxation times.

Thermal demagnetisation was used to demagnetise any magnetite or haematite present in the samples. This technique was undertaken at Oxford University in a magnetically shielded lab using a magnetic measurements thermal demagnetiser.

2.11.3 Sampling technique

Samples were collected at 10 m intervals over ~ 1 km of stratigraphy. The deep-marine systems sampled include the top of the Gerbe, the Banastón and the majority of the Ainsa System. A total of 4 sections were selected across the Ainsa Basin to gain samples from these systems. There is some stratigraphic overlapping in some of these sections. Sampling for magnetostratigraphy was carried out along the sections selected for spectral gamma-ray logging. Two different sampling methods techniques were used for the palaeomagnetic study in the Ainsa Basin: core drilling and hand sampling techniques.

2.11.3.1 Core drilling technique

Cores were drilled using a diamond tipped drill-bit. Ideally, cores were 6-7 cm in length but in more weathered sections this was not always possible and the cores were shorter (3-4 cm in length). Cores were oriented using a Brunton compass (accuracy ± 0.5°) mounted on an orienter. The orienter was placed into the drilled core hole leaving the cored sample still in situ. The compass was then levelled and the strike from the compass and the dip from the orienter were annotated. Sun compass readings were also taken where possible to correct for possible high magnetic intensities interfering with the compass needle. The top of the core was marked with a pencil and then extracted

with the help of a brass rod. Cores were then cleaned and marked. The mark at the top of the core was extended to the rest of the core forming a line with the help of the brass rod and ticks were drawn pointing down to show the dip direction of the core. Approximately 3-4 samples were collected per site. Mostly siltstones and very fine-grained sandstone turbidites were the preferred lithology which allowed for the extraction of longer cores.

2.11.3.2 Hand sampling technique

Due to damage of the drill, core drilling had to be discontinued at the end of the Boltaña section and a hand sampling technique was used instead to finalise this section and to sample the Forcaz and the Gerbe sections. Nevertheless, this sampling technique was considered the most appropriate to be used in the Forcaz and the Gerbe sections because they both are more difficult to access with steep slopes and are lacking a nearby water source needed to operate the drill. These two sections were characterised by more weathered areas which caused siltstones and finer lithologies to break more easily with the main lithology sampled being very-fine to fine-grained sandstone turbidites. Hand samples were oriented using a compass clinometer. The strike and dip of the surface was measured and it was marked with an arrow to the right and tick down-dip respectively. The sample was then hammered into a fist size block. Due to the weight of the collected samples using this technique only 2 samples were collected per site.

2.11.4 Sample preparation and magnetostratigraphic analysis

Sample preparation and analyses were completed at the Palaeomagnetic Laboratory at Oxford University. MSc geology student Kyrre Johansen prepared and analysed all the

samples collected as part of his Master's project under the supervision of Dr Conall MacNiocaill.

Hand specimens were converted into field cores by placing them in plaster and then drilling them to obtain cores. Cores were extracted with the help of a brass bar. The samples were then marked using the same technique as described for the drilled cores. All the core samples were cut into 2.5 cm sized core using a table saw and then cleaned and remarked. The NRM of each sample was recorded before undertaking any demagnetisation procedures. Samples were then demagnetised using AF and/or thermal demagnetisation.

AF demagnetisation used batches of 8 samples per run. In order to remove any secondary NRM components, the samples were exposed in a stepwise manner, to progressively higher peak fields up to 100 mT (Johansen, 2014). Thermal demagnetisation heated the samples using thermal treatment steps. The samples were heated rapidly at a rate of 30°C/min until a temperature of ~ 30°C below the desired peak temperature was achieved. Then, the samples were progressively heated at a slower rate of 10°C/min until reaching the peak temperature. This temperature was maintained for ~ 45 min and then the samples were cooled rapidly until they could be handled. Samples were rotated 180° between steps to prevent the influence of any possible field propagating in the furnace (Johansen, 2014).

Most of the samples were demagnetised by ~ 350°C (Johansen, 2014). This temperature is well below the Curie temperature of magnetite of 580°C. Above this temperature all NRM will be removed (Butler, 1992).

The field orientation of the samples were corrected by inserting the strike and dip into the 2G Magnetometer software and applying a tectonic correction factor. The data was analysed using the Super-IAPD2000. Anomalous peaks in magnetic

intensities were removed from the sample paths. The primary NRM was then obtained from the remaining data points by fitting lines using the LINEFIND function (Kent *et al.*, 1983). Statistical analysis were also implemented to test the reliability of the data (Johansen, 2014). Results were plotted in a Zijderveld plot (Z-plot), a stereonet and a plot of magnetic intensity (Johansen, 2014). Figure 2.10 shows a 3D representation of a Z-plot diagram.

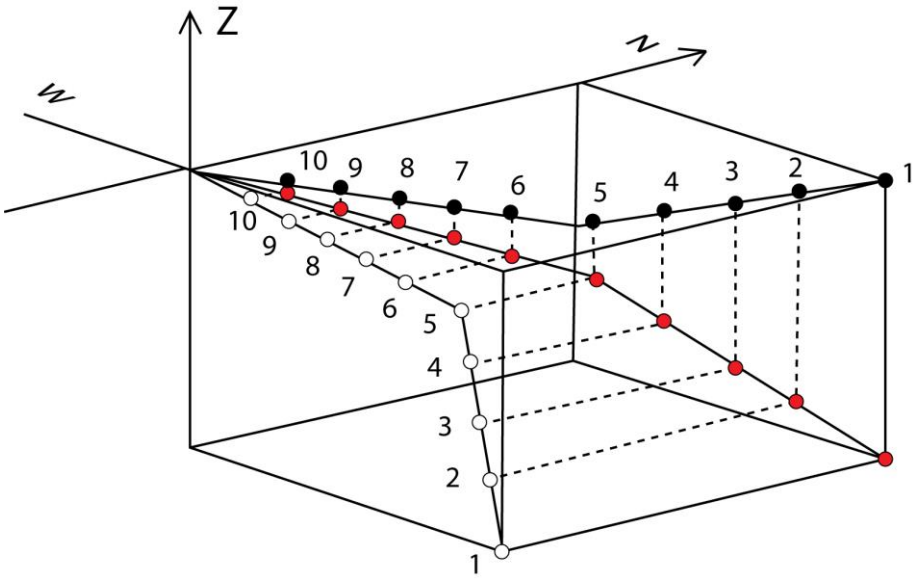

Figure 2.10 3D representation of a Zijderveld diagram. After Zijderveld (1967).

Z-plots are the standard method to represent the results of a stepwise demagnetization process. The direction and the intensity at each demagnetization step for a specific sample is represented by the direction and length of a vector in a 3D space. This vector is projected onto two planes at right angles of each other. Solid black symbols are projections of the vectors on a horizontal plane containing the axes NS and EW. The open symbols are the vectors projected on a vertical plane with axes NS and Up-Down. The NRM is placed at the origin of the coordinate system. The diagrams show the change in the direction of the vector during the progressive thermal or alternating field demagnetization process.

2.12 Cyclostratigraphy

Spectral analysis is an important tool in climate research because it allows the extraction of periodic signals from a dataset. The purpose of this analysis is to estimate the power spectrum (strength) of periodic components at all possible frequencies. The identification of cyclic patters within a time-series can then be related to environmental change. Time-series analysis was performed in the spectral gamma-ray field data and in the XRF and carbon isotopes records from the A6 core. A work-flow of the methods used for time-series analysis in this study can be seen in Figure 2.11.

2.12.1 Data conditioning

The data was processed prior to performing spectral analysis to reduce the likeliness that the resulting spectra would be influenced by mathematical artefacts (Weedon, 2005). Processing of the time-series included interpolation, detrending and the removal of outliers from the data. These parameters have the potential to cause distortion of the spectrum.

2.12.1.1 Interpolation

Some of the methods employed in this study to perform time-series analysis use a constant time interval or spacing to perform cyclostratigraphic calculations. Gaps in the spectral gamma-ray field data included unreachable areas within the selected sections and small-scale sediment slides, slumps, and other chaotic sediments, although the presence of these types of distorted sediments were very localised and never reached more than 40 cm in thickness.

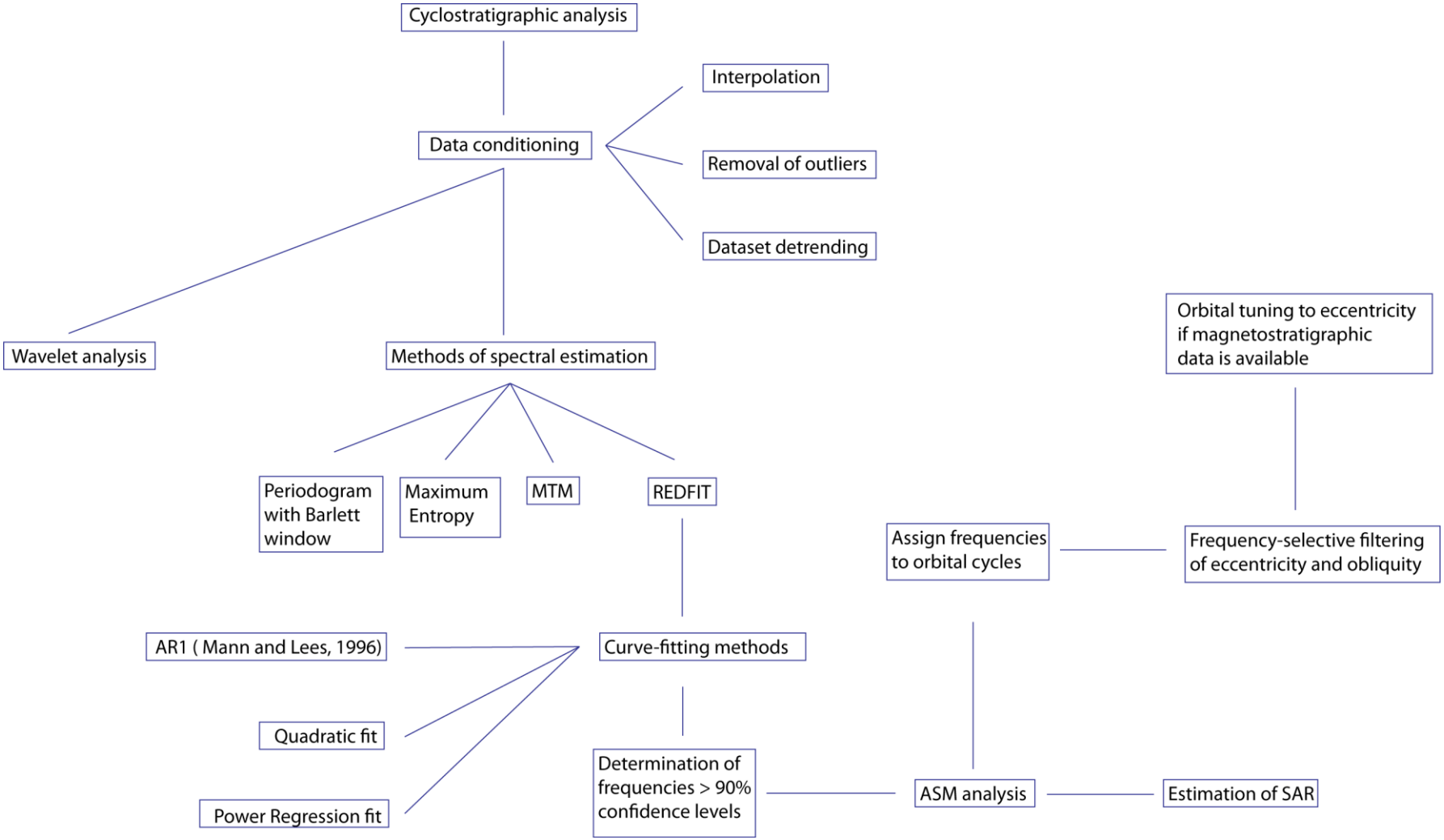

Figure 2.11 Work-flow of the cyclostratigraphic analysis used in this study.

Additional missing points can be added during removal of outliers (see Section 2.9.1.2). Most of the field sections are, however, continuous and if gaps were present, these constituted less than 0.5% of the total data points. Carbon isotope data was continuous and did not require any interpolation. XRF data from the A6 core contained relatively low percentages of missing data points associated with rocks fractures and interpolation was used to estimate the missing values from adjacent data. Different methods of interpolation have been summarised by Press *et al.* (1992) but the method used in this study was a simple linear interpolation which estimates the missing value by drawing a straight line between adjacent points. This method can introduce spurious high frequencies in the data because climatic time-series tend to possess a curved rather than a straight appearance and is not recommended when there is a lot of high-frequency noise (Weedon, 2005). However, it was considered adequate to apply this interpolation method due to the small percentage of missing points and because computations used with this method did not add new frequencies when compared with other methods of spectrum estimation which allowed unevenly-spaced datasets such as REDFIT.

2.12.1.2 Removal of outliers

Outliers are data points which have a very high or very low value, and are off from the range of the other data points. These points need to be removed from the time-series because they can cause severe distortion in the spectra and raise the level of high-frequency noise (Weedon, 2005).

Outliers were present in the XRF data usually associated with fractures. These outliers were removed and missing data was interpolated before applying time-series analysis computations.

2.12.1.3 Dataset detrending

The mean and the variance in a dataset should remain constant. If the time-series changes by progressively increasing or decreasing the trend of mean values over the length of the studied interval, interpretation of the spectrum would be difficult since the methods of spectral estimation treats the data as if it was untrended (Weedon, 2005).

The data was detrended by fitting a simple linear-square regression line to the data. Then the line was subtracted for each of the points of the series. This technique results in the trend and the mean being removed and the data oscillating around the zero line.

2.12.2 The discreet Fourier Transform

The Fourier Transform is a mathematical tool which can deconstruct any waveform into a sum of regular sine and cosine waves of different wavelengths and amplitudes. Sine and cosine waves form a set of orthogonal functions which can describe any time-series.

The frequencies investigated are defined by integer divisors of the number of data points in a time-series (N) multiplied by the sampling interval (SI). The higher frequency examined is the Nyquist frequency that is defined by Equation 2:

$$\text{Nyquist} = 2 \times SI \qquad \textbf{Equation 2}$$

The discreet Fourier Transform consists in multiplying every data point of the time-series by a cosine wave of a particular frequency. The results are added up and multiplied by a constant which is 2/N. This computation is then repeated, but,

this time the time-series is multiplied by a sine wave of the same frequency and the results are summed up and multiplied by the same constant. The final amplitude of the time-series is calculated by averaging the results of the sine and cosine products times two and divide them by N (Weedon, 2005).

The results of the discreet Fourier Transform are presented as power spectra analysis where the results of the relative amplitudes and wavelengths of all the regular components in the time-series are represented. The frequency (1/wavelength) of the cycles is plotted against the squared amplitude, referred to as power, as it represents energy per time interval. The higher the power, the greater the importance of a specific frequency in controlling the shape of the time-series.

The discreet Fourier Transform is a slow computation and a new numerical algorithm known as the Fast Fourier Transform (FFT) was developed to speed the time-series analysis (Press *et al.*, 1992). The application of the FFT has very rapidly extended to many fields within the science, mathematics and engineering domains.

2.12.3 Methods of spectral estimation

The spectrum of the outcrop gamma-ray data and the sandstone turbidite intensity of the A6 core have been calculated using four main methods: the periodogram, the maximum entropy, the multi-taper method (MTM) and the REDFIT methods. The MTM and the REDFIT methods have been extensively used in the literature to create time-series analysis of palaeoclimate data. The significant levels of the spectrum can easily be applied to both methods. The maximum entropy method has become more significant over the last few years as an applied method to palaeoclimatic data (e.g., Pardo-Igúzquina and Rodriguez-Tovar, 2006). One of the advantages of this method, as discussed further in Section 2.9.3.2, is that it has a

very high resolution in the frequency domain and therefore is suitable to use as a complementary method to the MTM and REDFIT to identify with accuracy the frequency of significant regular cycles. The periodogram does not constitute a reliable spectral method due to the problems discussed in Section 2.9.3.1, but many spectral estimation methods are based on this method (Weedon, 2005). The periodogram has therefore been included in this study to allow comparison of the estimated spectra with the other methods.

Figure 2.12 shows the spectrum estimation using the REDFIT, the MTM, the maximum entropy and the periodogram using a Barlett window for the eccentricity data between 50 and 40 Ma using the La2010a orbital solution of Laskar *et al.* (2011). Eccentricity amplitude variations between 50 and 40 Ma can be seen in Figure 1.13. These four methods identify the 3 main peaks associated with eccentricity cycles during the Middle Eocene at ~ 400, 123 and 95 kyr. Confidence levels have not been plotted. The establishment of confidence levels and the estimation of the background noise is further discussed in Section 2.9.4.

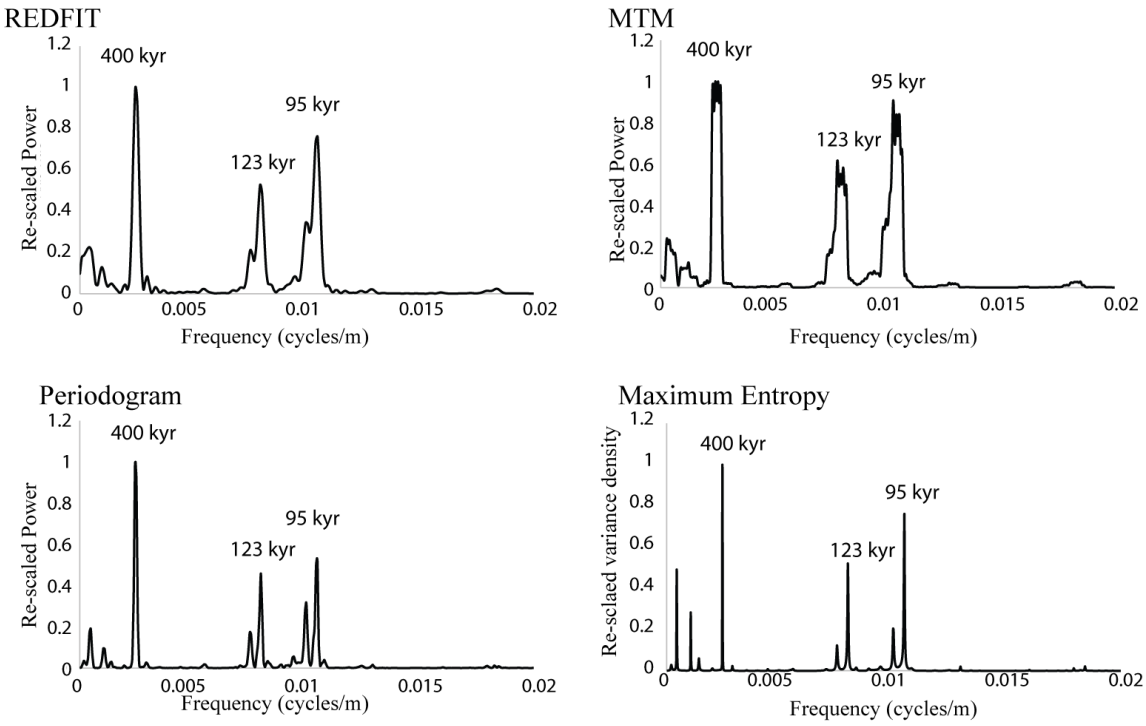

Figure 2.12 Time-series analysis of eccentricity using REDFIT, the MTM, the periodogram and the maximum entropy methods. Eccentricity data from the La2010a orbital solution of Laskar *et al.* (2011) between 50 and 40 Ma. REDFIT uses 6 WOSA segments and 8 degrees of freedom. MTM uses 6 tapers and ~ 12 degrees of freedom. The periodogram uses a Barlett window. The maximum entropy method uses number of lags M = N/3. See text for explanation.

2.12.3.1 The periodogram

The periodogram was invented by Schuster (1898) to estimate the spectral density of a spectra. The periodogram is the absolute value squared of the Fast Fourier Transform applied to evenly-spaced data. It forms the basis of many techniques in spectral estimation but should not be used for spectral analysis due to the spectral bias associated with this method (Weedon, 2005). The bias is caused by spectral leak and this bias is more significant if the time-series is short. Another problem associated with this method is the large variance of the spectrum. Increasing the number of data samples does not decrease the variance and this results in a general poor performance of the method. In order to improve performance of the

periodogram, the variance can be reduced by averaging (smoothing) using the Barlett method. This method was developed by Barlett (1948, 1950). The Barlett method consists of splitting the original time-series into a number of non-overlapping segments. For each of these segments a periodogram is calculated by computerising the square of the discreet Fourier Transform. The final spectrum is then calculated by averaging the estimates from the periodograms from each of the data segments. This method results in a reduction in the variance and the standard deviation but it also results in a reduction of the resolution when compared with other periodograms.

2.12.3.2 The maximum entropy method

The maximum entropy method (MEM) was first devised by Burg (1967, 1968). This method has been applied to astronomy, geophysics and other domains such as radar and speech processing. MEM has also been used in the analysis of climatic data (e.g., Currie and O'Brien, 1988; Pardo-Igúzquina and Rodriguez-Tovar, 2006; Laurent and Cai, 2007).

The MEM is considered a non-parametric method because it takes no assumption on the cyclicity of the data (Weedon, 2005). The MEM approximates the time-series by a linear autoregressive (AR) process (Percival and Walden, 1993). The order of the AR process is determined by the number of lags used (M). The MEM involves the calculation of the autocovariance sequence of the data out to the chosen lag M (Weedon, 2005). The choice of M determines the smoothness of the spectrum. The number of peaks in the spectrum increases with M regardless of the number of regular components present in the dataset and therefore the choice of an adequate M will have a great impact in the resulting maximum entropy spectrum.

The upper bound value of M is generally taken as N/2, with N being the number of data points in the time-series (Ghil *et al.*, 2002). M is more typically chosen between N/3 and N/20 (Weedon, 2005). The degrees of freedom in the time-series can be determined by N/M. The power associated with the spectral peaks is not determined by the spectral amplitude of the peak, but by the area under the curve.

This method has a high-frequency resolution and a good performance, especially when using in short time-series which has made it a popular method in cyclostratigraphic studies of climatic data (Pardo-Igúzquina and Rodriguez-Tovar, 2006). The main drawbacks of the MEM are the difficulty in assessing the statistical significance of the spectral peaks (Percival and Walden, 1993). Also, MEM can produce additional spectral peaks if time-series are non-stationary or not well approximated by an AR process which can result in errors by interpreting spurious peaks as having a physical origin. It is, therefore, recommended to use this method when reliable spectral peaks have been established with other methods to determine the significance of the MEM peaks (Ghil *et al.*, 2002; Weedon, 2005).

2.12.3.3 The multi-taper method (MTM)

The MTM is a common method employed to analyse palaeoclimatic records (Olsen and Kent, 1996; Mann and Lees, 1996; DeLong *et al.*, 2009; Wu *et al.*, 2012) The MTM is based on the periodogram. This method reduces the variance of spectral estimates of the periodogram by using a small set of orthogonal tapers or spectral windows. These tapers are constructed to minimise the spectral leakage (Percival and Walden, 1993). A set of independent estimates of the power spectrum is computed by multiplying the data by these orthogonal tapers. The resulting spectrum has well-supressed side-lobes which reduces the spectral bias and gives the spectrum

a smooth appearance. The number of tapers used are usually 4-8. The degrees of freedom doubles the number of tapers used (Percival and Walden, 1993). Therefore, in order to obtain a smooth spectrum a number of at least 8 degrees of freedom (4 tapers) is recommended. Weedon (2005) pointed out that this method has a tendency to produce flat-topped spectral peaks. An example of this effect can be observed in the MTM computation of eccentricity data in Figure 2.12. In this study most of the spectral gamma-ray data uses 4 tapers, but in shorter time-series, 4 tapers resulted in an over-smooth spectrum with flat-topped broad peaks which made difficult to estimate the significant frequencies. In these cases, the number of tapers were reduced to 3.

One of the drawbacks of this method is that it requires data evenly spaced in time, which may be problematic in most palaeoclimate datasets. In the presence of discontinuous data, interpolation of the data is necessary before computation. Interpolation introduces inevitable bias which can make it difficult to obtain an accurate estimate of the typical red-noise spectrum. The discontinuities present in the datasets used in this study are in general quite small. Therefore, interpolation errors associated with these discontinuities are likely to be small and the use of the MTM was considered adequate.

2.12.3.4 REDFIT method

The REDFIT algorithm was developed by Schulz and Mudelsee (2002). This method has been widely used in cyclostratigraphic analysis of palaeoclimatic data such as Stüben *et al.* (2003), Banerjee *et al.* (2010), Hodell *et al.* (2013) and Husson *et al.* (2014) among many others.

The REDFIT algorithm test peaks in the spectrum of a time-series against the red-noise background using a Gaussian first order autoregressive (AR1) process. An advantage of this method is that it can be used for unevenly-spaced data without the need to interpolate. This is done by applying the Lomb-Scargle Fourier Transform (LSFT; Lomb, 1976; Scargle, 1982, 1989) which is a derivative of the Discreet Fourier Transform adapted to even and unevenly-spaced data in combination with a Welch-Overlapped-Segment-Averaging Procedure (WOSA) (Welch, 1967). The WOSA algorithm divides a time-series into a number of n_{50} segments which overlap by 50% the final spectral estimate (Schulz and Mudelsee, 2002). The resulting spectrum is derived from averaging the n_{50} periodograms. The program SPECTRUM developed by Schulz and Stattegger (1997) was based on these computations. The REDFIT program adds to the SPECTRUM computations a bias correction of the LSFT which allows to overlie the spectrum calculated with a red-noise theoretical spectrum. The bias correction is calculated by running a number of randomly algorithms known as Monte Carlo simulations (N_{sim}) of red-noise spectra. The deviation of the average red-noise spectrum resulting from these calculations and the theoretical spectrum is used to calculate the bias correction. The number of Monte Carlo simulations established by default in the program are N_{sim} = 1,000. The oversampling factor (OFAC) determines the number of frequencies investigated in the LSFT. An OFAC of 4 is set as a default in the program and is considered a good compromise between computing time and the resulting smoothness of the spectrum (Schulz and Stattegger, 1997). A rectangular window which prevents the distortion of the time-series was used in the computation. The number of WOSA segments used was established in the majority of the analysis to 6 which resulted in a spectrum with 8 degrees of freedom. In those cases where the time-series were too

short, the WOSA segments were reduced to 4 or 5 which resulted in a spectrum with 5 and 6 degrees of freedom, respectively.

2.12.4 Curve-fitting models

Different curve-fitting models were tested to approximate the spectral background of the power spectrum. Inadequate models which do not approximate the spectral background shape can cause unrealistically high significance spectral frequencies which may have a negative impact on the interpretation of the data (Weedon, 2005). The different methods tested include the autoregressive model developed by Mann and Lees (1996), a quadratic and a power regression model. These three noise methods are well recognised in palaeoclimatology (Weedon, 2005). A spreadsheet was generated for each dataset and for the three methods tested. The method which appears to have the least deviation error in most of the time-series analysed in this study is the power regression method. This method uses the log power *versus* log frequency plot for distinguishing spectral peaks from the spectral background (Wunsch, 2000).

Figure 2.13 shows the three curve-fitting methods tested on the K spectrum of the outcrop spectral gamma-ray data of the Forcaz section. The method which contains a minor deviation error is the power regression method. The autoregressive model shows a good fit but the deviation error is higher than the power regression. The quadratic method does not fit well the background levels due to the presence of very strong spectral peaks at low-frequencies.

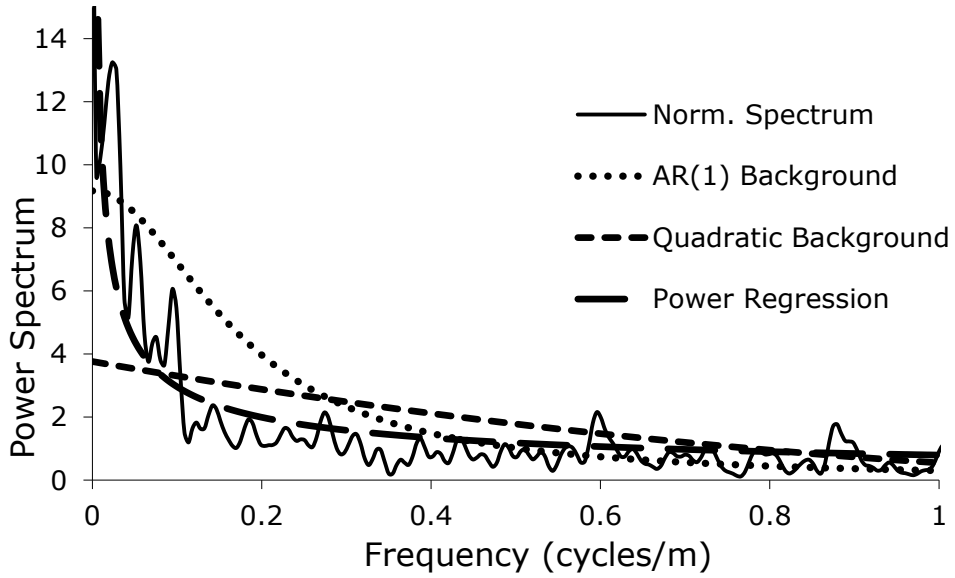

Curve Fitting method	Summative Square Error
AR(1) (Mann and Lees, 1996)	796
Quadratic fit	1082
Power regression	325

Figure 2.13 Comparison of difference curve-fitting methods for the K spectrum of the Forcaz section. The fitting-method with a lower summative square error is the power regression method.

2.12.5 Average spectral misfit

The Average spectral misfit (ASM) method was developed by Meyers and Sageman (2007) and is a useful method in palaeoclimatology when applied to records which lack adequate radiometric time control. The ASM method provides a quantitative evaluation of how well the time-series results fit the predicted orbital parameters. These orbital parameters are calculated from equations derived by Berger *et al.* (1992).

The frequencies used to determine SARs in the ASM analysis are those frequencies present in the REDFIT spectrum with confidence levels > 90%. This confidence level was chosen to isolate significant frequencies as recommended by the method of Meyers and Sageman (2007). Since there is very little variation in the

orbital periods between 40 and 50 Ma (Table 1.2), all the analyses used in this study have been carried out using the orbital parameters established at ~ 45 Ma using Berger *et al.* (1992) equations.

The ASM method uses these significant frequencies to conduct thousands (e.g., 100,000) Monte Carlo simulations over a range of plausible SARs which were chosen between 5 and 100 cm/kyr with an increment of 0.5 cm/kyr. This range of SARs was considered adequate for the sediments of the Ainsa Basin based on previous SARs estimations by Heard *et al.* (2008); Pickering and Corregidor (2005), Pickering and Bayliss (2009) and Scotchman (2012) which estimated average SARs between 30 and 40 cm/kyr (see Section 1.2.4.8). The average spectral misfit is then calculated for every SAR of interest. The method is complemented with the estimation of critical significant levels of rejection above which the null hypothesis (no orbital cyclicity) is rejected. The critical level in all the ASM analysis is 0.52%. Only the SARs which have a significant level lower than the critical level have been considered. The period duration of each of the frequencies has been calculated for each of the significant SARs in order to visualise the best fit possible to the Middle Eocene orbital parameters. The spectral frequencies present in more than one spectrum and with confidence levels > 90% are more likely to represent a physical process than those only present in one spectrum or with lower confidence levels. Therefore, when deciding the most adequate SAR, this argument has been taken into consideration and discussed individually for each of the gamma-ray sections.

2.12.6 Wavelet analysis

Wavelet analysis is becoming widely used for signal processing and analysis of ancient climatic records and other geological processes (Meyers *et al.*, 1993; Lau and Weng, 1995; Prokoph, and Barthelmes, 1996; Barrucand *et al.*, 2006). Wavelet analysis is a useful tool to analyse time-series with non-stationary changes in frequency (Torrence and Compo, 1998) because it divides a continuous time-series into segmented time-frequency components and therefore, not only is able to determine the dominant cyclic components at specific wavelengths in the data but also identify changes of variability of these components in time (Torrence and Compo, 1998). This analysis, therefore, permits to characterise whether signals have a significant amplitude throughout the whole of the dataset or if they are only present at certain intervals (Kumar and Foufoula-Georgiou, 1997). This signal characterisation in the time domain is an advantage over the Fourier Transform which can recognise all the frequencies present in a dataset but is unable to determine how these signal vary as a function of time.

Wavelets are orthogonal functions of finite length with varying amplitude which begins at zero, increases and then decreases back to zero, rather than being maintained stable indefinitely. An example of a wavelet can be seen in Figure 2.14. A wavelet transform is produced by multiplication of a wavelet in a time-series. Different shapes of wavelets can be applied to the time-series and these are known as mother wavelets. The resulting wavelet transform is represented by a finite number of daughter wavelets which are copies of the mother wavelet, but, have been scaled (stretched or compressed) and translated at different stratigraphic positions or time periods to match the time-series using an appropriate coefficient. A correlation coefficient can, therefore, be calculated for every scale and every time (interval).

Computations at one scale will construct rows in the time-scale plane and computations at different scales construct columns in the time-scale plane. As a result of these computations, a contour plot can be constructed and is illustrated in Figure 2.15.

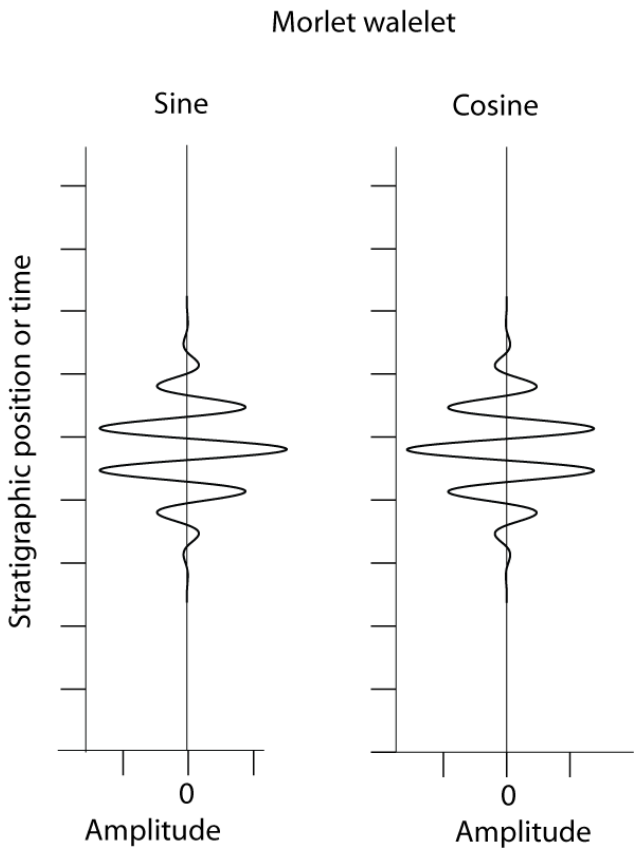

Figure 2.14 Morlet mother wavelet. The figure shows a Morlet mother wavelet containing five oscillations. Modified after Weedon (2005).

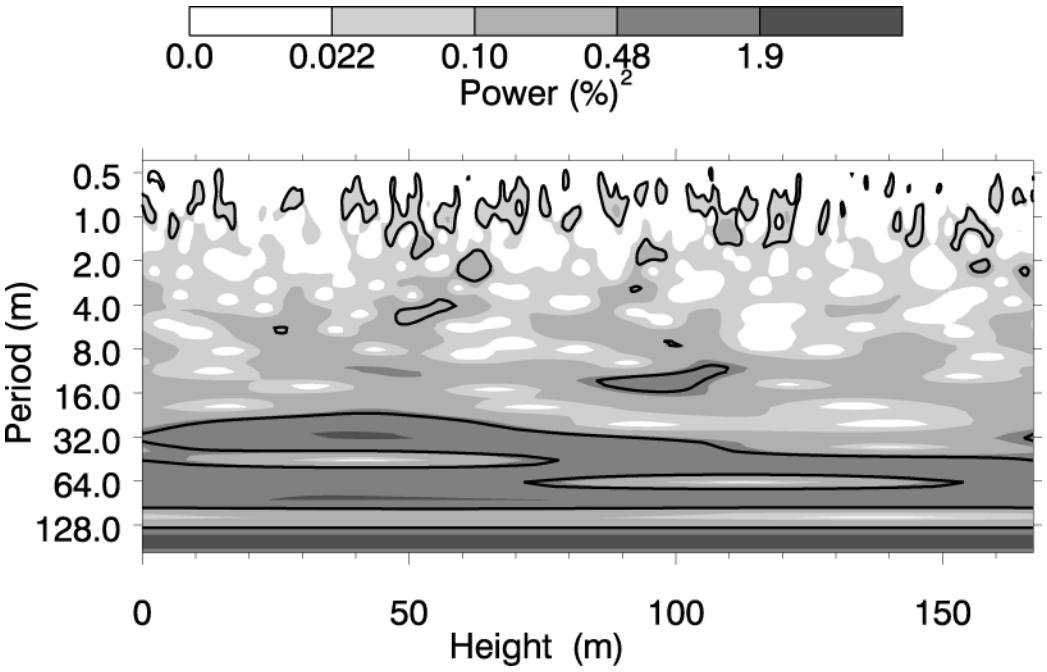

Figure 2.15 Wavelet analysis contour plot. Time here is represented as stratigraphic height (m) and frequencies can be established by applying the relation frequency =1/period. The grey scaled colours represent the amplitude (power of the signal) with the black contours indicating the 10% significance regions. Computations used the online tool http://paos.colorado.edu.research/wavelets.

The data is analysed using a time-frequency wavelet tiling (Figure 2.16). Wavelet tiling consists in filtering the time-series analysis into low and high-frequency components. The high-frequency component is multiplied by the smallest scale version of the mother wavelet chosen. Then, the low-frequency component of the time-series is again divided into high and low-frequency components and the high-frequency component is been multiplied by a larger scaled mother wavelet. This process is repeated until the lowest frequency component of the time-series is transformed. This process causes that at low frequencies, there is a good frequency resolution (the height of the boxes are shorter) but poor time resolution (the width of the boxes are longer). At high frequencies, the resolution is inversed with good time resolution but poor frequency resolution.

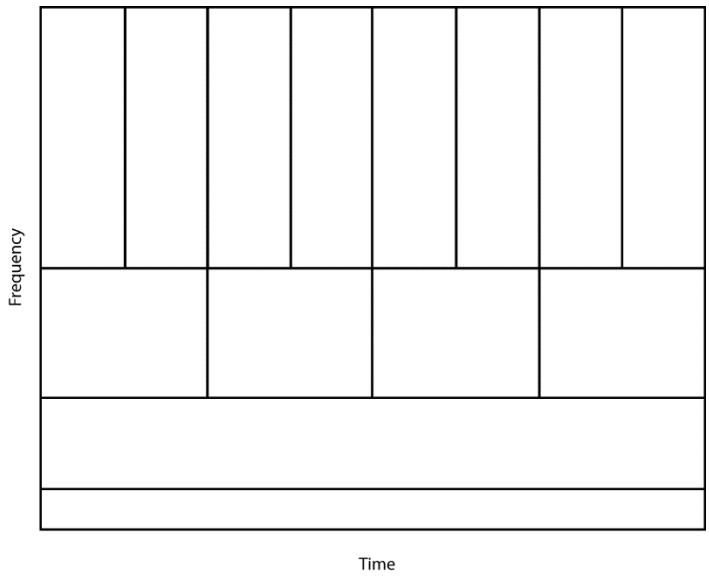

Figure 2.16 Wavelet tiling. This figure shows the data compartmentation in the time-frequency plane during wavelet analysis. At low frequencies the frequency resolution is good (the height of the boxes is small) but it has a poor time resolution (width of the boxes is large and is not possible to specify the exact value of time). At lower frequencies the frequency resolution gets poorer but the time resolution improves. Modified from Weedon (2005).

Significant levels in the wavelet analysis can be determined by adjusting an appropriate noise background levels to the dataset. Any peak which is significantly above the background spectrum is assumed to be a real feature with a certain confidence level which is calculated using a chi-squared distribution. This is achieved by multiplying the background level to a chi-squared value which corresponds to the confidence level aimed to calculate.

2.12.6.1 Wavelet analysis parameters

The K, Th, total-gamma, sandstone turbidite intensity and major and minor chemical elements datasets acquired from outcrop spectral gamma-ray studies, sedimentary logging analysis and elemental analysis of core data using XRF scanning were

applied to a fast wavelet transform computation using the online tool available at http://paos.colorado.edu.research/wavelets. This tool is based upon the mathematical algorithms of Torrence and Compo (1998). There are a number of parameters that need to be set to perform the calculations and are summarised in Table 2.2.

Table 2.2 Wavelet analysis parameters.

Wavelet parameters	Wavelet type	Morlet
	Wave number	6
	Scale width and start scale	Varied depending on dataset
	Powers of two	11
	Pad with zeroes	No
	Cone of influence	No
Significance	Background spectrum	Red noise
	Significance level	10%

(a) Wavelet shape

Lau and Weng (1995) have suggested that best results in the wavelet analysis are achieved when the chosen mother wavelet has a shape which contains certain resemblance to the signal results. The mother wavelet chosen to perform wavelet analysis on field and laboratory-based time-series is the Morlet wavelet. The Morlet wavelet is a continuous wavelet which consists of a plane wave modified by a Gaussian envelope. The shape of this wavelet is characterised by a constant wavelength and is ideally employed in wavelike time-series to capture oscillatory behaviour. This type of wavelet has been commonly applied to climatic cyclostratigraphic studies (e.g., Lau and Weng, 1995; Prokoph and Barthelmes, 1996). The Morlet wavelet is a complex wavelet function which combines positive and negative peaks into a single broad peak and can provide information on both,

time-dependent amplitude and phase for different frequencies (Lau and Weng, 1995).

(b) Wave number

The wave number is the number of oscillations within the wavelet itself. A number of 6 is recommended as the errors due to non-zero mean are smaller (Farge, 1992; Torrence and Compo, 1998).

(c) Scaling parameters

Setting adequate scaling parameters is important to ensure that all the frequencies present in the time-series are sampled. Start scales define the smallest scale which can be resolved. At a sampling interval of 0.2 m in the field data, the smallest resolvable scale is $2\ \delta t = 0.4$ m. Different parameters were used until adequate frequency ranges were achieved. The resulting resolution of the wavelet analysis will depend on the chosen width of the wavelet function (Torrence and Compo, 1998). It is desirable that the wavelet width shows a good balance between the width of the wavelet in real space and in Fourier space. A narrow wavelet will have good time resolution but poor frequency resolution, while a broad wavelet will have the opposite effects with a poor time resolution but a good frequency resolution. Different parameters were investigated to determine the best value of wavelet width for each of the datasets. This value was maintained below 0.5 which is the largest value that still gives adequate sampling in scale in the Morlet wavelet.

(d) Number of scales

The number of scales used in the computation of the wavelet transform is written as fractional powers of two. The number of scales used was maintained at 11 which is the default value in the Torrence and Compo (1998) wavelet algorithm.

(e) Pad with zeroes and cone of influence

Wavelet computations can result in errors at the beginning and at the end of the time-series. These errors are associated with edge effects produced by the Fourier Transform dealing with a finite length of the dataset. Torrence and Compo (1998) have recommended padding at the beginning and at the end of the time-series with zeroes and then removing them using a cone of influence once the wavelet transform has been produced. However, as the authors discuss, this approach can also result in errors since it introduces discontinuities at the endpoints and also affects the amplitude near the edges.

(f) Significance parameters

A red noise background characterised by an increase in power with decreasing frequencies is the most likely background noise associated with climatic data (Mann and Lees, 1996) and therefore a red noise wavelet power spectra has been applied to all the wavelet analysis. The significance level chosen is 10% which refers to a confidence level > 90%. A black contour line in the wavelet plot image marks the 10% significance region.

2.9.6.2 Wavelet analysis parameters used in this study

Wavelet studies in the gamma-ray logged sections have been performed on sandstone turbidite intensity, K, total gamma and Th records. The continuous wavelet transform has been produced by applying the mathematical algorithms developed by Torrence and Compo (1998) available at http://paos.colorado.edu/reserach/wavelets. All the analysed records have been detrended and interpolated prior to computation. The mother wavelet selected is the Morlet wavelet and a wave number of 6 have been applied to the computation. A scale width of 0.1 and 11 powers-of-two have been considered adequate to obtain good resolution wavelet analysis. Data has not been padded with zeroes and therefore a cone of influence has not been used. A red noise background has been set with a significance level established at 10%.

2.12.7 Frequency-selective filtering

Filtering is a helpful tool in spectral studies which involves manipulation of the time-series in order to isolate the signal from the noise. There are different procedures to achieve a filtered time-series. One of the most common used in cyclostratigraphic studies is frequency-selective filtering which involves the isolation of some bands of frequencies which are of interest from those which are not. Frequency-selective filtering includes high-pass, low-pass and band-pass filtering. The high-pass filters reduce the low-frequency variations and leave the high-frequency variations unaffected. Low-pass filters eliminate or reduce high-frequency variations and band-pass filters out low and high frequencies and leave a narrow band of middle frequencies unaltered. In this study, low-pass filters and band-pass filters have been used to analyse the time-series.

2.12.7.1 Low-pass filters

A simple type of low-pass filter which can be used in signal processing is the simple moving average method. This filter is a type of convolution which can be used in unevenly-spaced records. The moving average filter averages a number of points from the original data to produce a new point in the filtered signal. A filtered record is created by moving one point along the original data at each step. Because this filter removes the high-frequency variance, the filtered records have a lower variance than the original time-series.

This type of filter is very effective at reducing white random noise whilst keeping a sharp step response. The higher the number of averaged points (weight number) used, the higher the reduction of the noise. For instance, a weight-5 moving average reduces the noise by a factor of two and a weight-100 moving average reduces the noise by a factor of ten. One of the drawbacks of this method is that the filtered record is shorter than the original time-series. This is because points are loss at the beginning and at the end of the record due to the requirements of the start-up values. The total value lost from each end depends on the number of average points (n) used to filter the time series being (n-1)/2. For instance, a 5-weight moving average filtered series has a centred value at point 3 of the original time series and would result in 2 points lost at the beginning and at the end of the time-series. The shortening effect can cause undesirable effects such as shifting values in relation to their original position in the time-series. Therefore, it is important to keep a balance between noise reduction and reduction in the length of the filtered time-series. The simple moving average used in this study uses a 5-weight value to low-band pass filter K, Th, U, Th/U and Th/K spectral field data, a 3-weight value to low-band

filter TOC and $CaCO_3$ data from core study and a 25-weight value to low-pass filter XRF data obtained from the A6 core using a sampling interval of 4 cm.

2.12.7.2 Band-pass filters

Band-pass filters are used to isolate individual frequencies or a small and delimited range of frequencies. These filters are useful in cyclostratigraphic studies because they can show the amplitude of the signal and reflect the changing importance over time of individual frequencies in the records.

Weedon (2005) suggested that only frequencies which form statistically significant peaks in the time-series spectrum should be used for band-pass filtering. The reason for this is that filtering non-statistically significant frequencies may give a faux impression of regular cyclicity.

The frequencies which have been employed in this study to filter the total gamma-ray records are those frequencies which consistently appear in all or at least in the majority of the REDFIT spectra of the analysed data with confidence levels > 90% and which have been associated with eccentricity and obliquity orbital cycles using a combination of spectral techniques such as REDFIT, ASM and wavelet analysis. Total-gamma records have been chosen as the time-series records suitable for band-pass filtering because they tend to consistently show all the frequencies associated with orbital cycles. Sandstone turbidite intensity records have not been used because they strongly depend on outcrop exposure and weathered areas can affect the quality of the records. Th and U records are generally very noisy and cyclic trends are more difficult to visualise. K records usually show the same frequencies as the total-gamma records but the amplitude of the spectral peaks are lower and found at lower confidence levels and have therefore not been filtered.

The program used for filtering is the Macintosh program Analyseries 2.0.3 (Paillard *et al.*, 1996). This program uses a band-pass Gaussian filter which modifies the original data by convolution with a Gaussian probability density function. This Gaussian function is centred at the specified frequency and the width of the function is determined by the filter bandwidth. The bandwidth used is the same as the one determined by spectral analysis using REDFIT. This bandwidth varies for each of the datasets but all the values range between 0.01-0.07 cycles/m. The filtered record is shown on top of the original data, using the same amplitude scale so it allows for a better comparison between the original data and the filtered records. Figure 2.17 shows an example of frequency-selective filtering by using an artificially created time-series.

(a)

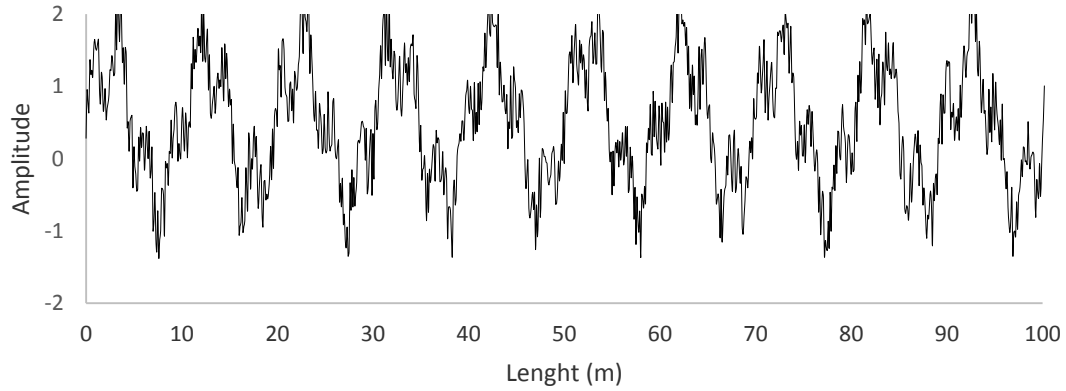

(b)

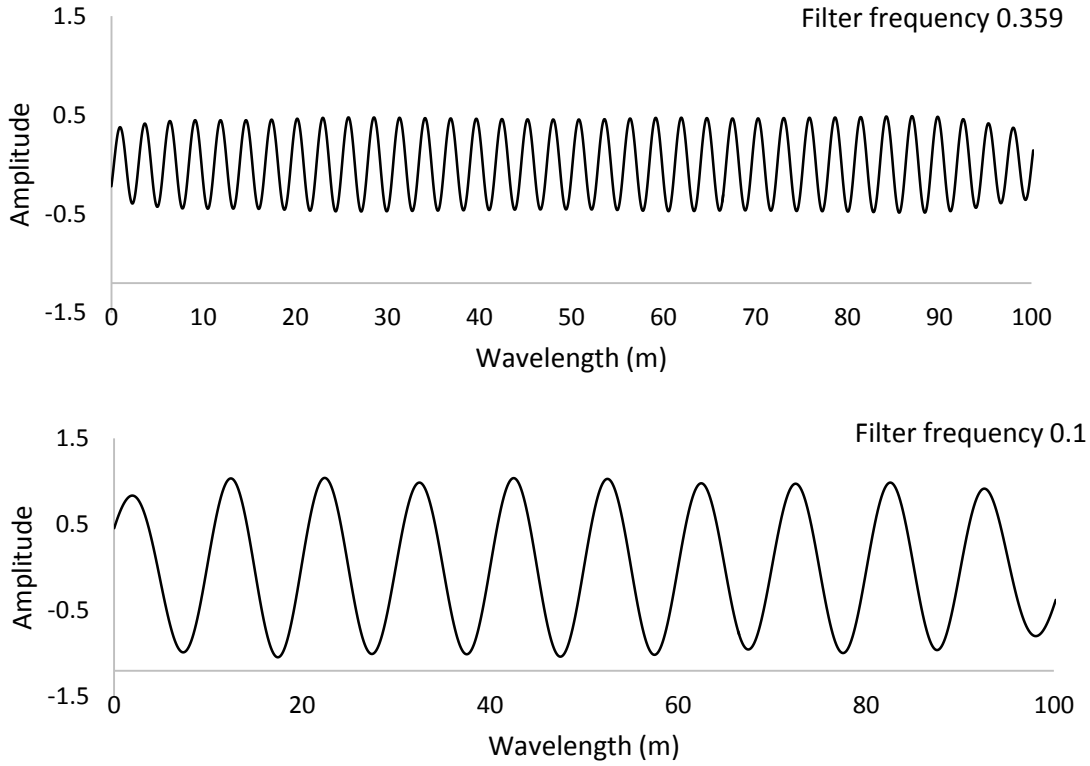

Figure 2.17 Frequency-selective filtering. (a) Time-series artificially created by adding two sinusoids and some random noise. The first sinusoid has a wavelength of 2.78 m and an amplitude of 0.5 and the second sinusoid has a wavelength of 10 m and an amplitude of 1. **(b)** Frequency-selective filtering at 0.1cycles/m (1/10 m) and 0.359cycles/m (1/2.78 m) of the time-series using the program Analyseries 2.0.3 (Paillard *et al.*, 1996) shows the presence of the two components with different amplitudes.

2.12.8 Orbital tuning

Orbital tuning is a method that can be used to refine the time scale of the time-series. This method consists in aligning the geological records to the calculated orbital periodicities of Milankovitch cycles. Since most of the geological records are in depth, this is a very useful method to obtain numerical ages from the records. Orbital tuning was first used by Hays *et al.* (1976) and since then, many other authors have followed (e.g., Imbrie *et al.*, 1984; Gale *et al.*, 1999; Bender, 2002; Weedon *et al.*, 2004; Lisiecki and Raymo, 2005; Westerhold *et al.*, 2013).

However, the development of an accurate orbital time-scale is influenced by the presence of temporal gaps in the stratigraphic record. These temporal gaps are the result of periods of erosion or non-deposition. Scouring by bottom currents or by erosive turbidites can lead to the removal of sediments and the formation of sedimentary hiatus in deep-marine basins. These chronostratigraphic gaps may not always be reflected in the biostratigraphy or in the sedimentological character of the strata (e.g., presence of erosional surfaces or abrupt changes in facies). Significant chronostratigraphic gaps can result in the distortion of the time-series resulting in the lost of periodicity of the orbital signals (Weedon, 1989; Meyers *et al*., 2001). Other sources of error which can effect the original cyclical signal in deep-marine hemipelagic sediments is the variation in sediment accumulation rates, sediment mixing on the seafloor, either through the movement of bottom currents or as a result of bioturbation (e.g., Walker, 2005).

Although small temporal gaps in the stratigraphy of the Ainsa Basin are possible and may contribute to an increase in the signal-to-noise ratio and distortion of the time-series in some of the sedimentary successions analised, absolute dating methods such as biostratigraphy (Scotchman et al., 2014) in combination with

magnetostratigraphy (Chapter 3) do not suggest major stratigraphic gaps or unconformities present in the stratigraphy of the basin.

2.12.8.1 Orbital tuning methodology

Orbital tuning of palaeoclimatic records consists first in band-pass filtering the records to the frequencies which are significant in the time-series and have been associated with orbital periodicities. The frequencies which have been linked to eccentricity, obliquity and precession can be compared with the orbital history of eccentricity, obliquity and precession, respectively. The tuning target of old cyclostratigraphic records is the orbital solution (e.g., Laskar *et al.*, 2004, 2011) for that time interval. In the absence of accurate radiometric dates, counting the regular cycles in the filtered records can also be used to refine the geological timescale. This strategy which is known as interval dating to differentiate it from absolute dating (Weedon *et al.*, 1997), allows the estimation of the duration of a geological record.

The best evidence which shows that orbital tuning has been successful and that the time scale is accurate is reflected if there is a significant increase and sharpening of the orbital-frequency bands which have not been tuned (Imbrie *et al.*, 1984, Hilgen *et al*., 1993; Karner *et al*., 2002). For instance, successful orbital tuning may cause obliquity cycles to be strengthened and showed an increase in spectral power when the records are tuned to eccentricity. However, authors have highlighted that coherency can also occur when the record has been aligned to the wrong set of orbital cycles or to the wrong part of the orbital history (Neeman, 1993; Shackleton, 1995; Weedon, 2005; Huybers and Aharonson, 2010).

Muller and MacDonald (2000) have discussed the risks of over-tuning the time-series records to match the target curve. For instance, manipulating the data to

match the target orbital curve may result in unphysical SARs. It is important therefore to reduce the number of tuning points to a minimum and to check for each interval that SARs are consistent and do not show large spikes in the time-depth plot.

The time-series analysis of field data has been tuned to eccentricity since this cycle seems to be dominant in most of the time-series analysis. Stratigraphic sections such as the Sieste and Guaso sections which are only 40 m in length or Labuerda section 1 which is 93 m long but has a much higher SAR (~ 41 cm/kyr) are too short to be able to establish eccentricity cycles with confidence. Weedon (2005) has argued that for a frequency to be detected with accuracy in the time-series, at least 4-5 cycles should be present in the records. Also, the Tierrantona section in the Arro System has not been tuned because there is a very poor radiometric control with no biostratigraphic or palaeomagnetic studies undertaken in this system. It is also very difficult to establish where in the stratigraphy of the Ainsa Basin this section is located, due to complex tectonic deformation in the Arro System. In the Morillo-reservoir and Morillo-Bruello sections located in the Morillo and Guaso systems respectively, only age determinations using biostratigraphic studies are available. Since the radiometric control in these sections is poorer, orbital tuning has not been attempted. The Gerbe, Labuerda 1 and 2, Boltaña and Forcaz sections have a good radiometric age control from biostratigraphic studies (Scotchman *et al.*, 2014) and magnetostratigraphic studies (Chapter 3). The two identified polarity reversals in the Gerbe I and in the Labuerda section 2 have enabled the orbital tuning of these sections to the eccentricity curves of the Middle Eocene.

Orbital tuning has been performed by comparing the total-gamma records filtered to the frequency associated with eccentricity (from REDFIT and ASM spectral analysis) to the historical eccentricity curves using the La2010a orbital solution of Laskar *et al.* (2011). The total-gamma records have been preferred over the other analysed records such as K, Th and sandstone turbidite intensity for reasons given in Section 2.9.7.2. The control or anchor points used in the total-gamma filtered records are the depth points which constitute the top of each of the filtered cycles. These depth points have been matched with the eccentricity maxima points in the La2010a orbital solution of Laskar *et al.* (2011). In those cases where the top of the cycles in the total-gamma filtered records have a poorly defined curve shape, then the anchor points used are the lowest point in the cycle and these have been matched to eccentricity minima in the La2010a orbital solution of Laskar *et al.* (2010). The rest of the depth points in the total natural gamma time-series have been matched to absolute time by using a simple linear interpolation between anchor points.

Chapter 3

Magnetostratigraphy in the Ainsa Basin

3.1 Introduction and objectives

This chapter presents magnetostratigraphic work undertaken in the Ainsa Basin through ~ 1 km of stratigraphy on the deep-marine sediments of the Upper Hecho Group. The assessment of age-dating for the Ainsa Basin fill has been the focus of several biostratigraphic and magnetostratigraphic studies, although, most of them have been undertaken on the areas surrounding the basin. Magnetostratigraphic studies include the work of Mochales *et al.* (2012) in the shallow-marine sediments of the Boltaña Anticline and of Holl and Anastasio (1993) in the sediments of the Mediano Anticline. However, to date, no magnetostratigraphic study has been undertaken in the deep-marine sediments of the Ainsa Basin. As a consequence, there are still major uncertainties regarding the chronology of these sediments. This uncertainty also complicates the inter-basin correlation of the Upper Hecho Group sediments across the Tremp-Ager, Ainsa and Jaca basins.

The main objective of this chapter is to provide a magnetostratigraphically-constrained age model for the Ainsa Basin. This new age model can be used to test the accuracy in the age estimations of the recent biostratigraphic work of Scotchman *et al.* (2014) across the whole of the deep-marine stratigraphy of the basin. This study also permits improved sediment correlations by comparison with other age models undertaken in proximity to the basin or in nearby areas.

The absolute ages inferred from any polarity reversals identified in this study can also be used as anchor points to tune the gamma-ray logged records to orbital solutions to obtain a higher resolution age-model across the basin (Chapter 5).

Finally, results from this study, used in conjunction with cyclostratigraphic studies across the basin (Chapter 5) and high-resolution geochemical proxies undertaken on interfan sequences (Chapter 4), can help to understand the sedimentation history of the basin and to unravel the influence that climate and tectonics may have played in influencing the deposition of the sediments of the Ainsa Basin (Chapter 6).

3.2 Previous chronostratigraphic studies in the Ainsa Basin

The chronostratigraphy of the deep-marine sediments of the Ainsa Basin is largely based on correlations with shallow-marine successions from depositional systems along the margins of the basin (Holl and Anastasio, 1993; Bentham and Burbank, 1996; Payros *et al.*, 2009; Mochales *et al.*, 2012), or based on correlations with nearby basins such as the Graus-Tremp Basin (Serra-Kiel *et al.*, 1993; Nijman, 1998; Bentham and Burbank, 1996) and the Jaca Basin (Labaume *et al.*, 1985; Payros *et al.*, 1999; Oms *et al.*, 2003). Intra-basinal regional correlations are based mainly on the recognition of erosional truncations and unconformities with age estimates largely depending on the accuracy of these correlations. However, some correlations have proved to be controversial and contradict other chronostratigraphic studies. Inter-basinal correlations are also complicated by the fact that there is no general consensus on the stratigraphic nomenclature used for the various formation names. In addition, the Ainsa and Jaca basins are separated by the Boltaña Anticline where Hecho Group sediments are not represented, making it considerably more

difficult to establish correlations across these two basins (Das Gupta and Pickering, 2008).

There are a very limited number of chronostratigraphic studies published based on direct sampling of the deep-marine sediments of the Ainsa Basin. Some of these studies are limited to a specific stratigraphic interval including biostratigraphy studies undertaken by Pickering and Corregidor (2005) and Jones *et al.* (2005), restricted to the Ainsa System. The most complete biostratigraphic study in the Ainsa Basin has recently been undertaken by Scotchman *et al.* (2014). This study is based on high-resolution calcareous nannofossils and larger benthic foraminifera age determination with ~ 2 km of stratigraphy sampled across the Upper Hecho Group (Figure 1.9).

3.3 Stratigraphy sampled in this study

The methodology used in this magnetostratigraphic study is described in detail in Section 2.8. The study sampled ~ 1 km of stratigraphy at 10 m intervals and included the upper part of the Gerbe System and all of the Banastón and the Ainsa systems. Four magnetostratigraphic sections were selected across the basin to sample these systems. From oldest to youngest, these sections are: Gerbe, Labuerda, Boltaña and Forcaz. There is some degree of stratigraphic overlap between these sections to ensure that the entire stratigraphic interval was sampled. However, the degree of overlap is difficult to quantify since there is considerable lateral variability in the geometry of the sandbodies and interfan successions. Figure 3.1 shows the location of the magnetostratigraphic sections within the Ainsa Basin and Figure 3.2 shows the position of the magnetostratigraphic sections within the stratigraphy.

The magnetostratigraphic sections coincide with the outcrop spectral gamma-ray logged sections of similar name (Table 3.1). Since the whole of the Labuerda magnetostratigraphic section is not suitable for spectral outcrop gamma-ray logging, this section has been broken into Labuerda 1 and Labuerda 2 gamma-ray logs separated by an interval of ~ 238 m of unlogged sediments. The Boltaña gamma-ray section is slightly shorter than the magnetostratigraphic section as the top 50 m are poorly exposed and unsuitable for gamma-ray logging. Aerial photographs, geological maps and cross-sections employed to determine the geographical location and the position of the sections within the basin stratigraphy, together with detailed sedimentary logs, outcrop photographs and other relevant analysis are available and discussed in detail in Chapter 5.

The Gerbe section is 200 m long and the base of the section is located in the fine-grained off-axis interfan sediments of the Gerbe I and Gerbe II sandbodies. The section terminates at the base of the Banastón II sandbody (Figure 3.2 and Figure 3.3). The Labuerda section is the longest of all sections at 680 m and sample most of the Banastón System. The section starts approximately in the Banastón I-II sandbodies although the exact position within the stratigraphy cannot be determined due to the presence of a thrust located a few metres below the beginning of the section. The Labuerda section ends at the base of the Ainsa I System. The Boltaña section is 220 m long and is located between the Banastón VI and the Ainsa III sandbodies. The Forcaz section is 190 m long and onsets in the Ainsa II System and finishes in the interfan sediments of the Ainsa and Morillo systems.

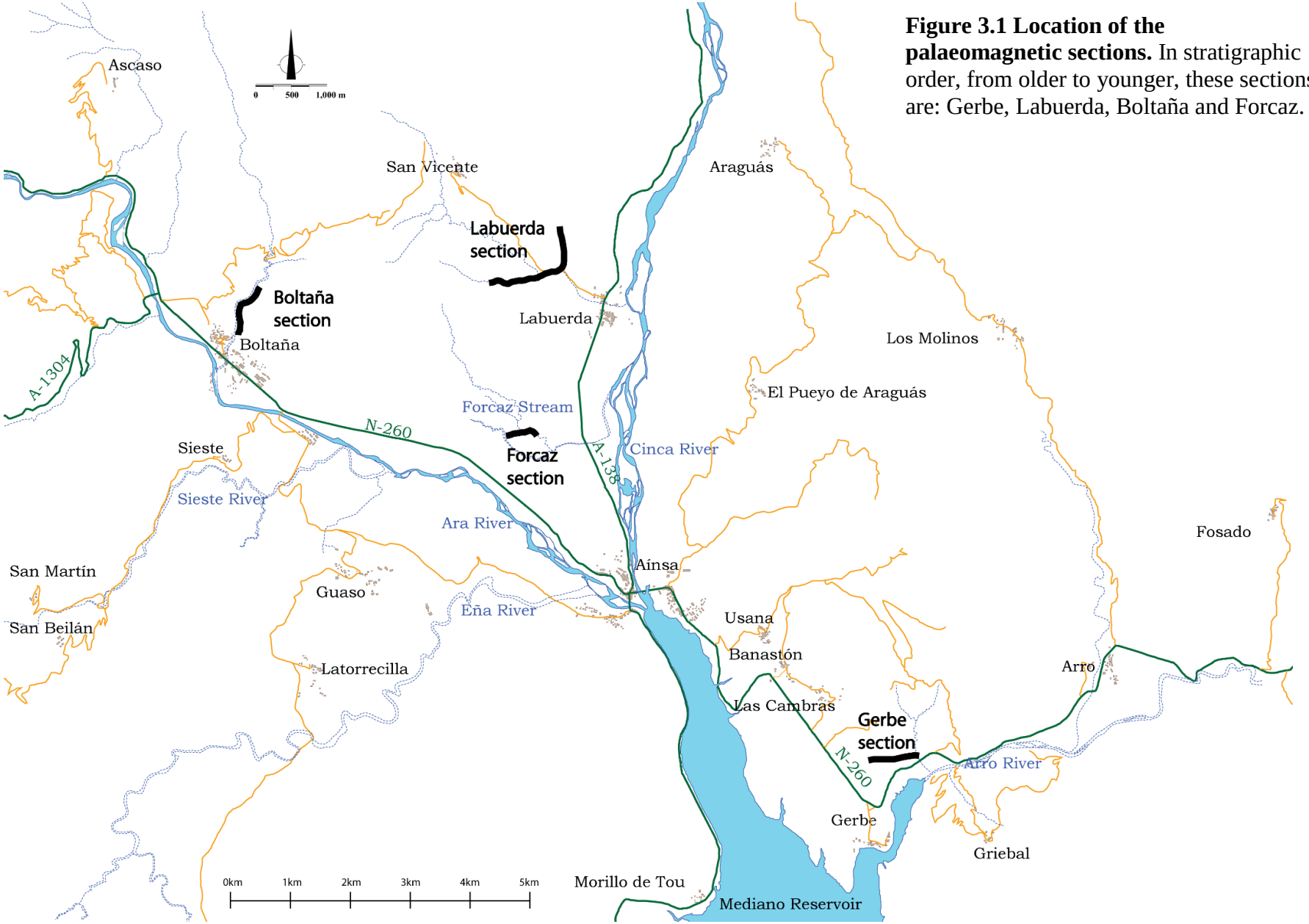

Figure 3.1 Location of the palaeomagnetic sections. In stratigraphic order, from older to younger, these sections are: Gerbe, Labuerda, Boltaña and Forcaz.

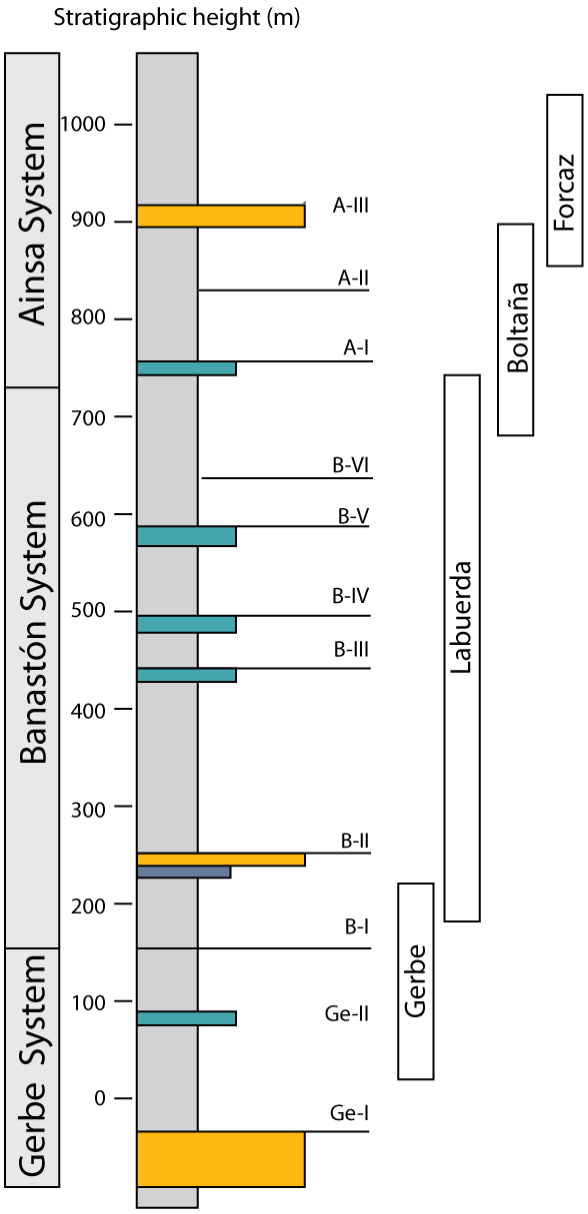

Figure 3.2 Composite section showing the location of the four magnetostratigraphic sections within the Ainsa Basin stratigraphy.

Table 3.1 Comparison between magnetostratigraphic and gamma-ray logged sections.

Deep-marine system	Magnetostratigraphic section	Length (m)	Gamma-ray logged section	Length (m)
Gerbe	Gerbe	200	Gerbe section	200 m
Banastón	Labuerda	680	Labuerda 1 No logged section Labuerda 2	92 m 238 m 350 m
Ainsa	Boltaña Forcaz	220 190	Boltaña Forcaz	167 m 186 m

Plate 3.1 Field photographs of the magnetostratigraphic study undertaken in the Ainsa Basin. (a) Field photograph showing MSc Geology student Kyrre Johansen using a diamond tipped drill attached to a water tank. **(b)** Field photograph showing Dr Conall MacNiocaill (Earth Sciences, Oxford University) extracting drilled cores with the use of a brass rod. **(c)** Field photograph showing Brunton compass mounted on an orienter inserted in the drilled hole to orient the core samples before extraction. Sun compass also attached to measure sun readings where possible. **(d)** Photograph showing a collection of drilled cores, typically between 3-6 cm long, already oriented and labelled.

Figure 3.3 (next page) Geological maps showing the position of the four palaeomagnetic sections within the stratigraphy. The Ainsa Basin geological map (Figure 2.4) has been mounted on Google Earth aerial photographs to show a topographic effect. The Gerbe section is 200 m long and is composed of 2 subsections, the Arro section (Ar) is 90 m long and the Gerbe section (Ge) is 110 m long. The Labuerda section (Lb) is 680 m long and starts immediately above a thrust area probably in the Banastón I-II sandbodies. This section finishes at the base of the Ainsa I sandbody which forms a significant ridge at this location. The Boltaña section is 220 m long and is located between the Banastón VI and the Ainsa III sandbodies. The Ainsa III forms a significant ridge where the Boltaña town was built. The Forcaz section is 190 m long. The section starts in the Ainsa II sandbody and finishes in the interfan sediments between the Ainsa and Morillo systems.

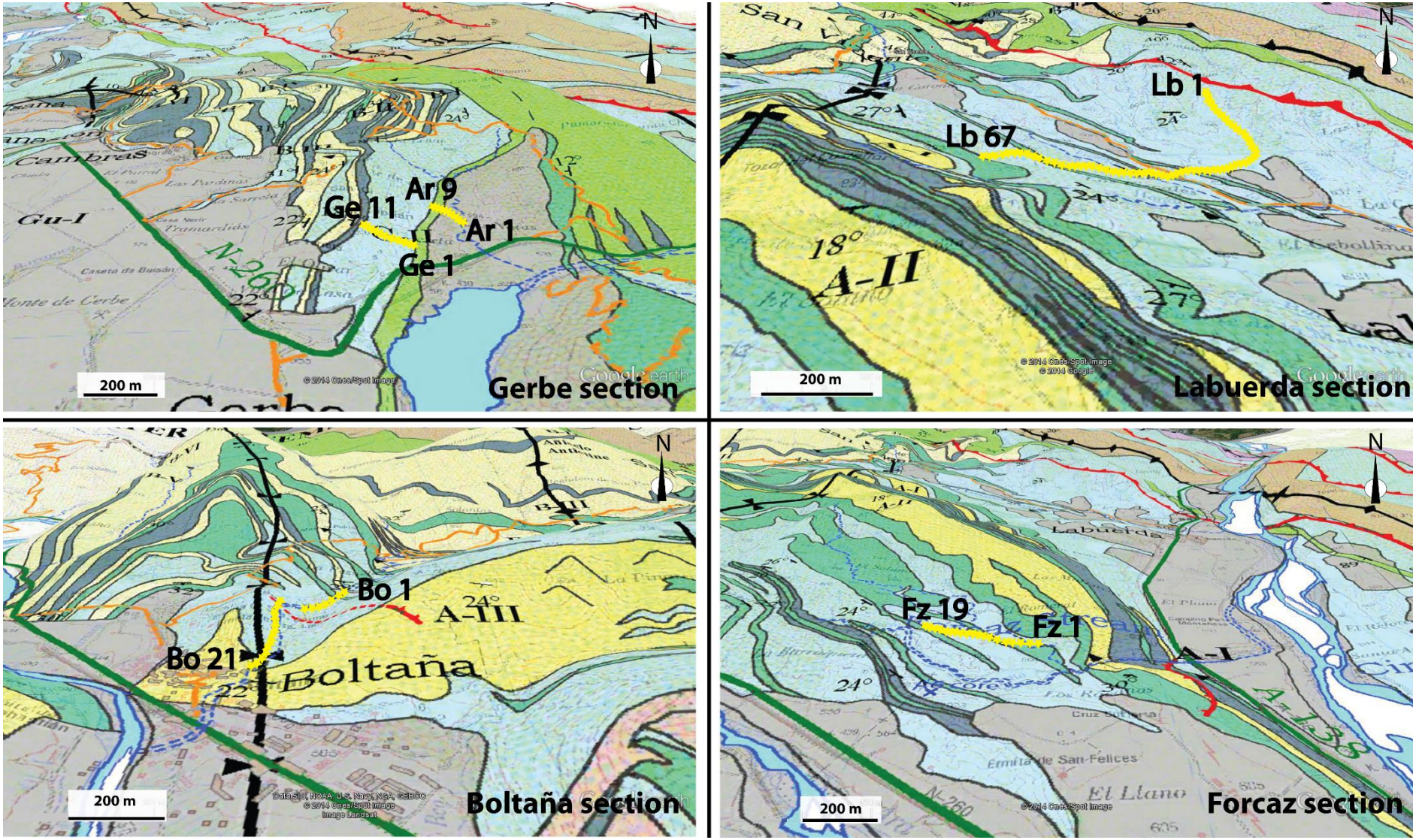
Gerbe section
Ge 11
Ar 9
Ar 1
Ge 1
Gu-I
Cambras
N-260
200 m
Labuerda section
Lb 1
Lb 67
A-II
18°
200 m
Boltaña section
Bo 1
Bo 21
A-III
Boltaña
200 m
Forcaz section
Fz 19
Fz 1
A-1
A-138
Labuerda
Emita de San Felices
El Llano
N-260
200 m

3.4 Data quality and reliability of the study

The quality of the data was evaluated by using three classification categories, designated from highest to lowest quality, A, B and C (Figure 3.4). Category A included all samples which showed a smooth demagnetisation trend. Lines of MAD (Mean Angle of Deviation) < 15-20° fitted easily into these trends. The samples showed a clear polarity and an obvious natural remnant magnetism. Only a small percentage of the samples showed a secondary overprint at a lower coercivity but in most cases a high coercivity was present (Johansen, 2014). The total percentage of samples classified under this category was 41%. An example of category A demagnetisation trend can be seen in Figure 3.4a.

Category B included all the samples which showed a more chaotic demagnetisation trend which made it difficult to fit lines of MAD < 15-20° to the trends (Figure 3.4b). However, the general sense of polarity of the sample, whether it was reverse or normal, was still clear. It is likely that the generally low intensity magnetisation of the rock (averaged values = 0.588 mA/m) was responsible for these more chaotic trends. 45% of all the samples analysed were classified under this category.

Category C samples showed very chaotic demagnetisation trends which prevented the visualisation of the polarity of the sample (Figure 3.4c). The polarity of these samples was inferred from demagnetisation trends of other samples from the same site (repeats) or from samples immediately above or below the sampling site.

Figure 3.5 shows the percentage of samples for each category in the magnetostratigraphic sections. Category B is prevalent in most of the sections and dominates in the Arro/Gerbe and Forcaz sections where the majority of the samples

belong to this category. The exception is the Boltaña section where category A is dominant. In all the sections, the percentage of category C constitutes 11-23% of all the samples. There is a clear reduction in the data quality in the Forcaz section with a very low percentage of category A samples.

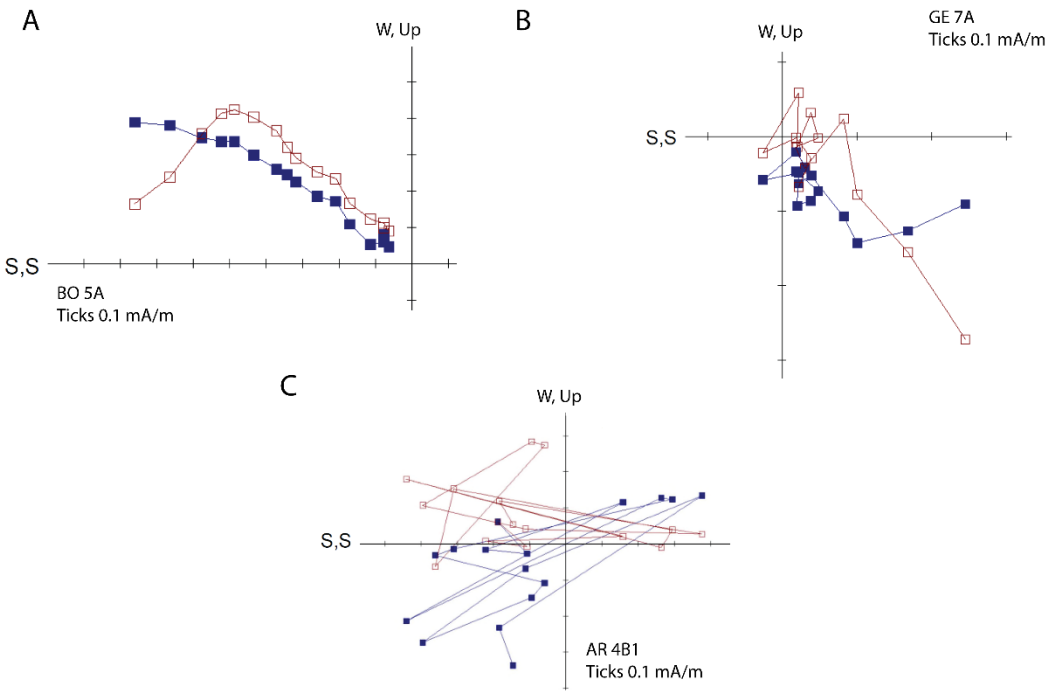

Figure 3.4 Z-plots showing the three demagnetization trend categories. The filled blue symbols show the magnitude and direction of the vectors in the horizontal plane (declination) and the open symbols show the magnitude and direction of the vector in the vertical plane (inclination). **(a)** Sample BO 5A of the Boltaña section showing a demagnetisation trend of category A. There is a clear demagnetisation trend indicating reverse polarity. **(b)** Sample GE 7A of the Gerbe section showing a demagnetisation trend of category B. Although the demagnetisation trend is more chaotic, the sample clearly shows a normal polarity, c) Sample AR 4B1 of the Gerbe section showing a demagnetisation trend of category. **(c)** In this sample, the polarity of the sample cannot be inferred. Modified after Johansen (2014).

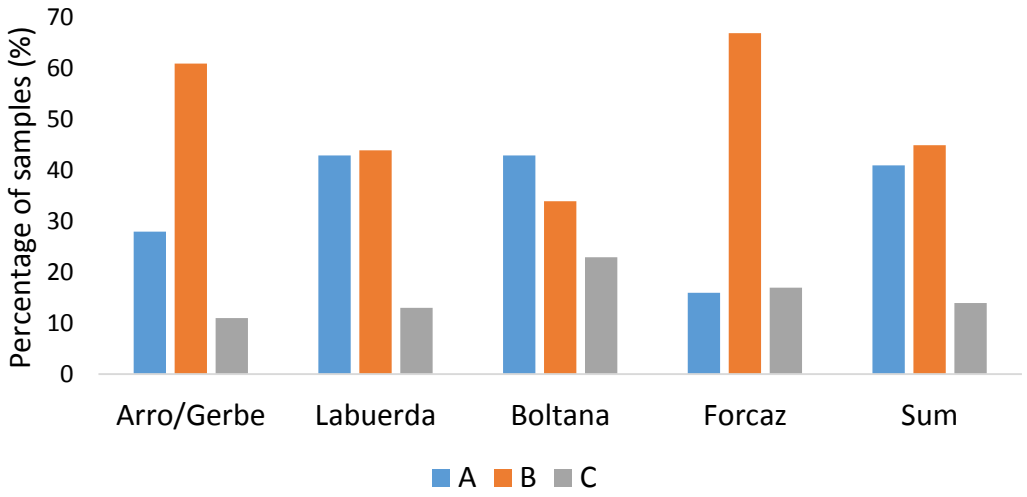

Figure 3.5 Data quality in the magnetostratigraphic sections. Category B is prevalent in most of the sampling sites with the exception of the Boltaña section where category A is dominant. The Boltaña section also contains the highest percentage of samples of category C. The quality of the Forcaz section is clearly reduced with a very low percentage of category A samples.

Most of the repeats in this study showed a similar trend to the original sample, making the interpretation of the results very consistent. All the data have been tectonically corrected. Declination, inclination and NRM intensity results are shown in Figure 3.6. The declination is the angle between the geographic North and the magnetic North. The inclination is the angle between the horizontal and a magnetic vector. If the magnetic vector points down below the horizontal the inclination is considered positive and if it points up is considered negative. Positive inclination in the Northern Hemisphere indicates normal polarity and negative inclination indicates reverse polarity. The average inclination of the samples is 62.3° (Johansen, 2014). Equation 3 allows the calculation of palaeolatitude from inclination data. An inclination of 62.3°, results in a palaeolatitude of 43.6°. This palaeolatitude is similar to the present latitude of the Ainsa Basin ~ 42.2°. The relatively stable palaeolatitude of the area since the Eocene strengthens the reliability of the data.

$$\tan(\text{Inclination}) = 2 \times \tan(\text{palaeolatitude}) \qquad \textbf{Equation 3}$$

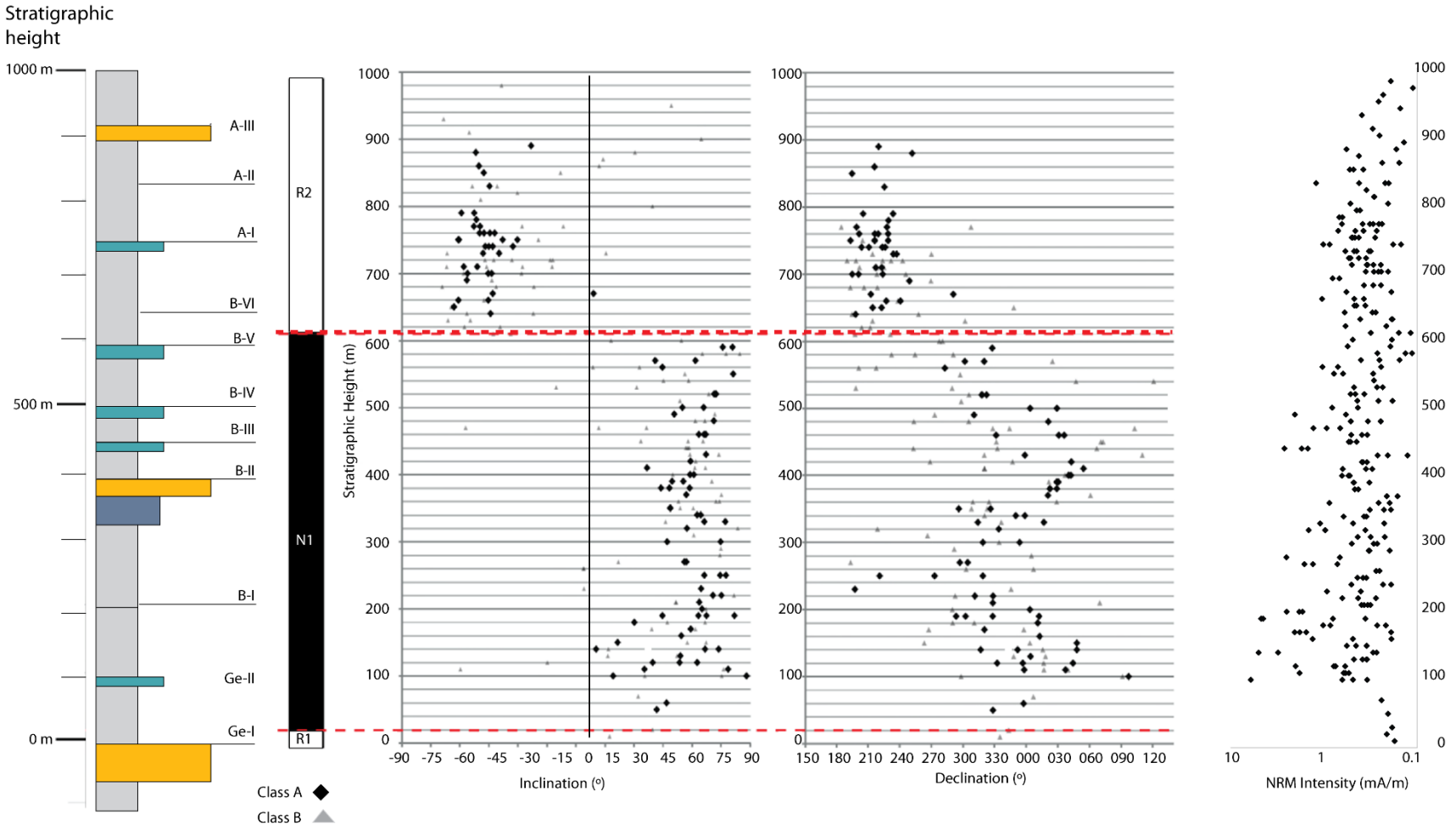

Figure 3.6 Stratigraphic log of the composite Ainsa palaeomagnetic section showing polarity, inclination, declination and natural remanent magnetization (NRM) intensity. NRM averaged values are 0.588 mA/m. Modified after Johansen (2014).

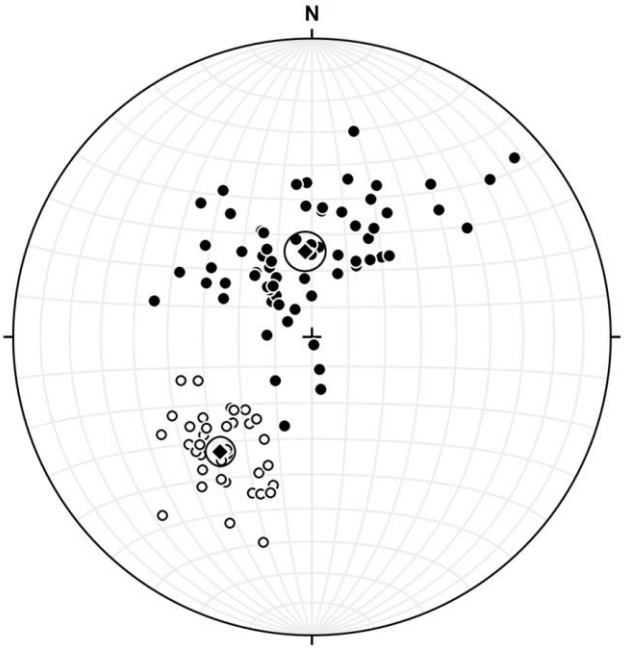

Figure 3.7 Equal area stereoplot including all category A samples. Black-filled circles indicate NRM oriented down (normal polarity) and open circles indicate NRM oriented up (reverse polarity), N = 103. From Johansen (2014).

Figure 3.7 shows an equal area stereoplot where all category A samples have been plotted. Two distinct groups can clearly be recognised in this figure. There is a larger group of samples which are oriented down and north (normal polarity samples) and are represented as black-filled dots. The smaller group oriented up and south (reverse polarity samples) is represented as unfilled circles. Normal polarity samples appear to show more spread out declination values than reverse samples which are more closely clustered. This higher degree of variability in the declination data is likely to reflect a secondary overprint on the normal polarity samples (Johansen, 2014). Although, this overprint does not affect the polarity results of the dataset, it has an influence on the statistical results applied to the dataset to check the reliability of the data, such as the reverse and the McElhinny fold test. Both tests were applied by Johansen (2014) and rejected with a confidence level > 95%. Despite this, the clear polarity for the majority of the samples (86%), the consistency

in the polarity results of the repeat samples and of the overlapped sections (Figure 3.8) and the reasonable palaeolatitude of the dataset, support the robustness and the reliability of the results from this study.

3.5 Magnetostratigraphic results

In the cases where the original sample did not demagnetise to origin, most of the repeats helped to establish the polarity at the sampled site by showing clear demagnetisation trends. Despite this, there are 12 sites where none of the samples successfully demagnetised to origin. The polarity of these sites was marked with a red dot in Figure 3.8 indicating the uncertainty of the polarity at that specific location. Their polarity was inferred by looking at adjacent sites or at the stratigraphic overlapped sections. The majority of these unresolved polarity sites were isolated and therefore could not contain a missed true reversal under the inclusion criteria defined in this study (see Section 3.5.1). The only exception is seen at the sites Ar-4 and Ar-5. These two sites are also very close to the boundary of a polarity reversal at site Ar-2. This polarity reversal is therefore not well-constrained and will be discussed further in Section 3.5.2.

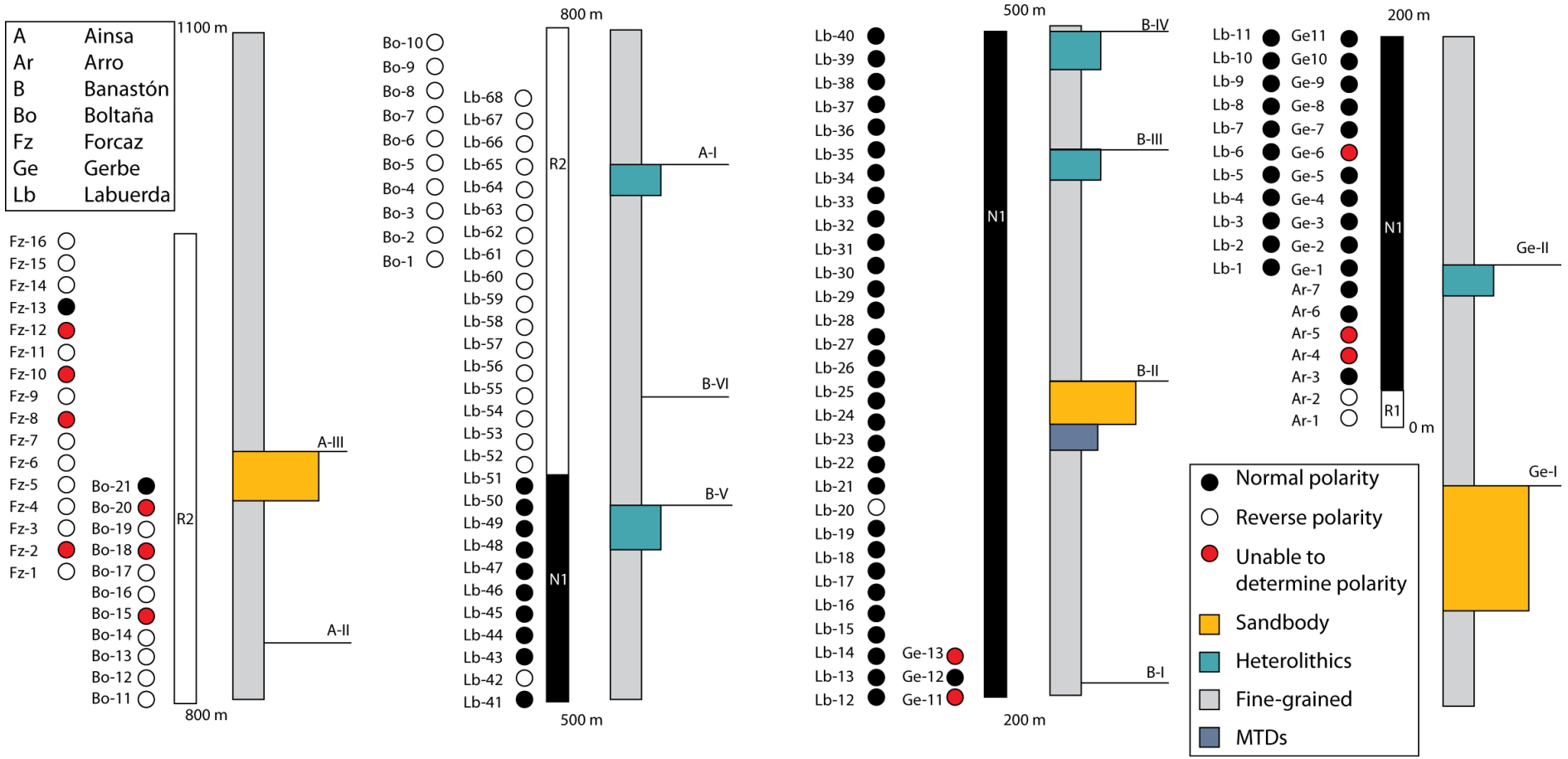

Figure 3.8 Magnetostratigraphic results of the Ainsa Basin. Three polarity chrons identified as R1, N1 and R2. There are 12 sites where the polarity was unable to be determined (red dots). There is a clear consistency in the polarity of the overlapped sections increasing the robustness of the results. Modified after Johansen (2014).

3.5.1 Polarity reversals classification criteria

A classification criterion has been developed to differentiate true polarity reversals from other phenomena including polarity excursions or secondary RM overprints. This classification criterion has taken into consideration a number of factors such as the sampling interval, the availability of magnetic data sample repeats and the quality of the demagnetised data.

A true reversal has been considered only when two or more adjacent site samples of category A and/or B showed a similar polarity. Opposite polarities shown at a single site were considered too brief to represent a true global polarity change. It is more likely that these sites correspond to polarity excursions or to secondary overprints associated with chemical RM and caused by diagenetic processes.

3.5.2 Polarity reversals

The results of this magnestostratigraphic study have identified three polarity chrons: reverse-1 (R1), normal-1 (N1) and reverse-2 (R2) (Figure 3.8).

The R1 interval is poorly constrained with only two samples (Ar-1 and Ar-2) which are located at the very beginning of the stratigraphic interval sampled in the Arro/Gerbe section. These two samples are category B and have a negative inclination and components of secondary RM (Johansen, 2014). The N1-R1 reversal boundary is located at ~ 70 m below the Gerbe II sandbody in the interfan deposits between Gerbe I and Gerbe II sandbodies.

The normal-1(N1) interval is constrained between 30 m and 610 m of stratigraphic height, from Ar-3 site to Lb-51 site. The stratigraphic intervals covered by this chron are the interfan successions of Gerbe I and II, and Banastón I to V

sandbodies. This interval includes a total of 161 samples with an average of 2-3 samples per site. Most of the samples were of category A (43%) and B (42%). Five samples, all of category B showed reverse polarity. These samples were from sampling sites LG17, 20, 42, 44 and 45. Sample repeats at localities LG17, 44 and 45 showed normal polarity whilst repeats for the samples LG20 and LG42 were unsuccessful. Sites LG 20 and LG42 were therefore considered as sites of reverse polarity (Figure 3.8). It is possible that these sites correspond to polarity excursions or that they are secondary overprints. The duration of the N1 interval is 560 m long. Since the boundary between chrons R1 and N1 is poorly constrained, the thickness of the N1 chron is therefore considered as minimal.

The R2 chron starts at 610 m stratigraphic height at sample site Lb-52 and continues throughout the stratigraphic interval sampled to the Forcaz Fz-16 site. The top of the R2 chron is not present in the sediments sampled and therefore the total thickness of this chron cannot be constrained. Nevertheless, this interval of reverse polarity can be estimated to be at least 490 m thick. The R2 interval probably starts during deposition of the Banastón V sandbody and continues up to the interfan sediments of the Ainsa III and Morillo I sandbodies. The R2 chron includes a total of 95 samples and most of the sites have an average of 2 samples since the majority of the Boltaña section and the totality of the Forcaz section samples were collected using a hand-drilling technique and only two samples were recovered per site. Most of the samples were of category A and B, 38% and 47%, respectively. Only two samples of category B showed normal polarity. These samples were from sampling site BO21 and FZ13 and repeats from these two sites were unsuccessful. As discussed above, it is likely that these sites correspond to excursions or have secondary overprints.

3.5.3 Polarity interpretations

The results of this study have been interpreted in conjunction with the biostratigraphic results of Scotchman *et al.* (2014). The stratigraphic nomenclature that these authors used is the same as the one used in this study, facilitating the correlation and interpretations between these two studies. The age calibration is from Gradstein *et al.* (2012). A comparison between these two studies can be seen in Figure 3.9.

The biostratigraphic study of Scotchman *et al.* (2014) uses calcareous nannofossils and larger benthic foraminifera data across a ~ 2 km composite section in the Ainsa Basin. The stratigraphic interval starts at the base of the Gerbe System and finishes at the top of the Sobrarbe Formation, and therefore all the stratigraphy sampled in this study is included in the Scotchman *et al.* (2014) age model.

This age model predicted the polarity reversal C21r-C21n (47.349 Myr) during the deposition of the Banastón II sandbody. It is likely that this polarity boundary is the R1-N1 shown identified in the interfan deposits between the Gerbe I and Gerbe II sandbodies. Similarly, the C21n-20r polarity reversal (45.724 Ma) is predicted by Scotchman *et al.* (2014) to be in the Ainsa I sandbody. The most likely match is the N1-R2 polarity reversal identified in the Banastón V sandbody. The R1, N1 and R2 chrons can therefore be associated with the C21r, C21n and C20r chrons, respectively. The C20r-C20n reversal, not sampled in this study, is likely to be found in the Morillo I or II sandbodies. These correlations suggest that the sediments are ~ 1 Myr younger than the age model proposed by Scotchman *et al.* (2014) (Figure 3.9).

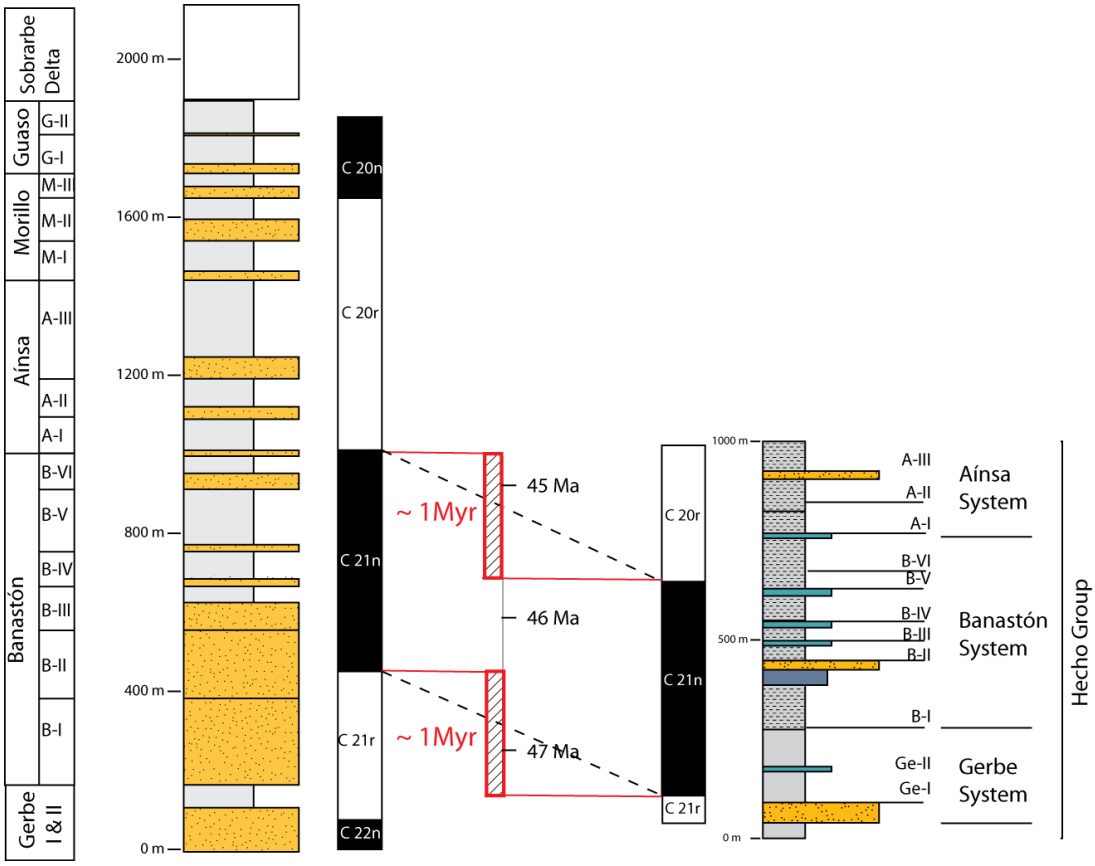

Figure 3.9 Comparison between the biostratigraphic study of Scotchman *et al.* (2014) and this study. The chron N1 identified in this study is likely to refer to the chron C21n. The red square shows the mismatch between both studies, indicating that the sediments are ~ 1 Myr younger than the proposed age model of Scotchman *et al.* (2014).

SARs have been calculated for the interval C21n. Table 3.2 shows the chron C21n durations using different GPTS. The two most recent studies, Gradstein *et al.* (2012) and Gee and Kent (2007) show a very similar duration for this chron at ~ 1.6 Myr. This chron has a thickness of 560 m in the Ainsa Basin and covers most of the Gerbe and Banastón systems. The SAR for this interval is 34.5 cm/kyr (Figure 3.10). This SAR is slighly slower than the SAR calculated by the biostratigraphic model of Scotchman *et al.* (2014) which inferred a SAR for the Banastón System of ~ 43 cm/kyr in Banastón I to III sandbodies to 35 cm/kyr in the Banastón V-VI sandbodies. The model by Scotchman *et al*. (2014) together with other estimates

from cyclostratigraphic studies (Heard *et al.*, 2008), suggest that the SAR in the Ainsa Basin slightly decreased during deposition of the Ainsa, Morillo and Guaso systems to ~ 30 cm/kyr.

Table 3.2 Absolute ages and chron durations using different GPTS from C21n-C20n.

GPTS	Polarity boundary (Myr)			Chron duration (Myr)			
	C21r-21n	C21n-20r	C20r-20n	C20n	C20r	C21n	C21r
Gradstein *et al.* (2012)	47.349	45.724	43.432	1.132	2.292	1.625	1.217
Gee and Kent (2007	47.906	46.264	43.789	1.253	2.475	1.642	1.131
Gradstein *et al.* (2004)	47.25	45.4	42.8	1.2	2.6	1.85	1.35

Cande and Kent (1995) have same absolute ages and chron durations than Gee and Kent (2007).

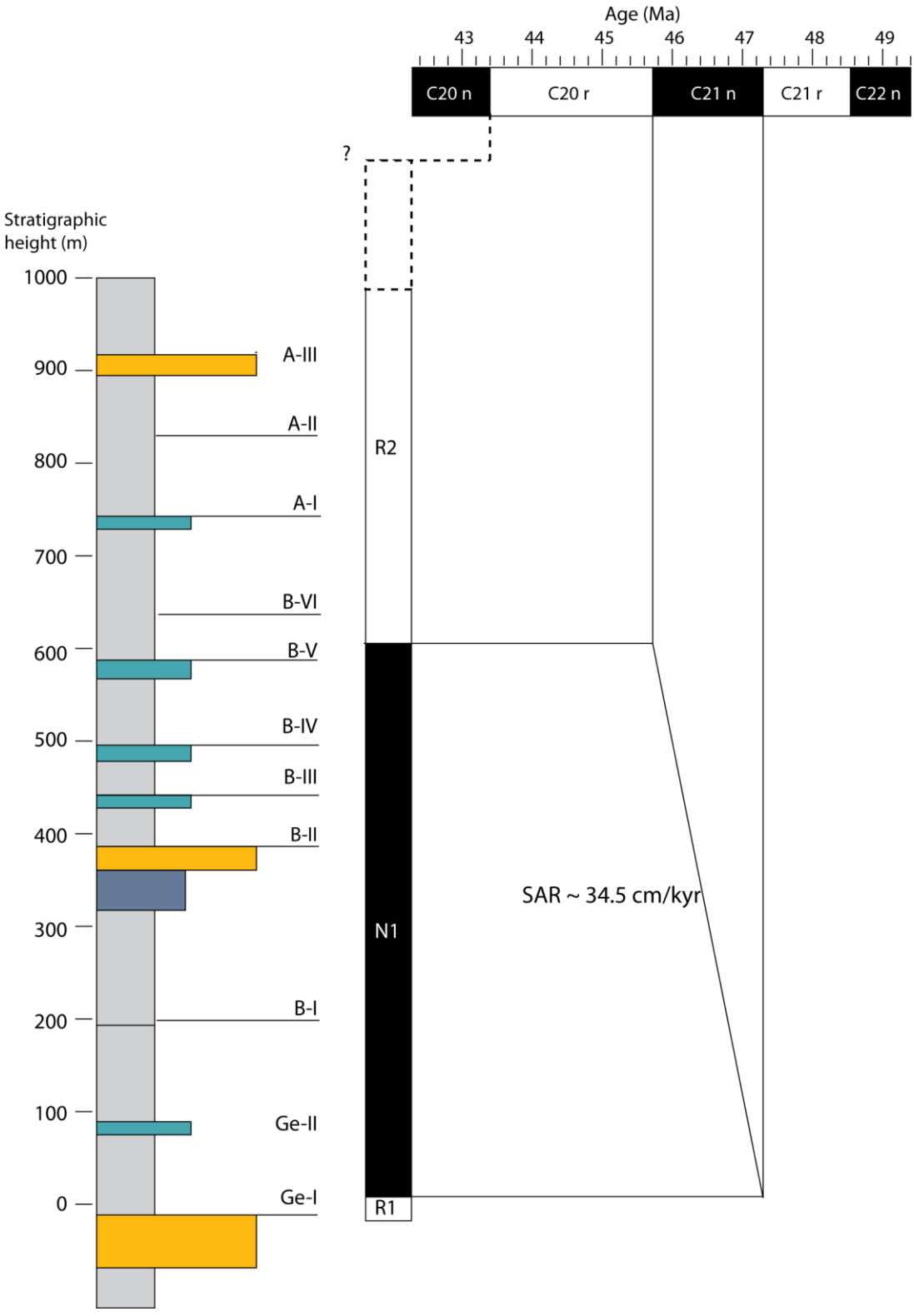

Figure 3.10 Magnetostratigraphic age model. The SAR calculated for the chron C21n is 34.5 cm/kyr. This is estimated for most of the Gerbe and the Banastón systems. The C20r-C20n polarity reversal is likely to be located within the Morillo System. GPTS of Gradstein *et al.* (2012).

3.6 Comparison with other magnetostratigraphic age models of the Ainsa Basin

There are two magnetostratigraphic studies carried out in the proximity of the Ainsa Basin. The study of Mochales *et al.* (2012) sampled shallow-marine sediments exposed at the Boltaña Anticline in the eastern and southern edges of the Ainsa Basin. The study by Holl and Anastasio (1993) was undertaken on the eastern edge of the Ainsa Basin and sampled both limbs of the Mediano Anticline.

3.6.1 Comparison between Mochales *et al.* (2012) and this study

Mochales *et al.* (2012) undertook a magnetostratigraphic study on ~ 2.4 km of Tertiary sediments cropping out at the Boltaña Anticline on the southern and western edges of the Ainsa Basin. The stratigraphic nomenclature which these authors used is based on the work of De Federico (1981) and refers to local formation names which cannot be applied regionally, therefore, making correlations difficult. The main lithologies sampled in this study are shallow-marine shelf deposits, mainly carbonates and siliciclastics. The lateral equivalents of the deep-marine deposits of the Hecho Group are the shallow-marine deposits of the Boltaña (Barnolas *et al*., 1991) and the San Vicente formations (Van Lunsen, 1970). These formations are well represented in the Coscollar section, located on the eastern limb of the Boltaña Anticline, between the villages of El Coscollar and Castellazo.

The Boltaña Formation represents a mixed shelf with siliciclastic and shallow-marine carbonates. The San Vicente Formation conformably overlies the Boltaña Formation and consists of distal carbonate ramp marls and marly limestone facies which appear frequently slumped. Two members have been recognised within the San Vicente Formation: the Paules Member and the La Patra Member (De Federico, 1981). The lower part of the Paules Member represents a retrogradational

ramp with very slow sedimentation rates which change towards a progradational regime in the upper part of the Paules Member. La Patra Member (or Coscollar Member by Barnolas *et al.*, 1991) represents a base-of-slope carbonate breccia interlayered with slope marls and distal clastic turbidites. Figure 3.11 compares the magnetostratigraphic results of Mochales *et al.* (2012) and this study. The lower part of the Upper Hecho Group (Gerbe, Banastón and Ainsa systems) appear to correlate with the Paules Member of the San Vicente Formation.

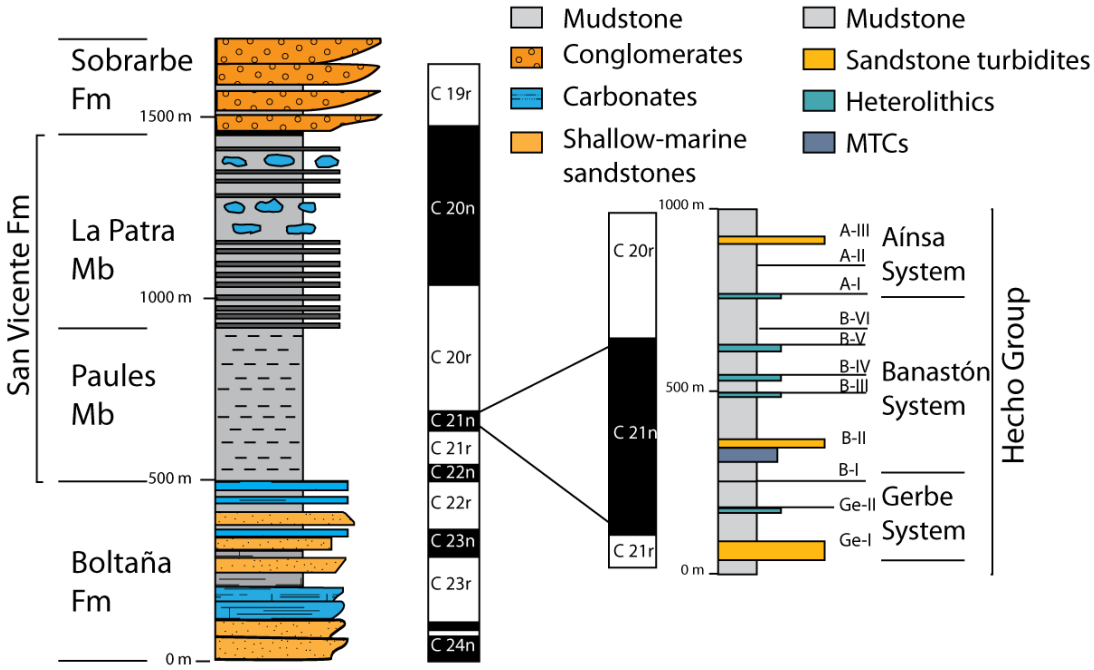

Figure 3.11 Magnetostratigraphic correlation between Mochales *et al.* (2012) and this study. The Gerbe, Banastón and Ainsa systems correspond to the Paules Member of the San Vicente Formation. Simplified stratigraphy of the Boltaña Anticline from Mochales (2011).

Mochales *et al.* (2012) calculated SARs in the order of 2-5 cm/kyr in the Boltaña Anticline, whilst the SARs in the Ainsa Basin for the same interval were estimated to be ~ 34.5 cm/kyr (Figure 3.9). The marly and micritic character of the Paules Member has been interpreted as the drowning of the carbonate platform and

its retrogression towards the foreland (Mochales *et al.*, 2012). This retrogressive sequence probably indicates an overall relative rise in sea levels. During this interval, the Gerbe and the Banastón systems were deposited in the Ainsa Basin. These two systems are characterised by forming the thickest sandy sucessionss of all the Ainsa Basin deep-marine sandbodies (Pickering and Bayliss, 2009). This could be construed as contrary to the view that the initiation of submarine fans occurred during periods of relative lowstands in sea-level (Pickering and Corregidor, 2005). It is, therefore, likely that basin accomodation space differed greatly across the basin and was influenced by the different growing ages of the basin bounding anticlines (Fernández et al., 2012).

The upper part of the Paules Member shows a dramatic increase in SARs from 2-5 cm/kyr to ~ 18 cm/kyr (Mochales *et al.*, 2012). Facies interpretation suggests that the Upper Paules Member is a progradational sequence (De Federico, 1981; Mochales *et al.*, 2012), likely to reflect a fall in relative sea-level. In the Ainsa Basin, this interval correlates with the deposition of the Ainsa and Morillo systems which show an increase of structural confinement in relation to previous deep-marine systems (Pickering and Corregidor, 2005; Bayliss and Pickering, 2014a, 2014b). During this time, the basin was incorporated into the hangingwall of the Gavarnie-Sierras Exteriores Thrust (Muñoz *et al*., 1998; Dreyer *et al*., 1999; Fernández *et al*., 2004; Fernández *et al*., 2012) and as a result, the Boltaña and Mediano anticlines undergone a period of growth (Fernandez *et al.*, 2012), which probably resulted in a progradational sequence in the Boltaña area and an increase in shallowing and confinement of the deep-marine basin (Bayliss and Pickering, 2014a, 2014b).

3.6.2 Comparison between Holl and Anastasio (1993) and this study

The palaeomagnetic study of Holl and Anastasio (1993) was undertaken on syn-orogenic strata in the areas surrounding the Mediano Anticline, located on the eastern edge of the Ainsa Basin. Sediment gravity flow deposits (mainly turbidites) and mudstones are exposed at the flanks of the anticline and show angular unconformities caused by pulses of anticline growth. The stratigraphic formations sampled in the study include the Castisent Group, the Santa Liestra Group and the lower part of the Campodarbe Group (after Mutti *et al.*, 1989). Although, the study presents data from both limbs of the Mediano Anticline, only the western limb is shown in Figure 3.12.

Correlations between the study of Holl and Anastasio (1993) and this study suggest that the Gerbe and part of the Banastón System (probably BI-BIII) are coeval with the Castissent Group outcropping at the Mediano Anticline (Figure 3.12). The Santa Liestra Group probably includes the sediments of the Ainsa, Morillo and Guaso systems.

3.7 Ainsa Basin chronostratigraphy

This section considers the chronostratigraphy of each of the systems forming part of the deep-marine infill of the basin. The older systems, Fosado and Los Molinos have not been discussed due to the high level of deformation in the area and the lack of chronostratigraphic studies undertaken in these two systems.

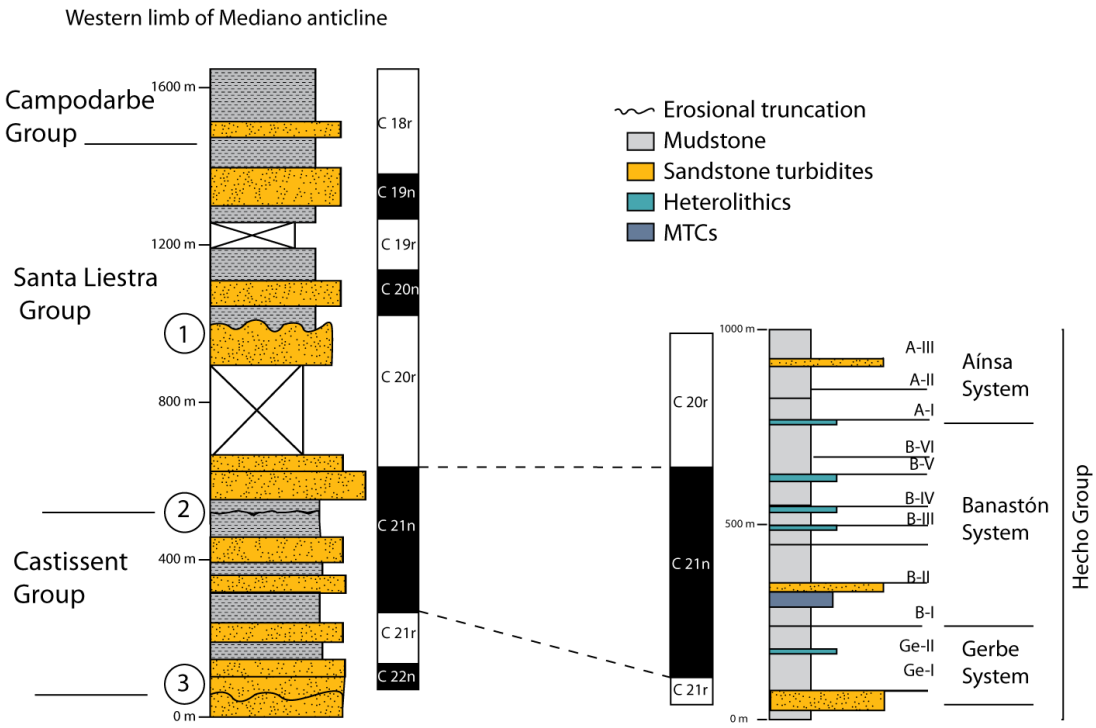

Figure 3.12 Magnetostratigraphic correlation between Holl and Anastasio (1993) and this study. The Castissent Group have the same age as the Gerbe and Banastón deep-marine systems. The upper part of the Upper Hecho Group (Ainsa, Morillo and Guaso systems) can be correlated with the Santa Liestra Group.

3.7.1 The Arro System

Detailed mapping by Millington and Clark (1995) linked the erosional surface of the Charo Canyon to the Arro deep-marine depositional system. Biostratigraphic studies undertaken on the infill of the canyon has been assigned to zone NP15a by Payros *et al.* (2009) within chron C21n. The study of Scotchman *et al.* (2014) suggests that the deposition of this system occurred much earlier, within zone NP13 in chron C22r.

The C21r-C21n magnetic-reversal found in the Gerbe System (this study) suggests that the timing of deposition of the Arro System is more likely to have occurred within chrons C21r and C22n. This new age estimation, positions the Arro system in the middle ground between the age estimation of Payros *et al.* (2009) and Scotchman *et al.* (2014), although the lack of direct magnetostratigraphic sampling

of this system, makes it impossible to establish its chronology with any great certainty.

3.7.2 The Gerbe System

The erosional unconformity of the Lascorz Canyon has been associated with the submarine fan deposits of the Gerbe System (Mutti *et al.*, 1985). The Gerbe System of Mutti *et al.* (1985) correlates with the Castissent Group which is dated within chron C21n (Holl and Anastasio, 1993) (Figure 3.12). The biostratigraphic study by Scotchman *et al.* (2014) suggests that the deposition of the Gerbe System occurred at an earlier stage within biozone NP14, placing the estimated age of the Gerbe System within chrons C22n and C21r.

Magnetostratigraphic work carried out on the Gerbe System (this study) shows that this system was deposited within chrons C21r-21n with the polarity reversal located at ~ 50-100 m above the initiation of the Gerbe System. Most of the Gerbe System deposition is therefore located within chron C21n. These results are consistent with the previous estimations of Holl and Anastasio (1993) and will place the top of the Gerbe System ~ 1 Myr younger than the age estimates of Scotchman *et al.* (2014).

3.7.3 The Banastón System

Scotchman *et al.* (2014) have established the deposition of the Banastón System between 45.82 and 48.31 Myr (late Ypresian-early Lutetian), during nannofossil zones NP14b- NP15a and shallow benthic foraminifera zone SBZ13.

Magnetostratigraphic work carried out in the Banastón System (this study) shows the C21n-C20r polarity reversal estimated at 44.72 Ma (Gradstein *et al.*, 2012) in the Banastón V sandbody. These results show that the Banastón System is ~ 1 Myr younger than the estimations from Scotchman *et al.* (2014) (Figure 3.9).

The deposition of the deep-marine Banastón System has been linked to the Formigales Canyon located at the eastern edge of the Ainsa Basin (Mutti *et al.*, 1985). This canyon erodes underlying deltaic sediments of the Capella Formation which has been dated within chrons C21n and C20r (Cuevas-Gonzalo, 1989; Bentham and Burbank, 1996). The results from the palaeomagnetic studies support this interpretation that the Formigales Canyon was probably active during the deposition of the Ainsa and Morillo systems, in agreement with the interpretations of Scotchman *et al.* (2014).

3.7.4 The Ainsa System

Previous age estimations using biostratigraphic horizon, has placed the deposition of the Ainsa Basin between foraminifera zones P11-P12 and calcareous nannofossil NP14-NP15 (Pickering and Corregidor, 2005) within chron C21n. Remacha *et al.* (2003) has established a younger deposition for the Ainsa System within foraminifera zones P12-P13 (~ NP16). More recent biostratigraphic studies suggest that the deposition of the Ainsa System occurred within nannofossil zone NP15 and shallow benthic zone SBZ13 (Scotchman *et al.*, 2014). This latest interpretation place the Ainsa System in chron C20r.

Magnetostratigraphic work carried out in the Ainsa System (this study) shows reverse polarity throughout the deposition of this system, corroborating the

age model of Scotchman *et al.* (2014) that the Ainsa System was deposited within chron C20r. Although this study suggests that the sediments of the Ainsa System are younger by ~ 1 Myr than the model by Scotchman *et al.* (2014). These authors infer the C21n-C20r magnetic reversal to be at the base of the Ainsa System, but this study has shown that this reversal occurred earlier during the deposition of the Banastón V sandbody. The estimated ages from this palaeomagnetic study place the deposition of the Ainsa System within calcareous zone NP15 at approximately 45-44 Ma between the estimations of Pickering and Corregidor (2005) and Remacha *et al.* (2003).

3.7.5 The Morillo System

The Morillo System was deposited between 43.2 and 44.24 Ma (late Lutetian), during nannofossil zone NP15-NP16 and shallow benthic foraminifera zone SBZ14-SBZ15 (Scotchman *et al.*, 2014). These estimated ages are in agreement with studies from Mochales *et al.* (2012) who estimated the end of the Morillo System at 43.2 Ma. Although this study has not directly sampled the Morillo System, it predicts (considering a SAR of ~ 30 cm/kyr) that the C21r-C20n polarity reversal at 43.43 Ma is located in the Morillo I and Morillo II sandbodies, indicating again slightly younger age predictions than the model of Scotchman *et al.* (2014).

3.7.6 The Guaso System

Biostratigraphic studies suggest that the beginning of the Guaso System occurred at ~ 43.23 Ma (Scotchman *et al.*, 2014). The top of the Guaso System represents the termination of the deep-marine deposition and the beginning of the deposition of

deltaics and fluvial deposits of the Sobrarbe and Escanilla formations. The cessation of the deep-marine sedimentation has been estimated to be between 41.6 to 42.3 Ma in SBZ15 and at the top of chron C20n (Bentham and Burbank, 1996; Dreyer *et al.*, 1999; Mochales *et al.*, 2012). Scotchman *et al.* (2014) suggested the top of the Guaso System to be a dark-shale anoxic horizon estimated at 42.55 Ma. This horizon was recognised as well by Mochales *et al.* (2012) who dated it at 42.4 Ma using magnetostratigraphy.

3.8 Correlations between the Jaca and the Ainsa basins

The palaeomagnetic study undertaken by Oms *et al.* (2003) was based on the Jaca Basin and sampled deep-marine clastics of the Hecho Group. The study covered a 2.2 km thick composite section. The lower part of the section sampled the Santa Liestra Allogroup (Cotefablo turbidites). These sediments are overlain by the Banastón Allogroup which includes deep-marine clastic depositional systems. This allogroup is composed of a long sucession of tabular sandstone turbidites and mudstones which are occasionally interrupted by catastrophic events which resulted in the deposition of carbonate megaturbidites (MT). The upper part of the section is characterised by channelised turbidites (Rapitán System) (Remacha *et al.*, 1995), followed by prodelta deposits (Larres marls Formation) and platform deposits (Sabiñánigo sandstone Formation) (Puigdefábregas, 1975). A summary of the Jaca stratigraphy is shown in Figure 3.13.

The study by Oms *et al.* (2003) suggests that the reversed polarity observed in the Cotefablo Allogroup can be associated with chron C20r. This interval correlates in this study with the uppermost part of the Banastón System (Banastón VI sandbody), Ainsa System and probably part of the Morillo System (interval not

sampled) (Figure 3.13). However, these results differ from age estimations from biostratigraphic and from intrabasinal correlations based on petrographic studies undertaken in the Ainsa and Jaca basins. The Banastón Allogroup in the Jaca Basin has been associated with the Banastón System in the Ainsa Basin using petrographic comparisons (Das Gupta and Pickering, 2008; Caja *et al.*, 2010). Also, Payros *et al.* (1999) and Labaume *et al.* (1985) asigned planktonic foraminiferal Zone P9 to the Megaturbidite 4 (MT-4). This would imply that MT-5 occurred within chron C21r. Remacha *et al.* (2003) also places the initiation of the Banastón Allogroup close to the polarity reversal between C21r-C21n at ~ 47.3 Ma with most of the Banastón Allogroup occupying chron C21n. This is in close approximation with the results of this study which estimates the Banastón System at ~ 46.8 Ma within chron C21n. In order to have a better agreement between biostratigraphic and magnetostratigraphic data, the N1 chron interpreted as C20n by Oms *et al.* (2003) can be re-interpreted as C21n (Figure 3.13). This new proposed correlation between the Oms *et al.* (2003) study and this study suggests that the Cotefablo Allogroup is coeval with the Gerbe System and possibly the lowest part of the Banastón System (Banastón I and II sandbodies). The Banastón Allogroup in the Jaca Basin would therefore coincide with the rest of the Banastón System in the Ainsa Basin and may also include the lower part of the Ainsa System. Although, the lack of age control on the total thickness of the chron C20r and the expected reduction of SARs during the deposition of the Ainsa and Morillo systems (Heard *et al.*, 2008, Scotchman *et al.*, 2014) may result in the Ainsa System completely correlating with the Jaca Allogroup. This interpretation is supported by biostratigraphic age models which have associated the Ainsa, Morillo and Guaso systems of the Ainsa Basin with the Jaca Allogroup of the Jaca Basin (Remacha *et al.*, 2003; Scotchman *et al.*, 2014).

There is a minor disagreement about the termination of the deep-marine sedimentation of the Hecho Group with Remacha *et al.* (2003) placing it at ~ 41 Ma in the Jaca Basin and Scotchman *et al.* (2014) estimating it at ~ 42 Ma in the Ainsa Basin. This study has demonstrated that the sediments of the Gerbe, Banastón and Ainsa system sediments are ~ 1 Myr younger than the age model proposed by Scotchman *et al.* (2014). If this relationship is maintained throughout the younger systems, then the termination of the Hecho Group deposition would be coeval in both basins at ~ 41 Ma.

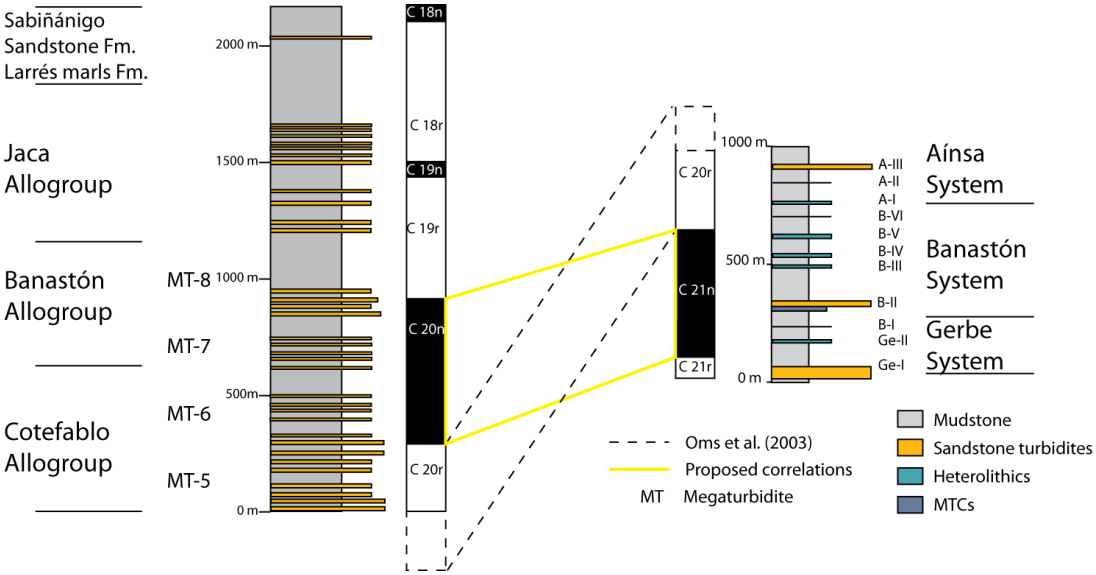

Figure 3.13 Magnetostratigraphic correlation between Oms *et al.* (2003) and this study. The poor image quality of the Oms *et al.* (2003) publication does not permit the visualisation of the stratigraphic interval with accuracy. This drawing is merely interpretative and may not coincide with the original data. Dash lines show the correlations between the interpreted magnetostratigraphic data of Oms *et al.* (2003) and this study. However, taking into consideration biostratigraphic studies, it is possible that the R1 interval of Oms *et al.* (2003) originally assigned to C20r is now reinterpreted to C21r (yellow lines).

3.9 Correlations between the Tremp-Ager Basin and the Ainsa Basin

The two most important chronostratigraphic studies undertaken in the Tremp Basin are the study by Nijman (1998) based on sequence stratigraphic correlations and the study by Bentham and Burbank (1996) which included extensive magnetostratigraphic work.

The deep-marine sediments of the Ainsa Basin were sourced from a large fluviodeltaic complex which entered the Tremp-Ager Basin from the east forming the Montanyana Group (Mutti *et al.,* 1985; Marzo *et al.,* 1988). Nijman (1998) divided the Montanyana Group into the Lower Montanyana (LM), Middle Montanyana (MM) and Upper Montanyana (UM) groups. The Lower Montanyana Group (Castigaleu Formation) can be subdivided into two megasequences (LLM and ULM) and this group is characterised by trunk river sheet sandstone facies (Nijman, 1998). The Middle Montanyana (Castissent Formation) only contains one megasequence. This group is characterised by amalgamated sheet sandstones typical of the main channel fluvial feeders. The Upper Montanyana Group is subdivided into five megasequences (UMA-UME) and contains the Capella and the Perarrua formations.

Three main fan-delta systems were active during the deposition of the Hecho Group sediment-gravity flow deposits, including turbidites, namely the Claramunt, San Esteban and Campanúe fans (Nijman, 1998). These fans are composed of coarse-grained sandstones and conglomerates (Puigdefábregas *et al.*, 1992; Nijman, 1998). The San Esteban Fan was active during the initiation of the Montanyana Group and prograded significantly into the Middle Montanyana Castissent fluvial environment. This fan continued its activity during the lower part of the Upper Montanyana. At the base of the UMB megasequence, sedimentation was then overtaken by the Campanué Fan.

The study undertaken by Bentham and Burbank (1996) used many magnetostratigraphic sections in the Tremp-Ager and in the Ainsa basins and attempted to correlate the stratigraphy between these two basins. However, these authors only differentiated the deep-marine sediments of the Hecho Group from the

overlying deltaics of the Sobrarbe Formation, and they did not attempt to break down the Hecho Group into the different deep-marine systems. As a consequence, the correlations established between these two basins are broad scale and cannot resolve the age uncertainties of the individual systems. Figure 3.14 shows a composite secion of the Tremp-Ager Basin stratigraphy using the Essera Valley section and the upper part of the Navarri section. This composite section is compared with the magnetostratigraphic results of this study. The Gerbe System correlates with the Perarrua Formation in the Upper Montanyana Group, suggesting that the older systems Los Molinos, Fosado and Arro correspond with the Middle Montanyana Castisent Formation and probably the upper part of the Lower Montanyana Group. The Banastón and the Ainsa systems appear coeval with the sediments of the Capella Formation in the Upper Montanyana Group, and the Morillo and Guaso systems are likely to correlate with the conglomeratic units of the Pano Formation (Figure 3.14).

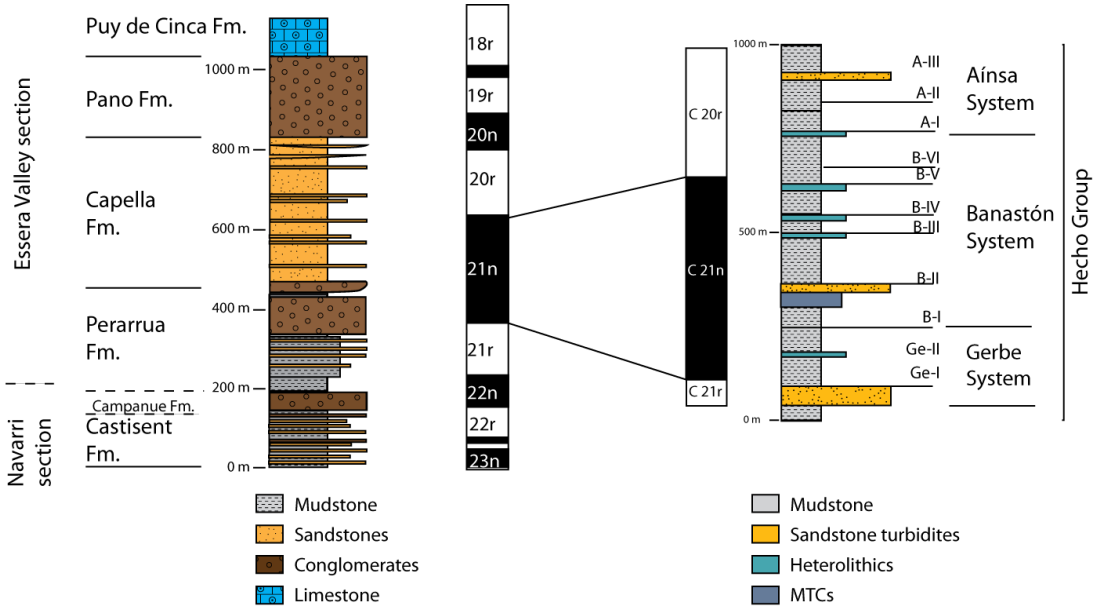

Figure 3.14 Magnetostratigraphic correlation between Bentham and Burbank (1996) and this study. The Gerbe System is coeval with the Perarrua Formation and the Banastón and the Ainsa systems are coeval with the sediments of the Capella Formation. The Morillo and Guaso systems are likely to be coeval with the conglomeratic units of the Pano Formation.

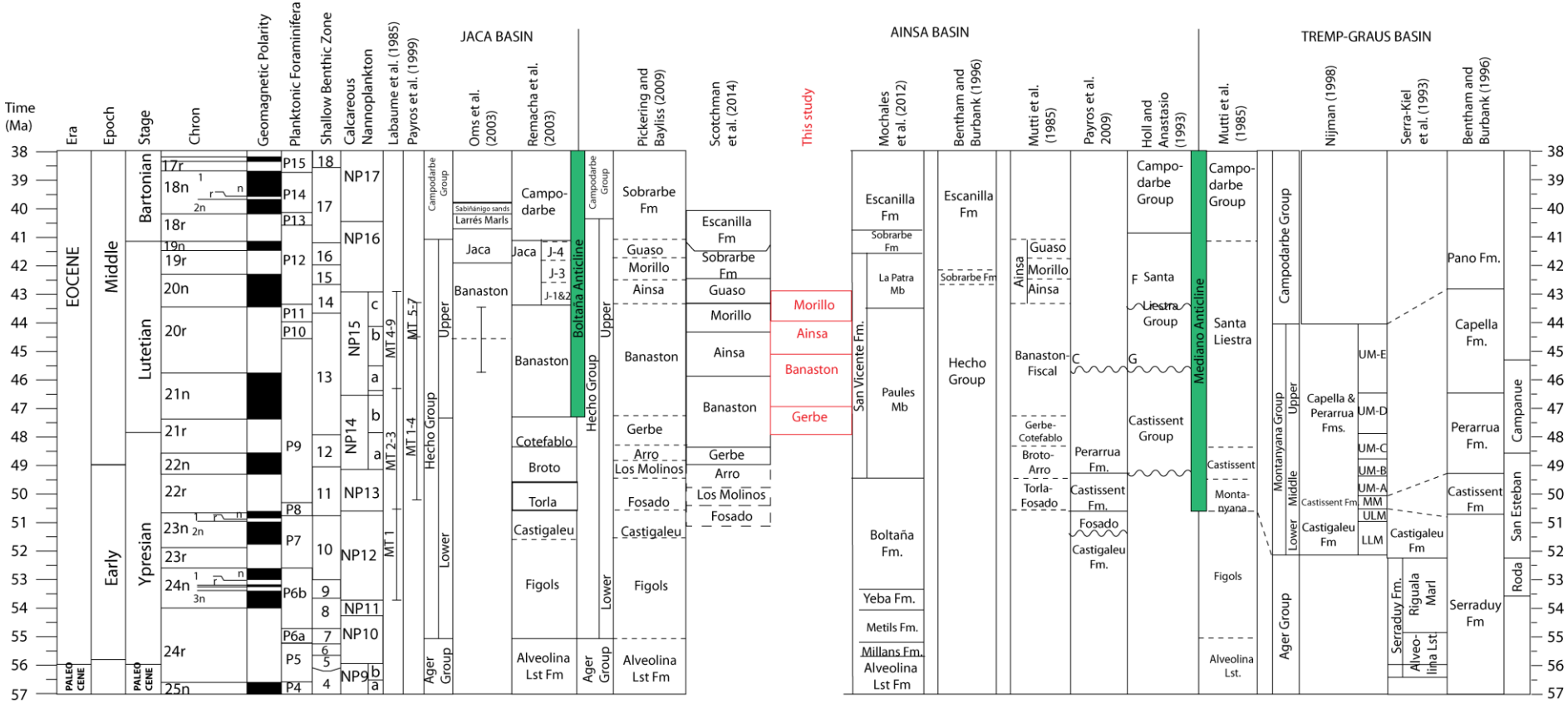

Figure 3.15 Summary of chronostratigraphic work undertaken in the Jaca, Ainsa and Tremp basins showing inter-basin correlations. Results from this study are highlighted in yellow. Modified after Scotchman *et al.* (2014).

3.10 Conclusions

This chapter has presented, for the first time, magnetostratigraphic work across ~ 1 km of stratigraphy of the deep-marine sediments of the Upper Hecho Group in the Ainsa Basin. The study sampled the majority of the Gerbe System and the totality of the Banastón and the Ainsa systems. This study has identified three main polarity chrons: R1, N1 and R2. Using the recent biostratigraphic study of Scotchman *et al.* (2014), the R1, N1 and R2 chrons has been associated to the chrons C21r, C21n and C20r, respectively. The C20r-C20n polarity reversal, although not sampled in this study is predicted to be found in the Morillo I- II sandbodies. These correlations suggest that the sediments are ~ 1 Myr younger than the age model proposed by Scotchman *et al.* (2014). The SARs during the deposition of the Gerbe and the Banastón systems have been established at ~ 34.5 cm/kyr.

Results from this study have been compared with the magnetostratigraphic studies carried out by Mochales *et al.* (2012) and Holl and Anastasio (1993) at the edges of the Ainsa Basin, in the Boltaña and in the Mediano anticlines, respectively. In the Boltaña Anticline, the shallow-marine retrogressive sequence of the lower part of the Paules Member has been linked with the deposition of the Gerbe and the Banastón systems whilst the progradational sequence of the upper part of the Paules Member is correlated with the deposition of the Ainsa and Morillo systems. Comparisons with the study of Holl and Anastasio (1993) in the Mediano Anticline suggest the Gerbe and part of the Banastón systems (probably BI-BIII sandbodies) are coeval with the Castissent Group and that the Ainsa, Morillo and Guaso systems are of a similar age as the Santa Liestra Group.

Interbasin correlations between the Jaca and Ainsa basins suggest that the Cotefablo Allogroup in the Jaca Basin is coeval mainly with the Gerbe System in the

Ainsa Basin and that the Banastón Allogroup coincides with most of the deposition of the Banastón System. The Ainsa and the Morillo systems seem to correlate with the Jaca Allogroup. In the Tremp-Ager Basin, the Gerbe System correlates with the Perarrua Formation; the Banastón and the Ainsa systems are coeval with the Capella Formation of the Upper Montanyana and the Morillo and Guaso systems are likely to be coeval with the conglomerates of the Pano Formation. A summary of all the chronostratigraphic studies undertaken in the Tremp-Ager, Ainsa and Jaca basins including results from this study can be seen in Figure 3.15.

Chapter 4

Well A6 core

4.1 Introduction and objectives

The fine-grained sediments of the Middle Eocene Ainsa Basin are finely laminated with an alternation of lighter and darker coloured bands and are characterised by thin sandstone turbidites packages forming cyclic sequences (this chapter and Chapter 5). In order to try and understand better the underlying causes for cyclic deposition of fine-grained siliciclastic deposits in a tectonically active basin, this chapter combines detailed sedimentological with multiple geochemical proxies of an essentially fine-grained siliciclastic deep-marine Middle Eocene core from the Ainsa Basin, Spanish Pyrenees. Detailed sedimentary logging, high-resolution multi-element XRF geochemistry, SEM and XRD results are combined to infer variations in grain size, weathering, organic content and changes in the geochemistry of the main recognised lithologies. TOC and stable carbon isotope studies are also included as they provide a useful means for prospective identification of the origin of organic matter and characterising the nature and provenance of the sediments in the basin.

Cyclostratigraphic techniques have been applied to the high-resolution sedimentological and geochemical records to determine the potential presence of Milankovitch orbital periodicities. Eccentricity, obliquity and precession cycles, can have an effect on sedimentation patterns as they affect the amount and distribution of incoming solar radiation and have a significant effect on precipitation and storminess, ice volume and sea-level change among others (see Section 1.3). Although the link between orbitally forced climatic variability and sedimentation is still poorly

understood (Meyers and Sageman, 2000), the recognition of Milankovitch forcing in a siliciclastic sequence can help our understanding of how these orbital cycles have affected the detrital and biogenic flux to deep-marine environments.

4.2 Geochemical proxies and sedimentation patterns in deep-marine environments

The geochemistry of ancient deep-marine sediments provide important information on sediment sources (e.g., Heller and Frost, 1988; McLennan *et al.*, 1993), sediment transport processes, palaeoclimatic and palaeoenvironmental conditions for example fluctuations in biological productivity and the redox state of bottom waters (Stein *et al.*, 1989; Shimmield and Mowbray, 1991; Salamy and Zachos, 1999; Werne *et al.*, 2000). Geochemical proxies are commonly used to deduce the likely environment for formation of deep-marine sedimentary rocks (Feng and Kerrich, 1990; Calvert and Pedersen, 1993; Schneider *et al.*, 1997; Schnetger *et al.*, 2000). Individual proxies have their limitations and therefore, a multi-proxy approach is preferred to obtain a comprehensive understanding of palaeoenvironments.

Analysis of deep-marine fine-grained thin-bedded turbidite and hemipelagic deposits provides an opportunity to interrogate sedimentation patterns, because this combines both a terrigenous detrital component (represented in the delivery of clays and terrestrial organic matter), and a pelagic biogenic component containing mineralised skeletal remains and marine organic matter. Additionally, the authigenic component reflects the burial and diagenetic history. The terrigenous component, mainly fluvial and aeolian, is affected by changes in precipitation, erosion, and weathering (e.g., White and Blum, 1995; Kostaschuk et al., 2002; Jacobson *et al*., 2003; Bouraoui et al. 2004; Riebe *et al*., 2004). The biogenic component is sensitive to

water column conditions which affect productivity. Climate can also influence the biogenic influx by regulating nutrient supply and by controlling water-column stability (e.g., Werne *et al.*, 2000; Moreno *et al.*, 2002). Tectonic processes can also exert a major control on the terrigenous and biogenic component via tectonic uplift/subsidence and basin accommodation space which, in turn, will affect rates of weathering and erosion and may cause relative sea-level changes (e.g., Watts and Thorne, 1984; Raymo *et al*., 1988; Rea, 1992; Riebe *et al*., 2001, 2004; Jacobson *et al*., 2003; Carey *et al*., 2005; Vött, 2007; Dixon *et al*., 2012)

4.3 The Well A6

4.3.1 Location of Well A6

The Well A6 was drilled ~ 1.9 km south of Labuerda and 2.4 km north of Ainsa towns, next to the Forcaz stream at ~ 400 m west of the road A-138 which connects the villages of Labuerda and Ainsa. Plate 4.1 shows an aerial photograph with the location of the A6 Well. The A6 Well was drilled to a subsurface depth of ~ 230 m with ~ 97% of core recovery.

4.3.2 Stratigraphic location of the A6 core

The A6 core was drilled between the Ainsa and Morillo submarine fan systems (Figure 4.1). The Ainsa System has been interpreted as a lower-slope and proximal basin-floor channelised fan system (Pickering and Bayliss, 2009), and the Morillo System is an erosional slope and base-of-slope channel system (Bayliss and Pickering, 2014).

The A6 core records deposition of both fine-grained sediments at the lateral margin and levée sites of the sandy Ainsa III Fan and the overlying interfan sediments

below the Morillo I Fan (Figure 4.2) and is characterised by the deposits of low-concentration and low-velocity turbidity currents.

The deep-marine systems of the Ainsa Basin appear to be characterised by only one major submarine channel being active at any time which fed from a point source towards the southeast over the growing Mediano Anticline (Pickering and Bayliss, 2009). The abandonment of the channel resulted in the switch-off of coarse clastic delivery to the basin and fine-grained sedimentation dominated these intervals. The stratigraphy of the Ainsa Basin shows this successive activation and abandonment of coarse-grained channelised systems. The relative linearity and confinement of the basin, makes the position of the A6 core ideal to study the temporal evolution of the deep-marine systems and the possible effects that allocyclic factors such as climate and tectonics exerted on the chemistry and sedimentation patterns of these sediments.

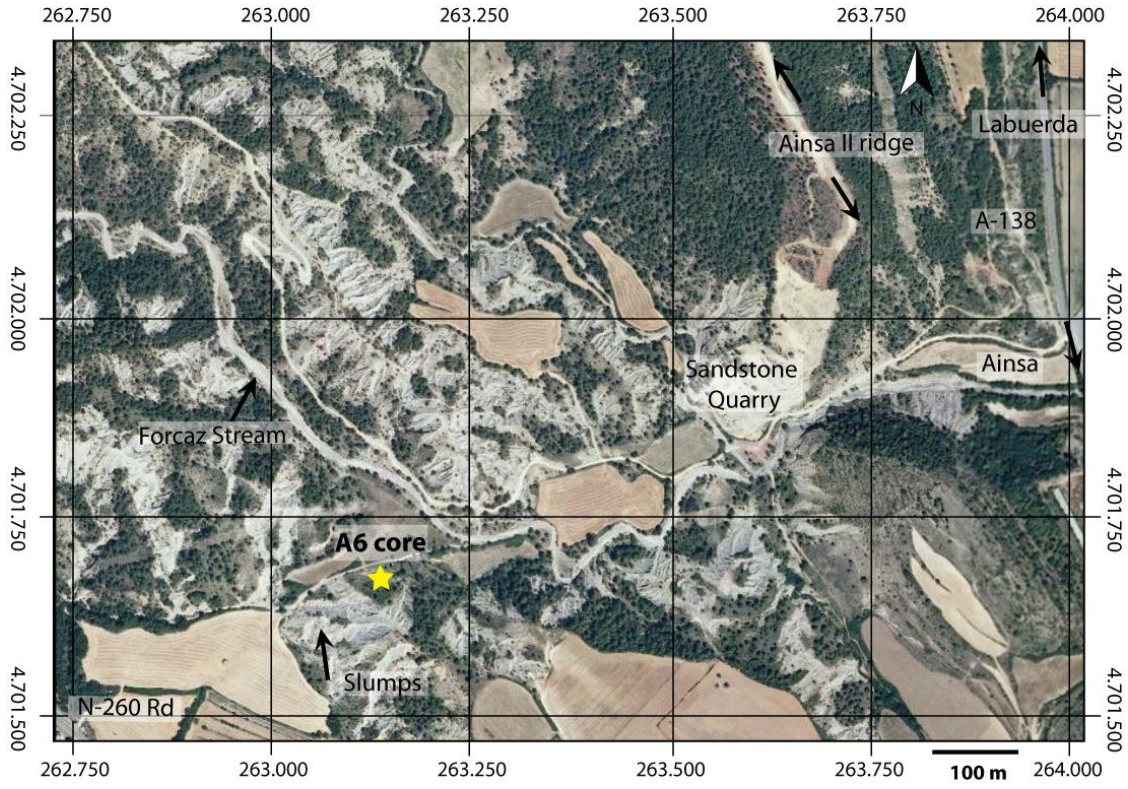

Plate 4.1 Aerial photograph showing the position of the Well A6. The Well A6 core site can be accessed from the road A-138 ~ 2 km north of Ainsa town and is located next to the Forcaz stream. Aerial photograph available from www.sigpac.mapa.es/fega/visor.

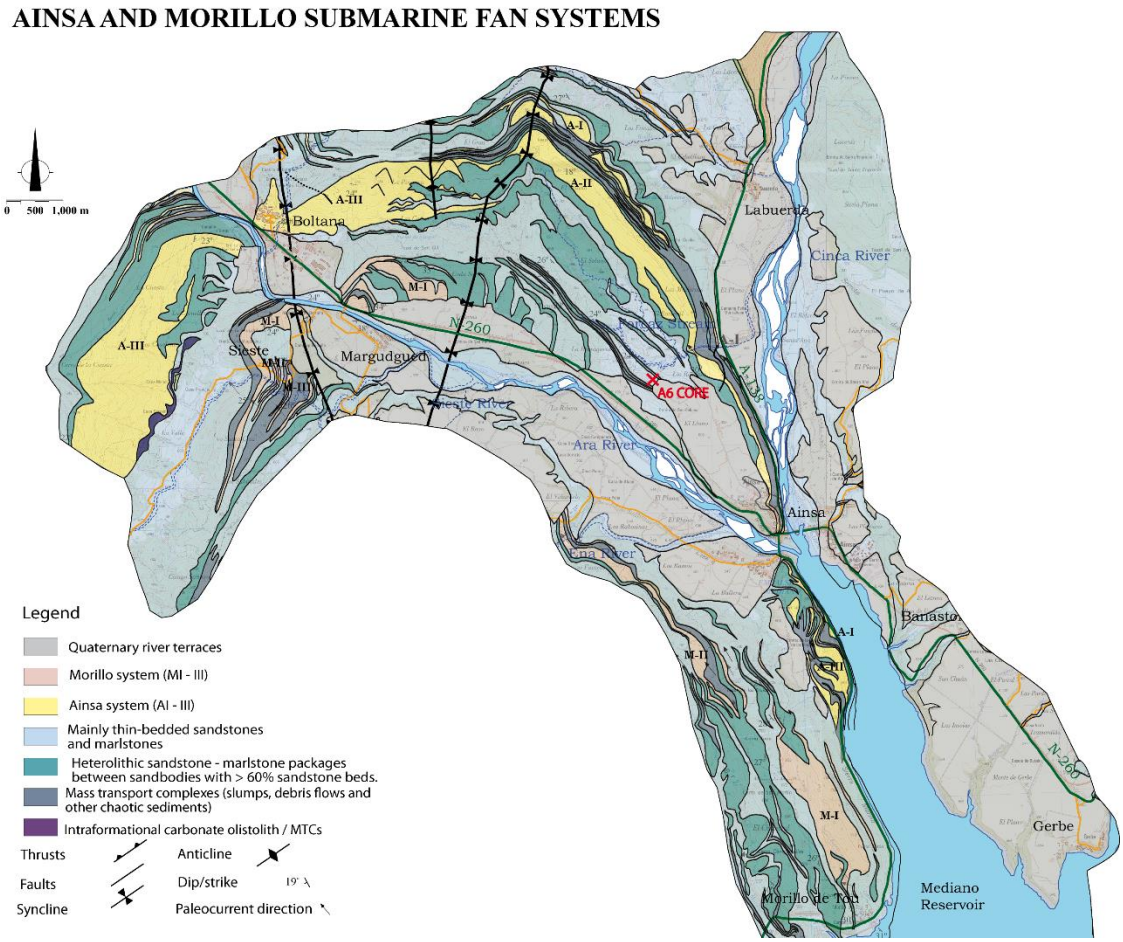

Figure 4.1 Geological map of the Ainsa Basin showing the position of Well A6. The well is positioned within the Ainsa and Morillo submarine fan systems. Modified after Pickering and Bayliss (2009).

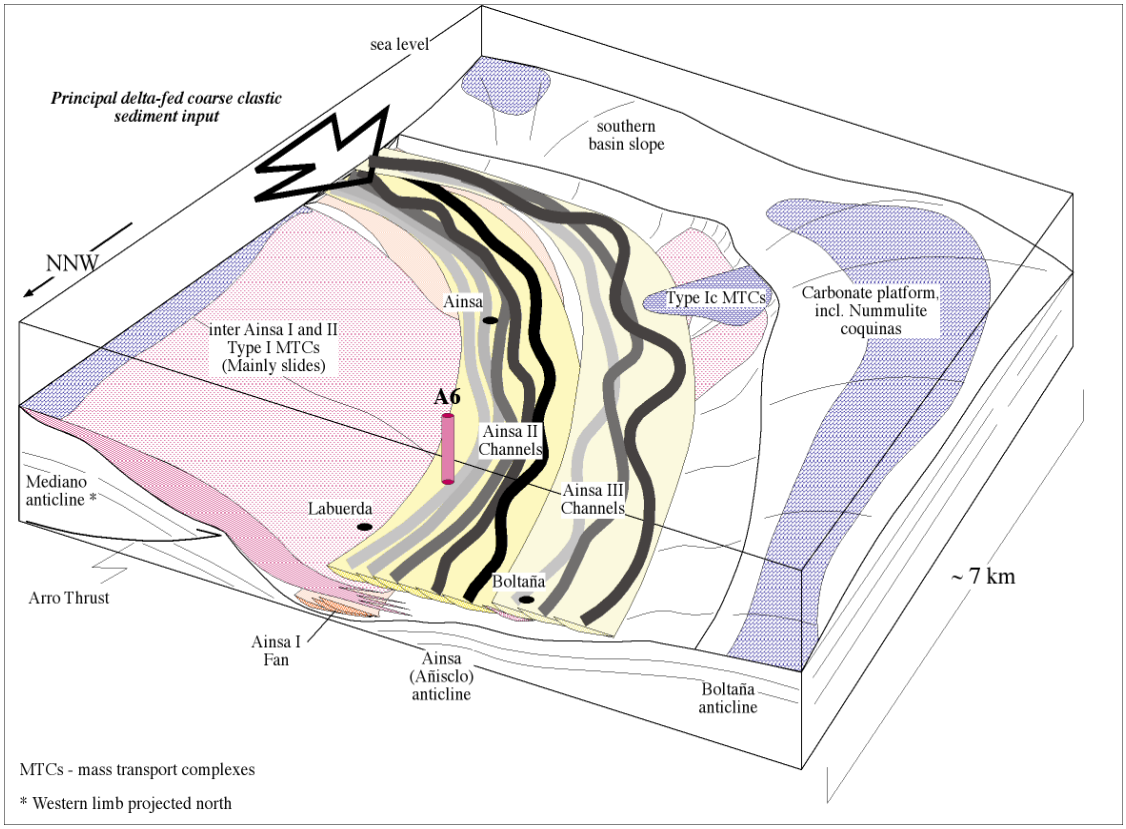

Figure 4.2 Reconstruction of the environment of deposition for the A6 core. The lower part of the A6 core represents the off-axis fan lateral-margin deposits to the Ainsa III Fan and the upper part represent interfan deposits between the Ainsa and Morillo sandy fans. Modified from Pickering and Bayliss (2009).

4.3.3 Age of the A6 core

Using a planktonic foraminifera zonation, the age of the core is constrained within the upper middle Lutetian, very close to the P11-P12 Biozones (Pickering and Corregidor, 2005). Spectral studies of bioturbation intensity suggest SARs of ~ 30 cm/kyr, yielding an estimate of 0.8 Ma of stratigraphy for the entire A6 core (Heard *et al.*, 2008).

4.4 Sedimentological study of the A6 core

220 m of detailed sedimentary logs have been produced from the A6 core (Appendix 3). All beds thicker than 2mm have been included in the logs. In addition, a total of six thin sections were taken from the core to understand some of the sedimentary features.

Special attention was given to the geometry of mm- to cm-sized fine-grained turbidite sandstones and the nature of muddy dark bands.

4.4.1 Sedimentary facies

The core shows colour variations from pale, medium and dark grey. Very rarely, light grey-orange-coloured bands are present. These changes in colour probably reflect compositional (both primary and diagenetic) changes and grain-size variations. The core is tightly carbonate cemented and locally contains abundant pyrite mainly as framboids in sandstone turbidites, hemipelagic mudstones, shells and burrows.

The A6 core comprises essentially hemipelagic marlstones, laminated, very thin-and thin-bedded normally-graded sandstone turbidites, silty and muddy-siltstones together with some chaotic sediment slide and slump deposits.

Fine-grained sandstone turbidites (Facies C2.3), mud and silt couplets (Facies D2.3) and graded siltstones (Facies D2.1) form part of the levée facies association. Apart from turbidites, other sediment gravity-flow deposits are present in minor amounts in the A6 core sediments. These include cohesive-flow deposits (slides and slumps) (Facies F2.1) and other laminar-flow deposits, as well as those resulting from the settling from suspension (Facies E1.1, interpreted as hemipelagites). There are mm-to-cm-sized bands in the core composed mainly of *nummulites*, *alveolinids* and disaggregated shell material (Plate 4.2c). They tend to occur towards the top of the A6 core. These nummulitic packstones were probably redeposited into deep-water from adjacent carbonate platforms during storm events (as tempestites).

Facies name	Description	Interpretation
Thin-bedded sandstones (C2.3)	Sandstones are moderately sorted and show subtle gradational fining upward trends (Plate 4.2a). Thickness range from mm to up to 6 cm thick. Bouma divisions are mainly T_c and T_d and may contain a thin mudstone cap (T_e division) (Plate 4.2c). Many beds are flat topped but locally may be current-rippled. Planar laminations generally occur in turbidites >1 cm thick. Turbidite bases are sharp but with little (mm) or no erosion. Pyrite is common in the turbidites and forms small cubic opaques that concentrate forming clusters (Plate 4.3b). Filaments of organic matter parallel to bedding are common (Plate 4.3e).	Dilute/low-density turbidity current deposits. The combination of biogenic and detrital elements is typical of re-sedimented deposits.
Regular siltstone and mudstone laminae (D2.3)	Thin regular silt and mud laminae. Siltstone laminae show generally sharp tops and bases. Intervals of silt and mud laminae can reach 2 m thick (Plate 4.2l).	Transportation by waning low-density turbidity currents. Deposition by suspension fall-out.
Structureless mudstones (E1.1)	Mudstones are dark grey in colour, homogeneous with a uniform grain-size distribution (Plate 4.2h and 4i). The mudstones lack primary sedimentary structures including fine laminations. Bed tops and bases are sharp. Thickness is typically between 1 and 6 cm. Burrowing structures are commonly present and pyritised burrow tubes can commonly be seen in these bands.	The lack of sedimentary structures and the presence of bioturbation suggests hemipelagic deposition by suspension fall-out.
Unstratified siltstones (D1.3) and silty-mudstones (E 1.3)	Pale grey in colour, commonly disorganised. Bed top and bases can be sharp or gradational. Sorting is poor to moderate. Bioturbation can be locally very intense and can totally homogenise the sediments.	Deposition by suspension fall-out.
Graded and stratified siltstones (D2.1)	Thin-to-medium-bedded, well sorted, light-grey in colour, normally graded from silt to clay-size particles and densely bioturbated (Plate 4.3h).The bases of beds are commonly sharp.	Transported *via* low-concentration turbidity currents.
Chaotic sediments-muddy slides and slumps (F2.1) and disorganised gravely muds (A1.2)	Folded and contorted siltstones and mudstones. Locally, sand packages and shallow marine debris including corals and shells are present (Plate 4.2e). Thickness varies from 10 cm to 4m. Locally, sedimentary structures such as siltstone-mudstone laminae are preserved (Plate 4.2f). Typically the folds are tight and most are recumbent relative to bedding. Bases are sharp and tops vary from planar to irregular. Bioturbation is absent to sparse.	Deposited *via* slumps and slides and cohesive debris flows. These events were caused by basin slope failure.
Disorganised nummulitic sandstones (A1. 4)	Carbonate cemented nummulitic sandstones form thin bands (up to 5 cm thick) of nummulites, broken thin shells and other shallow marine material (Plate 4.2c, 4.2e and 4.3f). Occur mainly in the uppermost 45 m of Well A6.	Storm deposits transferred from adjacent carbonate platforms. Re-deposited tempestites/storm layers.

Table 4.1 Summary of facies recognised in the A6 core. Facies classification scheme from Pickering *et al.* (1986b, 1989).

Locally, the core shows tectonic deformation, e.g., at 71 m core depth there is a 10 cm-thick duplex structure with calcite veining which is interpreted as a post-depositional thrust-fault zone (Plate 4.2a, Appendix 3). This area corresponds with pronounced peaks in the natural gamma and several XRF elements (Figure 4.3). These observations suggest that the duplex probably represents a zone of significant but non-quantifiable tectonic dislocation. Also, at 142 m core depth, there is a 15 cm-thick breccia with crystal-fibre slickensides caused by shearing (Plate 4.2b, Appendix 3). Unlike the duplex, this horizon is not represented by any natural gamma-ray or XRF anomalies (Figure 4.3), and although it is likely to be a thrust, it is possible that any tectonic dislocation was less significant than that for the duplex structure at 71 m core depth.

Locally, the core is intensively bioturbated and different ichnospecies have been recognised and studied by Heard and Pickering (2008), and Heard *et al.* (2008). The most common ichnotaxa identified from shallowest to deepest tier, are *Phycosiphon, Nereites, Planolites, Scolicia, Thalassinoides, Zoophycos* and *Chondrites*. Burrows appear flattened due to burial compaction and show a typical ratio of 4:3 mm suggesting a 60% degree of vertical compaction. Table 4.1 summarises the various facies identified in the A6 core adopting the hierarchical and descriptive facies classification scheme of Pickering *et al.* (1986b, 1989). Plates 4.2 and 4.3 show selected examples of facies and structures observed in the core.

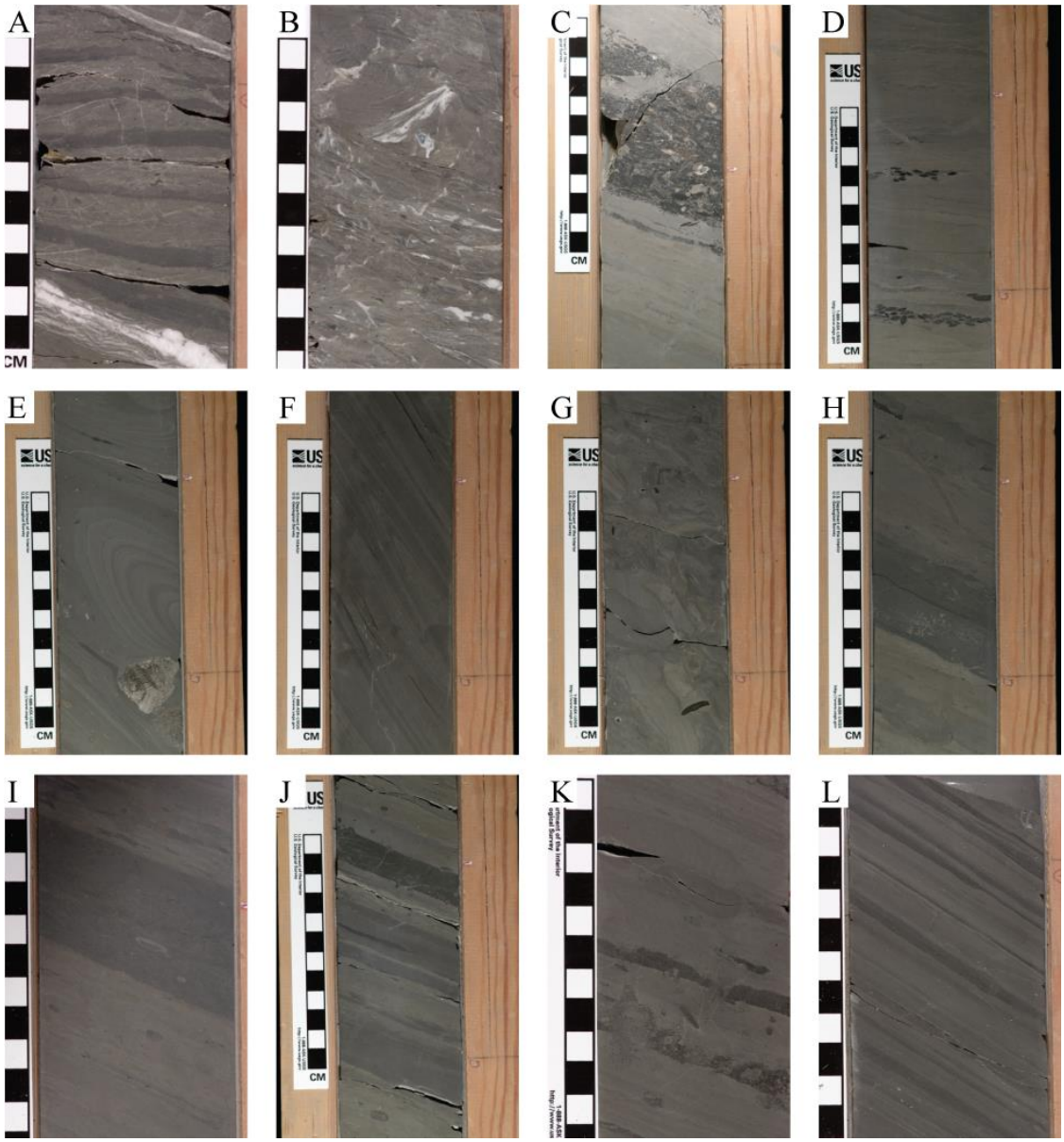

Plate 4.2 Close-up photographs of the A6 core (a) Duplex structure at 71 m core depth. **(b)** Breccia with crystal-fibre slickensides at 142 m core depth. **(c)** Nummulitic packstone (Facies A1.4) at 20 m core depth. **(d)** Nummulitic packstones at 52 m core depth associated with sediment slide unit (Facies F2.1). **(e)** Sediment slide at 22 m core depth showing folded siltstones (Facies F2.1), containing shallow-marine material such as nummulites and corals. **(f)** Sediment slide (Facies F2.1) at 41 m core depth showing and increase in dip in the finely laminated mudstone-siltstone laminae. **(g)** Debris flow deposits at 37 m core depth (Facies A1.2). **(h)** Muddy dark band with sharp boundaries at 69 m core depth showing bioturbation (Facies E1.1). **(i)** Dark band with sharp boundaries (Facies E1.1) at 114 m core depth. **(j)** Graded siltstones and structureless muds (Facies D2.1 and E1.1) at 72 m core depth. **(k)** Intense bioturbation of the core which has erased part of the original sedimentary structures at 222 m core depth. **(l)** Silt and mud laminae with very fine-grained sandstone turbidites (Facies D2.3 and C2.3) at 189 m core depth.

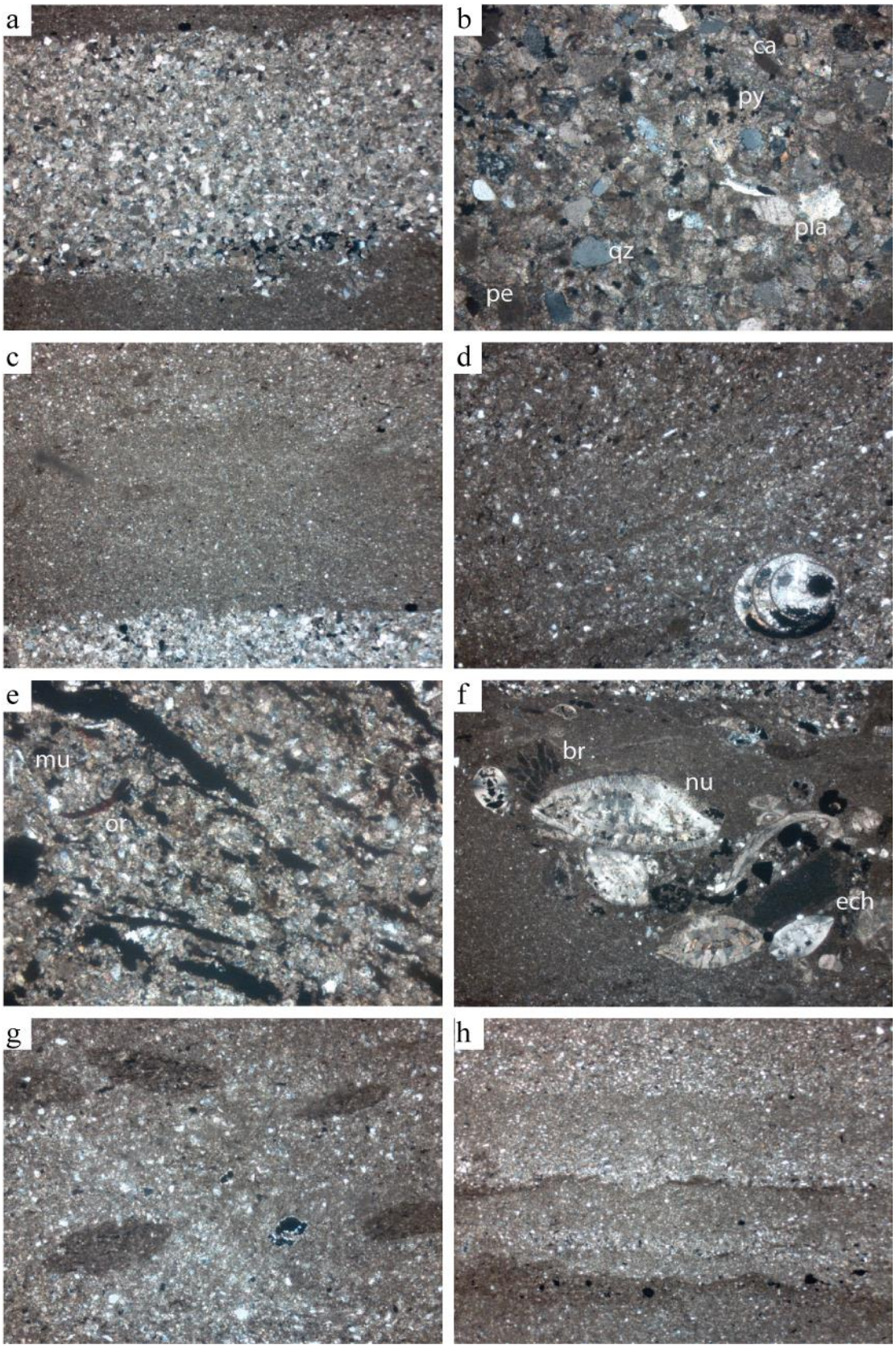
a
b
ca
py
pla
qz
pe
c
d
e
mu
or
f
br
nu
ech
g
h

Plate 4.3 Thin sections of the A6 core. (a) Field of view (FOV) 4.5 mm, cross-polarised light (XPL). Sandstone turbidite (Facies C2.3) showing sharp boundaries and subtle normal grading at 175 m core depth. **(b)** FOV 1.1 mm, XPL. Turbidite sandstone at 174 m core depth. Most grains are quartz (qz) and carbonates (ca) with some plagioclase feldspars (pla) showing characteristic lamellar twinning and alkali feldspars with perthitic textures (pe). Muscovite (mu), pyrite framboids (py) and Fe-oxides are present in minor amounts. Shell fragments and nummulites are commonly seen. **(c)** FOV 4.5 mm, XPL. Sandstone turbidite with 2mm mud cap at 175 m core depth. **(d)** FOV 2.25mm, XPL view. Foraminifera preserved in silty sediment at 112 m core depth. Initial geopetal infill with pyrite and then cavity finally filled with sparite calcite. **(e)** FOV 1.1mm, XPL. Organic matter and pyrite in sandstone turbidite at 65 m core depth. **(f)** FOV 4.5mm, XPL. Package of remobilised nummulites (nu), echinoids (ech) and bryozoans (br), pyrite also present at 64 m core depth. **(g)** FOV 2.25 mm, XPL. Flattened burrows in siltstones due to compaction at 112 m core depth. **(h)** Normally-graded silty beds at 175 m core depth. FOV 4.5 mm, XPL.

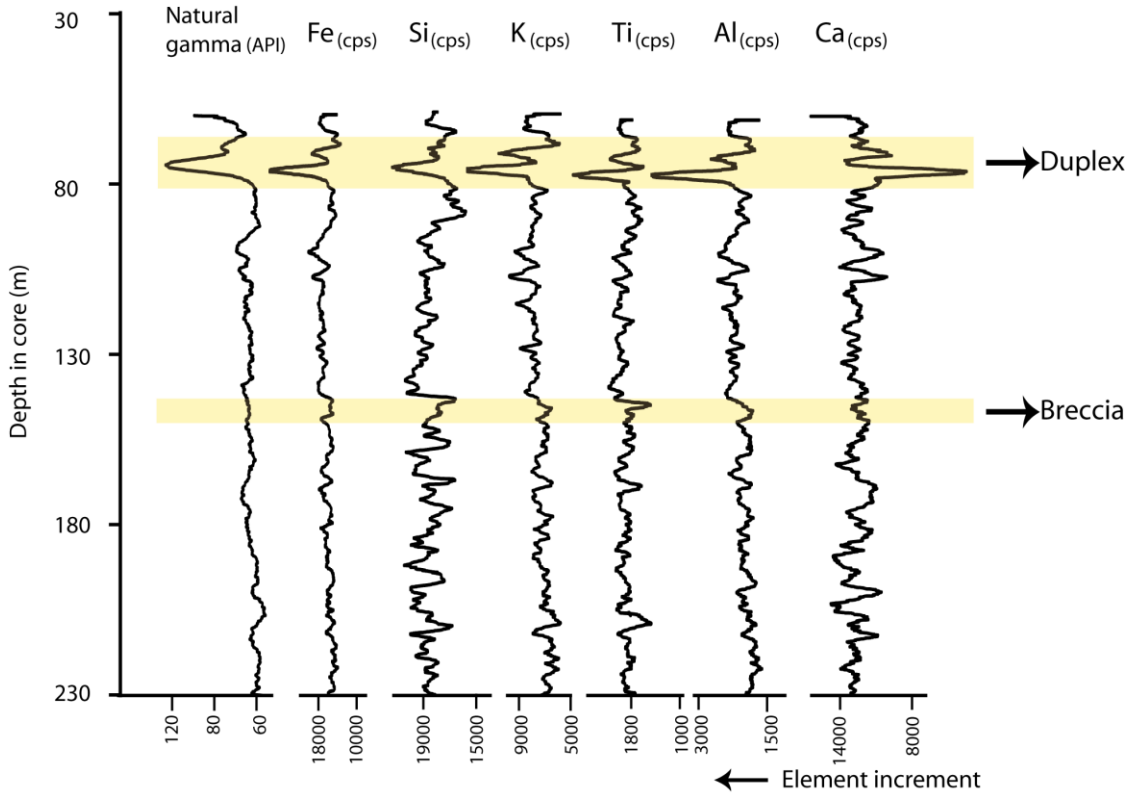

Figure 4.3 XRF elements showing thrust zone anomaly. Anomalous spike at ~ 71 m depth can be seen in the natural gamma and in most of the XRF elements. This spike is associated with a thrust zone (Plate 4.2a). The breccia seen at ~ 142 m (Plate 4.2b) does not show any anomaly in the XRF elements. cps - counts per second.

4.4.2 A6 core sedimentary divisions

The A6 core can be divided into three principal stratigraphic intervals. The lower (oldest) 50 m section is characterised by abundant thin-bedded, very fine and fine-grained sandstone turbidites. There are intervals of thin, regular, siltstone-mudstone laminae (Plate 4.2l) tens of cm thick and bioturbated siltstone and silty mudstones (Plate 4.2j). This core section corresponds to the top of the Ainsa II Fan and is deposited off-axis from the basin-floor Ainsa III Fan (Figure 4.1). In the middle part of the A6 core, there is a lower frequency of thin-bedded, fine and very fine-grained sandstone turbidites. These sandstone turbidites tend to be thinner (average 1-2 cm) than in the fan abandonment and off-axis deposits. Where bioturbation intensity is least, packages of siltstone and mudstone laminae with interbedded mm-size sandstone turbidites are well preserved. Mapping suggests that this middle section represents the interfan deposits between the Ainsa III and Morillo I fans (Pickering and Bayliss, 2009). The upper 45 m of the core comprises several MTDs consisting mainly of cm to m-scale sediment slides (Plate 4.2e and 4.2f), and debris-flow deposits (Plate 4.2g), containing redeposited nummulites (Plate 4.2d) and other shallow-marine material such as coral fragments redeposited from shallow-marine sites (Plate 4.2f). Sediment slides are identified by anomalous bed dips, folding, attenuation and disaggregation of beds. These MTDs probably resulted from the gravitational collapse of lateral-margin basin-slope sediments, as there is an absence of coarse detrital material. This upper core section possibly represents the initiation of the Morillo I sandbody (fan) (Figure 4.1). Representative sedimentary logs of the main sections of the A6 core can be seen in Figure 4.4.

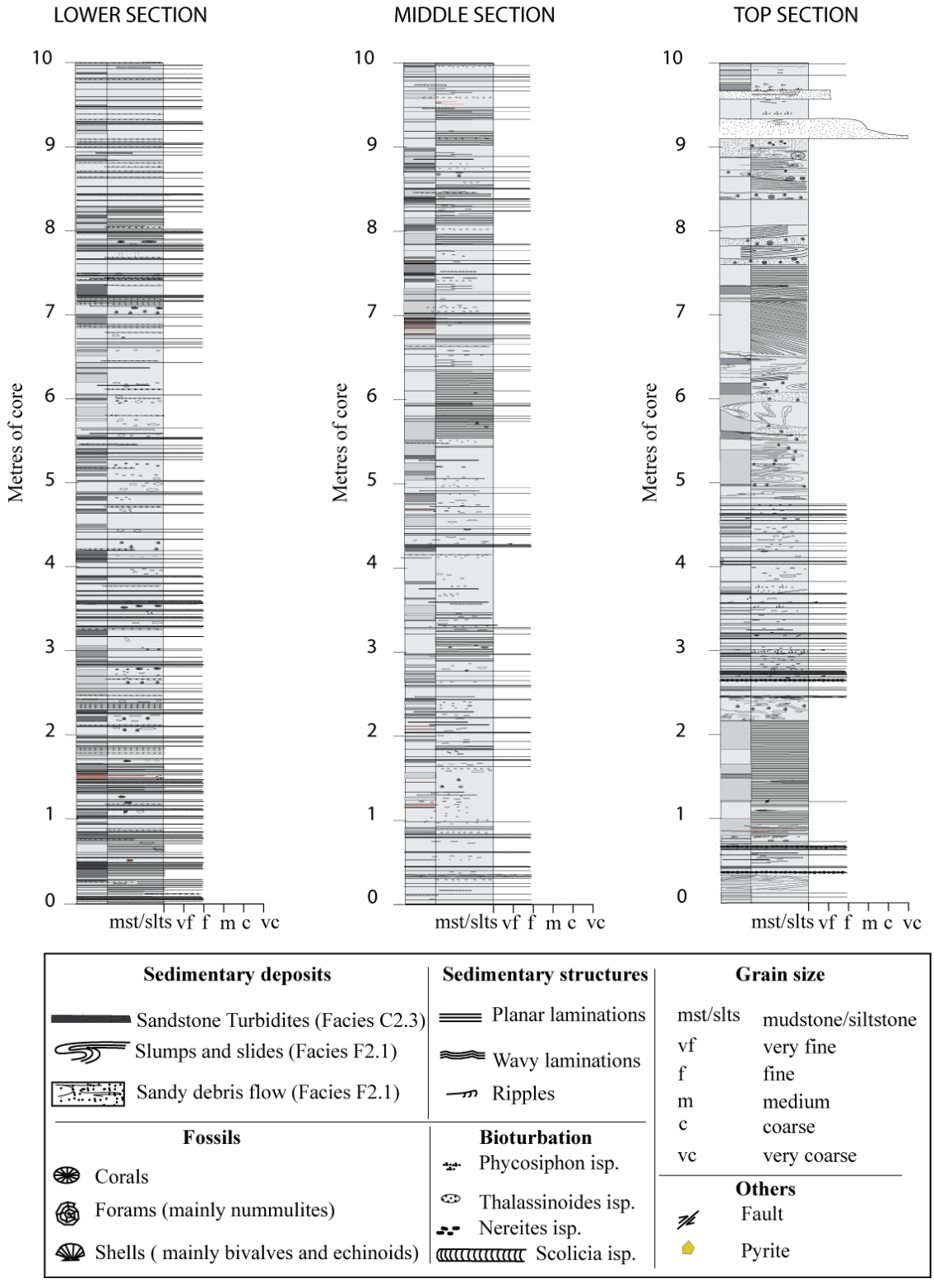

Figure 4.4 Representative sedimentary logs of the three main sections of the A6 core. This figure shows the variability in abundance of sandstone turbidites. The lower section is characterised by a larger number of turbidites, the middle section contains thick intervals of finely laminated mud-silt couplets and the top section is characterised by numerous sediment slides. Appendix 3 shows complete sedimentary logs of the A6 core.

4.5 Geochemical study of the A6 core

This section combines the results from the XRF scanning, XRD, SEM, TOC and carbon isotope analyses to interpret environmental and depositional changes in the chemistry of the sediments. Parameters such as bioturbation and sandstone turbidite abundance have also been included to link chemical changes to the sedimentology of the A6 core. Bioturbation intensity was studied by Heard and Pickering (2008) and Heard *et al.* (2008). Sandstone turbidite intensity was calculated by counting the number of sandstone turbidites ≥ 0.2 mm thick in successive 10 cm-thick vertical core intervals. Lithogenic elements have been normalised to aluminium content in order to account for carbonate dilution effects (Shimmield and Mowbray, 1991). Normalising data to a conservative element such as Al is useful to determine relative changes in other elements in settings where biological and diagenetic processes may influence their geochemistry (Löwemark *et al.*, 2011).

4.5.1 XRF results

Well A6 core was scanned using a multi-element XRF scanner from 230 to 60 m depth below the surface using a core spacing interval of 4 cm between measurements. This section avoids the top 60 m of chaotic sediments of the A6 core but contains the thrust at ~ 71 m core depth. Any geochemical work undertaken in the A6 core was therefore restricted to 230-80 m depth to prevent this deformed area. The methodology used for the XRF scanning has been detailed in Section 2.5.

4.5.1.1 Elemental distributions

Correlation-coefficient matrices between element pairs for a 31 m long dataset using a spacing interval of 3.5 mm (N = 8,300) were determined in order to examine potential relationships (Table 4.2) and any controls on the chemical composition of the sediments in the A6 core. Elements such as Al, Ti, K, Rb and Zr are exclusively present in the detrital component and are not influenced by biogenic or diagenetic processes. These elements can, therefore, reveal changes in the composition of the detrital inputs.

Table 4.2 Correlation coefficients calculated for pair of elements.

	Al	**Si**	**S**	**K**	**Ca**	**Ti**	**Mn**	**Fe**	**Cr**	**Rb**	**Sr**
Si	0,38										
S	-0,04	0,08									
K	**0,88**	0,19	0,01								
Ca	**-0,71**	-0,3	-0,07	**-0,64**							
Ti	0,44	0,42	0,08	**0,61**	-0,45						
Mn	-0,34	-0,06	0,07	-0,25	0,31	0,05					
Fe	**0,74**	0,32	0,08	**0,75**	-0,59	0,45	-0,24				
Cr	0,08	0,17	0,06	0.12	0,01	0.20	0.18	0,09			
Rb	**0,74**	0,38	0,08	**0,78**	**-0,6**	0,47	-0,26	**0,62**	0,09		
Sr	-0,19	0,07	0,03	-0,19	0,23	-0,12	0,18	-0,14	0,02	-0,15	
Zr	0,01	0,43	0,04	-0,08	-0,03	0,14	0,05	0,01	0,08	-0,02	0,22

Resolution 3.5mm spacing interval through 31 m of core stratigraphy. N = 8,300. Shown in bold strong correlation coefficients (>0.6).

The correlation matrices show positive association between Al, Ti, K, Rb, and Fe (Table 4.2), which reflects the continental, derived silicate fraction of the sediment. These elements are inversely related to Ca content, which represents the most important biogenic (and diluting) component in the Ainsa Basin sediments. The negative correlation between typical terrigenous and biogenic elements reflects the mixed marine and terrestrial sources of the sediments. Aluminium is principally derived from aluminosilicate clay minerals. The strong association between Al, K and

Rb (0.74-0.88) suggests detrital clay input of relatively uniform composition. Iron can appear incorporated into clay minerals such as chlorite, smectite and illite (Goldhaber and Kaplan, 1974). The strong association of Fe with K, Rb, and Al is evidence for the presence of detrital Fe-bearing clay minerals (Cosgrove, 1973). The Fe *versus* Al cross-plot, for example, shows this correlation (Figure 4.5).

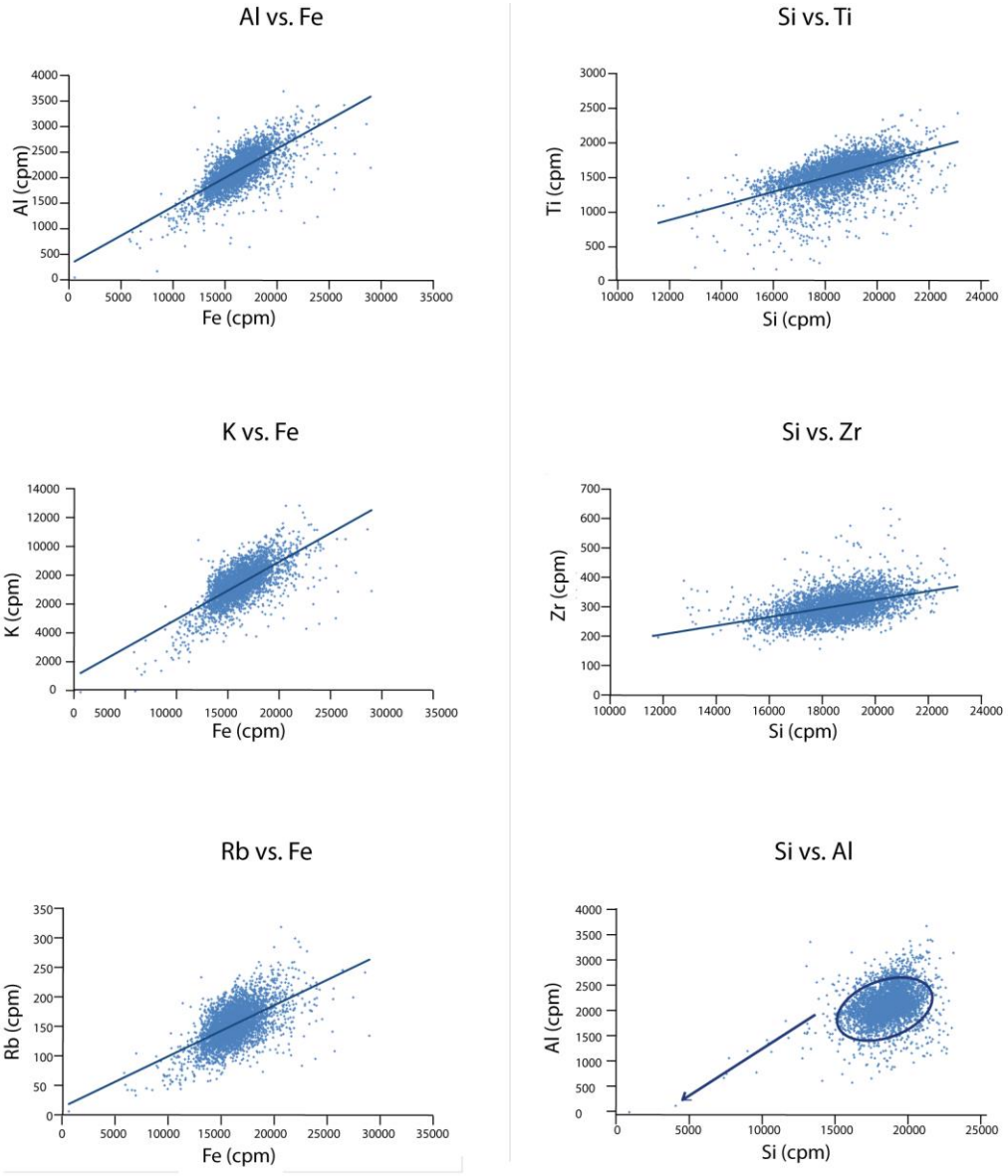

Figure 4.5 Cross-plots of selected elements in the A6 core. N = 8,300. There is a positive correlation between Al, K and Rb with Fe indicating the presence of Fe-bearing clay minerals. Si correlates well with Zr and Ti indicating that Zr and Ti mainly appear as zircon ($ZrSiO_4$) and sphene ($CaTiSiO_5$), respectively. The Si *versus* Al cross-plot shows a small compositional group that correlates positively with Al, and probably shows the association of some Si to clay minerals. There is a larger group that does not show correlation with Al and probably indicates that the majority of the Si resides in quartz.

Titanium is present in soils and sediments in the form of Ti-oxides and silicate mineral phases such as rutile (TiO_2), sphene ($CaTiSiO_5$) and ilmenite ($FeTiO_3$) (Force, 1976; Humphrey and Bowen, 1982). In the A6 core, Ti has a moderate correlation with elements such as K, Al, Rb and Fe (R = 0.44-0.61), and this probably indicates the presence of Ti in clay minerals. The positive association of Ti with Si (R = 0.42), which may indicate the presence of Ti-bearing mineral phases such as sphene, tend to be transported in the coarse fraction. This may indicate that the Ti is partitioned between the coarse and the fine fraction with some Ti associated with clay minerals and the rest transported in the coarse fraction associated with heavy minerals (e.g., Correns, 1954; Boyle, 1983).

Zirconium occurs in sediments mainly as the mineral zircon ($ZrSiO_4$). Zircon is a mineral chemically resistant to weathering due to its hardness and lack of cleavage (Sudom and St. Arnaud, 1971; Milne and Fitzpatrick, 1977; Dypvik and Harris, 2001). Cross-plots of Si *versus* Zr (Figure 4.5) show a compositional grouping probably indicating that most of Zr is present in the sediments in the form of zircon. Zirconium tend to be transported in the coarse fraction and is likely to be concentrated in the sandstone turbidites. Zirconium is likely to be sourced by granites and this inference is supported by petrographic analyses of Ainsa Basin sediments by Das Gupta and Pickering (2008) who found that the quartz grains in sandstone turbidites were exclusively derived from an igneous plutonic origin.

The correlation of silica with detrital elements is in general moderate (R = 0.4). Silica may be associated with detrital quartz or bonded in clay minerals such as aluminosilicates. Quartz will tend to be delivered in the coarse fraction while Si-bound in clay minerals would have been transported in the fine fraction. The cross-plot of Si *versus* Al shows that the majority of the data does not display any robust correlation.

There is, however, a small grouping indicated with an arrow in Figure 4.5 that shows a positive correlation and may indicate the association of Si with detrital clay minerals.

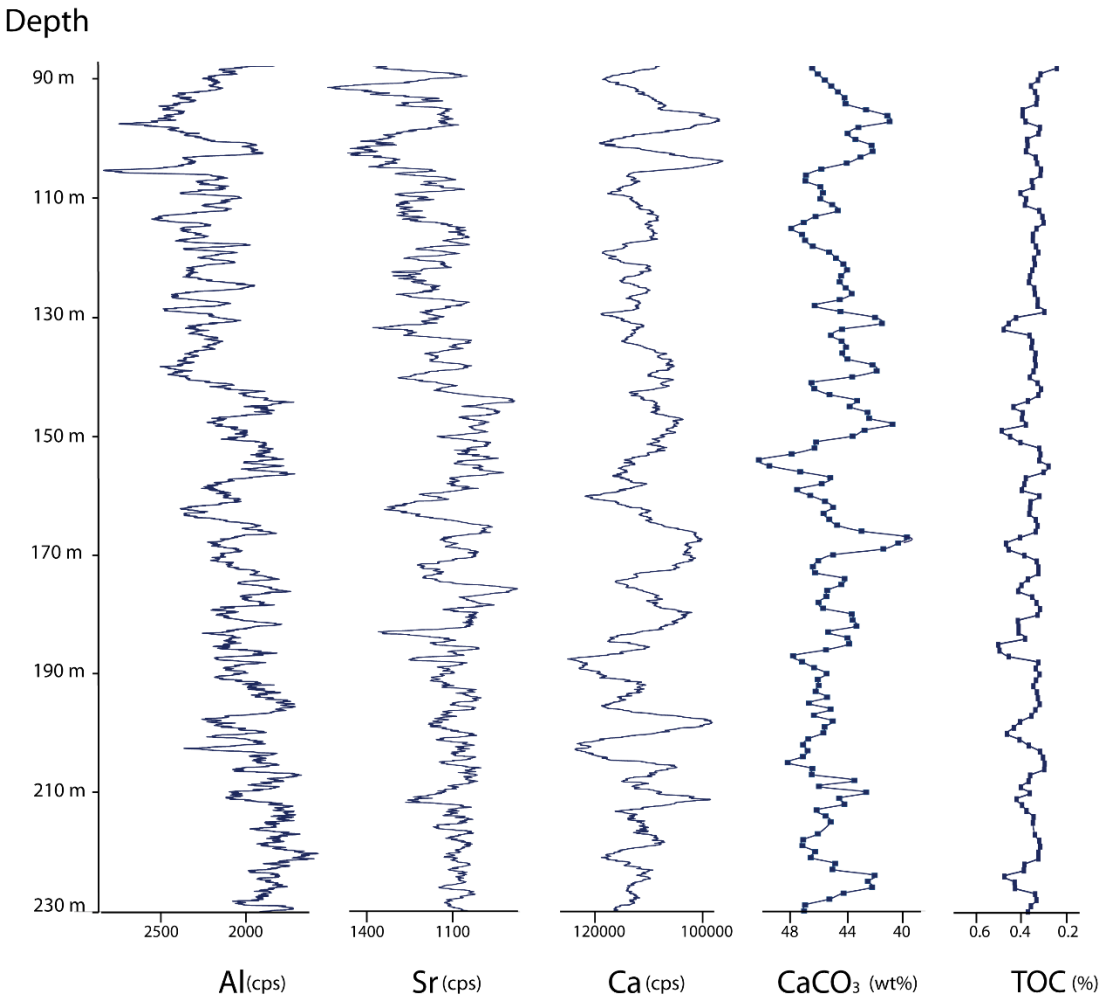

Figure 4.6 Al, Sr and Ca trends from XRF analysis compared with $CaCO_3$ and TOC results. TOC values are low and stable. Ca and $CaCO_3$ follow a similar profile indicating that most of the Ca in the rocks derives from $CaCO_3$. It does not appear to have major changes in productivity in the A6 core sediments. A weight-3 moving average has been applied to the $CaCO_3$ and TOC values and a weight-25 moving average has been applied to the XRF data.

Strontium occurs in a variety of rock-forming minerals including feldspars, calcite and dolomite. In marine carbonates, Sr tends to show a good association with Ca since Sr substitutes for Ca in the calcite lattice causing a strong linear relationship between these two elements (Deer *et al.*, 1966). Strontium can also be of detrital

origin. During weathering, Sr can be easily mobilised and incorporated into clay minerals where it has a strong adsorption. Figure 4.6 shows the profiles of Al, Sr and Ca. The Sr and Al profiles show a similar trend but they differ from the Ca profile. The similarities between the Sr and Al trend suggests that most of Sr present in the A6 sediments originated from the weathering of carbonates and was likely transported in rivers associated with clay minerals. A comparison between Ca from XRF and $CaCO_3$ from TC and TOC analyses shows a similar general profile (Figure 4.6), suggesting that the most important source of Ca in the A6 core material came from calcium carbonate. The lower 50 m of Well A6 has a lower degree of correlation between Ca and $CaCO_3$. This part of the core is characterised by a greater abundance of sandstone turbidites, and it is likely that the profile was affected by additional sources of Ca which may be present in plagioclase feldspars (as seen in thin-sections of sandstone turbidites) and in heavy minerals such as titanite ($CaTiSiO_5$), as inferred by the correlation index between Ca and Ti -0.45 (Table 4.2).

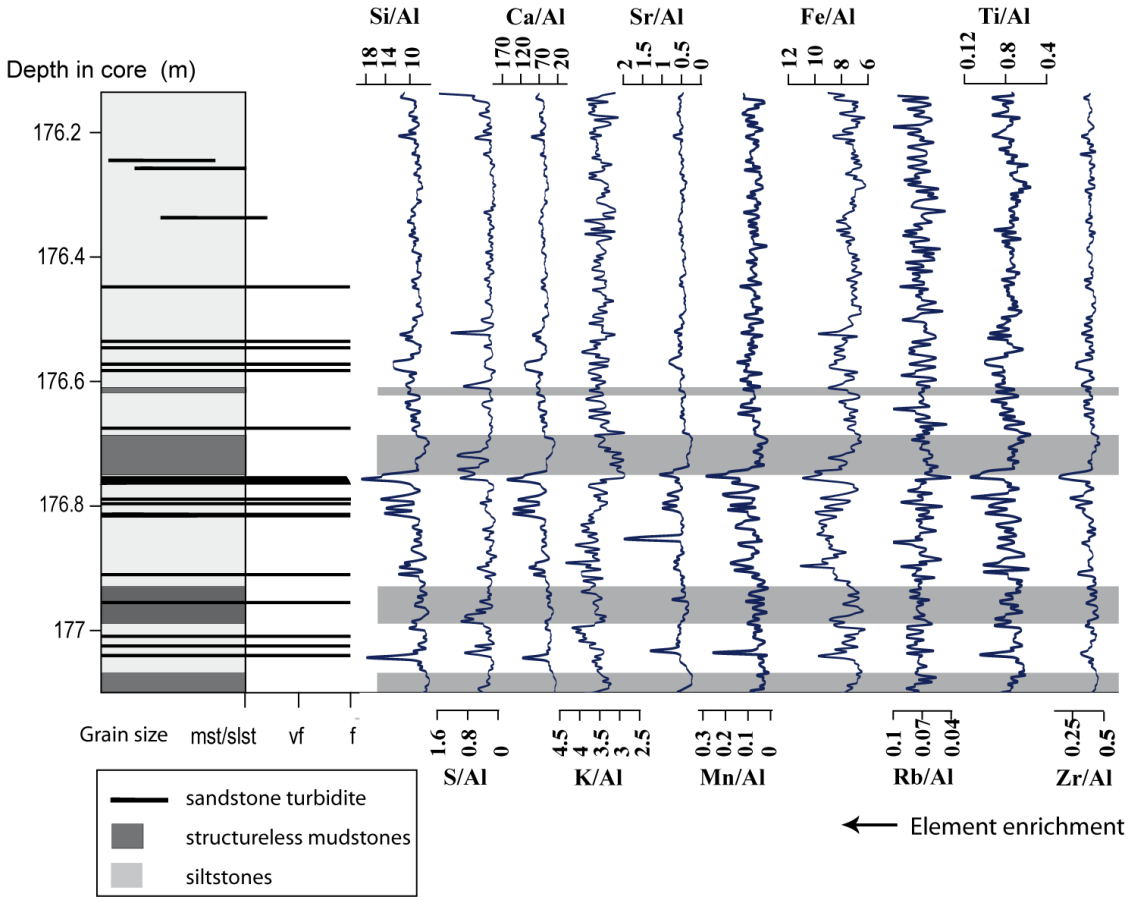

Figure 4.7 Sedimentary logs compared with 3.5mm spacing XRF data. Elements have been normalised to Al to account for dilution effects. Note the enrichments of Si, Ti, Fe, Zn, Zr, K, Sr, and Mn in the sandstone turbidites and the depletions of these same elements in the mudstones (grey bands).

Multi-element XRF data collected using a 3.5 mm spacing was compared with sedimentary logs to evaluate the relative abundance of chemical elements in the different sedimentary facies of the A6 core (Figure 4.7). Fine-grained sandstone turbidites are characterised by enrichments of Si, Ti, Fe, Zn, Zr, Ca, Sr, Mn and S relative to the surrounding siltstones. In contrast, structureless mudstones have a higher content of S at their base, but low contents of Ca, Si, K, Fe, Sr, Zr, Zn and Mn. Sandstones are, therefore, enriched in detrital elements such as Zr, K, Ti and Fe and in biogenic elements such as Ca whilst the mudstones are relatively depleted in these same elements. Mn forms insoluble compounds and accumulates in sediments

deposited under oxygenated conditions and its content is also high in the sandstones. The only element which appears to be elevated in both sandstones and mudstones in relation to the surrounding siltstones is S. The presence of S is confirmed by the visual observation of pyrite (FeS_2) mainly concentrated in these two sedimentary facies.

4.5.1.2 Grain-size distributions

Some elemental ratios in the A6 core can be used as a reliable proxy for grain size, e.g., Zr/Rb, Zr/Al, Si/Al and Ti/Al (Boyle, 1983; Schneider *et al.*, 1997; Schnetger *et al.*, 2000; Bloemsma *et al.*, 2012). Zirconium, silica and titanium are mainly transported with the sand and coarse-silt fractions and can be used as a representative of the detrital coarse fraction (Correns, 1954; Boyle, 1983; Brumsack, 1986). The use of Si/Al ratios may be affected by the presence of biogenic silica, although most of the Si in the Ainsa sediments appears to be associated with detrital quartz and clay minerals. The Ti/Al ratio is useful as a proxy for grain size since the origin of Ti is considered to be exclusively terrigenous (Murray and Leinen, 1996). In contrast, Al and Rb provide a proxy for the fine-size fraction: the latter two elements are strongly sorbed to clay minerals which prevent their environmental mobility (Arthur *et al.*, 1985). The use of Zr/Rb ratios as a proxy for grain-size, however, can be unreliable if there is a significant contribution of Rb from K-feldspars, commonly associated with coarse silt and sand size fractions. XRD results indicate that feldspar is present in a low percentage in both sandstone turbidites and siltstones. Graphs of Zr/Al, Ti/Al, Zr/Rb and Si/Al used as proxies for grain size, all show similar profiles with a progressive decrease in grain size towards the top of the A6 core (Figure 4.8). When compared with sandstone turbidite intensity, these grain-sized proxies show good agreement, suggesting that most of the Zr, Ti and Si is indeed contained within the

sandstone turbidite (Figure 4.8). These findings corroborate the interpretation that the lower part of the A6 core represents the off-axis deposits of the Ainsa III Fan. Figure 4.8 also compares sandstone turbiditite and mudstone intensities. Both facies appear to be more common in the lower part of the core. The turbidite intensity appears to decrease cyclically but the mudstone intensity is maintained relatively constant.

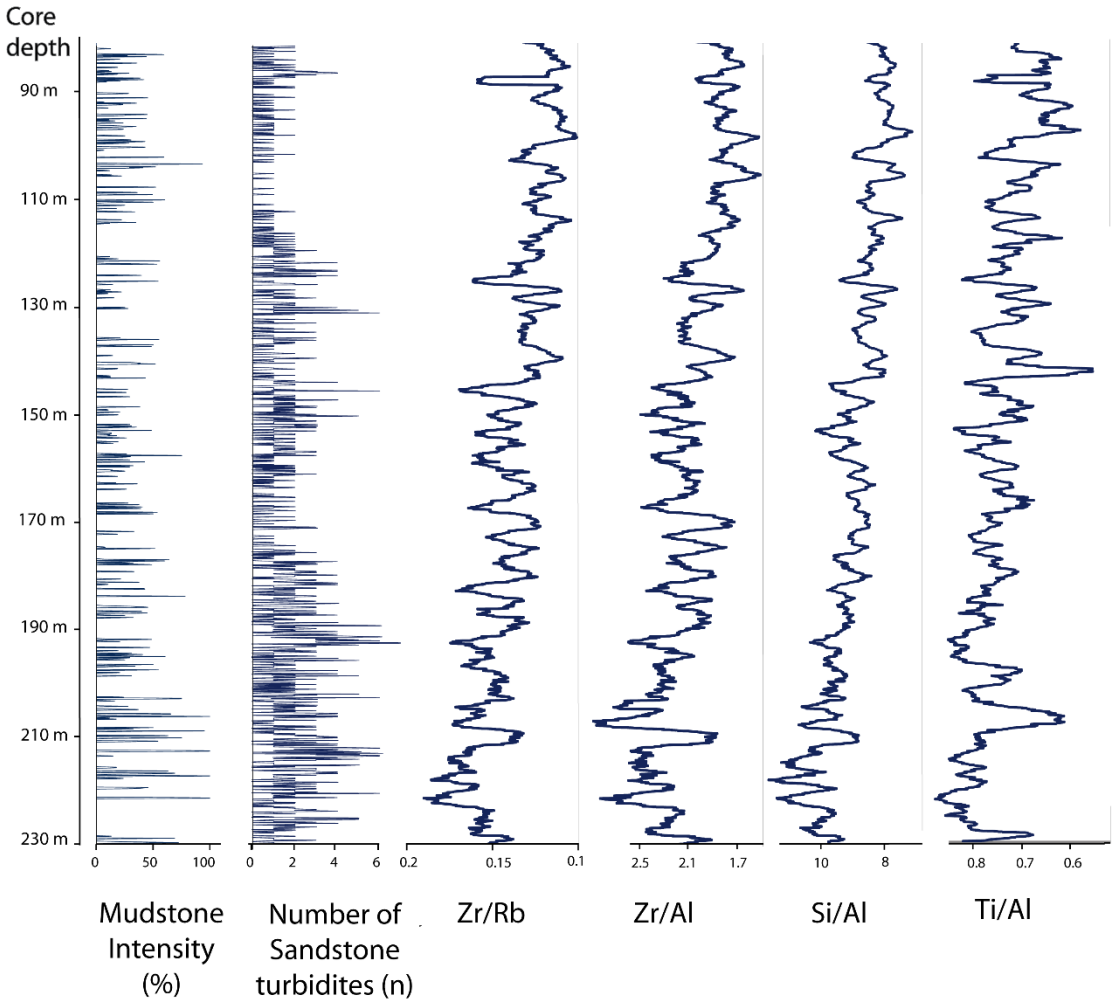

Figure 4.8 Comparison between mudstone intensity, sandstone turbidite intensity and grain-size palaeoproxy profiles. Higher sandstone and mudstone intensity occur in the lower parts of the core whilst turbidite intensity decreases cyclically, mudstone intensities are maintained relatively constant. There is a similar decrease trend in all the grain-size palaeoproxy profiles which is inversed to the sandstone turbidite profile. This inverse relationship suggests that most of the detrital quartz, Ti-rich minerals and heavy minerals (zircon) are associated with the sandstone turbidites. Note the progressive decrease in grain size in the core with a dominance of clay minerals towards the top of the core.

4.5.2 X-ray mapping

An x-ray elemental map of a 2.5mm thick sandstone turbidite surrounded by siltstones from the A6 core can be seen in Plate 4.4. X-ray mapping highlights the spatial variation of grain size in siltstone and sandstone turbidites. Minerals containing elements such as Si, Al, Ca, Rb and Sr show a significant increase in grain size in the sandstone turbidites, whilst minerals containing Fe, K, Ti and Zr do not display any significant grain-size distribution. S appears exclusively in the sandstone turbidites, mainly concentrated at the base of the beds.

Aluminium and K appear to be more abundant in the siltstones, whereas Ca, Si, Rb and Sr dominate in the sandstone turbidites. Zirconium shows a very subtle preferential distribution within the sandstone turbidites and Ti is partitioned equally between the sandstone and siltstones. It should be noted that this elemental mapping technique shows the bulk of the element distribution and does not take into consideration dilution effects of the carbonate content.

Plate 4.4 (next page) X-ray elemental mapping across a 2.5mm sandstone turbidite surrounded by siltstones. The X-ray photograph shows the spatial distribution of different chemical elements. Significant grain size variations between the sandstones and siltstones can be seen in minerals containing elements such as Al, Ca, Si, Rb and Sr whilst Fe, K, Zr and Ti do not show particular grain size changes. S is mostly concentrated in the sandstone turbidites.

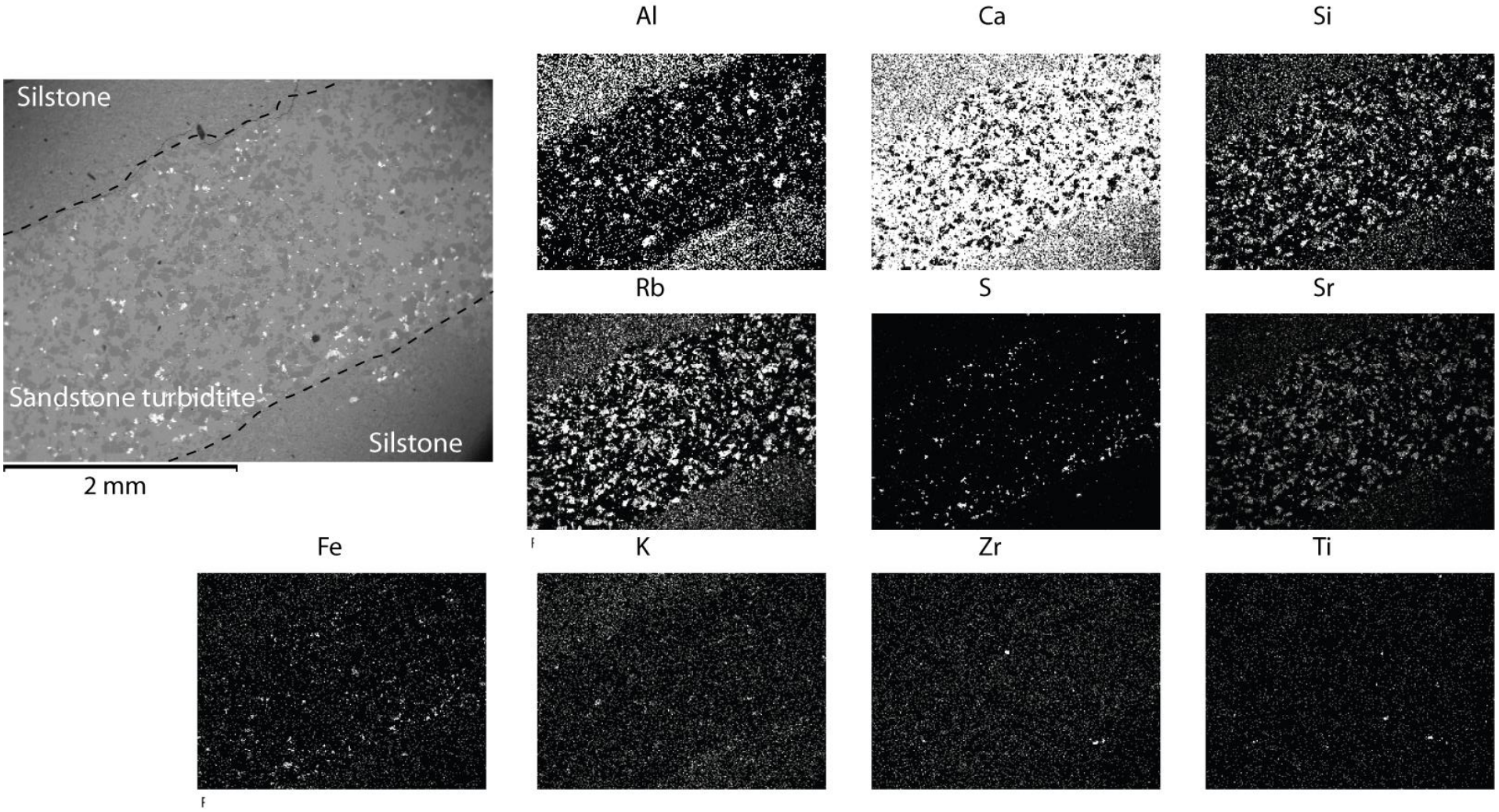
Silstone
Sandstone turbidtite
Silstone
2 mm
Al
Ca
Si
Rb
S
Sr
Fe
K
Zr
Ti

4.5.3 SEM and XRD results

The bulk mineralogy for samples from Well A6 were determined by XRD and analysed by SEM (Plate 4.5). XRD was undertaken in 6 samples: 2 siltstones, 2 unstructured mudstones and 2 sandstone turbidites. The XRD spectra plots of the 6 samples are shown in Figure 4.9.

Detrital quartz and calcite are present in major amounts, together with some phyllosilicates (chlorite and muscovite) and feldspars (probably albite) (Figure 4.9, Plate 4.5). Minor minerals such as framboids of pyrite are also present in the samples although they appear more concentrated at the base of the sandstone turbidites (Plate 4.3a and 4.4). Rare grains of titanite (sphene) are found in the sandstone turbidite (Plate 4.5). BSE images of the sandstone and siltstones show that the rocks are tightly cemented by calcite, ranging from micrite to microsparite and locally dolomite is present (appears less crystalline in the XRD analysis).

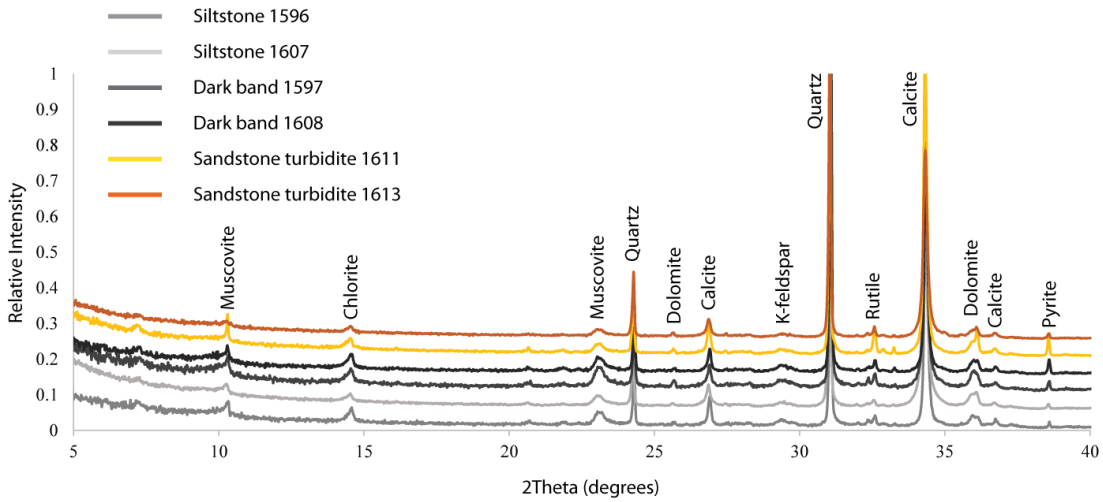

Figure 4.9 XRD spectra obtained from 6 bulk samples of the A6 core. The samples were analysed using X-ray powder diffractometry. The three main lithologies of the A6 core were sampled: sandstone (orangey colour), unstructured mudstones (dark grey colour) and siltstones (pale grey colour). Due to large differences in the total counts for each of the samples, intensities have been re-scaled to a total value of 1 and then each spectrum has been artificially separated by adding a constant small percentage. Despite these computations, the relative intensity between the peaks is maintained intact allowing for the determination of semi-quantitative mineral concentrations.

Figure 4.9 shows that all the samples have a very similar mineralogy, although there is probably some variation in the amounts of quartz and calcite relative to layer silicates. The spectral plots indicate that it seems quite likely that the siltstone 1607 and the sandstone turbidites 1611 and 1613 have rather more layer silicates in them. Trying to quantify the numerical differences in the proportion of these minerals was not attempted as it is likely that the results produced would not be reliable without including more samples.

The sandstone turbidite 1611 shows reflections from the mica mineral which are much sharper than in the other samples, implying better crystallinity and possibly larger grains. The reflections from the layer silicates in the other sandstone turbidite 1613, look somewhat different from those in the 1611 pattern; the 14 Ångström reflection (about 7 degrees 2 theta) is relatively weaker, so it is possible that either there is some difference in the composition of the chlorite or is due to the presence of a 1:1 layer silicate. Pyrite reflections seem to be more prominent in the sandstone turbidite and in the dark bands, whilst reflections of chlorite appear more significant in the dark bands.

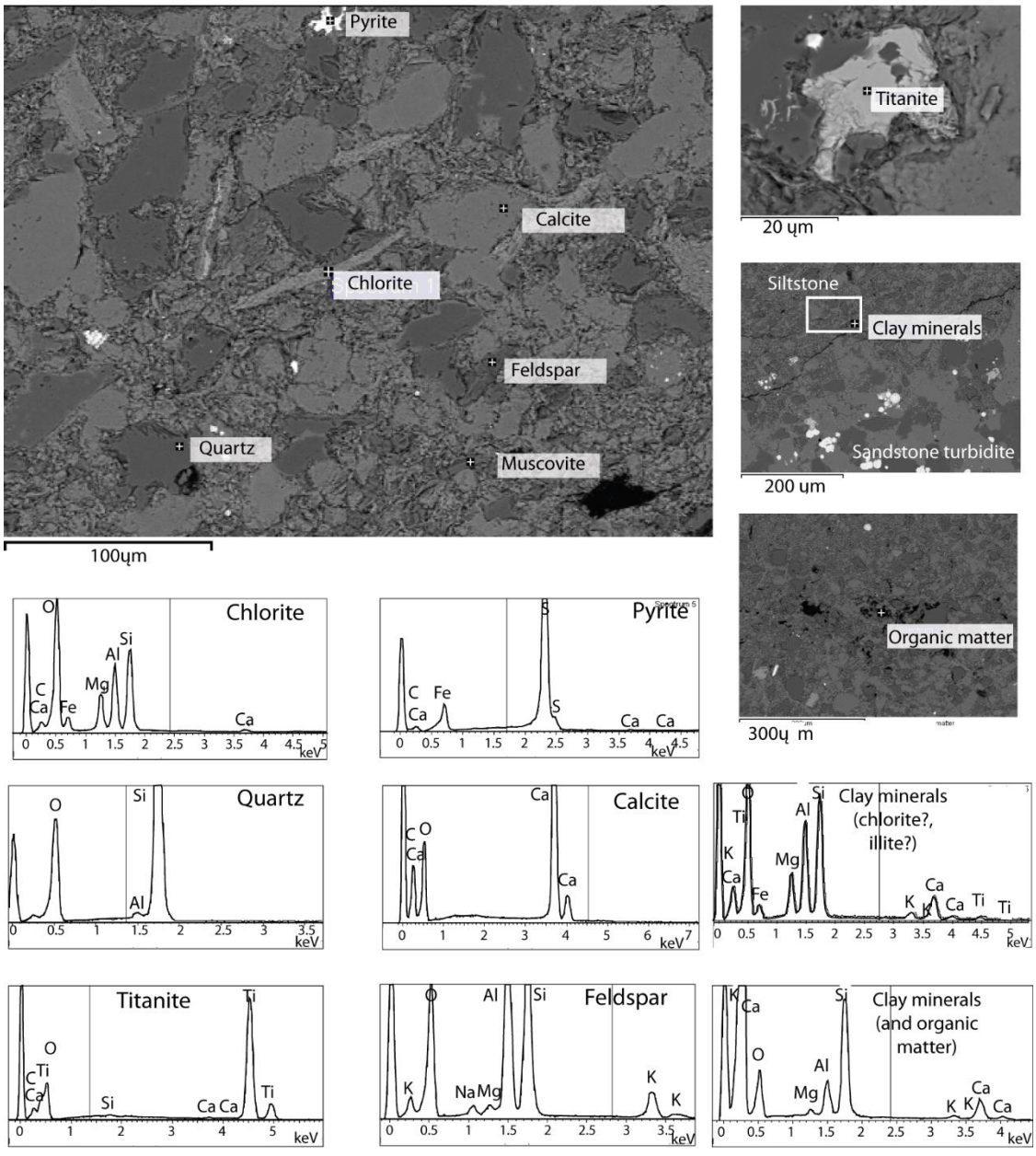

Plate 4.5 BSE images of the A6 core. The plate shows a 2.5mm thick sandstone turbidite surrounded by siltstones from the A6 core. Angular quartz and calcite grains constitute the majority of the grain compositions. Laths of phyllosilicates such as chlorite and muscovite and plagioclase and perthite feldspars are present in minor amounts. Pyrite forms framboids and tend to concentrate at the base of the sandstone turbidite. Rare grains of titanite (sphene) are found in the sandstone turbidite. Ti is also found in the siltstone matrix probably forming part of clay minerals. Grains are tightly cemented by calcite cement, mostly micritic, but, patches of microsparitic calcite are also present.

4.5.4 TOC and stable carbon isotope results

Throughout the Well A6, values for TOC content are typically low, ranging from 0.24-0.7 wt% (averaging 0.36%) (Figure 4.6). These values are typical for modern open-marine environments (McIver, 1975). TOC shows no trend with depth.

The relative amount of terrestrial and marine-sourced organic matter preserved in sediments is commonly determined using C/N ratios, since the C/N ratio of marine zooplankton and phytoplankton differs from those of land plants (Stein *et al.*, 1989). The low values of organic carbon and nitrogen in the A6 core sediments increase the uncertainty of the results (Leventhal, 2004) and C/N ratios were, therefore, not used in this study.

In Well A6 samples, carbon isotope compositions range between -25$^{o}/_{oo}$ and -21$^{o}/_{oo}$ with average values of approx. -23$^{o}/_{oo}$ (Figure 4.10). These results are consistent with mixing of terrigenous and marine organic matter. The oldest 40 m of the A6 core are characterised by slightly more negative $\delta^{13}C$ values ($\delta^{13}C$ = -24 ± 0.81 $^{o}/_{oo}$) than the younger sediments ($\delta^{13}C$ = -23.7 ± 0.67 $^{o}/_{oo}$), suggesting a higher proportion of terrestrial organic matter. It is possible that the the more negative carbon isotope values are linked to the higher percentage of sandstone turbidites (~ 8.4%) in the first 40 m of the core, showing a much sandier interval than the younger core section (3.9%). From 170 m to 88 m core depth, results appear to vary in a cyclical manner. This section corresponds to the interfan deposits between the Ainsa III and Morillo I fans. Figure 4.10 compares the stable carbon isotope values with the sandstone turbidite intensity in the A6 core. Periods of enhanced coarse-grained delivery to the basin are associated with lighter carbon isotope values and a higher content of terrestrial organic carbon delivery.

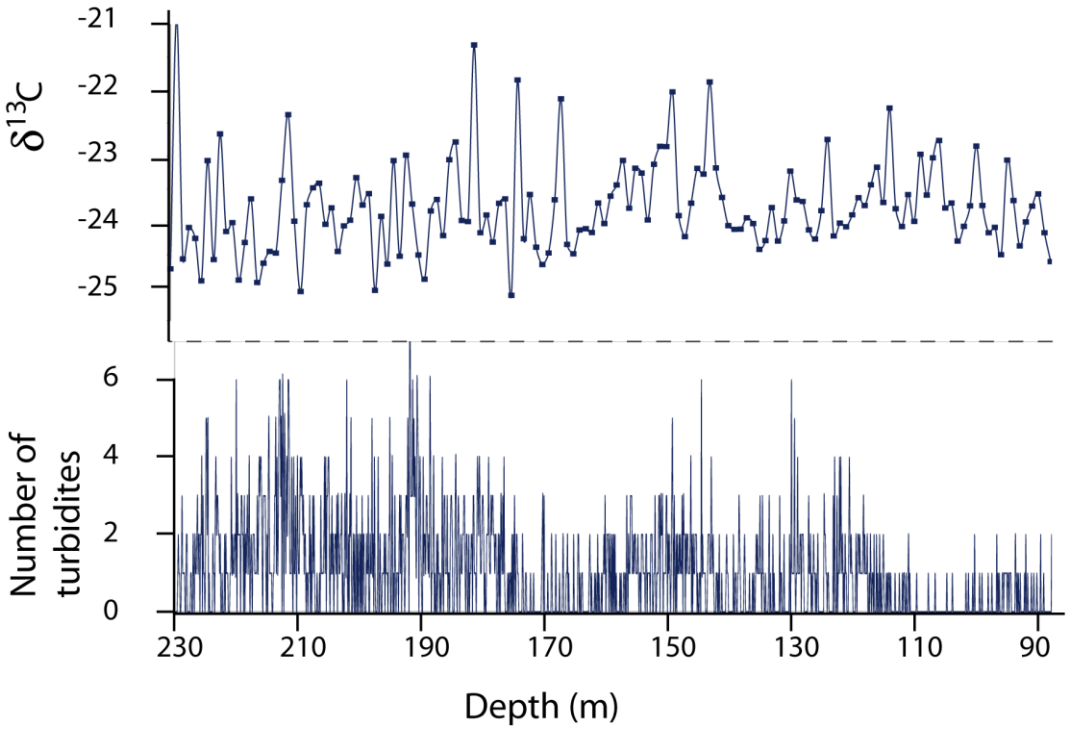

Figure 4.10 Stable carbon isotopes of the A6 core and sandstone turbidite intensity. From 230 m to 170 m core depth, the stable carbon isotope values are slightly more negative than younger sediments. Sandstone turbidites are also more frequent in the oldest 40 m of the core.

4.5.5 Cyclostratigraphic analysis

Time-series analyses of multi-element XRF data, sandstone turbidite intensity and $\delta^{13}C$ were undertaken in order to ascertain if there is any cyclicity in the geochemical proxies of the A6 core. Heard *et al.* (2008) have already demonstrated that the bioturbation intensity in Well A6 was controlled by orbital changes.

4.5.5.1 Methods of spectral estimation

The spectrum of the sandstone turbidite intensity data has been estimated using four different methods: the REDFIT, the MTM, the maximum entropy and the periodogram modified with a Barlett window. Each of these methods is explained in detail in Section 2.9. Figure 4.11 shows the spectral results obtained from applying each of these methods and Table 4.3 summarises the main frequencies present from 0-0.3

cycles/m. There are three main frequencies which consistently appear in all of the spectra analysed: ~ 0.032 cycles/m (1/30 m), 0.09 cycles/m (1/11 m) and 0.14 cycles/m (1/7 m).

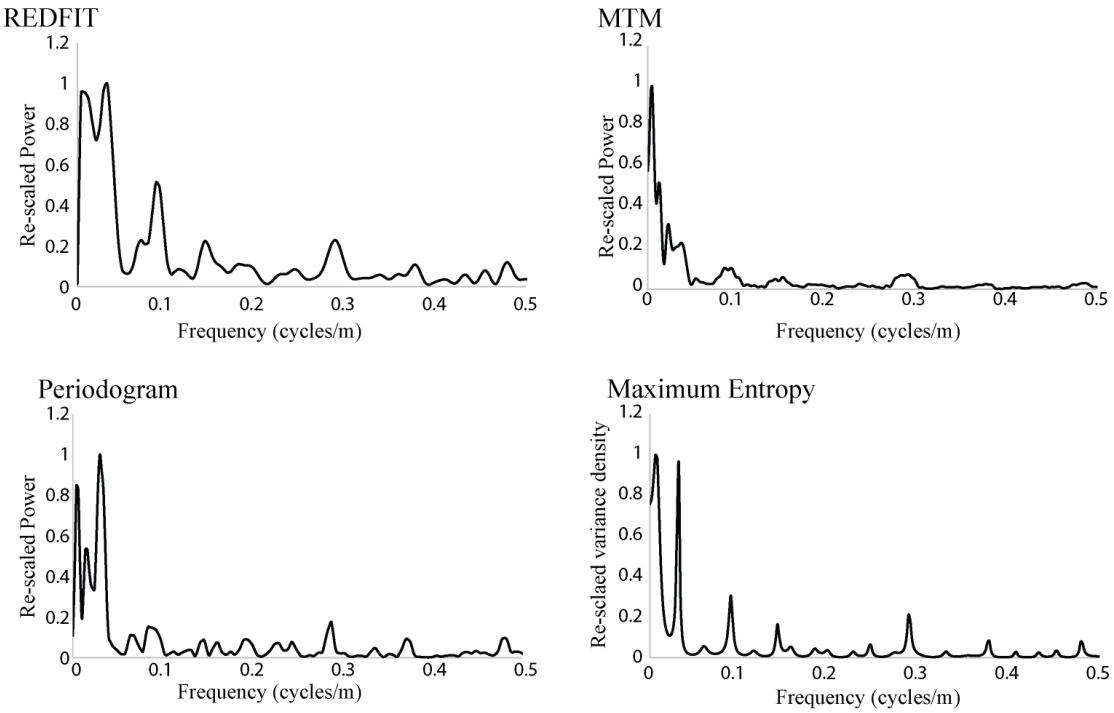

Figure 4.11 Methods of spectral estimation using the sandstone turbidite intensity data of the A6 core. REDFIT spectrum uses 4 WOSA segments, ~ 6 degrees of freedom and a bandwidth of 0.02 cycles/m. The MTM method uses 3 tapers and ~ 6 degrees of freedom. The periodogram has been modified with a Bartlett window. The maximum entropy method uses numbers of lags M = N/3 = 501). REDFIT spectral computations used the REDFIT software developed by Schulz and Mudelsee (2002). The periodogram, maximum entropy and the MTM spectra used the Analyseries software developed by Paillard *et al.* (1996).

Table 4.3 Methods of spectral estimation of the sandstone turbidite intensity data in the A6 core.

Spectral Method	Frequency (cycles/m)♠	Period (m)	Spectral Method	Frequency (cycles/m)♠	Period (m)
REDFIT	0.008	125	Periodogram	0.006	166.7
	0.033	30.3		0.016	62.5
	0.0875	11.4		**0.03**	33.3
	0.1416	7.06		0.07	14.3
				0.088	11.4
				0.146	6.8
				0.162	6.2
				0.196	5.1
				0.23	4.3
				0.248	4.0
				0.288	3.5
MTM	0.00488	204.9	Maximum	0.008	125
	0.0122	81.9	entropy	**0.032**	31.2
	0.023	43.5		**0.09**	11.1
	0.037	27		**0.142**	7
	0.092	10.9		0.288	3.5
	0.15	6.7			

♠ Frequencies from 0-0.3 cycles/m.

4.5.5.2 REDFIT time-series analysis

REDFIT time-series analysis has been undertaken on sandstone turbidite intensity, stable carbon isotopes and multi-element XRF elemental data normalised to Al. Three different curve-fitting models have been applied to the REDFIT spectrum: the AR1 model of Mann and Lees (1996), a quadratic model and a power regression model. Table 4.4 summarised the summative square error associated with each of these models. The best curve fit model in most cases is the power regression method. This model results in the lower summative square error indicating a better fit of the background spectral noise. This curve-fitting model has been applied to all the data analysed using REDFIT. The time-series results have been re-scaled to allow comparison between different variables.

Time-series analysis confirms that cyclicity exists in the sediments of Well A6 (Fig 4.12). There are four recurring peaks which appear to be present in most of the elements, i.e., 0.032, 0.095, 0.15 and 0.196 cycles/m (Table 4.4). All the peaks are > 95% confidence levels, although elements such as Ca, Sr, and Ti show very distinctive peaks > 99%. Most of the elements only show one prominent value indicating that the abundances of these elements must be controlled by a dominant orbital parameter.

Table 4.4 Curve-fitting methods for the sandstone turbidite intensity in the A6 core.

Data	Summative square errors		
	AR1	Quadratic	Power regression
Sandstone turbidite intensity	3118	3014	**1152**
Bioturbation Intensity	**12015**	38931	24776
Ca/Al	3047	2961	**1737**
Sr/Al	5724	5553	**2903**
K/Al	7484	10308	**3417**
Mn/Al	944	860	**723**
Fe/Al	2664	2497	**708**
Ti/Al	3297	3271	**1422**
$\delta^{13}C$	39.9	39.8	**39**
Cr/Al	439	**259**	701
S/Al	2010	2470	**981**
Si/Al	1610	1448	**1210**

Summative square errors using the AR1 model of Mann and Lees (1996), a quadratic curve and a power regression method. The method with the least summative square error indicating the most adequate fitting curve method is shown in bold numbers. In most cases, the power regression method has the least summative square error. AR1 method derived from Mann and Lees (1996) equations.

Figure 4.12 (next page) REDFIT time-series analysis of A6 core data. Time-series analysis of XRF elements uses a 4 cm spacing interval and 6 WOSA segments; bioturbation and sandstone turbidite intensity uses a 10 cm spacing interval and 4 WOSA segments. $\delta^{13}C$ uses 1 m interval and 4 WOSA segments. Power-regression curve fitting method is applied to all the spectral analysis. Spectra have been re-scaled to allow spectral comparison from different variables (Weedon, 2005). The most prominent peaks in the data appears to be associated with eccentricity and obliquity, whilst frequencies associated with precession are less prominent for most elements. The Si/Al and Fe/Al spectra are noisy. This is probably associated with the fact that these elements appear fractioned between coarse and fine fractions. Milankovitch frequencies have been labelled (E-eccentricity, O-obliquity, P-precession).

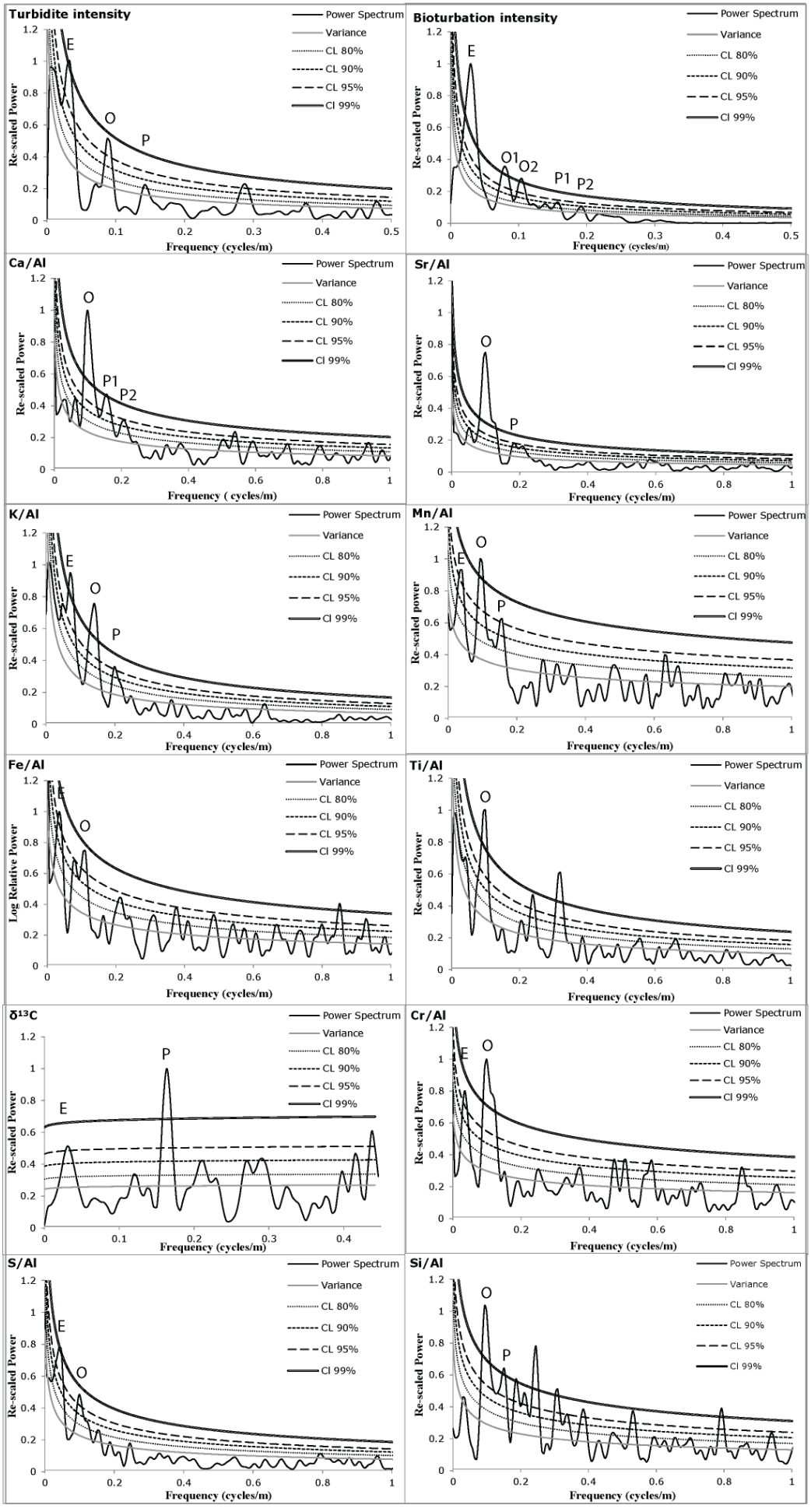
Turbidite intensity
Power Spectrum
Variance
CL 80%
CL 90%
CL 95%
Cl 99%
E
O
P
Re-scaled Power
Frequency (cycles/m)
Bioturbation intensity
E
O1
O2
P1
P2
Re-scaled Power
Frequency (cycles/m)
Ca/Al
O
P1
P2
Re-scaled Power
Frequency (cycles/m)
Sr/Al
O
P
Re-scaled Power
Frequency (cycles/m)
K/Al
E
O
P
Re-scaled Power
Frequency (cycles/m)
Mn/Al
E
O
P
Re-scaled power
Frequency (cycles/m)
Fe/Al
E
O
Log Relative Power
Frequency (cycles/m)
Ti/Al
O
Re-scaled Power
Frequency (cycles/m)
δ13C
E
P
Re-scaled Power
Frequency (cycles/m)
Cr/Al
E
O
Re-scaled Power
Frequency (cycles/m)
S/Al
E
O
Re-scaled Power
Frequency (cycles/m)
Si/Al
O
P
Re-scaled Power
Frequency (cycles/m)

Table 4.5 REDFIT spectral results of the A6 core data.

Data	Principal frequencies (cycles/m)				
S/Al	0.041	0.111			
K/Al		0.087	0.134	0.20	
Mn/Al	0.04	0.099	0.157		
Ca/Al		0.099	0.151	0.192	
Si/Al		0.09	0.151	0.192	0.245 and 0.31
Cr/Al	0.029	0.087			
Fe/Al	0.029	0.08 and 0.11			
Sr/Al		0.099		0.19	
Ti/Al		0.099			0.244 and 0.32
Bioturbation intensity	0.029	0.08 and 0.104	0.1585 (90%)	0.196 (90%)	
Sandstone turbidite intensity	0.029	0.093	0.141 (80%)		
$\delta^{13}C$	0.03		0.163		
MEDIAN	**0.032**	**0.095**	**0.15**	**0.195**	**0.24 0.31**

All results show a confidence levels are > 95% unless otherwise stated.

4.5.5.3 ASM analysis

The ASM method developed by Meyers and Sageman (2007) has been applied to the turbidite and bioturbation intensity data, first to test if the results reject the null hypothesis of no orbital cyclicity and, secondly, to determine the best fit between the spectral frequencies identified in the time-series analysis and the expected orbital periods for the Middle Eocene. For the Middle Eocene, the expected orbital parameters for eccentricity (E), obliquity (O) and precession (P) (~ 45 Ma) taken from Berger *et al.* (1992) are the following: E1 = 404 kyr, E2 = 124 kyr, E3 = 95 kyr, O1 = 52 kyr, O2 = 40 kyr, P1 = 23 kyr, P2 = 19 kyr.

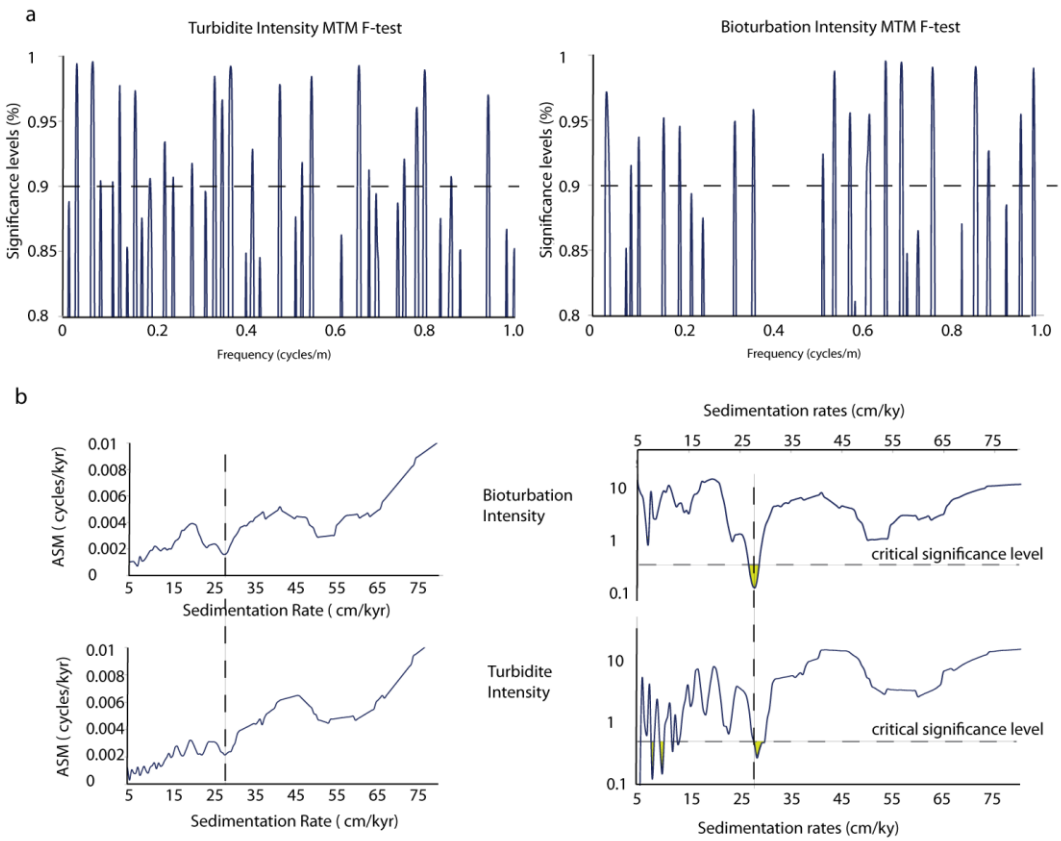

Figure 4.13 ASM results of the sandstone turbidite and bioturbation intensity of the A6 core. (a) F-test results for bioturbation and sandstone turbidite intensity using a 3-taper 4π MTM power spectrum. Dotted line marks the 90% F-test significant level. **(b)** Average misfit results for bioturbation and sandstone turbidite intensity for SARs between 5 and 80 cm/kyr. The significant levels for bioturbation and sandstone turbidite intensity are calculated using 37 and 56 frequencies per spectrum respectively and 100,000 Monte Carlo simulated spectra. Dash lines indicate the critical significance level.

Figure 4.13a shows the results from the MTM harmonic F-test. Frequencies > 90% significance level are present above the dash line. The average spectral misfit recognises an optimal SAR of 28 cm/kyr which exceeds the critical significance level of 0.5% in the bioturbation intensity spectrum (ASM = 1.6 x 10^{-3} cycles/kyr, 0.12% significance level) (Figure 4.13b). The ASM method for the sandstone turbidite intensity identifies 5 possible SARs which exceed the critical significance levels (8, 10, 11, 13 and 28.5 cm/kyr); of these, 8, 10 and 28.5 cm/kyr contain the highest H_0 significance level (Figure 4.13b). The 8 and 10 cm/kyr values suggest that the 0.03 cycles/m frequency can be linked to the 400 kyr long eccentricity period which is

unlikely to be represented in the record as the core length is too short to contain this frequency. The most reasonable sediment accumulation rate chosen is 28.5 cm/kyr (ASM = 2.1 x 10^{-3} cycles/kyr, 0.27% significance level), a value that is in good agreement with the estimated SAR for the bioturbation data of Heard *et al.* (2008). The estimated length of the orbital periods using 28 cm/kyr SARs can be seen in Table 4.6.

Table 4.6 Temporal period duration of significant frequencies in the A6 core.

Bioturbation Intensity			Sandstone turbidite intensity		
Frequency (cycles/m)	MTM Probability (%)	Periodicity (kyr) using 28 cm/kyr	Frequency (cycles/m)	MTM Probability (%)	Periodicity (kyr) using 28.5 cm/kyr
0.032	0.97	**112.2**	**0.032**	0.99	**108.6**
0.085	0.91	**41.7**	**0.066**	0.99	**52.3**
0.103	0.94	34.7	**0.084**	0.90	**40.9**
0.158	0.95	**22.6**	0.111	0.90	31.0
0.193	0.94	**18.5**	0.127	0.98	27.2
			0.1611	0.97	21.4
			0.194	0.90	**17.7**

The table shows calculated cycle duration for each significant frequencies (> 90% confidence levels) at a SAR of 28 cm/kyr in the bioturbation intensity and 28.5 cm/kyr in the sandstone turbidite intensity data. At these SARs the frequency at 0.032 cm/kyr represents eccentricity ~ 110 kyr, the frequency 0.085 cycles/m represents obliquity 40 kyr and the frequencies 0.15 and 0.19 cycles/m represent precession 22 and 18 kyr, respectively. These periodicities are consistent with calculations of orbital periodicities in the Middle Eocene using Berger *et al.* (1992) equations (eccentricity 123.8 and 94.8 kyr, obliquity 52.3 and 40 kyr and precession 22.6 and 18.8 kyr).

Applying the results of ASM analysis to the frequencies observed in the XRF elements and carbon isotope values, it can be inferred that the four recurrent frequencies at 0.032, 0.095, 0.15 and 0.196 cycles/m represent E1 (~ 110 kyr), O2 (~ 40 kyr), P1(~ 23 kyr) and P2 (~ 19 kyr), respectively. All the elements show very prominent obliquity cycles, whilst eccentricity and precession are not always represented. An exception is $\delta^{13}C$ which shows a very prominent precession cycle (Figure 4.12). Elements such as Si and Fe shows a noisy spectrum, which is associated

with the partitioning of the element between the coarse- and fine-grained sediment fractions. Elements such as Ti, Si and $\delta^{13}C$ show an additional significant frequency at 0.24 and 0.32 cycles/m which may represent a harmonic of obliquity and precession, but could also represent sub-Milankovitch cycles.

4.5.5.4 Wavelet analysis

Wavelet analysis has been performed in the sandstone turbidite and bioturbation intensity records and also in the stable carbon isotope records (Figure 4.14). XRF data has not been analysed using the wavelet method because the high-resolution sampling interval (4 cm) resulted in records too large (N = 3600) to be computerised with this method. The wavelet method used the available online tool http://paos.colorado.edu/reesearch/wavelets based on the algorithms of Torrence and Compo (1998).

Wavelet analysis of the analysed records shows a number of significant frequencies > 90% confidence levels. The most spatially persistent frequency, present in all the analysed records > 90% confidence level is ~ 0.03 cycles/m (1/33 m). This frequency has been associated with short eccentricity combining REDFIT and ASM analysis. This frequency is present in all of the stratigraphic records. The turbidite and bioturbation intensity records appear continuous throughout the A6 core interval but in the stable carbon isotopes it is only present in the second half of the records. The frequency present at ~ 0.09cycles/m (~ 1/11 m) is significant in the turbidite and bioturbation intensity records but completely absent in the stable carbon isotopes. This frequency is spatially discontinuous, and is significant mainly in the first half of the records. This frequency has been associated with obliquity 40 kyr using ASM analysis. The frequency at ~ 0.14 cycles/m (1/7 m) is present but spatially sporadic in the three

spectra investigated, with only short intervals where this frequency is > 90% significant levels. However, in the stable carbon isotopes, there is an increase in spectral power mostly continuous at this frequency throughout the records (Figure 4.14). This frequency has been associated with orbital precession using REDFIT and ASM analysis and appears to be more dominant at controlling the distribution of $\delta^{13}C$ in the A6 core.

Figure 4.14 (next page) Wavelet analysis of the sandstone turbidite and bioturbation intensity and the stable carbon isotopes of the A6 core. (a) The wavelet power spectrum identifies spectral power at different frequencies throughout a ~ 150 m thick sequence of the A6 core. Black contours mark the 10% significant regions. **(b)** Global wavelet shows the scale-averaged wavelet power across the studied frequency bands. Values to the right of the dashed line are significant > 90% confidence level. Significant spectral peaks which have been linked to Milankovitch frequencies using REDFIT and ASM analysis have been labelled (E-eccentricity, O-obliquity, P-precession). Data computerised using the online tool http://paos.colorado.edu/research/wavelets.

Turbidite intensity data

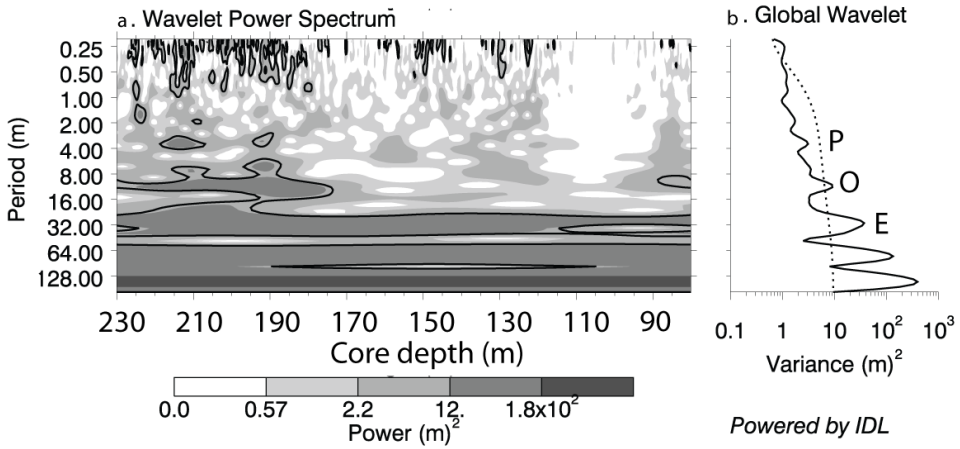

Bioturbation Intensity data

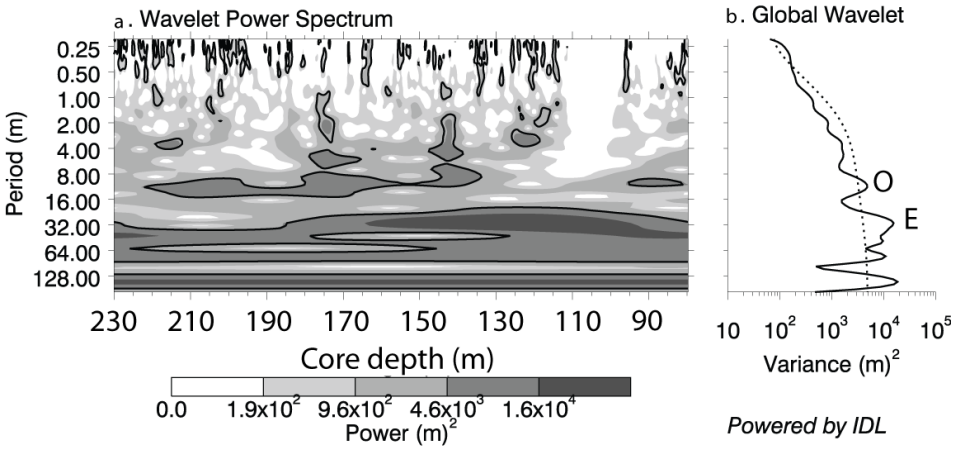

Stable carbon isotopes

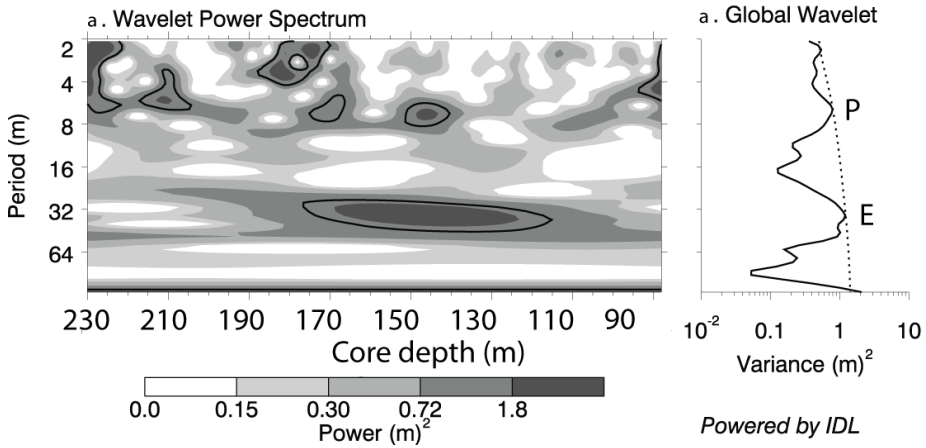

4.6 Discussion

4.6.1 Origin of the sediments of the A6 core

Sandstone turbidites are enriched in ‘terrestrial’ minerals, such as quartz grains, feldspars, sphene and zircon, which were probably transported in the coarse fraction. Calcite grains enrichment in the turbidites reflects a greater entrainment of detrital carbonate grains from shallow-marine environments. Sandstone turbidites composition, therefore, shows the mixing of terrestrial and marine sediments in shallow-marine environments where biogenic material from ocean productivity was mixed with the terrestrial input of river-derived and aeolian sediments. The concentration of pyrite in the sandstone turbidites is likely to be associated with higher rates of sediment accumulation (Lyons and Berner, 1992), because such rates result in a decrease of oxic respiration and a corresponding increase in sulphate reduction (Canfield, 1991).

The sediment gravity-flows that produced the sandstone turbidites probably originated from fluvio-deltaic environments, with the detrital minerals (such as quartz, feldspars and heavy minerals) transported as mixed loads in the river discharge. These flows entered the marine environment as hyperpycnal flows. The high content of Ca and the presence of abundant nummulites and other shallow-marine biogenic material is indicative of material eroded and entrained into the flows.

The structureless mudstones have a higher content of clay minerals. They have a lower content of elements such as Ca and of other elements that are commonly associated with the coarse detrital fraction, such as Si, Zr and Ti. High content of S is probably associated with the precipitation of pyrite, especially at the base of these layers. The mudstones are generally bioturbated, but the low content of Mn in the dark

layers suggests deposition under slightly reducing conditions (Calvert and Pedersen, 1996). Pyritised burrows and some small thin shells of bivalves occur in these bands. The increased preservation of organic matter in these layers may have caused enrichments of pyrite and the characteristic dark colouration. The uniform grain-size distribution, the lack of internal current structures and the pervasive bioturbation, all support the interpretation that the mudstones are hemipelagites (e.g., Rupke and Stanley, 1974; Stow and Tabrez, 1998).

The higher content of detrital clay minerals in the structureless mudstones, and the low content of marine biogenic elements such as Ca, suggests that these sediments probably originated from dilute riverine flows (suspended-load plumes or hypopycnal flows). When a river carrying fine-grained material enters the sea, the temperature and density contrast between river and salt water can generate a hypopycnal plume which remains at the surface (Nittrouer *et al.*, 2007) The mixture of muddy freshwater with seawater may have facilitated the flocculation of clay particles and a relatively rapid settling of these particles (*cf.* Leeder, 2011). Thus, the sediments of the A6 core appear to have formed by a combination of hyperpycnal (sandstone turbidites) and hypopycnal flows (mudstones) (Figure 4.15).

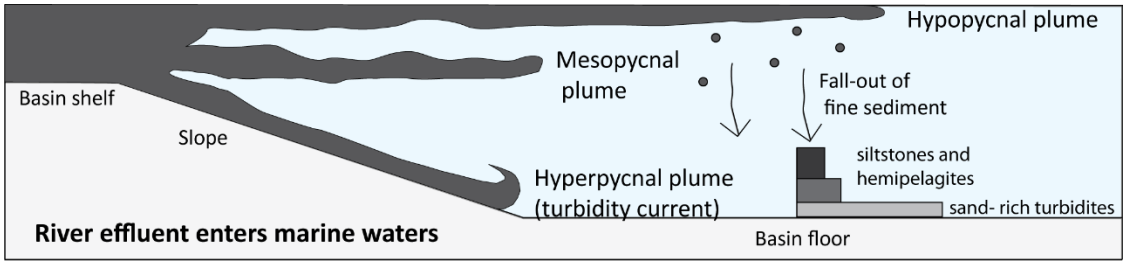

Figure 4.15 Hypopycnal, mesopycnal and hyperpycnal flows. Diagram modified from Parsons *et al.* (2001) to show the formation of hyperpycnal flows from the convection instability of hypopycnal flows. The hyperpycnal flow (turbidite current) will result in the deposition of sandy turbidites. Sediment fall-out of suspension from the remnant hypopycnal flow will result in the formation of hemipelagites which in the core are represented by unstructured dark mudstones. Note, the "idealised" tripartite unit reflects three discrete depositional events (beds).

4.6.2 Variations in the organic content of the A6 core

Three processes are known to control changes in the carbon records through geological time: (a) changes in the productivity of the ocean; (b) variation in the oxygenation of the bottom waters, and (c) variations in the flux of terrigenous organic carbon (Fahl and Stein, 1997). Variations in any of these variables can affect bioturbation intensity.

4.6.2.1 Changes in the productivity of the ocean

TOC has been used by some researchers as a proxy for changes in productivity (e.g., Stein *et al.*, 1989; Werne *et al.*, 2000; Moreno *et al.*, 2002). TOC values in the A6 core are uniformly low, with no significant vertical changes which may suggest changes in productivity (Figure 4.6).

Shimmield and Mowbray (1991) used Ca values from XRF measurements to estimate the calcareous biogenic component, whilst other authors have used HCO_3 content (Moreno *et al.*, 2002). The $CaCO_3$ can be of *in-situ* marine biogenic origin or detrital, but the percentage of each component cannot be determined by visual inspection of the geochemical profiles. Ca and $CaCO_3$ show no trends or significant enrichments or depletions (Figure 4.6). These results, together with the lack of significant changes in the TOC values, could be interpreted as indicating that no significant events of enhanced production or preservation of organic matter occurred.

4.6.2.2 Variation in the oxygenation of the bottom waters

Increased bottom-water oxygenation generally results in increased rates of degradation of organic matter (Moodley *et al.*, 2005), in a high-diversity trace-fossil assemblage (Ekdale, 1985), and intensity of bioturbation. The overall high bioturbation intensity throughout the A6 core is indicative of generally highly oxygenated depositional

environments. Heard *et al.* (2008) observed significant variation in bioturbation in the A6 core and postulated that changes in oxygenated marine bottom-waters might have caused changes in bioturbation intensity. However, the inverse relationship between sandstone turbidite intensity and bioturbation intensity (Figure 4.16) suggests that temporal variations in SARs may have been the dominant control on bioturbation intensity. Temporal reduction in SARs may have provided an opportunity for burrowing organisms to colonise the sediment. Higher SARs during periods of high turbiditic intensity may have regulated the bioturbation patterns observed in the core.

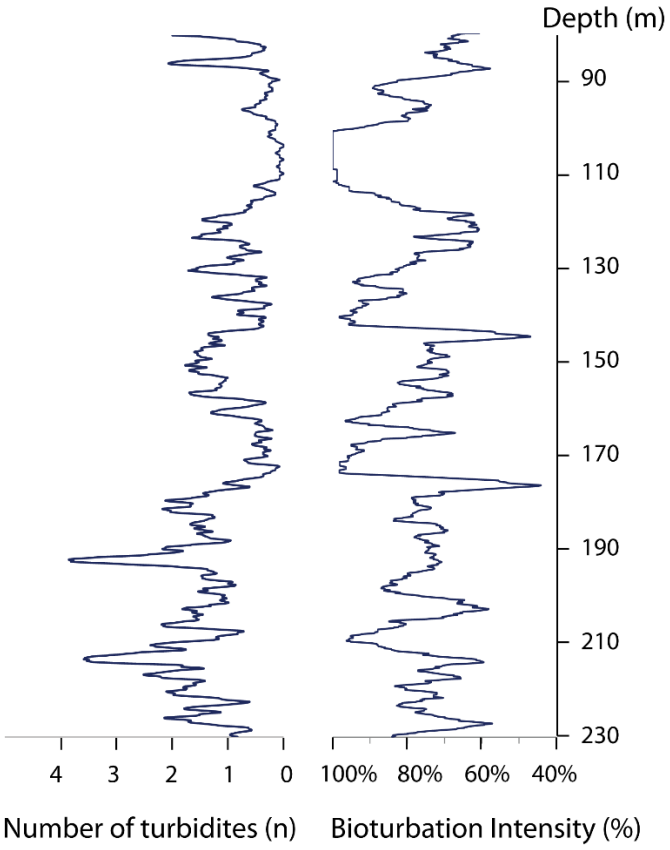

Figure 4.16 Sandstone turbidite intensity versus bioturbation intensity. Periods of high bioturbation intensity coincide with periods of low sandstone turbidite intensity. It is likely that bioturbation intensity has been controlled by changes in SARs of coarse-grained sediment delivery. Sandstone turbidite intensity from Heard *et al.* (2008). A weight-5 moving average has been applied to both records.

Alternatively, salinity changes may have been the dominant control on bioturbation intensity, with periods of increased river discharge associated with fresh-water flushing of the enclosed Ainsa Basin. At such times, one might expect a dramatic die-back of marine organisms (bioturbators) and increased turbidite accumulation and preservation as the enhanced river discharge would have brought greater sediment volumes into the basin with a greater propensity for hyperpycnal flows in the less dense waters (underflows), with commensurate increased rates of sediment accumulation.

4.6.2.3 Variations in the flux of terrigenous organic carbon

$\delta^{13}C$ data shows the variation of terrestrial and marine organic matter in the A6 core. Figure 4.10 compares sandstone turbidite frequency with carbon isotope values and shows an association between low isotopic values and abundance of sandstone turbidites. The oldest 40 m of the A6 core are characterised by slightly more negative $\delta^{13}C$ values ($\delta^{13}C$ = -24 ± 0.81 ‰) than the younger sediments ($\delta^{13}C$ = -23.7 ± 0.67 ‰). Isotopically lighter values of $\delta^{13}C$ are indicative of greater amounts of land-derived organic matter present in the sediments. The variation which is observed in the $\delta^{13}C$ is probably an effect of the dilution of the marine organic matter by terrestrial input. In periods of decreased turbidite frequency we observe a shift towards heavier isotopic values (Figure 4.10). These results are in agreement with those from Waseda *et al.* (1995) in Pliocene to Pleistocene sediments from the Chile continental margin, who found that turbiditic sections have lighter $\delta^{13}C$ and that the sections interpreted as pelagic fallouts have heavier $\delta^{13}C$ values. It should be noted that stable carbon isotope ratios may be affected by microbial sulphate reduction, since this mechanism preferentially uses the more metabolisable marine organic matter to produce FeS and

pyrite (FeS_2) (Westrich and Berner, 1984; Berner and Westrich, 1985). Diagenetic effects may cause a ~ -2 $^{o}/_{oo}$ shift (difference) in the isotopic carbon results (Hayes *et al.*, 1989; Meyers, 1994). The presence of pyrite throughout the core suggests that the actual content of marine organic matter in the sediments may have been initially much higher. Pyrite tends to be concentrated in the sandstone turbidites, mainly at the base as observed in thin-sections (Plate 4.3a) and in X-ray elemental mapping (Plate 4.4). It seems plausible that an increase in sandstone turbidite intensity may have caused an increase in burial rates and pyrite formation, which may have shifted $\delta^{13}C$ results towards the lighter values observed.

4.6.3 Causes of cyclicity in the A6 core

Time-series analysis of the various sedimentological and geochemical data all reflects a strong cyclicity at Milankovitch-like frequencies. It, therefore, seems reasonable to conclude that a generic linkage exists between these variables and any cyclicity. Here, it is argued that this association is likely to result from the variable supply of relatively coarser and finer-grained sediment to the deep-marine basin. Within the interfan and fan lateral-margin deposits, the coarser-grained sandstone turbidite intensity shows a Milankovitch-like cyclicity (Figure 4.12). This means that the turbidity currents transported mixed-load river sediments into deep-water and also entrained detrital and biogenic shallow-marine material to deposit sandstone turbidites with this periodicity. Periods of high sandstone turbidite intensity were associated with higher sediment supply and accumulation rates that may have affected the bioturbation intensity and the preservation of organic carbon. Rapid SARs linked to periods of active turbidite deposition reduced the time for organisms to bioturbate the sediment and oxidise organic matter. Rapid burial probably led to the reduction of organic matter by

sulphate-reducers and resulted in the precipitation of pyrite in the sandstones. During periods of hemipelagic deposition, lower SARs may have resulted in greater bioturbation of sediment and oxidation of organic matter, limiting the formation of pyrite. The $\delta^{13}C$ isotopes show that greater sandstone turbidite accumulation corresponds with lighter $\delta^{13}C$ isotopic values, suggesting a greater terrestrial supply of organic carbon. Since bioturbation intensity and carbon-isotope values appear to be linked with intensity of the turbidite accumulation, time-series analysis of these parameters shows a similar cyclical behaviour.

The principal processes which drive high-frequency modulation of sediment flux to deep-marine environments and, therefore, create cyclicity in the sedimentary record, include high-frequency climatic cycles (linked with changes in chemical and physical weathering and erosion), tectonics, autocyclicity and/or eustatic sea-level changes. These processes are discussed in detail in Chapter 6.

4.7 Conclusions

The A6 core is a siliciclastic succession of deep-marine siltstones, fine-grained sandstone turbidites and hemipelagic mudstones (marlstones) which were deposited as overbank off-axis and interfan deposits in the Ainsa System submarine fan environments (Pickering and Bayliss, 2009). The combined palaeo-proxies used in this study show that there is a combination of terrigenous and biogenic components in these sediments. Grain-size proxies suggest there is an overall fining upwards trend throughout Well A6, recorded as a progressive decrease in the number and thickness of sandstone turbidites. Sandstone turbidites show enrichments of detrital elements such as Si, Zr and Ti, which suggest that they have higher contents of quartz and heavy minerals than the surrounding siltstones while hemipelagic unstructured mudstones are

low in all these components and have a higher content of clay minerals. The detrital fraction in the sediments is likely to be derived from fluvial sources and transported by waning low-density turbidity currents to the deep-marine environment.

TOC values are in general low and typical of open-marine conditions, in strong agreement with the micropalaeontological data which suggests essentially continuous and fully marine conditions throughout the deposition of these sediments. $CaCO_3$ values do not show major changes which might imply important changes in palaeo-productivity. Isotopically lighter $\delta^{13}C$ isotopes appear to be associated with periods of higher turbidite occurrence. It is possible that the carbon isotopic signal may reflect terrestrial organic matter supplied to the deep-marine basin preferentially by sandy turbidity currents that led to deposition from hyperpycnal flows. High bioturbation intervals are associated with periods of low turbidity-current frequency, and are likely to have been associated with times of reduced SARs. However, salinity changes linked with times of high fluvial discharge and freshwater flushing of the Ainsa Basin (associated with increased sandy turbidity currents) remains a plausible mechanism to account for the observations, e.g., changes in bioturbation intensity.

Cyclostratigraphic studies reveal a strong Milankovitch cyclicity in the sediments of Well A6, i.e. results of ASM analysis to the frequencies observed in the XRF elements and carbon isotope values suggests the presence of four recurrent frequencies representing ~ 110 kyr (eccentricity), (~ 40 kyr (obliquity), and ~ 23 kyr and ~ 19 kyr (precession couplet). All the elements studied show prominent obliquity cycles, although, eccentricity and precession are not always represented - an exception being $\delta^{13}C$ which shows a very prominent precession cycle.

Chapter 5

Orbital forcing in the sediments of the Ainsa Basin

5.1 Introduction and objectives

Chapter 4 examined the detailed sedimentology and geochemistry of a ~ 230 m long deep-marine siliciclastic core (the Well A6 core). The multiple geochemical proxies applied and the use of multiple cyclostratigraphic techniques have demonstrated the cyclic delivery of coarser-grained sediment by turbidity currents associated with Milankovitch forcing. The first objective of this chapter is to expand this study to other fine-grained successions in the Ainsa Basin to demonstrate that Milankovitch forcing has driven these sediments throughout the entire deep-marine stratigraphy of the basin. In order to achieve this, high-resolution spectral gamma-ray logging has been undertaken on long and undeformed sections of fine-grained sediments in many interfan and overbank successions within the deep-marine systems of the Hecho Group. Similar cyclostratigraphic techniques to those ones used in the analysis of the A6 core have been applied to each of these successions. This chapter, not only tries to recognise regular components within these sections but also gives an insight into the sedimentary and geochemical evolution of the basin in deep time by looking at changes in the sand content, SARs and chemical signatures (e.g., U, Th and K content) in each of the deep-marine systems.

The second main objective of this chapter is to determine the timing of deposition of the coarse-grained sandbodies. This can be achieved by estimating stratigraphic thicknesses of the interfan deposits by using geological mapping and building cross-sections across the gamma-ray logged sections in the basin. The timing

between the sandbodies can then be determined by applying the SARs calculated from cyclostratigraphic studies to the interfan stratigraphic thicknesses.

In addition, this chapter integrates spectral results from the gamma-ray logged sections with magnetostratigraphic results (Chapter 3) and published biostratigraphic studies in the basin (Pickering and Corregidor, 2005; Scotchman *et al.*, 2014) or in the vicinities of the basin (e.g., Holl and Anastasio, 1993; Mochales *et al.*, 2012) to permit the tuning of the data to orbital parameters using the La2010a orbital solution of Laskar *et al.* (2011). Orbital tuning has only been applied to gamma-ray logged sections within the Gerbe, Banastón and Ainsa systems where magnetostratigraphy can provide robust age control points. These calculations permit to adapt the basin depth-stratigraphy into an age-stratigraphy which can help to establish any associations between the initiation of the sandbodies and specific orbital periods (e.g., during the 400 kyr eccentricity minima).

5.2 Gamma-ray logged sections

Ten continuous and undeformed successions of fine-grained sediments were selected for gamma-ray logging across the basin. These sections span a time interval from ~ 48 to ~ 41 Ma and sample the Ainsa Basin systems from the Arro to the Guaso systems. The two older systems in the basin, Fosado and Los Molinos have not been sampled as these systems are tectonically deformed and no suitable sections for gamma-ray logging were identified. Table 5.1 summarises the gamma-ray sections logged, their length and the stratigraphic system in which they are located. Fine-grained sediments in the Morillo and Guaso systems are generally weathered and poorly exposed. Locally, these successions contain large-scaled sediment slides and slumps which cause discontinuities in the vertical succession of hemipelagic fine-grained

stratigraphy. It is, therefore, difficult to identify long and undeformed sections suitable for gamma-ray logging in these two systems. The Sieste and Guaso sections located in the Morillo and Guaso systems, respectively, are only 40 m in length. Figure 5.1 shows the location of the gamma-ray logged sections within a composite stratigraphic column of the Ainsa Basin built by integrating numerous cross-sections across the gamma-ray logged areas.

Table 5.1 List of gamma-ray logged sections in the Ainsa Basin.

Gamma-ray section♠	Length (m)	Stratigraphic system
Tierrantona	167 m	Arro
Gerbe	200 m	Gerbe
Labuerda	92 m	Banastón
Labuerda Banastón	350 m	Banastón
Boltaña	167 m	Ainsa
Forcaz	185 m	Ainsa
Morillo-Reservoir	122 m	Morillo
Sieste	40 m	Morillo
Morillo-Bruello	108 m	Guaso
Guaso	40 m	Guaso

♠The sections have been named after the name of the village closest to the gamma-ray logged section.

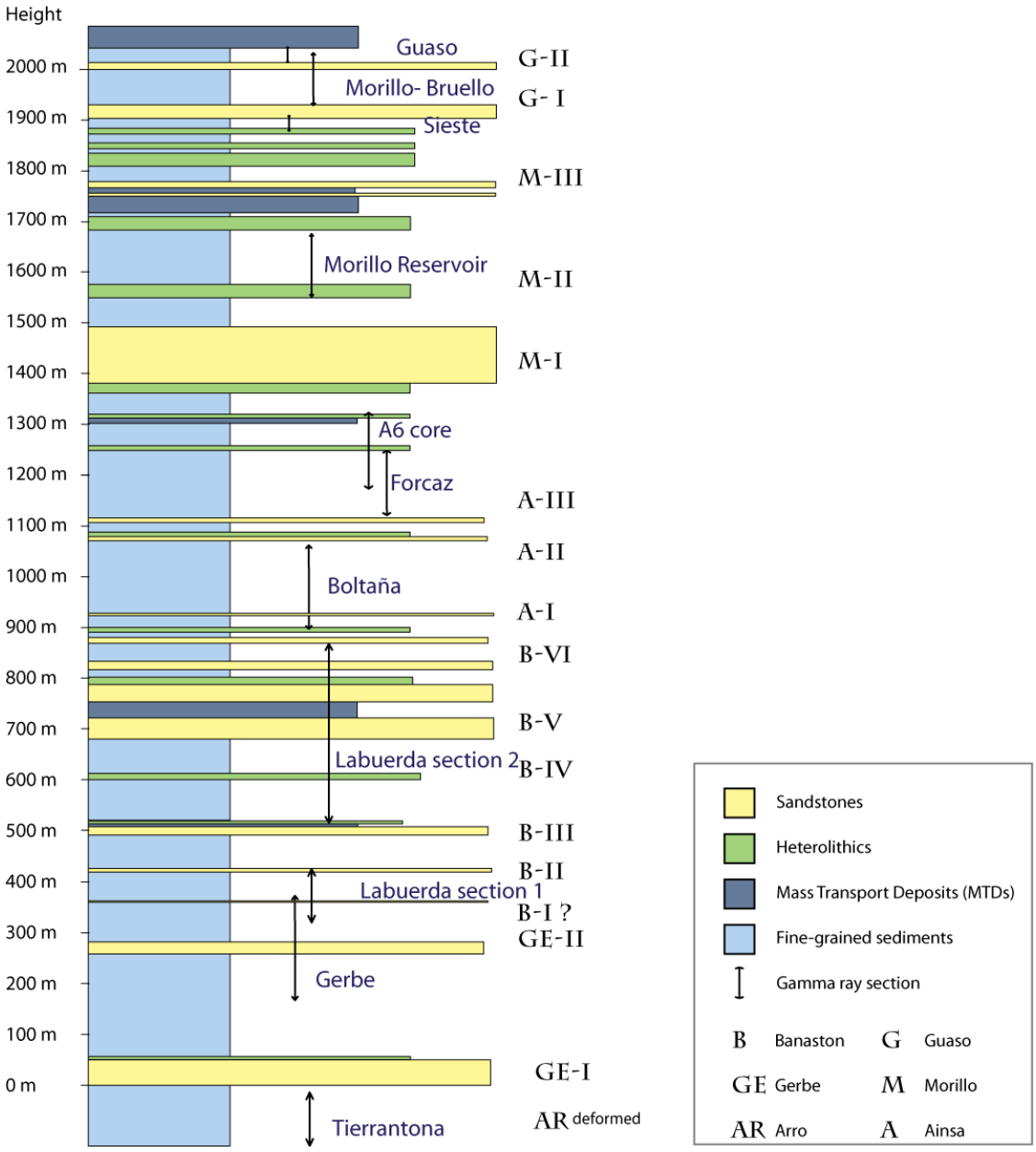

Figure 5.1 Location of the gamma-ray logged sections in the stratigraphy of the Ainsa Basin. The stratigraphy of the Ainsa Basin has been created by joining cross-sections drawn across the gamma-ray logged sections. Stratigraphic overlapping is seen in some of the gamma-ray sections. In all the cases, the gamma-ray logs have been undertaken in interfan and overbank off-axial deposits from the main sandbodies (submarine fans). The exact location of the Tierrantona section within the stratigraphy cannot be established due to the high degree of tectonic deformation of the Arro System.

5.2.1 Type of sediments in the gamma-ray logged sections

The types of sediments present in the gamma-ray logged sections have been classified using the descriptive facies classification scheme of Pickering *et al.* (1986b, 1989). The sediments consist mainly of hemipelagic marlstones, laminated, very thin-, thin- and medium-bedded normally-graded and ungraded sandstones (Facies C2.3), silty and muddy-siltstone turbidites. The sandstone turbidites are generally very-fine and fine-grained, and are typically cm in size. However, some sections can contain coarser-grained turbidites (medium to coarse) which can reach up to 60 cm in thickness, although these turbidites are rare in the fine-grained sediments and constitute less than 1% of the total sandstone turbidite beds. Mud and silt couplets (Facies D2.3) are common and form metre-size laminated successions. Apart from turbidites, other sediment gravity-flow deposits are present in minor amounts such as cohesive-flow deposits (sediment slides and slumps) (Facies F2.1) and other laminar-flow deposits, although, these are rare and commonly do not exceed ~ 1 m in thickness. The Tierrantona and the Labuerda section 2 contain small-scale Type 1a MTCs and some debris flows (Pickering and Corregidor, 2005). Gamma-ray measurements have not been undertaken across these deformed areas as anomalous readings can affect the cyclostratigraphic studies of these successions. These small-scaled chaotic intervals have resulted in discontinuities in some of the gamma-ray logged records. Locally, the Forcaz section contains mm- to cm-sized nummulitic packstones which were probably redeposited into deep-water from adjacent carbonate platforms during storm events (as tempestites). These sediments have also been seen in the Ainsa-Morillo interfan deposits of the Well A6 core but are rare in any other deep-marine systems. A detailed description of the facies identified within the fine-grained gamma-ray logged sections and the sedimentary processes involved can be seen in Table 4.1.

The fine-grained sediments are locally intensively bioturbated and it is possible to observe different ichnospecies. Plate 5.1 shows examples of bioturbation in the fine-grained sections. Examples of the ichnospecies identified are *Skolithos, Phycosiphon, Nereites, Planolites, Scolicia, Thalassinoides, Zoophycos* and *Chondrites*. Detailed bioturbation studies in the Ainsa Basin based on core and outcrop samples have been undertaken by Heard and Pickering (2008), Heard *et al.* (2008) and Heard *et al.* (2014).

Sedimentary logs have been produced for each of the gamma-ray logged sections. These logs include every bed that is thicker than 0.5 cm. The logs record information on sedimentary structures, grain-size variations, bioclastic content and bioturbation. The logs also include information on sediment colour, recording the presence of cm-sized dark-grey bands and orangey bands which are probably both primary and diagenetic in origin. The key symbols used in the sedimentary logs can be seen in Figure 2.5.

Plate 5.1 (next page) Ichnofacies in the fine-grained successions. **(a)** Sandstone turbidite dominated by *Nereites*. Ainsa System, Boltaña section. **(b)** Intense bioturbated sandstone turbidite consisting mainly of *Ophiomorpha Annulata,* interfan deposits between Guaso I and Guaso II sandbodies. **(c)** *Helminthorhaphe* in the Ainsa System, Forcaz section. **(d)** *Scolicia* in the Ainsa System, Boltaña section. (**e)** *Arenicolites* burrows in the Banastón System, Labuerda section 1. **(f)** *Arenicolites* forming vertical branches in the Sieste stream section. **(g)** Sandstone bed containing *Spiroraphe* (*Nereites* ichnofacies), Ainsa System, Boltaña section. **(h)** *Cosmorhaphe* forming meandering feeding traces in a sandstone turbidite in the interfan deposits of Gerbe and Banastón systems, Gerbe section.

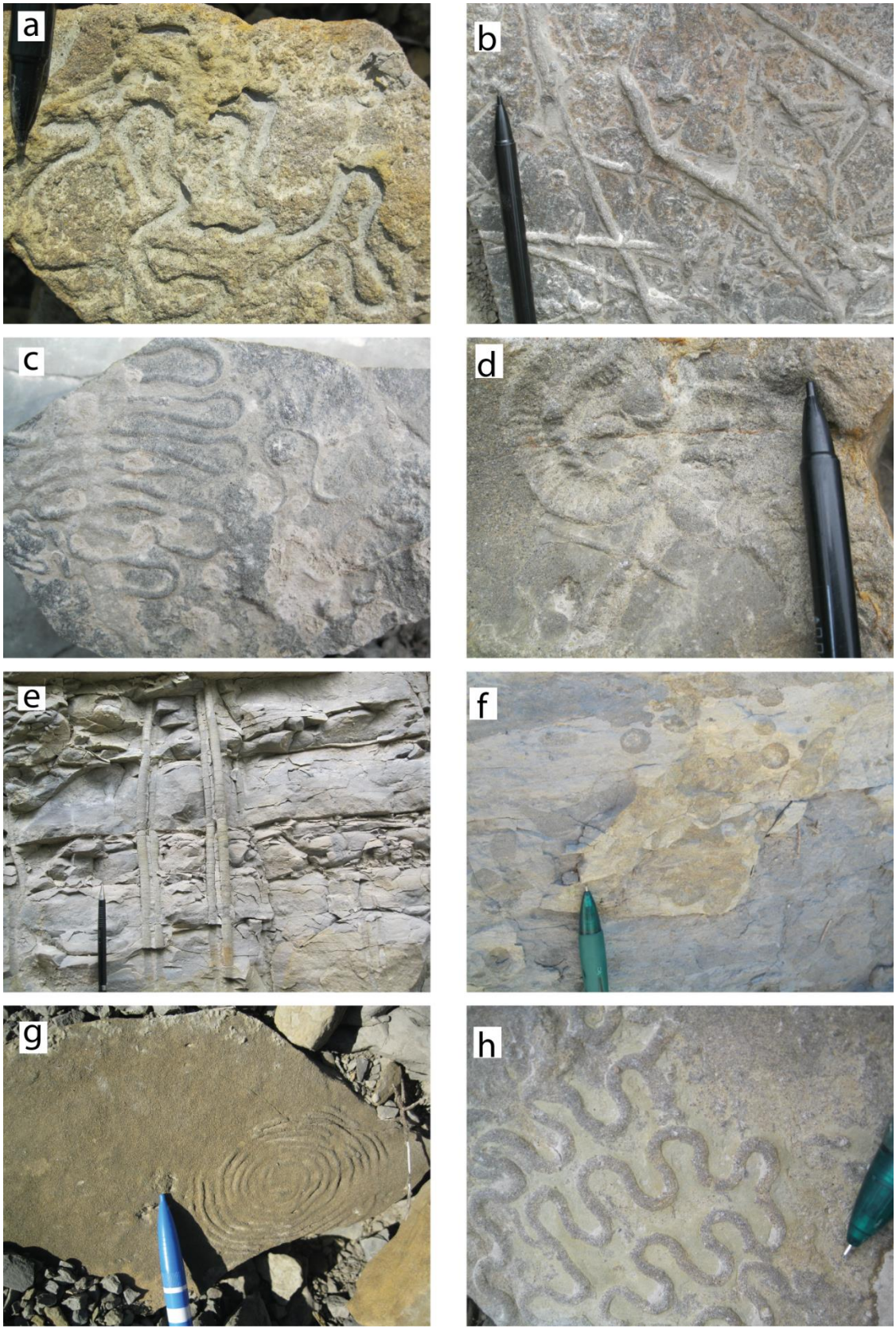
a
b
c
d
e
f
g
h

5.2.2 Environment of deposition of the fine-grained sequences

The fine-grained gamma-ray logged sections are mainly interpreted as interfan successions and channel levée-overbank deposits. Figure 5.2 shows a schematic representation of the typical environments of deposition seen in the deep-marine sediments of the Ainsa Basin.

The deposition of levée and overbank deposits occurs when sediment gravity flows such as turbidity currents, are confined within a submarine channel and overtop the channel margins to deposit sediment beyond the channel axis (Mutti and Normark, 1987). Levée deposits are characterised by packages of very thin-bedded siltstones interbedded with thin-bedded sandstone turbidites. Climbing-ripple and cross-lamination are observed in some of these sandstone turbidites. There are significant thickness variations in the sandstone turbidites which tend to decrease away from the channel margins.

Overbank deposits are lithologically very similar to levée deposits and can be interpreted as the lateral continuation of a levée. These deposits are, in general, characterised by a lower net-to-gross ratio as many sandstone turbidites have already pinched out away from the channel. Interfan deposits are very similar to overbank deposits although they tend to be characterised by larger intervals of laminated siltstone and mudstone couplets.

In the absence of detailed mapping and lateral correlations, similarities in the sedimentology of levées, overbank and interfan deposits make the distinction between these three types of sedimentary environments difficult to differentiate. As a result, interpretations have been made by taking into consideration the location of the gamma-ray sections in relation to the channel axis using the Ainsa Basin geological map.

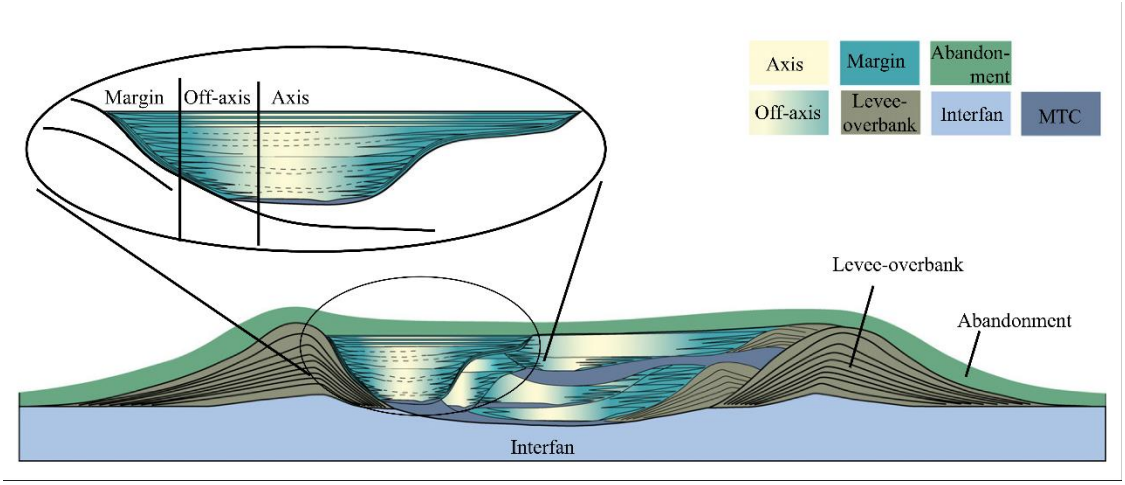

Figure 5.2 Environments of deposition of the Ainsa Basin channel systems. The figure shows a schematic cross-section of a channel levée-overbank system. The three main environments of deposition seen in the fine-grained successions are levée-overbank, fan abandonment and interfan. After Heard *et al.* (2014).

5.2.3 K, Th and U content of the gamma-ray sections and environmental constraints

The K (%), U (ppm) and Th (ppm) contents of the fine-grained sediments are in general, higher in the older sections (Arro, Gerbe and Banastón systems) than in the younger sections (Ainsa and Morillo systems) (Figure 5.3a and 5.3c), although the Morillo-Bruello and Guaso sections shows a mild increase in the content of these elements. The recalculated content of these elements to 100% shows that the K in the rocks has remained relatively stable throughout the stratigraphy at ~ 13-14%, whilst the Th and the U tend to compensate the win and the loss for each other (Figure 5.3e). The Labuerda 2 and Boltaña sections, for instance, appear to be particularly enriched in Th relative to U, whilst the Sieste Stream and Morillo-Bruello sections appear to be particularly enriched in U relative to the Th content (Figure 5.3e).

Ternary diagrams of these three elements show a similar compositional trend in all the gamma-ray logged sections with all the values plotting in the lower left corner

of the K-Th-U triangle indicating a dominance of Th in the rock composition (Figure 5.4). The four youngest sections Morillo-reservoir, Sieste, Morillo-Bruello and Guaso sections located within the Morillo and Guaso systems show a subtle change of values spreading towards the U field (Figure 5.4).

The sand percentage for each of the fine-grained successions has been calculated to estimate whether there has been any significant differences in the sand content of the interfan and overbank deposits of the different deep-marine systems. Sand percentage has been calculated by adding the thickness of all the sandstone turbidites present in each fine-grained succession (Figure 5.3b). The Ainsa System, for example, shows the lowest sandstone content (3.6%) represented in the Boltaña and the Forcaz sections whilst the Banastón System contains the highest sandstone percentage, close to ~ 11% in both Labuerda sections. Comparison of sedimentary logs with total-gamma and K content shows that periods of high-frequency sandstone turbidite deposition appear to be associated with low gamma-ray counts and low K contents. This association can clearly be seen in the Tierrantona section (Figure 5.10), although in other sections, such as the Boltaña section (Figure 5.51), this correlation is more difficult to establish. It is likely that there is some sand content present in the siltstones, interfering the signal.

Cross-plots of Th *versus* U, Th *versus* K and U *versus* K have been produced for each of the sections to determine the presence of any association between these pair of elements. Although the correlation coefficient (R) between Th and U is low for all the gamma-ray sections (average R = -0.29 ± 0.13) (Table 5.2), most of the cross-plots of Th *versus* U tend to show a negative trend with the exception of the Gerbe section where there is no trend observed (Figure 5.5). The Th *versus* K cross-plots show a

moderate positive association with averaged values of R = 0.39 ± 0.08 (Table 5.2, Figure 5.6). This moderate correlation probably reflects that there is some association between K and Th as part of clay minerals in mudstones and very-fine lithologies, but the presence of thoriferous minerals and feldspars in coarser lithologies may be responsible for the scattering observed in the cross-plots. There is no association between U and K (R = 0.013) in any of the gamma-ray sections (Table 5.2).

The Th/K ratios show little variation in all the sections with values remaining relatively stable between 4.3-4.9 (Figure 5.3d). Th/U ratios show a higher degree of variation with values ranging from 3.2-4.9 (Figure 5.3d). Most upper crust rocks have a typical Th/U ratio of between 3.5 and 4 (McLennan *et al.*, 1993). Weathering and sedimentary recycling may result in the loss of U and result in an increase in the Th/U ratios. Th/U values > 4 are considered to indicate significant weathering in the source areas (McLennan *et al.*, 1993). The Labuerda section 2 and the Boltaña section have relatively high Th/U values (~ 4.9), suggesting that an increase in weathering and/or sediment recycling may have occurred during the deposition of the Banastón and Ainsa systems. However, the relative stability of the Th/K ratios across the whole stratigraphy, suggests there were no significant variations in rock weathering patterns occurring in the source areas.

Th/U ratios can also reflect water oxygenation conditions during sediment deposition. Wignall and Twitchell (1996) considered that values between 0 and 2 were characteristic of anoxic conditions, whilst values of ~ 8 reflected strongly oxidising conditions. The Th/U values in the Ainsa Basin reflect in general oxic conditions throughout the stratigraphy. The four youngest sections (Morillo-reservoir, Sieste, Morillo-Bruello and Guaso) have slightly lower Th/U ratios (between 3.2 and 3.5) and this may reflect a reduction in basin oxygenation. The significant growth of the

bounding anticlines of the Ainsa Basin during the deposition of these systems may have contributed to a restricted environment.

Table 5.2 Correlation coefficient (R) in the spectral gamma ray data.

Gamma-ray sections	Th/U	U/K	Th/K
Tierrantona	-0.36	-0.049	0.388
Gerbe	0.052	0.331	0.604
Labuerda section 1	-0.257	0.111	0.369
Labuerda section 2	-0.312	0.0068	0.416
Boltaña	-0.368	-0.057	0.344
Forcaz	-0.378	-0.065	0.3036
Morillo-reservoir	-0.337	-0.123	0.3991
Sieste	-0.396	-0.122	0.29
Morillo-Bruello	-0.31	-0.0022	0.4
Guaso	-0.25	0.107	0.433
Average	-0.29	0.013	0.395
Standard deviation	0.13	0.13	0.08

The Th *versus* U cross-plots shows a week relationship and the Th *versus* K cross-plots show a moderate relationship. The U *versus* K cross-plots does not show any association.

a

		Total %	Average	St Dev
Tierrantona	K (%)	13.7%	2.41	0.27
	Th (ppm)	19.1%	3.36	0.89
	U (ppm)	67.2%	11.91	1.7
	Th/K		4.97	0.73
	Th/U		3.97	2.18
Gerbe	K (%)	14.84%	2.85	0.39
	Th (ppm)	19.09%	3.68	0.98
	U (ppm)	66.07%	12.79	2.09
	Th/K		4.5	0.61
	Th/U		3.76	1.41
Labuerda 1	K (%)	14.25%	2.61	0.29
	Th (ppm)	19.68%	3.59	0.87
	U (ppm)	66.06%	12.15	1.7
	Th/K		4.69	0.67
	Th/U		3.66	1.46
Labuerda 2	K (%)	14.23%	2.31	0.28
	Th (ppm)	17.6%	2.85	0.79
	U (ppm)	68.17%	11.16	1.64
	Th/K		4.86	0.72
	Th/U		4.43	2.56
Boltaña	K (%)	14.02%	2.14	0.25
	Th (ppm)	17.4%	2.65	0.79
	U (ppm)	68.57%	10.54	1.57
	Th/K		4.5	2.03
	Th/U		4.97	0.78
Forcaz	K (%)	14.61%	2	0.27
	Th (ppm)	19.47%	2.66	0.89
	U (ppm)	65.91%	9.11	1.7
	Th/K		4.58	0.73
	Th/U		3.81	2.18
Morillo-reservoir	K (%)	14.61%	1.81	0.22
	Th (ppm)	21.23%	2.62	0.75
	U (ppm)	64.16%	8.01	1.36
	Th/K		4.46	0.73
	Th/U		3.45	1.8
Sieste	K (%)	14.34%	1.56	0.21
	Th (ppm)	22.14%	2.41	0.77
	U (ppm)	63.5%	7	1.29
	Th/K		4.53	0.88
	Th/U		3.45	2.18
Morillo-Bruello	K (%)	14.88%	1.93	0.28
	Th (ppm)	21.83%	2.82	0.73
	U (ppm)	63.28%	8.28	1.46
	Th/K		4.34	0.79
	Th/U		3.24	1.45
Guaso	K (%)	13.85%	1.76	0.27
	Th (ppm)	21.6%	2.74	0.71
	U (ppm)	64.55%	8.31	1.47
	Th/K		4.75	0.83
	Th/U		3.33	1.45

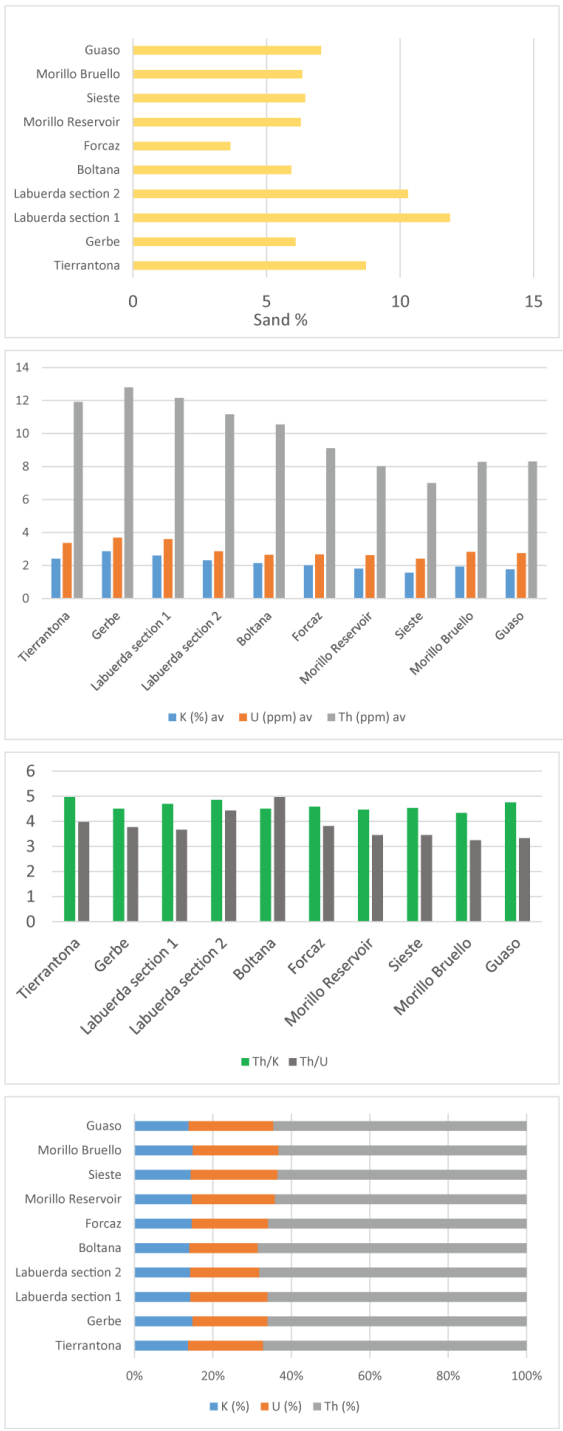

Figure 5.3 K, Th and U content of the gamma-ray logged sections. (a) Table showing the K, U, Th, Th/K and Th/U content of the gamma-ray logged sections. Average and standard deviation values are shown. **(b)** Graph comparing the sand percentage of all the gamma ray-logged sections. Values calculated from sandstone turbidite intensity studies. **(c)** Graph showing the K, U and Th content variation in the gamma-ray logged sections. **(d)** Graph showing the Th/K and Th/U variation in the gamma-ray logged sections. **(e)** Graph showing the K, Th and U contents recalculated to 100% in all the gamma ray logged sections. U content appears to increase across the stratigraphy.

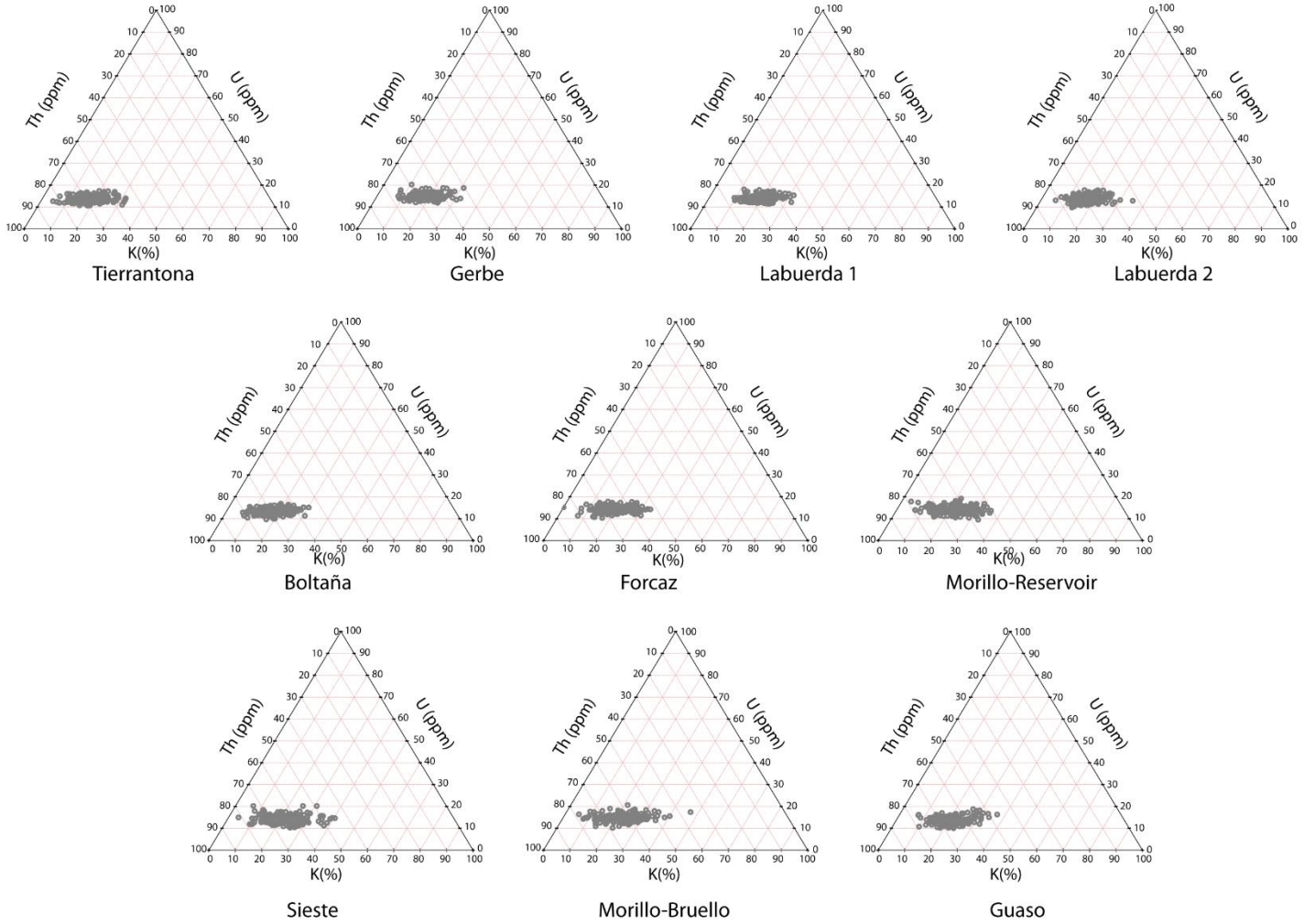

Figure 5.4 Ternary diagrams of all the spectral gamma-ray logged sections. All the sections show a similar compositional trend with all the values plotting in the lower left corner of the Th-U-K triangle indicating a dominance of Th in the rock composition.

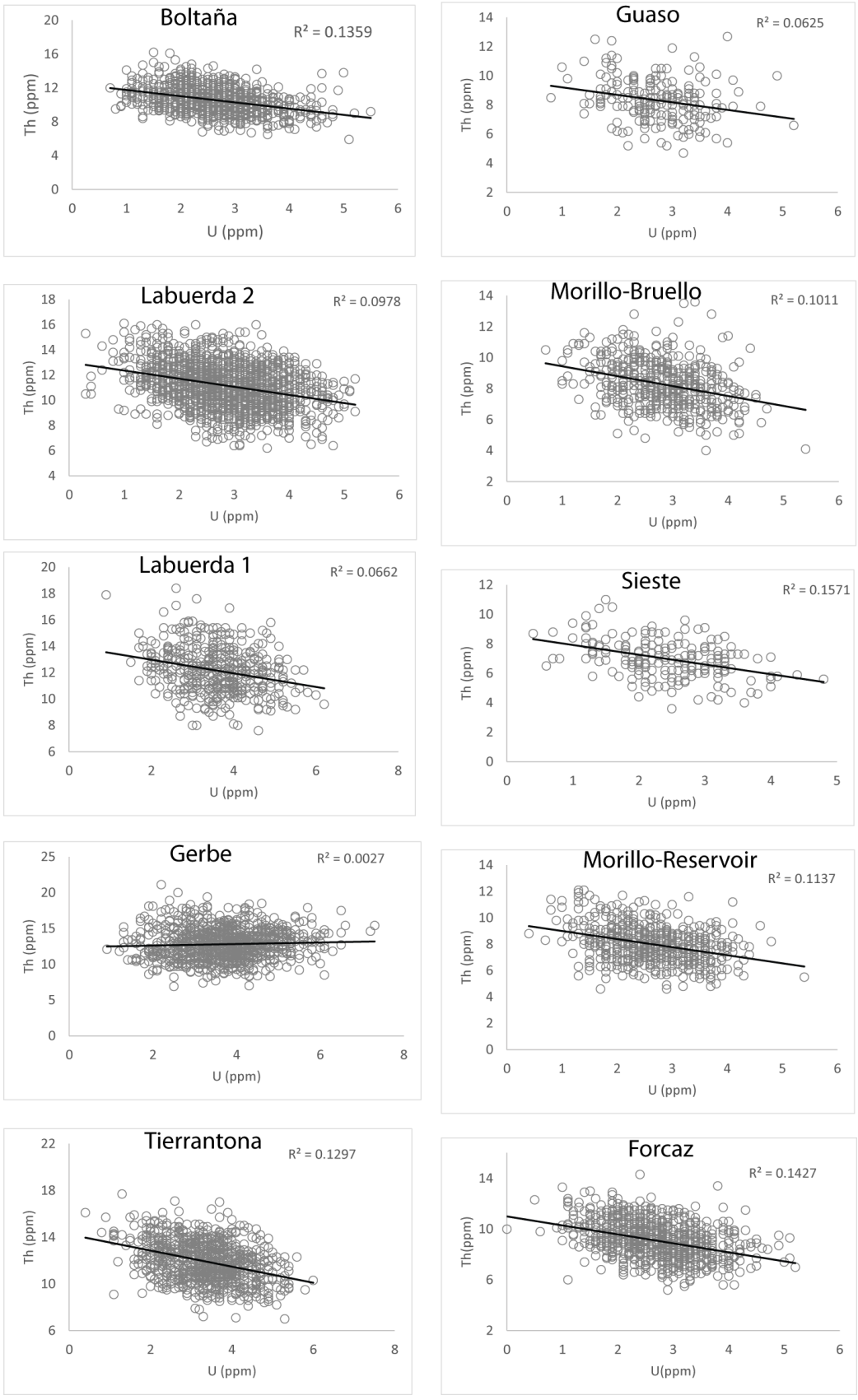

Figure 5.5 Cross-plots of Th *versus* U in the spectral gamma-ray sections. There is a weak negative correlation between the Th and U in all the gamma-ray sections (averaged values R = -0.29) with the exception of the Gerbe section where there is no correlation.

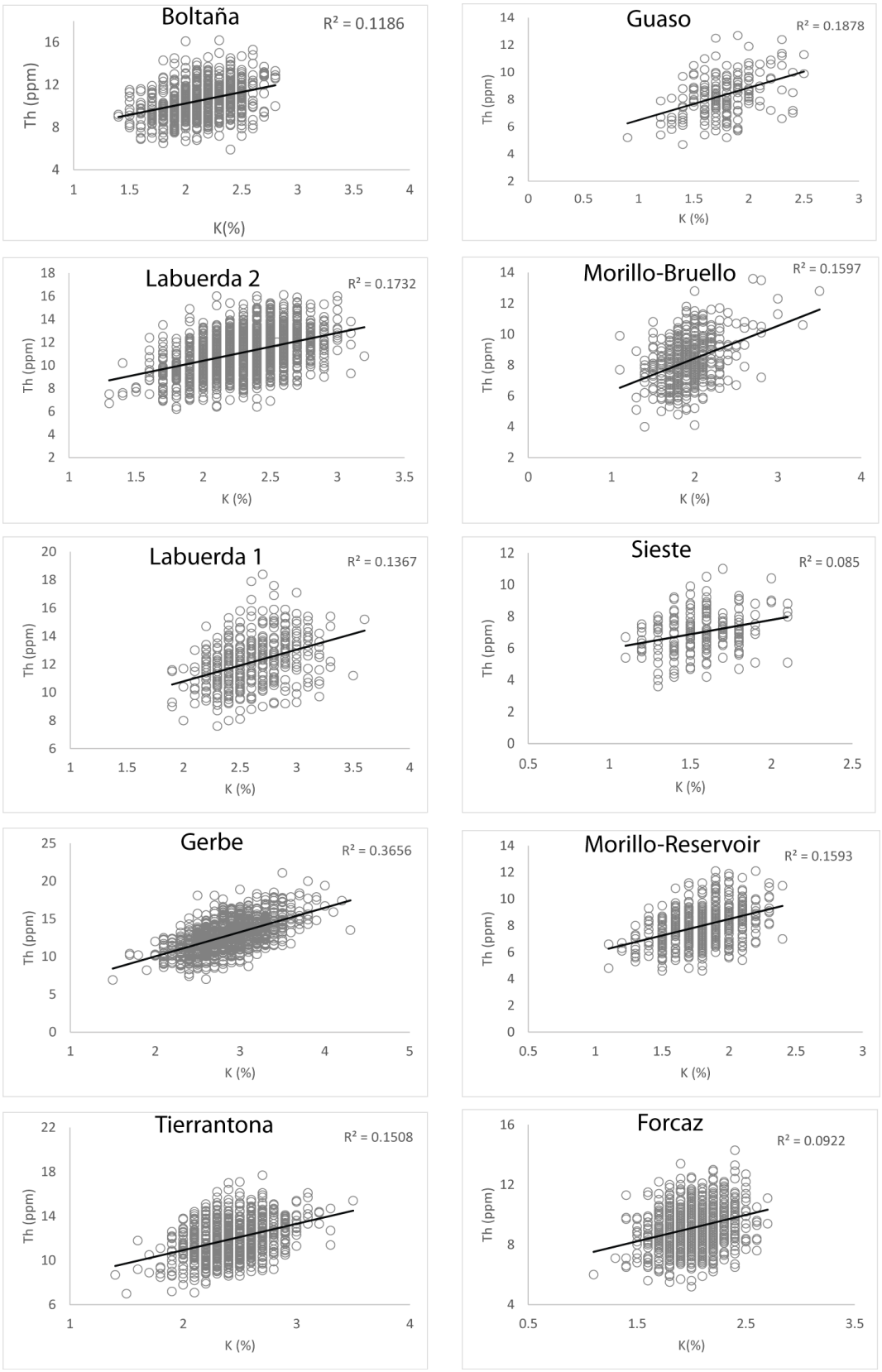

Figure 5.6 Th and K cross-plots of the spectral gamma-ray sections. There is a moderate positive correlation between Th and U in all the gamma-ray sections (averaged values R = 0.395).

5.2.4 Spectral analysis of the spectral gamma-ray sections

Detailed information on the spectral gamma-ray methodology used in this study can be found in Section 2.4. The cyclostratigraphy analysis work-flow used for the interpretation of the gamma-ray logged sections can be seen in Figure 2.11.

Time-series analysis of the total-gamma (cpm), K (%) and Th (ppm) has been undertaken for each of the gamma-ray logged sections. The U (ppm), Th/U and Th/K plots are in general noisy and this is probably associated with the relatively low content of U and K in the rocks. Preliminary time-series results of these records have not shown any significant cyclicity and therefore they have not been included in the time-series analysis of the outcrop gamma-ray logged sections. Sandstone turbidite intensity has also been calculated for each of the gamma-ray logged sections by counting the number of sandstone turbidites ($\geq$ 0.5 mm thick) in successive 20 cm-thick vertical intervals. A spacing interval of 20 cm was considered adequate to match the sampling resolution of the gamma-ray logging technique. Time-series analysis of the sandstone turbidite intensity records has also been undertaken for each of the gamma-ray sections to provide an additional estimate of the cyclicity present in these fine-grained successions.

Methods of spectral estimation include the software packages REDFIT (Schulz and Mudelsee, 2002) and Analyseries (Paillard *et al.,* 1996). The methodology and program input parameters have been described in Section 2.9. The power spectrum of the total-gamma data created using the REDFIT method has been compared with the spectra derived from other methods such as the MTM, the maximum entropy and the modified periodogram to show that these four methods can produce a similar spectrum with the most significant spectral peaks present at similar frequencies. The preferred method of analysis in this study is considered to be REDFIT because it has the

advantage of being used in unevenly-spaced data without introducing interpolation errors. In addition, this method resulted in smoother spectral results (high degrees of freedom) without losing frequency resolution. Time-series analysis of the total-gamma, K, Th and sandstone turbidite intensity has also been undertaken using this method. Different system parameters have been tried for each of the gamma-ray sections with the aim of obtaining the best frequency resolution/smooth power spectrum. Shorter sections require, in general, a reduction in the number of WOSA segments and in the degrees of freedom, to prevent over-smoothing the spectrum and causing loss of frequency resolution. A summary of the parameters used for each spectral computation is described in each of the gamma-ray logged sections. Comparison of the power of the spectrum for the four different parameters was facilitated by re-scaling the spectra.

In order to estimate the spectral noise and establish reliable confidence levels of the power spectrum, three different methods to fit the background noise have been applied to all the REDFIT spectra. These models include: the AR(1) of Mann and Lees (1996), a power regression and a quadratic fitting-curve method (see Section 2.9.4). A table with the square errors resulting from applying each of these methods is included for each of the gamma-ray logged sections. Most of the field sections show that the least summative square error and therefore the best noise background fitting method is the power regression, although, there are a few exceptions in some of the shorter sections where the least error is produced by the AR(1) method of Mann and Lees (1996). Finally, each section includes a table with all the main frequencies identified > 90% confidence levels, unless otherwise stated.

Wavelet analysis has also been included in this study to complement the time-series analyses by adding information about the spatial variability of certain

frequencies throughout the records. This method permits to characterise the stratigraphic intervals where the frequencies have enough amplitude to be significant.

The significant frequencies determined by REDFIT have been selected for ASM analysis. ASM studies estimate the SAR which best fit the expected Milankovitch periodicities for the Middle Eocene (~ 45 Ma). ASM analysis has been carried out using the method of Meyers and Sageman (2007) which includes critical significant levels of rejection of 90% above which the null hypothesis of no orbital cyclicity is rejected. The frequencies which have been associated with eccentricity and obliquity cycles from ASM studies have then been used to filter the total-gamma records to determine changes in the amplitude of these cycles throughout the stratigraphy.

Finally, orbital tuning has been applied to the Gerbe, Labuerda 2, Boltaña and Forcaz sections. These four gamma-ray sections have a good radiometric control from biostratigraphy (Scotchman *et al.*, 2014) and palaeomagnetic studies (Chapter 3) and have a sufficient length to recognise eccentricity cycles with confidence.

5.3 Gamma-ray logged sections in the Ainsa deep-marine systems

5.3.1 The Arro System

5.3.1.1 Sedimentology of the Arro System

The Arro System is part of the Lower Hecho Group and is stratigraphically located between the Los Molinos and the Gerbe systems. The sediments of the Arro System were incorporated into a major thrust system which caused intense distortion, faulting, major fault-propagation-folds and stratigraphic duplications. As a result, the Arro System is one of the most tectonically deformed deep-marine systems in the Ainsa Basin. Despite this intense deformation, there are a number of well-exposed outcrops which have allowed its study and interpretation by several researchers (e.g., Mutti *et al.*, 1985; Millington and Clark, 1995; Clark and Pickering, 1996; Remacha *et al.*, 2003).

The total thickness of the Arro System has been investigated by several authors. Mutti *et al.* (1985) and Clark and Pickering (1996) have estimated a thickness of ~ 145 m. These estimations are in close proximity to those of Millington and Clark (1995) who estimated a variation from 120 m in the proximal sections to 150 m in the distal sections. Remacha *et al.* (2003) gave an estimation of ~ 280 m. However, these authors included the underlying sandbodies of the Los Molinos System into the Arro System.

The sedimentology of the Arro System has been described and interpreted by Millington and Clark (1995) and Bayliss (2011). This system is composed of three sandy successions or sandbodies classified from older to younger, Arro I to III sandbodies. The Arro System has been interpreted as a base-of-slope sheet-like sand-prone system developed in front of a canyon mouth. The sediments of the Arro System

can be traced directly into its canyon source, the Charo Canyon. The Arro sandbodies are characterised by medium to coarse-grained erosive sandstone turbidites interpreted as sediments deposited at the canyon mouth. Petrographic studies indicate that these sandstones are subarkose arenites enriched in shallow-marine faunas such as echinoderms and bivalves (mainly oyster shells) and large foraminifera such as *nummulites* and *alveolines* (Das Gupta and Pickering, 2008). The abundance of marine faunas probably indicates that the sediments were sourced from shelfal areas and fed the canyon by littoral drift (Millington and Clark, 1995). The Arro II and III sandbodies also contain large amounts of wood material which may indicate progradation of rivers which fed directly into the canyon mouth. Interbedded with these erosively-based turbidites, there are large intervals of contorted muddy sediments (Type Ia MTDs) containing large open shear-fold structures interpreted as sediment slides. These MTDs, which are mainly found at the base of the Arro II sandbody, have incorporated distorted sand rafts into their flow which probably suggest that they were very erosive events able to incorporate semi-lithified sediment from the seafloor (Bayliss, 2011). These sediment slides were sourced from the collapse of nearby slopes (Millington and Clark, 1995).

The Arro System rapidly thins downslope, away from the canyon mouth, forming a heterolithic package containing sheet-like, thin to medium-bedded sandstones (Millington and Clark, 1995). This change in facies, from highly erosive sandstone turbidites to thin sheet-type facies, has been interpreted as density flows which underwent a hydraulic jump due to an inferred break of slope at the canyon mouth (Millington and Clark, 1995).

There is a general paucity of extra-formational rounded pebbles within the Arro System and also, in older turbidite systems including the Fosado and Los Molinos.

This paucity of pebbles most likely indicates the source of sediments to the Ainsa Basin were mature fluvial systems which developed in the Tremp-Graus Basin at this time. From the Gerbe System onwards, larger amounts of rounded pebbles were delivered to the Ainsa Basin. This change in the amount of pebbles between the Arro and the Gerbe systems suggests a period of significant uplift in the Tremp-Ager Basin source areas. The increase in slope gradients probably resulted in the transition from mature to immature rivers with the ability to transport down the system significant volumes of pebbles from well-developed alluvial fans and store them on shelfal areas (Heard, 2007; Scotchman *et al.*, 2014).

5.3.1.2 Tectonic history during the deposition of the Arro System

The deposition of the Arro System is synchronous with a major uplift event associated with the motion of the Montsec-Peña Montañesa Thrust (Mutti *et al.*, 1988; Fernández *et al.*, 2012) which resulted in significant intrabasinal tectonic activity and the emplacement of the Arro Thrust System. This intense tectonic activity resulted in an increase in slope gradients which caused slope instabilities, collapses and resulted in the large quantities of slump and slide sediments observed in the Arro System.

The Los Molinos Thrust is part of the Arro Thrust System and is responsible for overturning the Arro I sandbody in the southwestern section of the basin. The Arro System developed coevally with the onset and first stages of this thrust and of the Mediano detachment fold (Mutti, 1992). Bentham and Burbank (1996) proposed that the initiation of the development of the Mediano Anticline probably occurred during the late Ypresian/early Lutetian, although the most prominent growth did not commence until the middle Lutetian coinciding approximately with the deposition of

the Ainsa System (Fernández *et al.*, 2004). The lack of thickness changes in the Arro System across this structure could suggest an onlapping relationship. Poblet *et al.* (1998) suggest this structure did not form a significant topographic high at the time of this system deposition.

5.3.1.3 Age of the Arro System

The timing of deposition of the Arro System is likely to have occurred within chrons C22n-C21r (this study). These estimations are in close agreement with the ages proposed by Scotchman *et al.* (2014), suggesting that the deposition of this system occurred within zone NP13 in chron C22.

5.3.1.4 Tierrantona gamma-ray logged section

5.3.1.4.1 Geographical location

The Tierrantona section is 167 m long and is located ~ 2.5 km west of Arro town and ~ 4 km south of the village of Tierrantona. The section is exposed along the road HU-V-6442 which joins the N-260 main road with the village of Tierrantona (Plate 5.2).

The first 60 m of the section are weathered and locally are covered by scree (Plate 5.3a). Gamma-ray logging of this area required the removal of the weathered material with a hammer and a brush to allow the portable gamma-ray spectrometer to sit on fresh rock. This poorly-exposed area may have resulted in inaccuracies whilst recording the sandstone turbidite intensity in the sedimentary logs. As a result, the cyclostratigraphic studies of the sandstone turbidite intensity of this section may have been affected. Rock exposure clearly improves from 60 m onwards and remains

satisfactory until the end of the logged section. Some small scale slumps are found towards the top of the section (Plate 5.3c). There is a general increase in the sand content throughout the section with thicker sandstone turbidites found towards the top (Plate 5.3b). The gamma-ray logged section was discontinued at 167 m due to the sediments immediately above appearing to be tectonically distorted and highly fractured with the presence of numerous calcite veins also being observed across the outcrop. This tectonically deformed area is likely to be associated with a thrust which crosses the northwestern part of the geological map (Figure 5.7).

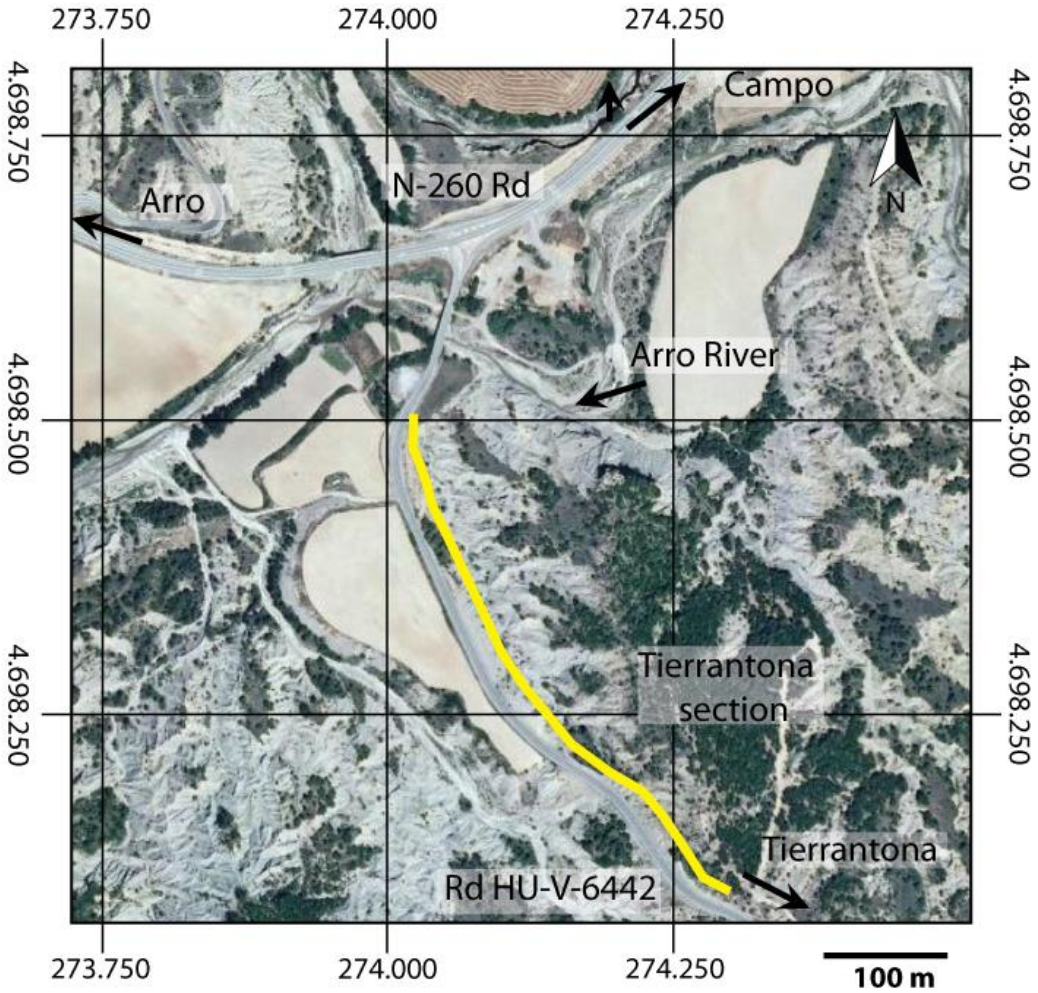

Plate 5.2 Aerial photograph of the Tierrantona gamma-ray logged section. The Tierrantona section is exposed next to the HU-V-6442 road. This road joins the N-260 road to the village of Tierrantona. The first 60 m of the section are weathered and locally thick scree covers fresh surfaces making it difficult to undertake sedimentary and gamma-ray logging of the section. Aerial image from www.sigpac.mapa.es/fega/visor.

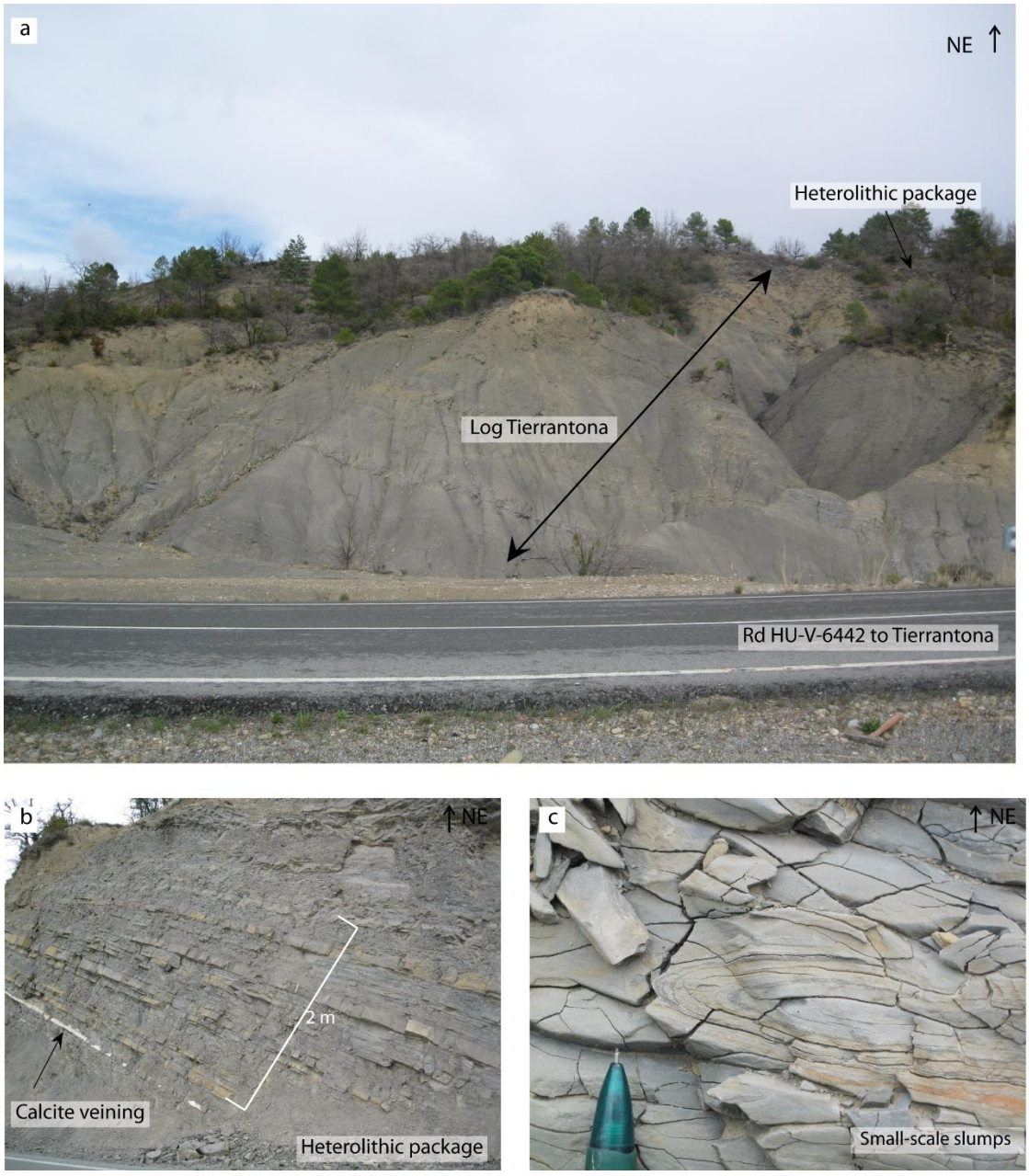

Plate 5.3 Outcrop photographs of the Tierrantona gamma-ray logged section. (a) Photograph showing the lower-part of the Tierrantona gamma-ray section by the side of the HU-V-6442 road. This part of the section is very weathered and covered by thick scree. **(b)** Outcrop photograph of a heterolithic package seen at ~ 150 m height towards the top of the Tierrantona section. The top 30 m contains some calcite veining, up to 5 cm-thick which seems to follow the strike of the beds. Fracture zones become more common immediately above the Tierrantona section with sheared and deformed sediments also common indicating a nearby thrust. **(c)** Close-up photograph of a syn-sedimentary fold seen in the fine-grained sediments. Sediment slumps and slides in the Tierrantona section are common towards the top of the section but are in general small and do not exceed ~ 15 cm in thickness. Slumps within the Arro System, however, are numerous and can reach up to 20 m in thickness.

5.3.1.4.2 Stratigraphic location

The Tierrantona section is located within the Arro System. Figure 5.7 shows a geological map and a cross-section of the area. The Arro System is tectonically deformed with many thrusts and fault-propagation-folds trending in a north-south direction and with a main displacement direction towards the west and the southwest. The intense tectonic deformation of the area has not permitted to determine the exact location of the Tierrantona section within the stratigraphy of the Arro System. As a result of this, a stratigraphic column for this section has not been constructed.

Plate 5.4 shows some outcrop photographs showing the degree of deformation which has mainly affected the sediments of the Lower Hecho Group (Arro, Los Molinos and Fosado systems) and some parts of the Gerbe System in the Upper Hecho Group. These deformed areas are mainly restricted to the northwestern area of the Ainsa Basin forming part of the Arro Thrust System.

Figure 5.8 shows the sandstone turbidite intensity variation of the Tierrantona section. The sandstone turbidite intensity appears to vary cyclically and two cycles with a period of 30-40 m can easily be distinguished in the middle and upper part of the section. There is a general increase in the sandstone turbidite intensity throughout the Tierrantona section (Figure 5.8). Figure 5.9 shows detailed sedimentary logs of the Tierrantona section. Electronic versions of these logs are available in Appendix 3. Figure 5.10 shows the variation in the content of the K, Th, U, Th/K and Th/U throughout the Tierrantona section. Heterolithic packages containing thick sandstone turbidites are characterised by low total-gamma counts and a decrease in the K content.

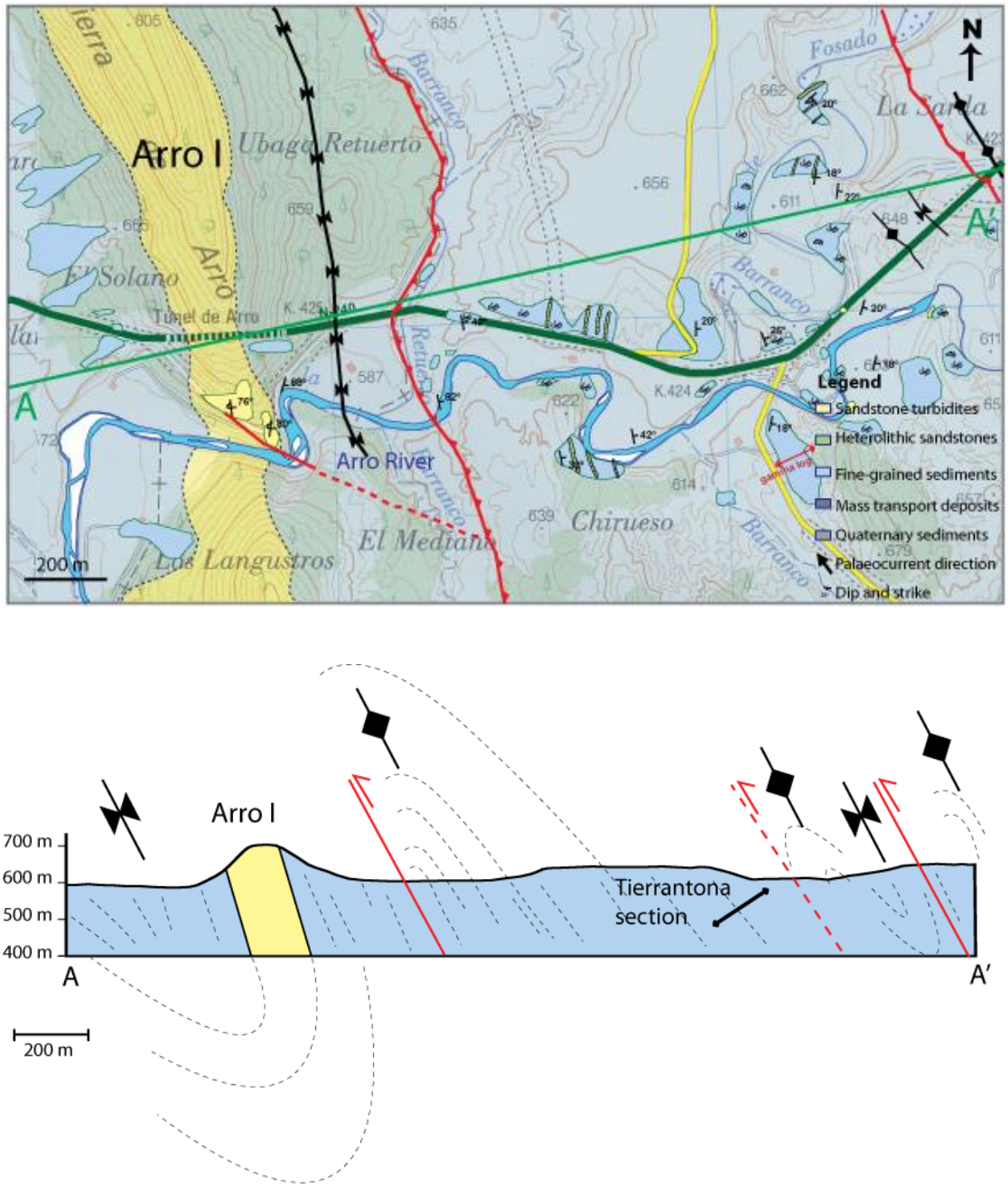

Figure 5.7 Geological map and cross-section of the Tierrantona section. (a) Geological map of the area surrounding the Tierrantona gamma-ray section. The Arro System is severely deformed and two main thrusts can be observed in the area. The area is also characterised by large-scale fault-propagation-folds The Arro I sandbody occupies the western part of the map and is upside-down with beds dipping 75-85°. There are large changes in the stratigraphic dip in the area ranging from 20° dip to completely vertical strata. There are also numerous large-scale slumps within the fine-gained sediments of the Arro System but they have not been mapped in detail due to mapping time-constraints. **(b)** Cross-section showing the position of the Tierrantona gamma-ray logged section. Due to the large-scale deformation within this system is not possible to infer the exact location of the Tierrantona section within the stratigraphy.

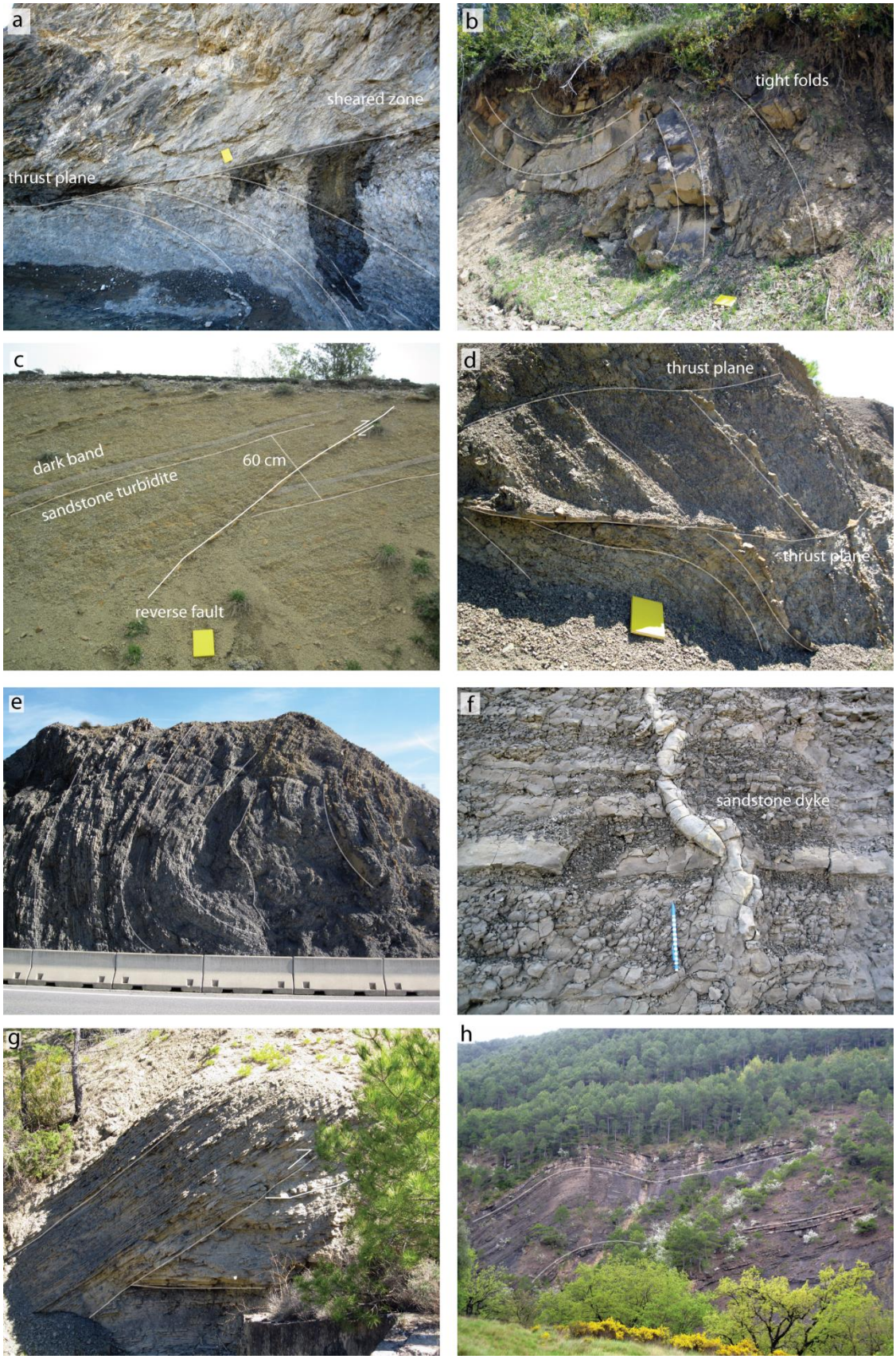
a
sheared zone
thrust plane
b
tight folds
c
dark band
sandstone turbidite
60 cm
reverse fault
d
thrust plane
thrust plane
e
f
sandstone dyke
g
h

Plate 5.4 (previous page) Outcrop photographs showing tectonic deformation in the Ainsa Basin. (a) Outcrop photograph of a thrust plane exposed in the Arro stream. This thrust is located ~ 50 m below the Arro sandbody and fault displacement has resulted in folding and overturning the strata in the area. **(b)** Outcrop photograph exposed along a path ~ 500 m north of San Vicente town showing tight folds in the sandstone turbidites of the Gerbe System. **(c)** Outcrop photograph of reverse faults seen on the road that joins the N-260 with Fosado village, 2 km south of Fosado. These faults are located in Los Molinos System. **(d)** Photograph of a distorted outcrop exposed along the road which joins Ainsa and El Soto town, ~ 1 km SW of El Soto. The outcrop shows faulted beds in the fine-grained sediments with numerous calcite veining. This deformed area is located in the Gerbe System. **(e)** Outcrop photograph exposed along the road N-260, ~700 m SW of the village of Fuendecampo, showing large scale folds with vertical and overturned strata in Los Molinos System. **(f)** Outcrop photograph showing a 70 cm vertical sandstone dyke exposed at the Arro stream in the Los Molinos System. **(g)** Outcrop photograph showing a thrust plane well exposed at a stream cut, ~ 1.5 km south of Los Molinos town. This thrust is located in the Los Molinos-Fosado systems. The main thrust direction is towards 240°. **(h)** Outcrop photograph of a broad anticline exposed at a stream cut, visible from the road that joins Ainsa and Araguás towns, ~ 600 m west of Araguás, in the Arro System.

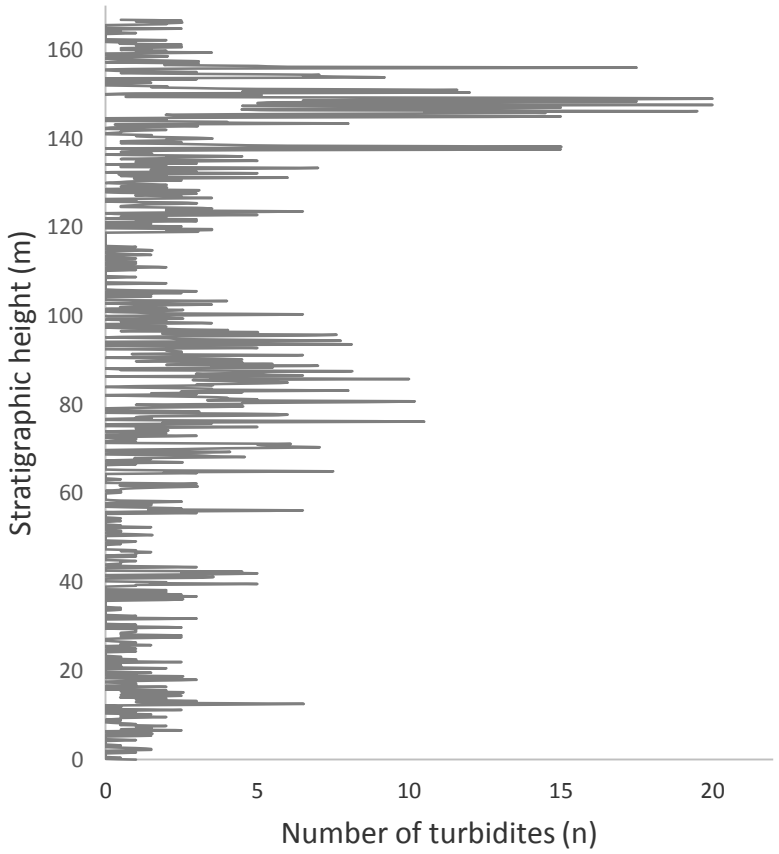

Figure 5.8 Sandstone turbidite intensity of the Tierrantona section. There are two well defined cycles with a period of 35-40 m. The lack of clear cyclicity in the first 60 m of the section is probably due to poor outcrop exposure. The averaged sand percentage for the whole section is ~ 8.7%.

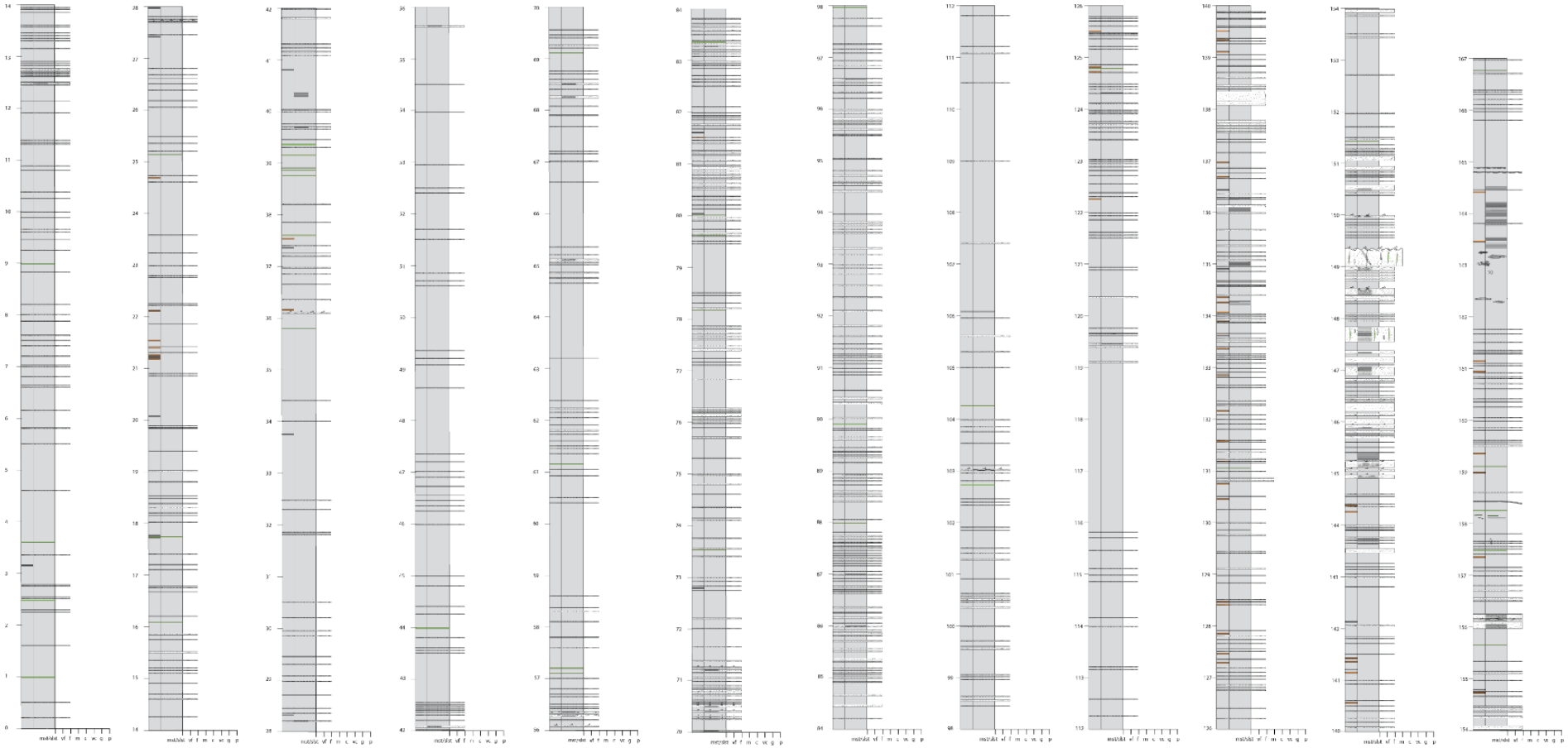

Figure 5.9 Sedimentary logs of the Tierrantona section. The low degree of sandstone turbidite intensity in the first 60 m of the section is likely to have resulted from poor exposure of the outcrop. Towards the end of the section, between 144-152 m, there is a significant heterolithic package containing thick sandstone turbidites. Sedimentary logs include every bed thicker than 0.5 cm. Figure 2.5 includes a legend of the symbols used in the sedimentary logs. Appendix 3 includes an electronic version of these sedimentary logs for detailed visualisation.

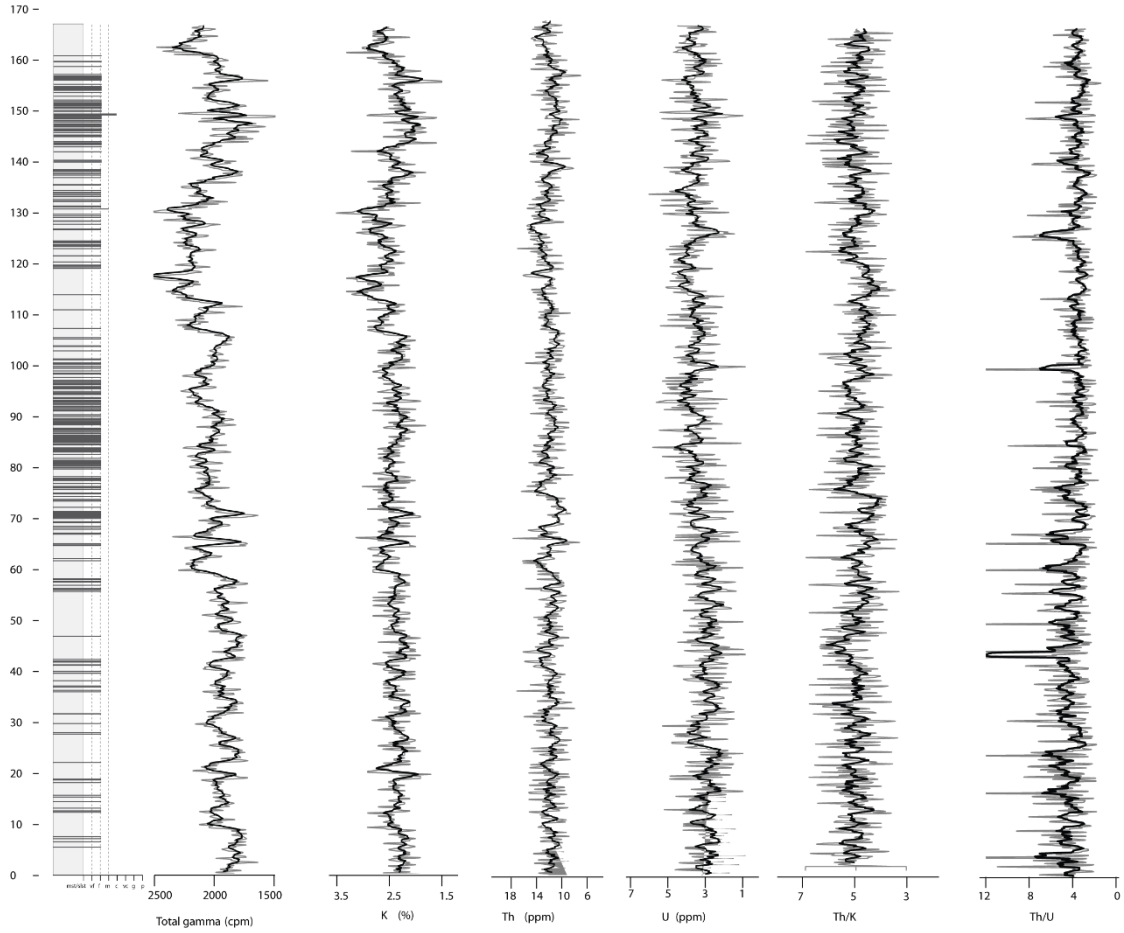

Figure 5.10 Total-gamma, K, Th, U, Th/K and Th/U data plotted against simplified sedimentary logs of the Tierrantona section. Sedimentary logs only showing sandstone turbidites ≥ 1.5 cm, for complete logs refer to Figure 5.9 and Appendix 3. The black line is a 4-weight moving average. The heterolithic package between 144-152 m containing thick sandstone turbidites is characterised by low gamma-counts and a low K content.

5.3.1.4.2. Cyclostratigraphic studies of the Tierrantona section

(a) Methods of spectral estimation

The total-gamma spectrum has been estimated using four different methods: the REDFIT, the MTM, the maximum entropy and the periodogram modified with a Bartlett window. Figure 5.11 shows the spectral results obtained from applying each of these methods and Table 5.3 summarises the main frequencies present from the frequency range 0-0.2 cycles/m. The spectrum created is similar using these four

methods, although frequencies in the MTM method appear flattened and poorly defined. The MTM significance test does, however, shows very similar frequencies to the other spectra. The frequency range 0.019-0.022 cycles/m (1/44-1/52 m) and the frequencies 0.059 cycles/m (1/16 m), 0.089 cycles/m (1/11 m), 0.15 cycles/m (1/6.7 m) and 0.19 cycles/m (1/5 m) consistently appear in all of the spectra analysed.

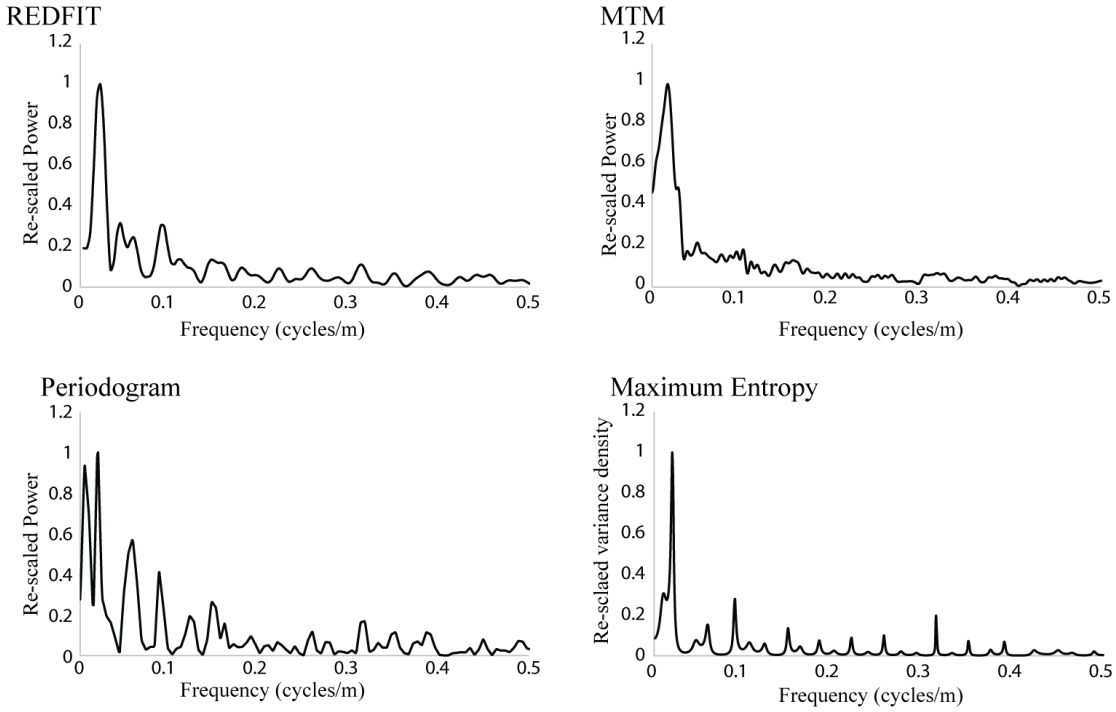

Figure 5.11 Methods of spectral estimation using spectral total-gamma data of the Tierrantona section. REDFIT spectrum created using 4 WOSA segments, 6 degrees of freedom and a bandwidth of 0.018 cycles/m. MTM method uses 4 tapers and ~ 8 degrees of freedom. The periodogram spectrum is modified with a Bartlett window. The maximum entropy method uses numbers of lags M = N/3 = 280). Computations were made with the REDFIT software developed by Schultz and Mudelsee (2002) and the Analyseries software package developed by Paillard *et al.* (1996).

Table 5.3 Methods of spectral estimation in the Tierrantona section.

Spectral Method	Frequency (cycles/m)♠	Period (m)	Spectral Method	Frequency (cycles/m)♠	Period (m)
REDFIT	**0.0224**	44.6	Periodogram modified with a Bartlett window	0.006	166.7
	0.0449	22.3		**0.02**	50
	0.0598	16.7		**0.059**	16.9
	0.0898	11.1		**0.089**	11.2
	0.1459	6.9		0.126	7.9
	0.183	5.5		**0.15**	6.7
				0.162	6.2
				0.19	5.3
MTM□	0.006	166.7	Maximum entropy	**0.02**	50
	0.0195	51.3		**0.06**	16.7
	0.034	29.4		**0.09**	11.1
	0.058	17.2		**0.149**	6.7
	0.089	11.2		**0.185**	5.4
	0.1232	8.1			
	0.148	6.8			
	0.191	5.2			

♠ Frequencies from 0-0.2 cycles/m.
□ Frequencies obtained from the MTM significance test (> 80% confidence levels).
The frequencies that consistently appear in all the spectra are represented in bold numbers.

(b) REDFIT spectral results

REDFIT time-series analyses of the Tierrantona section were undertaken on the total-gamma, K, Th and sandstone turbidite intensity records. Figure 5.12 shows the estimated spectra using 4 WOSA segments, ~ 6 degrees of freedom and a bandwidth of 0.018 cycles/m. Table 5.4 compiles all the significant frequencies present in the analysed spectra. The background noise has been estimated using a power regression method (Table 5.5).

Various significant frequencies can be recognised within the range 0-0.5 cycles/m (Figure 5.12). The frequency range 0.018-0.022 cycles/m (1/53-1/44 m) is present with a confidence level > 99% in all the analysed parameters. Total-gamma, K and Th spectra show another frequency at 0.059 cycles/m (1/17 m) with confidence levels > 90%. The frequency ~ 0.088 cycles/m (1/11 m) is present in the sandstone turbidite intensity and total-gamma with confidence levels > 95% and 99%,

respectively. The Th spectrum shows another frequency at 0.11 cycles/m (1/8 m) with a confidence level > 90%. Finally, the total-gamma and Th spectra show a significant frequency range 0.14-0.15 cycles/m (1/6 m) with a confidence level > 90%.

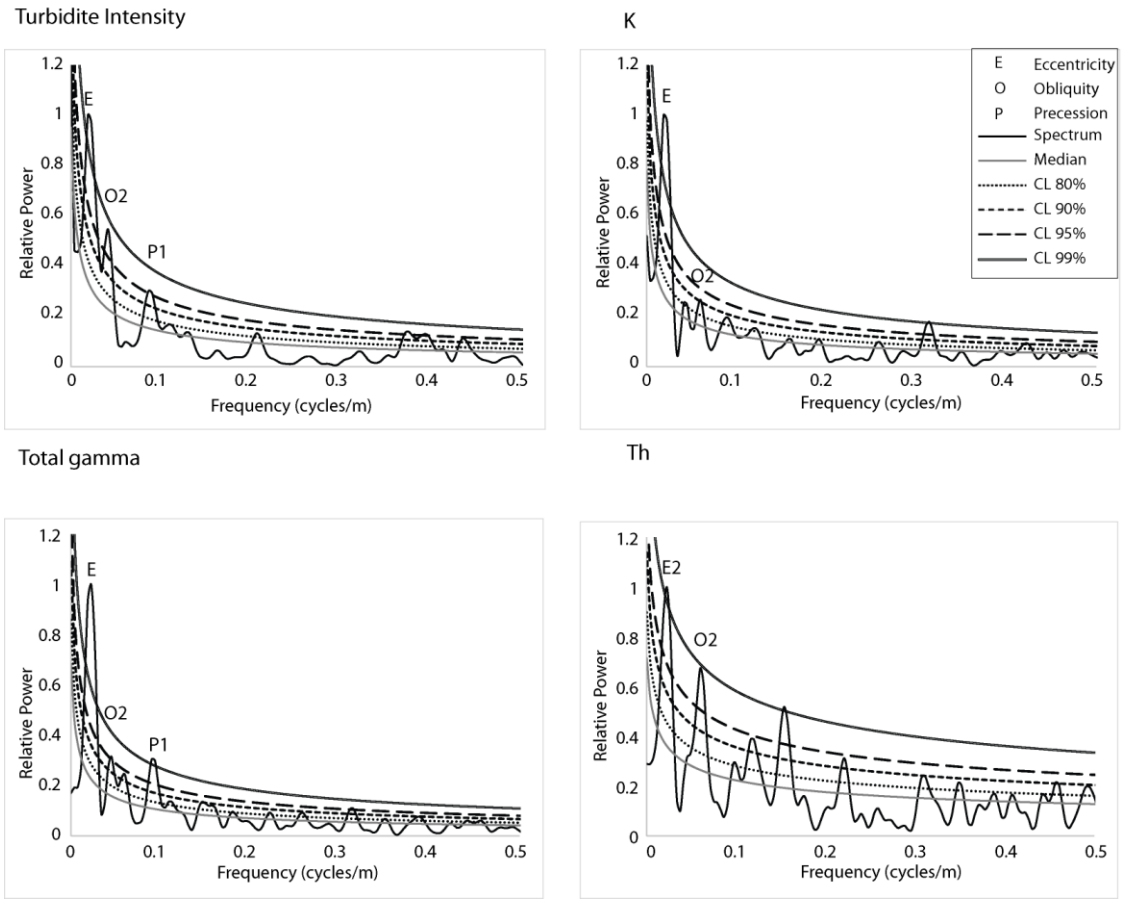

Figure 5.12 Time-series analysis of spectral gamma ray and sandstone turbidite intensity data of the Tierrantona section using REDFIT. REDFIT spectral results used 4 WOSA segments and 6 degrees of freedom. REDFIT results were plotted using a power regression noise background curve-fitting model. Graphs have been re-scaled. Analysis used the REDFIT software developed by Schulz and Mudelsee (2002).

Table 5.4 Significant frequencies of the Tierrantona section using REDFIT.

Data	Frequencies (cycles/m)♠	Period (m)	Confidence level (%)
Total-gamma	0.0224	44.64	99%
	0.0449	22.27	95%
	0.0598	16.72	90%
	0.0898	11.13	99%
	0.1459	6.85	90%
	0.3143	3.18	95%
K	0.0187	53.47	99%
	0.0598	16.72	90%
	0.3143	3.18	99%
	0.4229	2.36	90%
Th	0.0224	44.64	99%
	0.0598	16.72	95%
	0.116	8.62	90%
	0.1534	6.51	99%
	0.2245	4.45	90%
	0.4565	2.19	90%
Sandstone turbidite intensity	0.0187	53.47	99%
	0.0411	24.33	95%
	0.0860	11.62	95%
	0.3742	2.67	95%
	0.3929	2.54	95%
	0.4341	2.3	90%

REDFIT spectral results using 4 WOSA segments and 6 degrees of freedom.
♠Frequencies shown between 0-0.5 cycles/m > 90% confidence levels.

Table 5.5 Noise-background estimation methods for the Tierrantona section.

Data	AR1 (Mann and Lees, 1996)	Quadratic curve	Power regression
Total-gamma	2551	3140	**2540**
K	1454	1639	**985**
Th	460	421	**347**
Sandstone turbidite intensity	2746	2204	**988**

Summative square errors using the AR1 model of Mann and Lees (1996), a quadratic curve and a power regression method. The best noise-estimation method has the least summative square error and is represented in bold numbers.

(c) ASM results

ASM analysis has been undertaken using the software developed by Meyers and Sageman (2007). A total of 10 frequencies have been included in the ASM analysis (Table 5.6). These frequencies are present in the REDFIT spectral gamma-ray and sandstone turbidite intensity analysis with confidence levels > 95%.

ASM analysis of the Tierrantona section (Figure 5.13) shows significant SAR values within the range 11.5-100 cm/kyr with a small interval of non-significant SAR between 18 and 24 cm/kyr. The most significant SARs are found within three main SAR groups. Group 1 (13.5-14.5 cm/kyr) and Group 2 (29.5-31 cm/kyr) has a null hypothesis significant level of 0.001%. Group 3 (50-51 cm/kyr) has a null hypothesis significance level of 0.002% (Figure 5.13). Taking into consideration those frequencies which have higher confidence levels and those which appear in the spectra of more than one investigated parameters, the SAR which most closely reflects the Middle Eocene orbital cycles is 50 cm/kyr (Table 5.6). At a SAR of 50 cm/kyr, the frequency range 0.0187-0.0224 cycles/m can be linked to eccentricity 95 kyr, the frequency range 0.0411-0.059 cycles/m represents obliquity 40 kyr and the frequency 0.088 cycles/m represents precession 23 kyr cycles.

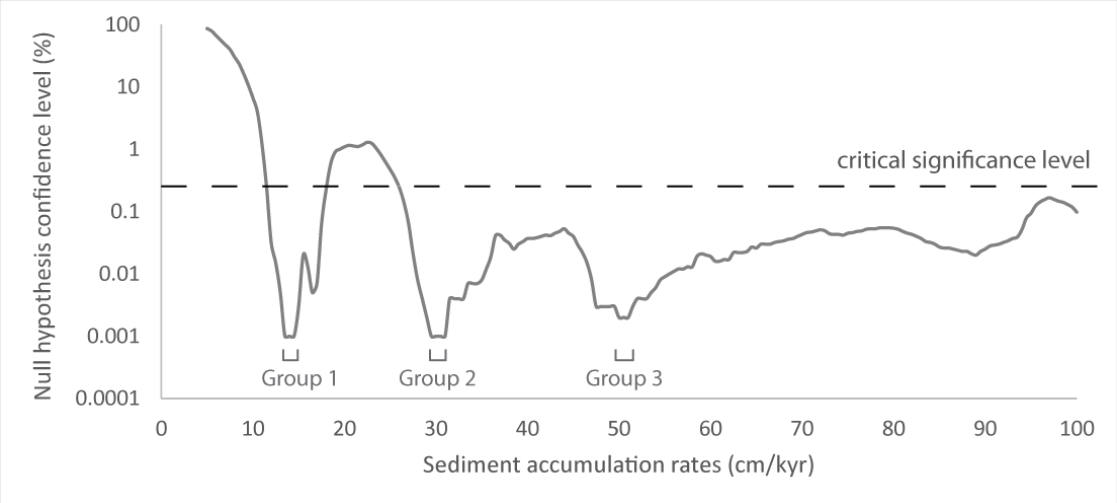

Figure 5.13 ASM results of the Tierrantona section. A total of 10 frequencies identified from spectral analysis of spectral gamma-ray and sandstone turbidite intensity with a confidence level > 95% have been applied to the ASM analysis. For a list of frequencies refer to Table 5.6. The analysis used a Rayleigh number of 2.38948626 x 10^{-4} and a Nyquist frequency of 2.4 cycles/m. Orbital parameters were established at ~ 45 Ma using Berger *et al.* (1992) equations. A total of 191 SAR ranging from 5-100 cm/kyr with an increment of 0.5 cm/kyr have been investigated using 100,000 Monte Carlo simulations. The critical level was established at 0.52%. ASM analysis has identified significant SAR values ranging from 11.5-100 cm/kyr with a small interval of non-significant SAR between 18 and 24 cm/kyr. The most significant SARs are found within the SAR ranges 13.5-14.5 cm/kyr, 29.5-31 cm/kyr and 50-51 cm/kyr. All 7 orbital parameters including eccentricity, obliquity and precession have been included in the ASM studies. Analysis used the ASM software developed by Meyers and Sageman (2007).

Table 5.6 Temporal period duration of significant frequencies in the Tierrantona section.

Frequency (cycles/m)♠	C.L (%)	N□	Period (m)	Period duration (kyr) at different SARs							
				Group 1		Group 2			Group 3		
				13.5 cm/ kyr	14 cm/ kyr	29.5 cm/ kyr	30 cm/ kyr	31 cm/ kyr	**50 cm/ kyr**	50.5 cm/ kyr	51 cm/ kyr
0.0187	99	2	53.5	396.1	382	181.3	178.2	172.5	**107**	104.9	104.9
0.0224	99	2	44.6	330.7	319	151.3	148.8	144	**89.3**	88.4	87.5
0.0411	95	1	24.3	180.2	173.8	82.5	81.1	78.5	**48.7**	48.2	47.7
0.0449	95	1	22.3	165	159.1	74.5	74.2	71.8	**44.5**	44.1	43.7
0.0598	95	3	16.7	123.9	119.4	56.7	54.7	54	**33.4**	33.1	32.8
0.088	99	2	11.4	84.2	81.2	38.5	37.9	36.7	**22.7**	22.5	22.3
0.1534	99	1	6.5	48.3	46.6	22.1	21.7	21	13	12.9	12.8
0.3143	95	1	3.2	23.6	22.7	10.8	10.6	10.3	6.4	6.3	6.2
0.3742	95	1	2.7	19.8	19.1	9.1	8.9	8.6	4.3	4.3	4.2
0.3929	95	1	2.5	18.9	18.2	8.6	8.5	8.2	4.1	5	5

The table shows calculated cycle duration for each significant frequency > 95% confidence levels (CL) at different SARs. The SARs which are more closely associated with the orbital periods of the Middle Eocene appear highlighted in bold numbers. Underlined frequencies indicate those frequencies which are contained in more than 1 spectrum with at least 1 confidence level > 95%. Estimated orbital cycles for the Middle Eocene (~ 45 Ma) using Berger *et al.* (1992) equations are: eccentricity 123.8 and 94.8 kyr, obliquity 52.3 and 40 kyr and precession 22.6 and 18.8 kyr.

♠ include all frequencies within the range 0-0.5 cycles/m with confidence levels > 90%.

□ number of parameters containing that specific frequency in the REDFIT spectrum.

Figure 5.14 (next page) Wavelet analysis of the sandstone turbidite intensity, K, total-gamma and Th data of the Tierrantona section. (a) The wavelet power spectrum calculates spectral power at different frequencies throughout the Tierrantona section. Black contours mark the 10% significant regions. **(b)** Global wavelet shows the scale-averaged wavelet power across the studied frequency bands. Values to the right of the dashed line are significant > 90% confidence level. Significant spectral peaks which have been associated with Milankovitch frequencies using REDFIT and ASM analysis have been labelled (E-eccentricity, O-obliquity, and P-precession). The analysis has used the online tool available at http://paos.colorado.edu.research/wavelets based on the algorithms of Torrence and Compo (1998).

Figure 5.14 Wavelet analysis of the Tierrantona section.

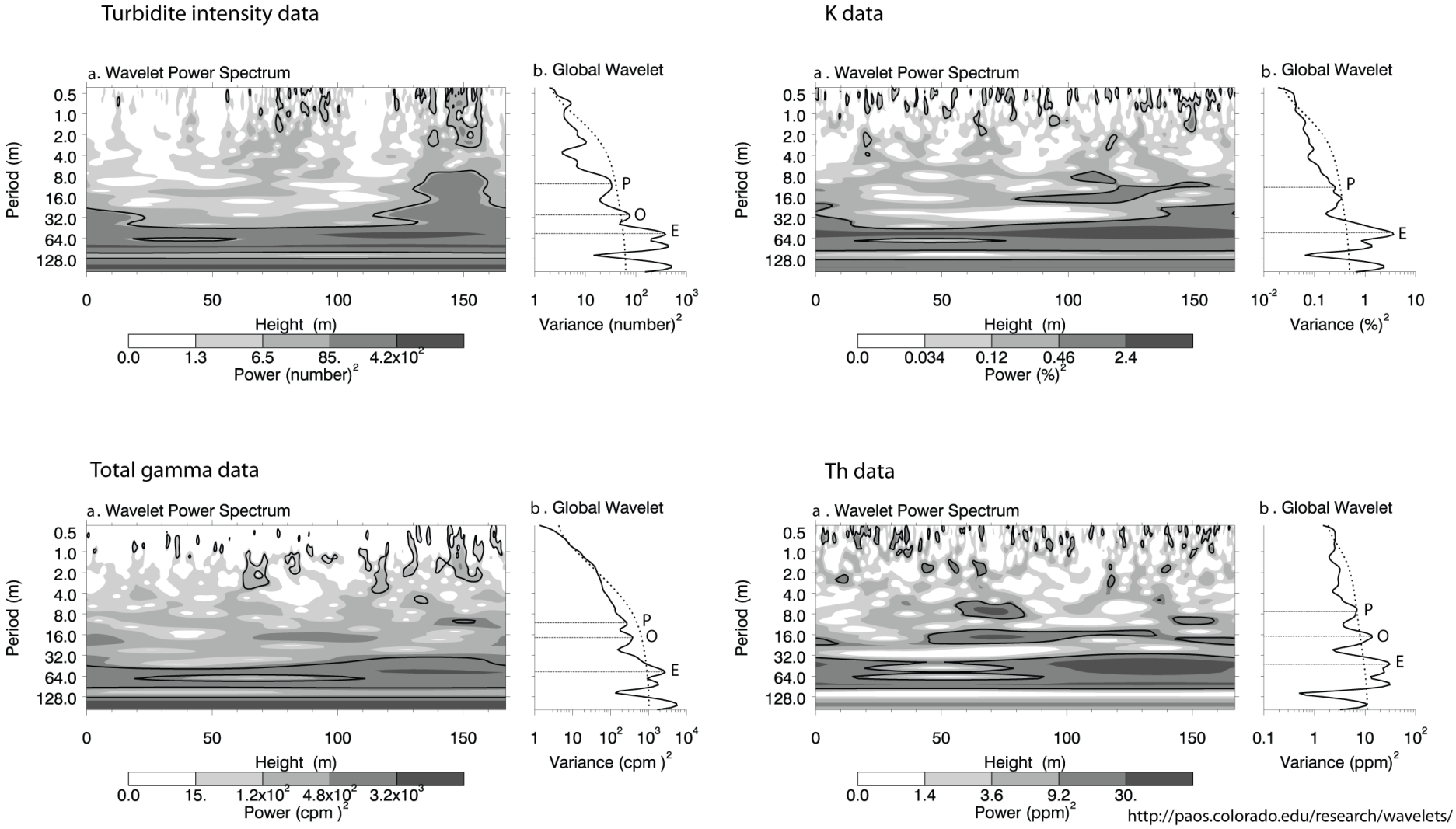

(d) Wavelet analysis

Results from the wavelet analysis include a number of significant frequencies > 90% confidence levels (Figure 5.14). The most spatially persistent frequency, present in all the analysed records with confidence levels > 90% is the frequency range 0.018-0.022 cycles/m (1/53-1/44 m). Spectral analyses using REDFIT and ASM have associated this frequency to eccentricity 95%.

The frequency range ~ 0.041-0.059 cycles/m (~ 1/17-1/24 m) is significant in the K wavelet spectrum between 80 and 130 m and is significant throughout the Th records. In the total-gamma records, there is an increase in the power spectra at around this frequency but it is not sufficient to be significant > 90% confidence levels. In the sandstone turbidite intensity records, this frequency is not well defined and only present sporadically towards the top of the Tierrantona section. This frequency range has been associated with obliquity using ASM analysis.

The frequency 0.088 cycles/m (1/11 m) is present in all the records but is only spatially significant (> 90% confidence levels) across a narrow stratigraphic interval between 130 and 160 m height. This frequency has been associated with precession by ASM analysis.

(e) Frequency-selective filtering

The total-gamma records have been frequency-selective filtered by applying a Gaussian filter. The methodology used is described in Section 2.9.7. Two frequencies, 0.0224 and 0.0598 cycles/m have been filtered using a bandwidth of 0.018 cycles/m (Figure 5.15). The frequency 0.0224 cycles/m is present in the total-gamma records

with a confidence level > 99% and has been linked to eccentricity cycles. The frequency 0.0598 cycles/m is present with confidence levels only > 90% but it has been chosen in preference of the frequency 0.0449 cycles/m as a representative of obliquity because the latter is not significant in any of the other analysed spectra (K, Th and sandstone turbidite intensity). It is also probable that the frequency 0.0449 cycles/m is a second harmonic of the frequency 0.0224 cycles/m. Since the 0.0598 cycles/m is also present in the K and Th spectra, it is likely that this frequency represents a real event.

The oldest 100 m of the total-gamma records filtered at a frequency of 0.0224 cycles/m show very broad low-amplitude eccentricity cycles (Figure 5.15). These cycles appear better defined from 100 to 167 m. Similarly, in the wavelet spectrum, this frequency shows an increase in the spectral power during this same stratigraphic interval in all the analysed data.

The total-gamma records filtered at a frequency of 0.059 cycles/m (1/17 m) show well developed cycles mainly in the central part of the records, from 50 to 150 m, but the amplitude of the cycles is significantly attenuated towards the edges of the section.

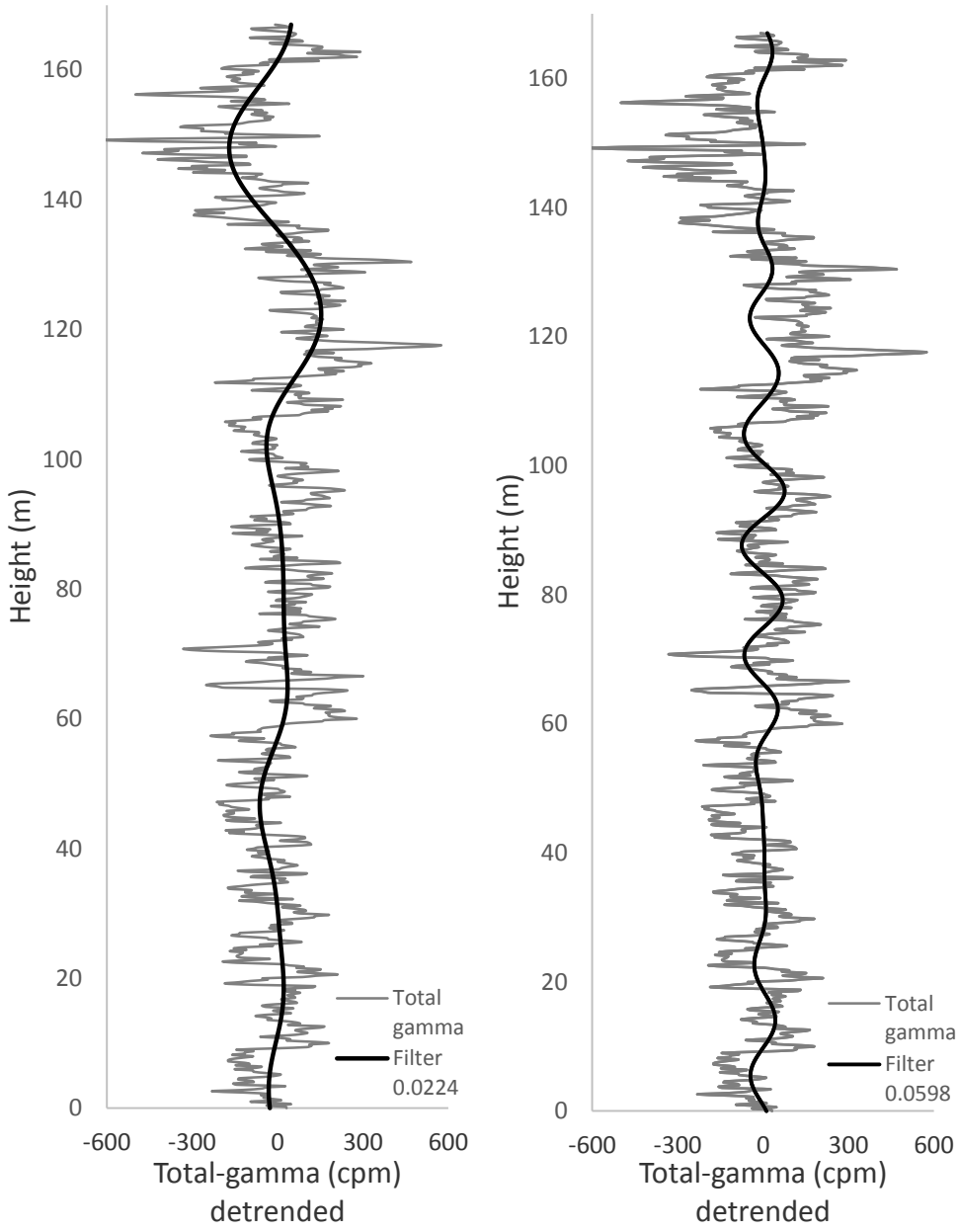

Figure 5.15 Frequency-selective filtering of the Tierrantona section. Total-gamma records have been interpolated and detrended prior to analysis. Filtering has been undertaken using a band-pass Gaussian filter and a bandwidth of 0.018 cycles/m using the software package Analyseries developed by Paillard *et al.* (1996). Total-gamma records have been filtered to the frequency 0.022 and 0.0598 cycles/m. These two frequencies have been respectively associated with eccentricity and obliquity using REDFIT spectral analysis and ASM studies.

5.3.2 The Gerbe System

5.3.2.1 Sedimentology of the Gerbe System

The Gerbe System is stratigraphically located between the Arro and the Banastón systems. It has been interpreted as a canyon-erosive submarine channel system (Clark and Pickering, 1996). The Gerbe System comprises two sandbodies designated, from older to younger, Gerbe I and Gerbe II. These sandbodies are typically tens of meters thick and are separated by a thick interval of fine-grained sediments. The Gerbe sandbodies have been deposited in an upper/mid-slope canyon to lower-slope erosional channel setting (Millington and Clark, 1995; Pickering and Bayliss, 2009). The sediments of the Gerbe System were sourced from the Charo Canyon (Mutti *et al.*, 1985) near the village of Charo. The initiation of this system is marked by an angular unconformity and is overlain by abundant Type Ia and II MTDs/MTCs suggesting mass wasting and collapse of the outer shelf and upper slope environments (Millington and Clark, 1995). The Charo Canyon cuts into the underlying fine-grained basin-slope forming a large-scale subaerial erosional surface with several tens of metres of erosional cut down. This deep basal unconformity caused the confinement of the Gerbe succession in the most proximal setting resulting in significant sediment bypass and erosion forming large scours which were infilled by pebbly lag deposits and finer-grained backfilling sandstone successions (Bayliss, 2011).

The Gerbe sandbodies can be interpreted as slope channelised submarine fans. The channel fill is heterogeneous and is characterised by different types of MTCs such as conglomerates (FA2b), pebbly sandstones (FA3a) and mud- and sand-filled scours (FA3g) (Bayliss, 2011). The sandstone turbidites are generally medium-bedded sandstones, fine to medium-grained, moderately to poorly sorted and can be classified

as subarkose arenites (Das Gupta and Pickering, 2008). Locally, the sandstone beds show truncated geometries and have well-developed cross bedding structures. Some of the sandstone beds contain embedded pebbles and shallow-marine material. This facies association is characteristic of erosive, highly concentrated turbidity currents and debris flows and probably indicate substantial sediment bypass (Bayliss, 2011).

5.3.2.2 Tectonic history during the deposition of the Gerbe System

Millington and Clark (1995) recognised a change in depositional style from a canyon-base-of-slope sheet system during the deposition of the Arro System to a canyon-submarine channel during the deposition of the Gerbe System. This rapid change was attributed to a significant reduction in the sediment supply that followed the period of thrust propagation and tectonic uplift which occurred during the deposition of the Arro System. These authors also argue that a change in the basin configuration and slope gradients could explain the change in the depositional style of these two systems. After a period of slope over-steepening and massive slope failures during the deposition of the Arro System, it followed a period of re-equilibration and healing of the slope which allowed a typical canyon-submarine channel complex to develop.

The Gerbe System marks the first significant volume of extra-formational rounded pebbles to enter the deep-marine Ainsa Basin. The deposition of gravelly material in the Ainsa Basin probably marks the transition from mature to immature, high energy, braided fluvial systems in the Tremp-Ager Basin in response to tectonic activity in the hinterland and increase in slope gradient and sediment supply *via* alluvial fans (Heard, 2007; Scotchman *et al.*, 2014).

5.3.2.3 Age of the Gerbe System

Magnetostratigraphic work carried out in the Gerbe System (this study) shows a polarity reversal, from reverse to normal, in the interfan deposits of the Gerbe I and Gerbe II sandbodies, at ~ 100 m above the Gerbe I sandbody. Normal polarity remains throughout the rest of the Gerbe section. It is likely that the changed in polarity refers to the chron C21r- C21n magnetic reversal estimated to have occurred at 47.35 Ma (Gradstein *et al.*, 2012). These results place the top of the Gerbe System ~ 1 Myr younger than the age estimates by Scotchman *et al.* (2014). For further discussion, see Section 3.7.

5.3.2.4 The Gerbe gamma-ray logged section

5.3.2.4.1 Geographical location of the Gerbe section

The Gerbe section is 200 m long and is located ~ 1.5 km north of Gerbe town and ~ 3 km west of Arro town. The section can be accessed from the main road N-260 and is exposed along a small stream (Plate 5.5 and Plate 5.6a).

The section is composed of two subsections: Gerbe 1 (72 m) and Gerbe 2 (128 m) which are separated ~ 50 m. Gerbe 1 starts at a stream cut and finishes at a prominent heterolithic package located at the top of a small hill. The area immediately below the beginning of the Gerbe 1 section is tectonically faulted. Sediments appear dislocated and heavily fractured with numerous calcite veins running through the outcrop (Plate 5.6b). The Gerbe 1 gamma-ray logged section starts immediately above this deformed area and was discontinued at the top of the heterolithic package which has been identified as the off-axial Gerbe II submarine fan. These same heterolithics are well exposed at the road cut ~ 50 m to the west of the Gerbe 1 log and mark the beginning of the Gerbe 2 section (Plate 5.6e). The first 30 m of this section are slightly weathered and contain a ~ 1 m thick Type 1a MTD which was not included in the gamma-ray log. The rest of the Gerbe 2 section is clean and well-exposed. The section was discontinued at the top of a hill immediately below a 20 m slump which marks the initiation of the Banastón II System (Plate 5.6d). Figure 5.16 shows the variation in the content of the K, Th, U, Th/K and Th/U throughout the Gerbe section.

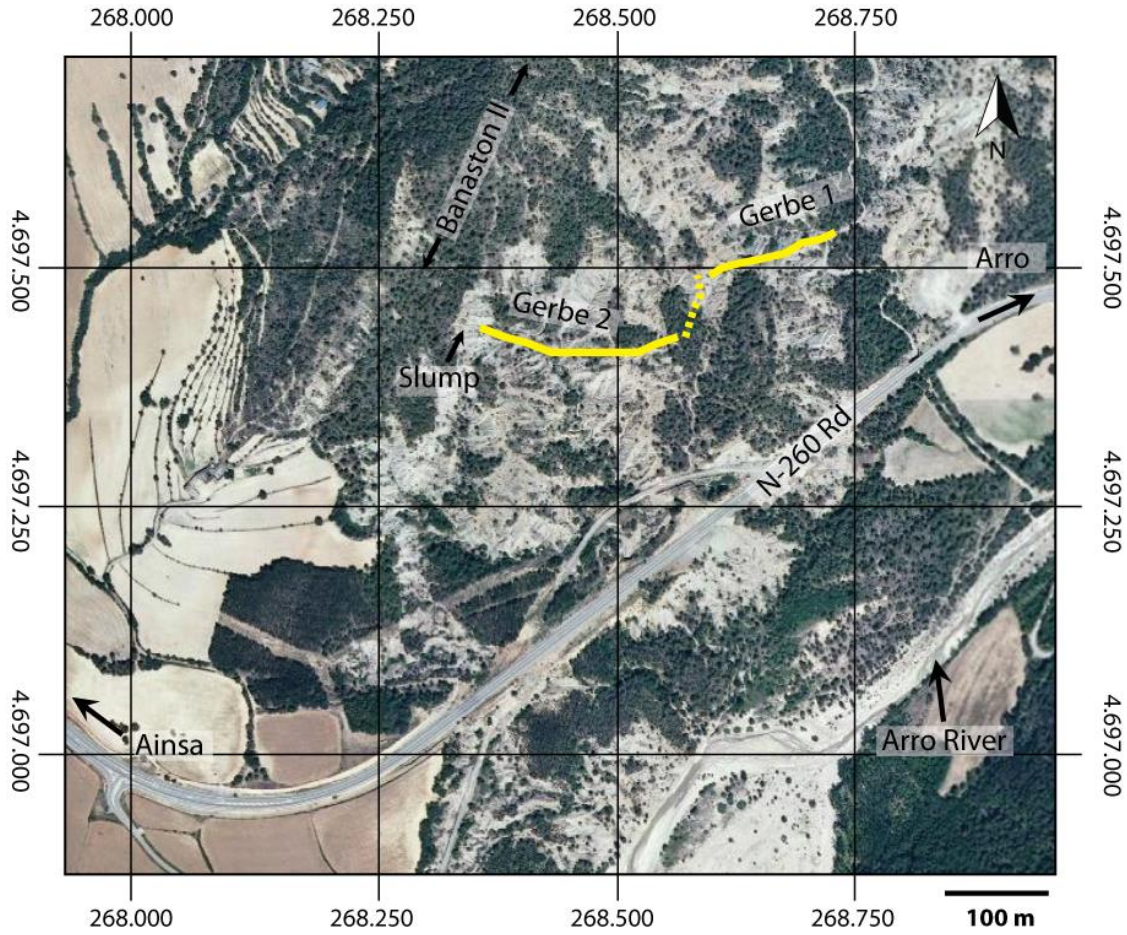

Plate 5.5 Aerial photograph of the Gerbe gamma-ray logged section. The Gerbe section is fragmented into Gerbe 1 and Gerbe 2 logs. Gerbe 1 forms a small hill which is capped by the Gerbe II sandbody and the Gerbe 2 log is well exposed along a river cut. There is a ~ 20 m slump at the top of the Gerbe 2 log which marks the initiation of the Banastón II submarine fan. The Banastón II sandbody constitutes a vegetated hill striking towards the NE. Aerial image from www.sigpac.mapa.es/fega/visor.

Plate 5.6 (next page) Outcrop photographs of the Gerbe gamma-ray logged section. (a) Photograph showing the Gerbe 2 gamma-ray logged section. The top 40 m of this log is not shown in the photograph. The section starts in the interfan sediments between the Gerbe I and Gerbe II sandbodies and finishes immediately below the Banastón II submarine fan. The Banastón I sandbody has completely pinched out at this location and its exact location within the stratigraphy cannot be determined. **(b)** Outcrop photograph showing a faulted area with numerous calcite veins located immediately below the Gerbe 1 log. This tectonically deformed area has not been included in the gamma-ray logged section. **(c)** Outcrop photograph showing some well-developed ripples in a sandstone turbidite bed. Palaeocurrent directions from ripples in this area suggest a preferential direction towards 240°. **(d)** Photograph showing a 20 m chaotic interval classified as a Type 1a MTC (Pickering and Corregidor, 2005). This sediment slide is located at the base of the Banastón II sandbody and the base of this chaotic event marks the top of the Gerbe gamma-ray logged section. **(e)** Photograph showing the Gerbe II sandbody exposed at the N-260 road, here off-axis forming a prominent heterolithic package.

Plate 5.6 Outcrop photographs of the Gerbe gamma-ray logged section

5.3.2.4.2 Stratigraphic location of the Gerbe section

The Gerbe section comprises mainly of the fine-grained and overbank deposits of the upper section of the Gerbe System and the lower part of the Banastón System. Figure 5.17 shows a geological map, a cross-section and a stratigraphic column indicating the exact location of the Gerbe section within the Ainsa Basin stratigraphy. The base of the section contains 70 m of the interfan deposits between the Gerbe I and Gerbe II sandbodies. The Gerbe II sandbody is present at 70 m height and constitutes a prominent sand-rich package of ~ 10 m (Plate 5.6e) which can easily be distinguished in the sedimentary logs (Figure 5.18) and in the sandstone turbidite intensity graph (Figure 5.19). The rest of the logged section comprises the fine-grained interfan sediments between the Gerbe II and Banastón I systems and between the Banastón I and Banastón II systems. The Banastón I sandbody has completely pinched out at this location and is only present as a thin sandbody ~ 500 m north of this location. The Banastón II sandbody forms a vegetated ridge (Plate 5.5) located immediately above the top of the Gerbe section.

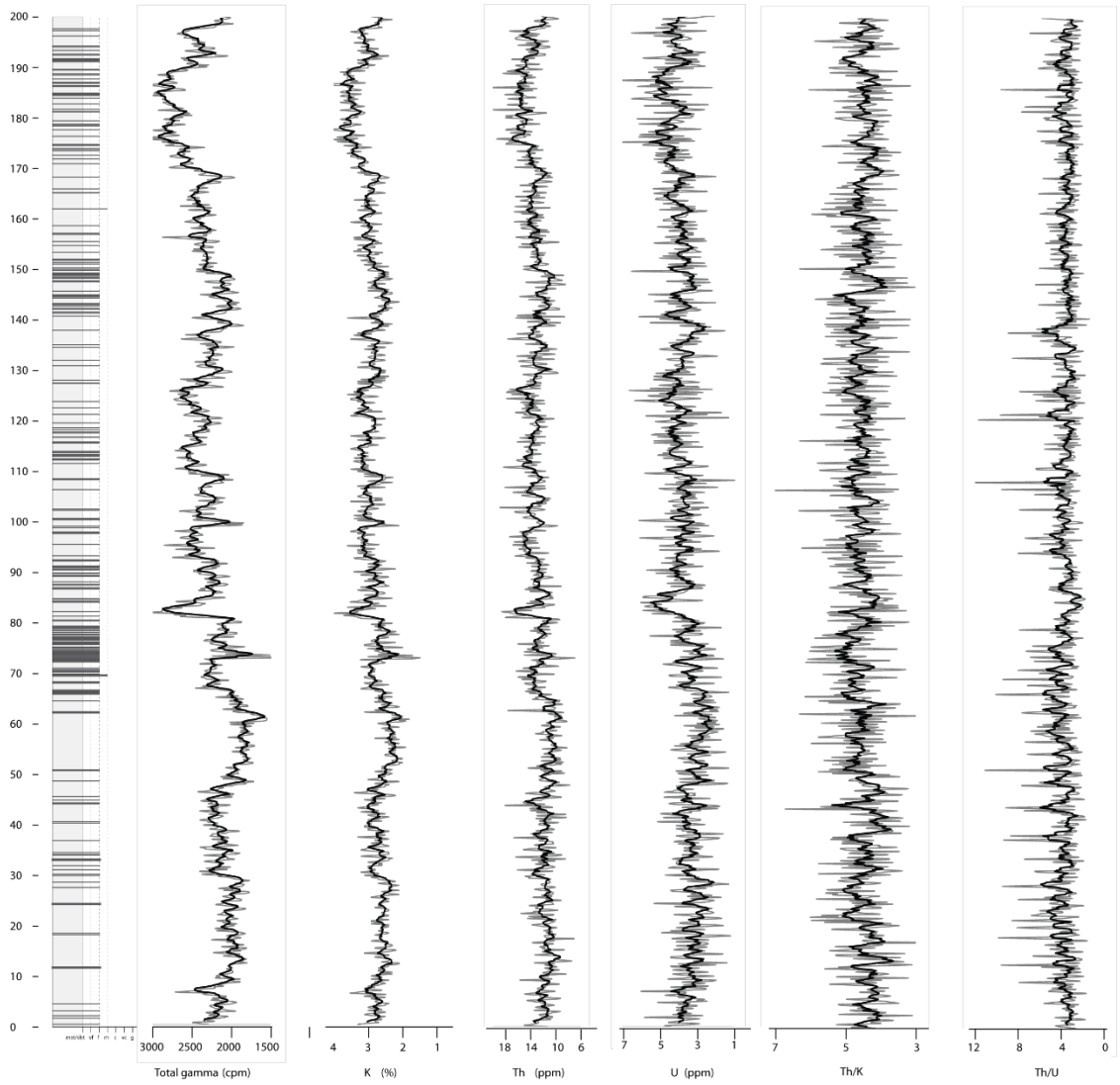

Figure 5.16 Total-gamma, K, Th, U, Th/K and Th/U data plotted against simplified sedimentary logs of the Gerbe section. The black line is a 4-period moving average. Simplified logs only show sandtone turbidites ≥ 1.5 cm, for complete logs refer to Figure 5.18 or Appendix 3.

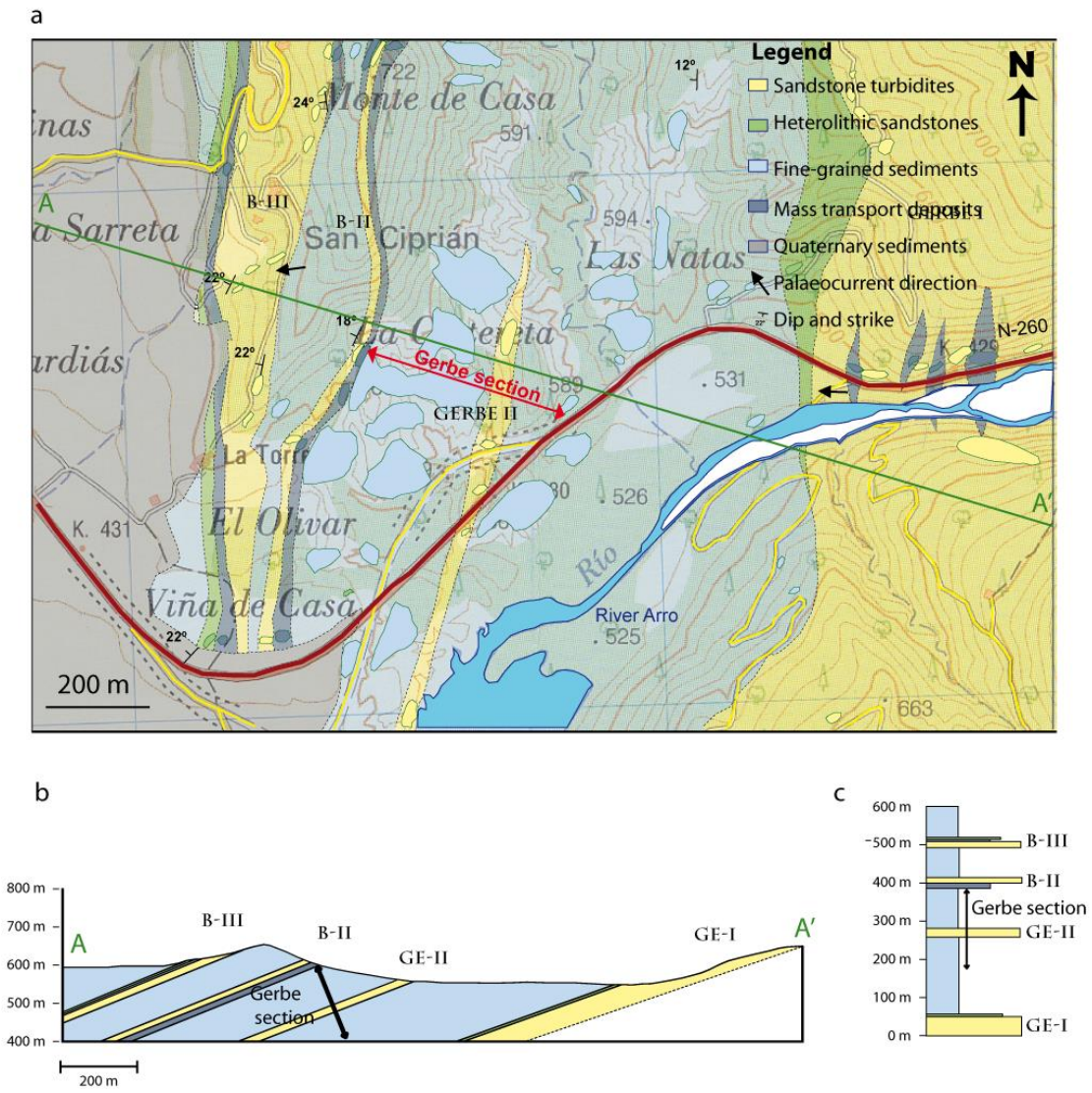

Figure 5.17 Geological map, cross-section and vertical stratigraphic column of the Gerbe gamma-ray logged section. (a) Geological map of the Gerbe section. The green line indicates the position of the cross-section A-A' which is parallel to the Gerbe gamma-ray logged section and perpendicular to the main outcrop strike to facilitate the calculation of true stratigraphic thicknesses. **(b)** Cross-section of the Gerbe area showing the position of the gamma-ray logged section in the interfan sediments between the Gerbe I and the Banastón II sandbodies. **(c)** Stratigraphic column showing the exact position of the Gerbe section within the stratigraphy.

Figure 5.18 Sedimentary logs of the Gerbe section. Sedimentary logs include every bed thicker than 5 mm. Gerbe I and Gerbe II logs have been joined to produce a 200 m Gerbe log. The key symbols used in the sedimentary logs can be seen in Figure 2.5. Electronic versions of these logs to allow for a more detailed study are included in Appendix 3.

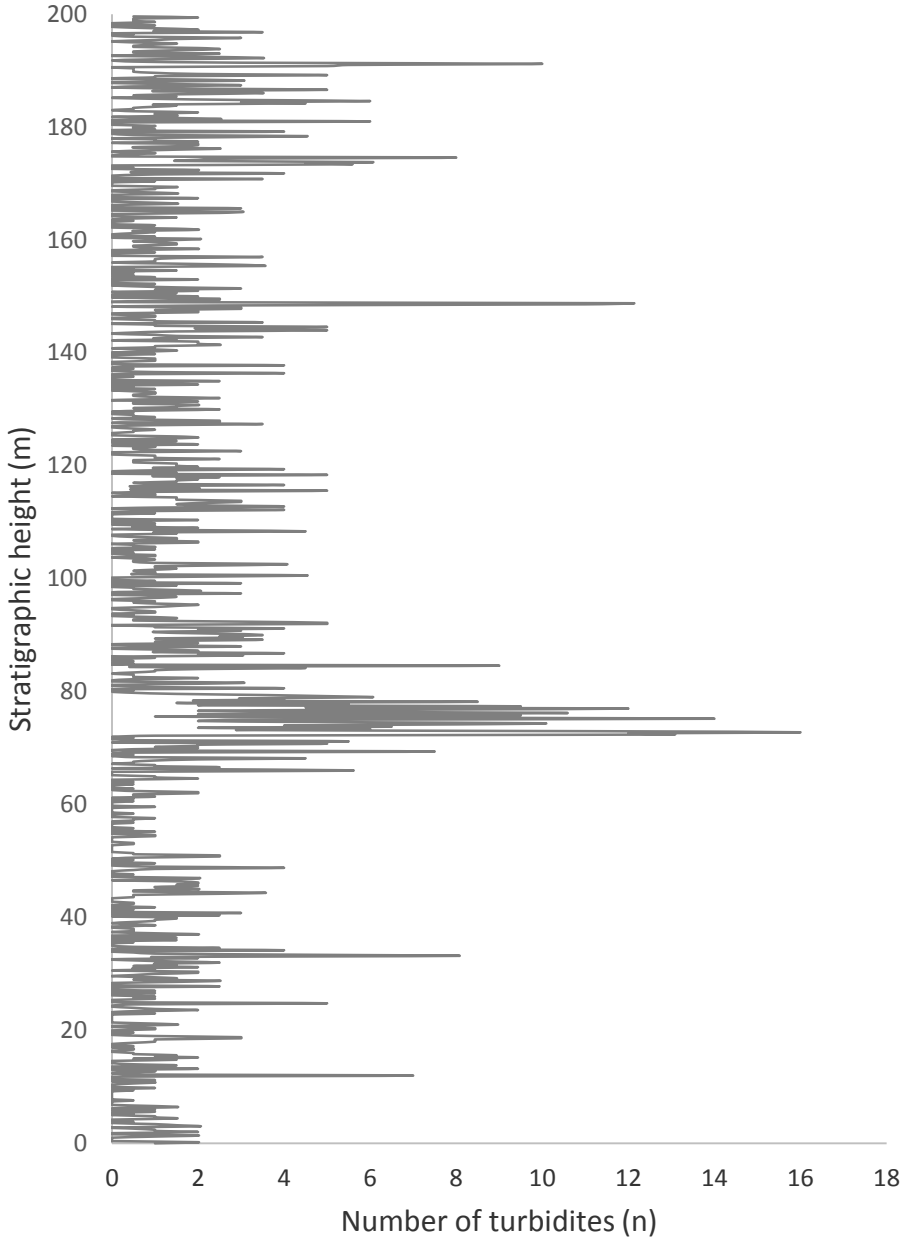

Figure 5.19 Sandstone turbidite intensity in the Gerbe section. The prominent heterolithic package between 65 and 80 m height is the Gerbe II sandbody. The averaged sandstone content for the Gerbe section is ~ 6%.

5.3.2.4.3 Cyclostratigraphic studies of the Gerbe section

(a) Methods of spectral estimation

The total-gamma spectrum of the Gerbe section has been estimated using four different methods: the REDFIT, the MTM, the maximum entropy and the periodogram modified with a Bartlett window. Figure 5.20 shows the spectral results obtained from applying each of these methods. Table 5.7 summarises the main frequencies present within the frequency range 0-0.2 cycles/m. The general spectrum created is similar using these four methods (Figure 5.20). There are 3 frequencies which consistently appear in all the spectra: the frequency range 0.019-0.024 cycles/m (1/42-1/53 m), and the frequencies 0.07 cycles/m (1/14 m) and 0.098 cycles/m (1/10 m).

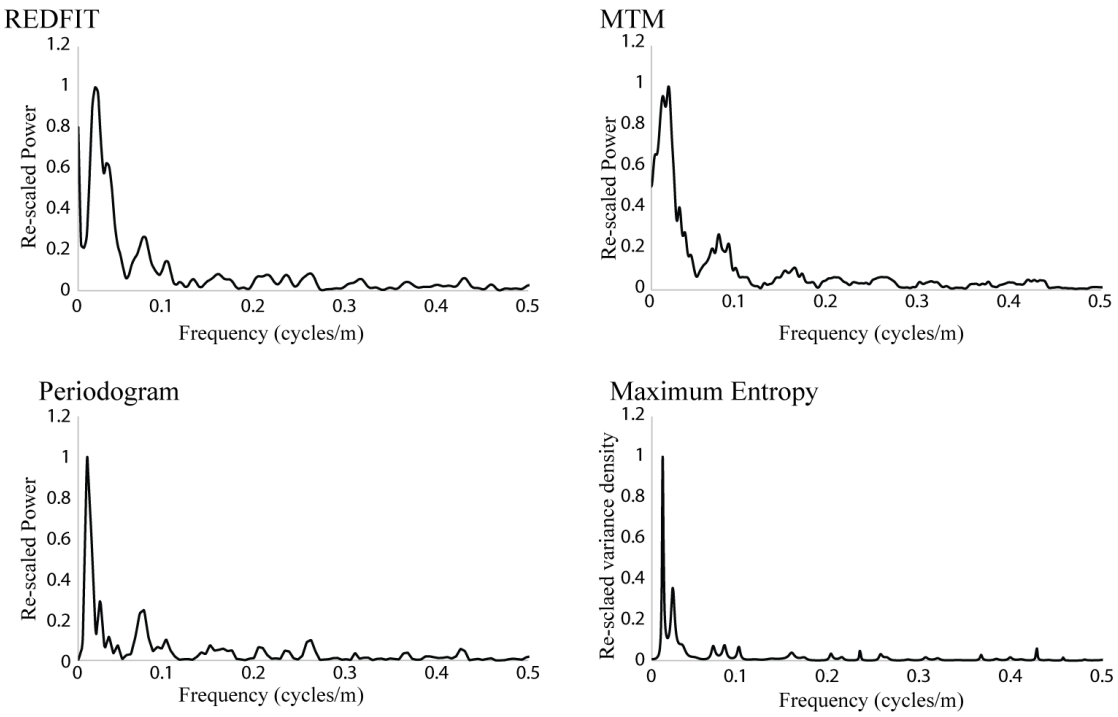

Figure 5.20 Methods of spectral estimation using Gerbe spectral total-gamma data. The REDFIT spectrum has been created using 4 WOSA segments, 6 degrees of freedom and a bandwidth of 0.014 cycles/m. The MTM method uses 4 tapers and ~ 8 degrees of freedom. The periodogram uses a Bartlett window. The maximum entropy method uses a numbers of lags M= N/3= 335). Analysis used the REDFIT software developed by Schultz and Mudelsee (2002) and the Analyseries software package developed by Paillard *et at.* (1996).

Table 5.7 Methods of spectral estimation in the Gerbe section.

Spectral Method	Frequency (cycles/m)♠	Period (m)	Spectral Method	Frequency (cycles/m)♠	Period (m)
REDFIT	**0.019** 0.031 **0.072** **0.099** 0.159	53.5 32.2 13.9 10 6.3	Periodogram modified with a Bartlett window	0.01 **0.024** **0.073** **0.098** 0.151	100 41.7 13.7 10.2 6.6
MTM□	0.012 **0.023** 0.035 0.045 **0.071** **0.098** 0.12 0.2	82 43.5 28.6 22.2 14.1 10.2 8.3 5	Maximum entropy	0.012 **0.024** **0.067** 0.08 **0.098** 0.155 0.198	83.3 41.7 14.9 12.5 10.2 6.5 5.1

♠ Frequencies from 0-0.2 cycles/m.
□Frequencies present in the MTM significant test with confidence levels > 80%.
Frequencies which appear consistently in all the spectra are represented in bold numbers.

(b) REDFIT spectral results

REDFIT time-series analysis of the Gerbe section was undertaken on the total-gamma, K, Th and sandstone turbidite intensity records using 4 WOSA segments and ~ 6 degrees of freedom (Figure 5.21). The most significant frequencies found in each spectrum within the frequency range 0-0.5 cycles/m are summarised in Table 5.8. The background noise has been estimated by using a power regression method (Table 5.9).

REDFIT analysis reveals three main significant frequencies within the 0-0.5 cycles/m range. Sandstone turbidite intensity, total-gamma and K spectra show two main frequencies: 0.0187 cycles/m (1/53 m) and 0.07 cycles/m (1/14 m). These two frequencies are significant > 95% confidence levels and in some cases the spectral peaks are well > 99% confidence levels. The 0.0187 cycles/m frequency is also present in the Th spectrum with a confidence level > 95%, being this, the only significant frequency found in the spectrum of this element. The frequency range 0.031-0.034

cycles/m (1/32-1/29 m) is significant in the total-gamma and K data > 99% confidence levels, however, this frequency is absent in the other spectra.

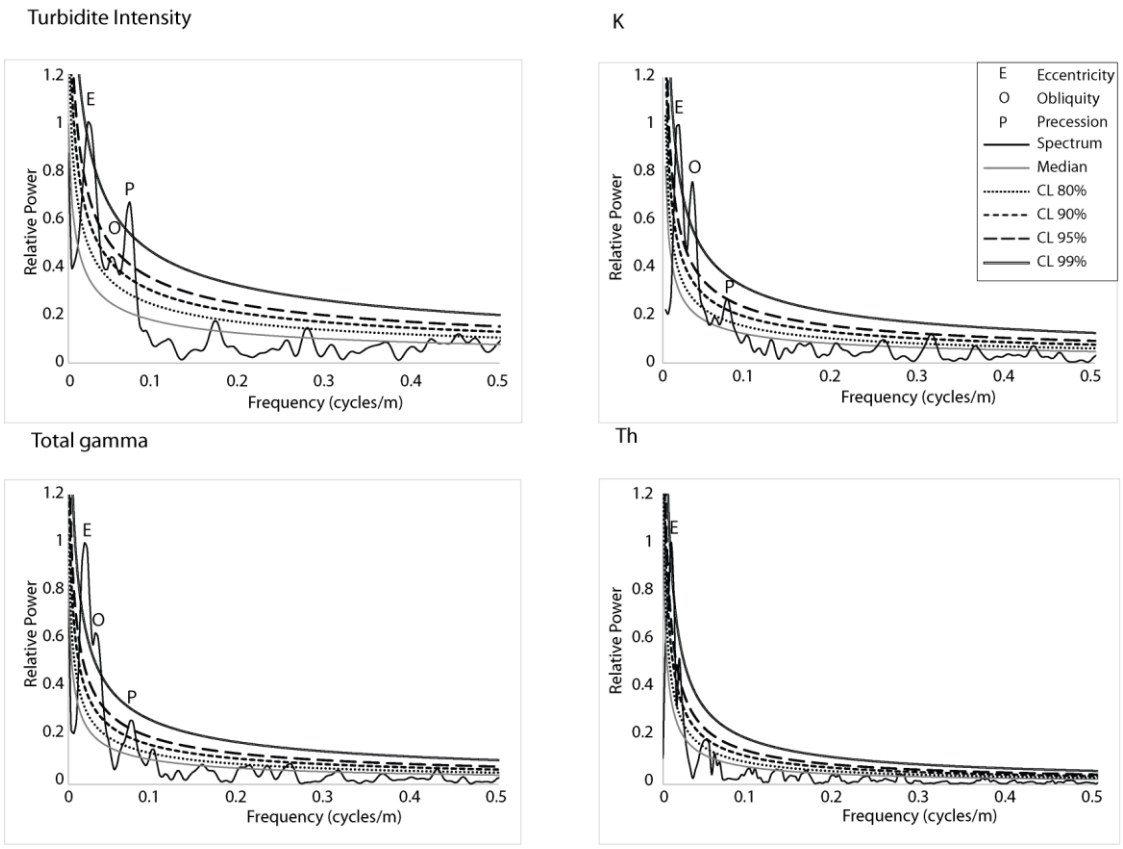

Figure 5.21Time-series analysis of spectral gamma-ray and sandstone turbidite intensity data of the Gerbe section using REDFIT. REDFIT spectral results used 4 WOSA segments, 6 degrees of freedom and a bandwidth of 0.014 cycles/m. REDFIT results plotted using a power regression fitting model. Graphs re-scaled to allow comparison between variables. The analysis used the REDFIT software developed by Schulz and Mudelsee (2002).

Table 5.8 Significant frequencies of the Gerbe section using REDFIT.

Data	Frequencies (cycles/m)	Period (m)	Confidence level (%)
Total-gamma	0.01871 0.03112 0.0717	53.44 32.13 13.95	99% 99% 95%
K	0.0186 0.0342 0.0747 0.3114	53.76 29.24 13.4 3.21	99% 99% 95% 90%
Th	0.0187	53.47	95%
Sandstone turbidite intensity	0.0187 0.045 0.0713	53.47 22.22 14.02	99% 90% 99%

REDFIT spectral results using 4 WOSA segments and 6 degrees of freedom. The frequencies shown are all frequencies between 0-0.5 cycles/m > 90% confidence levels.

Table 5.9 Noise background estimation methods for the Gerbe section.

Data	AR1 (Mann and Lees, 1996)	Quadratic curve	Power regression
Total-gamma	8910	7558	**5181**
K	4793	4164	**2196**
Th	6702	5856	**2524**
Sandstone turbidite intensity	1684	1307	**783**

Summative square errors using the AR1 model of Mann and Lees (1996), a quadratic curve and a power regression method. The method with the least summative square error indicating the most adequate fitting curve method is represented in bold numbers.

(c) ASM results

The ASM analysis identifies two main significant SAR ranges: 16.5-17.5 cm/kyr and 42-100 cm/kyr (Figure 5.22). The lowest significant level at 0.002% is found in the SAR range between 54.5 and 71 cm/kyr. Table 5.10 calculates the duration of the cycles for different frequencies at specific SARs. The SAR which most closely mirrors the orbital periods of the Middle Eocene is 57 cm/kyr. This SAR associates the most significant frequency 0.0187 cycles/m, present in all the analysed spectra, with eccentricity 95 kyr. Higher SARs do not link this frequency to any orbital cycles and therefore have been discarded as no significant, since eccentricity cycles are the most dominant orbital cycles in all the other gamma-ray sections in the Ainsa Basin. At 57 cm/kyr, the frequencies 0.034 cycles/m and 0.045 cycles/m are associated with obliquity, and the frequency 0.07 cycles/m is linked to precession 23 kyr. However, it is likely that the frequency 0.034 cycles/m represents a second harmonic of 0.0187 cycles/m since the ~ 0.034 value closely approximates the double of this frequency. Harmonics can occur in records which show a change in SARs. Variations in the SAR can result in non-linear distortion of the time-series resulting in the development of harmonics (Weedon, 2005).

Orbital tuning of the Gerbe records in Section 5.3.2.4.3f indicates that the most likely SAR rate for the Gerbe section is 47 cm/kyr (Table 5.10). The good age control in the Gerbe section with the C21r/C21n polarity reversal identified at the beginning of the section implies that the SAR inferred from tuning the records to eccentricity are likely to be correct. The SAR 47 cm/kyr is significant in the SAR analysis with a significant level of 0.082%. This SAR also considers that the most predominant spectral peak at 0.0187 cycles/m can be interpreted as eccentricity (~ 114 kyr in duration), and the frequency 0.045 cycles/m will therefore be considered as obliquity.

However, at this SAR the frequency 0.07 cycles/m have a duration of ~ 29 kyr which could represent precession, although, its duration is slightly on the high side. Orbital tuning of the records also suggests that SARs may have varied a lot in the Gerbe section from 28 to 63 cm/kyr and this variation may have affected the periodicity of the precession cycles and the presence of harmonics (Weedon, 2005). A SAR of 47 cm/kyr in the Gerbe System closely approximates the SAR estimated for the stratigraphically older Arro System at 50 cm/kyr.

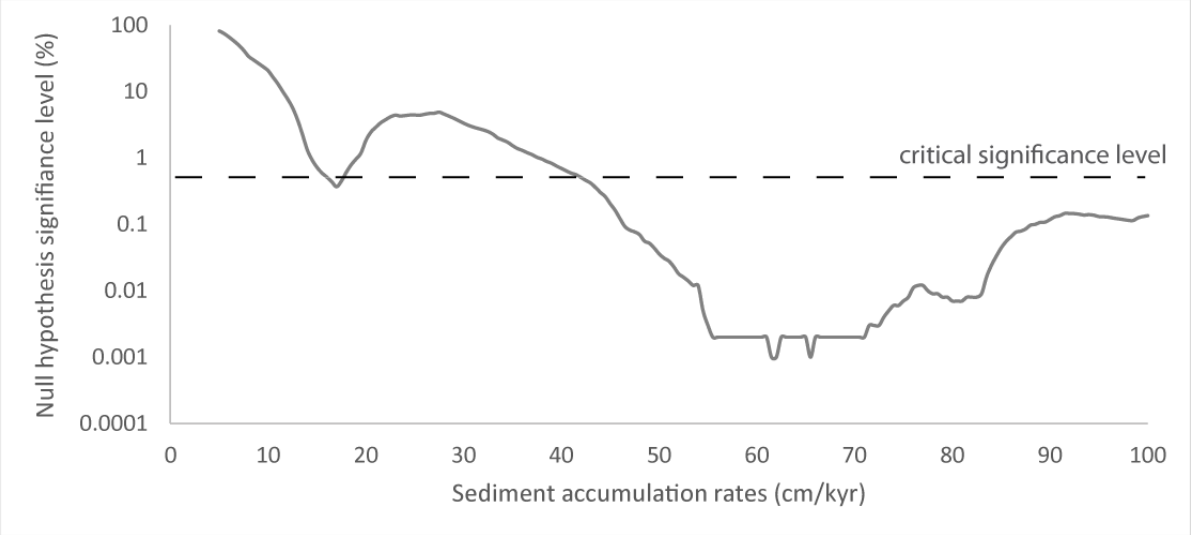

Figure 5.22 ASM results of the Gerbe section. ASM analysis includes a total of 7 frequencies identified from the spectral analysis of the spectral gamma-ray and sandstone turbidite intensity data with a confidence level > 90%. For a list of frequencies refer to Table 5.10. The analysis used a Rayleigh number of 1.99004975 x 10^{-4} and a Nyquist frequency of 2.4 cycles/m. Orbital parameters were established at ~ 45 Ma using Berger *et al.* (1992) calculations. A total of 191 SARs ranging from 5-100 cm/kyr with an increment of 0.5 cm/kyr were investigated using 100,000 Monte Carlo simulations. Critical levels were established at 0.52%. ASM analysis has identified significant SAR values ranging from 42-100 cm/kyr. All 7 orbital parameters (eccentricity, obliquity and precession) have been included in the ASM studies. Analysis used the ASM software developed by Meyers and Sageman (2007).

Table 5.10 Temporal period duration of significant frequencies in the Gerbe section.

Frequency (cycles/m)	C.L (%)	N□	Period (m)	Period duration (kyr) at different SAR									
				47 cm/ kyr	**57 cm/ kyr**	58 cm/ kyr	60 cm/ kyr	62 cm/ kyr	64 cm/ kyr	66 cm/ kyr	68 cm/ kyr	70 cm/ kyr	72 cm/ kyr
0.018	99	4	53.5	**113.8**	**93.8**	92.2	89.1	86.2	83.5	81	78.6	76.4	74.3
0.031	99	1	32.1	68.4	56.4	54.4	53.6	51.9	50.2	48.7	47.3	46	44.7
0.034	99	1	29.2	62.2	**51.3**	50.4	48.7	47.2	44.7	44.3	43	41.8	40.6
0.045	90	1	22.2	**47.3**	**39**	38.3	37	34.8	34.7	33.7	32.7	31.7	30.9
0.071	95	2	14.1	**29.7**	**24.7**	24.3	23.5	22.7	22	21.3	20.7	20.1	19.6
0.074	95	1	13.4	**28.5**	**23.5**	23	22.3	21.6	20.9	20.3	19.7	19.1	18.6
0.311	90	1	3.2	6.8	4.6	4.5	4.3	4.2	5	4.9	4.7	4.6	4.46

The table shows calculated cycle duration for each significant frequency (> 90% confidence level) at different SARs. The SAR which most closely matches the orbital periods of the Middle Eocene (~ 45 Ma) is 57 cm/kyr (bold numbers). The SAR at 47 cm/kyr is also considered as significant. See text for further explanation. The frequencies underlined are contained in more than 1 spectrum with confidence levels > 95%. Estimated orbital cycles for the Middle Eocene (~ 45 Ma) using Berger *et al.* (1992) equations are: eccentricity 123.8 and 94.8 kyr, obliquity 52.3 and 40 kyr and precession 22.6 and 18.8 kyr.

♠ include all frequencies within the range 0-0.5 cycles/m with confidence levels > 90%.

□ number of parameters containing that specific frequency in the REDFIT spectrum.

Figure 5.23 (next page) Wavelet analysis of the sandstone turbidite intensity, K, total-gamma and Th data in the Gerbe section. (a) The wavelet power spectrum identifies spectral power at different frequencies throughout the Gerbe stratigraphic section. Black contours mark the 10% significant regions. **(b)** Global wavelet shows the scale-averaged wavelet power across the studied frequency bands. Values to the right of the dashed line are significant > 90% confidence level. Significant spectral peaks which have been associated with Milankovitch frequencies using REDFIT and ASM analysis have been labelled (E-eccentricity, O-obliquity, and P-precession). Analysis used the online tool available at http://paos.colorado.edu.research/wavelets based on the algorithms of Torrence and Compo (1998).

Figure 5.23 Wavelet analysis of the Gerbe section.

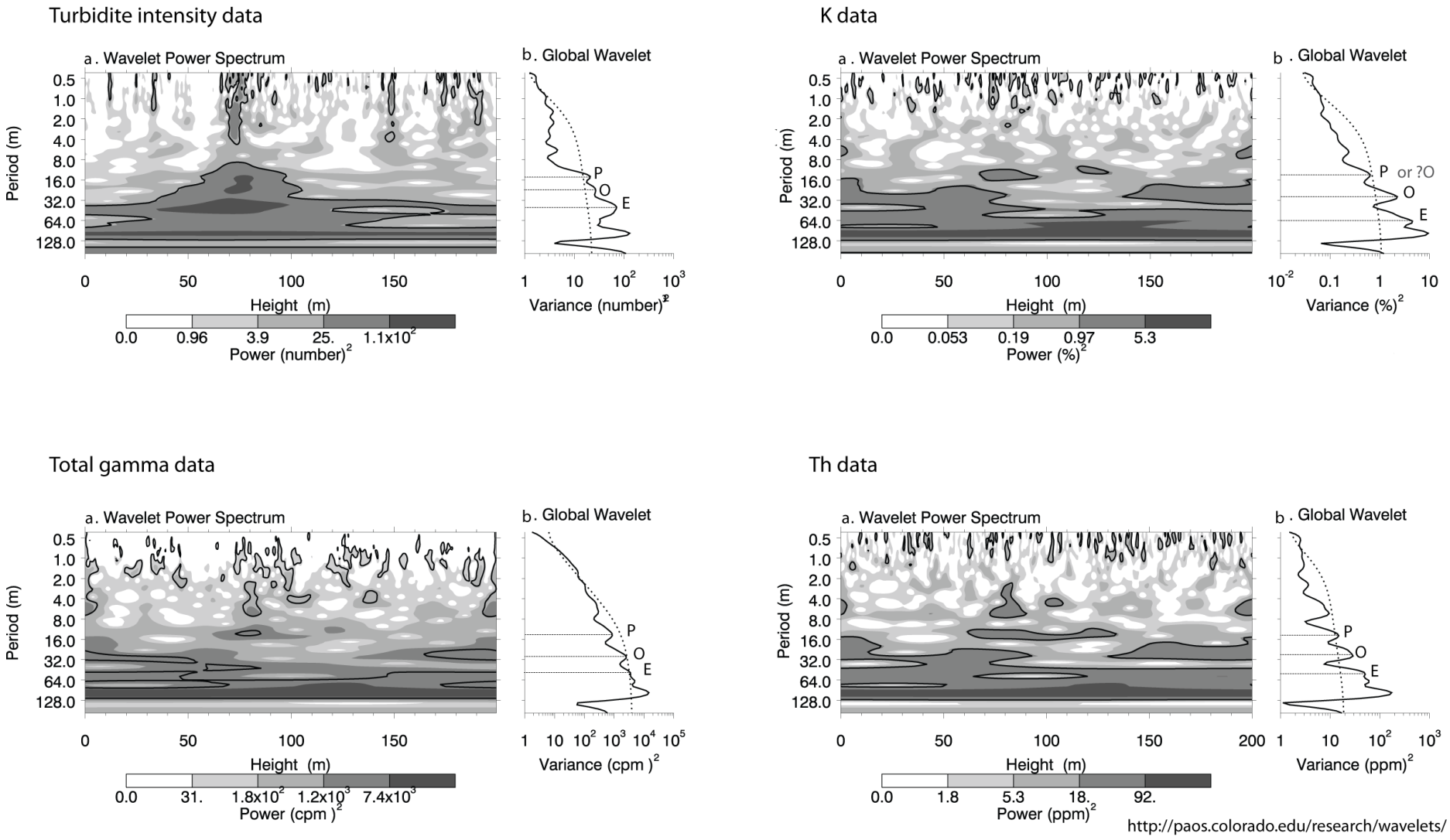

(d) Wavelet analysis

Results from the wavelet analysis include a number of significant frequencies > 90% confidence levels (Figure 5.23). The most spatially persistent frequency, present in all the analysed records with confidence levels > 90% is 0.0187 cycles/m (1/53 m). This frequency has been associated with short eccentricity combining REDFIT and ASM analysis. This frequency is present in all of the stratigraphic records. In the sandstone turbidite intensity and Th wavelet spectra, this frequency appears continuous throughout the stratigraphy but in the total-gamma and K records it shows some spatial discontinuities mainly in the central part of the records.

The frequency 0.045 cycles/m (1/22 m) is also significant and spatially persistent in the wavelet spectra of all the records analysed. The sandstone turbidite intensity data shows this frequency is significant throughout the records, but, the K, Th and total-gamma spectra show a decrease in power in the central part of the records at ~ 80-130 m. This frequency has been associated with obliquity using ASM studies.

There is another frequency present at ~ 0.07 cycles/m (1/14 m) which is significant between 60 and 130 m in all the studied records. This frequency is associated with precession cycles.

(e) Frequency-selective filtering

Three frequencies, 0.0187, 0.03 and 0.07 cycles/m have been filtered using a bandwidth of 0.014 cycles/m which has been determined by REDFIT analysis. The frequencies 0.0187 and 0.03 cycles/m are present in the total-gamma records with confidence levels > 99% and the frequency 0.07 cycles/m has confidence levels > 95%.

The filtered records of the Gerbe section using a frequency of 0.0187 cycles/m and 0.03 cycles/m (Figure 5.24) show a very similar number of well-defined broad cycles. This figure shows that it is unlikely the frequency 0.03 cycles/m represents obliquity and can better be interpreted as a second harmonic of the eccentricity caused by variations in the SAR. The figure also shows how eccentricity cycles become less defined in the central part of the total-gamma records and this probably reflects the decrease in power and significance identified in the wavelet spectrum of the total-gamma records (Figure 5.23).

The filtered records at 0.07cycles/m (1/14 m) show well developed cycles throughout the records. The cycles seem to increase in amplitude in the central part of the section where eccentricity cycles are less dominant.

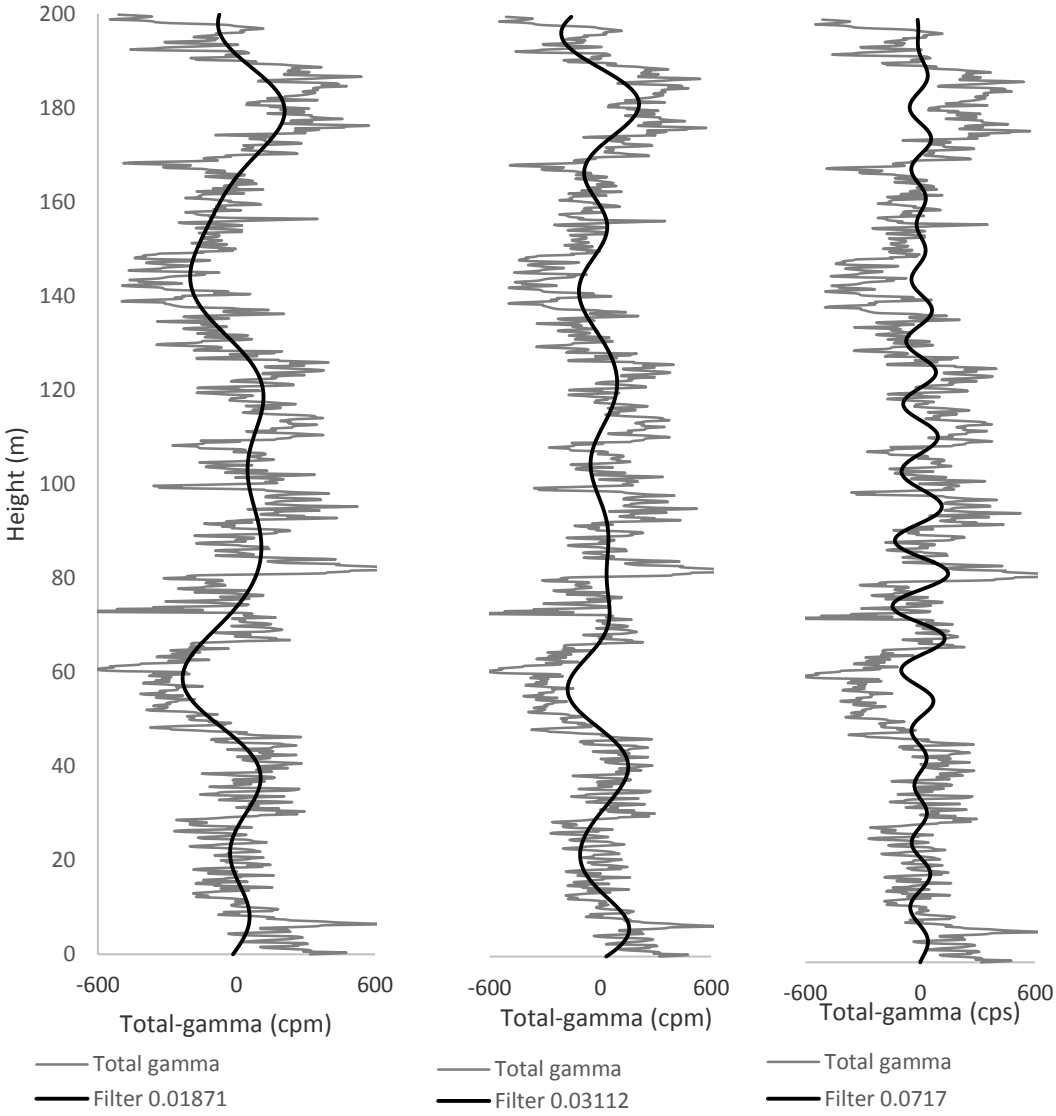

Figure 5.24 Frequency-selective filtering of the Gerbe section. The records have been interpolated and detrended before analysis. Filtering has used a band-pass Gaussian filter and a bandwidth of 0.015 cycles/m. Total-gamma data has been filtered to 0.0187, 0.031 and 0.07 cycles/m. The frequency 0.0187 cycles/m has been linked to eccentricity and the frequency 0.07 cycles/m has been associated with precession. The program used for filtering was Analyseries of Paillard *et al.* (1996).

(f) Orbital tuning

Orbital tuning of the Gerbe section has been performed by comparing the total-gamma records filtered to 0.0283 cycles/m which is the frequency associated with eccentricity (from REDFIT and ASM spectral analysis) to the eccentricity curves for the Middle

Eocene using the La2010a orbital solution of Laskar *et al.* (2011). Five anchor points have been used for tuning the records (Table 5.11).

Table 5.11 Anchor points used for tuning in the Gerbe section.

Stratigraphic height (m)	Age (Ma)♠	Cycle
7.6	47.338	Eccentricity maxima
37.4	47.236	Eccentricity maxima
58.3	47.189	Eccentricity minima
102.5	47.082	Eccentricity minima
179.5	46.960	Eccentricity maxima

The table shows the 5 anchor points employed to tune the Gerbe section to the eccentricity time scale.
♠Ages obtained from the GPTS of Gradstein *et al*. (2012).

The best match between the total-gamma filtered records of the Gerbe section and the eccentricity curves of the La2010a orbital solution of Laskar *et al.* (2011) (Figure 5.25), suggests that the base of the Gerbe section can be dated at 47.36 Ma. This is in agreement with the age of the C21r-C21n polarity reversal found at the base of the section (~ 10 m stratigraphic height). The top of the Gerbe section which has been interpreted as the base of the Banastón II System, can be established at 46.93 Ma, giving a total duration for the Gerbe section of ~ 420 kyr.

Figure 5.26 shows that tuning the records to eccentricity has strengthened the power of the obliquity peak (~ 47 kyr). This peak can be associated with the obliquity O1 orbital period of 52 kyr which is now significant with confidence levels > 99%. The peak at 32 kyr is also more prominent in the tuned data. This peak is likely to be associated with the obliquity O2 40 kyr orbital period. Tuning the records has also strengthened the precessional cycles (21 kyr and possibly 16 kyr) which were not significant in the original spectrum (below the 80% confidence levels).

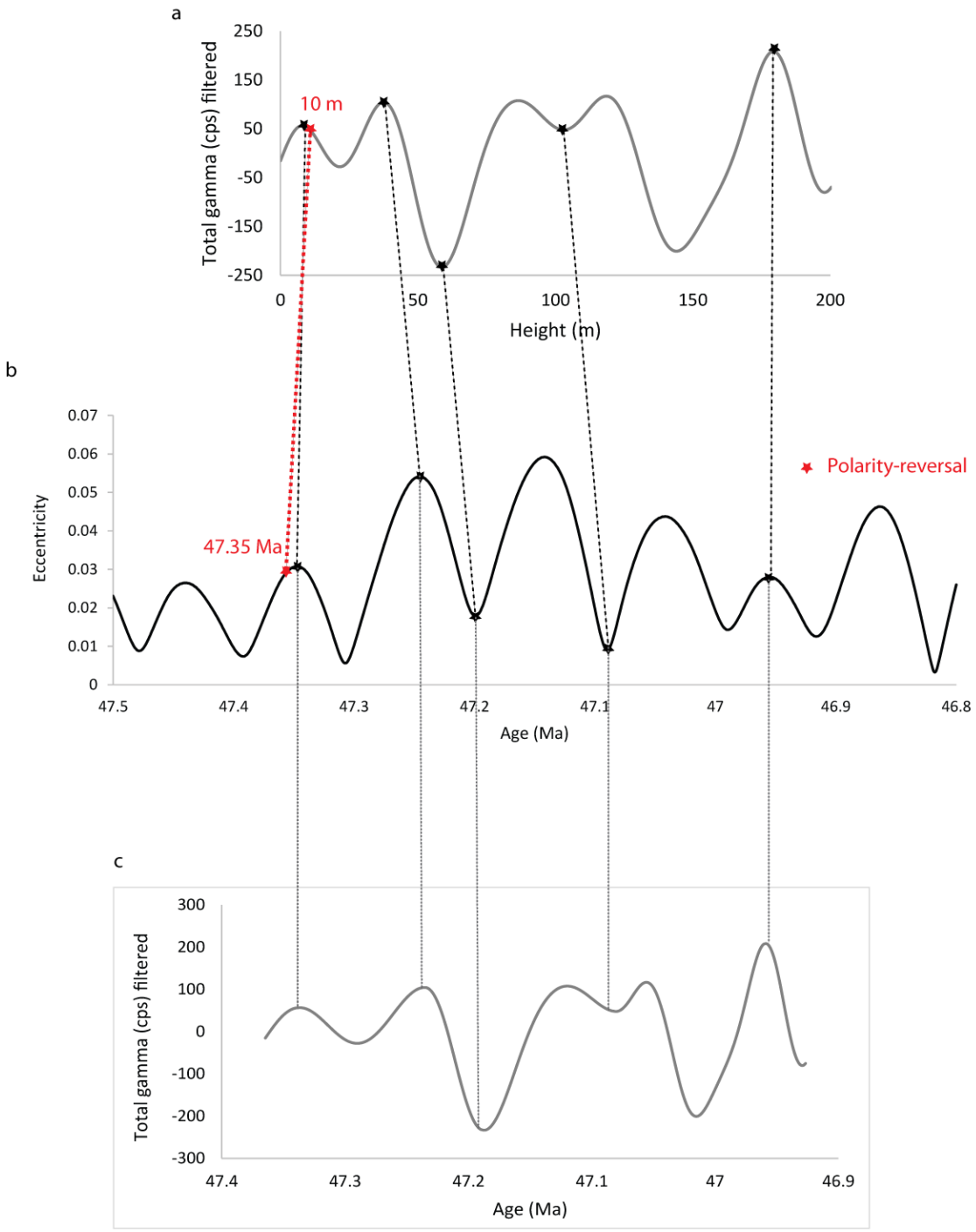

Figure 5.25 Orbital tuning of the Gerbe section. The filtered total-gamma records of the Gerbe section (Figure a) have been matched to the eccentricity cycles of the La2010a orbital solution of Laskar *et al.* (2011) orbital solution (Figure b) using 5 anchor points designated with an asterisk (*). The resultant tuned records (Figure c) show the distortion of the original data. The C21r-C21n polarity reversal dated at 47.35 Myr identified at ~ 10 m stratigraphic height in the Gerbe section has also been used as a control point.

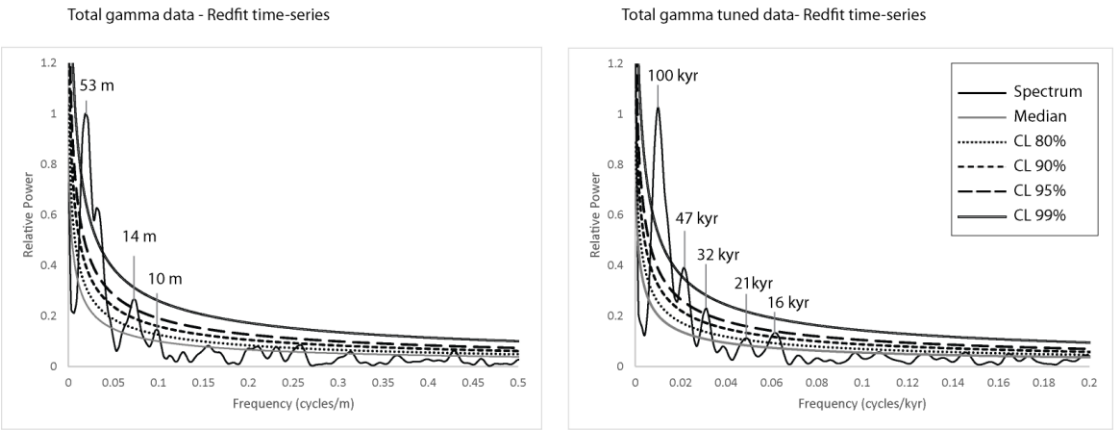

Figure 5.26 Spectral analysis using REDFIT of total-gamma records tuned to eccentricity. The tuned records show a strengthening of the obliquity peak (~ 47 kyr) which is now present > 99% confidence levels. It is likely that the 32 kyr peak > 95% confidence levels is also associated with obliquity and may indicate some variation in the duration of the obliquity cycles (e.g., obliquity O1 52 kyr and obliquity O2 40 kyr orbital periods). Tuning the records has also strengthened the precessional cycles (21 kyr and possibly 16 kyr) which were no significant in the original spectrum.

SARs have been calculated for each of the intervals between anchor points to ensure that the tuned total-gamma records of the Gerbe section have not resulted in unrealistic SARs (Table 5.12). The SARs have varied between 28.6 cm/kyr and 63.2 cm/kyr although averaged values are around 47 cm/kyr. Figure 5.27 shows the variation of SAR across the tuned Gerbe section and the averaged SAR of the section is represented as a linear trend. This averaged SAR is lower than the most significant SAR ranges identified from ASM analysis, between 54.5 and 71 cm/kyr, but is still located within the range of significant SARs (Figure 5.22).

Table 5.12 SARs in the Gerbe section calculated from tuning the records to eccentricity.

Height interval (m)	Age interval (Ma)	SAR (cm/kyr)
0-7,6	47.365-47.338	28.6 cm/kyr
7.6-37.4	47.338-47.236	29.2 cm/kyr
37.4-58.3	47.236-47.189	44.4 cm/kyr
58.3-102.5	47.189-47.082	41.3 cm/kyr
102.5-179.5	47.082-46.96	63.1 cm/kyr
179.5-200.6	46.96-46.9266	63.2 cm/kyr

The table shows SAR calculated at different time intervals throughout the Gerbe section length. Averaged SAR is 47 cm/kyr.

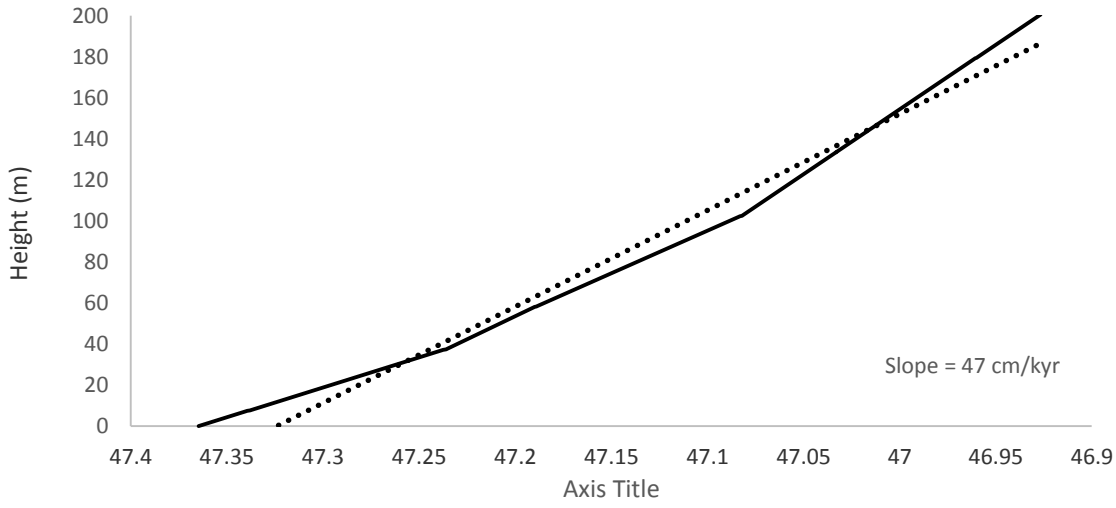

Figure 5.27 SARs in the Gerbe section calculated from orbital tuning the total-gamma records to eccentricity. The figure shows the variation of SARs across the Gerbe section. The averaged SAR is 47 cm/kyr and is represented in the figure as a linear trend. This averaged SAR is much lower than the one estimated from ASM analysis at 57 cm/kyr.

5.3.3 The Banastón System

5.3.3.1 Sedimentology of the Banastón System

The Banastón System forms the thickest accumulation of sandstone turbidites in the Ainsa Basin. The thickness of the system varies from ~ 500 m in the most proximal areas to ~ 700 m in the most distal areas (Bayliss, 2011). The Banastón System has been extensively mapped and interpreted in detail by Bayliss (2011) and Bayliss and Pickering (2014b). The system comprises 6 sandbodies, designated from older to younger, Banastón I to Banastón VI. These sandbodies show a transitional depositional style from lower-slope erosional channel canyon infill in the eastern part of the Ainsa Basin to a more proximal basin-floor and overbank environments ~ 3 km to the northwest, in the proximities of the San Vicente and Boltaña towns (Bayliss and Pickering, 2014b). The transitional change in the environment of deposition of these sand-prone systems is reflected in the architectural elements which constitute these sandbodies (Bayliss and Pickering, 2014b). The proximal lower-slope channels are characterised by vertically-stacked erosional channels. These channels have an erosive base in the scale of tens of metres and are overlain by thick chaotic intervals, mainly Type II MTC deposits, comprising of mainly distorted mudstones with sand rafts which range from metres to hundreds of metres in length. The more distal deposits of the Banastón System have been deposited in a basin-floor setting and are characterised by less confined sediments with sand accumulation occupying a wider area. The channels show a lower degree of erosion at the base.

Palaeocurrent directions determined from current ripples, cross-stratified beds and sole marks suggest that the current direction of the most eastern slope channels

have a dominant westerly direction (290°) and the basin-floor channels have a more north to northwest dominant direction (320°) (Bayliss and Pickering, 2014b).

5.3.3.2 Tectonic history during the deposition of the Banastón System

The sediment distribution patterns of the sandbodies of the Banastón System are characterised by structural confinement between intrabasinal structural highs and the edges of the basin margins. The Banastón sandbodies onlap and pinch out against the Boltaña and the Mediano structural highs, indicating these structures played an important role in confining these flows (Bayliss and Pickering, 2014b).

Cross-sections drawn perpendicular to the main palaeoflow direction, show a lateral migration of the depositional axis of the Banastón System towards the SSW. Bayliss and Pickering (2014b) have associated this lateral migration with the syn-sedimentary growth of the Añisclo Anticline during the deposition of the Banastón System. The progressive growth of this intrabasinal structure has resulted in an offset-stack of successive channels towards the SSW away from the deformation front. Growth rates of this anticline probably exceeded the SAR during the deposition of the Banastón I and II sandbodies and resulted in the structural confinement of these two sandbodies between the Boltaña and the Añisclo anticlines. The Banastón III and IV sandbodies do not show a significant change in thickness across this structure and have a lower degree of confinement. This may indicate that this structure was latent or the depositional accumulation of these two sandbodies exceeded structural growing rates (Bayliss and Pickering, 2014b). The Banastón V and VI sandbodies are thicker towards the west indicating SARs did not keep pace with the growth of this structure (Bayliss and Pickering, 2014b).

5.3.3.3 Age of the Banastón System

Magnetostratigraphic work carried out in the Banastón System (Chapter 3) shows that most of the Banastón System has a normal polarity. There is a change in the magnetic polarity, from normal to reverse, in the interfan deposits between the Banastón IV and V systems. Normal polarity remains throughout the rest of the Banastón System. The polarity reversal probably marks the transition between chrons C21n and C20r which is estimated to have occurred at 44.72 Ma (Gradstein *et al.*, 2012). This result suggests that the Banastón System is ~ 1 Myr younger than the estimations from Scotchman *et al.* (2014) (see Chapter 3).

5.3.3.4 Labuerda gamma-ray logged sections

Two sections have been logged in the Banastón System, ~ 1 km northwest of Labuerda town. Labuerda section 1 has a thickness of 92 m and Labuerda section 2 is 365 m thick. These two sections are separated by ~ 240 m of fine-grained sediments. The fine-grained sediments in between these two sections contain some large-scale slumps and locally outcrop exposure can be very poor causing discontinuous vertical successions. As a result, this intermediate section was considered unsuitable for high-resolution gamma-ray logging and therefore not included in this study. Labuerda section 1 and 2 can be accessed from the road which joins the villages of Labuerda and San Vicente and both sections are well exposed along small stream valleys (Plate 5.7).

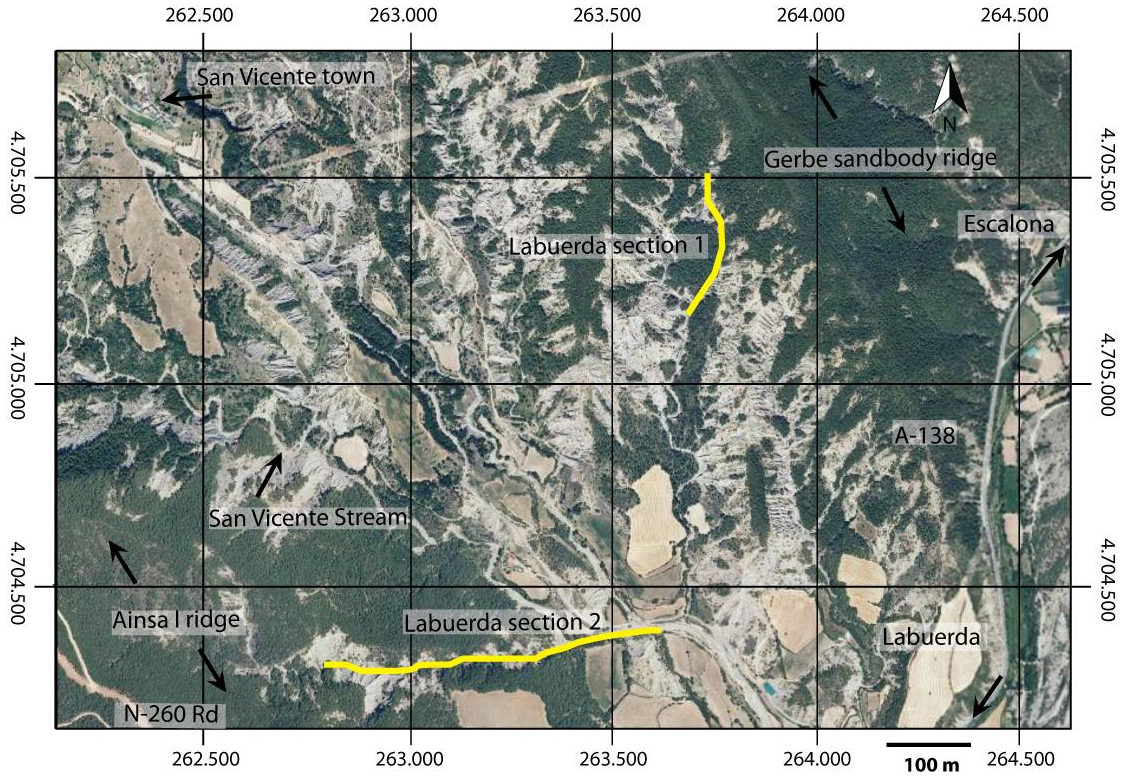

Plate 5.7 Aerial photograph of the Labuerda gamma-ray logged sections. This plate shows the location of the Labuerda 1 and 2 sections outcropping at stream valleys between the towns of Labuerda and San Vicente. The area between these two sections is poorly exposed and not suitable for gamma-ray logging. To the northwest and southeast of the plate there are two vegetated ridges which correspond to the Gerbe I and Ainsa I sandbodies, respectively. Aerial image from www.sigpac.mapa.es/fega/visor.

5.3.3.5 Stratigraphic location of the Labuerda sections

The Labuerda 1 and 2 sections are both located in the Banastón System and these sections mainly represent the fine-grained overbank deposits and interfan sediments of the Banastón submarine fans. Figure 5.28 shows a geological map, cross-section and stratigraphic column of the area surrounding the Labuerda sections.

The Labuerda section 1 starts immediately above a tectonically deformed area which contains numerous small-scale reverse faults. The sediments in this area also show an increase in the sedimentary dip of up to 30°. Towards the NE, ~ 120 m from

the beginning of the Labuerda 1 section, there is a densely vegetated ridge which contains at the top a thin sandstone package. This thin sandbody has been interpreted as the Gerbe I sandbody (Plate 5.7, Figure 5.29). It is inferred that the deformed area between the Gerbe sandbody and the beginning of the Labuerda section is associated with a thrust which can be traced towards the NW and SE of this location (Figure 2.4). This thrust belongs to the Arro Thrust System and has deformed certain areas of the Gerbe System (Plate 5.4). The Gerbe System was thrusted over the first successions of the Banastón System (Banastón I and possibly part of Banastón II). It is therefore very difficult to determine the exact stratigraphic location of the beginning of the Labuerda section 1. A stratigraphic overlapping between the Labuerda section 1 and the Gerbe section is likely, although it is not possible to determine with accuracy, the exact degree of overlapping.

The fine-grained sediments of the Labuerda section 1 and 2 are sandy-rich (~ 11.8 and 10.3% sand, respectively). This high percentage of sand content makes the overbank and interfan deposits of the Banastón System the sandiest of all the systems of the Ainsa Basin. Interestingly, the Banastón System also comprises the thickest turbidite successions of all the Ainsa deep-marine systems. The Banastón V and VI sandbodies have completely pinched out at this location and their exact position within the stratigraphy cannot be determined with certainty. The top of the Labuerda season 2 log is located ~ 40 m below the Ainsa I sandbody which is represented in Plate 5.7 by a vegetated ridge. The top of the Labuerda season 2 log finishes in a very steep and narrow valley with a large heterolithic package at the top which marks the initiation of the Ainsa I Fan. Access to this heterolithic package is not possible due to the steepness of the slopes.

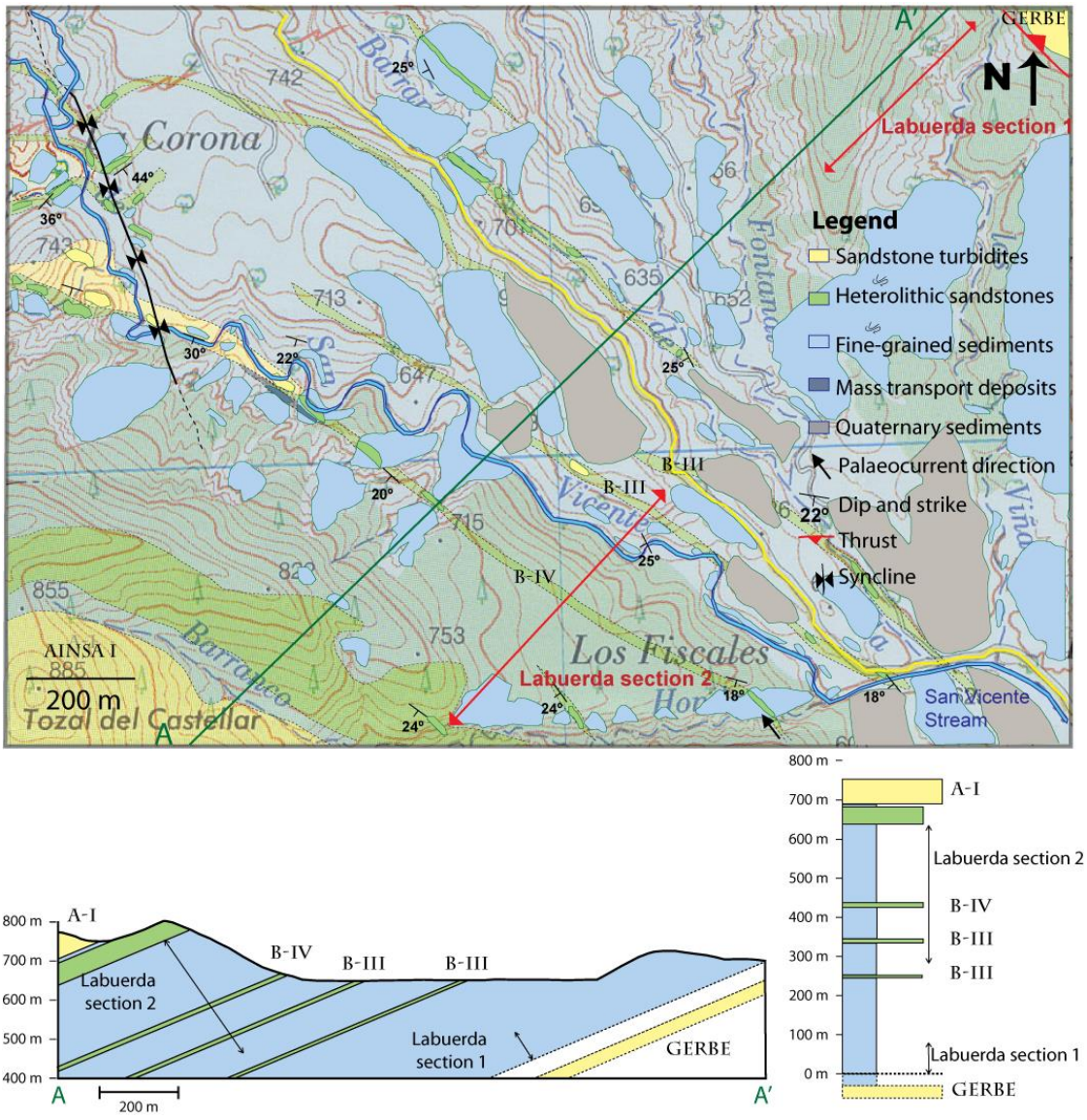

Figure 5.28 Geological map, cross-section and vertical stratigraphic column of the Labuerda gamma-ray logged section 1 and 2. (a) Geological map of the area west of the village of Labuerda showing the gamma-ray logged Labuerda section 1 and 2. In the northwestern part of the area, there is a significant ridge containing the Gerbe I sandbody. The area appears slightly deformed with reverse faults and the sediments show an increase in the depositional dip. It has been interpreted that the Gerbe System has been thrusted over the first successions of the Banastón System (Banastón I and possibly part of Banastón II which are absent in this area). The green line indicates the position of the cross-section A-A', parallel to the Labuerda gamma-ray sections. **(b)** Cross-section showing the position of the gamma-ray logged section in the interfan and overbank sediments between the Banastón II and the Ainsa I sandbodies. The Banastón II, V and VI sandbodies have completely pinched out at this location and it is not possible to determine their exact position within the stratigraphy. **(c)** Stratigraphic column showing the thickness of the sediments and the position of the Labuerda gamma-ray logged sections 1 and 2. The total stratigraphic thickness of the sediments in between the Labuerda section 1 and 2 is ~ 240 m.

5.3.3.6 Labuerda gamma-ray logged section 1

The Labuerda section 1 has a significant interval ~ 13 m thick between 28 and 41 m height that shows a large occurrence of *Arenicolites* burrows (Plate 5.8). This bioturbated interval is quite remarkable and only one other area in the Ainsa Basin, associated with the Gerbe 1 sandbody has shown such a high concentration of *Arenicolites* burrows (Heard, 2007). These burrows cut the strata vertically and are typically 50 cm in length. However, locally they can reach up to a few metres thick. The burrows are sharp-walled, U-shaped and ~ 1 cm in diameter. These burrows have been interpreted as dwelling and feeding structures and are associated with suspension-feeding annelids or small crustaceans (Ekdale and Lewis, 1991; Pervesler and Uchman, 2004). The abundance of vertically orientated *Arenicolites* in the Labuerda section 1 is probably indicative of a high energy environment with significant sediment bypass (Heard, 2007). *Arenicolites* burrows are infilled with coarser grained sand than the surrounded siltstones and mudstones indicating sediment bypass of coarse-grained turbidites or sandy MTDs/MTCs.

Figure 5.29 shows complete sedimentary logs of the Labuerda section 1. The interval of *Arenicolites* can be easily distinguished in the logs. The last 30 m of the Labuerda section 1 are characterised by thick intervals of siltstone-mudstone couplets. Figure 5.30 shows the sandstone turbidite intensity variation of the Labuerda section 1. The turbidite intensities appear to vary cyclically from 40 m height to the end of the section with periodicities of ~ 10 m. Figure 5.31 shows the variation in the content of the K, Th, U, Th/K and Th/U throughout the Labuerda section 1.

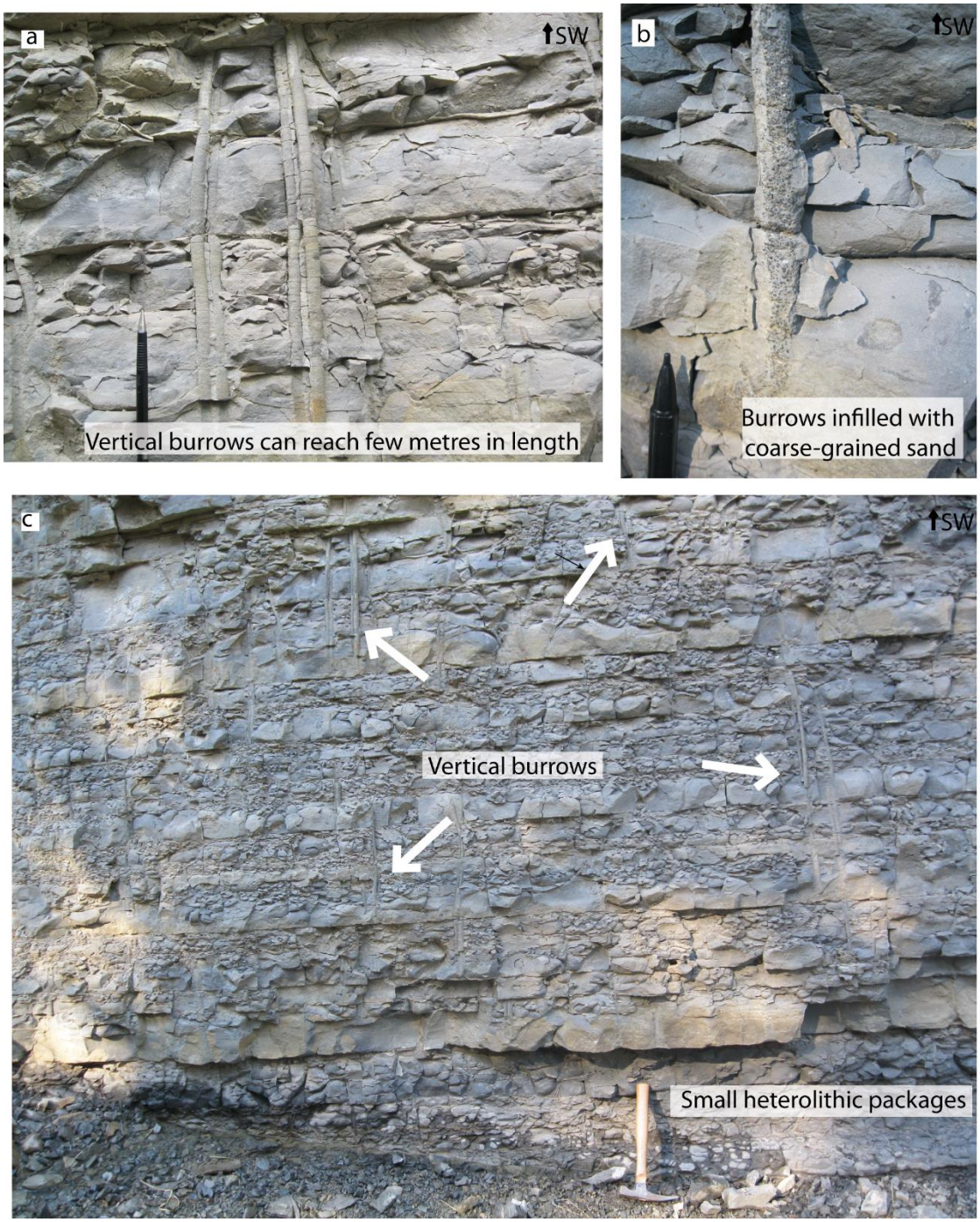

Plate 5.8 Outcrop photographs of the Labuerda section 1. The photographs show a large concentration of *Arenicolites* burrows in the Labuerda section 1 between 28 and 41 m height. **(a)** Close-up photograph of some *Arenicolites* burrows where it can be appreciated the verticality of this type of burrows cutting perpendicularly across bedding. **(b)** *Arenicolites* burrows are U-shaped, ~ 1 cm thick and typically 50 cm in length but they can reach up to few metres. *Arenicolites* burrows are infilled with coarser grained sand than the surrounding siltstones and mudstones. The coarse-grained infill has made these burrows more resistant to weathering and has contributed to their preservation. **(c)** Outcrop photograph showing a large concentration of *Arenicolites* burrows in the area.

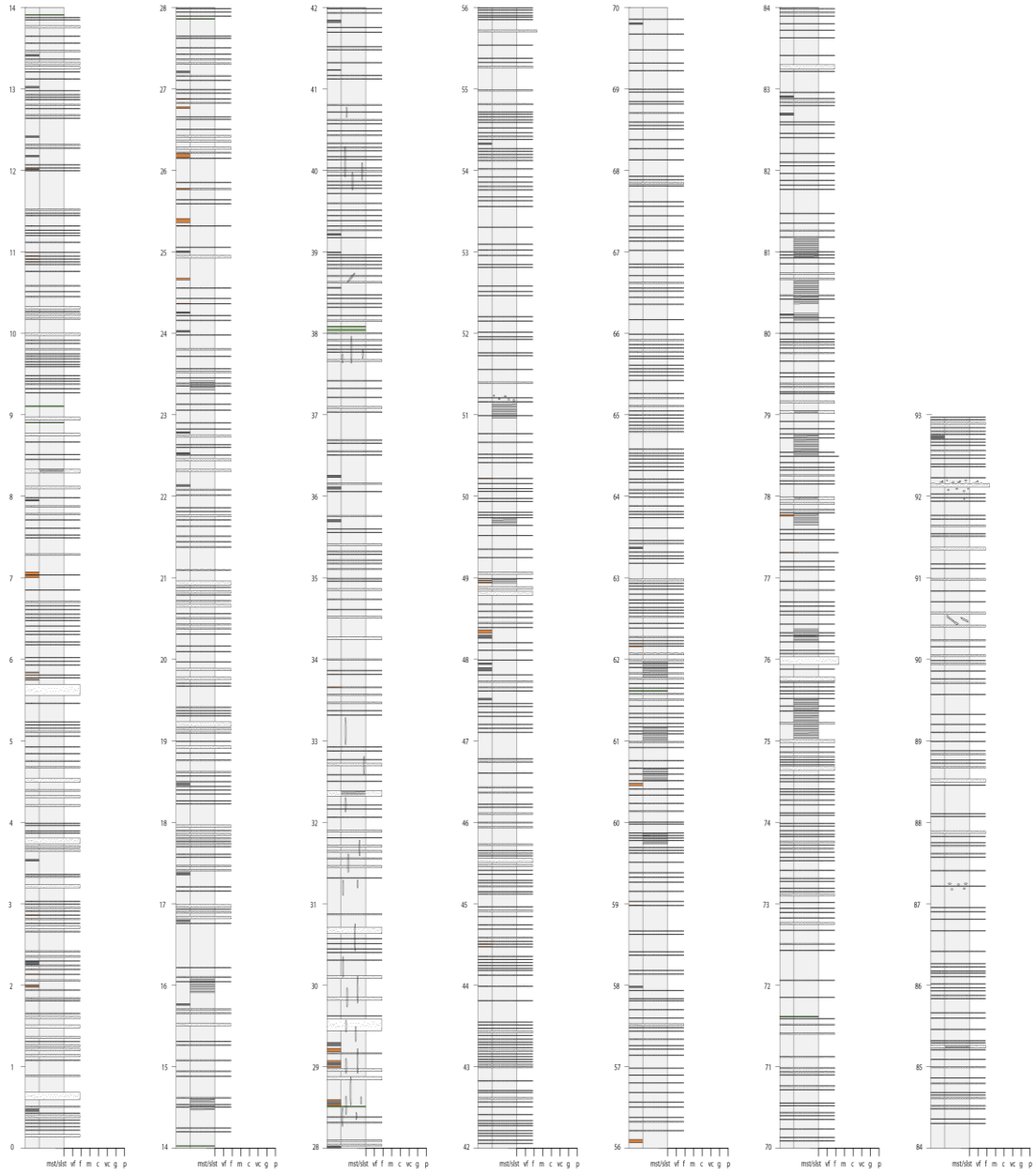

Figure 5.29 Sedimentary log of the Labuerda section 1. Sedimentary logs include every bed thicker than 0.5 cm. Figure 2.5 includes a legend of the symbols used in the sedimentary logs. The sedimentary logs show the *Arenicolites* horizon between 28 and 41 m height. The Labuerda section 1 is characterised by a high intensity of sandstone turbidites and contains many intervals of laminated siltstone-mudstone couplets. Appendix 3 includes an electronic version of these sedimentary logs for detailed visualisation.

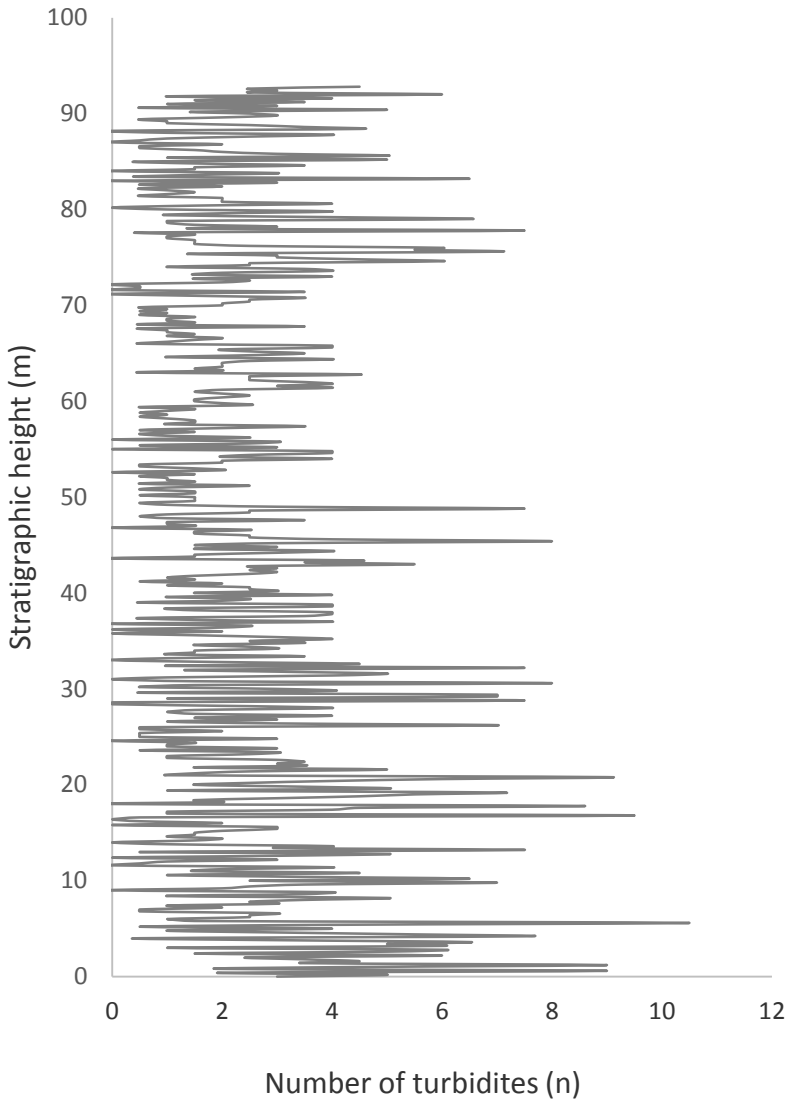

Figure 5.30 Sandstone turbidite intensity in the Labuerda section 1. The first 40 m of the section contains a higher number of sandstone turbidites. From 40 m to the top of the section, the sand content appears to have varied in a cyclical manner with periodicities of ~ 10 m. This 10 m period is associated with a precessional cycle (see Section 5.3.3.6.1). The averaged sand content for the whole section is ~ 11.9%.

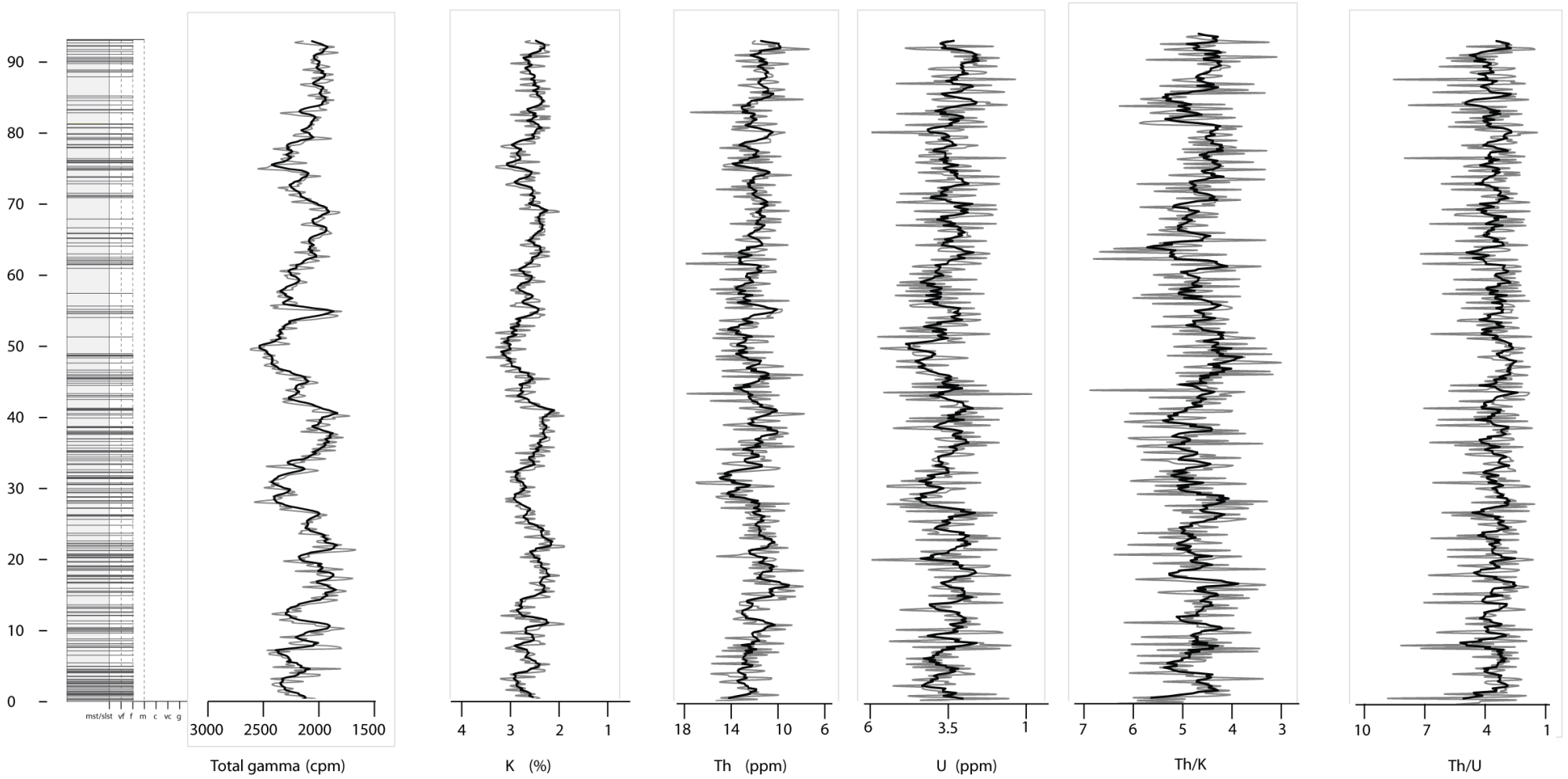

Figure 5.31 Total-gamma (cpm), K (%), Th (ppm), U (ppm), Th/K and Th/U data plotted against sedimentary logs of Labuerda section 1. Simplified sedimentary logs only showing sandtone turbidites ≥ 1.5 cm, for complete logs refer to Appendix 3.

5.3.3.6.1 Cyclostratigraphy of the Labuerda section 1

(a) Methods of spectral estimation

The total-gamma spectrum of the Labuerda section 1 has been estimated using four different methods: the REDFIT, the MTM, the maximum entropy and the periodogram modified with a Bartlett window. Figure 5.32 shows the spectral results obtained from applying each of these methods. Table 5.13 summarises the main frequencies identified within the range 0-0.2 cycles/m. The four methods result in spectra which contain spectral peaks at similar frequencies. The frequencies 0.04 cycles/m (1/25 m), 0.068 cycles/m (1/14 m) and 0.11 cycles/m (1/9 m) consistently appear in all the spectra analysed.

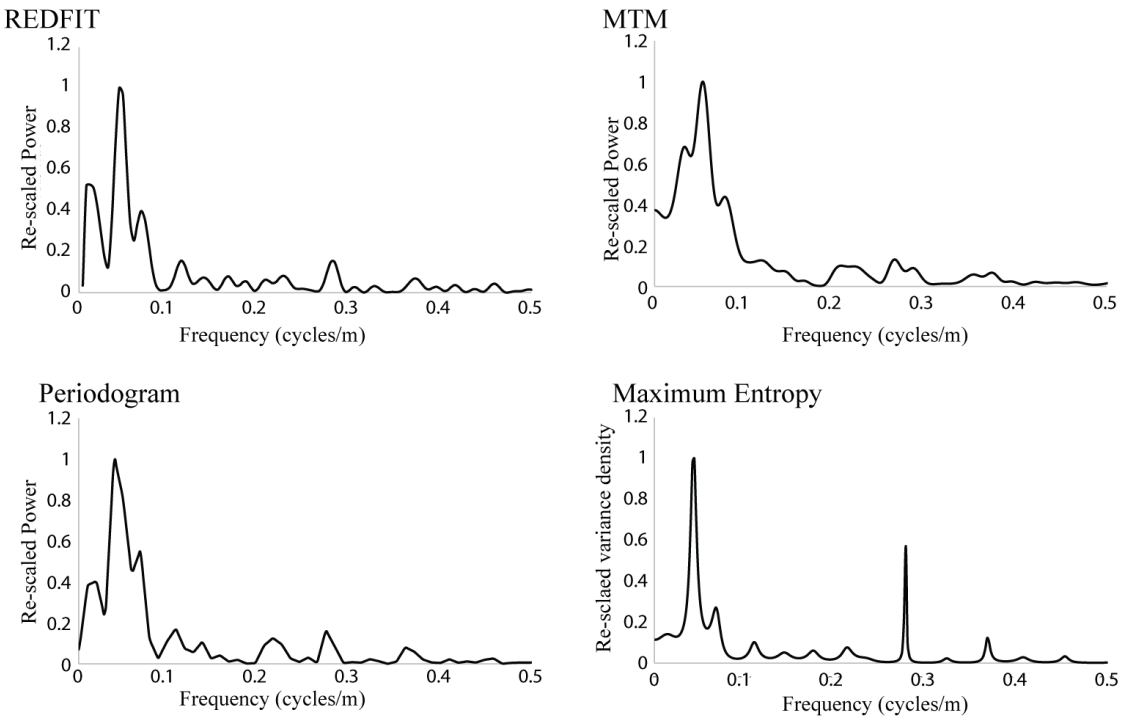

Figure 5.32 Methods of spectral estimation using Labuerda section 1 spectral total-gamma data. REDFIT spectrum used 2 WOSA segments, 3 degrees of freedom and a bandwidth of 0.0194 cycles/m. MTM method used 2 tapers, ~ 4 degrees of freedom. The periodogram spectrum used a Bartlett window. The maximum entropy method used number of lags M = N/3 = 155). The analysis used the REDFIT software developed by Schultz and Mudelsee (2002) and the Analyseries software package developed by Paillard *et al.* (1996).

Table 5.13 Methods of spectral estimation in the Labuerda section 1.

Spectral Method	Frequency (cycles/m)♠	Period (m)	Spectral Method	Frequency (cycles/m)♠	Period (m)
REDFIT	0.012 **0.048** **0.068** **0.117**	83.3 20.8 14.7 8.5	Periodogram modified with a Bartlett window	0.012 **0.04** **0.068** **0.11** 0.14	83.3 25 14.7 9.1 7.1
MTM□	0.0158 **0.041** **0.068** **0.105** 0.135	63.3 24.4 14.7 9.5 7.4	Maximum entropy	**0.042** **0.07** **0.112**	23.8 14.3 8.9

♠ Frequencies from 0-0.2 cycles/m.
□Frequencies present in the MTM significant test with confidence levels > 80%.
The frequencies that appear consistently in all the spectra are represented in bold numbers.

(b) REDFIT spectral results

REDFIT analyses of the Labuerda season 1 section have been undertaken using 2 WOSA segments (Figure 5.33). Table 5.14 summarises the most significant frequencies found within the frequency range 0-0.5 cycles/m. Table 5.15 shows the summative square errors for different background noise fitting methods. The method used is the Labuerda section 1 is the autoregressive AR1 method of Mann and Lees (1996) with the exception of the sandstone turbidite intensity spectrum where a power regression method has shown to fit better the spectral background noise (Table 5.15).

The most significant frequency identified is 0.047 cycles/m (1/21 m). This frequency is present in the total-gamma and K spectrum > 95% confidence levels and in the Th spectrum > 99% confidence levels. At 0.0645 cycles/m (1/15 m) and at 0.104 cycles/m (1/9 m) the sandstone turbidite intensity spectrum shows two spectral peaks well > 99% confidence level. These frequencies are characterised by relatively low power peaks below the 80% confidence levels in the total-gamma, Th or K spectra.

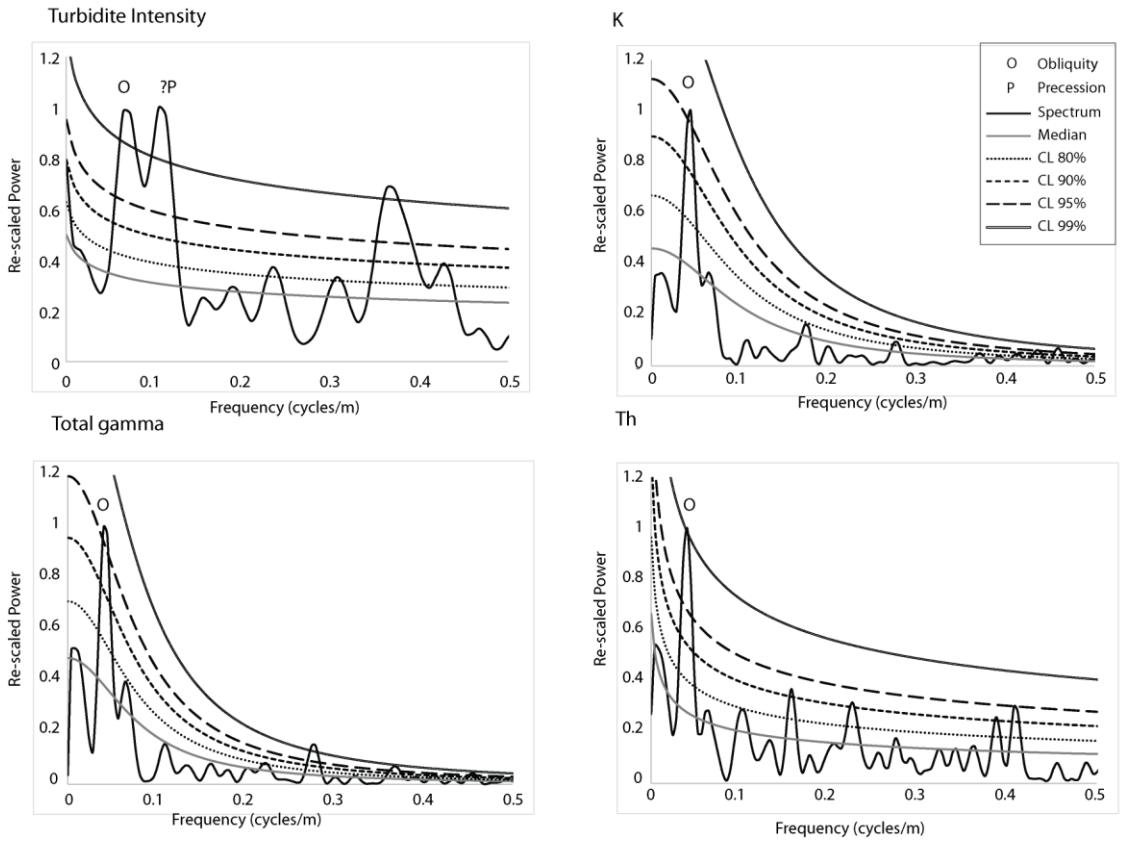

Figure 5.33 Time-series analysis of spectral gamma ray and sandstone turbidite intensity data using REDFIT. REDFIT spectral results used 2 WOSA segments, 3 degrees of freedom and a bandwidth of 0.0194 cycles/m. REDFIT results plotted using the autoregressive model AR1 of Mann and Lees (1996) with the exception of sandstone turbidite intensity data which uses a power regression method. Graphs have been re-scaled to allow comparisons between variables.

Table 5.14 REDFIT time-series analysis results of the Labuerda 1 section.

Data	Frequencies (cycles/m)♠	Period (m)	Confidence levels (%)
Total-gamma	0.0472 0.2764	21.2 3.6	95 99
K	0.0472	21.2	95
Th	0.047	21.2	99
Sandstone turbidite intensity	0.0645 0.1048 0.3629	14.5 9.5 2.7	99 99 99

REDFIT spectral results using 2 WOSA and 3 degrees of freedom.
♠ Frequencies shown are all frequencies between 0-0.5 cycles/m > 95% confidence levels.

Table 5.15 Noise background estimation of the Labuerda section 1.

Data	AR1 (Mann and Lees, 1996)	Quadratic curve	Power regression
Total-gamma	**3032**	6123	4306
K	**2232**	3824	2977
Th	**555**	498	427
Sandstone turbidite intensity	116	110	**104**

Summative square errors using the AR1 model of Mann and Lees (1996), a quadratic curve and a power regression method. The method with the least summative square error indicates the most adequate fitting-curve method and is represented in bold numbers.

(c) ASM results

The five frequencies present in the REDFIT spectra > 99% confidence levels have been applied to the ASM studies. Table 5.16 shows a list of the frequencies used. Considering that the gamma-ray logged sections in the Arro and Gerbe systems have yielded high SARs (~ 50 cm/kyr) it is unlikely that the Labuerda section 1 can determine eccentricity cycles with confidence due to no more than 2 eccentricity cycles probably represented in the total length of the section Therefore, only the obliquity and precession parameters have been included in the ASM analysis.

ASM analysis of the Labuerda section 1 shows significant SAR within the range 37-91 cm/kyr (Figure 5.34). The most significant SARs range from 41-43 cm/kyr with a null hypothesis significance level of 0.04%. Taking into consideration those frequencies which have higher confidence levels and those which appear in the spectra of more than one investigated parameters, the SAR which most closely reflects the Middle Eocene orbital cycles is 41 cm/kyr (Table 5.16). At a SAR of 41 cm/kyr, the frequencies 0.047 cycles/m (1/21 m) and 0.0645 cycles/m (1/14 m) represent obliquity 52 kyr and 40 kyr, respectively. The frequency 0.1048 cycles/m (1/10 m) is likely to represent precession 23 kyr.

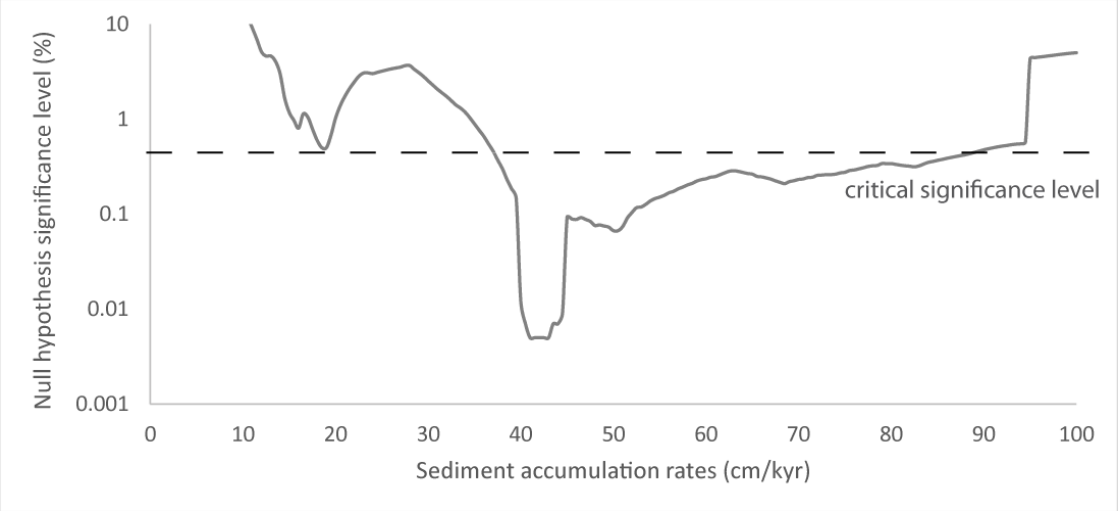

Figure 5.34 ASM results of the Labuerda section 1. ASM analysis includes a total of 5 frequencies identified from spectral analysis. For a list of the frequencies used, refer to Table 5.16. The analysis used a Rayleigh number of 4.29184549 x 10^{-4} and a Nyquist frequency of 2.4 cycles/m. Orbital parameters were determined by using Berger *et al.* (1992) equations at ~ 45 Ma. A total of 191 SAR ranging from 5-100 cm/kyr with an increment of 0.5 cm/kyr were investigated using 100,000 Monte Carlo interactions. Critical levels were established at 0.52%. ASM analysis has identified significant SAR values ranging from the 37-91 cm/kyr range with the most significant SAR between 41 and 43 cm/kyr. Only obliquity and precession parameters were investigated (O1, O2, P1, P2). The analysis used the ASM software developed by Meyers and Sageman (2007).

Table 5.16 Temporal period duration of significant frequencies in the Labuerda section 1.

Frequency (cycles/m) ♠	CL (%)	N□	Period (m)	Period duration (kyr) at different SARs				
				41 cm/kyr	41.5 cm/kyr	42 cm/kyr	42.5 cm/kyr	43 cm/kyr
0.047	99	3	21.3	**51.9**	51.3	50.7	50	49.5
0.0645	99	1	14.5	**37.8**	37.4	37	36.5	36
0.1048	99	1	9.5	**23.3**	23	22.7	22.4	22.2
0.2764	99	2	3.6	8.8	8.7	8.6	8.5	8.4
0.3629	99	1	2.8	6.7	6.6	6.5	6.5	6.4

The table shows calculated cycle duration for each significant frequency (> 90% confidence level) at different SARs. The SAR that is most closely associated with the orbital periods of the Middle Eocene (~ 45 Ma) is 41 cm/kyr.

♠ Includes all the frequencies from 0-0.5 cycles/m with confidence levels > 99%.

□ Number of spectra containing that specific frequency.

Underlined are frequencies which are contained in more than 1 spectrum with at least 1 confidence level > 95%.

Estimated orbital cycles in the Middle Eocene at 45 Ma using Berger *et al.* (1992) equations are eccentricity 123.8 and 94.8 kyr, obliquity 52.3 and 40 kyr and precession 22.6 and 18.8 kyr.

Figure 5.35 (next page) Wavelet analysis of the sandstone turbidite intensity, K, total-gamma and Th data in the Labuerda section 1. (a) The wavelet power spectrum calculates spectral power at different frequencies throughout the Labuerda section 1 using sandstone turbidite intensity, K, Th and total-gamma records. Black contours mark the 10% significant regions. **(b)** Global wavelet shows the scale-averaged wavelet power across the studied frequency bands. Values to the right of the dashed line have a significance > 90% confidence levels. Significant spectral peaks which have been associated with Milankovitch frequencies using REDFIT and ASM analyses, have been labelled (E-eccentricity, O-obliquity, and P-precession). Analysis used the online tool http://paos.colorado.edu.research/wavelets based on the algorithms of Torrence and Compo (1998).

Figure 5.35 Wavelet analysis of the Labuerda section 1.

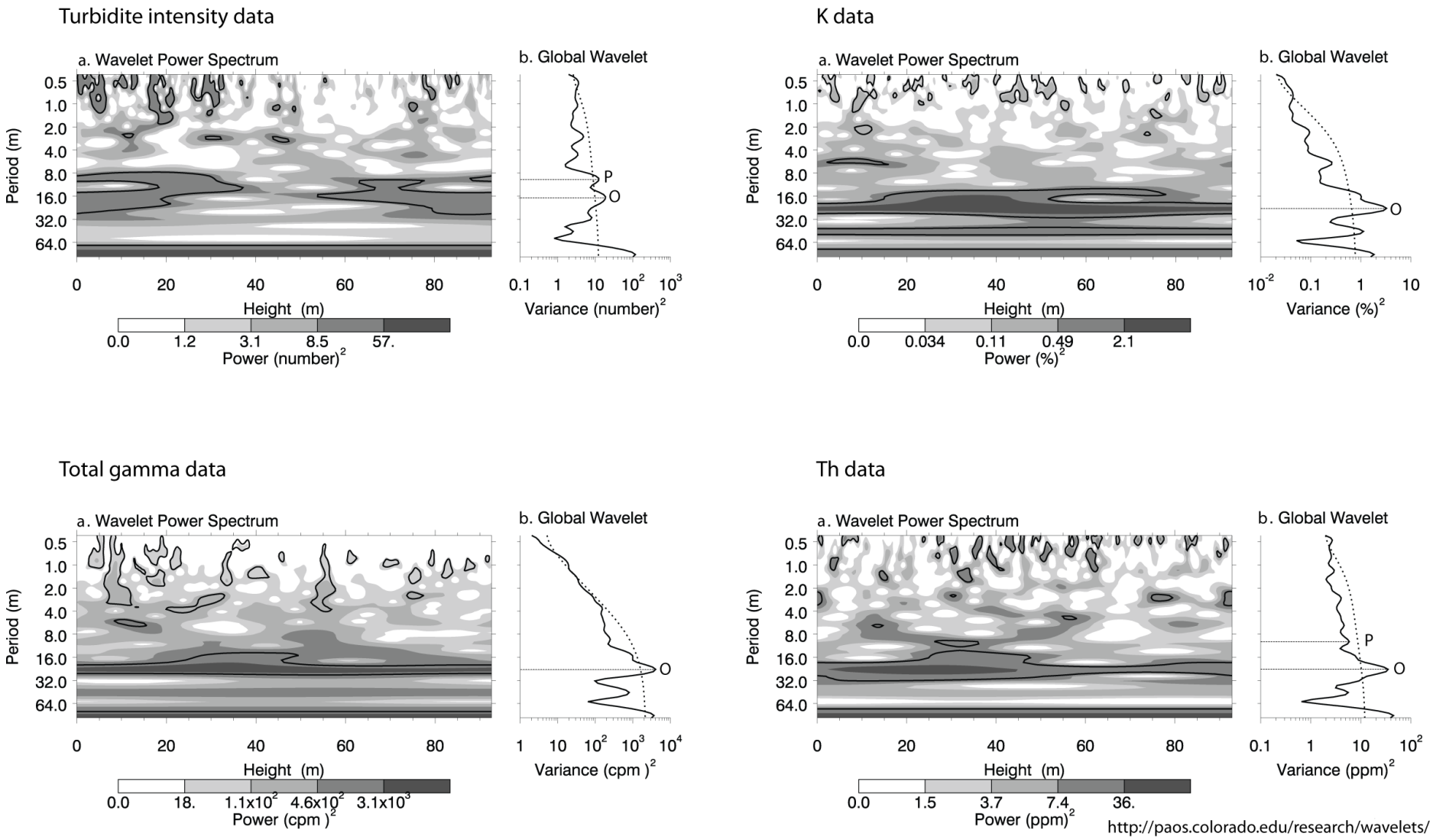

(d) Wavelet analysis

Wavelet analysis shows two main frequency ranges > 90% confidence levels (Figure 5.35). The most spatially persistent frequency range is ~ 0.047-0.065 cycles/m (1/21-1/15 m). This frequency range is significant with a confidence level > 90% in the total-gamma, K and Th throughout the total length of the section. In the sandstone turbidite intensity records, this frequency range is also significant but is spatially discontinuous and present only in the first 25 m and top 35 m of the records. Spectral analysis using REDFIT and ASM has associated this frequency to obliquity.

The frequency at 0.1048 cycles/m (~ 1/10 m) which has been linked to precession is only present in the wavelet spectra of the sandstone turbidite intensity and Th data. This frequency is spatially sporadic in the Th spectrum but is more spatially persistent in the sandstone turbidite intensity data, mainly in the first 30 m and top 40 m of the section.

(e) Frequency-selective filtering

The frequency 0.0472 cycles/m (1/21 m) has been filtered using a bandwidth of 0.0194 cycles/m (Figure 5.36). This frequency is present in the total-gamma records with confidence levels > 90% and in the Th and K records with confidence levels > 90% and 99%, respectively. This frequency has been linked to obliquity.

The total-gamma records filtered at the frequency 0.0472 cycles/m show well developed high-amplitude obliquity cycles throughout the stratigraphy. The spatial distribution of this frequency coincides roughly with the distribution of the wavelet analysis in the total-gamma, Th and K records which have shown the persistent significance of this frequency throughout the length of the Labuerda section 1.

The frequency 0.1048 cycles/m shows well developed cycles in the first 70 m of the records. From 70 m to the top of the section, these cycles appear to lose amplitude and disappear.

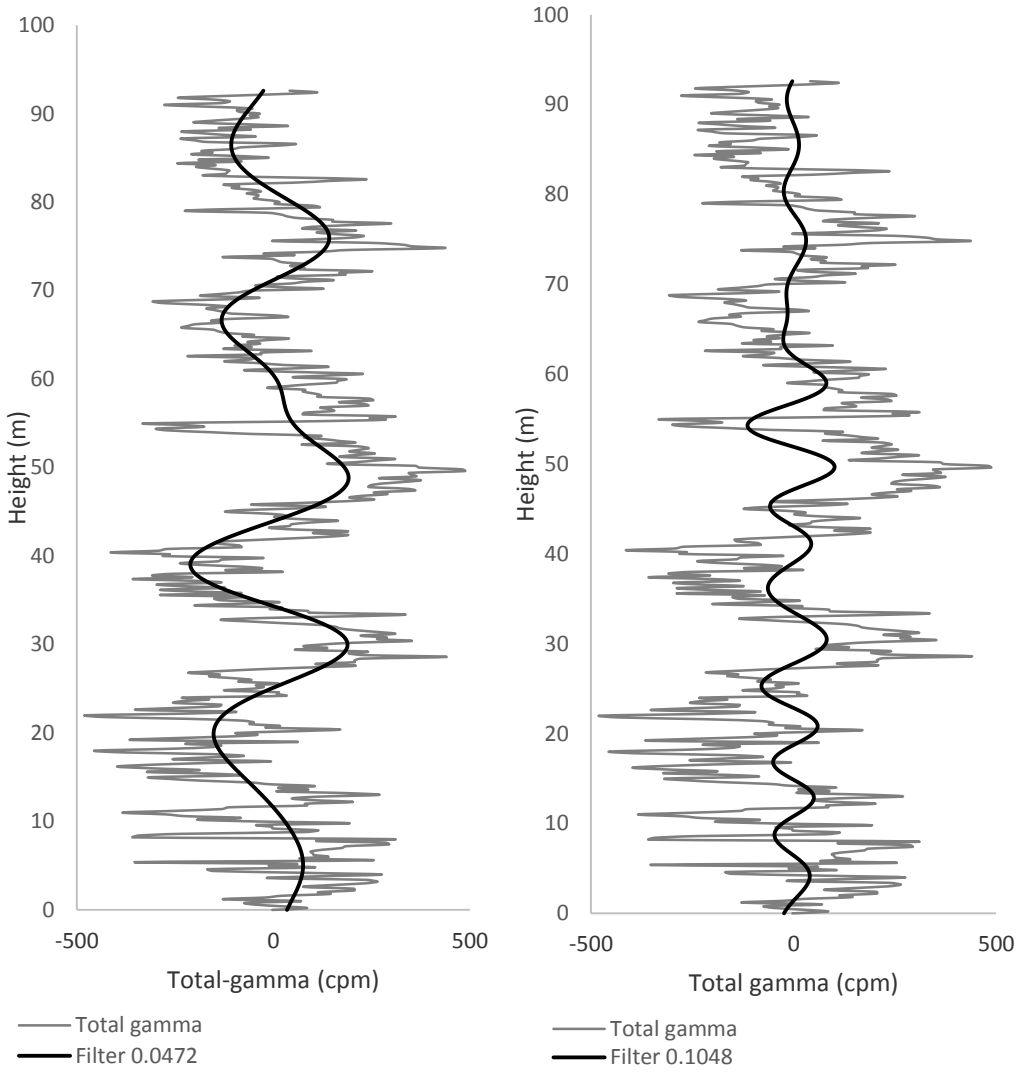

Figure 5.36 Frequency-selective filtering of the Labuerda section 1. Total-gamma-ray records have been interpolated and detrended prior to analysis. Filtering has been undertaken using a band-pass Gaussian filter and a bandwidth of 0.0194 cycles/m. The total-gamma records have been filtered to the frequencies 0.0472 cycles/m and 0.1048 cycles/m. These two frequencies have been associated with obliquity and precession using REDFIT and ASM spectral analysis. The program Analyseries of Paillard *et al.* (1996) has been used for filtering.

5.3.3.7 Labuerda gamma-ray logged section 2

The Labuerda section 2 comprises fine-grained and overbank sediments from the Banastón III to the Ainsa I submarine fan systems. The off-axial sediments of the Banastón III and IV channelised sandbodies are represented by heterolithic packages at ~ 30 m and ~ 150 m height, respectively. Towards the end of the Labuerda section 2, there are a number of chaotic events represented by muddy debris flows containing distorted sandstone rafts. These events are generally less than 1 m in thickness. The Labuerda section 2 log finishes ~ 20 m below the base of a thick heterolithic package which marks the initiation of the Ainsa I sandbody. This heterolithic package is not accessible due to steep slopes in a narrow stream valley.

The Labuerda section 2 has been gamma-ray logged by two MSc Geology students, Rachel Quarmby and Pierre R. C. Warburton in 2010, as part of their final MSc research project. Since their work did not include geological mapping, detailed sedimentary logs, sandstone turbidite intensity studies, magnetostratigraphy or extended time-series analysis, new work has been undertaken in this area.

Figure 5.37 shows detailed sedimentary logs of the Labuerda section 2 and Figure 5.38 shows the sandstone turbidite intensity variation throughout the section. There is a significant increase in the sand content of the section between 110 m and 150 m height. The Labuerda section 2 is one of the sandiest fine-grained sections logged in the Ainsa Basin with a total sand percentage of 10.3%.

Figure 5.37 Sedimentary logs of the Labuerda section 2. Sedimentary logs include every bed thicker than 5 mm. Electronic versions of these logs to allow for a more detailed visualisation are included in Appendix 3.

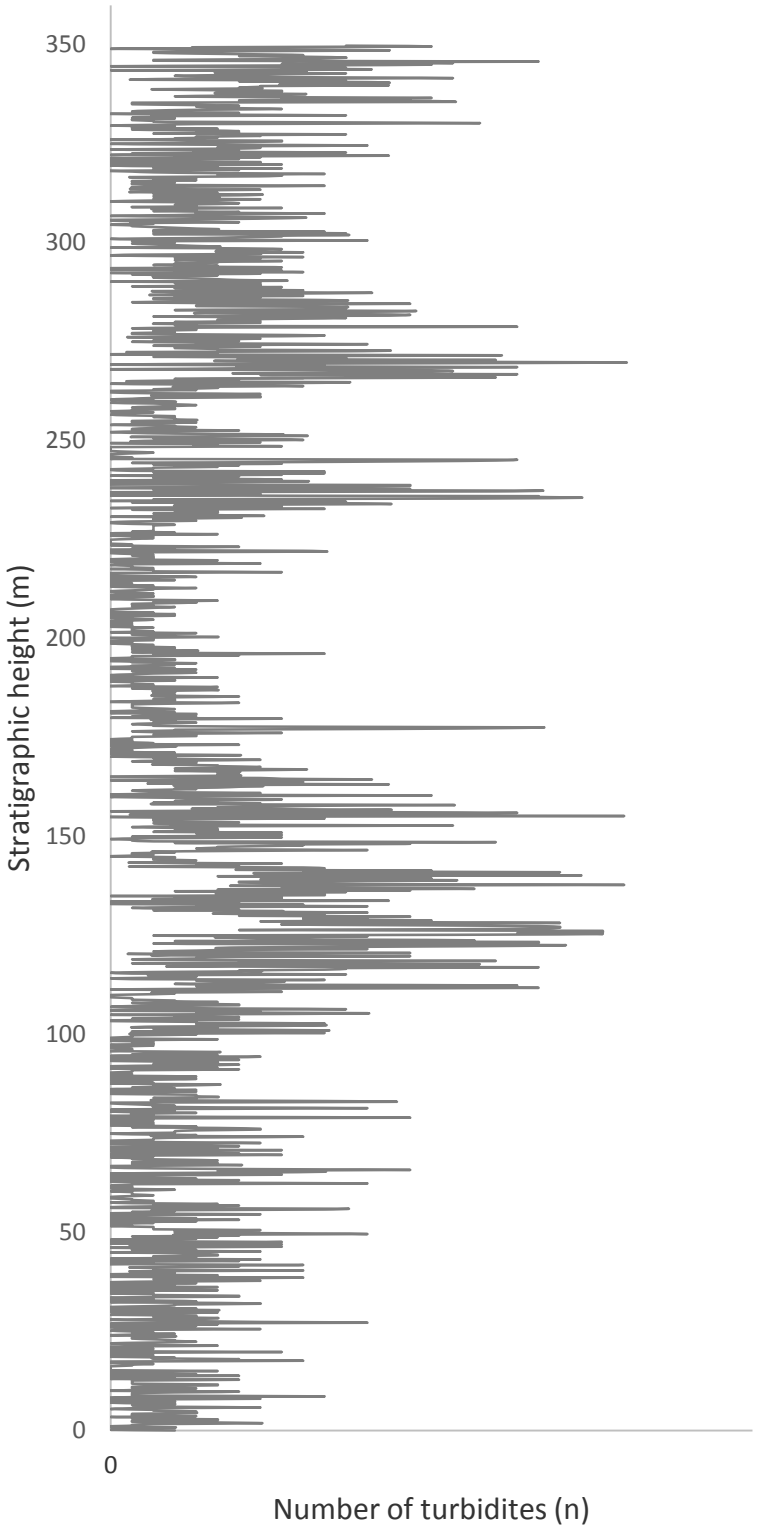

Figure 5.38 Sandstone turbidite intensity in the Labuerda section 2. There is a significant increase in the sand content of the section from 110 m to 150 m and towards the top of the log. The total sand percentage for the Labuerda section 2 is 10.3%.

5.3.3.7.1 Cyclostratigraphic studies of the Labuerda section 2

(a) Methods of spectral estimation

The total-gamma spectrum of the Labuerda section 2 has been estimated using four different methods: the REDFIT, the MTM, the maximum entropy and the periodogram modified with a Bartlett window. Figure 5.39 shows the spectral results obtained from applying each of these methods. Table 5.17 summarises the main frequencies identified within the frequency range 0-0.2 cycles/m. The spectrum created in all cases is similar, although, the MTM is characterised by flat topped frequencies. The MTM significance test does, however, show similar frequencies to the other spectra. There are four frequencies which persistently appear in all the spectra such as 0.012, 0.055, 0.107 and 0.157 cycles/m. For a list of all the frequencies, refer to Table 5.17.

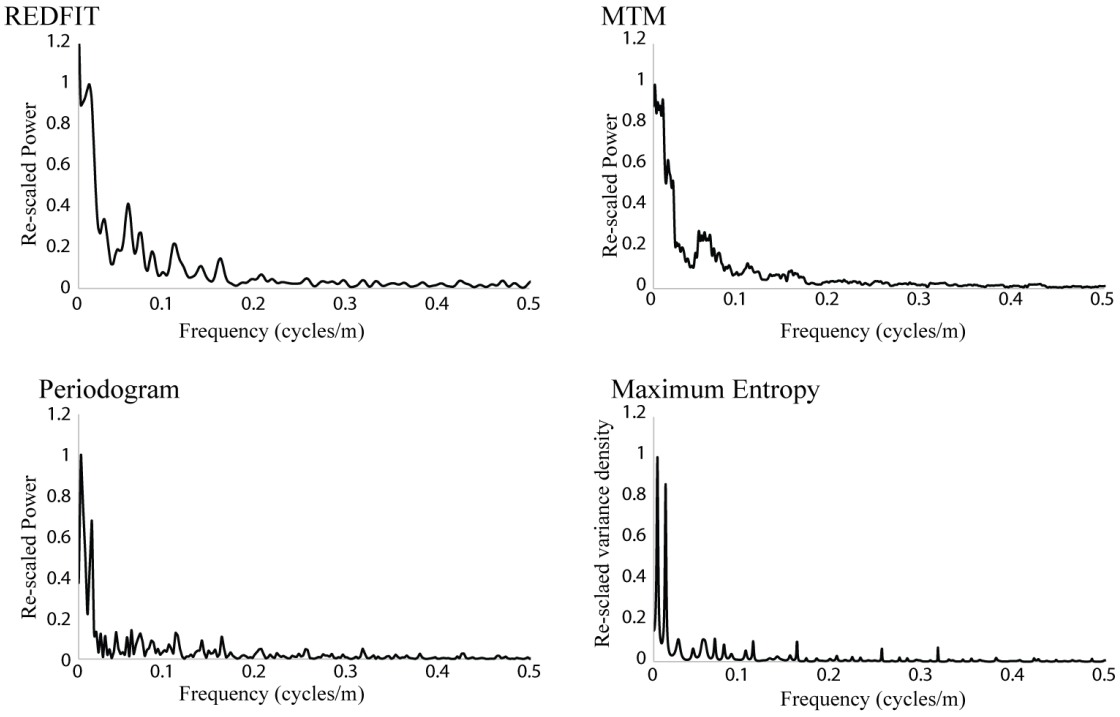

Figure 5.39 Methods of spectral estimation using Labuerda section 2 spectral total-gamma data. The REDFIT spectrum uses 6 WOSA segments and 8 degrees of freedom. MTM method uses 6 tapers. The periodogram spectrum uses a Bartlett window. The maximum entropy method uses numbers of lags M= N/3= 613). Analysis used the programs REDFIT (Schultz and Mudelsee, 2002) and Analyseries (Paillard *et al.*, 1996).

Table 5.17 Methods of spectral estimation in the Labuerda section 2.

Spectral Method	Frequency (cycles/m)♠	Period (m)	Spectral Method	Frequency (cycles/m)♠	Period (m)
REDFIT	**0.012**	83.3	Periodogram modified with a Barlett window	0.002	500
	0.028	35.7		**0.014**	69
	0.055	18.2		0.042	23.8
	0.069	14.5		**0.059**	17
	0.083	12		0.069	14.5
	0.107	9.3		**0.11**	9.1
	0.157	6.4		0.137	7.3
				0.16	6.2
MTM□	**0.0137**	73	Maximum entropy	0.004	250
	0.0244	41		**0.013**	76.9
	0.0293	34.1		0.028	35.7
	0.042	23.8		0.044	22.5
	0.054	18.5		**0.056**	17.9
	0.059	16.9		0.068	14.7
	0.108	9.3		0.079	12.6
	0.125	8		**0.11**	9.1
	0.137	7.3		**0.159**	6.3
	0.16	6.2			
	0.168	5.9			
	0.18	5.6			
	0.184	5.4			

♠ Frequencies from 0-0.2 cycles/m.
□Frequencies present in the MTM significance test with confidence levels > 90%.
The frequencies which consistently appear in all the spectra are represented in bold numbers.

(b) REDFIT spectral results

REDFIT analyses of the Labuerda section 2 have been undertaken using 6 WOSA segments. There are several significant frequencies within the 0-0.5 cycles/m range in the time-series analyses of the total-gamma, K, Th and sandstone turbidite intensity datasets (Figure 5.40). The frequency 0.01 cycles/m (1/84 m) is present in the Th spectrum with confidence levels > 95%. The frequency 0.025-0.026 cycles/m (1/38-1/40 m) is present in the Th (> 90% confidence levels) and in the sandstone turbidite intensity spectrum (> 95% confidence levels). The frequency 0.055 cycles/m (1/18 m) also has good confidence levels in the total-gamma and Th time-series > 99% and 95%, respectively. The frequency 0.07 cycles/m (1/14 m) is present in all the analysed

parameters with a confidence level > 95% in all cases. Other significant frequencies are 0.1 cycles/m (1/9 m) which is present in the total-gamma records > 95% confidence levels and the frequency 0.157 cycles/m (1/6 m) present in the total-gamma and K spectra (confidence levels > 90%). A list of all significant frequencies are summarised in Table 5.18. The noise background estimation method used in this analysis was the power regression fitting method (Table 5.19).

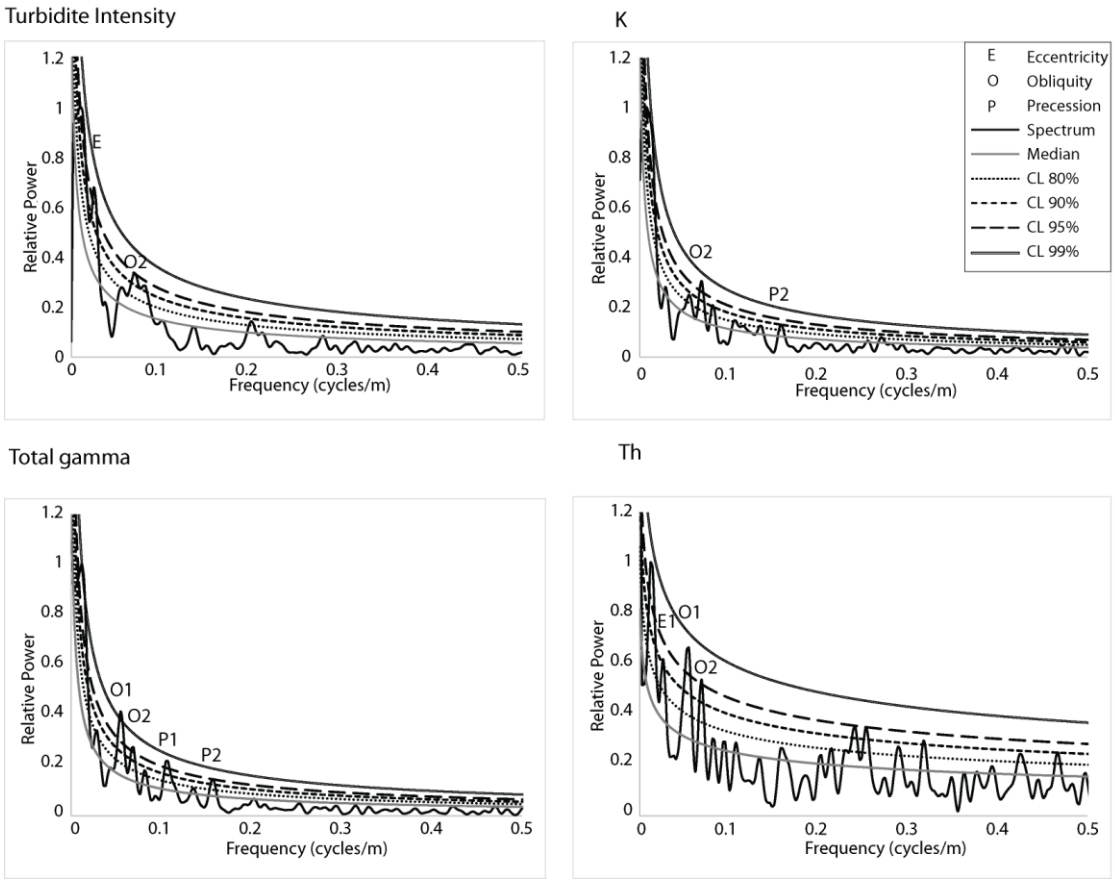

Figure 5.40 Time-series analysis of spectral gamma ray and sandstone turbidite intensity data using REDFIT. REDFIT spectral results used 6 WOSA segments, 8 degrees of freedom and a bandwidth of 0.011 cycles/m. REDFIT results plotted using a power regression fitting model. Graphs showing re-scaled power to allow comparison between variables.

Table 5.18 REDFIT time-series analysis results of the Labuerda section 2.

Data	Frequency (cycles/m)♠	Period (m)	Confidence level (%)
Total gamma	0.0549 0.06922 0.105 0.15753	18.25 14.44 9.52 6.34	99 95 95 90
K	0.0691 0.081 0.1573	14.47 12.35 6.35	95 90 90
Th	0.0119 0.0262 0.0548 0.0691 0.2406 0.2525 0.3169	84.03 38,17 18.25 14.47 4.15 3.96 3.15	95 90 95 95 90 90 90
Sandstone turbidite intensity	0.025 0.07 0.08	40 14.28 12.5	95 95 90

REDFIT spectral results using 6 WOSA segments and 8 degrees of freedom.
♠ Frequencies shown are all frequencies between 0-0.5 cycles/m > 90% confidence levels.

Table 5.19 Noise background estimation of the Labuerda section 2.

Element	AR1 (Mann and Lees, 1996)	Quadratic curve	Power regression
Total-gamma	3289	10467	**2623**
K	3866	5497	**1309**
Th	846	776	**285**
Sandstone turbidite intensity	2398	2803	**818**

Summative square errors using the AR1 model of Mann and Lees (1996), a quadratic curve and a power regression method. The method with the least summative square error indicating the most adequate fitting curve method is represented in bold numbers.

(c) ASM studies

ASM analysis of the Labuerda section 2 shows significant SAR values within the 13.5-100 cm/kyr range (Figure 5.41). Within this large range of significant SAR, there are five main groups of SARs which show the lowest null hypothesis significance levels at

0.001% : Group 1 (16-17.5 cm/kyr), Group 2 (28.5-37.5 cm/kyr), Group 3 (50.5-51.5 cm/kyr), Group 4 (63.5-68.5 cm/kyr) and Group 5 (74.5-81.5 cm/kyr). The frequencies 0.055 cycles/m (1/18 m), 0.069 cycles/m (1/14 m) and the frequency range 0.025-0.026 cycles/m (~ 1/40 m) appear in more than one investigated parameters and have confidence levels > 95% in at least one of the parameters. These frequencies are likely to be the most reliable and have been taken into consideration when determining which of the five groups of significant SARs better reflects the Middle Eocene orbital cycles. Examples of the duration of the cycles for each of these SAR groups can be seen in Table 5.20.

In Group 1 (16-17.5 cm/kyr), the significant frequency range 0.025-0026 cycles/m has a duration of 238-250 kyr which do not approximate any significant orbital cycle. Similarly, Group 3 (50.5-51.5 cm/kyr) and Group 4 (63.5-68.5 cm/kyr) are unlikely to represent the most likely SAR for the Labuerda section 2, since the frequency range 0.025-0.026 cycles/m has an approximate duration of 78 kyr and 60 kyr respectively. These two periods do not approximate any of the known orbital cycles. The SAR which better matches the orbital cycles is 37 cm/kyr in Group 2 and 78 cm/kyr in Group 4.

The Labuerda section 1 which is stratigraphically below the Labuerda section 2, but, also located within the Banastón System, has a SAR of 41 cm/kyr (Table 5.16). Spectral analysis has shown that the SAR has decreased from ~ 50 cm/kyr in the older sections (Tierrantona and Gerbe sections) to ~ 41 cm/kyr in the Labuerda section 1. It is likely that the Labuerda section 2 follows this decreasing trend with a SAR of 37 cm/kyr. Also, further support for a SAR of ~ 37 cm/kyr comes from magnetostratigraphic studies (Chapter 3) which have suggested an average SAR of ~ 34.5 cm/kyr in the Banastón System (see Section 3.5.3, Figure 3.10).

A SAR of 37 cm/kyr suggests that the frequency range 0.025-0.026 cycles/m represents eccentricity; the frequencies 0.054 and 0.0262 cycles/m match the orbital parameters of obliquity 52 and 40 kyr, respectively, and the frequencies 0.105 and 0.157 cycles/m can be linked to the precession cycles 23 and 19 kyr, respectively (Table 5.20).

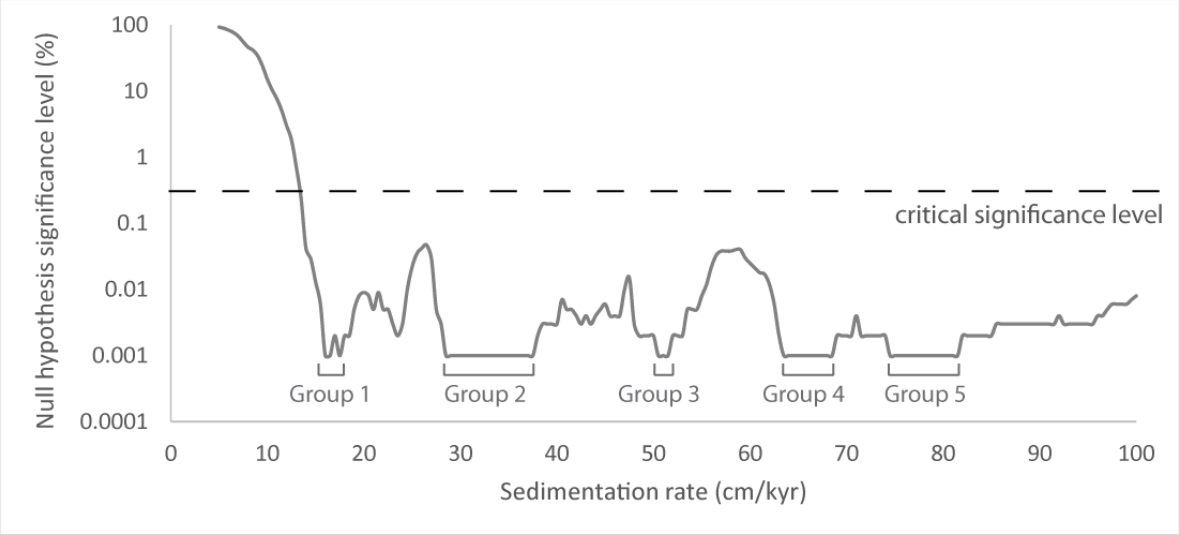

Figure 5.41 ASM results of the Labuerda section 2. ASM analysis includes a total of 11 frequencies identified from spectral analysis of the spectral gamma-ray and sandstone turbidite intensity data with a confidence level > 90%. For a list of frequencies refer to Table 5.20. The analysis used a Rayleigh number of 1.08873163x 10^{-4} and a Nyquist frequency of 2.4 cycles/m. Orbital parameters were established at ~ 45 Ma using Berger *et al.* (1992) equations. A total of 191 SARs ranging from 5-100 cm/kyr with an increment of 0.5 cm/kyr were investigated using 100,000 Monte Carlo simulations. Critical levels have been estimated at 0.52%. ASM analysis has identified significant SAR values ranging from 13-100 cm/kyr. Seven orbital parameters including eccentricity, obliquity and precession have been included in the ASM studies. Analysis used the ASM software developed by Meyers and Sageman (2007).

Table 5.20 Temporal period duration of significant frequencies in the Labuerda section 2.

Spectral frequencies				Period duration (kyr) at different SAR										
Frequency♠	CL (%)	N□	Period (m)	Gr1 (cm /kyr)	Group 2 (28.5-37.5 cm/kyr)				Gr 3	Group 4 (63.5 -68.5 cm/kyr)		Group 5 (74.5-81.5 cm/kyr)		
				16	29	32	35	**37**	51	64	68	75	**78**	81
0.012	95	1	84	524.2	290	263	240	227	165	131	124	112	**106**	104
0.025	95	1	40	250	138	125	114	**108**	78	62.5	58.8	53	**51.3**	49.4
0.026	90	1	38.2	238.5	132	119	109	**103**	75	59.6	56.1	51	**49**	47.1
0.055	95	2	18.2	114.1	63	57	52	**49**	36	28.5	26.8	24	**23.4**	22.5
0.069	95	3	14.5	90.6	50	45	41	**39**	28	22.6	21.3	19	**18.6**	17.9
0.081	90	2	12.3	77.2	43	39	35	33.4	24	19.3	18.1	16	14.8	14.2
0.105	95	1	9.5	59.5	33	30	27	**26**	19	14.9	14	13	12.2	11.7
0.157	90	2	6.4	39.8	22	20	18	**17**	12	10	9.4	8.5	8.2	7.9
0.241	90	1	4.2	26	14	13	12	11	8.1	6.5	6.1	4.5	4.3	4.1
0.252	90	1	4	24.8	14	12	11	11	7.8	6.2	4.8	4.3	4.1	4.9
0.317	90	1	3.2	19.7	11	10	9	8	6.2	4.9	4.6	4.2	4	3.9

The table shows calculated cycle duration for each significant frequency (> 90% confidence levels) at different SARs. The SAR which most closely matches the orbital periods of the Middle Eocene (~ 45 Ma) is 37 cm/kyr.

♠ Includes all the frequencies from 0-0.5 cycles/m with confidence levels > 90%.

□ Number of spectra containing that specific frequency.

Underlined are those frequencies which are contained in more than 1 spectrum with confidence levels > 95%.

The Middle Eocene orbital cycles (~ 45 Ma) using Berger *et al*. (1992) equations are: eccentricity 123.8 and 94.8 kyr, obliquity 52.3 and 40 kyr and precession 22.6 and 18.8 kyr.

(d) Wavelet analysis

Wavelet analysis shows three main frequencies > 90% confidence levels (Figure 5.42). The most spatially persistent frequency is ~ 0.025 cycles/m (1/40 m). This frequency is continuous throughout the records in the sandstone turbidite intensity spectrum. In the K and Th wavelet spectra, it is significant in the first ~ 150 m height of the Labuerda section 2. However, in the total-gamma spectrum this frequency is not significant, although there is an increase in power in the first 150 m of the section as well. REDFIT and ASM spectral analysis has associated this frequency with the short eccentricity. The frequency range ~ 0.055-0.069 cycles/m (~ 1/14-1/18 m) which has been linked to obliquity, is present in the wavelet spectra of the sandstone turbidite intensity, K, Th and total-gamma > 90% confidence levels. But significant regions around this frequency are in general small and discontinuous. In the sandstone turbidite intensity spectrum, this frequency is spatially discontinuous throughout the section. However, in all the other spectra it seems to be more significant in the first 100 m. Finally, the frequency range 0.105-0.157 cycles/m (1/6-1/9 m), linked to precession, is significant in all the records but spatially sporadic.

Figure 5.42 (next page) Wavelet analysis of the sandstone turbidite intensity, K, total-gamma and Th data in the Labuerda section 2. (a) The wavelet power spectrum calculates spectral power at different frequencies throughout the Labuerda section 2 using the sandstone turbidite intensity, K, Th and total-gamma records. Black contours mark the 10% significant regions. **(b)** Global wavelet shows the scale-averaged wavelet power across the studied frequency bands. Values to the right of the dashed line are significant > 90% confidence level. Significant spectral peaks which have been associated with Milankovitch frequencies using REDFIT and ASM analysis have been labelled (E-eccentricity, O-obliquity, and P-precession). Analysis used the online tool http://paos.colorado.edu.research/wavelets based on the algorithms of Torrence and Compo (1998).

Figure 5.42 Wavelet analysis of the Labuerda section 2.

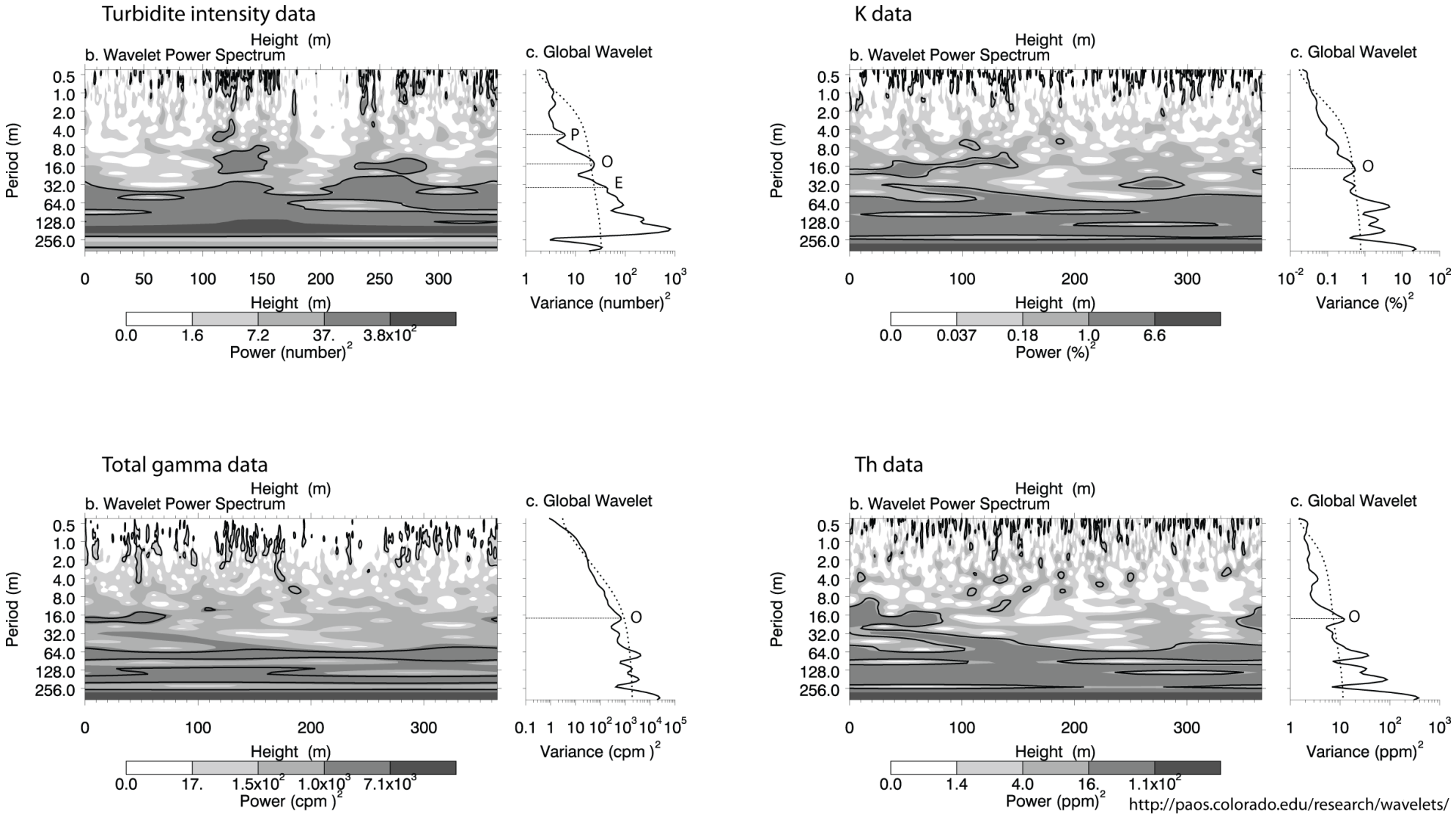

(e) Frequency-selective filtering

The total-gamma records have been filtered to the frequencies 0.025 cycles/m (1/40 m) and 0.0692 cycles/m (1/14 m) using a bandwidth of 0.0115 cycles/m (Figure 5.43). The frequency at 0.025 cycles/m is only significant in the total-gamma ray records with confidence levels > 80%, but, is also present as well in the Th and sandstone turbidite intensity records with confidence levels > 90 and 95%, respectively. Figure 5.44 shows a comparison between sandstone turbidite intensity and total-gamma filtered records using a frequency of 0.025 cycles/m and a bandwidth of 0.0114 cycles/m. Both spectra show a similar number of eccentricity cycles, but, there is some offset at certain intervals throughout the stratigraphy. This offset is probably associated with small disagreements in the outcrop correlations between the gamma-ray logging and the sedimentary logging, which took place in two different field seasons and carried out by different researchers. The 0.025 cycles/m frequency has been linked to eccentricity using results from REDFIT and ASM analysis. The records filtered at this frequency show well-developed high-amplitude cycles mainly in the first 150 m and between 220 m and 310 m stratigraphic height (Figure 5.43). The filtered total-gamma records coincide with the wavelet spatial distribution of this frequency which shows a mostly continuous significant (> 90% confidence levels) spectrum, but, with a central area of decreased wavelet power spectra between 150 m and 210 m.

The total-gamma records filtered at a frequency of 0.0692 cycles/m (1/14 m) has a cyclical appearance throughout the records, but, the amplitude of the cycles is higher in the first 200 m. From 200 m to the top of the section, cycles appear more attenuated with some areas showing some irregularities and loss of cyclicity. This

frequency is present in the total-gamma records with confidence levels > 95% and has been associated with obliquity cycles.

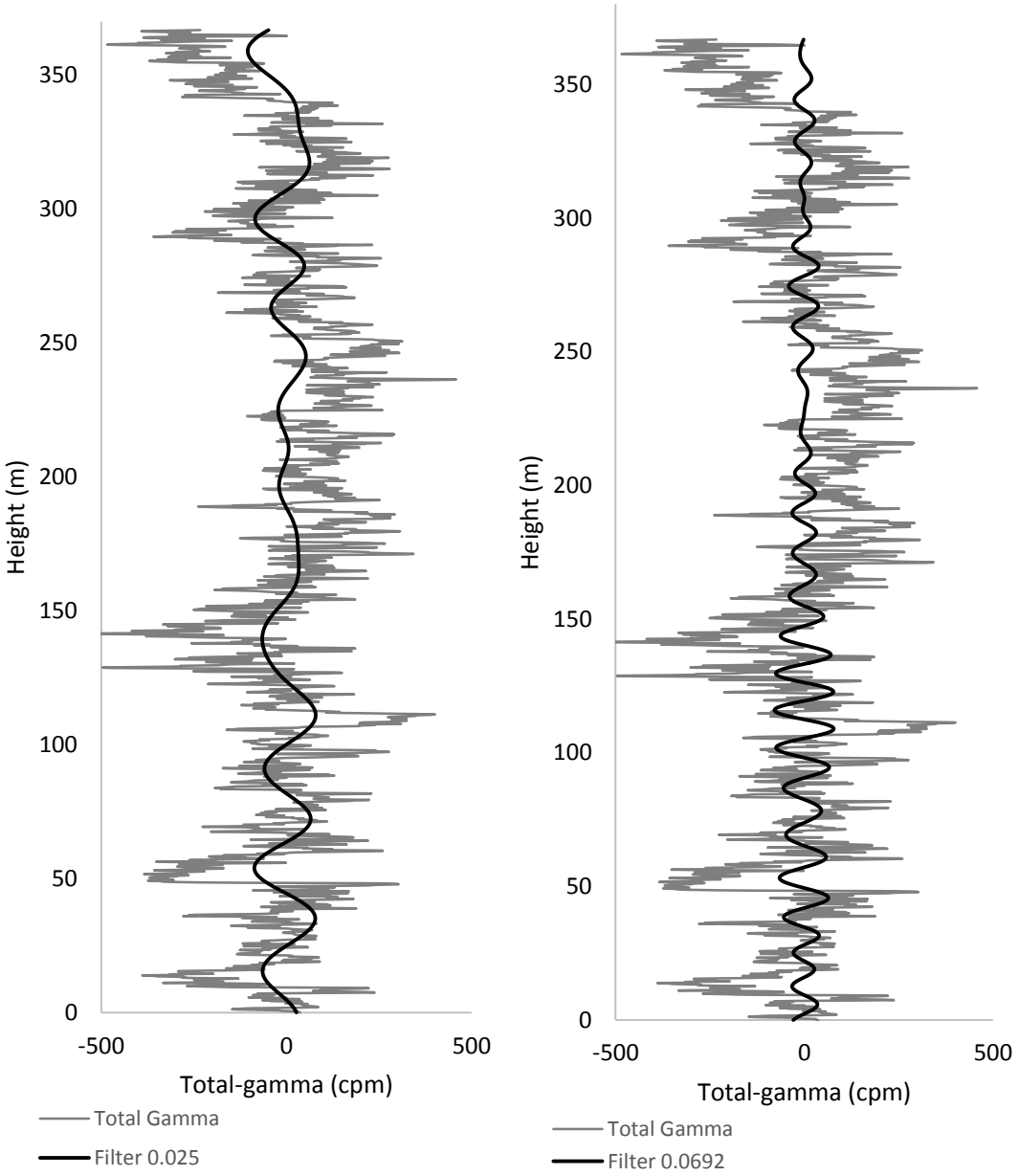

Figure 5.43 Frequency-selective filtering of the Labuerda section 2. Total-gamma-ray records have been interpolated and detrended prior to analysis. Filtering has been undertaken using a band-pass Gaussian filter and a bandwidth of 0.0114 cycles/m. The frequency 0.025 cycles/m has been associated with eccentricity and the frequency 0.0692 cycles/m has been linked to obliquity using REDFIT and ASM analysis. Filtering used the program Analyseries (Paillard *et al.*, 1996).

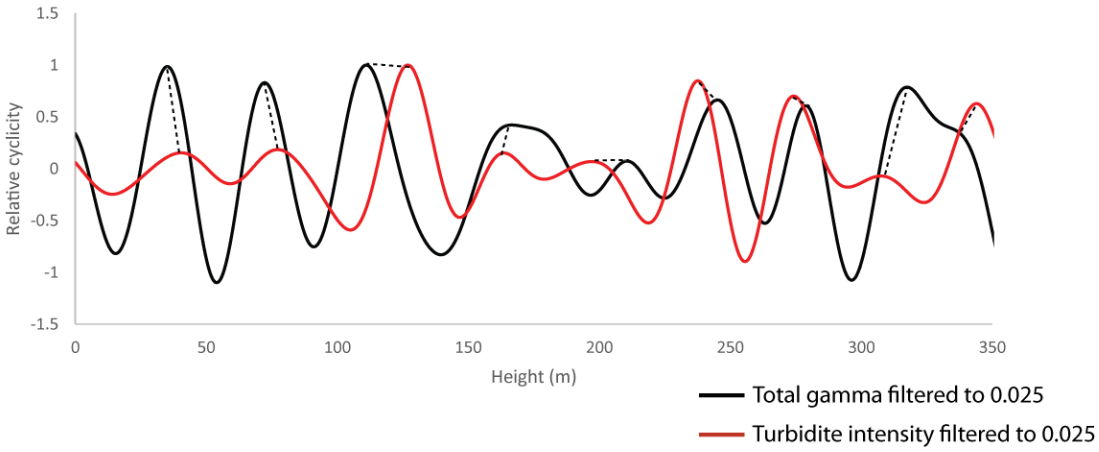

Figure 5.44 Comparison between total-gamma and sandstone turbidite intensity filtered records to the frequency 0.025 cycles/m. Filtered total-gamma and sandstone turbidite intensity records have been normalised to allow comparison between these two parameters. The dashed lines mark the offset in eccentricity maxima between the two records for each of the identified eccentricity cycles. Filtering used the program Analyseries (Paillard et al., 1996).

(f) Orbital tuning

Orbital tuning of the Labuerda section 2 has been performed by comparing the total-gamma records filtered to 0.025 cycles/m, which is the frequency associated with eccentricity (from REDFIT and ASM spectral analysis) to the eccentricity curves for the Middle Eocene using the La2010a orbital solution of Laskar *et al.* (2011) (Figure 5.45). Nine anchor points were used for tuning the records (Table 5.21).

The change in magnetic polarity from normal to reverse identified in the Labuerda section 2 at ~ 185 m height has been associated with the chron C21n-C20r magnetic reversal. The age of this reversal is estimated to have occurred at 45.72 Ma (Gradstein *et al.*, 2012). The best possible match found, taking into consideration the position of this magnetic reversal in the records, establishes the beginning of the Labuerda section 2 at 46.19 Ma. The top of the Labuerda section 2 is dated at 45.13 Ma, giving a total duration for the section of ~ 924 kyr.

Figure 5.46 shows that tuning the records to eccentricity have strengthened the power of the obliquity peaks (52 and 42 kyr) which are now both present > 99% confidence levels. These peaks indicate that there is some variation in the duration of obliquity cycles is present in the records (e.g., obliquity 52 and 40 kyr). Tuning the records has also strengthen the precessional cycles (26 kyr and possibly 17 kyr). The peak at 26 kyr is now well > 99% confidence level and the peak at 17 kyr is > 95% confidence levels.

Table 5.21 Anchor points for tuning in Labuerda section 2.

Height (m)	Age (Ma)	Cycle
34.974	46.098	Eccentricity maxima
71.958	45.994	Eccentricity maxima
110.55	45.891	Eccentricity maxima
166.026	45.789	Eccentricity maxima
209.442	45.618	Eccentricity maxima
243.813	45.512	Eccentricity maxima
277.38	45.409	Eccentricity maxima
314.771	45.323	Eccentricity maxima
356.976	45.278	Eccentricity minima

The table shows the 9 anchor points used to tune the Labuerda section 2 to the eccentricity curves of the La2010a orbital solution of Laskar *et al.* (2011).

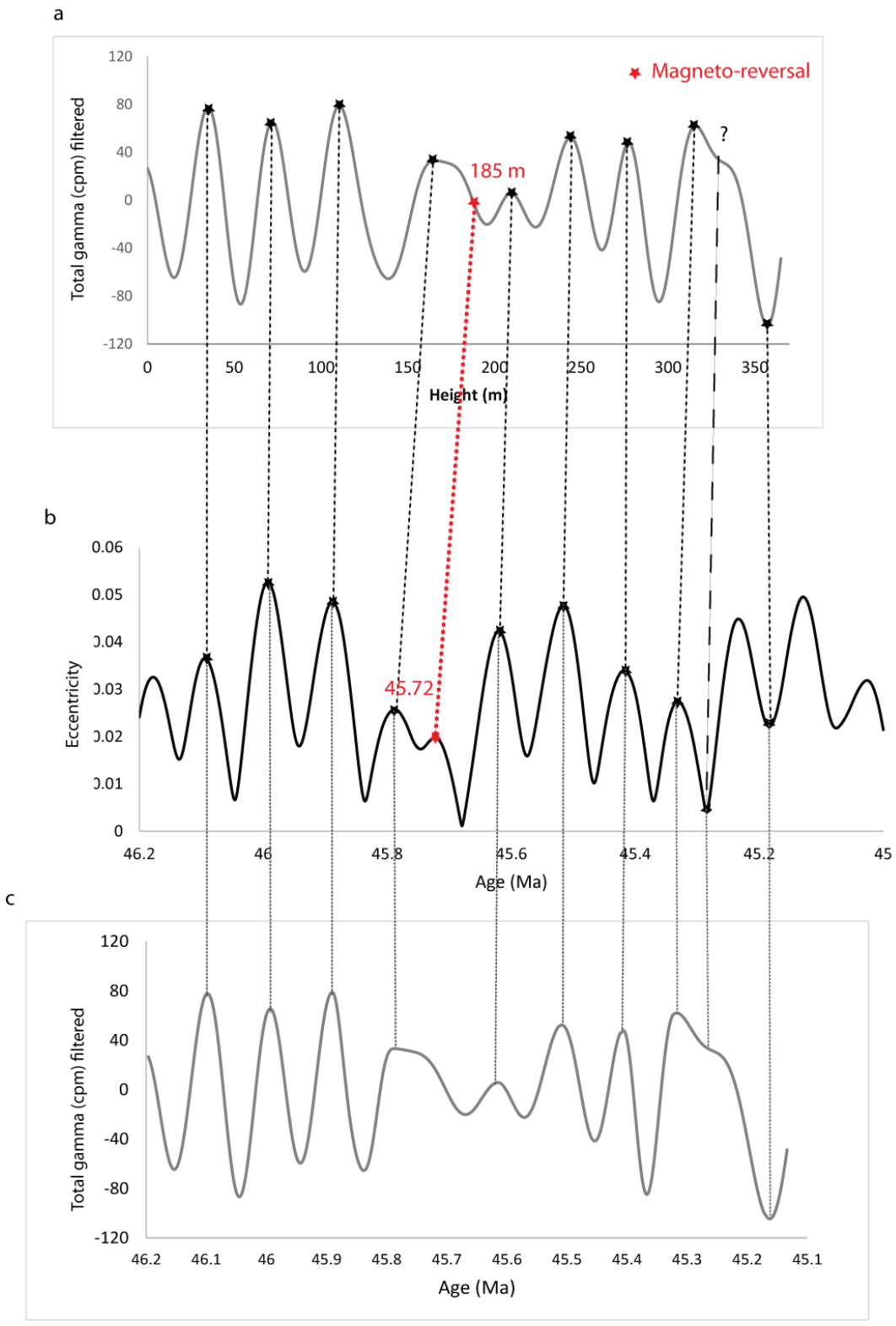

Figure 5.45 Orbital tuning of the Labuerda section 2. The filtered total-gamma records of the Labuerda section 2 (Figure a) have been matched to the eccentricity cycles of the La2010a orbital solution of Laskar *et al.* (2011) orbital solution (Figure b) using 9 anchor points designated with an asterisk (*). The resultant tuned records (Figure c) show the distortion of the original data. The C21n-C20r magnetic reversal dated at 45.72 Ma found at ~ 185 m height in the Labuerda section 2 has also been used as a control point.

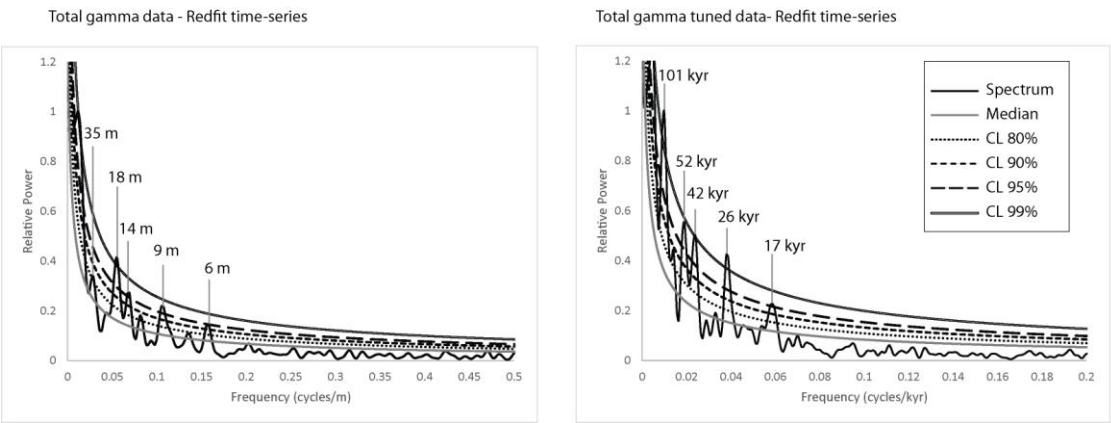

Figure 5.46 Spectral analysis using REDFIT tuned to eccentricity. The tuned records show a strengthening of the obliquity 42 kyr and of the precession 26 kyr cycles which are now both > 99% confidence levels. The precessional peak at 17 kyr has also strengthened and is now > 95% confidence level.

SARs have been calculated for each of the intervals in between anchor points to ensure the tuned total-gamma records of the Labuerda section 2 have not resulted in unrealistic SARs. The SARs have varied between 24.4 cm/kyr and 54.4 cm/kyr although averaged values are ~ 35 cm/kyr. Table 5.22 shows the variation of SAR across the Labuerda section 2. Figure 5.47 shows graphically the variation in SAR across the Labuerda section 2 and averaged SARs are represented as a linear trend. The 35 cm/kyr averaged SAR is very similar to the most representative SAR of the orbital periods for the Middle Eocene calculated by ASM analysis at 37 cm/kyr (Table 5.20) and from palaeomagnetic studies at ~ 34.5 cm/kyr (Chapter 3).

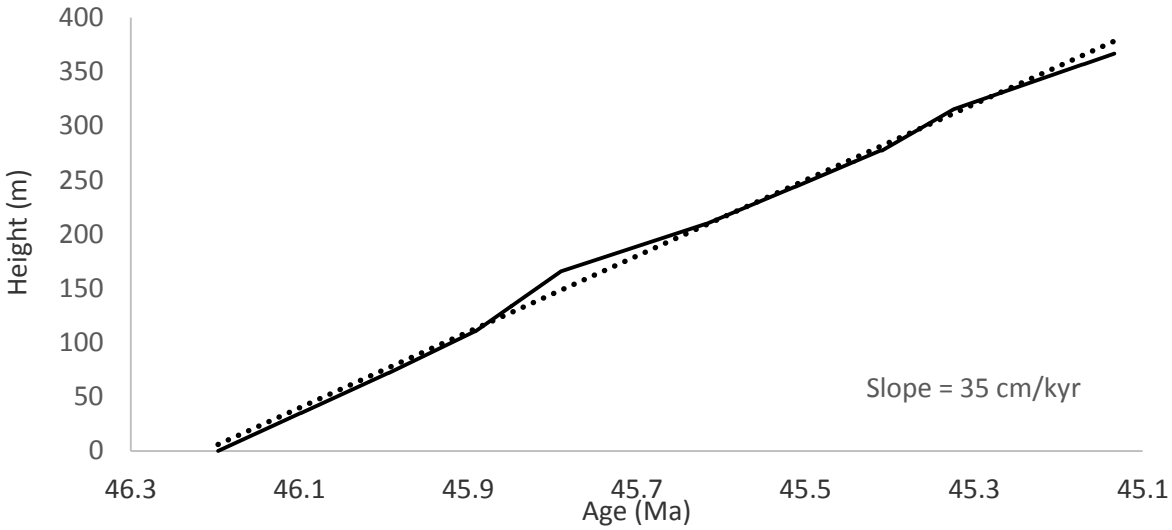

Figure 5.47 SAR in the Labuerda section 2 calculated from orbital tuning the total-gamma records to eccentricity. The SARs have varied between 24.4 cm/kyr and 54.4 cm/kyr. Averaged values are ~ 35 cm/kyr (linear trend). SARs in Labuerda section 2 have remained relatively stable.

Table 5.22 SARs in the Labuerda section 2 calculated from tuning the records.

Height interval (m)	Age interval (Ma)	SAR (cm/kyr)
0-35	46.1964 - 46.098	34.5
35-72	46.098 - 45.994	34.5
72-110.5	45.994 - 45.891	37.5
110.5-166	45.891 - 45.789	54.4
166-209.4	45.789 - 45.618	24.4
209.4-243.8	45,618 - 45.512	32.4
243.8-277.4	45.512 - 45.409	32.5
277.4-314.8	45.409 - 45.323	44.6
314.8-357	45.323 - 45.17	26.9
357-367	45.17 - 45.1336	26.7

The table shows SARs calculated at different time intervals throughout the Labuerda section 2. The averaged SAR is 35 cm/kyr.

5.3.4 The Ainsa System

5.3.4.1 Sedimentology of the Ainsa System

The Ainsa System is ~ 170 m thick and is stratigraphically located between the Banastón and the Morillo deep-marine systems, within the Upper Hecho Group. The Ainsa System has been studied by numerous authors (Mutti *et al.*, 1985; Mutti and Normark, 1987; Clark and Pickering, 1996; Pickering and Corregidor, 2000, 2005; Falivene *et al.*, 2010).

The Ainsa System comprises three sandy successions, designated Ainsa I-Ainsa III. These sandbodies have been interpreted as structurally confined, lower-slope erosional channels or proximal basin-floor channel systems (Pickering and Corregidor, 2005). The facies association in the Ainsa sandbodies suggests repeated episodes of channel incision, sediment bypass and channel deposition and infilling. The sandbodies are characterised by a number of vertical and laterally offset stacked channels forming channel complexes. The channels are typically a few metres deep (up to 30 m) and hundreds of metres wide. They are characterised by basal conglomerates and Type II MTCs representing an initial erosional phase and a sand-rich infill generally composed of thick-bedded sandstones which marks the depositional phase and backfilling of the channel (Pickering and Corregidor, 2000). Sandstones are typically medium-grained, moderately sorted and can be classified as sublitharenites (Das Gupta and Pickering, 2008). The Ainsa fans show an overall westward migration with time, away from the deformation front and also show an aerial expansion within the Ainsa Basin which reflects an increase in sediment supply from the Ainsa I to the Ainsa III systems (Pickering and Corregidor, 2000).

5.3.4.2 Tectonic history during the deposition of the Ainsa System

During the deposition of the Ainsa sandbodies, the confinement of the Ainsa Basin which had already started during the deposition of the Banastón System (Bayliss and Pickering, 2014b) continued to increase. The Mediano Anticline was actively growing during the deposition of the Ainsa System (Fernández *et al*., 2004) and the growth of the fold propagated from south to north (Fernández *et al*., 2012). Also, the Añisclo Anticline was in an active growing stage, as evidenced by the increase of sediment thickness between the Ainsa and Morillo deep-marine systems in the San Vicente Syncline (Fernández *et al*., 2004; Fernández *et al*., 2012). The growth of the Boltaña Anticline appears to have started soon after, during the Morillo and Guaso depositional systems (Fernández *et al*, 2012). The growth of these anticlines was associated with a compressional tectonic regime which resulted in the advancement of the Pyrenean deformation front and the incorporation of the Ainsa Basin into this front. The Ainsa System was probably deposited during a transitional stage where the basin evolved from a foredeep basin to a thrust-top basin when it was incorporated into the hanging wall of the Gavarnie-Sierras Exteriores (Muñoz *et al*., 1998; Dreyer *et al*., 1999; Fernández *et al*., 2004; Fernández *et al*., 2012).

5.3.4.3 Age of the Ainsa System

Magnetostratigraphic work carried out in the Ainsa System (Chapter 3) shows reverse polarity throughout the deposition of this system, corroborating the age model of Scotchman *et al.* (2014) which suggests that the Ainsa System was deposited during chron C20r. These authors infer the C21n-C20r magnetic reversal at the base of the Ainsa System. However, the magnetostratigraphic study undertaken has shown that

this reversal occurred earlier, during the deposition of the Banastón V sandy succession. The estimated ages from palaeomagnetic studies suggests that the deposition of the Ainsa System occurred within calcareous zone NP15 at approximately 45-44 Ma, between the estimations of Remacha *et al.* (2003) and those of Pickering and Corregidor (2005).

5.3.4.4 Boltaña gamma-ray logged section

5.3.4.4.1 Geographical Location of the Boltaña section

The Boltaña section is 167 m long and is located ~ 300 m north of Boltaña town. The section can be accessed from the Javierre road which joins the main road N-260 just outside Boltaña town. The section is in an international walking route which joins the villages of Boltaña and San Vicente along the San Martin gully (Plate 5.9).

The section is fragmented into three mini sections: Boltaña 1 (~ 37 m long), Boltaña 2 (~ 11 m long) and Boltaña 3 (~ 119 m long) sections. These three sections are separated ~ 20-50 m apart (Plate 5.10) and can easily be correlated due to the presence of some thick sandstone turbidites which can be used as marker beds. Boltaña 1 is exposed at the stream which crosses the Boltaña town and Boltaña 2 and 3 sections are located immediately below Boltaña castle (Plate 5.9).

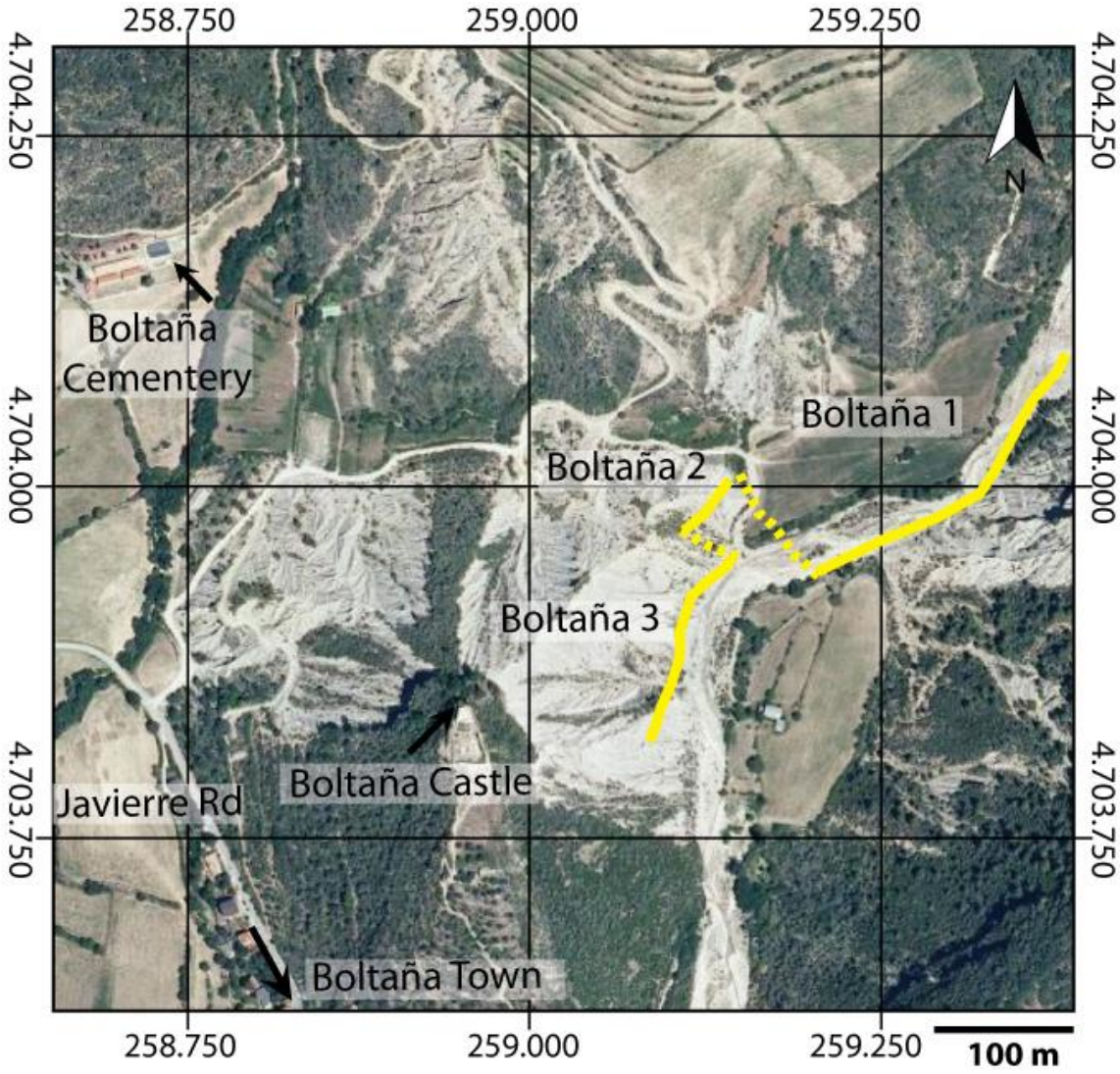

Plate 5.9 Aerial photograph of the Boltaña gamma-ray logged section. This plate shows the three correlated logged sections. Boltaña 1 is well exposed along a stream whilst Boltaña 2 and 3 are located inmediately underneath Boltaña Castle. Aerial image from www.sigpac.mapa.es/fega/visor.

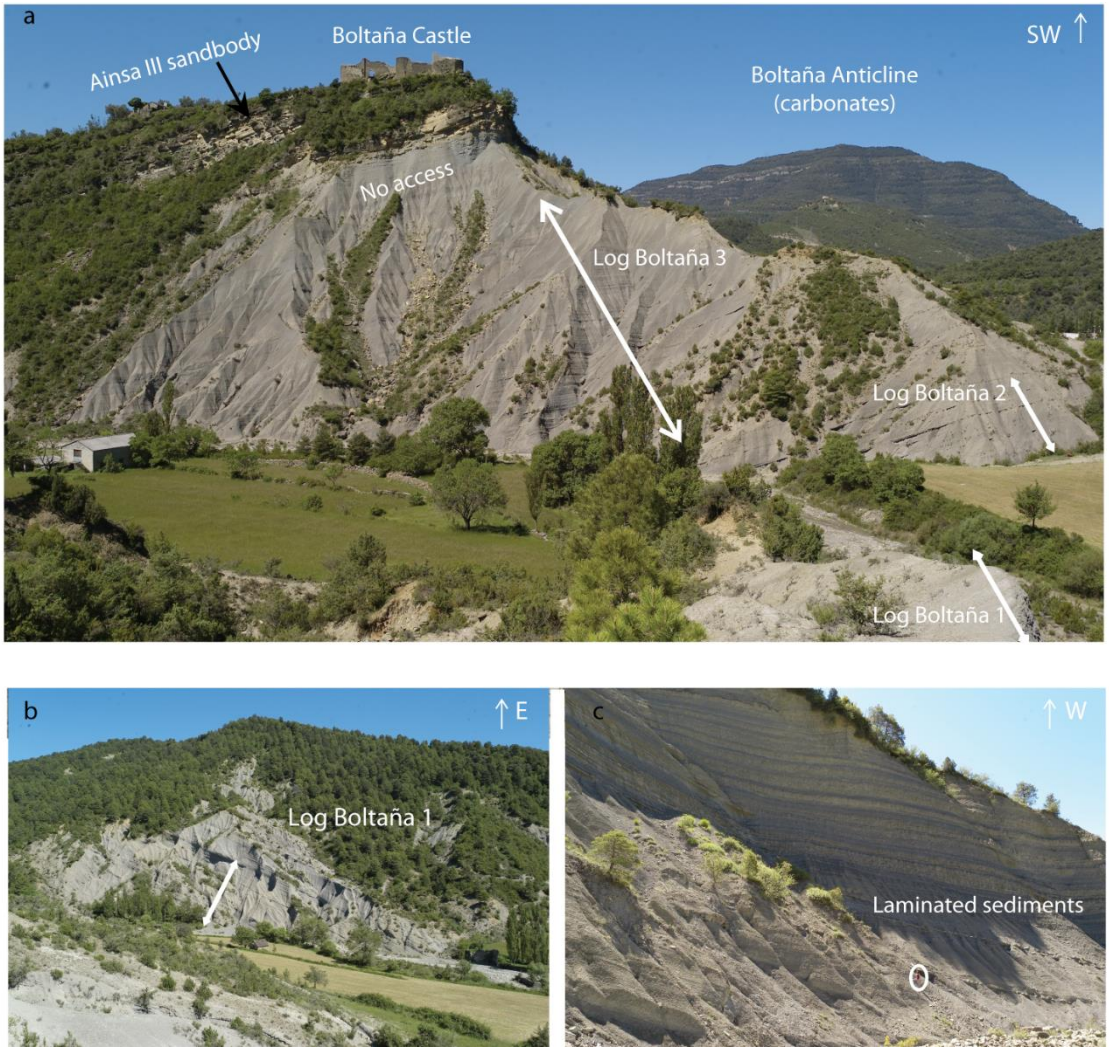

Plate 5.10 Outcrop photographs of the Boltaña gamma-ray logged section. (a) Photograph showing the three correlated logged sections. Boltaña 1 section is only partially exposed in this photograph. There is no access to the top 50 m of the fine-grained sediments located immediately below the Ainsa III sandbody due to very steep slopes. **(b)** Photograph shows the complete Boltaña 1 logged section well exposed along a stream cut. **(c)** Photograph showing the laminated nature of the fine-grained sediments with an alternation of darker and lighter bands forming cyclical packages. Human scale.

5.3.4.4.2 Stratigraphic location of the Boltaña section

The Boltaña section comprises the upper part of the Banastón System and most of the Ainsa System. Figure 5.48 shows a cross-section of the area and the position of the gamma-ray log within the stratigraphy. The logged section starts in the interfan deposits between the Banastón V and Banastón VI systems and ends ~ 50 m below the main axial part of the Ainsa III sandbody. The Banastón VI sandbody is off-axis at this location and is represented by a heterolithic package, ~ 15 m in thickness, which is present in the Boltaña 1 section between 15 and 30 m height (Figure 5.49). The sandstone turbidite intensity graph (Figure 5.50) shows clearly this sand-rich package at the same height (15-30 m). The Ainsa I and II sandbodies have completely pinched out at this location and their exact position within the stratigraphy cannot be established. The axial part of these two channelised sandbodies is located ~ 2 km from this location towards the east and the southeast. The Ainsa III sandbody is axial at this location and is well-exposed at the top of the hill where Boltaña castle and the rest of Boltaña town have been built upon (Plate 5.10a). The 50 m of fine-grained sediments immediately below the Ainsa III sandbody have not been logged as very steep slopes have prevented access to these sediments. Figure 5.51 shows the variation in the content of the total-gamma, K, Th, U, Th/K and Th/U data plotted against simplified sedimentary logs of the Boltaña section.

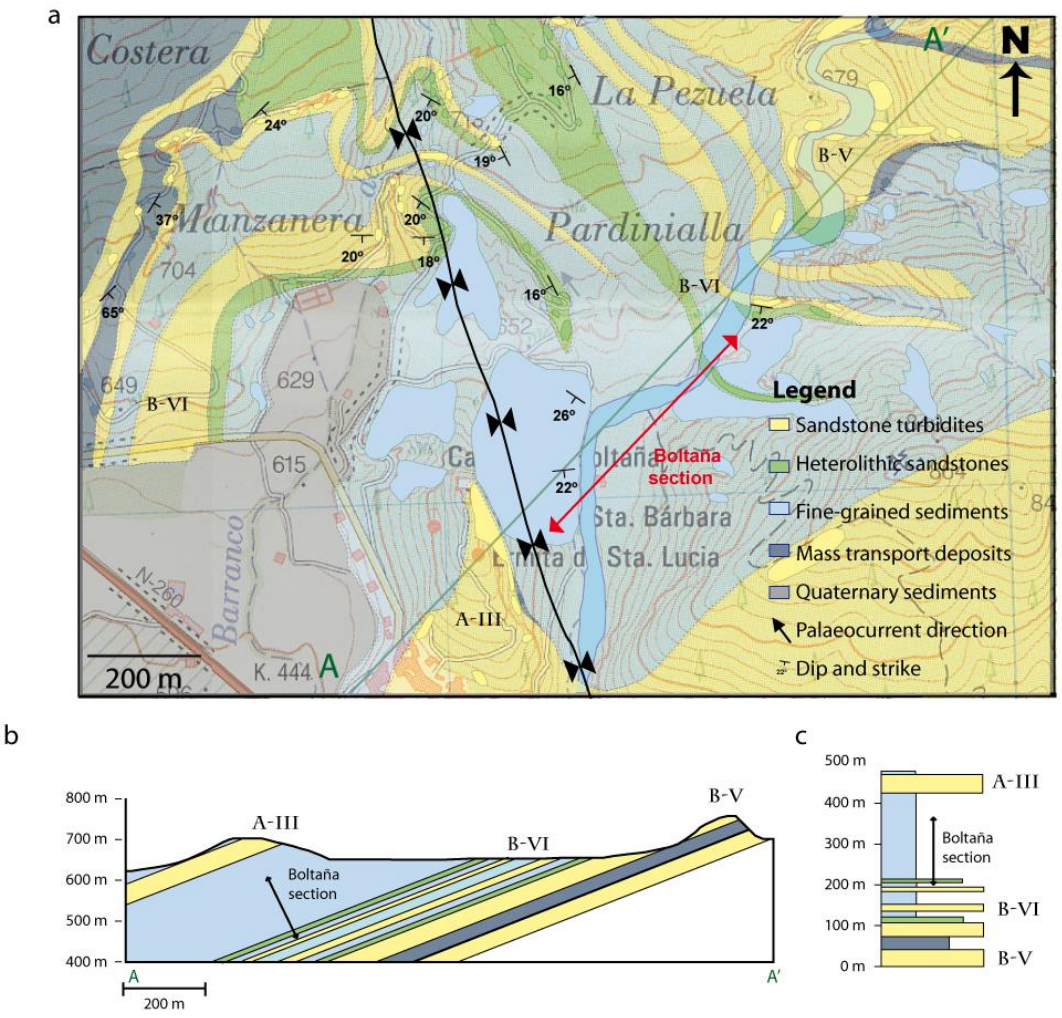

Figure 5.48 Geological map, cross-section and vertical stratigraphic column of the Boltaña gamma-ray logged section. (a) Geological map of the Boltaña section. The northeastern part of the map shows an area of tectonic deformation with a large-scale synclinal fold (Buerba Syncline). This syncline is located between the Añisclo and the Boltaña anticlines. The eastern part of the area is completely undeformed and suitable for gamma-ray logging. The green line indicates the position of the cross-section A-A' which is parallel to the Boltaña gamma-ray section. **(b)** Cross-section of the Boltaña area showing the position of the gamma-ray logged section in the interfan sediments between the Banastón VI and the Ainsa III sandbodies. The Ainsa I and II sandbodies have completely pinched out at this location and it is not possible to determine their exact position within the stratigraphy. **(c)** Stratigraphic column showing the thickness of the sediments and the position of the Boltaña gamma-ray logged section. The base of the Boltaña section contains the Banastón VI sandbody which forms a discrete heterolithic package indicating off-axial deposition. The logged section is discontinued ~ 50 m below the Ainsa III sandbody as the area is not accessible due to the steepness of the slopes.

Figure 5.49 Sedimentary logs of the Boltaña section. Sedimentary logs of the Boltaña section include every bed thicker than 0.5 cm and contain information on sediment colour, bioturbation, sedimentary facies and tectonic deformation. Figure 2.5 includes a legend of the symbols used in the sedimentary logs. An electronic version of these logs is available in Appendix 3.

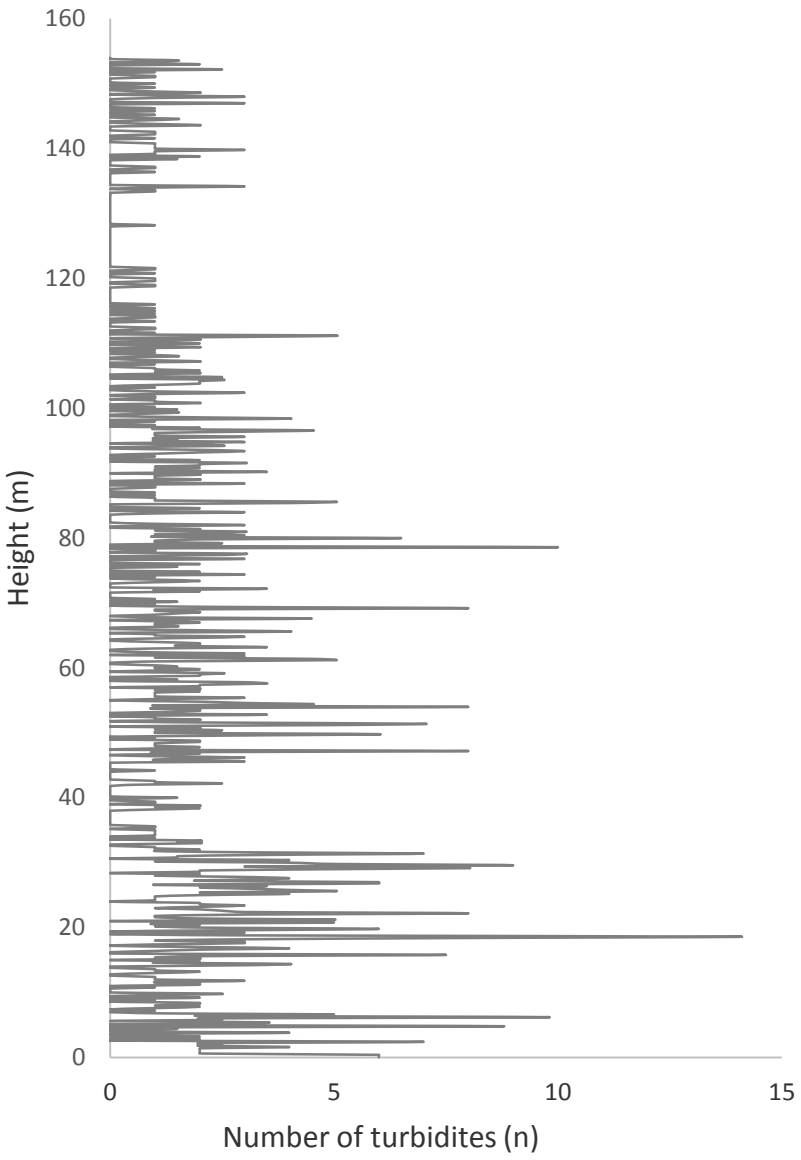

Figure 5.50 Sandstone turbidite intensity in the Boltaña section. There is a general decrease in the number of turbidites throughout the section. The averaged sandstone content of the section is ~ 6%. The last 13 m of the section (from 154 to 167 m height) is covered by thick scree. This poorly exposed section has not been included in the final sedimentary logs or in the sandstone turbidite intensity studies, but, is present in the gamma-ray logs.

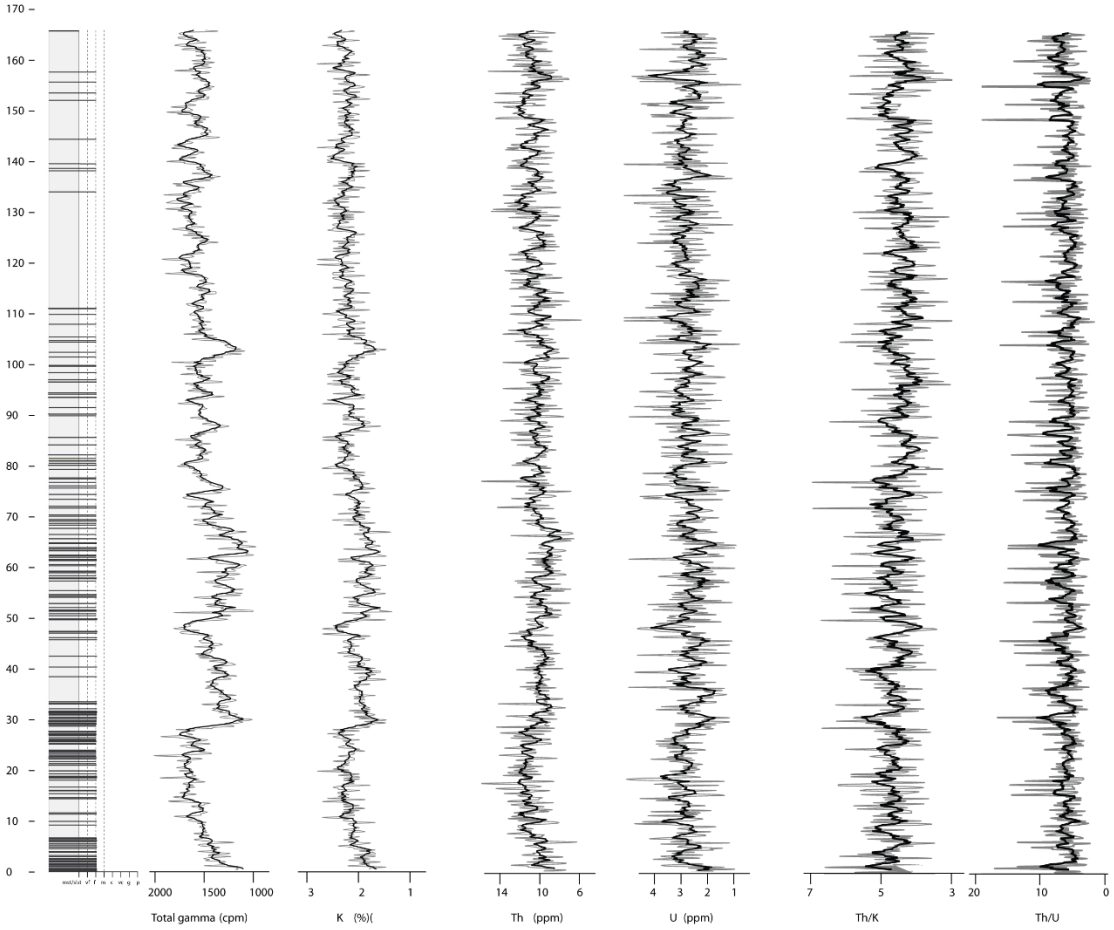

Figure 5.51 Total-gamma, K, Th, U, Th/K and Th/U data plotted against simplified sedimentary logs of the Boltaña section. Simplified sedimentary logs of the Boltaña section only showing sandstone turbidites ≥ 1.5 cm, for complete logs refer to Figure 5.49. The last 10 m of the outcrop are very weathered and no sedimentary logs are available. Black line is a 4-period moving average.

5.3.4.4.3 Cyclostratigraphic studies of the Boltaña section

(a) Methods of spectral estimation

The total-gamma spectrum of the Boltaña section has been estimated using four different methods: the REDFIT, the MTM, the maximum entropy and the periodogram modified with a Bartlett window. Figure 5.52 shows the spectral results obtained from applying each of these methods and Table 5.23 summarises the main frequencies present within the frequency range 0-0.2 cycles/m. The general spectrum created is

similar using these four methods with spectral peaks present in similar frequency positions. The frequencies 0.089 cycles/m (1/11 m), 0.14-0.16 cycles/m (1/6 m) and 0.189 cycles/m (1/5 m) consistently appear in all of the spectra analysed. The frequency range 0.029-0.031 cycles/m (~ 1/30 m) is also present in all the spectra with the exception of the MTM spectrum.

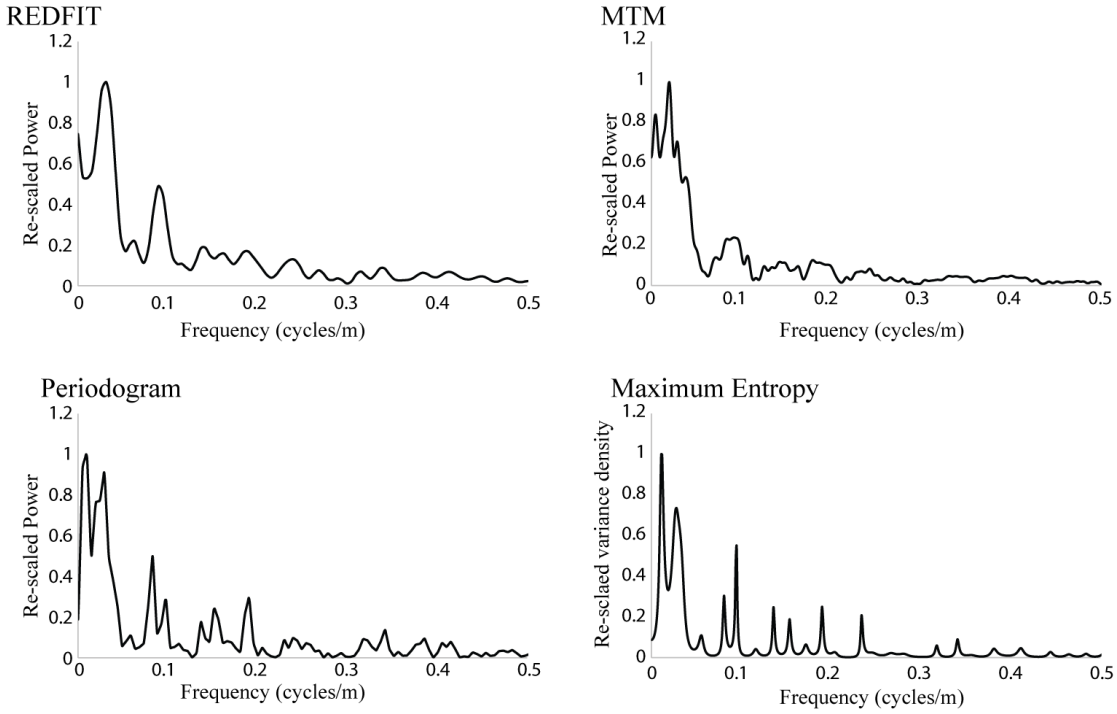

Figure 5.52 Methods of spectral estimation using the spectral total-gamma data of the Boltaña section. REDFIT spectral results used 6 WOSA segments, 8 degrees of freedom and a bandwidth of 0.024 cycles/m. MTM method used 4 tapers and ~ 8 degrees of freedom. The periodogram spectrum was computerised using a Bartlett window. The maximum entropy method used numbers of lags M = N/3 = 280). The analysis was undertaken using the REDFIT software developed by Schultz and Mudelsee (2002) and the Analyseries software package developed by Paillard *et al.* (1996).

Table 5.23 Methods of spectral estimation in the Boltaña section.

Spectral Method	Frequency (cycles/m)♠	Period (m)	Spectral Method	Frequency (cycles/m)♠	Period (m)
REDFIT	0.0315 **0.089** **0.147** **0.1628** **0.189**	31.7 11.2 6.8 6.1 5.3	Periodogram	0.01 0.029 **0.083** 0.098 **0.14** **0.153** **0.191**	100 34.5 12 10.2 7.2 6.5 5.2
MTM□	0.0085 **0.084** 0.095 **0.14** **0.153** **0.19**	118 11.9 10.5 7.2 6.5 5.3	Maximum entropy	0.012 0.029 **0.081** 0.095 **0.14** **0.153** **0.19**	83.3 34.5 12.3 10.5 7.4 6.5 5.3

♠ Frequencies from 0-0.2 cycles/m.
□Frequencies from the MTM significance test with confidence levels > 90%.
Frequencies which are consistently present in all the spectra are represented in bold numbers.

(b) REDFIT spectral results

REDFIT analyses of the Boltaña section using 6 WOSA segments reveal some significant frequencies within the 0-0.5 cycles/m frequency range (Figure 5.53). There is a clear significant frequency at 0.0315 cycles/m (1/31 m) which shows a prominent spectral peak in the total-gamma and K spectra well > 99% confidence level. This spectral frequency is also present > 99% confidence levels in the sandstone turbidite intensity spectrum. The frequency range 0.089-0.0942 cycles/m (1/11-1/10 m) is also present > 99% confidence level in the total-gamma and in the K spectra and > 95% confidence level in the Th spectrum. The frequency 0.147 cycles/m (1/7 m) is present in the total-gamma and in the K spectrum with confidence levels > 90%. Finally, the frequency range 0.18-0.19 cycles/m (1/6 m) is present in the total-gamma and Th spectra > 80% and 90% confidence levels, respectively. A list of all significant frequencies > 80% confidence levels within the frequency range 0-0.5 cycles/m can be

seen in Table 5.24. The confidence levels have been calculated after applying a power regression fitting curve to the background noise (Table 5.25).

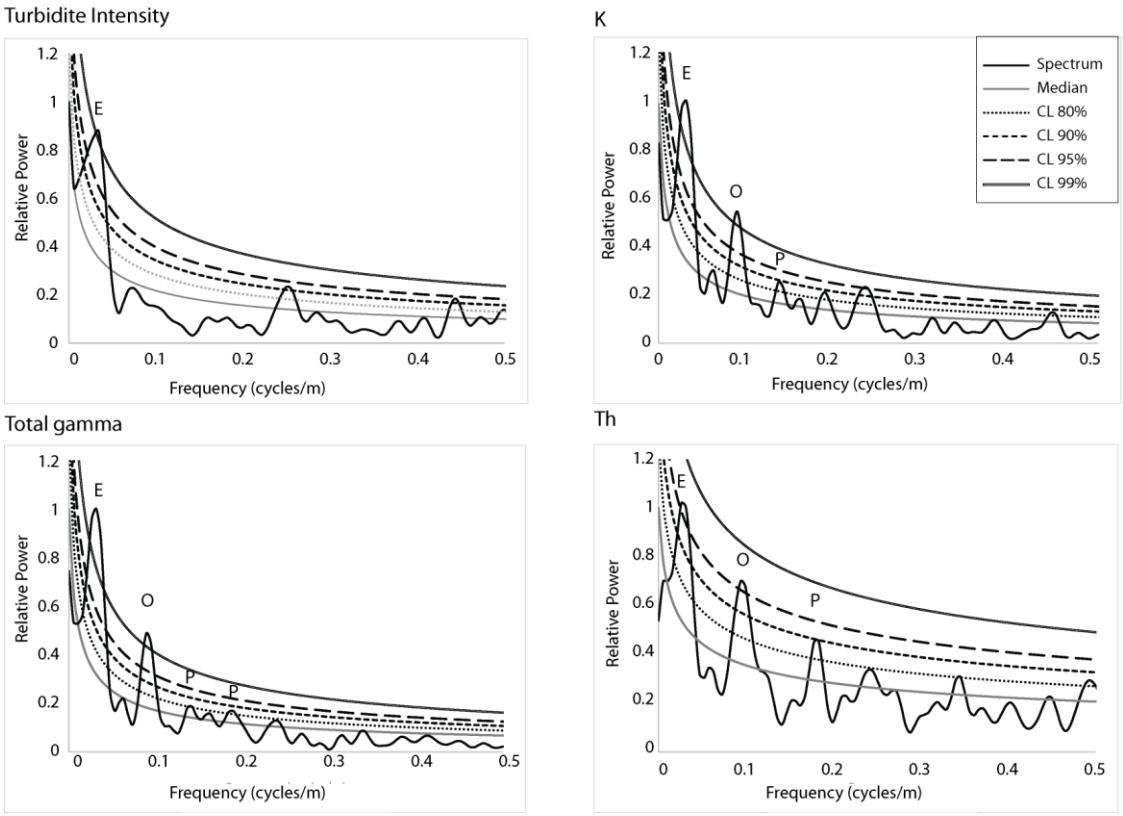

Figure 5.53 Time-series analysis of spectral gamma ray and sandstone turbidite intensity data using REDFIT. REDFIT spectral results used 6 WOSA segments; 8 degrees of freedom and a bandwidth of 0.024 cycles/m. REDFIT results are plotted using a power regression fitting model. Graphs have been re-scaled to allow comparison between variables. Analysis used the REDFIT software developed by Schulz and Mudelsee (2002).

Table 5.24 REDFIT time-series analysis results of the Boltaña section.

Data	Frequency (cycles/m)♠	Period (m)	Confidence level (%)
Total-gamma	0.0315 0.0892 0.147 0.1785	31.74 11.21 6.8 4.6	99 99 80 80
K	0.0315 0.0892 0.147 0.2363	31.74 11.21 6.8 4.2	99 99 90 90
Th	0.0261 0.0942 0.1883	38.31 10.61 4.31	95 95 90
Sandstone turbidite intensity	0.0315	31.74	99

REDFIT spectral results used 6 WOSA segments; 8 degrees of freedom and a bandwidth of 0.024 cycles/m.
♠Frequency range 0-0.5 cycles/m.

Table 5.25 Noise background estimation in the Boltaña section.

Data	AR1 (Mann and Lees, 1996)	Quadratic curve	Power regression
Total-gamma	2831	1988	**1150**
K	1523	1033	**588**
Th	158	145	**117**
Sandstone turbidite intensity	568	465	**210**

The table shows the summative squared error for different noise background curve-fitting methods. The best curve-fitting method contains the lowest summative square error and is shown in bold numbers. In the Boltaña section, the best fitting method for all the analysed data is the power regression method.

(c) ASM results

ASM analysis has identified significant SARs ranging from 19.5 to 68.5 cm/kyr (Figure 5.54). The most significant ASM results are the SARs between 26-30.5 cm/kyr with null hypothesis significance levels of 0.001%. Table 5.26 calculates the duration

of each cycle for all the frequencies at a specific SARs. A SAR of 30 cm/kyr very closely represents the duration of orbital cycles for the Middle Eocene using the equations of Berger *et al.* (1992). At a SAR of 30 cm/kyr, the frequencies 0.026 cycles/m (1/38 m) and 0.0315 cycles/m (1/32 m) represent eccentricity 123 and 95 kyr, respectively. The frequency range 0.089-0.094 cycles/m (1/10-1/11 m) can be linked to the obliquity 40 kyr cycle and the frequencies 0.147 cycles/m (1/7 m)) and 0.1883 cycles/m (1/4 m) represent precession 23 and 19 kyr cycles, respectively.

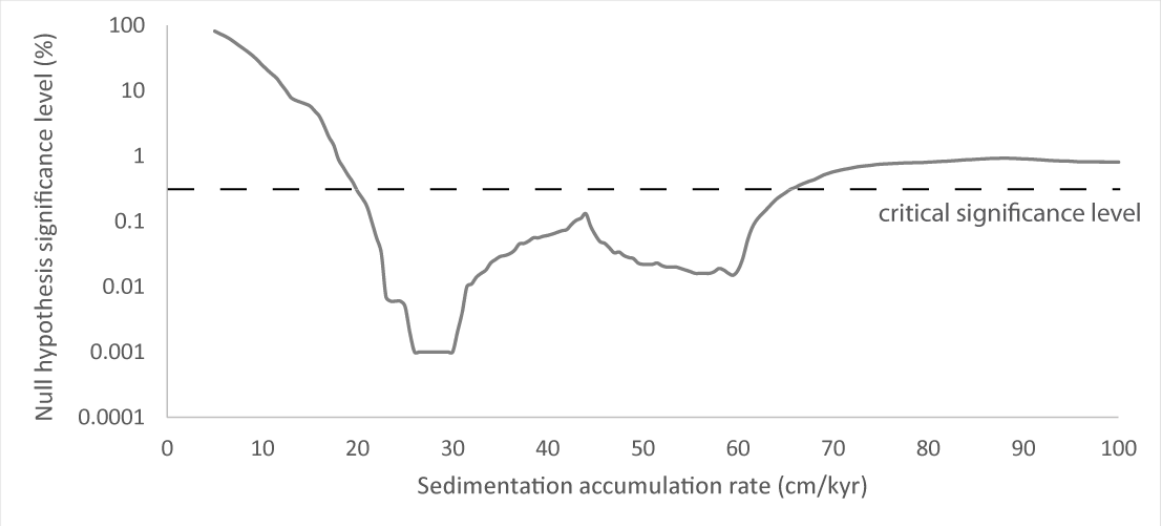

Figure 5.54 ASM results of the Boltaña section. A total of 7 frequencies identified from the spectral analysis of gamma-ray and sandstone turbidite intensity records and with a confidence level > 90% have been applied to the ASM analysis. For a list of all the frequencies refer to Table 5.26. The analysis used a Rayleigh number of 2.38948 x 10^{-4} and a Nyquist frequency of 2.4 cycles/m. Orbital parameters were established at ~ 45 Ma using Berger *et al.* (1992) equations. A total of 191 SARs ranging from 5-100 cm/kyr with an increment of 0.5 cm/kyr have been investigated using 100,000 Monte Carlo interactions. Critical levels were established at 0.52%. ASM analysis has identified significant SAR values ranging from 19.5 to 68.5 cm/kyr. The most significant ASM results are the SAR between 26-30.5 cm/kyr with null hypothesis levels of 0.001%. All 7 orbital parameters including eccentricity, obliquity and precession have been included in the ASM studies. The analysis used the ASM software developed by Meyers and Sageman (2007).

Table 5.26 Temporal period duration for significant frequencies in the Boltaña section.

Frequency (cycles/m)♠	C.L (%)	N □	Period (m)	Temporal periods (kyr) for each SAR									
				26 cm/kyr	26.5 cm/kyr	27 cm/kyr	27.5 cm/kyr	28 cm/kyr	28.5 cm/kyr	29 cm/kyr	29.5 cm/kyr	**30 cm/kyr**	30.5 cm/kyr
0.026	95	1	38.3	147	145	142	139	137	134	132	130	**128**	125
0.031	99	3	31.7	122	120	118	114	113	111	109	108	**105**	104
0.089	99	2	11.2	43.1	42.3	41.5	40.8	40	39.3	38.7	38	**37.4**	36.8
0.094	95	1	10.6	40.8	40.1	39.3	38.6	37.9	37.2	36.6	36	**34.4**	34.8
0.147	90	2	6.8	26.2	24.7	24.2	24.7	24.3	23.9	23.5	23	**22.7**	22.3
0.188	90	1	4.3	20.4	20	19.7	19.3	19	18.6	18.3	18	**17.7**	17.4
0.236	90	1	4.2	16.3	16	14.7	14.4	14.1	14.9	14.6	14.3	14.1	13.9

The table shows calculated cycle duration for each significant frequency (> 90% confidence levels) at different SARs. The SAR which is most closely associated with the Middle Eocene orbital periods (~ 45 Ma) is 30 cm/kyr. Underlined are frequencies which are contained in more than 1 spectrum with at least 1 confidence level > 95%. Estimated orbital cycles for the Middle Eocene (~ 45 Ma) using Berger *et al.* (1992) equations are: eccentricity 123.8 and 94.8 kyr, obliquity 52.3 and 40 kyr and precession 22.6 and 18.8 kyr.

♠ include all frequencies within the range 0-0.5 cycles/m with confidence levels > 90%.

□ number of parameters containing the specific frequency in the REDFIT spectrum.

(d) Wavelet analysis

The results from applying wavelet analysis are shown in Figure 5.55. There are a number of significant frequencies identified in the wavelet spectra with confidence levels > 90%. The most spatially persistent frequency is present at 0.03 cycles/m (1/33 m) and is significant in all the spectral data analysed. However, all the wavelet spectra show a decrease in power at this frequency in the 2nd half of the records, from 80 to 160 m height, below the 90% confidence levels. This frequency has been associated with eccentricity combining REDFIT and ASM analysis. The frequency 0.09 cycles/m (~ 1/11 m) has an intermittent spatial distribution and is better represented in the Th spectrum where it appears more continuous. This frequency is also present in the K and sandstone turbidite intensity spectra, but is not significant in the total-gamma spectrum. This frequency has been associated with obliquity. The 0.15 cycles/m (1/6 m) and 0.18 cycles/m (1/5 m) are only present sporadically in the wavelet spectra of all the parameters. These two frequencies have been linked to precession.

Figure 5.55 (next page) Wavelet analysis of the sandstone turbidite intensity, K, total-gamma and Th data in the Boltaña section. (a) Wavelet power spectrum represents spectral power at different frequencies throughout the Boltaña stratigraphic section. Black contours indicate the 10% significant regions. **(b)** Global wavelet shows the scale-averaged wavelet power across the studied frequency bands. Values to the right of the dashed line (90% confidence level) are significant. Significant spectral peaks which have been associated with Milankovitch frequencies using REDFIT and ASM analysis have been labelled (E-eccentricity, O-obliquity, and P-precession). Analysis used the online tool http://paos.colorado.edu.research/wavelets based on the algorithms of Torrence and Compo (1998).

Figure 5.55 Wavelet analysis of the Boltaña section.

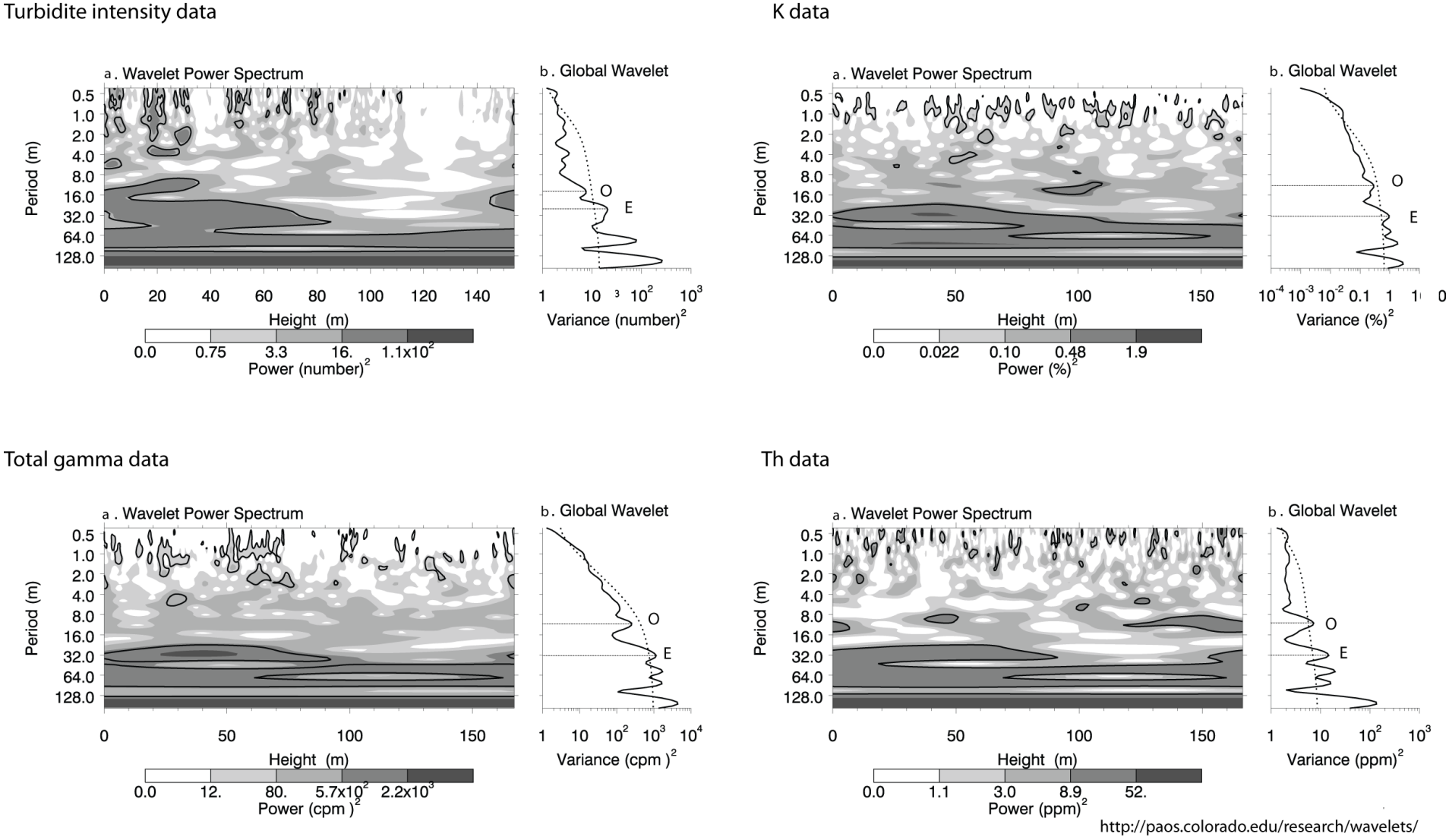

(e) Frequency-selective filtering

The two frequencies used for frequency-selective filtering were 0.0315 cycles/m (1/32 m) and 0.089 cycles/m (1/11 m) (Figure 5.56). These two frequencies are present in the REDFIT total-gamma spectrum > 99% confidence levels and have been associated with eccentricity and obliquity, respectively. The bandwidth used for filtering is 0.024 cycles/m which is the same determined by REDFIT analysis.

The filtered records using a frequency of 0.0315 cycles/m show well defined cycles only in the first half of the Boltaña section (0-80 m). These cycles become less defined and disappear in the second half of the filtered records. These results corroborate the wavelet analysis spectral results where this frequency was significant only in the first half of the section. The first half of the total-gamma record filtered at the frequency 0.089 cycles/m shows in general good amplitude obliquity cycles. These cycles become more evident and apparent in the second part of the records. The Boltaña record therefore, appears to be dominated by eccentricity in its first half and by obliquity in its second half.

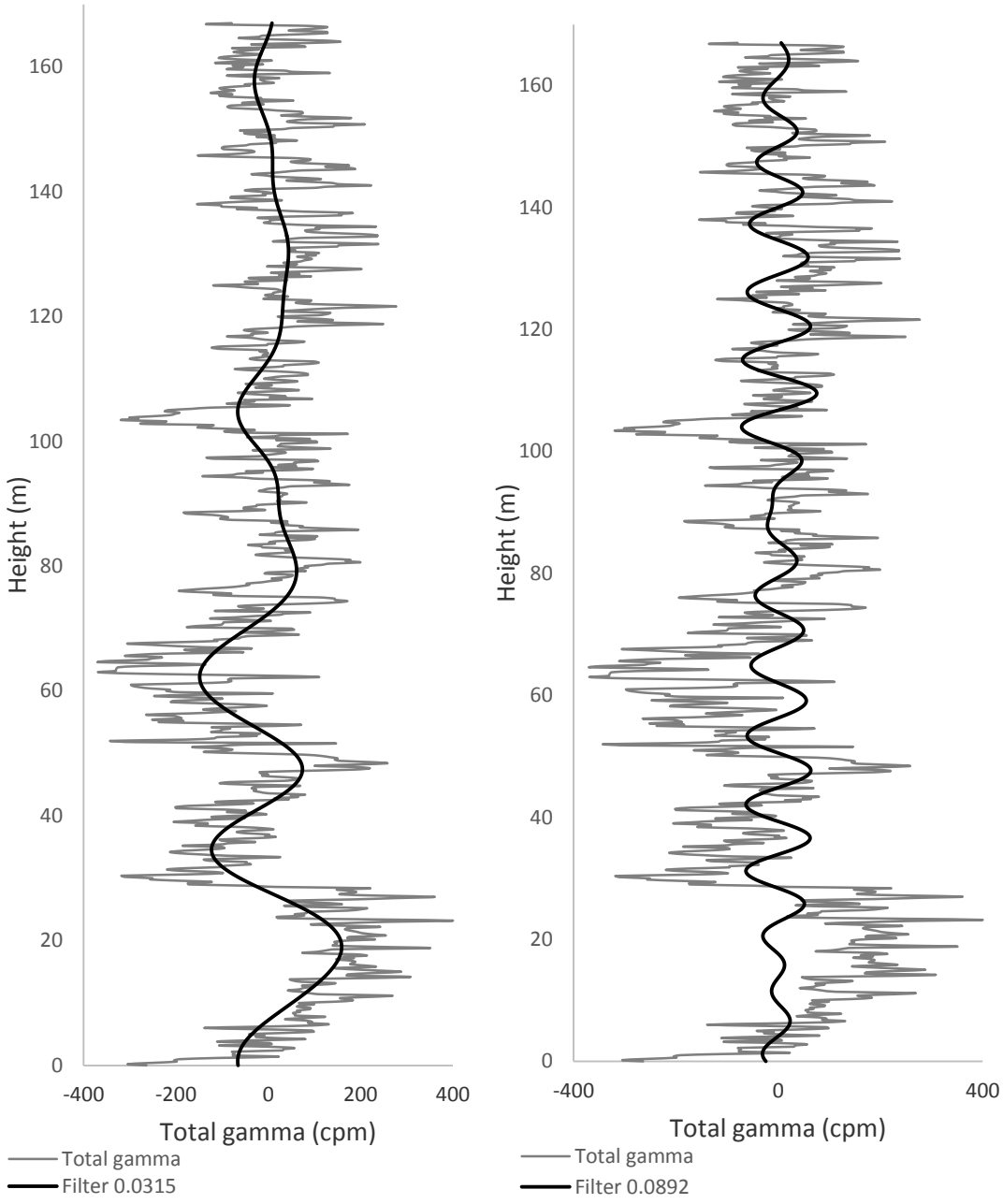

Figure 5.56 Frequency-selective filtering of the Boltaña section. Total-gamma records filtered to the frequencies 0.0314 and 0.0892 cycles/m. The frequency 0.0314 cycles/m has been associated with eccentricity 95 kyr cycles and the frequency 0.0892 cycles/m has been associated with obliquity 40 kyr cycles. Filtering used the program Analyseries (Paillard *et al.*, 1996).

(f) Orbital tuning

Orbital tuning of the Boltaña section has been performed by comparing the total-gamma records filtered to 0.0315 cycles/m which is the frequency associated with eccentricity to the eccentricity curves of the La2010a orbital solution of Laskar *et al.* (2011). A total of 6 anchor points have been used for tuning the records (Table 5.27). In the total-gamma filtered records, the depth points which constitute the top of each of the filtered cycles have been matched with eccentricity maxima points in the La2010a orbital solution of Laskar *et al.* (2011). The rest of the depth points in the total-gamma time series have been matched to absolute time by using a simple linear interpolation between the anchor points.

The Boltaña section has a good radiometric age control from biostratigraphic studies (Scotchman *et al.*, 2014) and magnetostratigraphic studies (Chapter 3). Age estimations using biostratigraphic studies suggest that the Ainsa System was deposited between 44.24 and 44.82 Ma (middle Lutetian), during nannofossil zone NP15 and shallow benthic foraminifera zone SBZ13- SBZ14 (Scotchman, *et al.*, 2014). Magnetostratigraphic studies show reverse polarity throughout the Boltaña section, likely to be within chron C20r. The C21n-C20r polarity reversal (45.72 Ma) has been identified at ~ 185 m height in the Labuerda section 2, approximately 165 m from the top of the section. This polarity reversal probably occurred during the deposition of the Banastón V succession. The Labuerda section 2 finishes in the Banastón VI System, no more than 50 m below the Ainsa I sandbody. The Boltaña section starts in the interfan deposits of the Banastón V and VI, ~ 15 m below the Banastón VI sandbody. It is not possible however, to estimate with accuracy the stratigraphic thickness which separates the Labuerda 2 and the Boltaña sections. Looking at the composite stratigraphy of the Ainsa Basin (Figure 5.1), the stratigraphic separation between these

two sections cannot be more than ~ 50 m. Therefore, it can be estimated that the Boltaña section is approximately 165-215 m above the C21n-C20r reversal at 45.72 Ma. SARs during the deposition of the Banastón and Ainsa systems from ASM studies (Figure 5.41, Figure 5.54) have been estimated to be between ~37 and 30 cm/kyr, respectively. Thus, the beginning of the Boltaña section is likely to have occurred between ~45.27-45 Ma.

Comparison between the eccentricity curves of the La2010a orbital solution of Laskar *et al.* (2011) and the total-gamma, filtered records, shows a similar curve pattern (Figure 5.57). The well-developed eccentricity cycles of the first half of the Boltaña records and the loss of cycle definition in the top 60 m can be matched to the eccentricity curves of the La2010a orbital solution of Laskar *et al.* (2011) between ~ 45.3 and 44.7 Ma (Figure 5.57). Several attempts have been undertaken to match the selected anchor points to the eccentricity maxima/minima points of the eccentricity curves of the orbital solution of Laskar *et al*. (2011) around this time interval. The best possible match between these two records (Figure 5.58) suggests the Boltaña section was deposited between 45.29 and 44.56 Ma which is close to the initial estimation from stratigraphic study. The Boltaña section is ~ 730 kyr in duration.

Table 5.27 Anchor points used for tuning the Boltaña section.

Height (m)	Age (Ma)	Matched cycle
19	45.226	Eccentricity maxima
47.4	45.120	Eccentricity maxima
79.4	45.015	Eccentricity maxima
104.8	44.9	Eccentricity minima
130.2	44.795	Eccentricity maxima
157.8	44.619	Eccentricity minima

The table shows the 6 anchor points used to tune the Boltaña section to eccentricity.

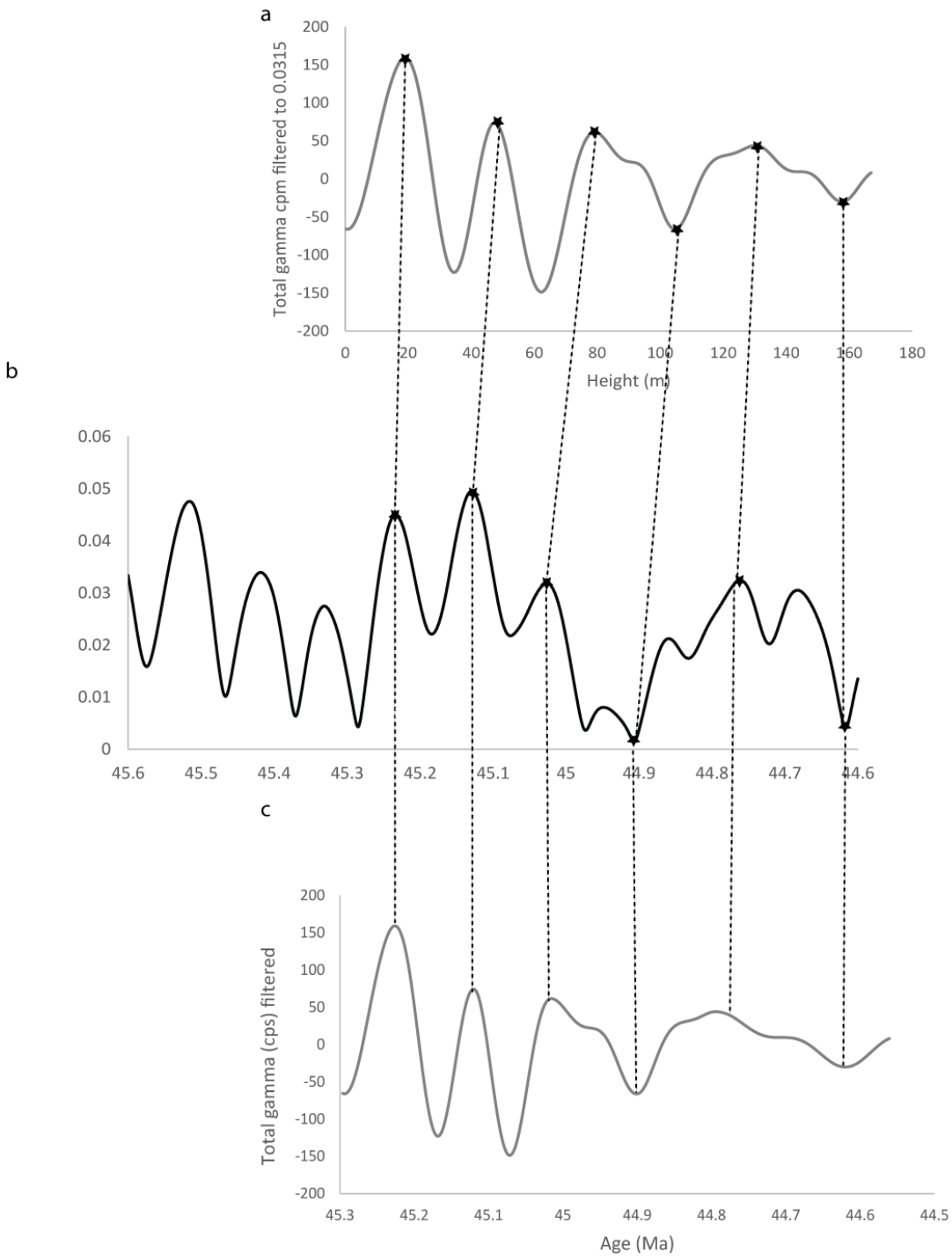

Figure 5.57 Orbital tuning of the Boltaña section. Filtered total-gamma records of the Boltaña section (Figure a) have been matched to eccentricity cycles of the La2010a orbital solution of Laskar *et al.* (2011) (Figure b) using 6 anchor points designated with an asterisk (*). The resulted tuned records (Figure c) show the distortion of the original data.

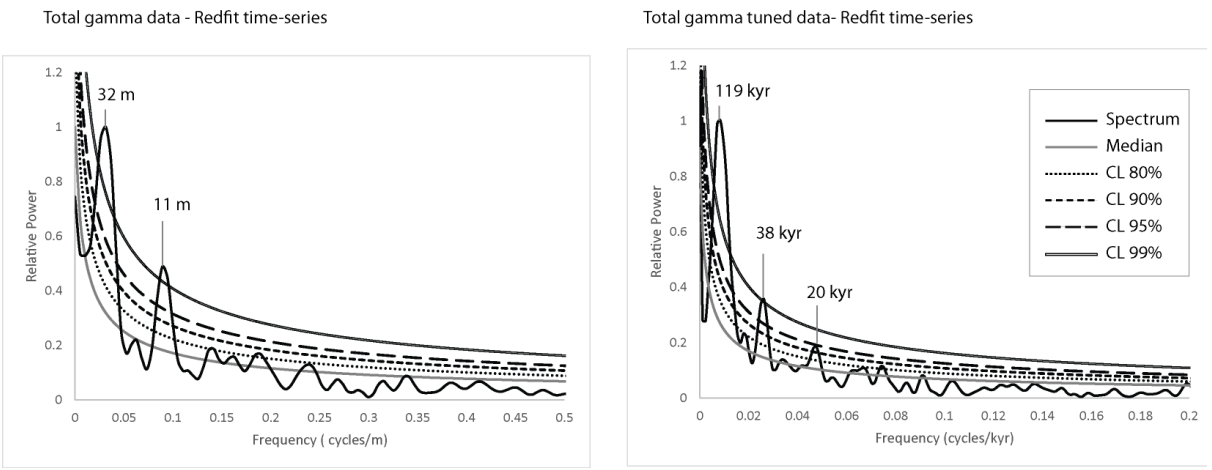

Figure 5.58 Spectral analysis using REDFIT of the Boltaña section tuned to eccentricity. The tuned records show eccentricity (119 kyr) and obliquity (38 kyr) cycles > 99% confidence levels and have a similar strength to the spectral peaks from non-tuned records. Tuning the records has strengthened a precession cycle (20 kyr) with a confidence level at 95% which was not significant in the original records.

SARs have been calculated from each of the intervals between anchor points to ensure the tuned records have not resulted in unrealistic SARs (Table 5.28). The SARs have varied between 14.6 cm/kyr and 30.5 cm/kyr although averaged values are ~ 24 cm/kyr. Figure 5.59 shows the variation of SAR across the Boltaña section and the averaged SAR of the section represented as a linear trend. The averaged value is similar to the one calculated using ASM analysis which yields an estimated averaged SAR of 26-30.5 cm/kyr.

Table 5.28 SARs in the Boltaña section calculated from tuning the records.

Height interval (m)	Age interval (Ma)	SAR (cm/kyr)
0-19	45.2964 - 45.226	27 cm/kyr
47.4-19	45.226 - 45.12	26.8 cm/kyr
79.4-47.4	45.12 - 45.015	30.5 cm/kyr
104.8-79.4	45.015 - 44.9	24.28 cm/kyr
130.2-104.8	44.9 - 44.795	24.2 cm/kyr
157.8-130.2	44.795 - 44.619	14.7 cm/kyr
167-157.8	44.619 - 44.56	14.6 cm/kyr

The table shows SAR calculated at different time intervals throughout the Boltaña section. SAR change from 14 to 30 cm/kyr and have averaged values of 24 cm/kyr.

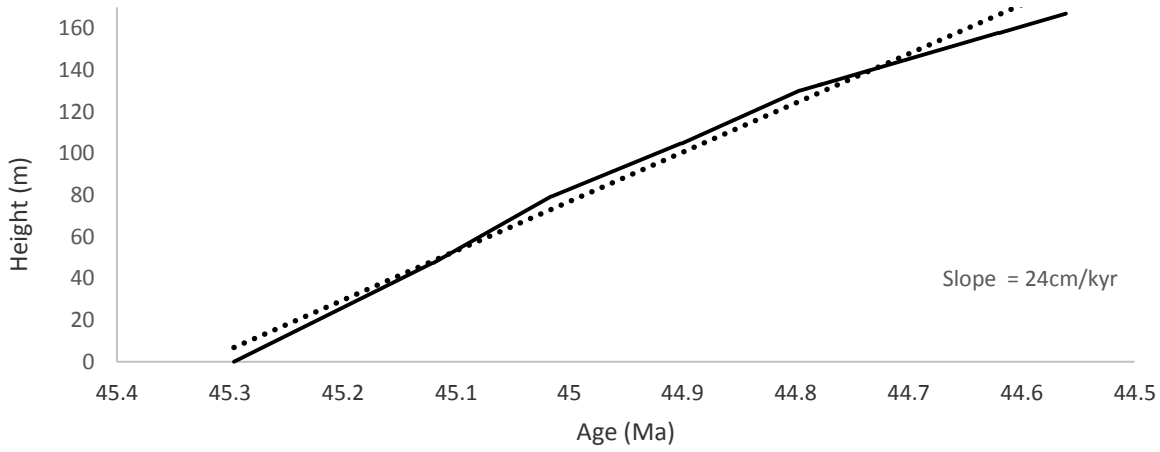

Figure 5.59 SAR in the Boltaña section calculated from orbital tuning the total-gamma records to eccentricity. Averaged SARs are ~ 24 cm/kyr and represented by a linear trend (dashed line). SARs in the Boltaña section have remained relatively stable, although the top of the section shows a decrease in the SAR.

5.3.4.5 Forcaz gamma-ray section

5.3.4.5.1 Geographical location of the Forcaz section

Forcaz section is 185 m long and is located ~ 1.9 km south of Labuerda town and ~ 2.4 km north of Ainsa town. The section can be accessed from the main road A-138 which joins the towns of Ainsa and Labuerda, and is located along the Forcaz stream, ~ 100 m to the west of the Labuerda sandstone quarry (Plate 5.11).

The section is fragmented into two subsections: Forcaz 1 (~ 105 m thick) and Forcaz 2 (~ 80 m thick) which are located ~ 100 m apart. Forcaz 1 is well exposed in a stream cut which joins the main Forcaz stream to the west, whilst Forcaz 2 forms a small hill. A small heterolithic package composed of medium-bedded turbidite allows the correlation between these two sections. Plate 5.11 also shows the position of the A6 core (Chapter 4). Plate 5.12 shows some of the outcrop photographs of the Forcaz section.

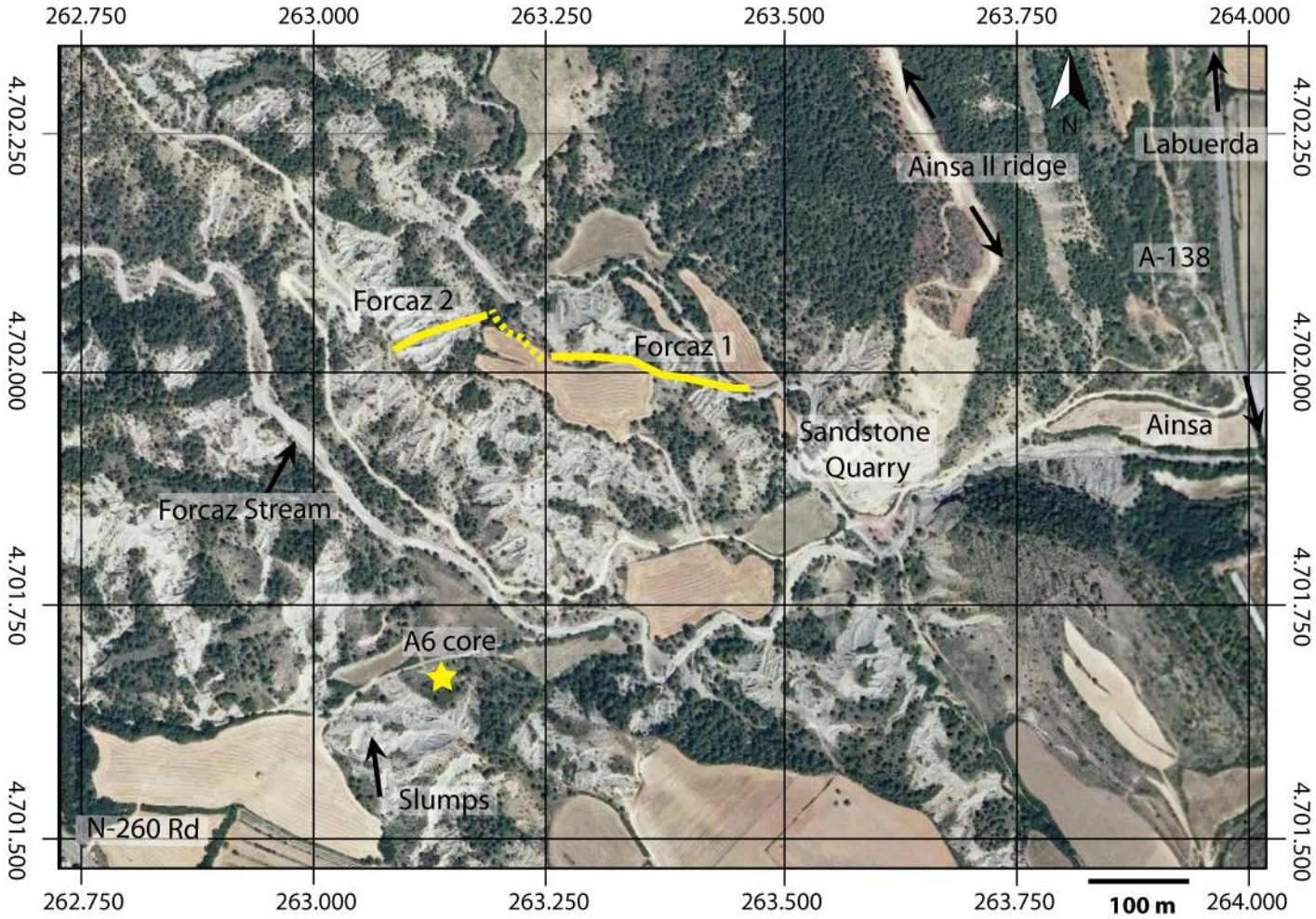

Plate 5.11 Aerial photograph of the gamma-ray logged Forcaz section. The photograph shows the two correlated sections Forcaz 1 and Forcaz 2. The location of the Well A6 (Chapter 4) is also shown. Aerial image from www.sigpac.mapa.es/fega/visor.

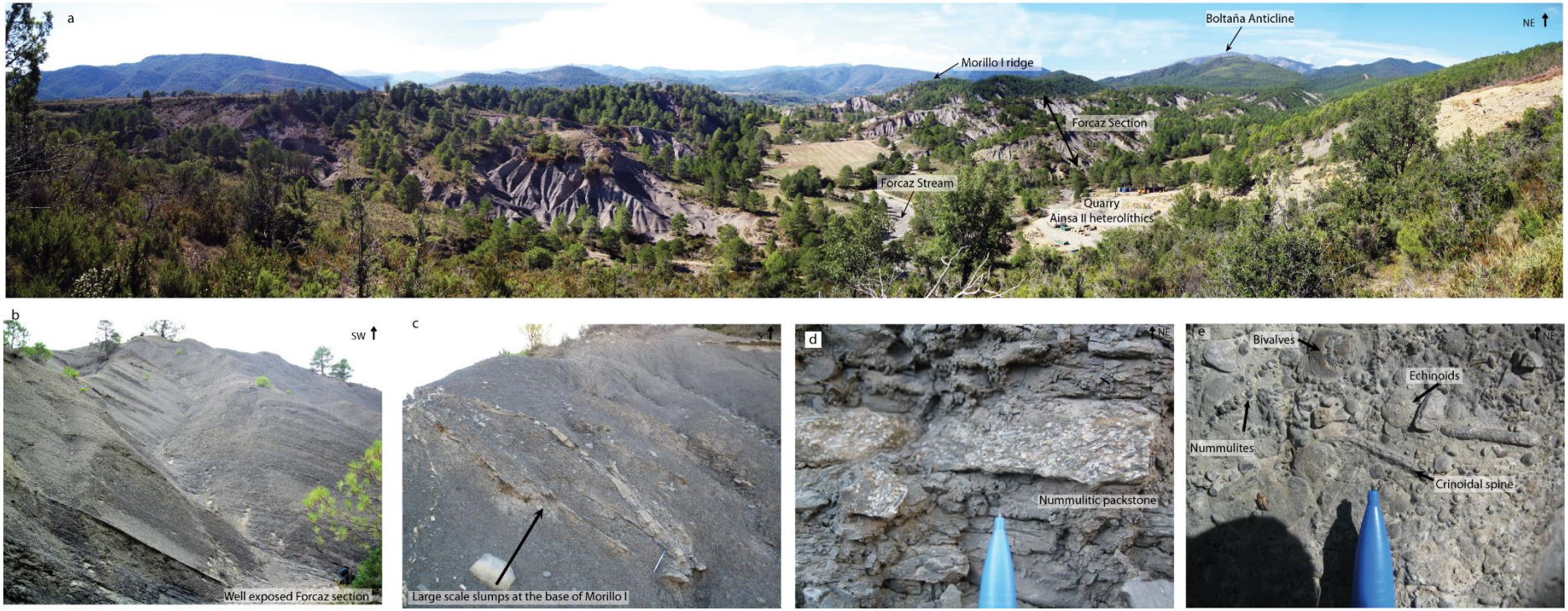

Plate 5.12 Outcrop photographs of the Forcaz gamma-ray logged section. (a) Panorama photograph showing the location of the Forcaz section in between the Ainsa II sandbody which has been extensively quarried at this locality and the Morillo I sandbody which forms a prominent, densely-vegetated ridge to the northeast of the Forcaz section. This area is characterised by a very good exposure of fine-grained sediments forming weathered hills incised by seasonal streams. **(b)** Outcrop photograph of the Forcaz section 1 showing the well exposed outcrop along the stream. **(c)** Outcrop photograph showing large-scale slumps present ~ 50 m above the top of the Forcaz section. These slumps have been studied in detail in the top 40 m of the A6 core and mark the initiation of the Morillo System. **(d)** Close-up photograph of a ~ 3 cm nummulite packstone associated with the slumped sediments in the area where the A6 core was drilled. These re-deposited fossiliferous beds are common towards the top of the A6 core and have also been observed in some beds of the Forcaz 2 log and have been interpreted as tempestites (Chapter 4). **(e)** Close-up photograph of a coarse-grained fossiliferous sandstone bed containing numerous bioclasts including nummulites, bivalves, crinoids and echinoids.

5.3.4.5.2 Stratigraphic location

The Forcaz section comprises the fine-grained overbank and interfan deposits between the Ainsa II and Morillo I sandbodies. Figure 5.60 shows a geological map, a cross-section and a stratigraphic column with the position of the Forcaz section. The Ainsa III sandbody is off-axis at this location and is represented by a ~ 15 m thick heterolithic package which is present at ~ 30 m height in the Forcaz section. The sedimentary logs (Figure 5.61) and the sandstone turbidite intensity graph (Figure 5.62) show this sandy-rich package. Although, there is some tectonic deformation in the area with a thrust affecting the Ainsa II System (Figure 5.60), the Forcaz section is completely undeformed. The base of the Morillo I System is off-axis at this location and is represented by a thin heterolithic package of ~ 15 m thick. This heterolithic package can be seen in the southeastern corner of Figure 5.60. It is estimated that the base of the Morillo I sandbody is ~ 130 m above the top of the Forcaz section and ~ 50 m above the top of the A6 core. There is an overlap between the sediments of the A6 core and the Forcaz section. The lowest 50 m of the A6 core contains a high concentration of sandstone turbidites interpreted as the off-axial Ainsa III sandbody (Chapter 4). This sandy interval in the core is likely to correlate with the heterolithic package present at ~ 30 m height in the Forcaz section. Therefore, it can be inferred that the Forcaz section is mostly contained within the sediments of the Well A6 core.

The sandstone turbidite intensity graph (Figure 5.62) shows that the Forcaz section contains the lowest sandstone percentage of all the gamma-ray logged sections. The Boltaña section which is also located within the Ainsa System shows relatively low sandstone turbidite intensity values when compared with other interfan systems. Therefore, it appears that the interfan and overbank sediments of the Ainsa System are

less sandy than the rest of the Ainsa deep-marine systems. Figure 5.63 shows the K, Th and U values of the Forcaz section.

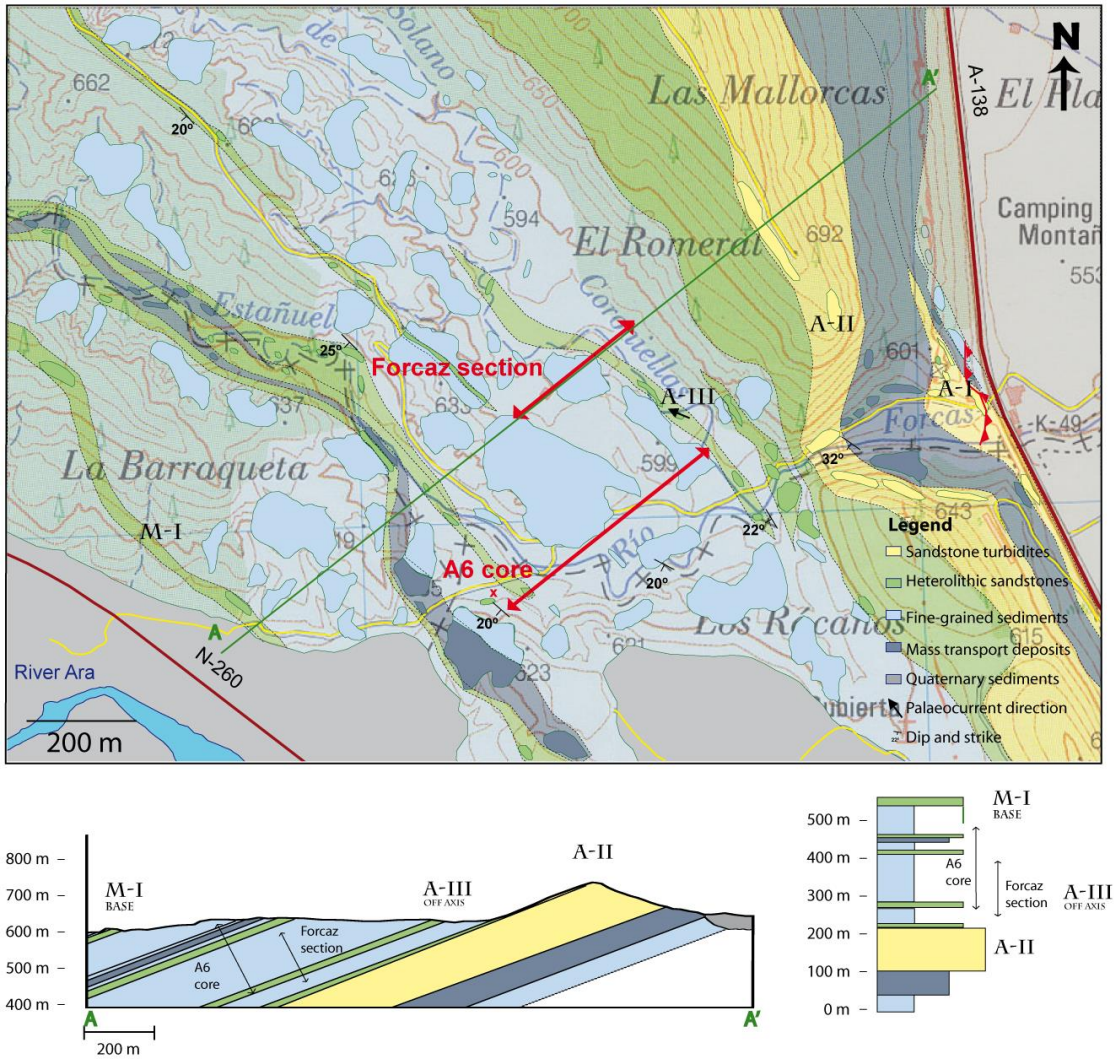

Figure 5.60 Geological map, cross-section and vertical stratigraphic column of the Forcaz section. (a) Geological map of the area surrounding the Forcaz gamma-ray section. The western part of the map shows an area of tectonic deformation in the proximities of the A-138 road. A thrust has caused deformation of the Ainsa 1 sandbody and shearing of the underlying fine-grained sediments exposed at the road cut. There is also another thrust at ~ 70 m depth of the A6 core but it is likely to be located just above the top of the Forcaz section. It has not been possible to trace this thrust across the geological map. The green line indicates the position of the cross-section A-A'. **(b)** Cross-section A-A' showing the position of the Forcaz gamma-ray logged section in the interfan sediments of the Ainsa II and Morillo I sandbodies. The Ainsa III sandbody is off-axial at this location and is represented by a small heterolithic package (~ 15 m thick) present at 30-45 m height in the Forcaz section. **(c)** Stratigraphic column of the Forcaz area showing the position of the Forcaz section and the Well A6 core.

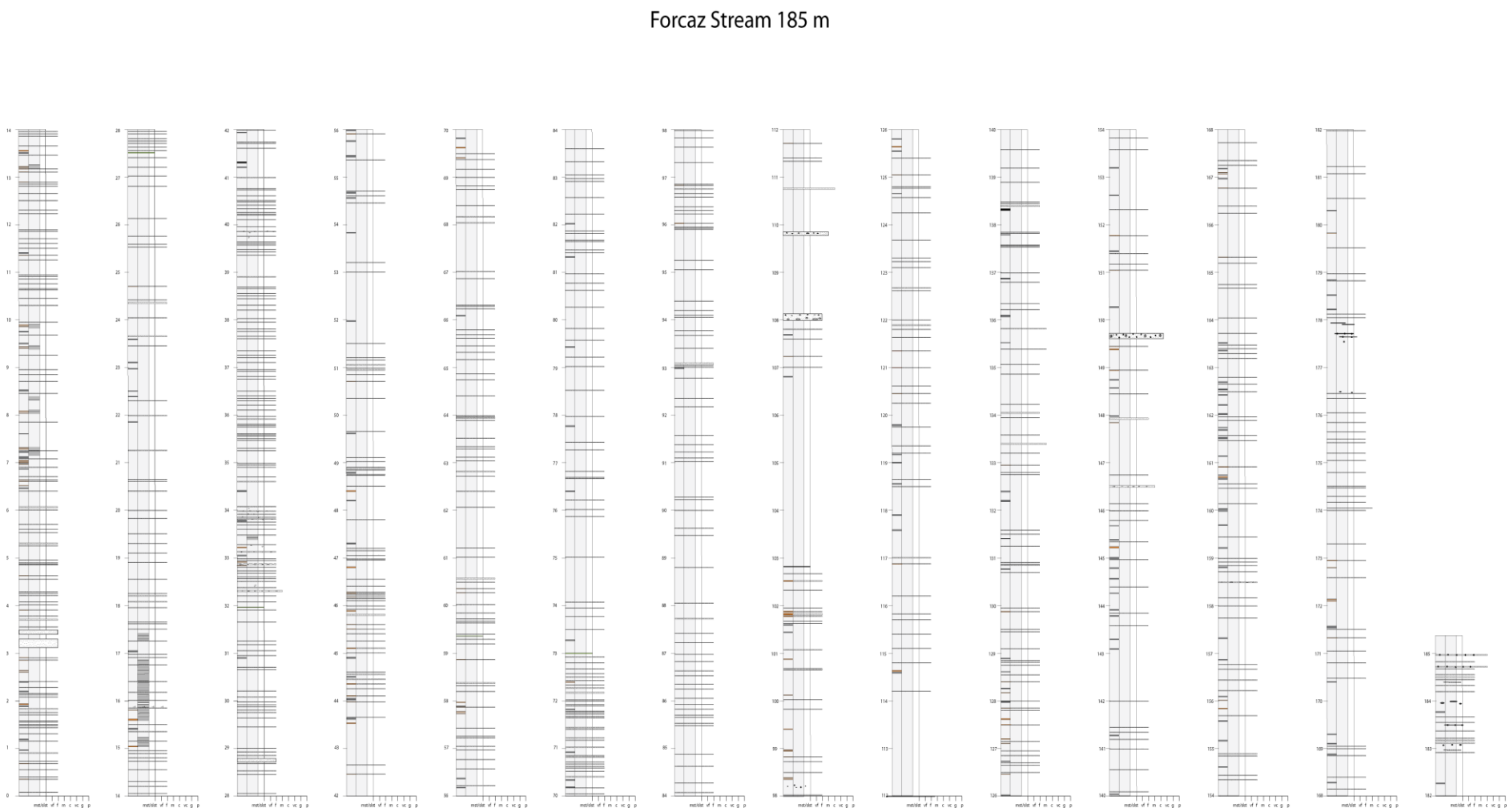

Figure 5.61 Sedimentary logs of the Forcaz section. Sedimentary logs of the Forcaz section including every bed thicker than 0.5 cm. Figure 2.5 includes a legend of the symbols used in the sedimentary logs. An electronic version of these sedimentary logs for detailed visualization is available in Appendix 3.

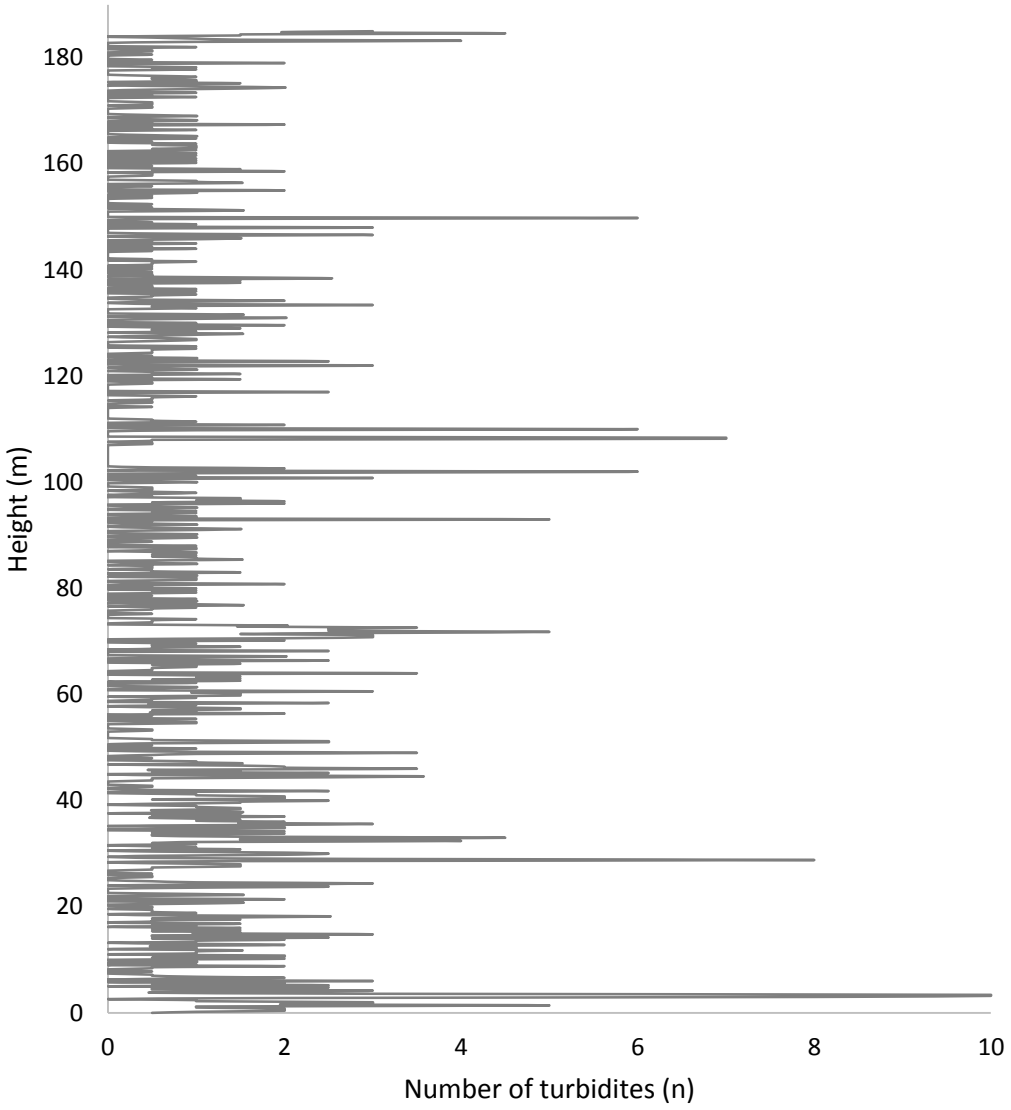

Figure 5.62 Sandstone turbidite intensity in the Forcaz section. The averaged sandstone percentage for the whole section is ~ 3.6%. The sandstone turbidite intensity of the Forcaz section together with the Boltaña section which is also located within the Ainsa System constitutes the lowest sandstone content of all the fine-grained deposits in the Ainsa Basin.

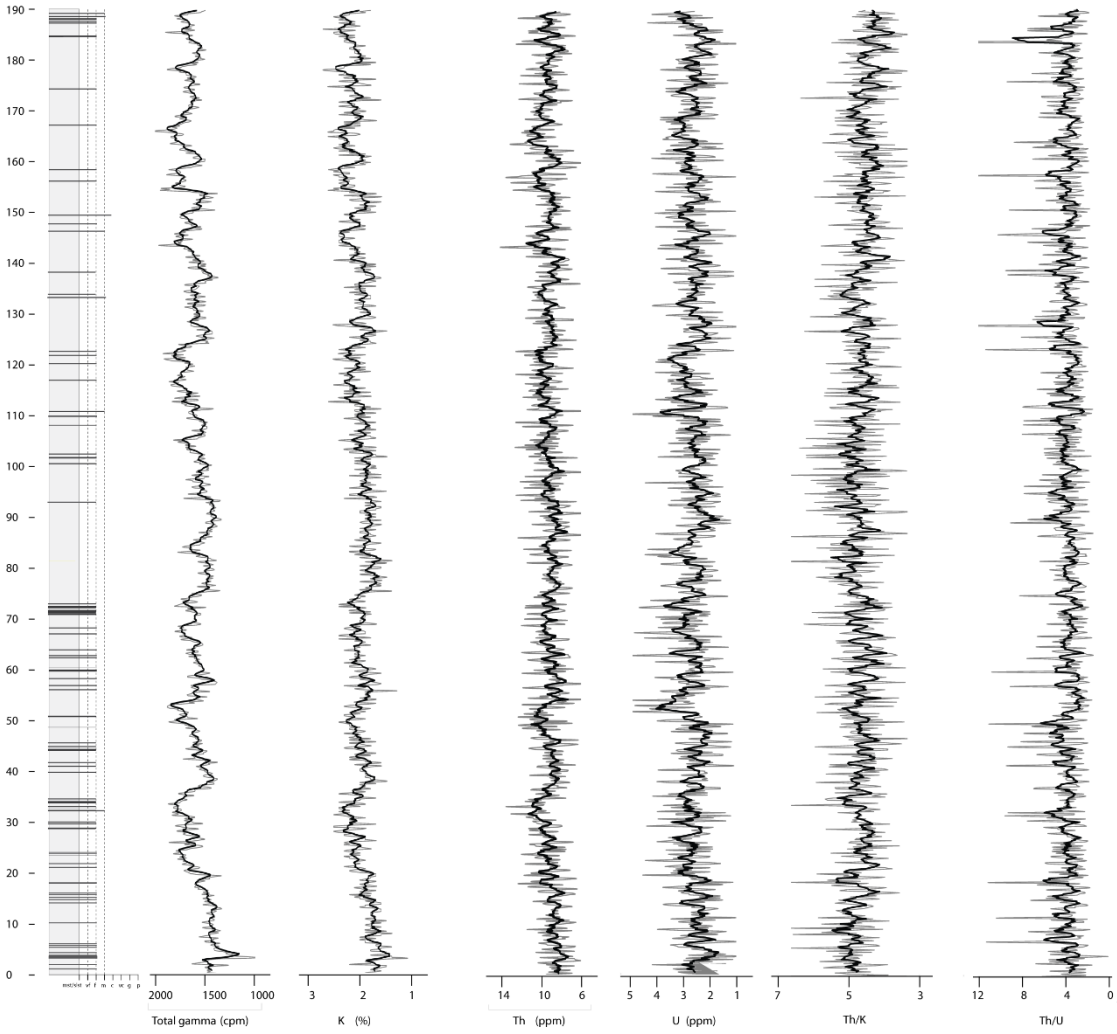

Figure 5.63 Simplified sedimentary logs of the Forcaz section plotted against total-gamma (cpm), K (%), Th (ppm) and U (ppm), Th/U and Th/K. Black line is a 4-period moving average. Simplified logs only show sandstone turbidites ≥ 1.5 cm, for complete logs refer to Figure 5.61 and Appendix 3.

5.3.4.5.3 Cyclostratigraphic studies of the Forcaz section

(a) Methods of spectral estimation

The total-gamma spectrum of the Forcaz section has been estimated using four different methods: the REDFIT, the MTM, the maximum entropy and the periodogram modified with a Bartlett window. Figure 5.64 shows the spectral results obtained from applying these four methods. All the spectra generated show a similar shape, although smoother results are achieved with the REDFIT method. Table 5.29 summarises the

main frequencies present within the frequency range 0-0.2 cycles/m. The frequency 0.024-0.028 cycles/m (1/35-1/41 m), 0.084-0.094 cycles/m (1/10-1/11 m) and 0.188 cycles/m (1/5 m) consistently appear in all of the spectra analysed.

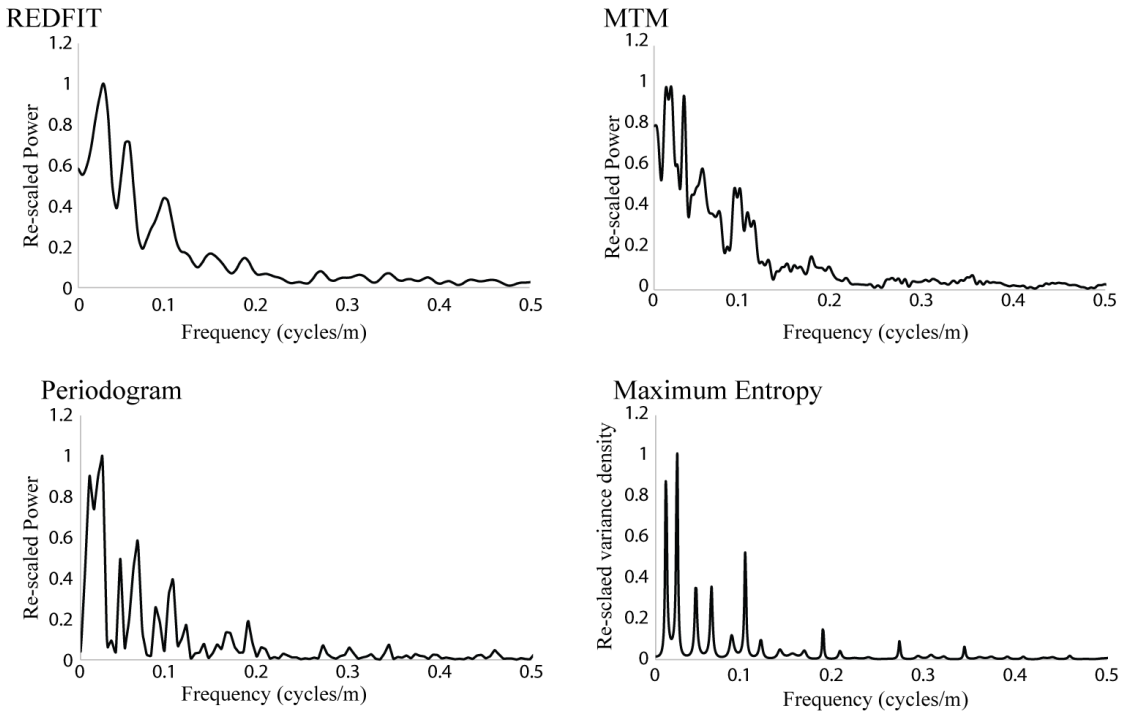

Figure 5.64 Methods of spectral estimation using Forcaz spectral total-gamma data. REDFIT spectrum uses 6 WOSA segments, 8 degrees of freedom and a bandwidth of 0.023 cycles/m. The MTM method uses 4 tapers and ~ 8 degrees of freedom. The periodogram spectrum uses a Barlett window. The maximum entropy method uses numbers of lags M = N/3 = 309). Analysis used the REDFIT software developed by Schultz and Mudelsee (2002) and the Analyseries software package developed by Paillard *et al.* (1996).

Table 5.29 Methods of spectral estimation in the Forcaz section.

Spectral Method	Frequency (cycles/m)♠	Period (m)	Spectral Method	Frequency (cycles/m)♠	Period (m)
REDFIT	**0.0283**	35.3	Periodogram	0.01	100
	0.056	17.9		**0.024**	41.7
	0.094	10.6		0.044	22.7
	0.151	6.6		0.063	15.9
	0.1889	5.3		**0.084**	11.9
				0.103	9.7
				0.117	8.5
				0.164	6.1
				0.187	5.3
MTM□	0.0079	127	Maximum entropy	0.011	90.9
	0.024	41.7		**0.024**	41.7
	0.043	23.3		0.045	22.2
	0.063	15.9		0.062	16.1
	0.084	11.9		**0.085**	11.8
	0.1	10		0.099	10.1
	0.117	8.5		0.117	8.5
	0.15	6.7		**0.186**	5.4
	0.186	5.4			

♠ Frequencies from 0-0.5 cycles/m.
□Frequencies present in the MTM significance test with confidence levels > 80%.
The frequencies that consistently appear in all the spectra are represented in bold numbers.

(b) REDFIT time-series

REDFIT analyses of the Forcaz section using 6 WOSA segments reveal some significant frequencies within the 0-0.5 cycles/m range (Figure 5.65). The analysis has used a power regression method to estimate the background noise. The summative error in the total-gamma spectrum is very similar when applying the AR1 fitting-curve method of Mann and Lees (1996) or the power regression method. The latter method was the one chosen as it was most adequate for the other datasets (Table 5.30). There are two main frequency ranges which are represented with good confidence levels in all the parameters analysed. The frequency range 0.024-0.028 cycles/m (1/42-1/35 m) is more significant in the total-gamma (> 99% confidence levels) and in the K and sandstone turbidite intensity spectra (> 95% confidence levels), but is less significant in the Th data (only > 80% confidence levels). The second most prominent frequency

range is the 0.08-0.099 cycles/m (1/10-1/12 m) which is present in all the analysed spectra with confidence levels > 95% and 99%. The sandstone turbidite intensity spectrum shows other significant frequencies at 0.137 cycles/m (1/7 m), 0.199 cycles/m (1/5 m) and 0.227 cycles/m (1/4 m), all > 95% confidence levels. A summary of all the significant frequencies can be seen in Table 5.31.

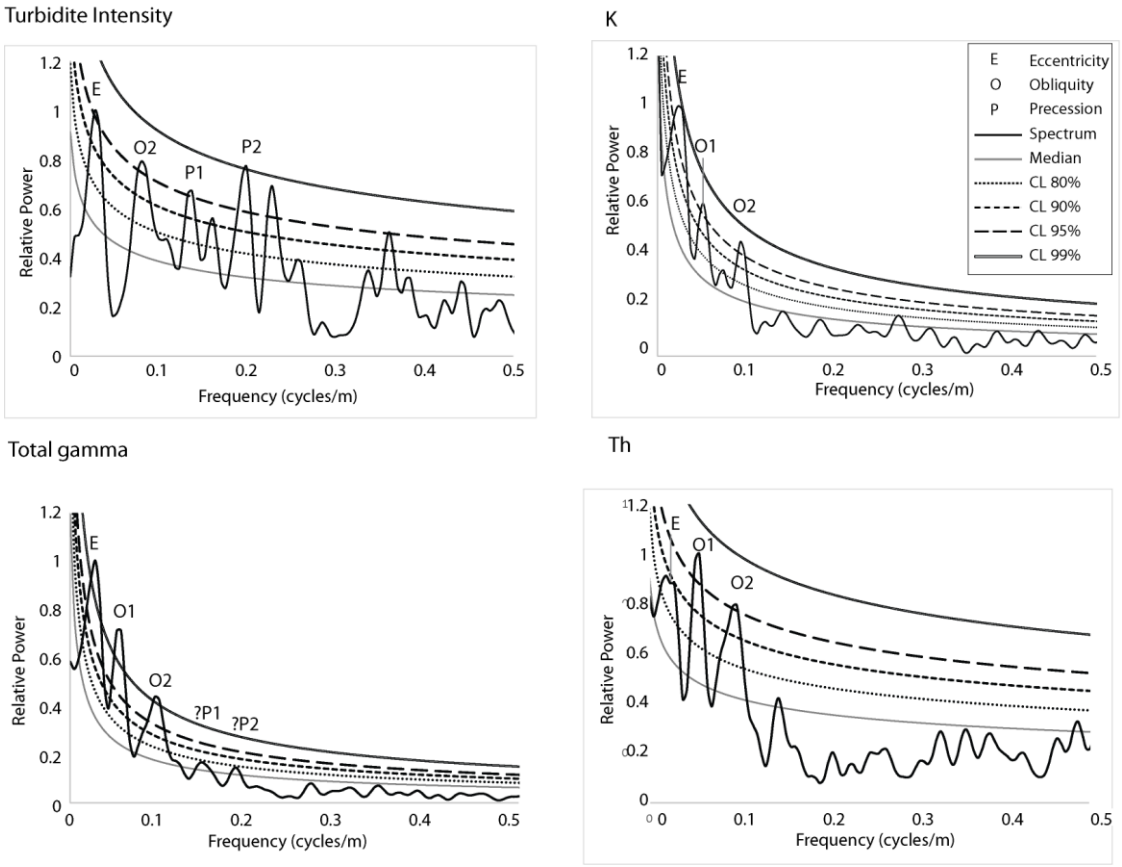

Figure 5.65 Time-series analysis of spectral gamma ray and sandstone turbidite intensity data using REDFIT. REDFIT spectral results used 6 WOSA segments, 8 degrees of freedom and a bandwidth of 0.023 cycles/m. REDFIT results plotted using a power regression fitting model. Spectra have been re-scaled to allow comparison between variables. Analysis used the REDFIT software developed by Schulz and Mudelsee (2002).

Table 5.30 Noise background estimation of the Forcaz section.

Data	AR1 (Mann and Lees, 1996)	Quadratic curve	Power regression
Total-gamma	1464	2462	**1475**
K	796	1082	**325**
Th	175	167	**139**
Sandstone turbidite intensity	190	167	**150**

Summative square errors using the AR1 model of Mann and Lees (1996), a quadratic curve and a power regression method. The method with the least summative square error indicates the most adequate fitting curve method (bold numbers).

Table 5.31 REDFIT time-series analysis of the Forcaz section.

Data	Frequencies (cycles/m)♠	Period (m)	Confidence level (%)
Total-gamma	0.0283 0.0566 0.094	34.27 17.64 10.58	99 99 99
K	0.0236 0.052 0.0945	42.28 19.22 10.57	95 95 95
Th	0.0283 0.0567 0.0993	34.33 17.64 10.07	80 95 95
Sandstone turbidite intensity	0.0284 0.0805 0.1374 0.1611 0.199 0.2275 0.3602	34.16 12.42 7.28 4.21 4.02 4.4 2.77	95 95 95 90 99 95 95

REDFIT spectral results using 6 WOSA segments and ~ 8 degrees of freedom.
♠Frequencies shown are between the frequency range 0-0.5 cycles/m.

(c) ASM studies

The ASM analysis identifies significant SARs ranging from 12 to 93 cm/kyr (Figure 5.66). The most significant ASM results are within the SAR ranges 22.5-24 cm/kyr

and the SAR 33.5 cm/kyr which have a null hypothesis level of 0.001%. Table 5.32 calculates the cycle duration for each frequency at different SARs. Using the equations of Berger *et al.* (1992), the SAR which most closely matches the orbital cycles for the Middle Eocene is 33.5 cm/kyr. At a SAR of 33.5 cm/kyr, the frequencies 0.0236 cycles/m and 0.0283 cycles/m can be linked to eccentricity 123 and 95 kyr respectively. The frequency 0.052 cycles/m and the cycles range 0.08-0.094 cycles/m can be matched to obliquity 52 kyr and obliquity 40 kyr, respectively. The frequencies 0.1374 and 0.199 cycles/m are probably associated with the precession cycles 23 and 19 kyr, respectively.

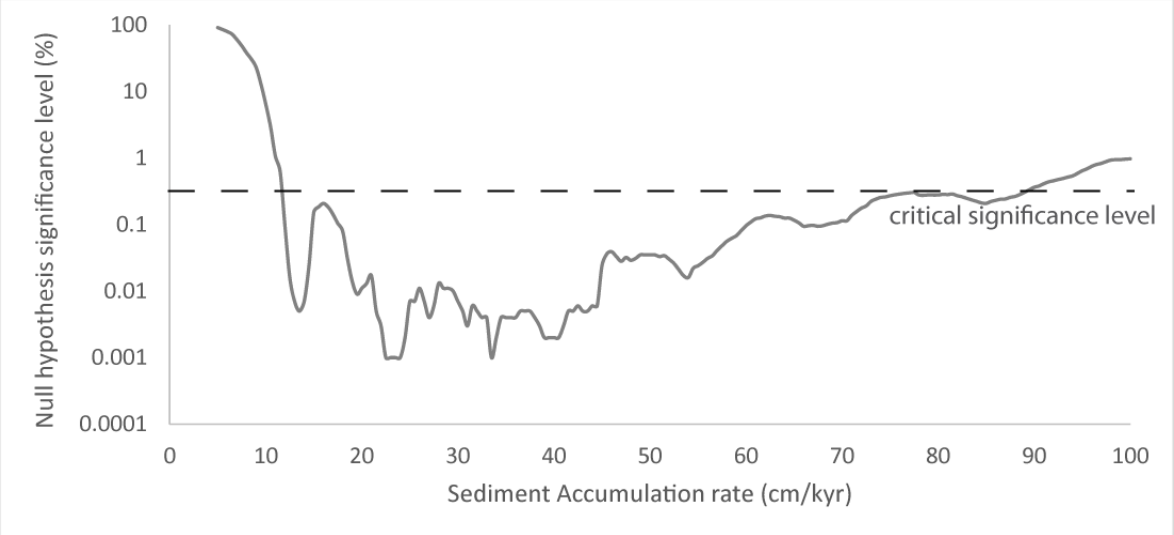

Figure 5.66 ASM results of the Forcaz section. A total of 11 frequencies identified from the spectral analysis of the spectral gamma-ray and the sandstone turbidite intensity records with confidence levels > 95% have been applied to the ASM analysis. For a list of the frequencies refer to Table 5.32. The analysis used a Rayleigh number of 2.152852 x 10^{-4} and a Nyquist frequency of 2.4 cycles/m. Orbital parameters were established at ~ 45 Ma using Berger *et al.* (1992) equations. A total of 191 SARs ranging from 5-100 cm/kyr with an increment of 0.5 cm/kyr were investigated using 100,000 Monte Carlo simulations. Critical levels were established at 0.52%. ASM analysis has identified significant SAR ranging from 12 to 93 cm/kyr. The most significant ASM results are the SAR between 22.5-24 cm/kyr and at 33.5 cm/kyr which have a null hypothesis level of 0.001%. All 7 orbital parameters including eccentricity, obliquity and precession have been included in the ASM studies. Analysis used the ASM software developed by Meyers and Sageman (2007).

Table 5.32 Temporal period duration of significant frequencies in the Forcaz section.

Frequency (cycles/m)♠	C.L (%)	N □	Period (m)	Period duration (kyr) at different SARs				
				22.5 cm/ kyr	23 cm/ kyr	23.5 cm/ kyr	24 cm/ kyr	**33.5 cm/ kyr**
0.0236	95	1	42.4	188.3	184.2	180.3	176.5	**126.4**
0.0283	99	3	34.3	157	153.6	150.4	147.2	**104.5**
0.052	95	1	19.2	84.5	83.6	81.8	80.1	**57.4**
0.0566	99	2	17.7	78.5	76.8	74.2	73.6	**52.7**
0.0805	95	1	12.4	54.2	54	52.9	51.7	**37.1**
0.094	99	2	10.6	47.3	46.2	44.3	44.3	**31.7**
0.099	95	1	10.1	44.9	43.9	43	42.1	30.1
0.1374	95	1	7.3	32.3	31.6	31	30.3	**21.7**
0.199	99	1	5	22.3	21.8	21.4	20.9	**15**
0.2275	95	1	4.4	19.5	19.1	18.7	18.3	13.1
0.3602	95	1	2.8	12.3	12.1	11.8	11.6	8.3

The table shows calculated cycle duration for each significant frequency (> 95% confidence levels) at different SARs. The SAR which most closely matches the orbital periods for the Middle Eocene appear highlighted in bold numbers.
Underlined are all the frequencies which are contained in more than 1 spectrum with at least 1 confidence level > 95%.
Estimated orbital cycles for the Middle Eocene (~ 45 Ma) using Berger *et al.* (1992) equations are: eccentricity 123.8 and 94.8 kyr, obliquity 52.3 and 40 kyr and precession 22.6 and 18.8 kyr.
♠ include all frequencies within the range 0-0.5 cycles/m with confidence levels > 90%.
□ number of parameters containing that specific frequency in the REDFIT spectrum.

(d) Wavelet analysis

Results from the wavelet analysis include a number of significant frequencies which approximate those frequencies identified using the REDFIT spectral estimation method (Figure 5.67). The most spatially persistent frequency is present at 0.024-0.028 cycles/m (1/42-1/34 m). This frequency has been associated with eccentricity combining REDFIT and ASM analysis and is significant > 90% confidence levels in all the analysed records. This frequency is present > 90% confidence levels throughout the stratigraphy in the K, Th and total-gamma wavelet spectra. Although, this frequency is significant in the sandstone turbidite intensity records, the wavelet spectrum shows an interval of 60 m, between 90 m and 150 m height, where this frequency is not significant. The frequency 0.08-0.09 cycles/m (~ 1/10-1/11 m) which has been associated with obliquity, has an intermittent spatial distribution in the wavelet spectrum and appears only at specific intervals in the stratigraphic records of all the analysed data. The frequencies 0.13 cycles/m (1/7 m) and 0.2 cycles/m (1/5 m), both linked to precessional cycles, have also an intermittent spatial distribution in the wavelet spectra of all the analysed records.

Figure 5.67 (next page) Wavelet analysis of the sandstone turbidite intensity, K, total-gamma and Th data of the Forcaz section. (a) The wavelet power spectrum shows spectral power at different frequencies throughout the Forcaz stratigraphic section. Black contours mark the 10% significant regions. **(b)** The global wavelet shows the scale-averaged wavelet power across the studied frequency bands. Values to the right of the dashed line are significant > 90% confidence level. Significant spectral peaks which have been associated with Milankovitch frequencies using REDFIT and ASM analyses, have been labelled (E-eccentricity, O-obliquity, and P-precession). Analysis used the online tool http://paos.colorado.edu.research/wavelets based on the algorithms of Torrence and Compo (1998).

Figure 5.67 Wavelet analysis of the Forcaz section.

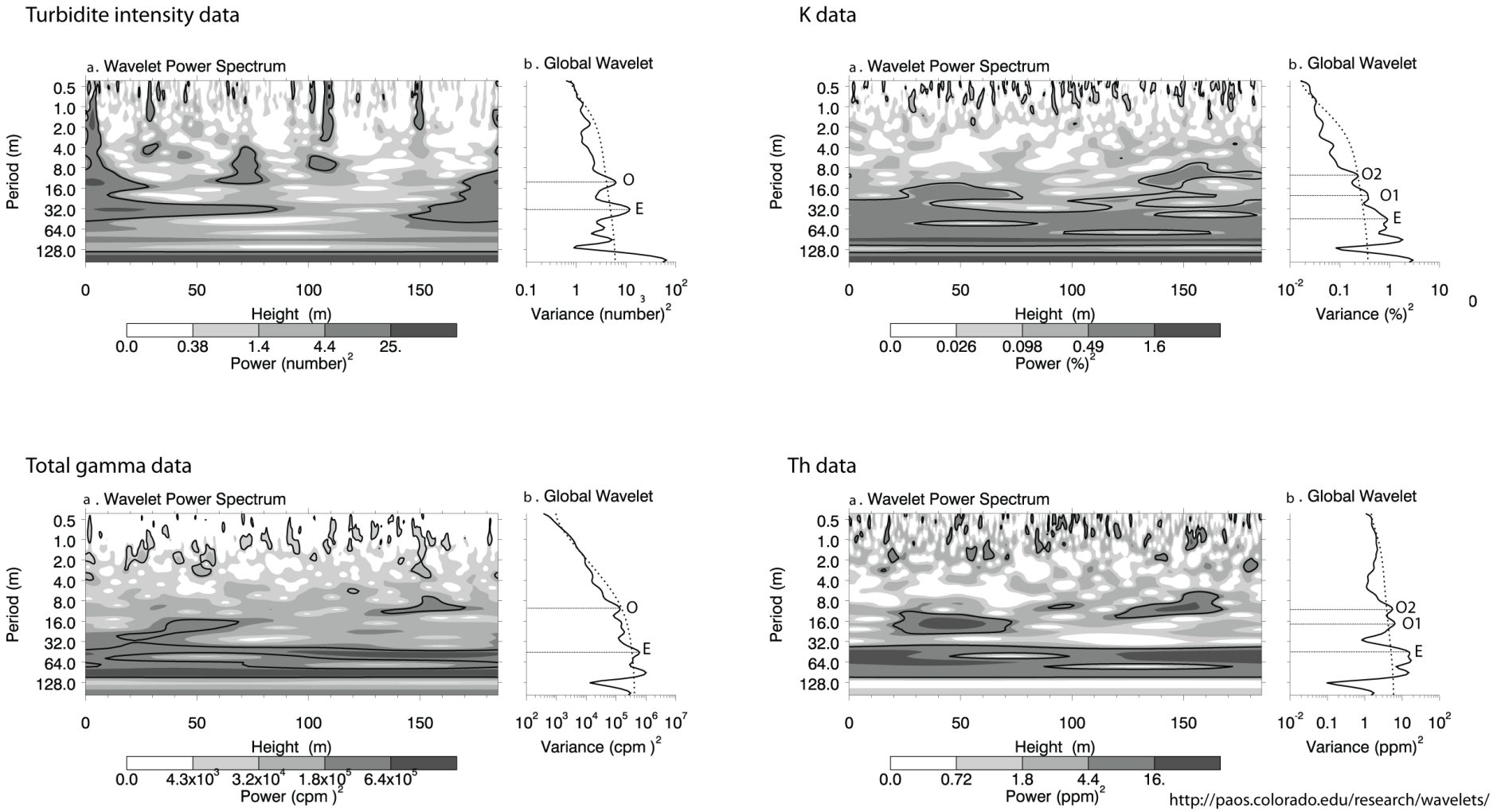

(e) Frequency-selective filtering

The total-gamma records of the Forcaz section have been filtered to 0.028 cycles/m and to 0.094 cycles/m using a Gaussian band-pass filter with a bandwidth of 0.023 cycles/m (Figure 5.68). These two frequencies have been associated with eccentricity and obliquity, respectively, and are both present in the REDFIT total-gamma spectrum with confidence levels > 99%.

The filtered records of the Forcaz section using a frequency of 0.028 cycles/m show eccentricity cycles throughout the stratigraphy. These cycles appear better defined and of larger amplitude between 0-40 m and 100-140 m height. The filtered records at a frequency of 0.094 cycles/m show well developed cycles throughout the records. These cycles appear less evident in those areas where eccentricity cycles are more dominant.

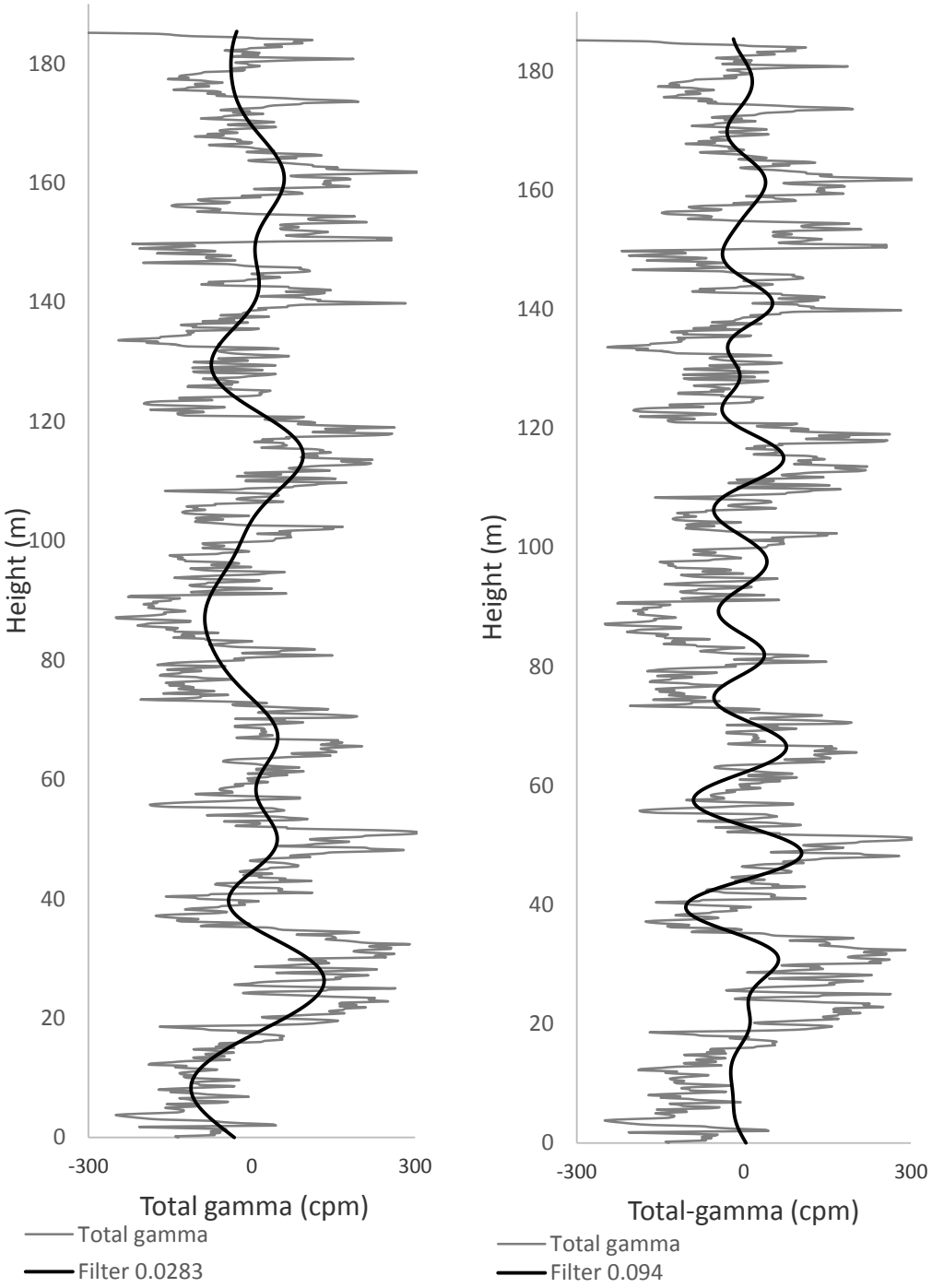

Figure 5.68 Frequency-selective filtering of the Forcaz section. The total-gamma records have been interpolated and detrended before being filtered. A band-pass Gaussian filter with a bandwidth of 0.023 cycles/m has been used for filtering. The total-gamma records have been filtered to the frequency 0.028 cycles/m which has been associated with eccentricity 95 kyr cycles and to the frequency 0.094 cycles/m which has been associated with obliquity 40 kyr using REDFIT and ASM spectral analysis. Filtering used the program Analyseries (Paillard *et al.*,1996).

(f) Spectral analysis comparison of the Forcaz section and the Well A6 core

The cross-section and stratigraphic section in the Forcaz area (Figure 5.60) suggests there is a large degree of overlapping between the Forcaz section and the A6 core. Spectral studies of these two sections should therefore show similar results.

REDFIT analysis of the XRF and stable carbon isotope records of the A6 core identified five recurrent frequencies at 0.032 cycles/m, 0.08 cycles/m, 0.095 cycles/m, 0.15 cycles/m and 0.196 cycles/m (Table 4.5). ASM analysis of the turbidite and bioturbation intensity data suggested that the most likely SAR of the A6 core sediments was 28.5 cm/kyr. At this SAR, the frequency 0.032 cycles/m represents eccentricity 110 kyr, the frequencies 0.08 and 0,095 cycles/m represent obliquity 40 kyr and the frequencies 0.15 and 0.196 cycles/m represents precession 23 kyr and precession 19 kyr, respectively.

In the Forcaz section, the SAR which most closely matched the orbital cycles for the Middle Eocene was 33.5 cm/kyr which is in close proximity to the one suggested for the deposition of the A6 sediments at 28.5 cm/kyr. REDFIT analysis recognised five main frequencies: 0.023 and 0.028 cycles/m linked to eccentricity 123 kyr and 95 kyr respectively, the frequency 0.052 cycles/m and the cycle range 0.08-0.094 cycles/m matched to obliquity 52 kyr and obliquity 40 kyr, respectively. The frequencies 0.14 and 0.199 cycles/m are associated with the precession cycles 23 and 19 kyr. Table 5.33 shows a summary of the spectral results of the Forcaz and the A6 core records.

Table 5.33 Forcaz section and A6 core spectral results comparison.

Section	SAR (cm/kyr)	Frequencies identified by spectral analysis (cycles/m)					
		Eccentricity		Obliquity		Precession	
		125 kyr	95 kyr	52 kyr	40 kyr	23 kyr	19 kyr
Forcaz	33.5	0.023	0.028	0.052	0.08-0.094	0.14	0.199
A6 core	28.5		0.031		0.08-0.095	0.15	0.196

Main frequencies identified in the Forcaz gamma-ray logged section and A6 core using REDFIT analysis (Table 5.30 and Table 4.5, respectively).

(g) Orbital tuning

Orbital tuning of the Forcaz section has been performed by comparing the total-gamma records filtered to the frequency 0.0283 cycles/m which has been associated with eccentricity to the eccentricity curves of the Middle Eocene using the La2010a orbital solution of Laskar *et al.* (2011). Eight anchor points have been used for tuning the records (Table 5.34).

The Forcaz section has a good radiometric age control from biostratigraphic studies (Scotchman *et al.,* 2014) and magnetostratigraphic studies (Chapter 3). Age estimations using biostratigraphic studies suggest the Ainsa System was deposited between 43.9 and 44.9 Ma (middle Lutetian), during nannofossil zone NP15 and shallow benthic foraminifera zone SBZ13 - SBZ14 (Scotchman *et al.*, 2014). Magnetostratigraphic studies show reverse polarity throughout the Forcaz section, likely to be chron C20r (44.72-43.43 Ma) (Gradstein *et al.*, 2012). The sediments of the Forcaz section post-date those of the Boltaña section. The top of the Boltaña section was located within the interfan deposits of the Ainsa II and Ainsa III sandbodies. Thickness estimations from sedimentary logging suggest that the top of

the Boltaña section is located ~ 50 m below the AIII sandbody (Figure 5.60). The Ainsa III sandbody in the Forcaz section is represented by a 15 m heterolithic package located at 30-45 m height (Figure 5.61). Therefore, it is reasonable to assume that the beginning of the Forcaz section coincides approximately with the end of the Boltaña section. Orbital tuning of the Boltaña section suggested that the sediments were deposited between 45.29 and 44.56 Ma. The base of the Forcaz section should, therefore, have accumulated close to ~ 44.56 Ma. Several attempts have been undertaken to match the selected anchor points to different eccentricity cycles around this time interval. The best curve match and the best response in the time-series analysis are shown in Figure 5.69. This figure shows that the interval between 60-90 m height has undergone more deformation to match the total-gamma filtered records to the eccentricity cycles of the orbital solution, whilst the rest of the data remained mostly unchanged. Although, there is no significant strengthening of the spectral peaks after tuning, the three main orbital parameters (eccentricity, obliquity and precession) are present with confidence levels > 99% (Figure 5.70). Tuning the Forcaz total-gamma data to other eccentricity cycles reduces the confidence levels of the obliquity and/or precession cycles significantly. Therefore, the Forcaz section has been more likely deposited between 44.63 and 44.02 Ma with a total duration of ~615 kyr.

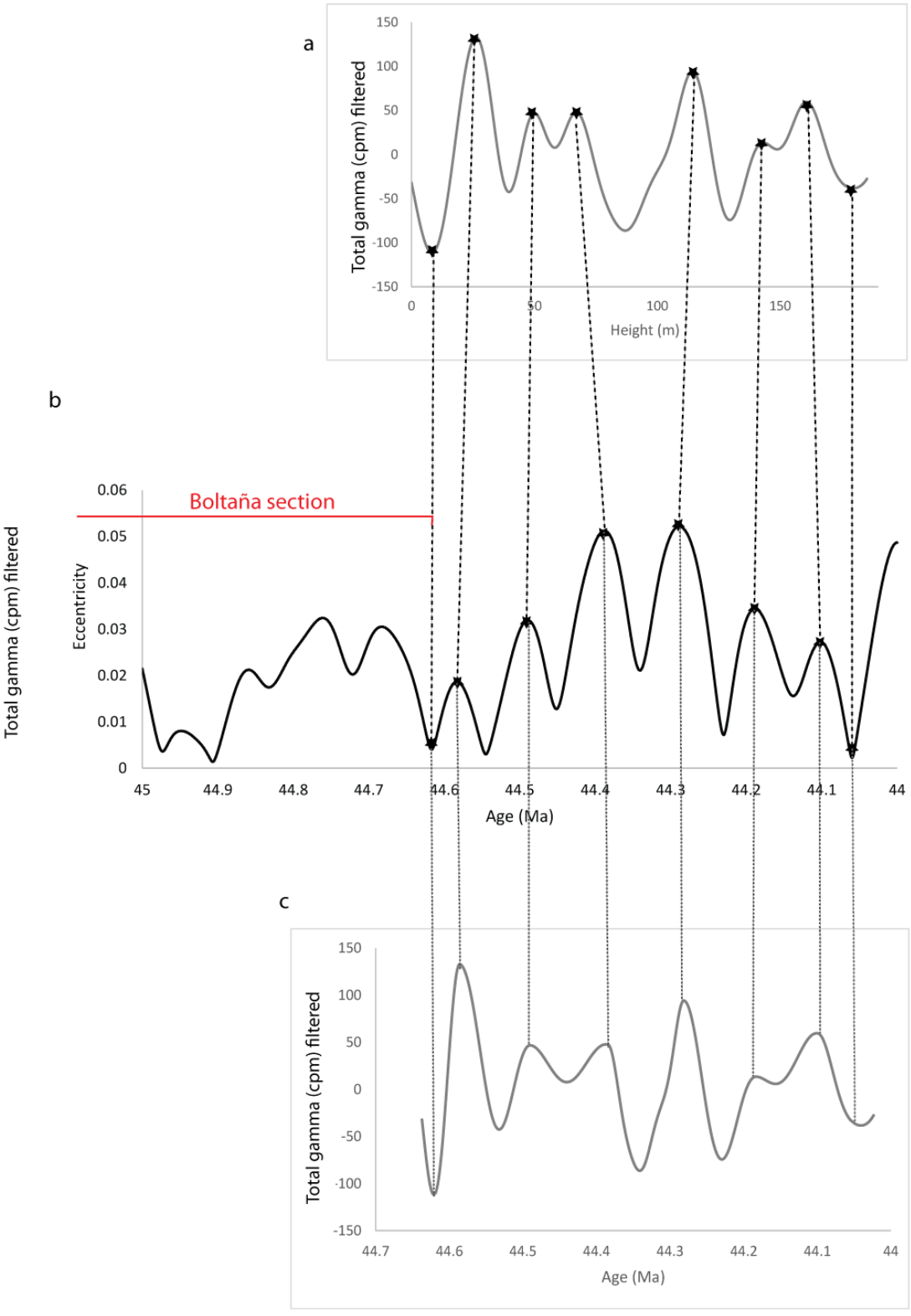

Figure 5.69 Orbital tuning of the Forcaz section. Filtered total-gamma records of the Forcaz section (Figure a) have been matched to eccentricity cycles of the La2010a orbital solution of Laskar *et al.* (2011) (Figure b) using 8 anchor points designated with an asterisk (*). The resultant tuned records (Figure c) show that the original data has undergone more distortion in the interval between 60 and 90 m height.

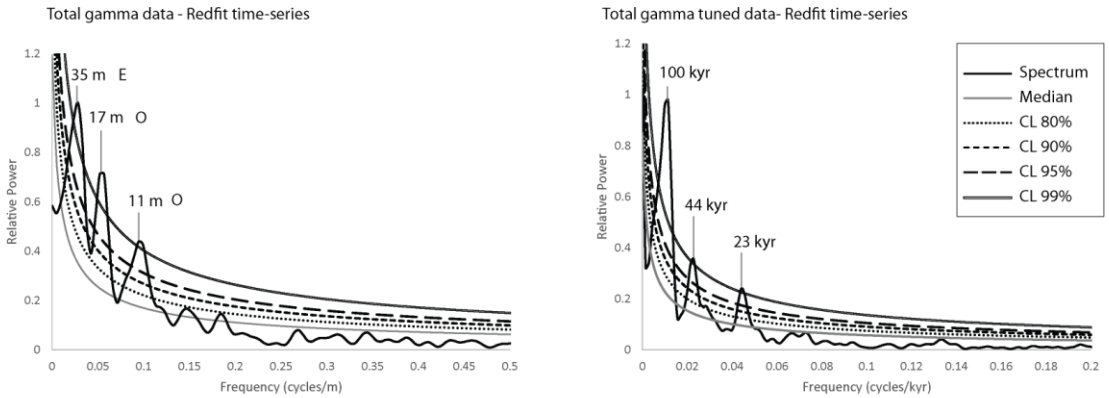

Figure 5.70 Spectral analysis using REDFIT of the Forcaz section tuned to eccentricity. The tuned total-gamma records of the Forcaz section show three well defined cycles at 100 kyr, 44 kyr and 23 kyr with confidence levels > 99%. No significant strengthening of the spectral peaks has occurred after orbital tuning, although the original data already showed three well-defined spectral peaks with confidence levels > 99%. Trying to tune the Forcaz total-gamma filtered records to any other eccentricity cycles reduces significantly the confidence levels in the obliquity and/or precession cycles.

Table 5.34 Anchor points for orbital tuning in the Forcaz section.

Height (m)	Age (Ma)	Cycle
9.2	44.619	Eccentricity minima
26.6	44.585	Eccentricity maxima
50.4	44.488	Eccentricity maxima
67.4	44.384	Eccentricity maxima
114.8	44.28	Eccentricity maxima
143.6	44.181	Eccentricity maxima
161	44.099	Eccentricity maxima
174.8	44.053	Eccentricity minima

The table shows the 8 anchor points employed to tune the Forcaz section to the eccentricity curves of the La2010a orbital solution of Laskar *et al.* (2011).

Table 5.35 SAR in the Forcaz section calculated from tuning the records.

Height interval (m)	Age interval (Ma)	SAR (cm/kyr)
0-9.2	44.6372-44.619	50.5 cm/kyr
9.2-26.6	44.619-44.585	51.1 cm/kyr
26.6-50.4	44.585-44.488	24.5 cm/kyr
50.4-67.4	44.488-44.384	16.3 cm/kyr
67.4-114.8	44.384-44.28	44.6 cm/kyr
114.8-143.6	44.28-44.181	29.1 cm/kyr
143.6-161	44.181-44.099	21.2 cm/kyr
161-174.8	44.099-44.053	32.1 cm/kyr
174.8-185	44.053-44.0236	34.8 cm/kyr

The table shows SAR calculated at different time intervals throughout the Forcaz section length. Average sedimentation rate is 29.4 cm/kyr. This SAR is very similar to the one calculated in the A6 core sediments at 28.5 cm/kyr.

SARs in the Forcaz section have been calculated for each interval between anchor points to ensure that the tuned total-gamma records of the Forcaz section have not resulted in unrealistic SARs. Calculating the SAR for each stratigraphic interval also allows the identification of periods where significant variations in the SAR have occurred (Table 5.35). The SARs have varied between 16.3 cm/kyr and 50.5 cm/kyr although averaged values are ~ 29.4 cm/kyr. Figure 5.71 shows the variation of SAR across the Forcaz section and the averaged SAR of the section is represented as a linear trend. The averaged SAR value is close to the SAR calculated using ASM analysis at 33 cm/kyr and to the SAR calculated in the A6 core at 28.5 cm/kyr.

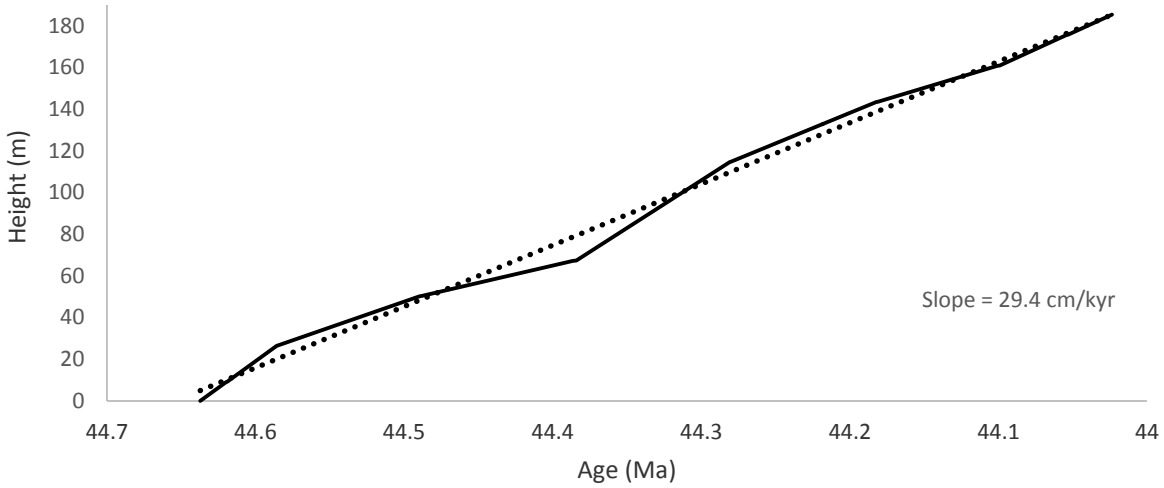

Figure 5.71 SARs in the Forcaz section calculated from orbital tuning the total-gamma records to eccentricity. The SARs have varied between 16.8 and 50.5 cm/kyr. The averaged SAR of the Forcaz section is represented as a linear trend. The averaged SAR 29.4 cm/kyr is slightly lower than the value estimated from ASM analysis at 33 cm/kyr, but, is very close to the one estimated for the A6 core at 28.5 cm/kyr.

5.3.5 The Morillo System

5.3.5.1 Sedimentology of the Morillo System

The Morillo System is ~ 260 m thick and is stratigraphically located between the Ainsa and the Guaso deep-marine systems. Some studies have focused on the sedimentology and environment of deposition of the Morillo System (Labourdette *et al.,* 2008; Moody *et al.,* 2012; Pohl and McCann, 2013; Bayliss and Pickering, 2014a). The Morillo System comprises three sandbodies, designated Morillo I-III. These sandbodies have been interpreted as structurally-confined, mid-slope canyon to lower-slope submarine fans channel systems (Bayliss and Pickering, 2014a).

The Morillo System sediments were sourced from a mid-slope canyon which cut across the Mediano Anticline and was located in the area surrounding the Coscojuela-de-Sobrarbe village. The canyon fill contains thick MTDs which comprise of mainly distorted mudstones and pebbly mudstones which represent the collapse of the shelf and mid-slope areas. These MTDs/MTCs also contain conglomerate deposits with abundant limestone boulders. These boulders probably reflect erosional down-cutting and canyon excavation of the flanks of the Mediano Anticline (Bayliss and Pickering, 2014a). The canyon infill thins and onlaps against the Mediano Anticline showing that this structure was a significant topographic high during the deposition of the Morillo System.

The Morillo sandbodies are characterised by an erosional base overlain by an MTD (typically Type II MTDs). The channel fills are a mixture of sediment gravity-flow deposits (including turbidites) and MTDs/MTCs, but they differ in that the Morillo I sandbody is sand-dominated, whilst the Morillo II and III sandbodies are MTC-dominated (Bayliss and Pickering, 2014a).

The Morillo System records an increase in structural confinement, reflected in a progressive decrease in channel width and a change from lateral offset-stacking between the Morillo I and II sandbodies to aggradational stacking between Morillo II and III (Bayliss and Pickering, 2014a). The abundance of MTDs/MTCs in the Morillo II and III sandbody fills also reflects an increase in depositional confinement with an increase in mass wasting deposits associated with an increase in slope gradients. This increase in structural confinement has been associated with the growth of the basin anticlines (Mediano, Añisclo and Boltaña) which narrowed the Ainsa Basin and caused a fall in relative base-level.

5.3.5.2 Tectonic history during the deposition of the Morillo System

During the deposition of the Morillo System, the Ainsa Basin was incorporated into the advancing Pyrenean deformation front. The emplacement of the Gavarnie thrust sheet, coeval with the deposition of the Upper Hecho Group, resulted in the development of the Mediano and the Boltaña anticlines and marked the evolution of the Ainsa Basin from a transitional foredeep basin to a thrust-top basin which was incorporated into the hanging wall of the Gavarnie-Sierras Exteriores (Muñoz *et al.,* 1998; Dreyer *et al.,* 1999; Fernández *et al.,* 2004; Fernández *et al.,* 2012). The Morillo System was probably deposited during a period characterised by tectonically-controlled shortening of the Ainsa Basin. The incorporation of the basin on the hangingwall of the Gavarnie-Sierras Exteriores Thrust as southwards propagation of the deformation front continued, also led to a significant swallowing of the basin with thrust-related uplift equalling or exceeding previous subsidence rates (Bayliss and Pickering, 2014a).

The growth of the Mediano Anticline during the deposition of the Morillo System resulted in sediment gravity flows being deflected southwards around this seafloor growth structure and entering the basin from a more southeastern point across the Mediano Anticline than in previous systems (Bayliss and Pickering, 2014a).

5.3.5.3 Age of the Morillo System

The Morillo System was deposited between 43.2 and 44.24 Ma (late Lutetian); during nannofossil zone NP15-NP16 and shallow benthic foraminifera zone SBZ14-SBZ15 (Scotchman *et al.,* 2014). These estimated ages are in agreement with studies from Mochales *et al.* (2012) who estimated the end of the Morillo System at 43.2 Ma. The Morillo System lacks any magnetostratigraphic age control, since this study (Chapter 3) only sampled from the Gerbe to the Ainsa systems. Due to previous disagreements between biostratigraphic and magnetostratigraphic work in older Hecho Group successions, orbital tuning of the gamma-ray logged sections in the Morillo and younger deep-marine systems has not been attempted.

5.3.5.4 Morillo-reservoir gamma-ray logged section

5.3.5.4.1 Geographical location of the Morillo-reservoir section

The Morillo-reservoir section is 122 m long and is located ~ 400 m southwest of the Morillo-de-Tou town and to the west of the Mediano Reservoir. The section can only be accessed when the water level in the reservoir is low, usually in summer and early autumn. The section is well exposed along a narrow stream valley which can be accessed from the Sarrato stream (Plate 5.13).

The Morillo-reservoir section contains few small-scaled slumps which rarely exceed 50 cm in thickness (Plate 5.14a). The section also contains some tectonic deformation with small-scale reverse faults which do not exceed tens of cm in displacement (Plate 5.14c). Sandstone turbidites in this area appear channelised and contain significant lateral changes in thickness (Plate 5.14d). Many of the thin sandstone turbidites show ripples and have a lenticular shape.

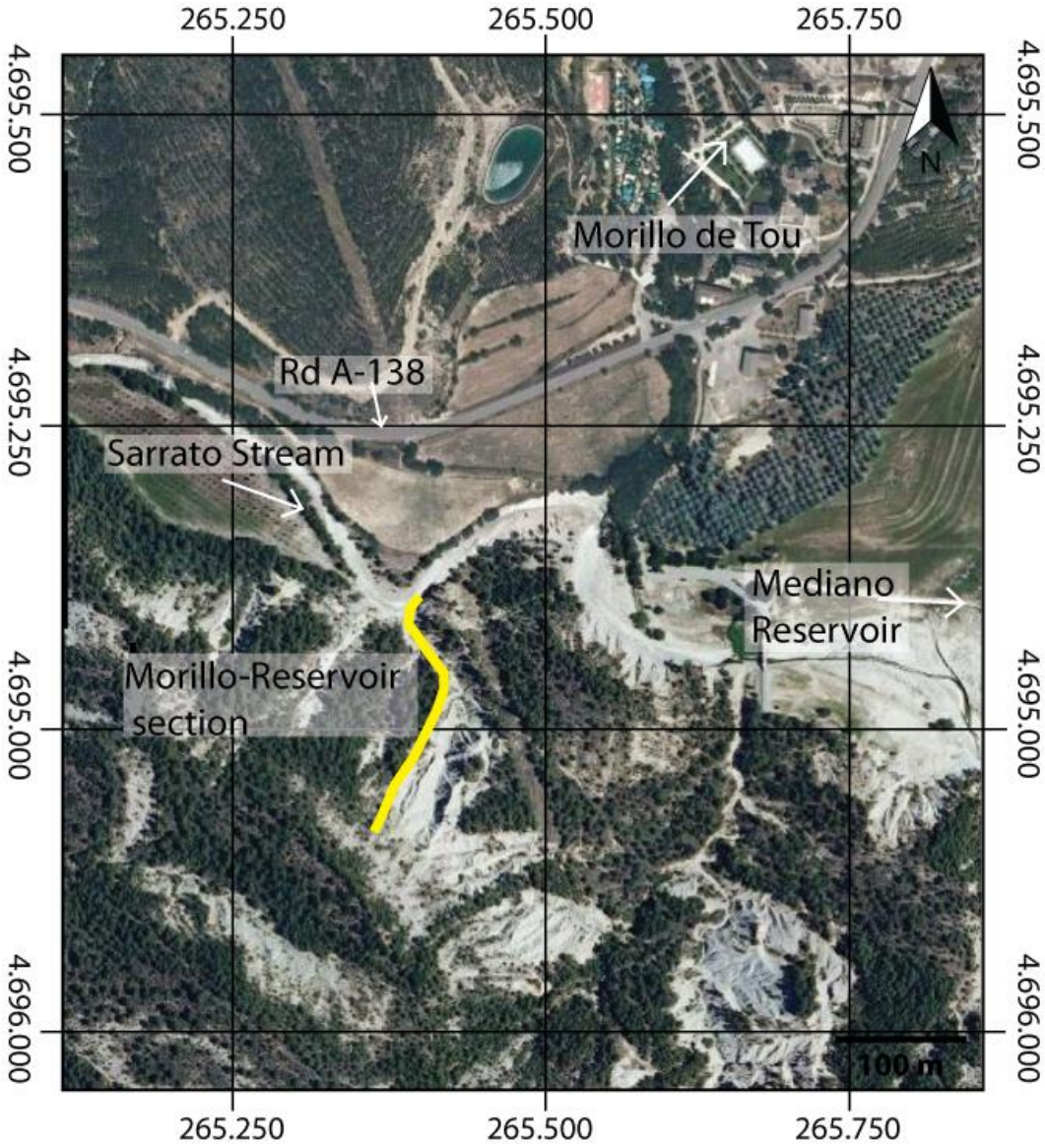

Plate 5.13 Aerial photograph of the area surrounding the Morillo-reservoir gamma-ray logged section. The section can be accessed easily from the Sarrato stream in proximity to the Morillo-de-Tou town but only when the water-level of the Mediano Reservoir is low. Aerial image from www.sigpac.mapa.es/fega/visor.

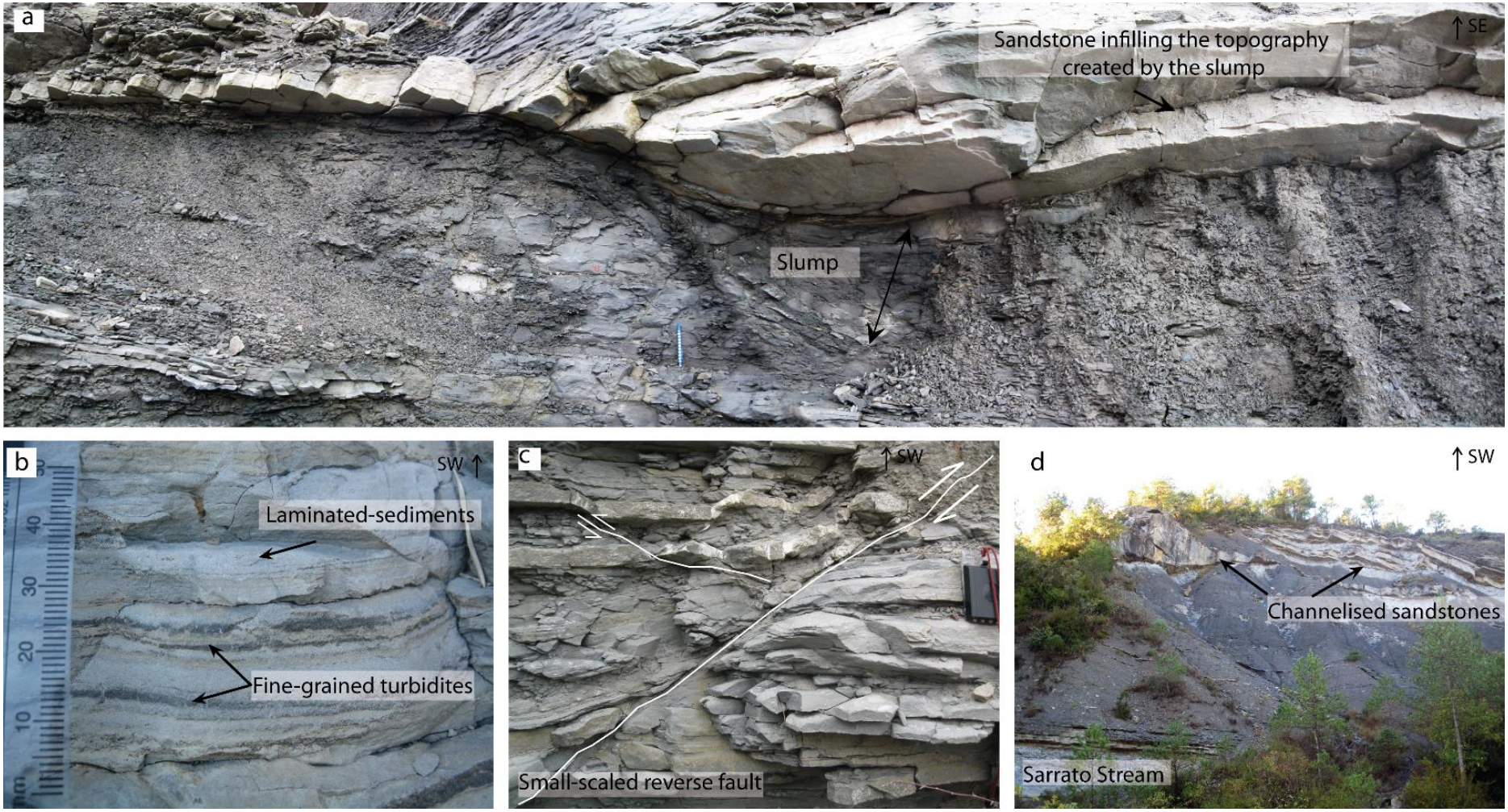

Plate 5.14 Outcrop photographs of the Morillo-reservoir gamma-ray logged section.

Plate 5.14 (previous page) Outcrop photographs of the Morillo-reservoir gamma-ray logged section. (a) Outcrop photograph of the Morillo-reservoir logged section at 45 m height. The section contains some small-scaled slumps which rarely exceed ~ 50 cm in thickness. Above the sediment slide, in the photograph a sandstone turbidite has infilled the topography created by the slump causing significant lateral changes in thickness. Sandstone turbidites have erosive bases and fining-upwards profiles. **(b)** Outcrop photograph showing the laminated character of the fine-grained sediments of the Morillo-reservoir section with an alternation of darker and lighter bands. Locally, orangey bands are present indicating a diagenetic origin. Sandstone turbidites are typically cm in size and on many occasions show planar laminations and ripples. **(c)** Outcrop photograph showing small reverse faults present at the beginning of the Morillo-reservoir section at ~ 35 m height. This reverse fault has a displacement of ~ 30 cm. **(d)** Photograph of channelised sand-prone deposits exposed at the Sarrato stream immediately above slumped fine-grained deposits. These deposits are ~ 50 m stratigraphically higher than the Morillo-reservoir section and are located within the Morillo III sandbody.

5.3.5.4.2 Stratigraphic location of the Morillo-reservoir section

The Morillo-reservoir section is located within the Morillo System. The heterolithic package located at the base of the section (5-20 m height) has been interpreted as the off-axial Morillo II sandbody (Figure 5.72). This package is ~ 15 m thick and can easily be distinguished in the sedimentary log (Figure 5.73) and in the sandstone turbidite intensity graph (Figure 5.74). The rest of the section comprises fine-grained interfan deposits between the Morillo II and the Morillo III sandy-successions. The base of the heterolithic package, forming the Morillo III off-axis fan sediments, is not accessible due to steep slopes. Figure 5.75 shows a simplified sedimentary log of the Morillo-reservoir section plotted against total-gamma, K, Th, U, Th/K and Th/U data.

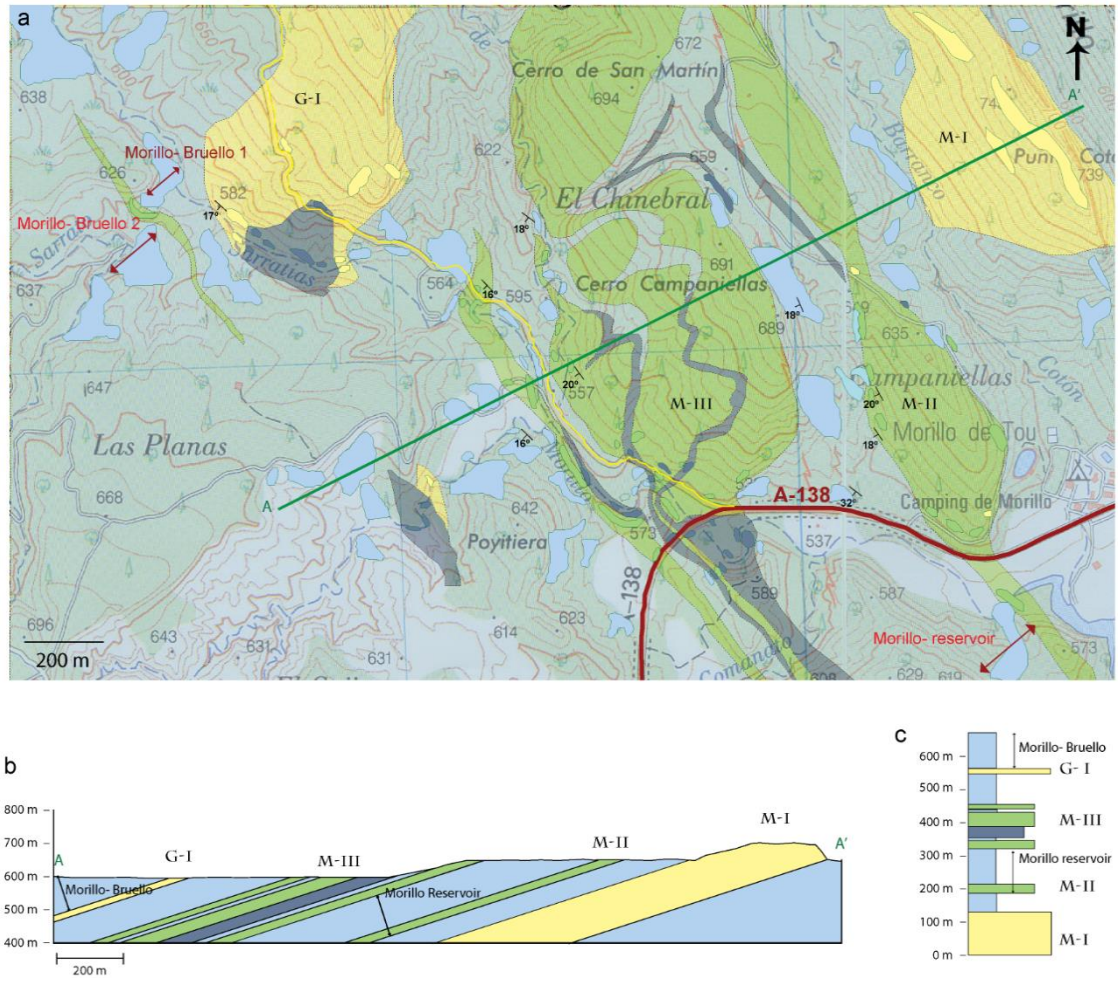

Figure 5.72 Geological map, cross-section and vertical stratigraphic column of the Morillo-reservoir and the Morillo-Bruello gamma-ray logged section. (a) Geological map of the area between the villages of Morillo-de-Tou and Bruello showing the position of the Morillo-reservoir and the Morillo-Bruello gamma-ray logged sections (see Section 5.3.6.4). The green line represents the cross-section A-A' running parallel to both gamma-ray logged sections and perpendicular to the main outcrop strike to facilitate the measurement of true stratigraphic thicknesses. **(b)** Cross-section A-A' showing the position of the Morillo-reservoir gamma-ray logged section within the interfan sediments of the Morillo II and Morillo III sandbodies and the position of the Morillo-Bruello section immediately above the Guaso I sandbody. **(c)** Stratigraphic thickness column based on the calculation of true thicknesses from the A-A' cross-section.

Figure 5.73 Detailed sedimentary log of the Morillo-reservoir section. Sedimentary logs include every bed thicker than 5 mm. There is a weathered, poorly-exposed area between 19-23 m height. An electronic version of this log to allow for a more detailed study is included in Appendix 3. Symbol key used for the sedimentary logs is available in Figure 2.5.

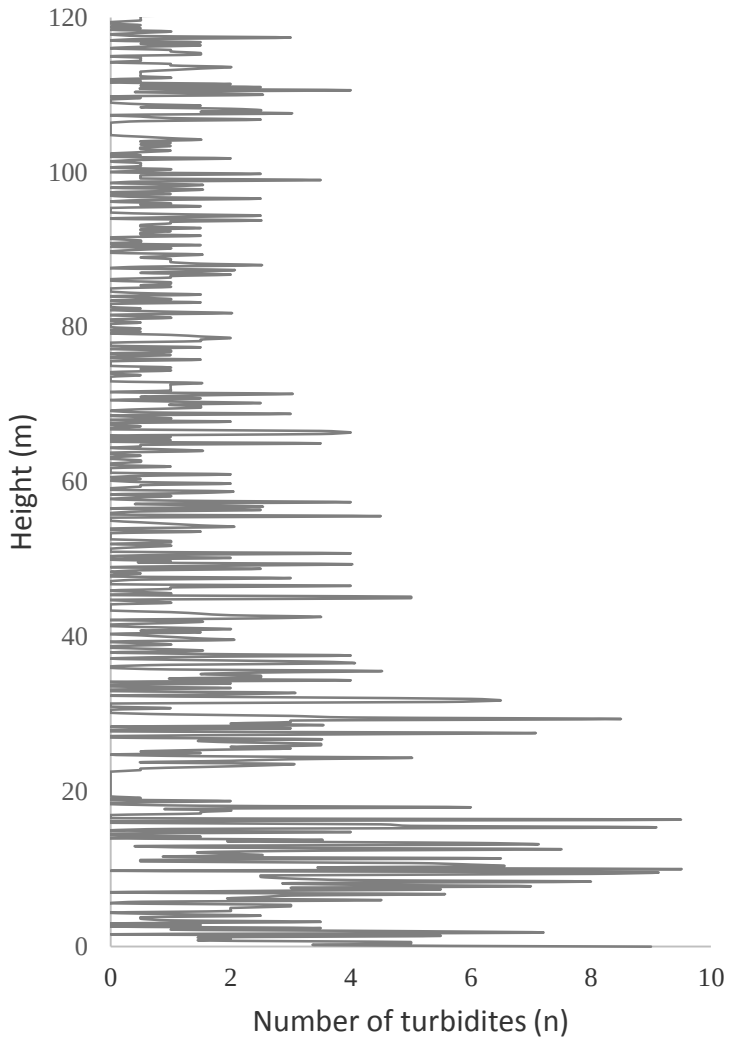

Figure 5.74 Sandstone turbidite intensity of the Morillo-reservoir section. There is a general decrease in the number of sandstone turbidites throughout the section. The area between 19 and 23 m height is poorly exposed with a thick layer of scree covering the outcrop, affecting the sedimentary logging of these sediments. The prominent heterolithic package at the beginning of the section (5-20 m height) has been interpreted as the off-axial Morillo II sandy succession. The averaged sandstone content for the whole section is ~ 6.3%.

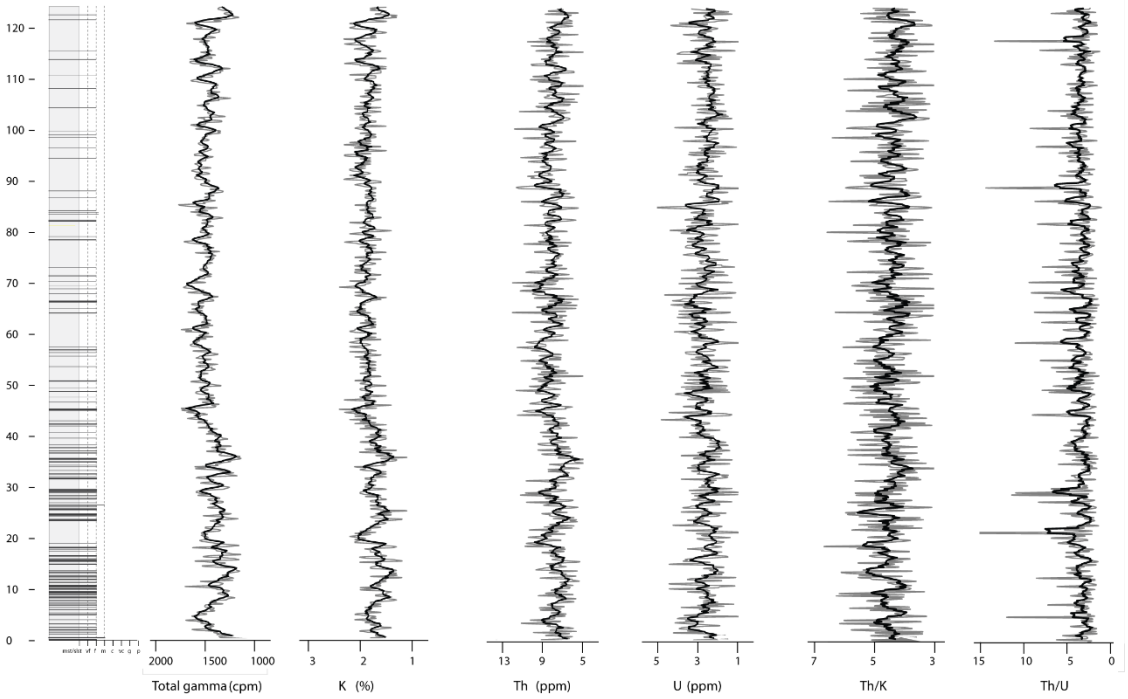

Figure 5.75 Simplified sedimentary logs of the Morillo-reservoir section plotted against total-gamma (cpm), K (%), Th (ppm), U (ppm), Th/K and Th/U data. The black line is a 4-period moving average. Simplified logs only show sandy turbidites ≥ 1.5 cm thick, for complete logs refer to Figure 5.73 and Appendix 3.

5.3.5.4.3 Cyclostratigraphic studies of the Morillo-reservoir section

(a) Methods of spectral estimation

The spectrum of the total-gamma data has been estimated using four different methods: the REDFIT, the MTM, the maximum entropy and the periodogram modified with a Bartlett window (Figure 5.76). The spectrum created with the REDFIT and the maximum entropy method is very similar, whilst the MTM method shows more similarities with the periodogram modified spectrum. Most of the frequencies, however, are common to all the spectra. Among those, the frequencies 0.05 cycles/m (1/20 m), 0.076 cycles/m (1/13 m), 0.122 cycles/m (1/8 m) and 0.147 cycles/m (1/6 m) consistently appear in the spectra of all the methods. Table 5.36 summarises the main frequencies present within the frequency range 0-0.2 cycles/m.

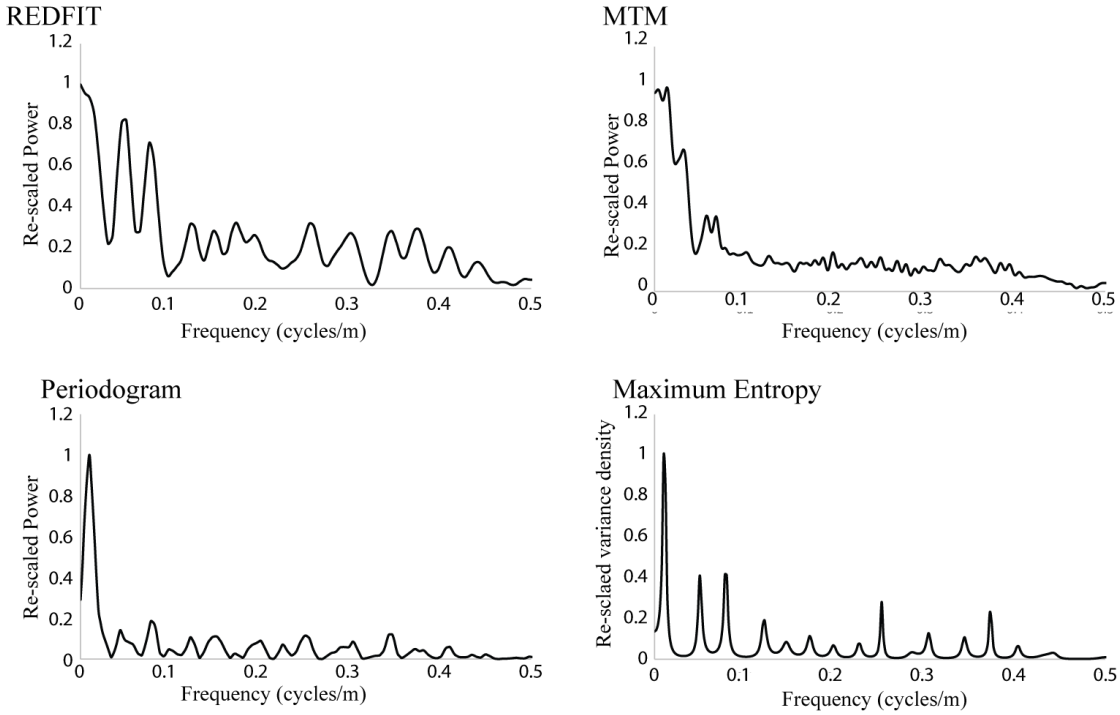

Figure 5.76 Methods of spectral estimation of the Morillo-reservoir total-gamma data. REDFIT spectrum using 4 WOSA segments, 6 degrees of freedom and a bandwidth of 0.024 cycles/m. The MTM method uses 6 tapers and ~ 12 degrees of freedom. The periodogram spectrum uses a Bartlett window. The maximum entropy method uses numbers of lags M = N/3 = 200). The analysis has used the REDFIT software developed by Schultz and Mudelsee (2002) and the Analyseries software package developed by Paillard *et al.* (1996).

Table 5.36 Methods of spectral estimation in the Morillo-reservoir section.

Spectral Method	Frequency (cycles/m)♠	Period (m)	Spectral Method	Frequency (cycles/m)♠	Period (m)
REDFIT	**0.051** **0.076** **0.122** **0.147** 0.173 0.193	19.6 13.2 8.2 6.8 5.8 5.2	Periodogram modified with a Bartlett window	0.01 **0.046** **0.08** **0.124** **0.15**	100 21.7 12.5 8.1 6.7
MTM□	0.01 **0.043** **0.081** **0.122** **0.156**	100 23.3 12.3 8.19 6.4	Maximum entropy	0.01 **0.05** **0.078** **0.122** **0.15** 0.174 0.2	100 20 12.8 8.2 6.7 5.7 5

♠ Frequencies from the 0-0.2 cycles/m range.
□Frequencies present in the MTM significance test with confidence levels > 80%.
Frequencies consistently present in all the spectra are represented in bold numbers.

(b) Spectral results using REDFIT

The REDFIT analysis of the Morillo-reservoir section has been undertaken using 4 WOSA segments (Figure 5.77). The preferred noise background estimation model is the power regression (Table 5.37) which has been applied to all the REDFIT spectra. There are six significant frequencies within the 0-0.5 cycles/m range which are well represented in the time-series analyses of the total-gamma, K, Th and sandstone turbidite intensity datasets. These frequencies are ~ 0.05 cycles/m (1/20 m), ~ 0.076 cycles/m (1/13 m), 0.17-0.19 cycles/m (1/4 m), 0.28-0.30 cycles/m (1/3 m) and 0.37 cycles/m (1/2 m). There are other significant frequencies, but, they only appear in one of the parameters investigated or have a relatively lower level of confidence and have not been discussed further in the text. Table 5.38 summarises all the frequencies present in the 0-0.5 cycles/m frequency range.

The frequency range 0.045-0.05 cycles/m (1/20-1/22 m) is present in the total-gamma and K with confidence levels > 95% and in the sandstone turbidite intensity spectrum as well > 99% confidence levels. A similar frequency at 0.04 cycles/m (1/24 m) is also present in the Th spectrum but with lower confidence levels (> 90%). The frequency 0.076 cycles/m (1/13 m) is present in the total-gamma and K spectra in both cases, well > 99% confidence level and in the Th spectrum > 90% confidence level. The frequency 0.173 cycles/m (1/4.6 m) is present in the total gamma (> 95% confidence levels) and K spectra (> 80% confidence levels). The frequency 0.197 cycles/m (1/4 m) is present in the Th and total-gamma spectra with a confidence level of 95% and 90%, respectively. The frequency range 0.259-0.28 cycles/m (1/3 m) is best represented in the total-gamma and K data. The 0.37 cycles/m (1/2 m) frequency is also present in all the four investigated parameters. This frequency forms a very

significant peak in the sandstone turbidite intensity spectrum well > 99% confidence levels.

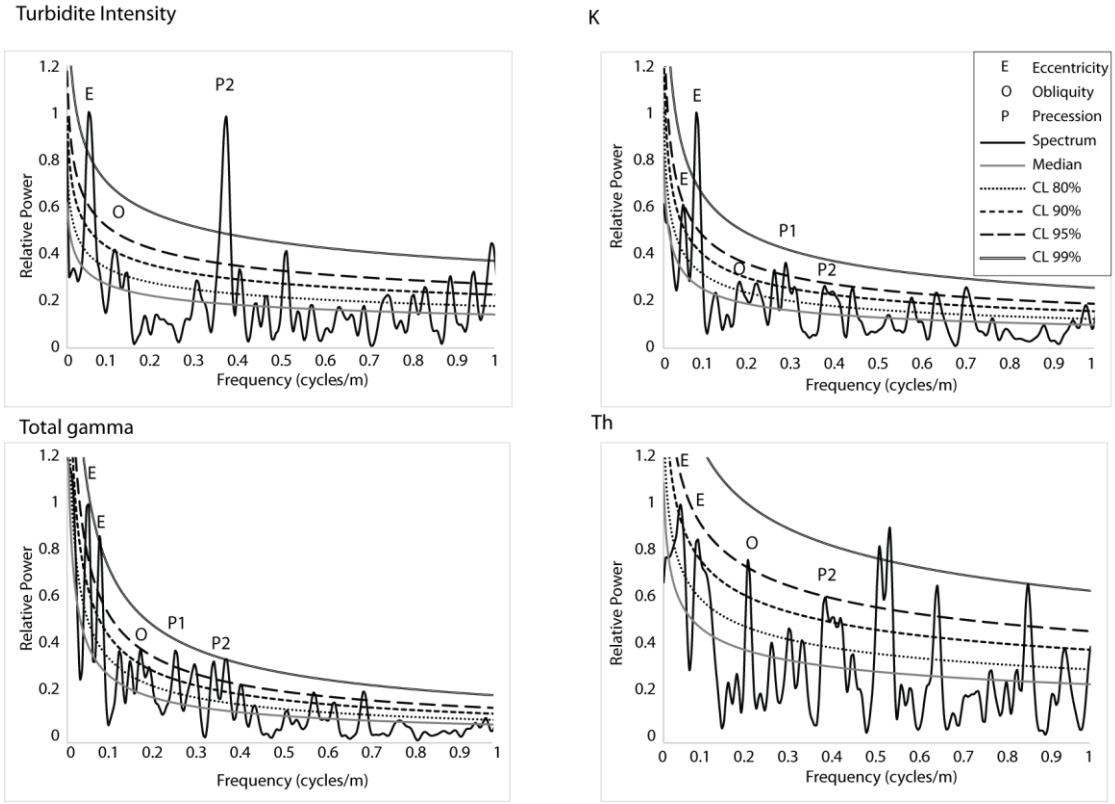

Figure 5.77 Time-series analysis of spectral gamma ray and sandstone turbidite intensity data using REDFIT. REDFIT spectral results used 4 WOSA segments, 6 degrees of freedom and a bandwidth of 0.024 cycles/m. The noise background fitting method is a power regression model. The spectra have been re-scaled power to allow comparison between variables. Analysis used the REDFIT software developed by Schulz and Mudelsee (2002).

Table 5.37 Noise background estimation of the Morillo-reservoir section.

Data	AR1 (Mann and Lees, 1996)	Quadratic curve	Power regression
Total-gamma	310	297	**251**
K	483	681	**360**
Th	201	191	**168**
Sandstone turbidite intensity	354	344	**313**

Summative square errors using the AR1 model of Mann and Lees (1996), a quadratic curve and a power regression method. The method with the least summative square error indicates the most adequate fitting curve method and is represented in bold numbers.

Table 5.38 REDFIT time-series analysis of the Morillo-reservoir section.

Data	Frequency (cycles/m)♠	Period (m)	Confidence level (%)
Total-gamma	0.0508	19.68	95
	0.0762	13.12	99
	0.1219	8.2	80
	0.1474	6.78	80
	0.1727	4.79	95
	0.1931	4.18	90
	0.2591	3.86	95
	0.2997	3.34	95
	0.34.55	2.89	95
	0.3760	2.66	99
	0.4065	2.46	90
K	0.0455	21.98	95
	0.0759	13.17	99
	0.1771	4.64	80
	0.2176	4.59	80
	0.2581	3.87	95
	0.2834	3.53	95
	0.3745	2.67	90
	0.4403	2.27	90
Th	0.0405	24.7	90
	0.0809	12.36	90
	0.1974	4.06	95
	0.2935	3.4	80
	0.3239	3.08	80
	0.3795	2.63	90
Sandstone turbidite intensity	0.0504	19.84	99
	0.1109	9.01	90
	0.1411	7.08	80
	0.3024	3.3	80
	0.373	2.68	99
	0.4032	2.48	90
	0.4637	2.16	80

REDFIT spectral results using 4 WOSA segments and 6 degrees of freedom.
♠Frequencies identified between the frequency range 0-0.5 cycles/m with confidence levels > 80%.

(c) ASM results

ASM analysis of the Morillo-reservoir has investigated 9 frequencies present in the REDFIT spectrum with confidence levels > 95% (Figure 5.78). Two main groups of significant SARs were identified in the ASM analysis. The first group of significant SARs ranges from 12 to 19 cm/kyr and the second group ranges from 20.5 to 31 cm/kyr. The most significant SAR is found at 14.5 cm/kyr with a null hypothesis

significance level of 0.07%. The SAR between 25-26 cm/kyr also has low significant levels at 0.031%. A slow SAR of ~ 14.5 cm/kyr implies the Morillo System was deposited over a large time interval and this causes conflict with previous estimations of the timing of deposition for the Guaso System and the Sobrarbe deltaics which would have occurred at a much later stage (~ 0.5-1.5 Ma) than most age-model estimations suggest (e.g., Bentham and Burkbank, 1996; Dreyer *et al.*, 1999; Mochales *et al.*, 2012; Scotchman *et al.*, 2014). Therefore, it is more reasonable to consider a SAR of ~ 25 cm/kyr as the most likely SAR for the Morillo-reservoir section. At this SAR, the frequencies 0.045 cycles/m represents eccentricity 95 kyr, the frequency 0.076 cycles/m represents obliquity 52 kyr and the 0.17-0.19 cycles/m represents precession 23 and 19 kyr, respectively (Table 5.39).

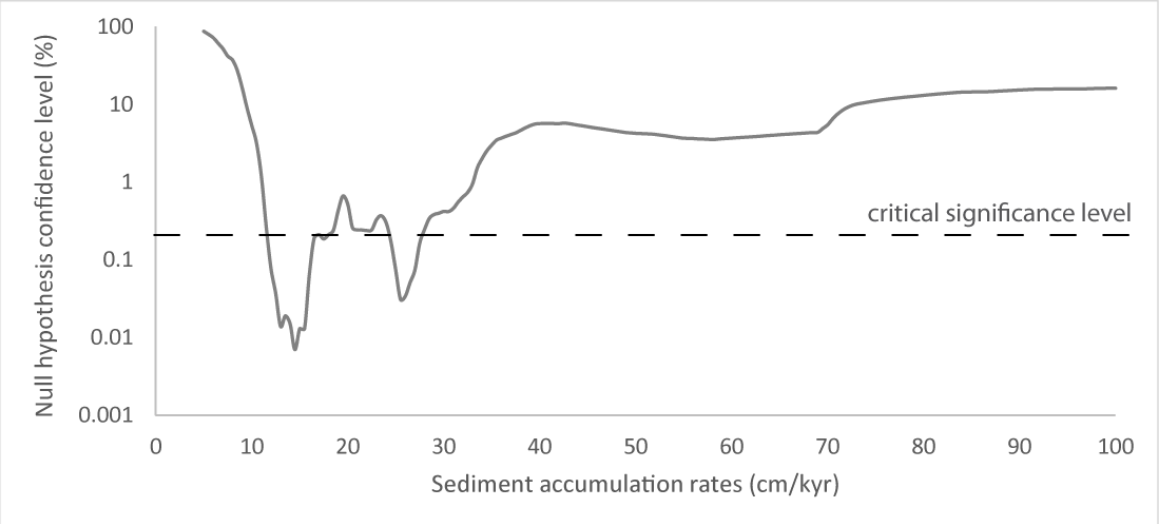

Figure 5.78 ASM results of the Morillo-reservoir section. The ASM analysis includes 9 frequencies identified from spectral analysis of the spectral gamma-ray and sandstone turbidite intensity data with a confidence level > 95%. The analysis used a Rayleigh number of 3.22580645 x 10^{-4} and a Nyquist frequency of 2.4 cycles/m. Orbital parameters were established at ~ 45 Ma using Berger *et al.* (1992) equations. A total of 191 SAR ranging from 5-100 cm/kyr with an increment of 0.5 cm/kyr were investigated using 100,000 Monte Carlo interactions. Critical significance levels were established at 0.52%. All 7 orbital parameters were included in the ASM studies. ASM analysis has identified 2 groups of significant SARs. The first group of significant SARs ranges 12 to 19 cm/kyr and the second group ranges from 20.5 to 31 cm/kyr. Analysis used the ASM software developed by Meyers and Sageman (2007).

Table 5.39 Temporal period duration of significant frequencies in the Morillo-reservoir section.

Frequency (cycles/m)♠	C.L (%)	N □	Period (m)	Period duration (kyr) at different SAR (cm/kyr)							
				Group 1 (SAR between 12-19 cm/kyr)						Group 2 (SAR 20-31 cm/kyr)	
				13 cm/kyr	13.5 cm/kyr	14 cm/kyr	**14.5 cm/kyr**	15 cm/kyr	14.5 cm/kyr	**25 cm/kyr**	26 cm/kyr
0.045	95	1	22	169.1	162.8	157	151.6	146.5	141.8	**87.9**	84.5
0.051	99	2	19.7	151.4	144.8	140.6	**134.7**	131.2	127	78.7	74.7
0.076	99	3	13.2	101.2	97.5	94	**90.7**	87.7	84.9	**52.6**	50.6
0.173	95	2	4.8	44.5	42.8	41.3	**39.9**	38.5	37.3	**23.1**	22.2
0.197	95	2	4.1	39	37.5	36.2	34.9	33.8	32.7	**20.3**	19.5
0.259	95	2	3.9	29.7	28.6	27.6	26.6	24.7	24.9	14.4	14.8
0.283	95	1	3.6	27.1	26.1	24.2	24.3	23.5	22.8	14.1	13.6
0.345	95	1	2.9	22.3	21.5	20.7	**20**	19.3	18.7	11.6	11.1
0.373	99	3	2.7	20.6	19.9	19.1	**18.5**	17.9	17.3	10.7	10.3

The table shows calculated cycle duration for each significant frequency (> 95% confidence levels (CL) at different SARs. The SAR which most closely matches the orbital periods for the Middle Eocene is highlighted in bold numbers.
Underlined are frequencies which are contained in more than 1 spectrum with at least 1 confidence level > 95%.
Estimated orbital cycles for the Middle Eocene (~ 45 Ma) using Berger *et al.* (1992) equations are: eccentricity 123.8 and 94.8 kyr, obliquity 52.3 and 40 kyr and precession 22.6 and 18.8 kyr.
♠ Frequencies within the range 0-0.5 cycles/m with confidence levels > 95%.
□ number of parameters containing that specific frequency in the REDFIT spectrum.

(d) Wavelet results

Results of the wavelet analysis include three main frequency ranges > 90% confidence levels (Figure 5.79). The frequency range 0.045-0.05 cycles/m (1/19-1/22 m) is present in the sandstone turbidite intensity and Th spectra, but, is not significant in the K and the total-gamma spectra, although, the K shows an increase in power at approximately this frequency. Spectral analysis using REDFIT and ASM has associated this frequency with eccentricity 95 kyr.

The most spatially persistent frequency 0.076 cycles/m (1/13 m) is present in all of the stratigraphic records and is persistently significant in the first 50 m of the Morillo-reservoir section and at the top 20 m of the records. Spectral analysis using REDFIT and ASM has associated this frequency with obliquity 40 kyr.

The frequency range ~ 0.17-0.19 cycles/m (~ 1/5 m) which has been linked to precession is identified in the K, Th and total-gamma spectra > 90% confidence levels. In general, however, significant regions at this frequency are both small and discontinuous, and in some of the spectra such as Th, very sporadic.

Figure 5.79 (next page) Wavelet analysis of the sandstone turbidite intensity, K, total-gamma and Th data of the Morillo-reservoir section. (a) The wavelet power spectrum calculates spectral power at different frequencies throughout the Morillo-Reservoir stratigraphic section using sandstone turbidite intensity, K, Th and total-gamma records. Black contours mark the 10% significant regions. **(b)** The global wavelet shows the scale-averaged wavelet power across the studied frequency bands. Values to the right of the dashed line have a significance level > 90% confidence level. Significant spectral peaks which have been associated with Milankovitch frequencies using REDFIT and ASM analysis have been labelled (E-eccentricity, O-obliquity, and P-precession). Analysis used the online tool http://paos.colorado.edu.research/wavelets based on the algorithms of Torrence and Compo (1998).

Figure 5.79 Wavelet analysis of the Morillo-reservoir section.

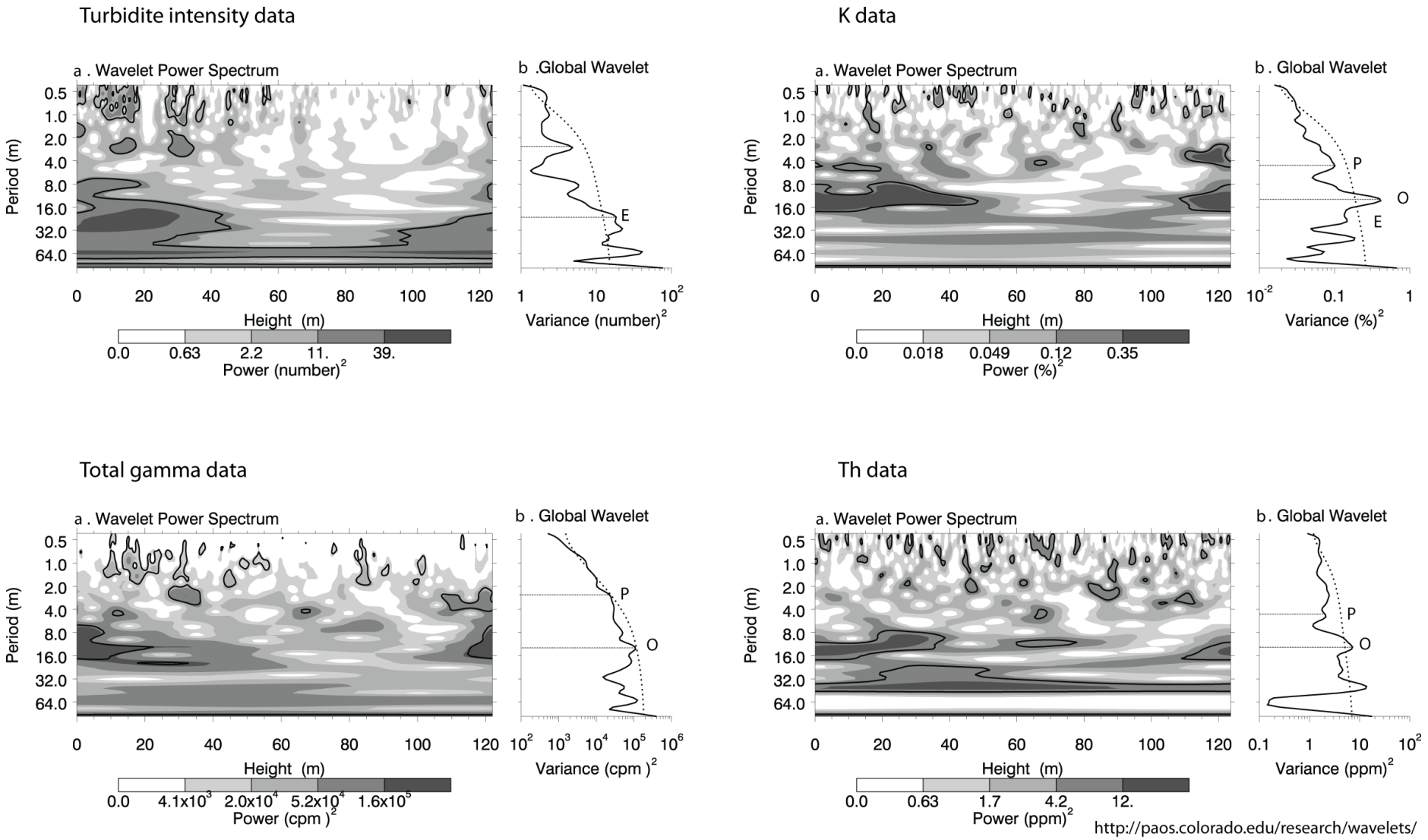

(e) Frequency-selective filtering results

Two frequencies, 0.0508 and 0.076 cycles/m have been filtered using a bandwidth of 0.0245 cycles/m determined by REDFIT spectral analysis (Figure 5.80). Both frequencies are present in the total-gamma records with confidence levels > 95%. REDFIT and ASM analysis has identified these frequencies as eccentricity and obliquity, respectively.

The total-gamma records filtered at the frequency 0.0508 cycles/m (1/19 m) shows well developed high-amplitude cycles mainly in the lower 50 m of the records and in the top 30 m. In the central part of the records, cycles have also been identified but the amplitude of these cycles appears attenuated.

The total-gamma records filtered at the frequency 0.076 cycles/m (1/13 m) show well develop cycles throughout the section, but, the amplitude of these cycles is higher in the first 50 m of the Morillo-reservoir section. In the wavelet spectrum, this frequency showed an increase in the spectral power during this same interval in all the analysed data.

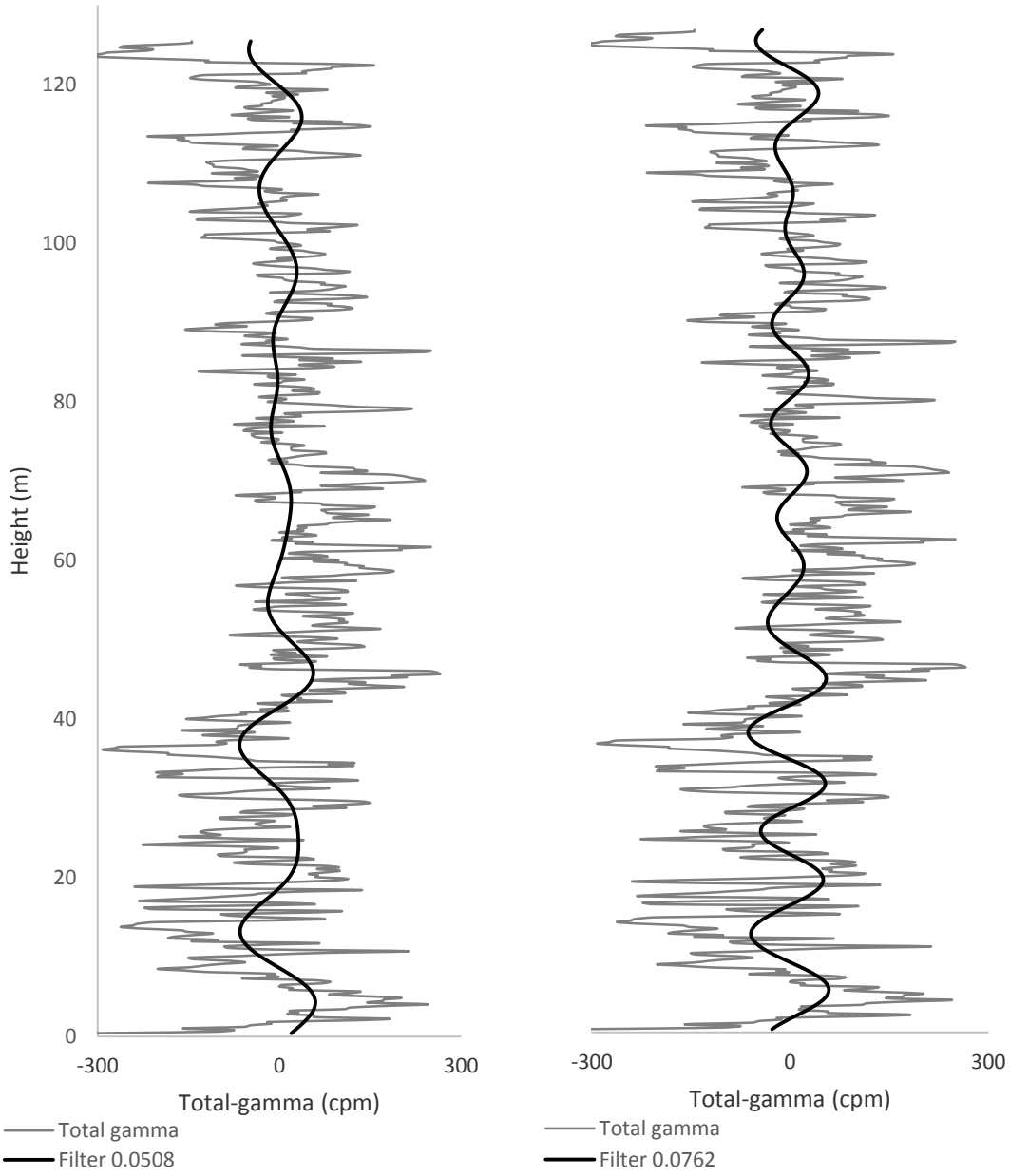

Figure 5.80 Frequency-selective filtering of the Morillo-reservoir section. Total-gamma-ray records have been interpolated and detrended prior to analysis. Filtering has been undertaken using a band-pass Gaussian filter and a bandwidth of 0.024 cycles/m. Total-gamma records have been filtered to the frequency 0.05 cycles/m and 0.0762 cycles/m. These two frequencies have been linked respectively to eccentricity and obliquity using REDFIT and ASM spectral analysis. The program Analyseries (Paillard *et al.*, 1996) was used for frequency-selective filtering.

5.3.5.5 Sieste gamma-ray logged section

5.3.5.5.1 Geographical location of the Sieste section

The Sieste section is 40 m long and located ~ 1.3 km south of Margudgued town and ~ 1 km southeast of the village of Sieste (Plate 5.15). The Sieste section is exposed along a small tributary of the Sieste River which can be accessed from the road A-2205 between the villages of Margudgued and Guaso. The oldest 20 m of the section are very clean and well-exposed along a stream (Plate 5.16a) and the remaining 20 m form a small hill capped by a heterolithic package. These heterolithics cannot be accessed due to very steep slopes and the gamma-ray log was discontinued ~ 30 m below them (Plate 5.16b).

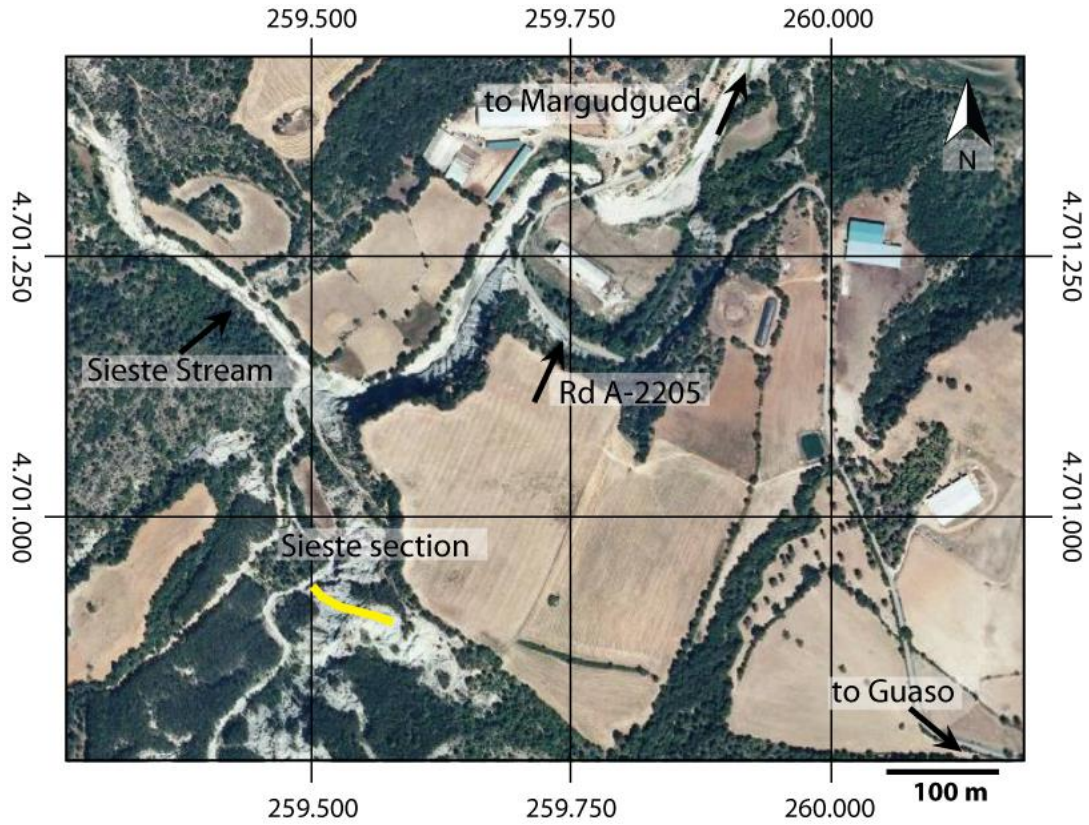

Plate 5.15 Aerial photograph of the area surrounding the Sieste gamma-ray logged section. The Sieste section is 40 m long and is well-exposed along a small stream in the proximities of the Sieste River. The section can be easily accessed from the road A-2205 between the villages of Guaso and Margudgued. Aerial image from www.sigpac.mapa.es/fega/visor.

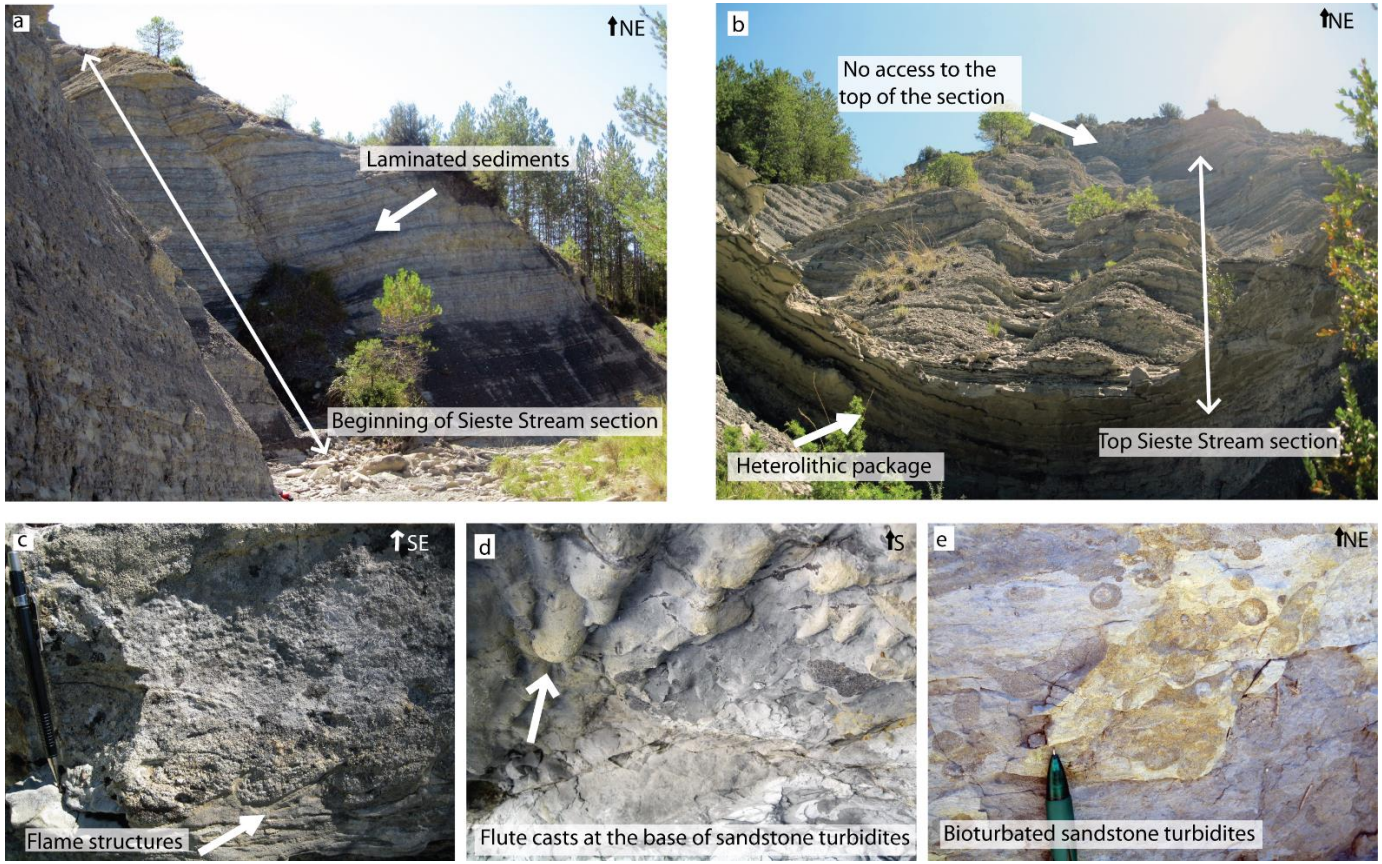

Plate 5.16 Outcrop photographs of the Sieste section. (a) Photograph showing the beginning of the Sieste section well-exposed along a tributary stream of the Sieste River. The outcrop shows the laminated character of the fine-grained sediments with an alternation of lighter and darker bands. **(b)** The top of the Sieste section forms a small hill capped by a thin heterolithic package interpreted to be the off-axial Guaso I sandbody. **(c)** Close-up outcrop photograph exposed at the Sieste River showing load structures in disorganised sandstone turbidite beds (Facies B1.2). **(d)** Close-up photograph showing the erosive base of a sandstone turbidite with well-developed flutes and grooves. **(e)** Close-up photograph showing intensely bioturbated intervals (probably *Arenicolite* burrows) within the fine-grained sediments of the Sieste section.

5.3.5.5.2 Stratigraphic location of the Sieste section

The Sieste section is located within the Morillo System and comprises the lower part of the fine-grained interfan deposits between the Morillo III and Guaso I sandbodies (Figure 5.81). The Morillo III Fan is represented by a mixed channel fill characterised by thin turbidite sandstone sequences and thick intervals of chaotic MTDs/MTCs. The Guaso I sandbody is very thin and off-axis at this location and constitutes a heterolithic package containing thick-bedded medium to coarse-grained sandstone turbidites. The Sieste gamma-ray log was discontinued ~ 60 m below this heterolithic package.

Figure 5.82 shows the sedimentary logs of the Sieste section. This section is in general, characterised by thin to very-thin sandstone turbidites and thick intervals of siltstone-mudstones couplets. Figure 5.83 shows that the sandstone turbidite intensity of the Sieste section has remained relatively constant throughout the section. At about 20 m above the base of this section, there is a thin (2 m thick) heterolithic package of sediments characterised by thicker sandstone turbidites. Figure 5.84 shows the variation in the content of the K, Th, U, Th/K and Th/U throughout the Sieste section. These values have also remained relatively stable throughout the Sieste section.

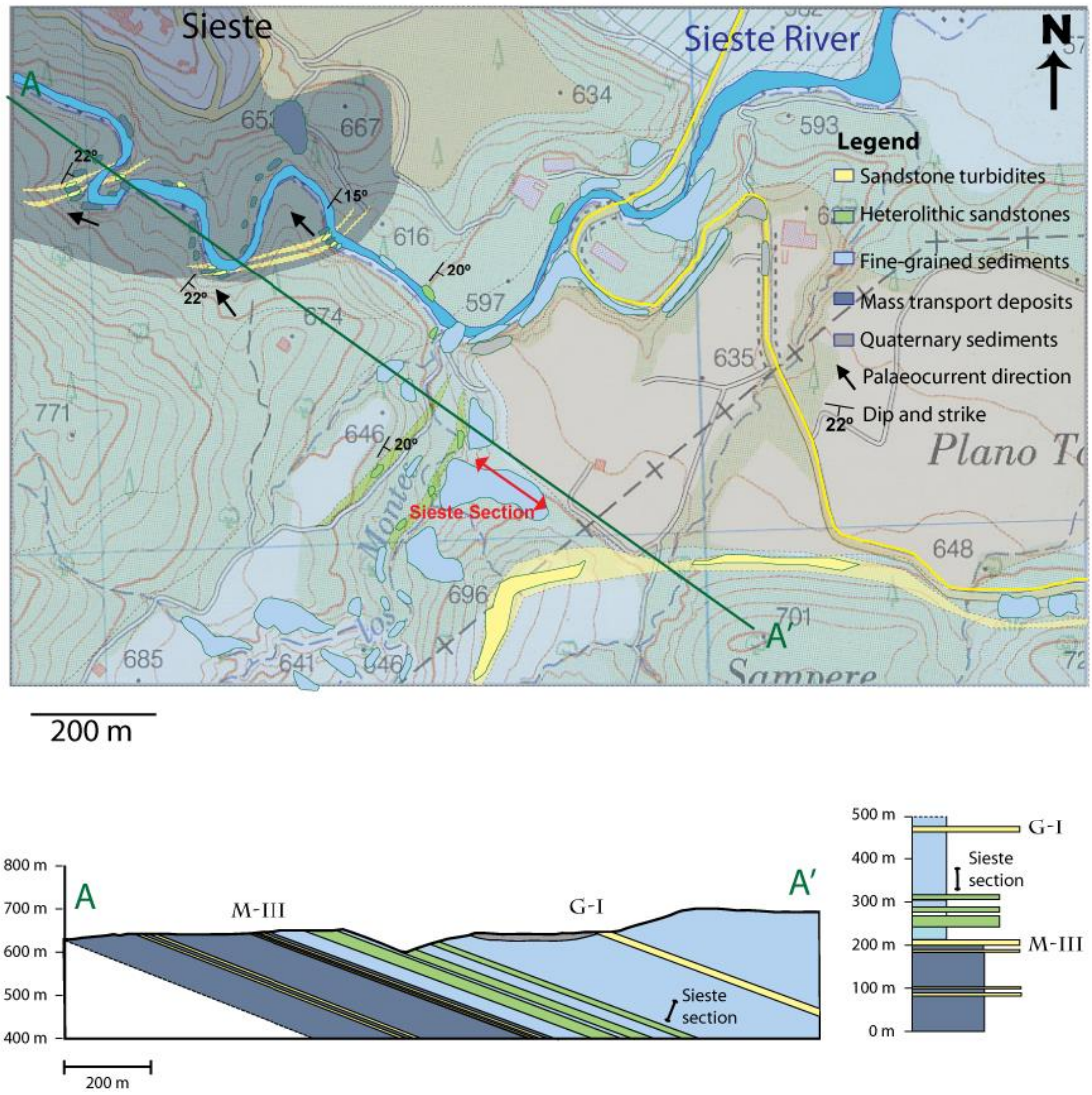

Figure 5.81 Geological map, cross-section and vertical stratigraphic column of the Sieste gamma-ray logged section. (a) Geological map of the area around the Sieste River in the proximities of the villages of Guaso and Margudgued showing the location of the Sieste gamma-ray logged section. The green line indicates the position of the cross-section A-A' which is parallel to the Sieste gamma-ray logged section and perpendicular to the main outcrop strike to facilitate the calculation of true stratigraphic thicknesses. (**b)** A-A' cross-section of the Sieste area showing the position of the gamma-ray logged section in the interfan sediments between the Morillo III and Guaso I sandy successions. **(c)** Vertical stratigraphic column showing the position of the Sieste gamma-ray logged section.

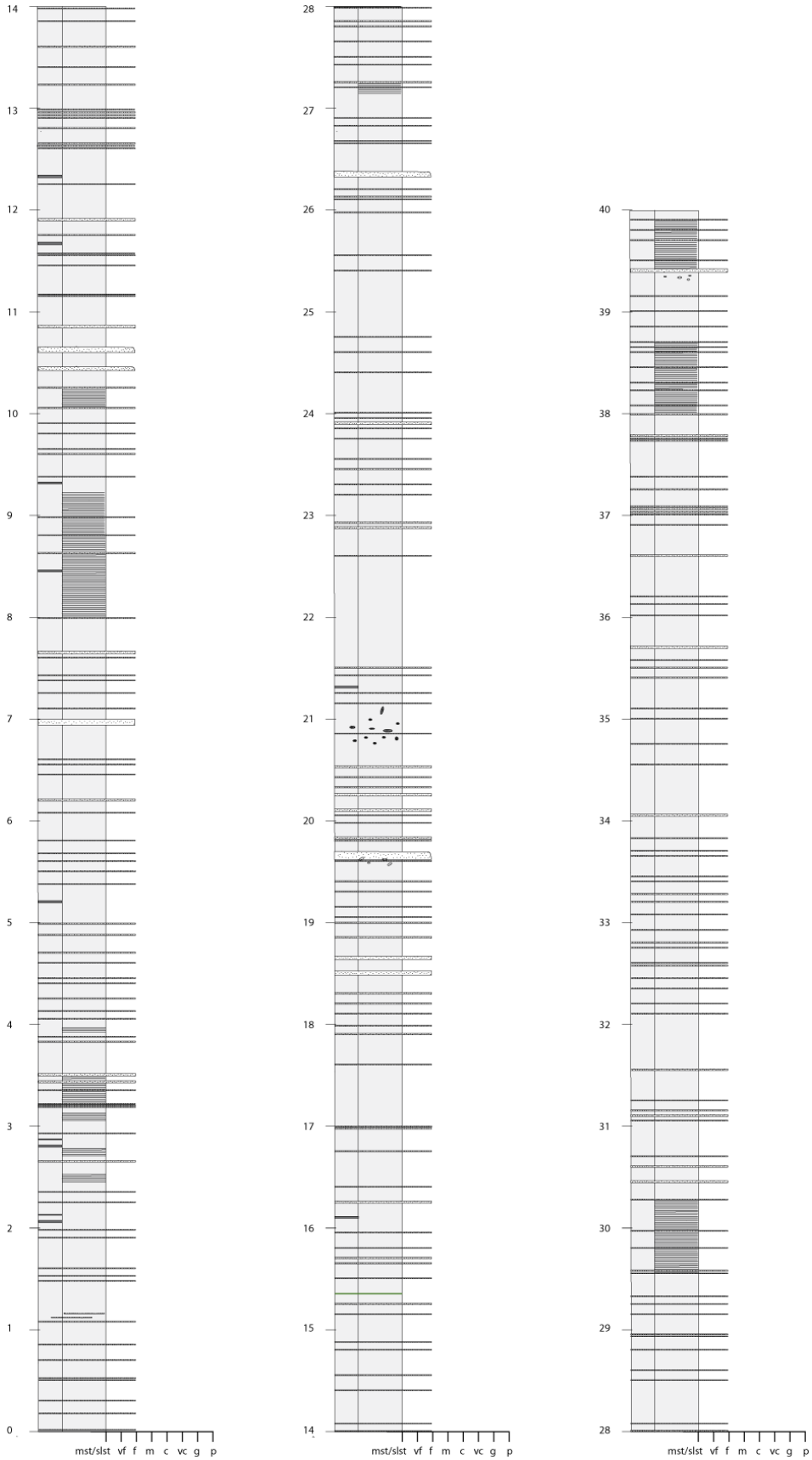

Figure 5.82 Detailed sedimentary log of the Sieste section. Sedimentary log includes every bed thicker than 5 mm. Figure 2.5 summarises the symbol key used in the sedimentary log. An electronic version of this log is available in Appendix 3.

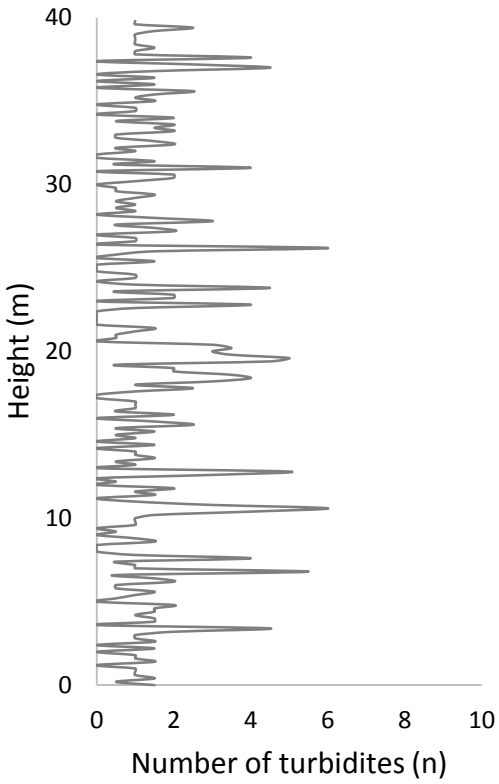

Figure 5.83 Sandstone turbidite intensity in the Sieste section. The thin heterolithic package between 18 and 20 m height can be seen in Plate 5.16b. The averaged sandstone content for the whole section is ~ 6.4%.

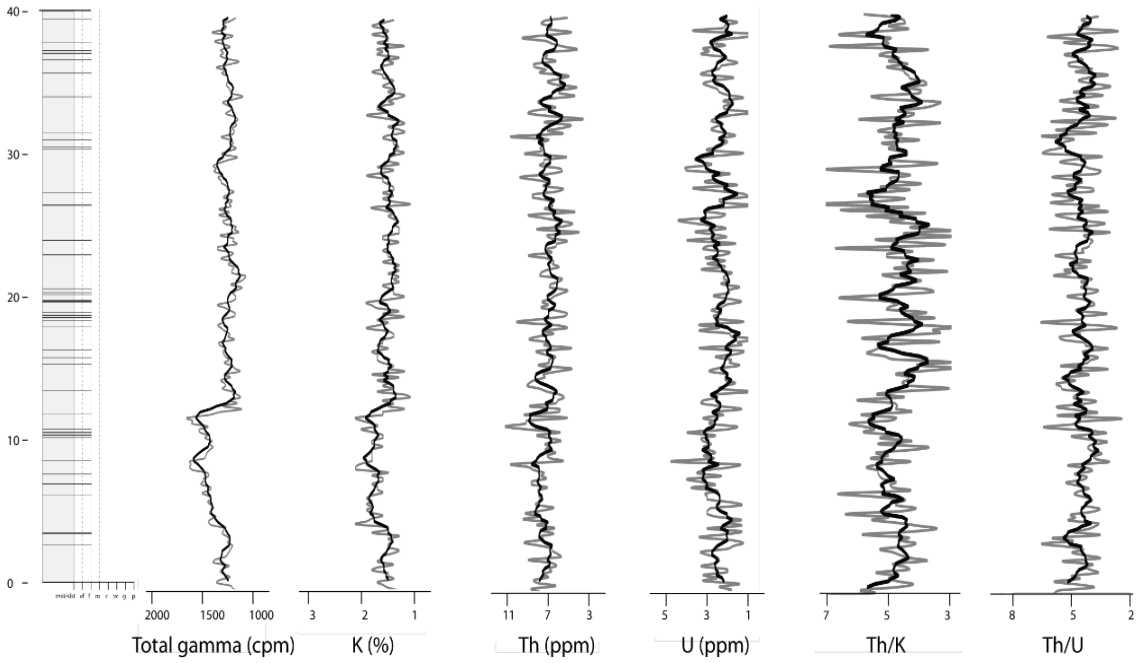

Figure 5.84 Simplified sedimentary logs of the Sieste section plotted against total-gamma (cpm), K (%), Th (ppm), U (ppm), Th/K and Th/U data. Black line is a 4-period moving average. Simplified logs only show sandy turbidites ≥ 1.5 cm, for complete sedimentary logs refer to Figure 5.82 and Appendix 3.

5.3.5.5.3 Cyclostratigraphic studies of the Sieste section

(a) Methods of spectral estimation

The total-gamma spectrum of the Sieste section has been estimated using four different methods: the REDFIT, the MTM, the maximum entropy and the periodogram modified with a Bartlett window. Figure 5.85 shows the spectral results obtained from applying each of these methods and Table 5.40 summarises the main frequencies present within the range 0-0.2 cycles/m. The MTM, the maximum entropy and the periodogram show very similar spectra which appear relatively flat with only a few well-defined spectral peaks. The REDFIT spectrum, however, appears noisier and contains spectral peaks at certain frequencies which are not identified in other spectra. Table 5.40 only shows a frequency range 0.4-0.05 cycles/m (1/18-1/25 m) which consistently appears in all of the spectra analysed. It is possible that the shortness of the Sieste section may have affected the reproductivity of the spectral results using different methodologies. Eccentricity cycles are not expected to be represented in this short section and the confidence levels of the obliquity cycles may have also been affected. The REDFIT method results in a noisier spectrum which will result in a decrease of the confidence levels, whilst the other methodologies result in the flattening of the spectral peaks which will also result in a reduction of the confidence levels.

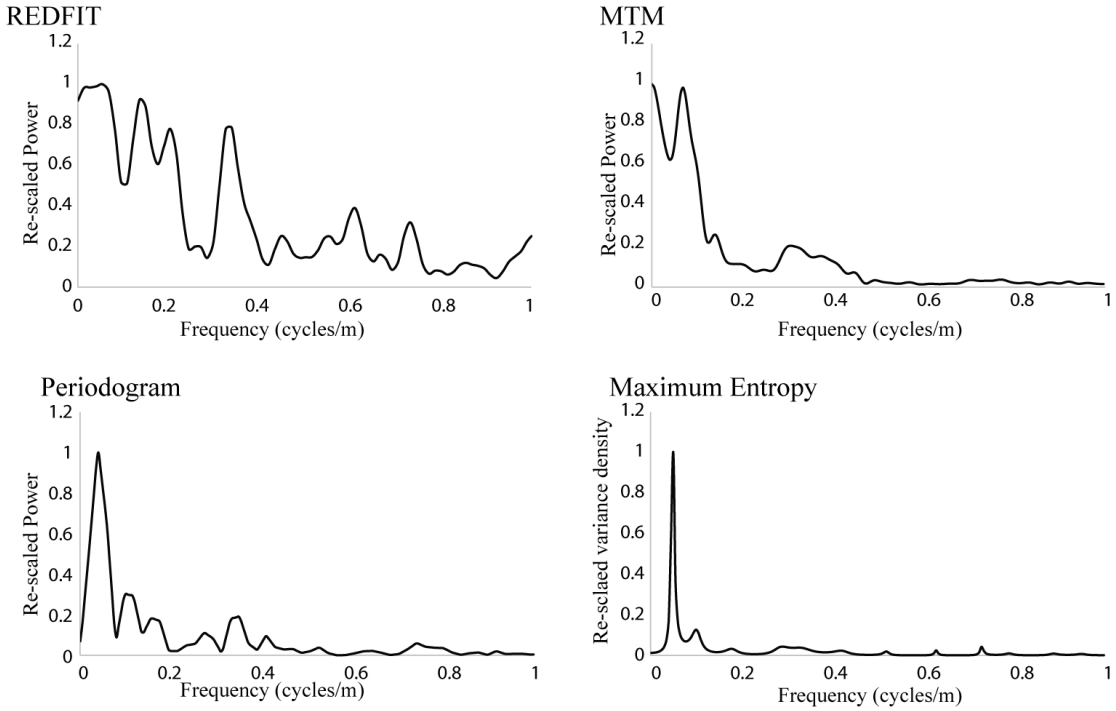

Figure 5.85 Methods of spectral estimation of the Sieste total-gamma data. REDFIT spectrum used 4 WOSA segments, 6 degrees of freedom and a bandwidth of 0.065 cycles/m. The MTM method used 3 tapers and ~ 6 degrees of freedom. The periodogram spectrum uses a Bartlett window and the maximum entropy method uses numbers of lags M = N/3 = 67). The REDFIT software developed by Schultz and Mudelsee (2002) and the Analyseries software package developed by Paillard *et al.* (1996) were used in the spectral analysis.

Table 5.40 Methods of spectral estimation of the Sieste section.

Spectral Method	Frequency (cycles/m)♠	Period (m)	Spectral Method	Frequency (cycles/m)♠	Period (m)
REDFIT	**0.054** 0.136 0.204 0.339	18.6 7.4 4.9 2.9	Periodogram modified with a Bartlett window	**0.04** 0.115 0.175 0.275 0.35	25 8.7 5.7 3.6 2.9
MTM□	**0.04** 0.112 0.171 0.347	25.6 8.93 5.85 2.9	Maximum entropy	**0.05** 0.105	20 9.5

♠ Frequencies within the range 0-0.4 cycles/m.
□Frequencies present in the MTM significance test with confidence levels > 90%.

(b) Spectral results using REDFIT

The Sieste section is too short to contain frequencies which can be associated with eccentricity cycles, but obliquity and precession cycles may well be reflected in the spectra. Significant frequencies identified in this section have been interpreted in association with other gamma-ray sections in the Morillo System such as the Morillo-reservoir section (see Section 5.3.5.4).

REDFIT analyses of the Sieste section have been undertaken using 4 WOSA segments (Figure 5.86). Results have been plotted using a power regression fitting model with the exception of the sandstone turbidite intensity data which has a better noise-background fit using the AR1 method of Mann and Lees (1996) (Table 5.41). The most significant frequency which appears to be represented in most of the investigated parameters is 0.14 cycles/m (1/7 m). This frequency has good confidence levels in the total-gamma and sandstone turbidite intensity (> 95%) and in the K spectrum (> 90%). The frequency range 0.20-0.23 cycles/m (1/4 m) is also present with good confidence levels (> 95%) in the total-gamma and sandstone turbidite intensity. Also, the frequency range at 0.34-0.36 cycles/m (1/2.7 m) has confidence levels > 99% and 95% in the total-gamma and Th data, respectively. Finally, the frequency 0.054 cycles/m (1/18 m) is only present in the total-gamma spectrum with a confidence level > 90%. This frequency is very similar to the frequency 0.05 cycles/m found in the stratigraphically lower Morillo-reservoir section, and interpreted to represent eccentricity cycles (see Section 5.3.5.4). Although the Sieste section is too short to represent this frequency with confidence, the presence of this frequency in other sections within the Morillo System may indicate that the SARs have remained relatively stable throughout the deposition of this system. Other frequencies within the frequency range 0-0.5 cycles/m are shown in Table 5.42.

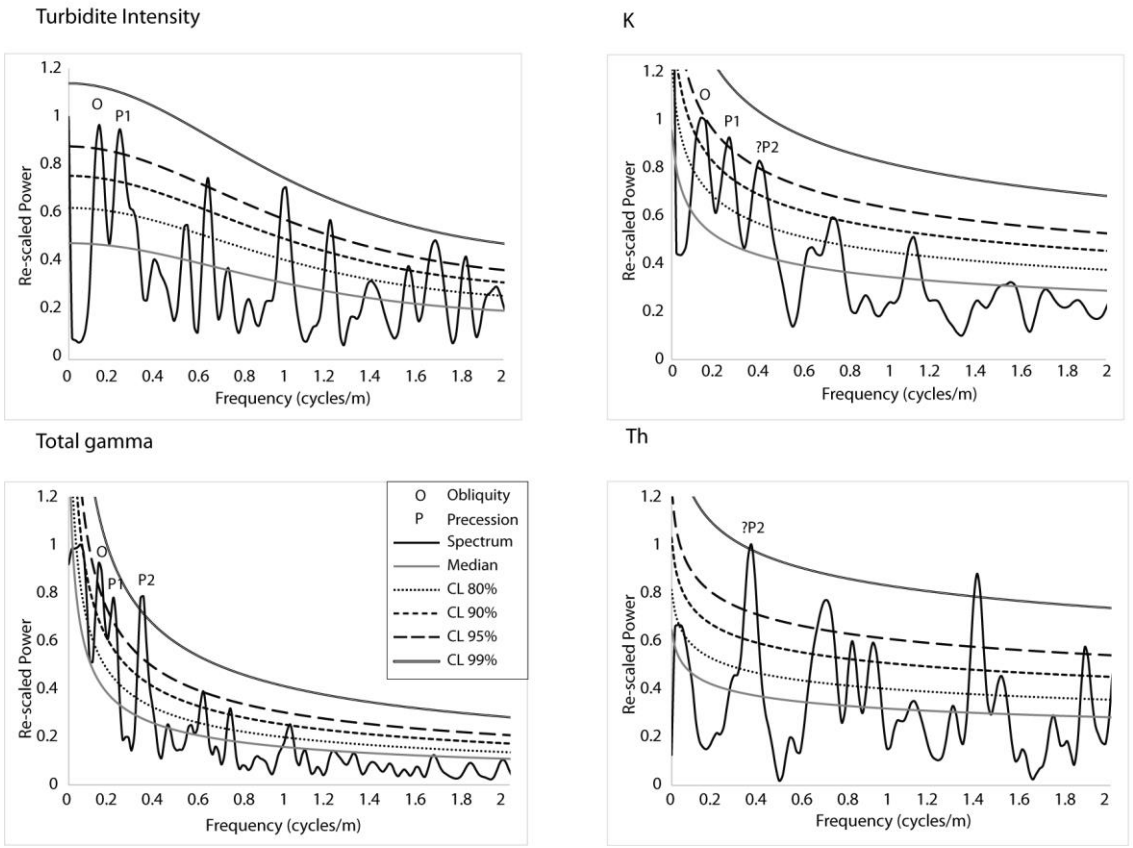

Figure 5.86 Time-series analysis of spectral gamma ray and sandstone turbidite intensity data of the Sieste section using REDFIT. The REDFIT spectral results used 4 WOSA segments, 6 degrees of freedom and a bandwidth of 0.065 cycles/m. REDFIT results plotted using a power regression fitting model with the exception of the sandstone turbidite intensity data that uses the AR1 method of Mann and Lees (1996). Spectra have been re-scaled to allow the comparison between different variables. Analysis used the software REDFIT developed by Schulz and Mudelsee (2002).

Table 5.41 Noise background estimation of the Sieste section.

Data	AR1 (Mann and Lees, 1996)	Quadratic	Power regression
Total-gamma	43	36	**20**
K	63	63	**63**
Th	100	105	**93**
Sandstone turbidite intensity	**57**	58	61

Summative square errors using the AR1 model of Mann and Lees (1996), a quadratic curve and a power regression method. The method with the least summative square error indicates the most adequate fitting-curve method and is represented in bold numbers.

Table 5.42 REDFIT time-series analysis results of the Sieste section.

Data	Frequencies (cycles/m)♠	Period (m)	Confidence level (%)
Total-gamma	0.054 0.1359 0.2038 0.3397	18.52 7.36 4.9 2.94	90 95 95 99
K	0.1339 0.2678 0.4018	7.47 3.73 2.49	90 95 95
Th	0.03164 0.3639	31.6 2.75	80 99
Sandstone turbidite intensity	0.1406 0.2343	7.11 4.27	95 95

REDFIT spectral results using 4 WOSA segments, 6 degrees of freedom and a bandwidth of 0.065 cycles/m.
♠Frequencies within the 0-0.5 cycles/m range with confidence levels > 80%.

(c) ASM results

A total of 9 frequencies were applied to the ASM studies (Figure 5.87). These frequencies were present in the REDFIT spectrum with confidence levels > 90%. The orbital parameters investigated were obliquity and precession, whilst eccentricity was excluded due to the shortness of the Sieste section.

Significant SARs range from 12 to 23 cm/kyr. The most significant ASM results are the SAR between 13-13.5 cm/kyr with null hypothesis significance levels of 0.003%. Other significant SARs are present between 14.5 and 16.5 cm/kyr with null hypothesis significance levels of 0.01% and between 18.5 and 19 cm/kyr with null hypothesis significance levels of 0.026% (Table 5.43). A SAR of 19 cm/kyr very closely represents the duration of orbital cycles for the Middle Eocene. At a SAR of 19 cm/kyr, the frequency range 0.135-0.141 cycles/m (1/7 m) represent obliquity 40 kyr and the frequencies 0.2343 cycles/m (1/4 m) and 0.2678 cycles/m (1/3 m) represent

precession 22 kyr and 19 kyr, respectively (Table 5.43). The frequency 0.054 cycles/m (1/18 m) is likely to represent eccentricity 95 kyr and this frequency is very similar to the frequency 0.054 cm/kyr linked to eccentricity in the Morillo-reservoir section.

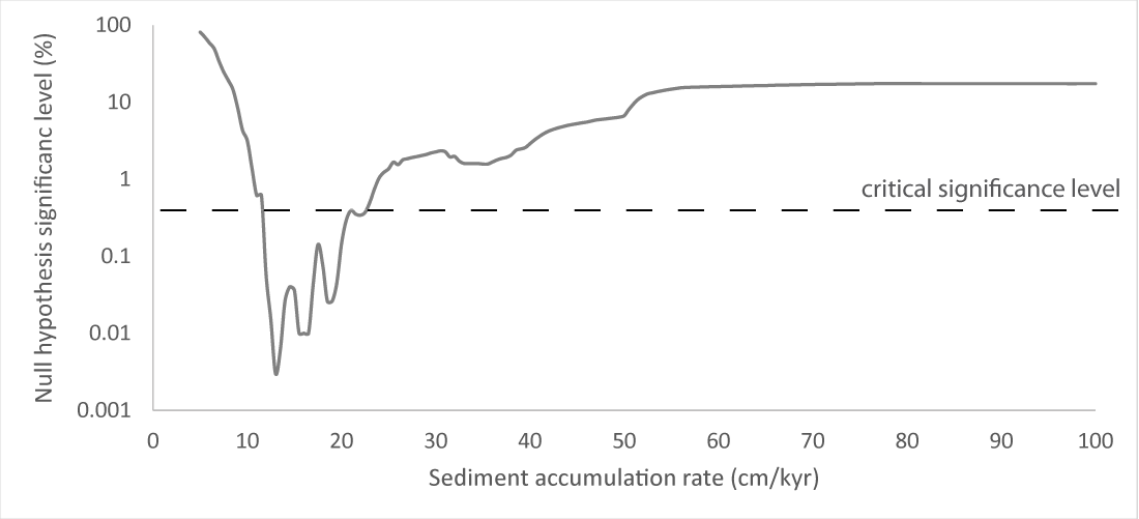

Figure 5.87 ASM results of the Sieste section. ASM analysis includes a total of 9 frequencies identified from spectral analysis of the spectral gamma-ray and sandstone turbidite intensity data with a confidence level > 90%. For a list of all significant frequencies refer to Table 5.43. The analysis used a Rayleigh number of 0.001 and a Nyquist frequency of 2.4 cycles/m. Orbital parameters were established at ~ 45 Ma using Berger *et al.* (1992) equations. A total of 191 SARs ranging from 5-100 cm/kyr with an increment of 0.5 cm/kyr were investigated using 100,000 Monte Carlo simulations. Critical significance levels were established at 0.52%. Only the orbital parameters obliquity and precession have been included in the ASM studies. ASM analysis has identified significant SAR values ranging from 12-23 cm/kyr. Analysis used the ASM software developed by Meyers and Sageman (2007).

Table 5.43 Temporal period duration of significant frequencies in the Sieste section.

Frequency (cycles/m)♠	C.L (%)	N□	Period (m)	Period duration (kyr) at different SARs						
				13 cm/kyr	13.5 cm/kyr	14.5 cm/kyr	16 cm/kyr	16.5 cm/kyr	18.5 cm/kyr	**19 cm/kyr**
0.054	90	1	18	142.4	137.2	119.5	114.7	112.2	100.1	**97.5**
0.135	95	2	7.4	56.9	54.9	47.8	46.3	44.9	40	**39**
0.1406	95	1	7.1	54.7	52.7	44.9	44.4	43.1	38.4	**37.4**
0.2038	95	1	4.9	37.7	36.3	31.7	30.7	29.7	26.5	24.8
0.2343	95	1	4.3	32.8	31.6	27.5	26.7	24.9	23.1	**22.5**
0.2678	99	1	3.7	28.7	27.7	24.1	23.3	22.6	20.2	**19.7**
0.3397	99	1	2.9	22.6	21.8	19	18.4	17.8	14.9	14.5
0.3639	99	1	2.7	21.1	20.4	17.7	17.2	16.7	14.9	14.5
0.4018	95	1	2.4	19.1	18.4	16.1	14.6	14.1	13.4	13.1

The table shows calculated cycle duration for each significant frequency (> 90% confidence levels) at different SARs. The SAR which most closely matches the orbital periods of the Middle Eocene (~ 45 Ma) is 19 cm/kyr.
♠Frequencies within the range 0-0.5 cycles/m present in the total-gamma, K, Th and sandstone turbidite intensity spectra with confidence levels > 90%.
□ N the number of spectra containing that specific frequency.
Underlined are frequencies which are contained in more than 1 spectrum with at least 1 confidence level > 95%.
Estimated orbital cycles in the Middle Eocene at 45 Ma using Berger *et al.* (1992) equations are: eccentricity 123.8 and 94.8 kyr, obliquity 52.3 and 40 kyr and precession 22.6 and 18.8 kyr.

(d) Wavelet analysis

Results of the wavelet analysis include two significant frequency ranges > 90% confidence levels (Figure 5.88). The most spatially persistent frequency range is 0.12-0.14 cycles/m (1/7-1/8 m). This frequency is significant with confidence levels > 90% in the total-gamma, K and sandstone turbidite intensity wavelet spectrum. In the sandstone turbidite intensity wavelet spectrum, this frequency range appears more significant in the middle section, whilst in the other records it is more consistent throughout the Sieste stratigraphic section. Spectral analysis using REDFIT and ASM has associated this frequency with obliquity.

The frequency range 0.23-0.26 cycles/m (1/3 -1/4 m) which has been linked to precession, is present in the wavelet spectra of the sandstone turbidite intensity, K and total-gamma records. This frequency range is spatially discontinuous and present in small significant regions. The Th spectrum does not contain any significant regions throughout the records.

Figure 5.88 (next page) Wavelet analysis of the sandstone turbidite intensity, K, total-gamma and Th data in the Sieste section. (a) The wavelet power spectrum calculates spectral power at different frequencies throughout the Sieste section using sandstone turbidite intensity, K, Th and total-gamma records. Black contours mark the 10% significant regions. **(b)** The global wavelet shows the scale-averaged wavelet power across the studied frequency bands. Values to the right of the dashed line have a significance > 90% confidence levels. Significant spectral peaks which have been associated with Milankovitch frequencies using REDFIT and ASM analysis have been labelled (E-eccentricity, O-obliquity, and P-precession). Analysis used the online tool http://paos.colorado.edu.research/wavelets based on the algorithms of Torrence and Compo (1998).

Figure 5.88 Wavelet analysis of the Sieste section.

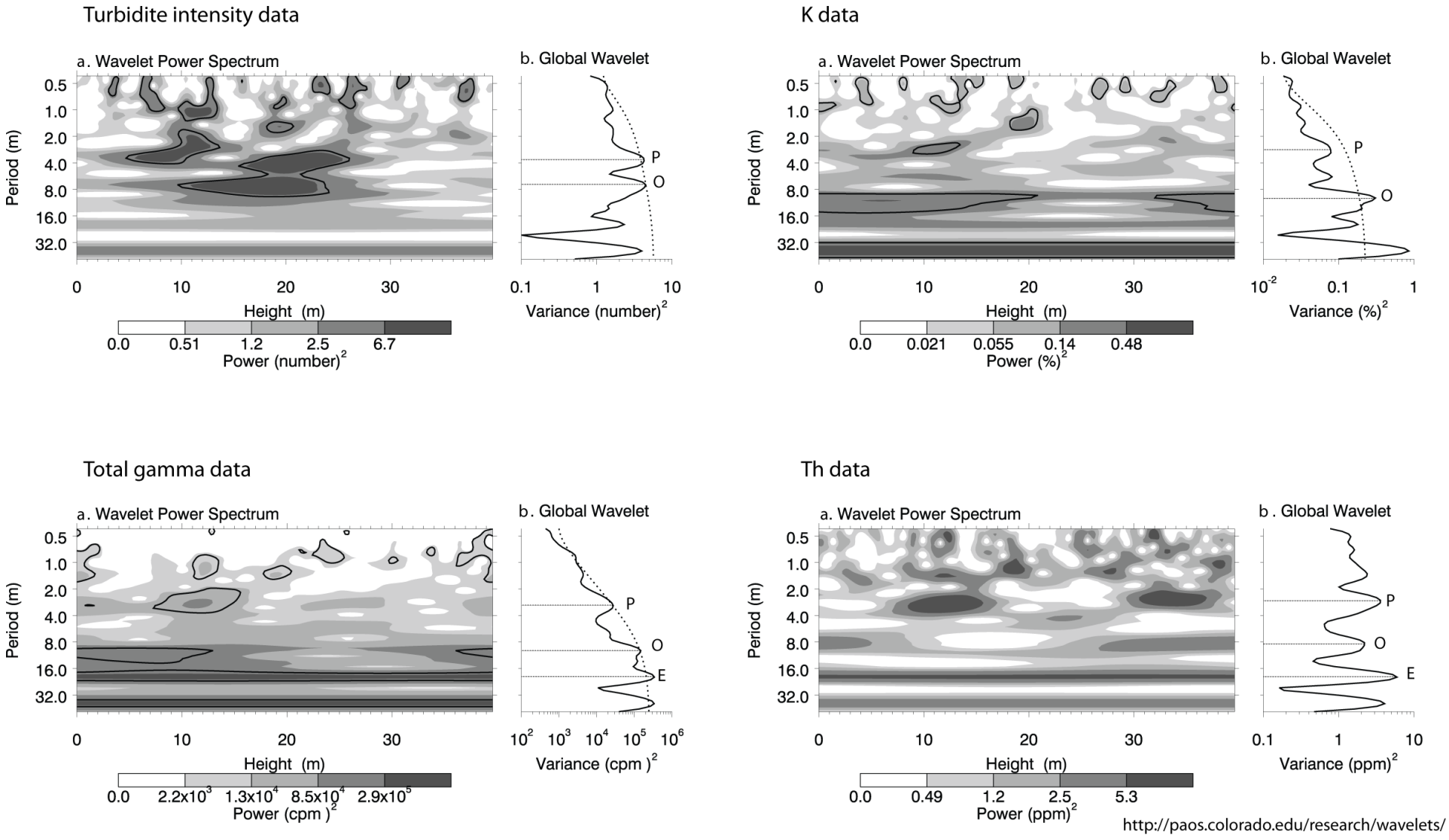

(e) Frequency-selective filtering

The frequencies 0.054 and 0.1359 cycles/m have been filtered using a bandwidth of 0.0658 cycles/m (Figure 5.89). These frequencies are associated with eccentricity and obliquity, respectively, and are present in the total-gamma records with confidence levels > 90%.

The total-gamma records filtered to the frequency 0.054 cycle/m (1/18 m) show a well-developed high amplitude cycle at the beginning of the section. The rest of the records, however, do not show clear cyclicity. Although this frequency has been linked to eccentricity, the Sieste section is too short to determine eccentricity cycles with confidence. As a result, the Sieste section has not been orbitally tuned and the timing of deposition for these sediments can only be estimated from biostratigraphic studies and from SAR estimates using the duration of obliquity and precession cycles.

The total-gamma records filtered at a frequency 0.1359 cycles/m (1/7 m) show poorly defined obliquity cycles throughout the section. The amplitude of the cycles is, in general low and the cycles appear irregularly spaced.

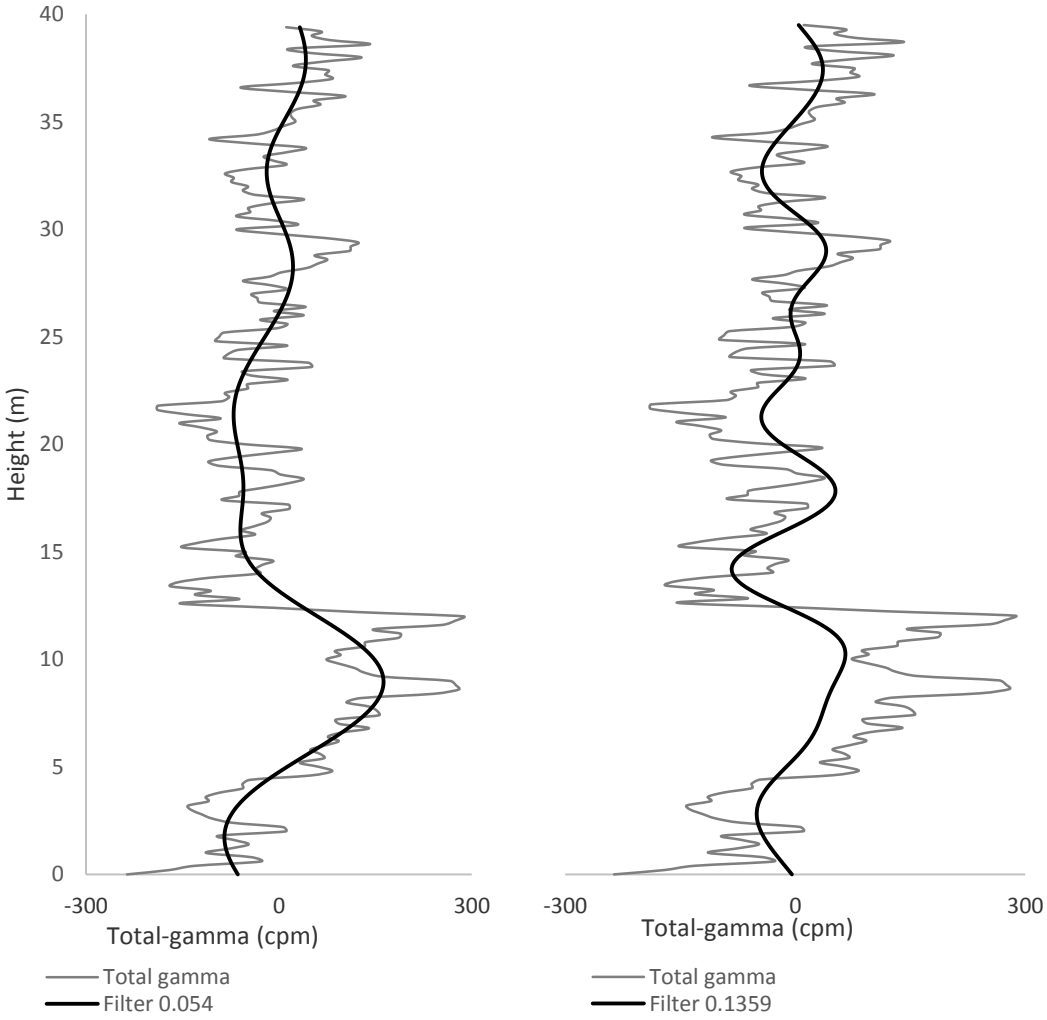

Figure 5.89 Frequency-selective filtering of the Sieste section. The total-gamma records have been interpolated and detrended prior to analysis. Filtering has been undertaken using a band-pass Gaussian filter and a bandwidth of 0.0658 cycles/m. Total-gamma records have been filtered to the frequencies 0.054 and 0.1359 cycles/m. These frequencies have been respectively associated with eccentricity, obliquity and precession using REDFIT and ASM analysis. Filtering has used the program Analyseries (Paillard *et al.*, 1996).

5.3.6 The Guaso System

5.3.6.1 Sedimentology of the Guaso System

The Guaso System is the youngest of all the deep-marine systems of the Ainsa Basin and stratigraphically, this system is located immediately above the Morillo System. The Guaso System is underlain by several hundreds of metres of very thin- and thin-bedded fine-grained sediments which constitute the interfan deposits between the Morillo III and the Guaso I sandbodies. Overlying the Guaso System is an upper basin slope and delta system of the Sobrarbe Formation and the subsequent fluvial deposits of the Escanilla Formation (Dreyer *et al*., 1999). The Guaso System outcrops at the core of the south-verging Buil Syncline and there are well-exposed outcrop sections in the proximities of the Sieste, Guaso and El Grado towns and along the Eña River. Nannofossil and foraminifera identification suggests that the Guaso System was deposited in fully marine conditions at upper bathyal depths, several hundred metres below wave-base (Sutcliffe and Pickering, 2009).

The sedimentology of the Guaso System has been described in detail by Sutcliffe and Pickering (2009). The Guaso System can be divided into two major clastic depositional units: the Guaso I and Guaso II submarine fans. Each of these units is mainly composed of a sandbody with a general fining upward profile. The sandbodies comprise thick-bedded, medium to coarse-grained, amalgamated sandstones and locally, they contain multi-event Type I MTDs (Sutcliffe and Pickering, 2009). The petrography of the Guaso sandstones show they are texturally and compositionally immature. They are classified as feldspathic litharenites and have a poor to moderate sorting (Das Gupta and Pickering, 2008).

The Guaso System has been interpreted as a low-gradient clastic system including base-of-slope deposition (Sutcliffe and Pickering, 2009). These authors based their conclusions on the laterally extensive geometry of the Guaso I and II sandbodies with multiple shallow channels and the paucity of coarse-grained Type II MTCs. The Guaso System is characterised by lateral structural confinement. This confinement is demonstrated by significant changes in the sandbody thickness. The axial part of the Guaso System is thicker at the Buil Syncline and the sediments thin and onlap onto the basin marginal slopes of the Boltaña and Mediano topographic highs. Sutcliffe and Pickering (2009) interpreted the Guaso System as a low-gradient clastic system. These authors also observed that the Guaso II sandbody is, in general, coarser grained than the Guaso I and they suggested delta progradation during the deposition of the Guaso II sandbody.

5.3.6.2 Tectonic history during the deposition of the Guaso System

The deposition of the Guaso System coincides with the latest stages of the emplacement of the Pyrenean lower thrust sheets including the propagation of the Gavarnie Thrust. This resulted in the thickening of the Pyrenean axial zone and resulted in the compartmentation of the southern foreland piggy-back basins. The continuous emplacement of the Gavarnie basement thrust resulted in regional uplift and resulted in the shallowing of the Ainsa Basin. As the Mediano and Boltaña anticlines continued to grow, the basin became narrower and resulted in the structural confinement of the Guaso sandbodies (Sutcliffe and Pickering, 2009).

The Guaso System was fed from a more southern sediment source than the Morillo System or any other previous deep-marine system of the Ainsa Basin.

Sediment gravity flows were deflected around the Mediano Anticline which at this time formed a prominent topographic high and entered the basin from a structurally confined frontal ramp area (Sutcliffe and Pickering, 2009).

5.3.6.3 Age of the Guaso System

Biostratigraphic studies suggest that the beginning of the Guaso System occurred at ~ 43.23 Ma (Scotchman *et al.,* 2014). The top of the Guaso System represents the end of deep-marine deposition and the beginning of the deposition of deltaics and fluvial deposits of the Sobrarbe and Escanilla formations. The termination of the deep-marine sedimentation has been estimated between 41.6 to 42.3 Ma in SBZ15 and at the top of chron C20n (Bentham and Burbank, 1996; Dreyer *et al.*,, 1999; Mochales *et al.*, 2012).

Scotchman *et al.* (2014) suggest that the top of the Guaso System was a dark-shale anoxic horizon which was dated using biostratigraphy at 42.55 Ma. This horizon was recognised as well by Mochales *et al.* (2012) and dated it at 42.4 Ma using magnetostratigraphy.

5.3.6.4 Morillo-Bruello gamma-ray logged section

5.3.6.4.1 Geographical location of the Morillo-Bruello section

The Morillo-Bruello section is 108 m long and is located ~ 1.5 km west of Morillo-de-Tou town and ~ 1.3 km south of the village of Bruello. The section can be accessed from the path which joins Morillo-de-Tou and Bruello towns, and is well exposed along the Sarrato stream (Plate 5.17). Plate 5.18 shows outcrop photographs of the Morillo-Bruello section.

The section is composed of two main subsections: Morillo-Bruello section 1 (~ 44 m thick) and Morillo-Bruello section 2 (~ 63 m thick). These two subsections are separated by a distance of ~ 20 m. The whole outcrop is generally well-exposed, with no slumps or tectonic activity noted. Morillo-Bruello 1 forms a small hill capped by a heterolithic package and Morillo-Bruello 2 is well-exposed along the Sarrato stream. The heterolithic package exposed at the top of Morillo-Bruello section 1 is also exposed along the Sarrato stream allowing the correlation between these two subsections.

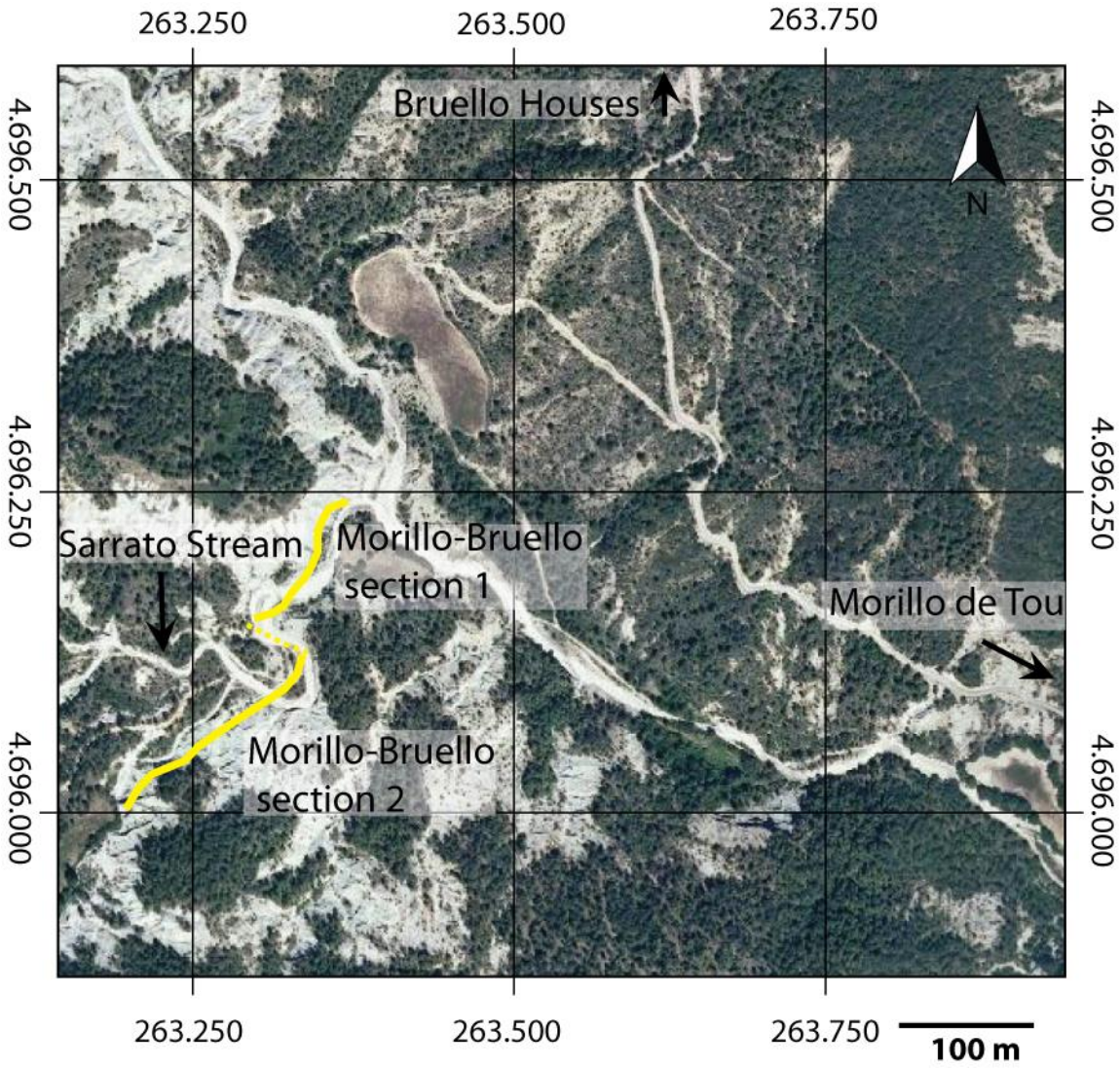

Plate 5.17 Aerial photograph of the Morillo-Bruello gamma-ray logged section. The Morillo-Bruello section is exposed along the Sarrato stream and is located between the villages of Morillo-de-Tou and Bruello. The section is 108 m long and comprises two subsections, Morillo-Bruello section 1 and 2 which are separated by ~ 20 m. Aerial image from www.sigpac.mapa.es/fega/visor.

Plate 5.18 (next page) Outcrop photographs of the Morillo-Bruello section. (a) Photograph of the Morillo-Bruello section 1, which forms a small hill with a heterolithic package at the top (vegetated area). **(b)** Photograph of the Morillo-Bruello section 2. The heterolithic package seen at the top of Morillo-Bruello section 1 is now well-exposed at the Sarrato stream allowing for lateral correlation of these two logs. **(c)** Outcrop photograph showing lenticular sandstone turbidites with well-developed ripples. **(d)** Close-up outcrop photograph showing the laminated nature of the Morillo-Bruello sediments. Dark bands appear heavily bioturbated. Note as well the presence of some orange-coloured bands which alternate with the dark bands. Sandstone turbidites are very thin and mm-sized.

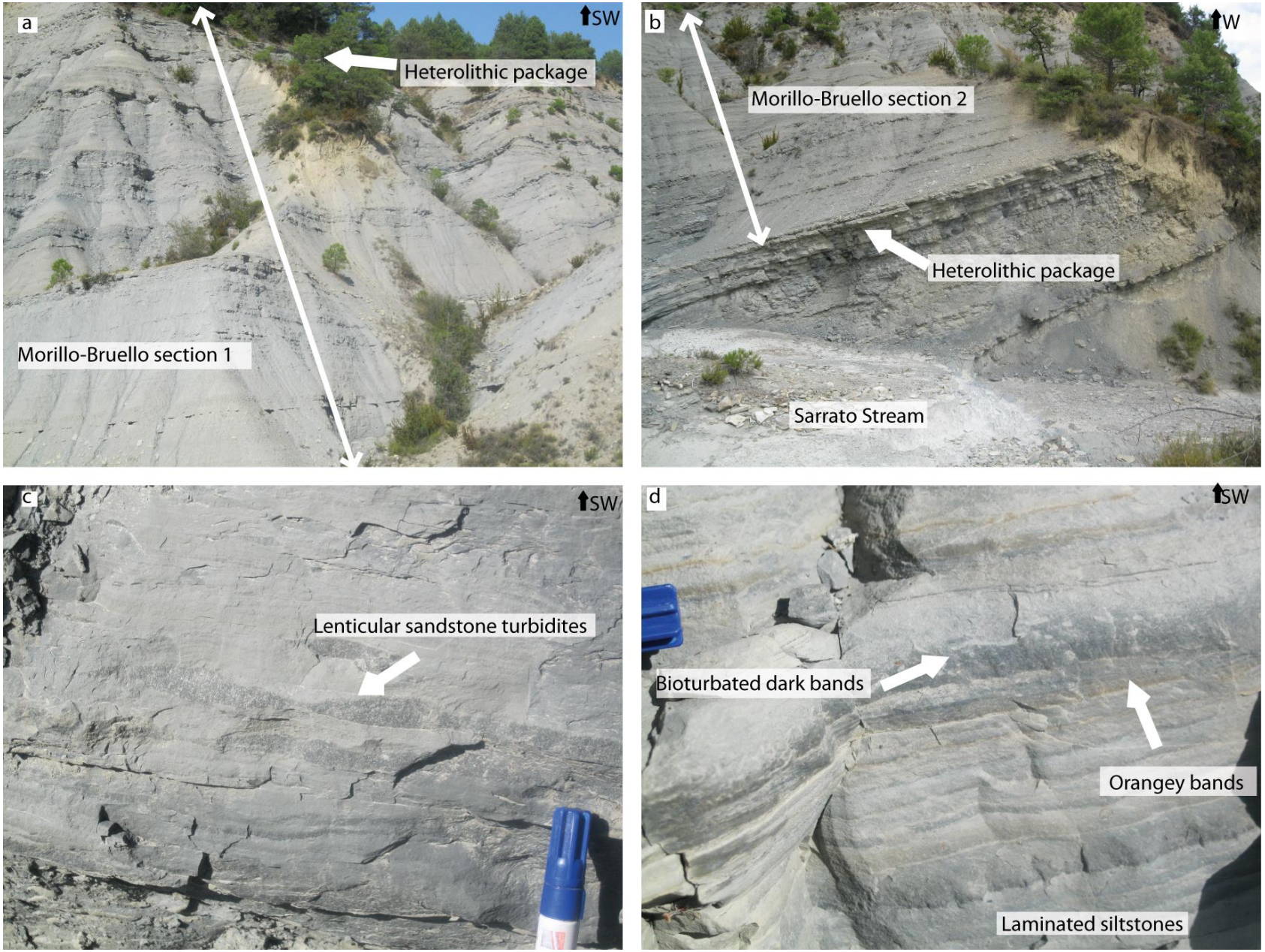
a
SW
Heterolithic package
Morillo-Bruello section 1
b
W
Morillo-Bruello section 2
Heterolithic package
Sarrato Stream
c
SW
Lenticular sandstone turbidites
d
SW
Bioturbated dark bands
Orangey bands
Laminated siltstones

5.3.6.4.2 Stratigraphic location of the Morillo-Bruello section

The Morillo-Bruello section is located within the Guaso System and this section mainly represents the fine-grained interfan sediments between the Guaso I and II sandbodies. The beginning of the section is found immediately above the Guaso I submarine fan which forms a thick sandbody at this location. The Guaso II sandbody has completely pinched out and the axial part of these channelised deposits can be found ~ 6 km towards the northwest. The heterolithic package present at ~ 45 m height in the Morillo-Bruello section could represent the off-axial Guaso II sandbody, but, this heterolithic package is small and discontinuous and could not be mapped laterally, making any association with the Guaso II sandbody uncertain. Figure 5.72 shows the geological map, cross-section and vertical stratigraphic column of the Morillo-Bruello section.

Figure 5.90 shows the sedimentary logs of the Morillo-Bruello section separated in Morillo-Bruello 1 and 2 subsections. Figure 5.91 shows the variation in the content of the K, Th, U, Th/K and Th/U throughout the section. Figure 5.92 shows the sandstone turbidite intensity variation of the section. The sandstone turbidite intensity appears to vary cyclically with cycles showing a periodicity of ~ 20 m throughout the section.

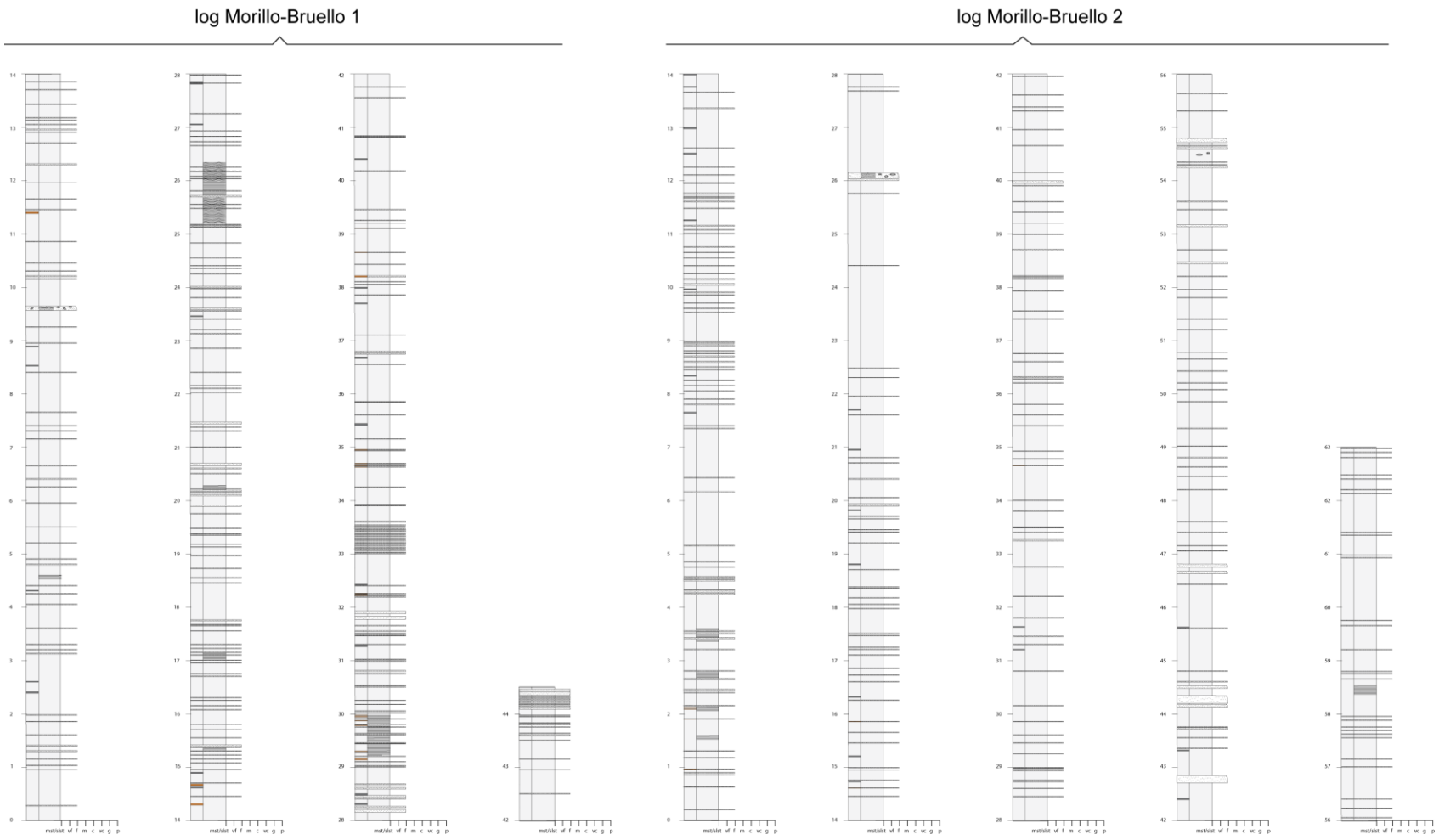

Figure 5.90 Detailed sedimentary logs of the Morillo-Bruello section. Morillo-Bruello section is composed of two main logs: Morillo-Bruello section 1 and 2. Sedimentary logs include every bed thicker than 5 mm. Figure 2.5 shows symbol key used in these logs. An electronic version of the sedimentary logs to allow for a more detailed study are included in Appendix 3.

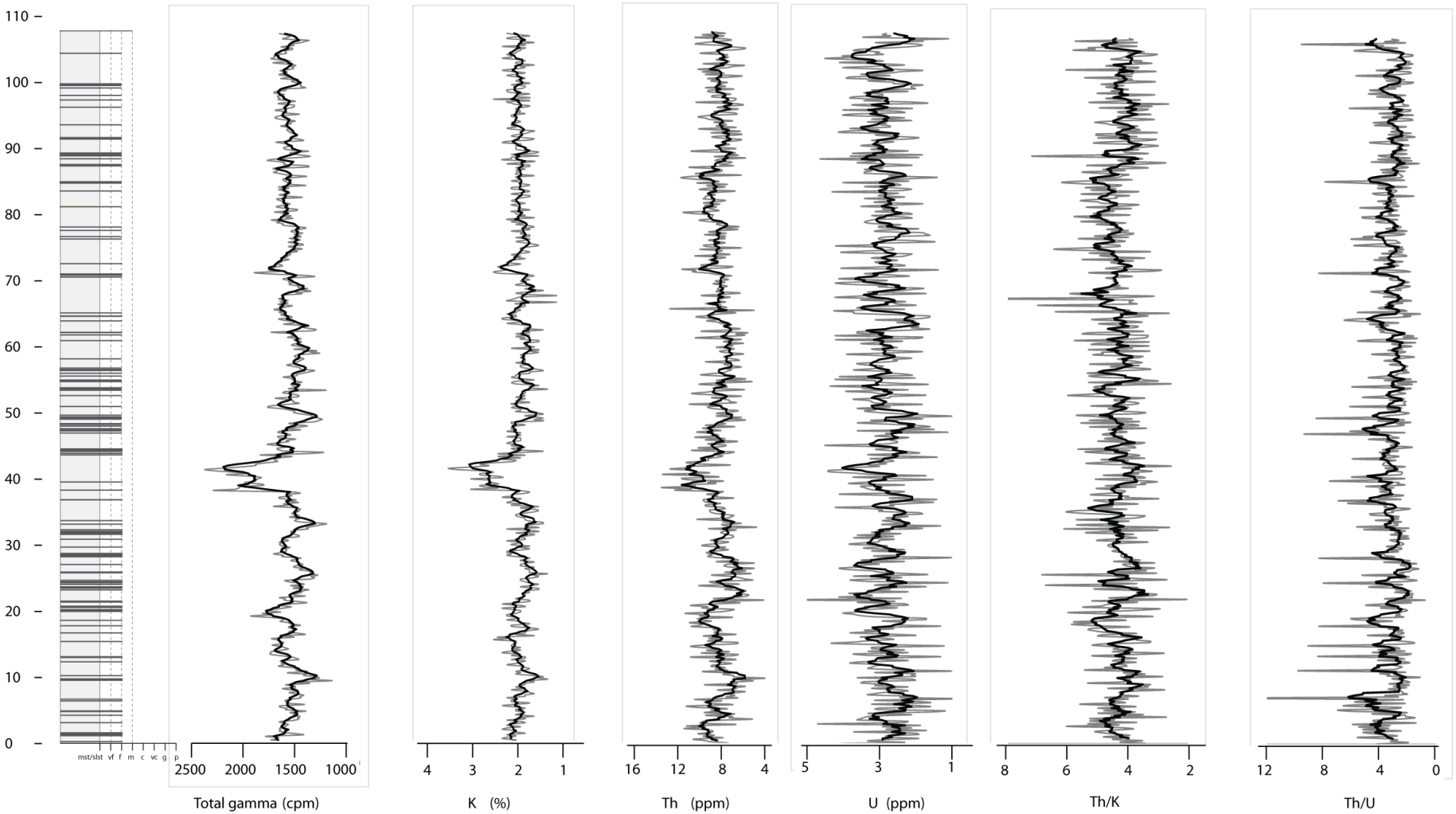

Figure 5.91 Total-gamma, K, Th, U, Th/K and Th/U data plotted against simplified sedimentary logs of the Morillo-Bruello section. Sedimentary log only showing sandy turbidites ≥ 1.5 cm, for complete log refer to Figure 5.90 and Appendix 3. Black line is a 4-weight moving average.

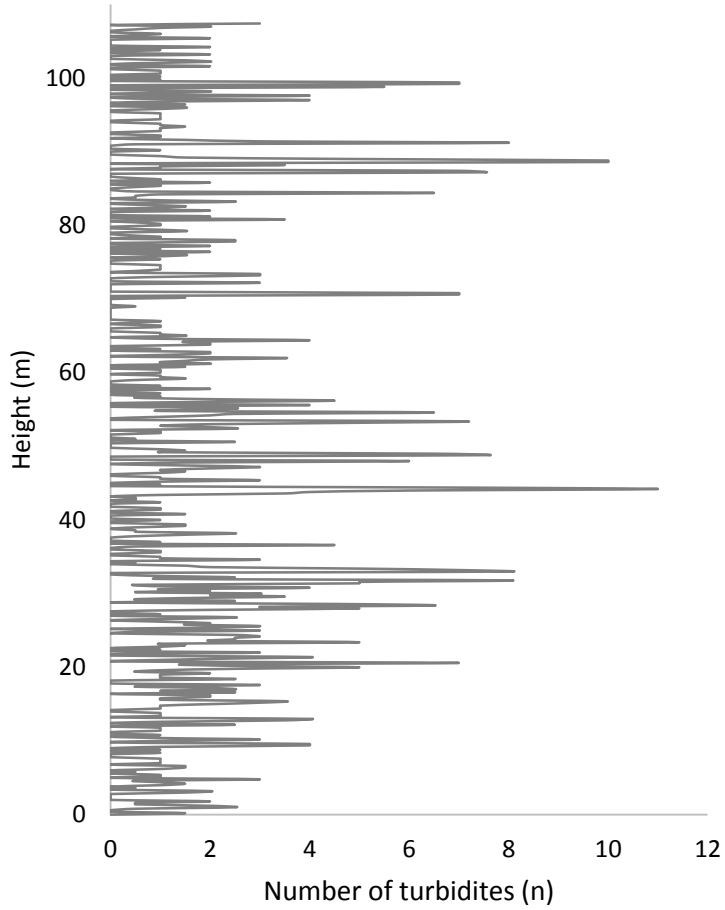

Figure 5.92 Sandstone turbidite intensity in the Morillo-Bruello section. The thin heterolithic package at 44 m allows correlation between the Morillo-Bruello log 1 and 2. The graph shows some cyclic packaging in the sandstone turbidites with a periodicity of ~ 20 m. The averaged sandstone content for the Morillo-Bruello section is ~ 6.3%.

5.3.6.4.3 Cyclostratigraphic studies of the Morillo-Bruello section

(a) Methods of spectral estimation

The total-gamma spectrum of the Morillo-Bruello section has been estimated using four different methods: the REDFIT, the MTM, the maximum entropy and the periodogram modified with a Bartlett window. Figure 5.93 shows the spectral results obtained from applying each of these methods. Table 5.44 summarises the main frequencies present within the range 0-0.2 cycles/m. The spectrum created using the four methods is very similar with spectral peaks found at similar frequencies. There are

three frequencies 0.15 cycles/m (1/6 m), 0.18 cycles/m (1/5 m) and 0.31 cycles/m (1/3 m) which consistently appear in all of the spectra analysed. The frequencies 0.08 cycles/m (1/12 m) and 0.42 cycles/m (1/2 m) are also present in all the spectra with the exception of the MTM spectrum.

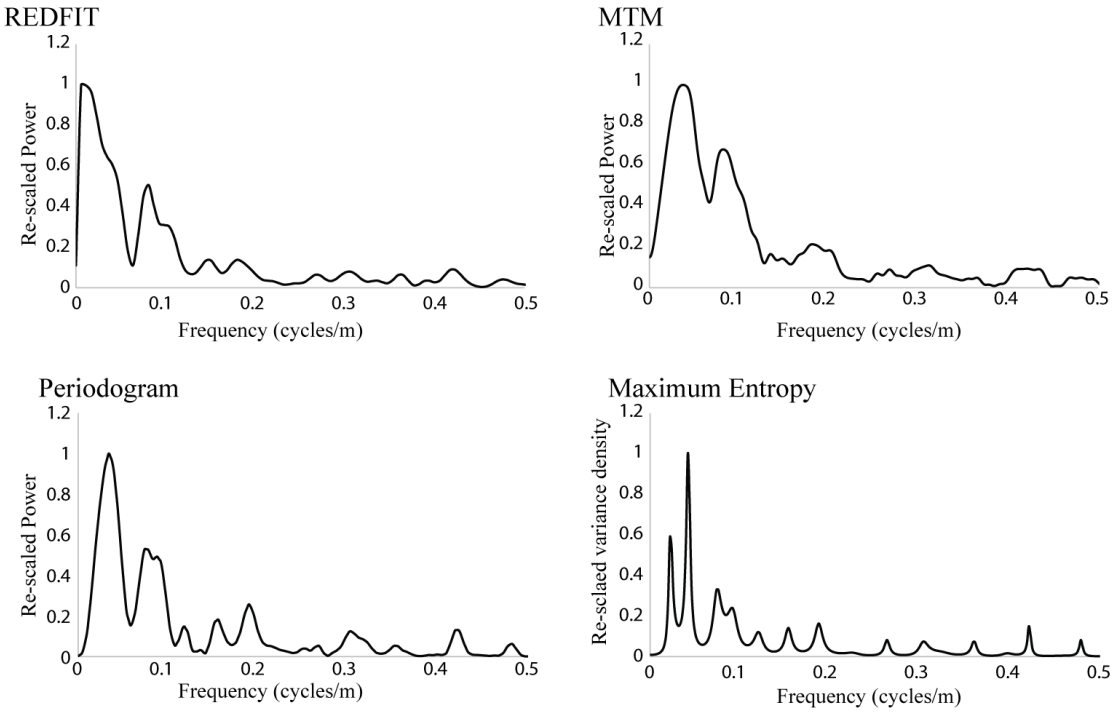

Figure 5.93 Methods of spectral estimation using the spectral total-gamma data of the Morillo-Bruello section. REDFIT spectrum uses 4 WOSA segments, 6 degrees of freedom and a bandwidth of 0.028 cycles/m. The MTM method uses 3 tapers and ~ 6 degrees of freedom. The periodogram spectrum uses a Bartlett window. The maximum entropy method uses numbers of lags M = N/3 = 180). Analysis used the REDFIT software developed by Schultz and Mudelsee (2002) and the Analyseries software package developed by Paillard *et al.* (1996).

Table 5.44 Methods of spectral estimation in the Morillo-Bruello section.

Spectral Method	Frequency (cycles/m)♠	Period (m)	Spectral Method	Frequency (cycles/m)♠	Period (m)
REDFIT	0.08 **0.15** **0.18** **0.31** 0.42	12.5 6.7 5.6 3.2 2.4	Periodogram modified with a Bartlett window	0.04 0.08 0.09 0.12 **0.16** **0.19** **0.31** 0.42	25 12.5 11.1 8.3 6.2 5.3 3.2 2.4
MTM□	0.12 **0.155** **0.19** 0.27 **0.35**	8.3 6.45 5.3 3.7 2.9	Maximum entropy	0.02 0.04 0.08 0.09 0.12 **0.16** **0.19** 0.27 **0.31** 0.36 0.42 0.48	50 25 12.5 11.1 8.3 6.2 5.3 3.7 3.2 2.8 2.4 2.1

♠ Frequencies from 0-0.5 cycles/m.
□Frequencies present in the MTM significance test with confidence levels > 80%.
Similar frequencies present in all the spectra are represented in bold numbers.

(b) REDFIT spectral results

REDFIT analyses of the Morillo-Bruello section have been undertaken using 4 WOSA segments. All the analyses have used a power regression background estimation method to approximate the noise background (Table 5.45). The total-gamma spectrum has very similar summative square errors using the power regression or the AR1 method of Mann and Lees (1996), although the power regression method fits better the noise background spectrum in all the other analysed spectra. Figure 5.94 shows several significant frequencies within the 0-0.5 cycles/m range in the time-series analyses of the total-gamma, K, Th and sandstone turbidite intensity datasets, although, the time-series analyses of the Morillo-Bruello section are characterised by generally low power spectral peaks and noisy spectra. The frequency 0.08 cycles/m (1/12 m) is present in

all the analysed parameters. In the total-gamma, K and Th spectra, the frequency has confidence levels > 95%, but in the sandstone turbidite intensity data the frequency is only present > 80% confidence levels. The frequency 0.18 cycles/m (1/5 m) is present in the total-gamma, Th and sandstone turbidite intensity time-series, although the confidence levels are in general low, > 80% in the Th and sandstone turbidite intensity spectra and > 90% in the total-gamma spectrum. A number of other frequencies are also present in the total-gamma and turbidite intensities: 0.38 cycles/m (1/2 m) (> 95% confidence level) and the frequency 0.42 cycles/m (1/2 m) (> 95% confidence level). A list of all the frequencies can be seen in Table 5.46.

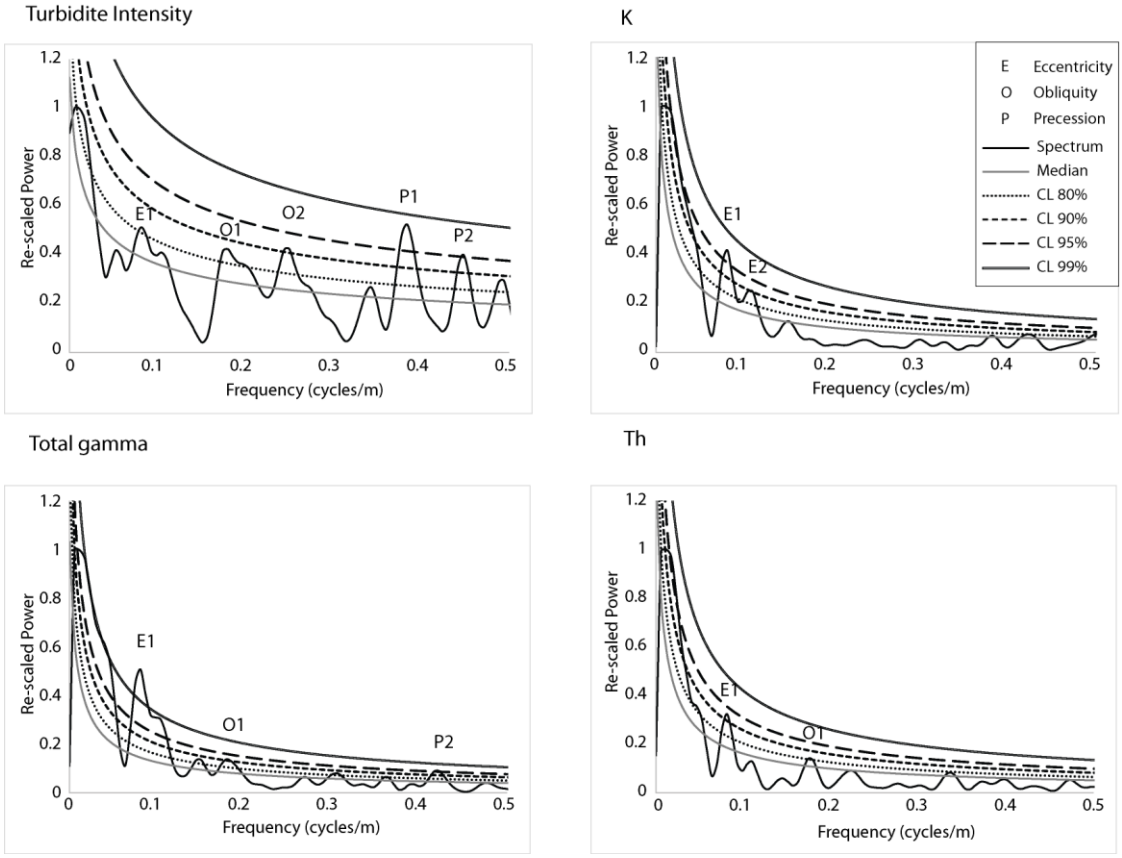

Figure 5.94 Time-series analysis of spectral gamma-ray and sandstone turbidite intensity data of the Morillo-Bruello section using REDFIT. REDFIT spectral results used 4 WOSA segments, 6 degrees of freedom and a bandwidth of 0.028 cycles/m. REDFIT results plotted using a power regression fitting model. Spectra have been re-scaled to allow comparison between variables. Analysis used the program REDFIT developed by Schulz and Mudelsee (2002).

Table 5.45 Noise background estimation of the Morillo-Bruello section.

Data	AR1 (Mann and Lees, 1996)	Quadratic curve	Power regression
Total-gamma	**732**	2562	770
K	957	2117	**527**
Th	1123	1415	**358**
Sandstone turbidite intensity	193	185	**143**

Summative square errors using the AR1 model of Mann and Lees (1996), a quadratic curve and a power regression method. The method with the least summative square error indicates the most adequate fitting curve method (bold numbers).

Table 5.46 REDFIT time-series analysis of the Morillo-Bruello section.

Data	Frequency (cycles/m)♠	Period (m)	Confidence level (%)
Total-gamma	0.081 0.1504 0.1794 0.3067 0.4224	12.34 6.64 4.57 3.26 2.36	99 80 90 80 95
K	0.0811 0.10436	12.33 9.58	95 90
Th	0.0811 0.1795	12.33 4.57	99 80
Sandstone turbidite intensity	0.0814 0.1802 0.25 0.3837 0.4476 0.4942	12.28 4.55 4 2.6 2.23 2	80 80 90 95 95 80

REDFIT spectral results using 4 WOSA segments and 6 degrees of freedom.
♠Frequencies between 0-0.5 cycles/m > 80% confidence levels.

(c) ASM results

The ASM analysis has used 7 frequencies which were identified with confidence levels > 90% in the REDFIT analyses (Figure 5.95). ASM analysis of the Morillo-Bruello section shows significant SAR within the range 9.5-14 cm/kyr. The most significant

SAR is found at 10.5 cm/kyr with a null hypothesis significance level of 0.004%. Taking into consideration the frequencies which have higher confidence levels and those which appear in the spectra of more than one investigated parameters, the two SARs which most closely reflect the Middle Eocene orbital cycles are 10.5 cm/kyr and 12.5 cm/kyr (Table 5.47). At these SARs, the frequency 0.08-0.104 cycles/m represents eccentricity 95-123 kyr. The frequency range 0.1794-0.25 cycles/m can be linked to obliquity 40 and 52 kyr. The frequency 0.38 cycles/m represents precession 23 kyr and the frequency range 0.42-0.44 cycles/m represents precession 19 kyr.

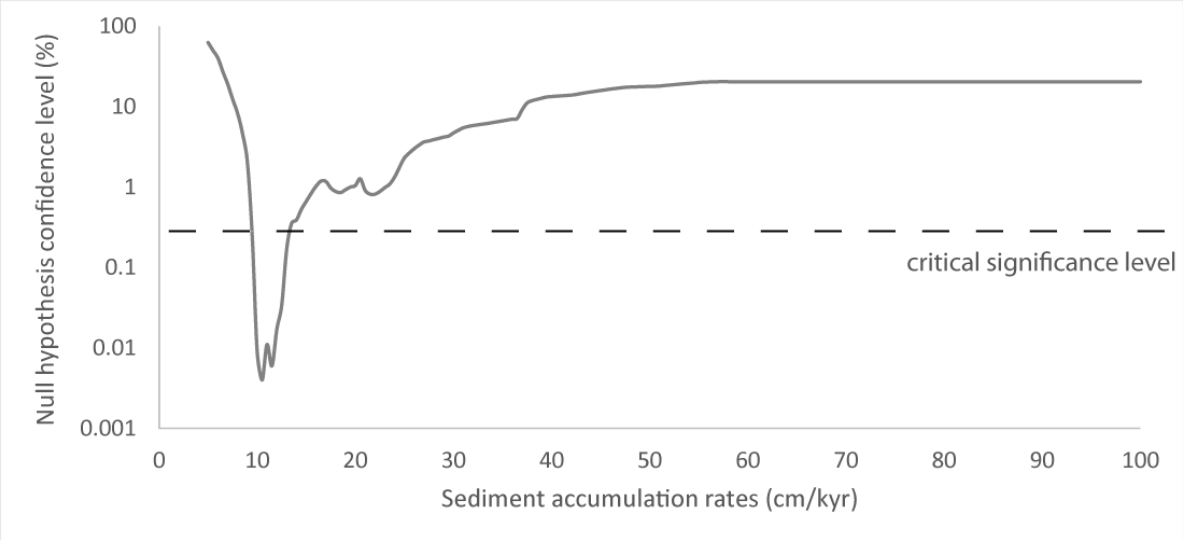

Figure 5.95 ASM results of the Morillo-Bruello section. ASM analyses include a total of 7 frequencies identified from spectral analysis of the spectral gamma-ray and sandstone turbidite intensity data with a confidence level > 90%. For a list of frequencies refer to Table 5.47. The analysis used a Rayleigh number of 3.69685767 x 10^{-4} and a Nyquist frequency of 2.4 cycles/m. Orbital parameters were established at ~ 45 Ma using Berger *et al.* (1992) equations. A total of 191 SARs ranging from 5-100 cm/kyr with an increment of 0.5 cm/kyr were investigated using 100,000 Monte Carlo interactions. Critical significance levels were established at 0.52 %. ASM analysis has identified significant SAR values ranging from 9.5-14 cm/kyr. The 7 orbital parameters including eccentricity, obliquity and precession have been included in the ASM studies. Analysis used the ASM software developed by Meyers and Sageman (2007).

Table 5.47 Temporal period duration of significant frequencies in the Morillo-Bruello section.

Frequency (cycles/m)♠	C.L (%)	N □	Period (m)	Period duration (kyr) at different SAR						
				9.5 cm/kyr	10 cm/kyr	**10.5 cm/kyr**	11 cm/kyr	11.5 cm/kyr	12 cm/kyr	**12.5 cm/kyr**
0.081	99	4	12.3	130	123.4	**117.6**	112.2	107.4	102.9	**98.8**
0.1044	90	1	9.6	100.9	94.8	**91.3**	87.1	83.3	80	77.2
0.1794	90	3	4.6	58.7	54.7	**53.1**	50.7	48.5	46.4	**44.6**
0.25	90	1	4	42.1	40	**38.1**	36.4	34.8	33.3	32
0.3837	95	1	2.6	27.4	26.1	**24.8**	23.7	22.7	21.7	**20.8**
0.4224	95	1	2.4	25	23.7	**22.6**	21.5	20.6	19.7	**18.9**
0.4476	95	1	2.2	23.5	22.3	**21.3**	20.3	19.4	18.6	**17.9**

The table shows calculated cycle duration for each significant frequency (> 90% confidence levels) at different SARs. The SAR which most closely matches the orbital periods of the Middle Eocene (~ 45 Ma) is 10.5 and 12.5 cm/kyr.

♠Frequencies present in the total-gamma, K, Th and sandstone turbidite intensity spectra with confidence levels > 90%.

□ N the number of spectra containing that specific frequency.

Underlined are frequencies which are contained in more than 1 spectrum with at least 1 confidence level > 90%.

Estimated orbital cycles in the Middle Eocene at 45 Ma using Berger et al. (1992) equations are: eccentricity 123.8 and 94.8 kyr, obliquity 52.3 and 40 kyr and precession 22.6 and 18.8 kyr.

(d) Wavelet analysis

The results from the wavelet analysis include a number of significant frequencies > 90% confidence levels (Figure 5.96). The most spatially persistent frequency, present in all the analysed records with a confidence level > 90% is the frequency range 0.08-0.01 cycles/m (1/9-1/12 m). This frequency range is present in all of the stratigraphic records and is persistently significant in the first half of the Morillo-Bruello section, mainly from 15 to 55 m height. In the second half of the records, the wavelet spectrum shows an increase in power around this frequency but not sufficiently high to be significant. Spectral analysis using REDFIT and ASM has associated this frequency to short eccentricity.

The frequency range 0.18-0.25 cycles/m (1/5-1/6 m) which has been linked to obliquity, is identified in the sandstone turbidite intensity, K and total-gamma > 90% confidence level. The significant regions associated with this frequency are in general small and discontinuous. Similarly, the frequency range 0.38-0.44 cycles/m (1/2 m), which has been linked to precession, is spatially sporadic in the sandstone turbidite intensity, K and total-gamma and is absent in the Th spectrum.

Figure 5.96 (next page) Wavelet analysis of the sandstone turbidite intensity, K, total-gamma and Th data in the Morillo-Bruello section. (a) The wavelet power spectrum calculates spectral power at different frequencies throughout the Morillo-Bruello section using sandstone turbidite intensity, K, Th and total-gamma records. Black contours mark the 10% significant regions. **(b)** The global wavelet shows the scale-averaged wavelet power across the studied frequency bands. Values to the right of the dashed line have a significance > 90% confidence level. Significant spectral peaks which have been associated with Milankovitch frequencies using REDFIT and ASM analysis have been labelled (E-eccentricity, O-obliquity, and P-precession). Analysis used the online tool http://paos.colorado.edu.research/wavelets based on the algorithms of Torrence and Compo (1998).

Figure 5.96 Wavelet analysis of the Morillo-Bruello section

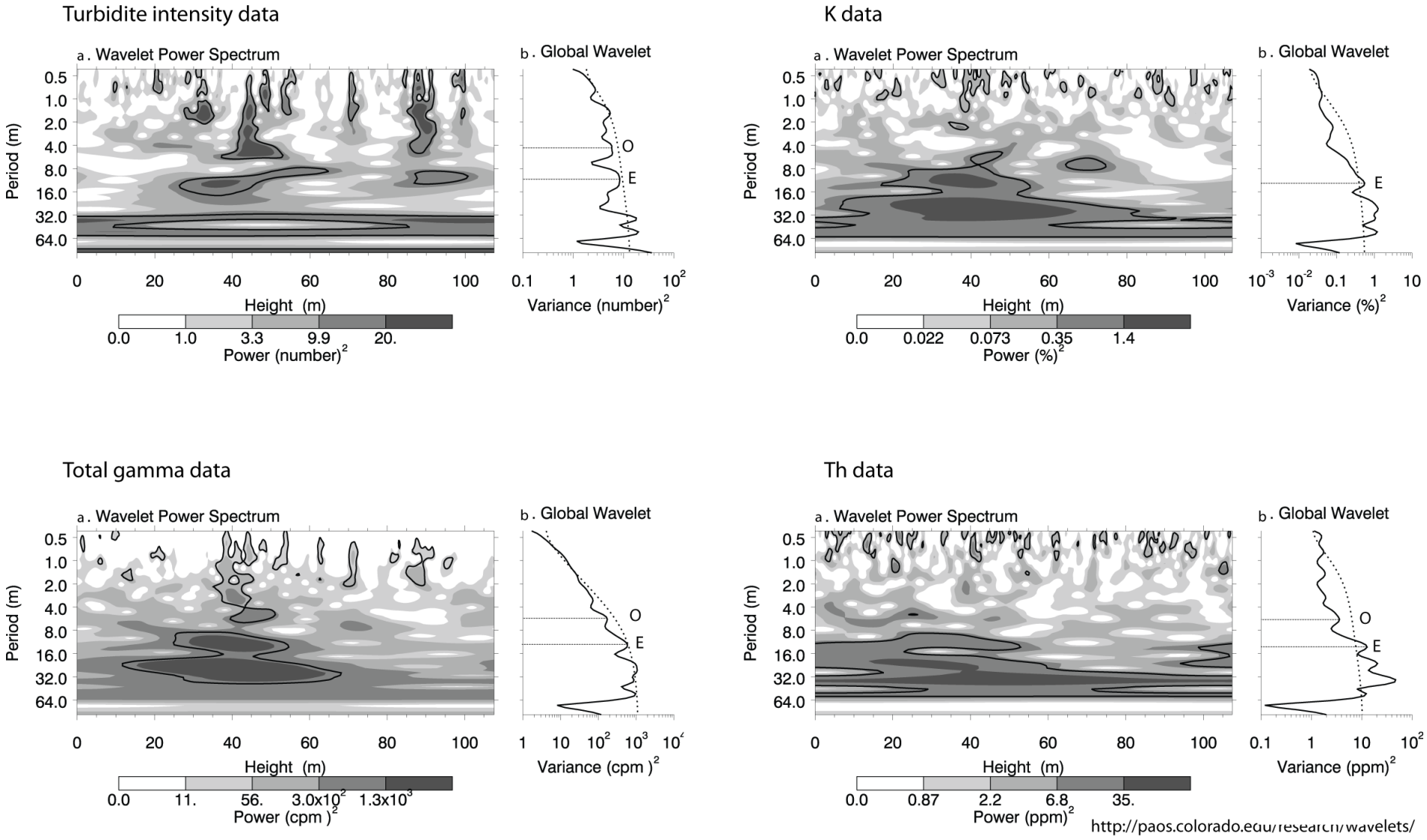

(e) Frequency-selective filtering

Two frequencies, 0.08 and 018 cycles/m have been filtered using a bandwidth of 0.028 cycles/m (Figure 5.97). The frequency 0.08 cycles/m is present in the total-gamma records with a confidence level > 99% and the frequency 0.018 cycles/m is present with confidence levels > 90%.

The total-gamma records filtered at the frequency of 0.08 cycle/m (1/12 m) shows well developed cycles mainly in the first half of the records. This corroborates the spatial distribution of this frequency in the wavelet spectrum which was significant > 90% confidence levels only in the first half of the records. In the second part of the section, there are also regular cycles but they appear attenuated and have a much lower amplitude.

The total-gamma records filtered at the frequency of 0.18 cycle/m (1/5 m) shows well developed cycles from 0-55 m height, but, then the cycles appear to lose amplitude towards the end of the section. In the wavelet spectrum, this frequency was only very sporadically significant in the central part of the Morillo-Bruello section.

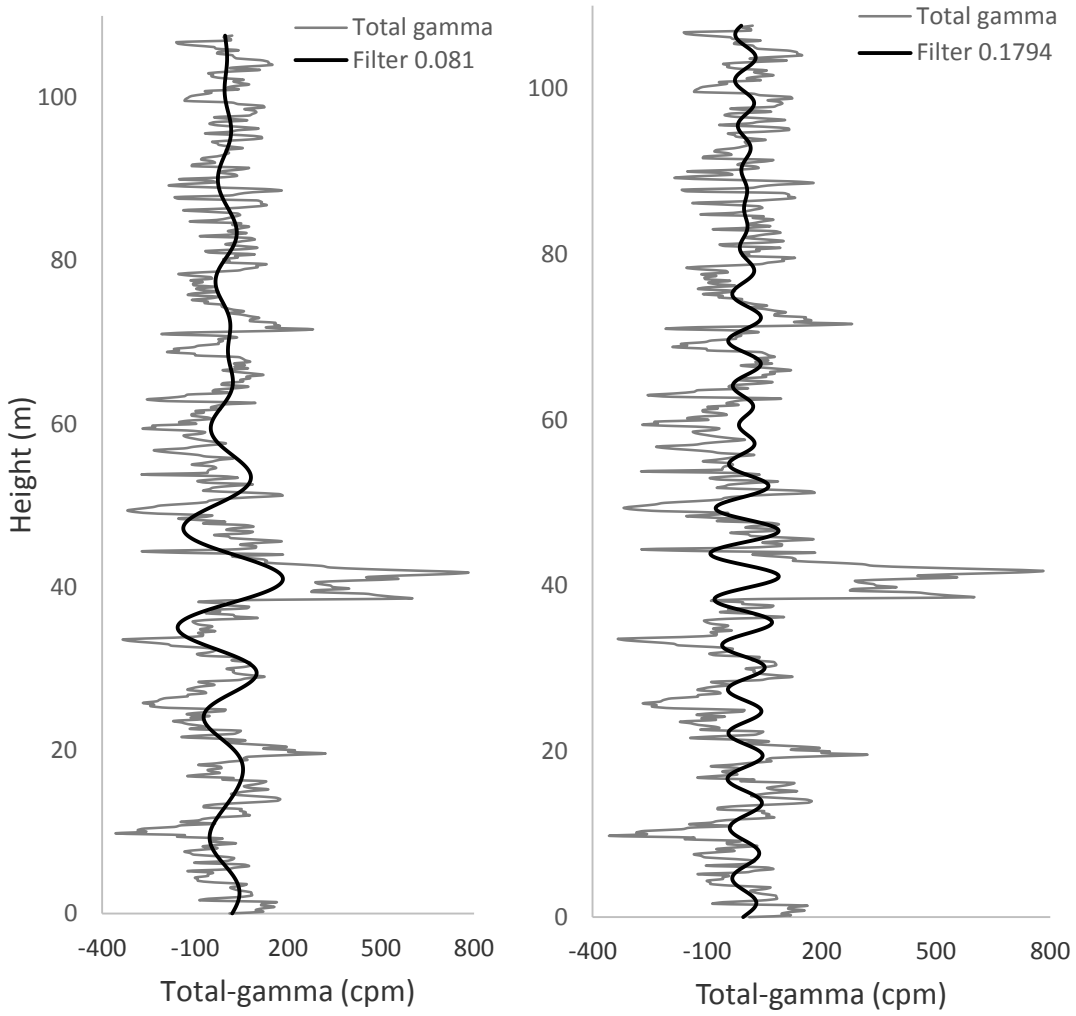

Figure 5.97 Frequency-selective filtering of the Morillo-Bruello section. Total-gamma records have been interpolated and detrended prior to analysis. Filtering has been undertaken using a band-pass Gaussian filter and a bandwidth of 0.028 cycles/m. Total-gamma records have been filtered to the frequency 0.008 cycles/m. which have been associated with the short eccentricity and to the frequency 0.018 cycles/m which has been associated with obliquity cycles. Filtering has used the program Analyseries (Paillard *et al.*, 1996).

5.3.6.5 Guaso gamma-ray logged section

5.3.6.5.1 Geographical location of the Guaso section

The Guaso gamma-ray logged section is 40 m long and is located ~ 400 m southwest of Guaso village and ~ 2 km southeast of the village of Sieste. The Guaso section can be accessed from the road A-2205 between the Margudgued and Guaso towns and is well exposed along a small stream (Plate 5.19). The Guaso section is small, but completely undeformed and well exposed. Immediately above the section there is a large interval of chaotic deposits, interpreted as sediment slides and slumps.

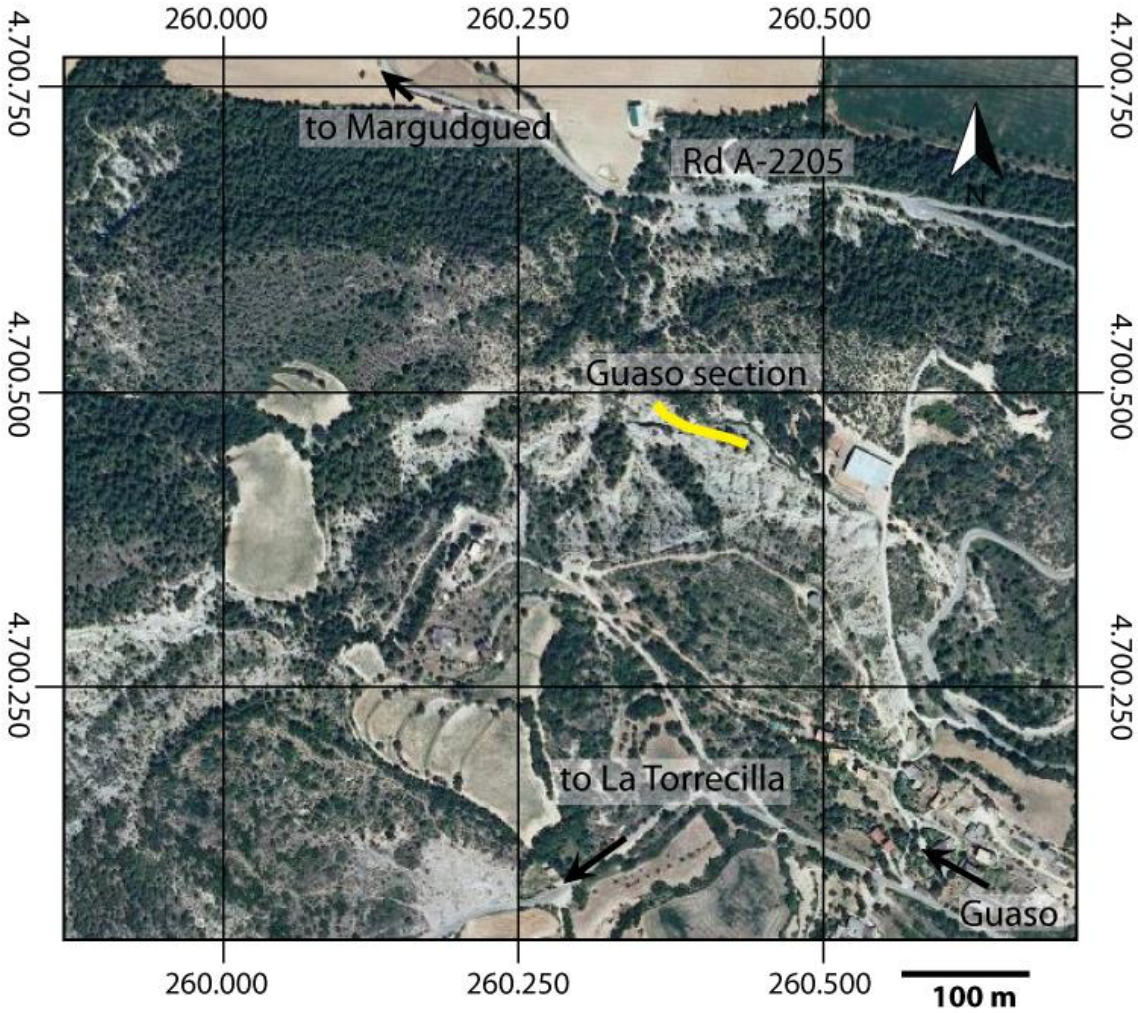

Plate 5.19 Aerial photograph of the area surrounding the Guaso gamma-ray logged section. The Guaso section is well exposed along a small stream. Access to the section can be gained from the road A-2205 between Margudgued and Guaso towns. Aerial image from www.sigpac.mapa.es/fega/visor.

5.3.6.5.2 Stratigraphic location of the Guaso section

The Guaso section is located within the Guaso System and comprises the youngest sediments of all the gamma-ray sections logged. The section is located just a few metres above the Guaso II sandbody and represents a fining upward succession associated with the abandonment of the Guaso II coarse-grained submarine fan (Figure 5.98). The stratigraphy above the Guaso II sandbody is characterised by large-scale slumps and numerous debris flows containing folded rafted sands. Although, two main sandbodies have been recognised within the Guaso System, Guaso I and II, other sandbodies which appear thinner and more localised are also present within this system (Figure 5.98).

Figure 5.99 shows sedimentary logs of the Guaso section. This section is characterised by intervals of orangey coloured bands associated with bioturbated siltstone and mudstone couplets. Figure 5.100 shows the variation in the content of the K, Th, U, Th/K and Th/U throughout the Guaso section. Intervals of high-frequency sandstone turbidites are associated with low total-gamma and K counts (Figure 5.100). Sandstone turbidite intensity graph (Figure 5.101) shows some cyclical packaging of the sandstone turbidites and the presence of thin heterolithic packages comprising thicker sandstone turbidites.

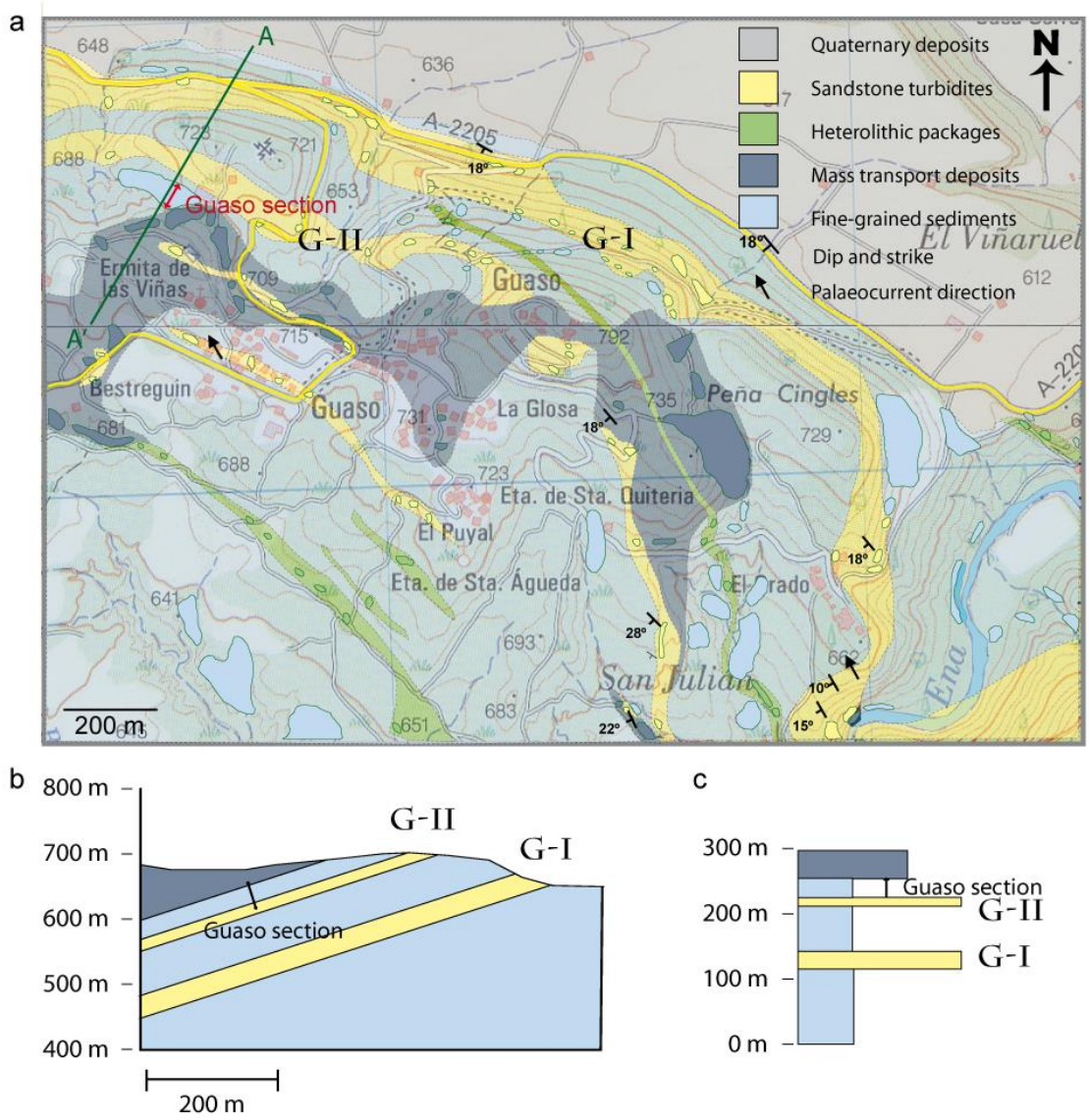

Figure 5.98 Geological map, cross-section and vertical stratigraphic column of the Guaso section. (a) Geological map of the area around Guaso town showing the location of the Guaso gamma-ray logged section. The green line indicates the position of the cross-section A-A' which is perpendicular to the main outcrop strike. **(b)** Cross-section of the Guaso area showing the position of the gamma-ray logged section in the interfan sediments immediately above the Guaso II sandbody. **(c)** Stratigraphic column showing the position of the Guaso section.

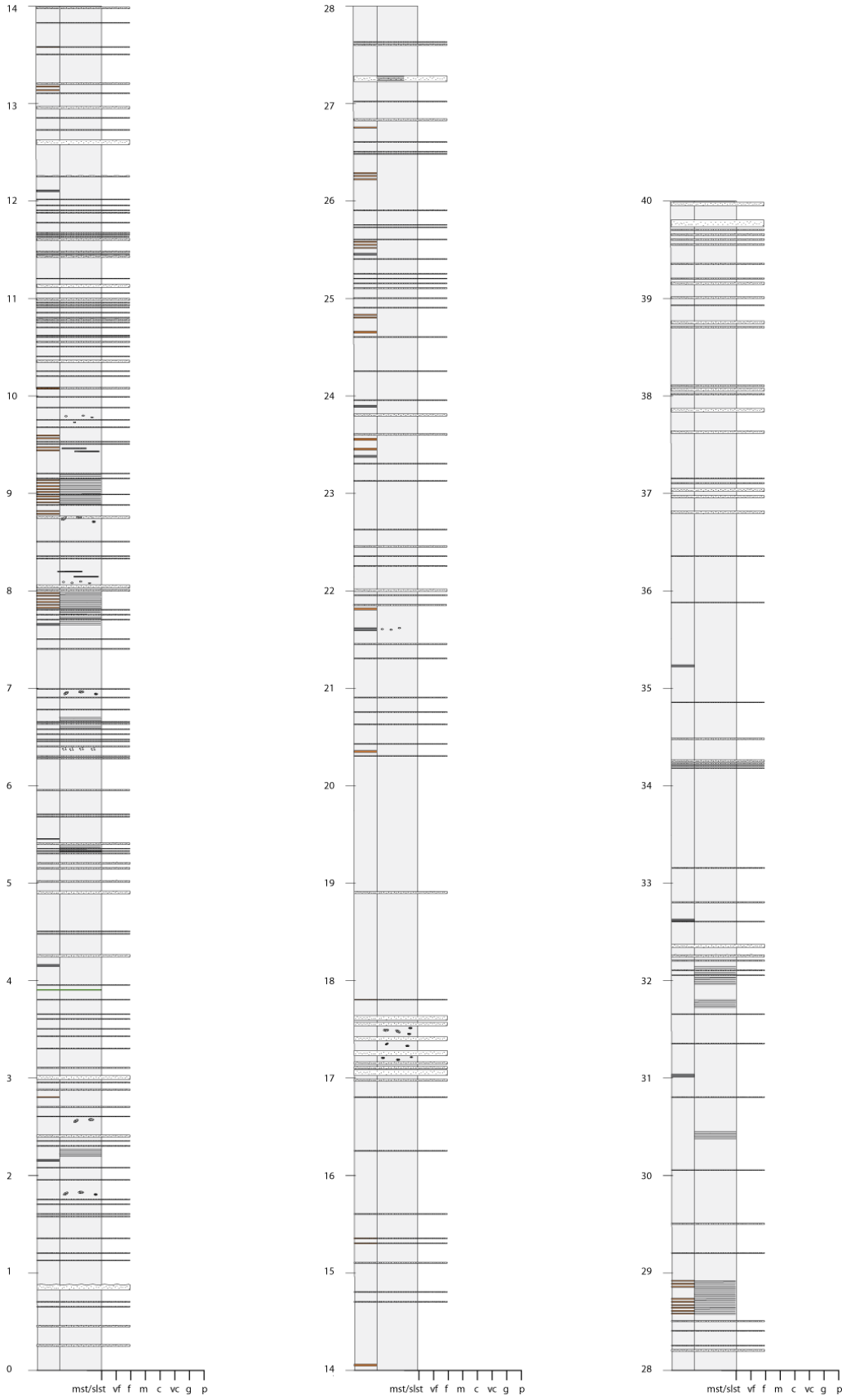

Figure 5.99 Detailed sedimentary log of the Guaso section. Sedimentary logs include every bed thicker than 5 mm. Figure 2.5 shows the symbol key used in the sedimentary logs. Electronic versions are included in Appendix 3.

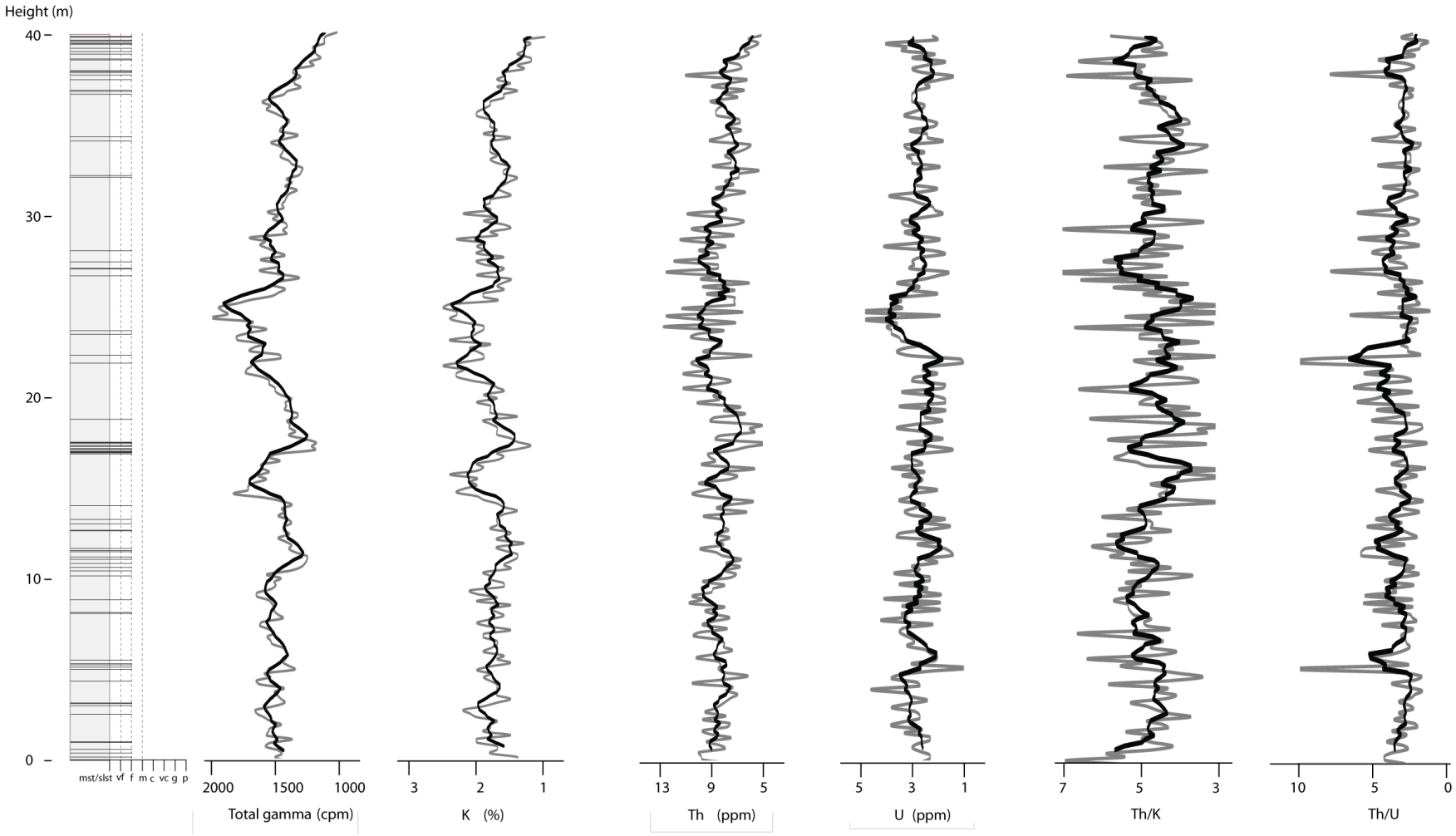

Figure 5.100 Simplified sedimentary logs of the Guaso section plotted against total-gamma (cpm), K (%), Th (ppm), U (ppm), Th/K and Th/U data. The black line is a 4-period moving average. Simplified logs only show sandy turbidites ≥ 1.5 cm, for complete logs refer to Figure 5.99 and Appendix 3.

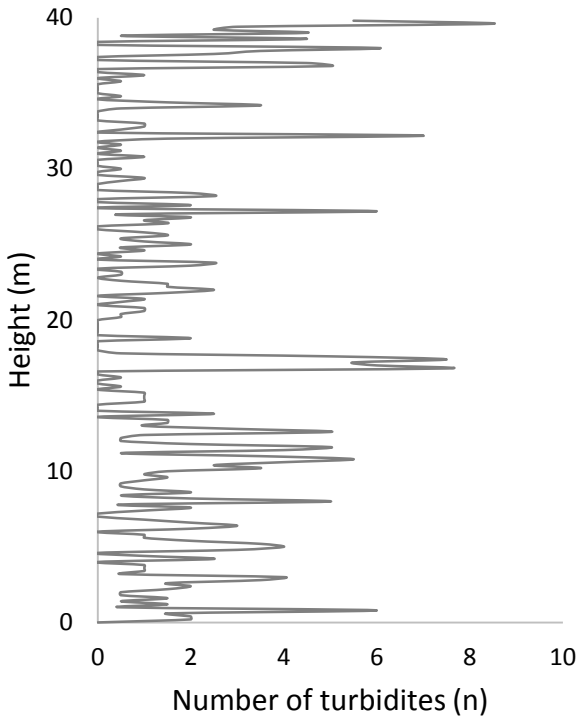

Figure 5.101 Sandstone turbidite intensity in the Guaso section. The averaged sandstone content for the section is ~ 7%.

5.3.6.5.3 Cyclostratigraphic studies of the Guaso section

(a) Methods of spectral estimation

The total-gamma spectrum of the Guaso section has been estimated using four different methods: the REDFIT, the MTM, the maximum entropy and the periodogram modified with a Bartlett window. Figure 5.102 shows the spectral results obtained from applying each of these methods and Table 5.48 summarises the main frequencies present from 0-0.5 cycles/m. All the spectra created are similar using the four spectral estimation methods, although frequencies in the MTM method appear flattened and poorly defined. The MTM significance test does, however, show very similar frequencies to the other spectra. The frequencies 0.046 cycles/m (1/21 m), 0.234 cycles/m (1/4 m) and 0.359 cycles/m (~ 1/3 m) are common in all the spectra.

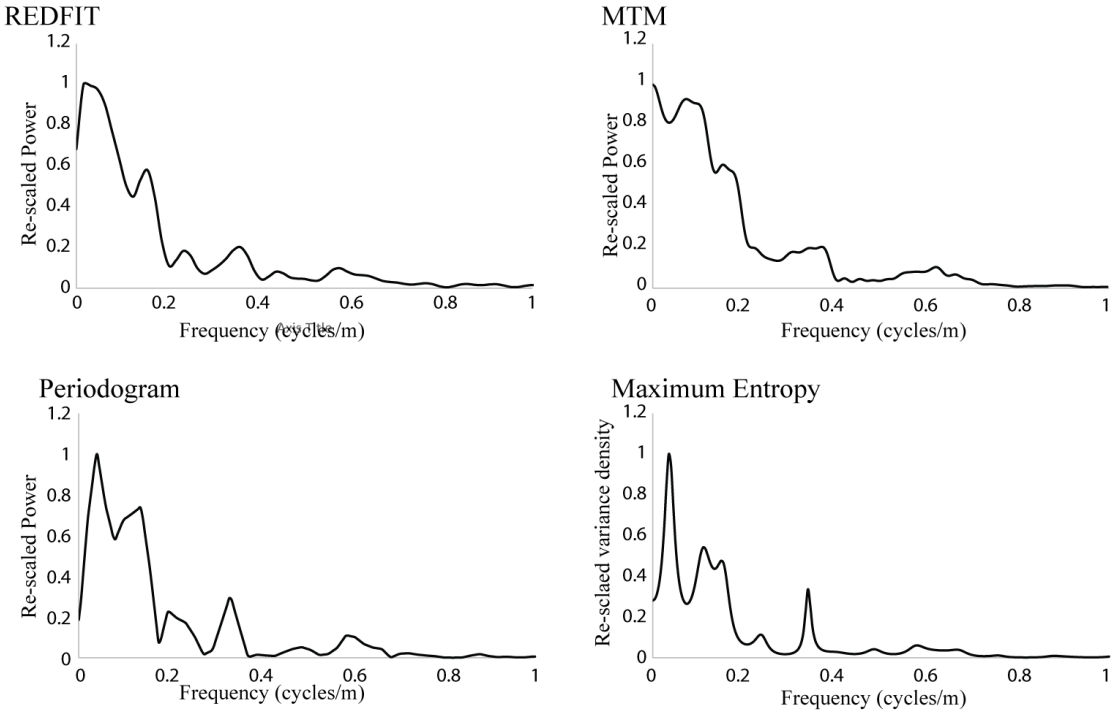

Figure 5.102 Methods of spectral estimation using the spectral total-gamma data of the Guaso section. REDFIT spectrum using 4 WOSA segments, 6 degrees of freedom and a bandwidth of 0.0756 cycles/m. The MTM method uses 3 tapers and ~ 6 degrees of freedom. The periodogram spectrum uses a Bartlett window. The maximum entropy method uses numbers of lags M = N/3 = 67). The spectral analysis used the REDFIT software developed by Schultz and Mudelsee (2002) and the Analyseries software package developed by Paillard *et al.* (1996).

Table 5.48 Methods of spectral estimation in the Guaso section.

Spectral Method	Frequency (cycles/m)♠	Period (m)	Spectral Method	Frequency (cycles/m)♠	Period (m)
REDFIT	**0.046** 0.156 **0.234** **0.359**	21.7 6.4 4.3 2.8	Periodogram modified with a Bartlett window	**0.04** 0.135 **0.205** **0.335**	25 7.4 4.9 3
MTM□	**0.039** **0.205** **0.332**	25.6 4.9 3	Maximum entropy	**0.035** 0.115 0.155 **0.245** **0.34**	28.6 8.7 6.5 4.1 2.9

♠ Frequencies from 0-0.5 cycles/m.
□ Frequencies present in the MTM significance test with confidence levels > 80%.
Frequencies which appear consistently in all the spectra are represented in bold numbers.

(b) REDFIT spectral results

The Guaso section is too short to show eccentricity cycles with confidence. Therefore, the only orbital periods investigated in the Guaso section are obliquity and precession. In order to support the reliability of the results from this short section, the significant frequencies identified in the Guaso section have been interpreted in association to the other gamma-ray logged section in the Guaso System (e.g., the Morillo-Bruello section).

REDFIT analyses of the Guaso section have been undertaken using 4 WOSA segments. The noise background fitting method used is the AR1 model of Mann and Lees (1996) with the exception of the Th spectrum, where the background noise has been approximated with a power regression method (Table 5.49). There are two main significant frequency ranges identified between 0-0.5 cycles/m which are present in the time-series analyses of the total-gamma, K, Th and sandstone turbidite intensity datasets: 0.14-0.17 cycles/m (1/5-1/7 m) and 0.32-0.36 cycles/m (1/3 m) (Figure 5.103). The frequency range 0.14-0.17 cycles/m is better represented in the K spectrum with a confidence > 99%, but, this frequency range is also significant in all the other parameters. The frequency range 0.32-0.36 cycles/m is present in the total-gamma and K spectra with confidence levels > 90% and 95%, respectively. These two frequency ranges are similar to the frequencies 0.15 and 0.38 cycles/m identified in the Morillo-Bruello section. Table 5.50 summarises all frequencies identified with the REDFIT method.

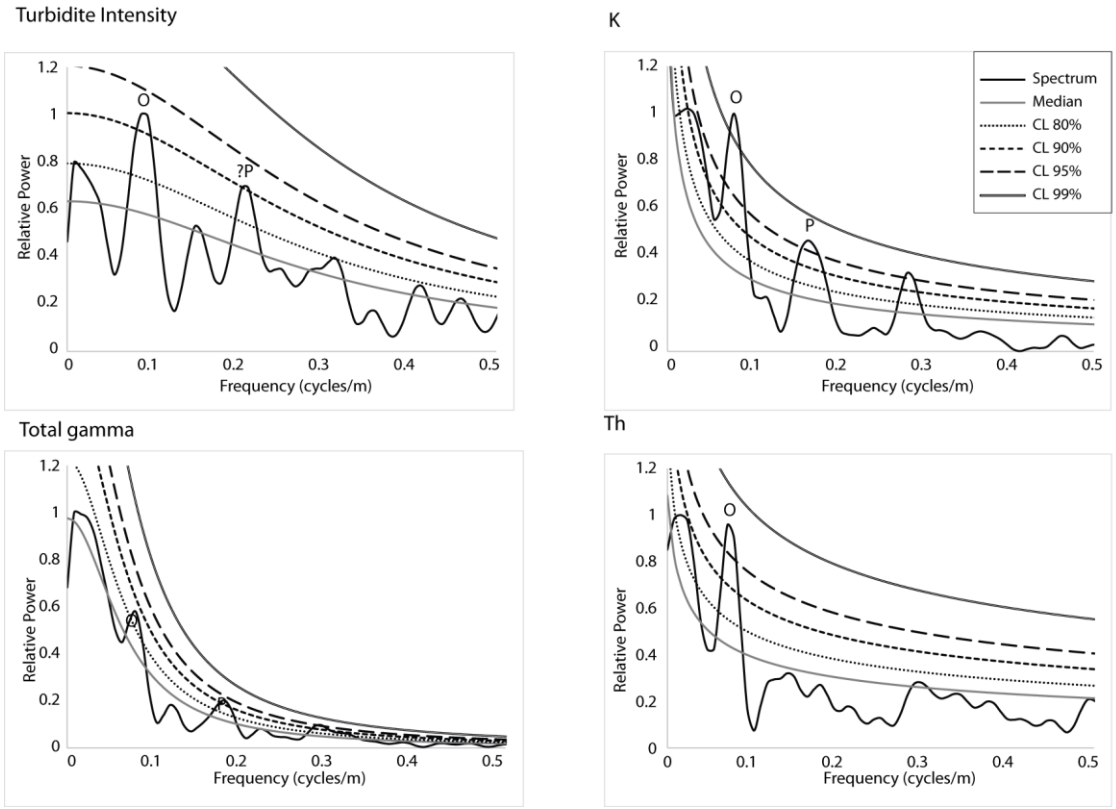

Figure 5.103 Time-series analysis of spectral gamma ray and sandstone turbidite intensity data using REDFIT. REDFIT spectral results used 4 WOSA segments, 6 degrees of freedom and a bandwidth of 0.0756 cycles/m. REDFIT results plotted using an AR1 noise background fitting model with the exception of the Th spectrum. Graphs showing re-scaled power to allow comparison between variables. Analysis used the REDFIT software developed by Schulz and Mudelsee (2002).

Table 5.49 Noise background estimation of the Guaso 40 m section.

Data	AR1 (Mann and Lees, 1996)	Quadratic curve	Power regression
Total-gamma	**45**	374	187
K	**70**	182	122
Th	83	69	**50**
Sandstone turbidite intensity	**39**	42	53

Summative square errors using the AR1 model of Mann and Lees (1996), a quadratic curve and a power regression method. The method with the least summative square error indicating the most adequate fitting curve method is represented in bold numbers.

Table 5.50 REDFIT time-series analysis results of the Guaso section.

Data	Frequency (cycle/m)	Period (m)	Confidence level (%)
Total-gamma	0.1563 0.3594	6.4 2.78	80 90
K	0.15625 0.3281	6.4 3.05	99 95
Th	0.1406	7.11	95
Sandstone turbidite intensity	0.1719 0.4219	4.81 2.37	90 90

REDFIT spectral results using 4 WOSA, 6 degrees of freedom and a bandwidth of 0.0756 cycles/m. The frequencies shown are all frequencies between 0-0.5 cycles/m > 80% confidence levels.

(c) ASM results

A total of 6 frequencies containing confidence levels > 90% have been applied to the ASM studies (Figure 5.104). ASM analysis of the Guaso section has investigated only obliquity and precession orbital cycles due to the shortness of the section.

Significant SARs range from 12 to 16 cm/kyr. The most significant ASM results are the SAR between 13.5-14.5 cm/kyr with null hypothesis significance levels of 0.002%. Table 5.51 investigates how closely these significant SARs relate to the orbital cycles in the Middle Eocene. At a SAR of 14 cm/kyr, the frequencies 0.14-0.156 cycles/m (1/6-1/7 m) represents obliquity 52 kyr and the frequency 0.1712 cycles/m (1/4.8 m) represents obliquity 40 kyr. The frequency range 0.32-0.36 cycles/m (1/3 m) probably represents precession.

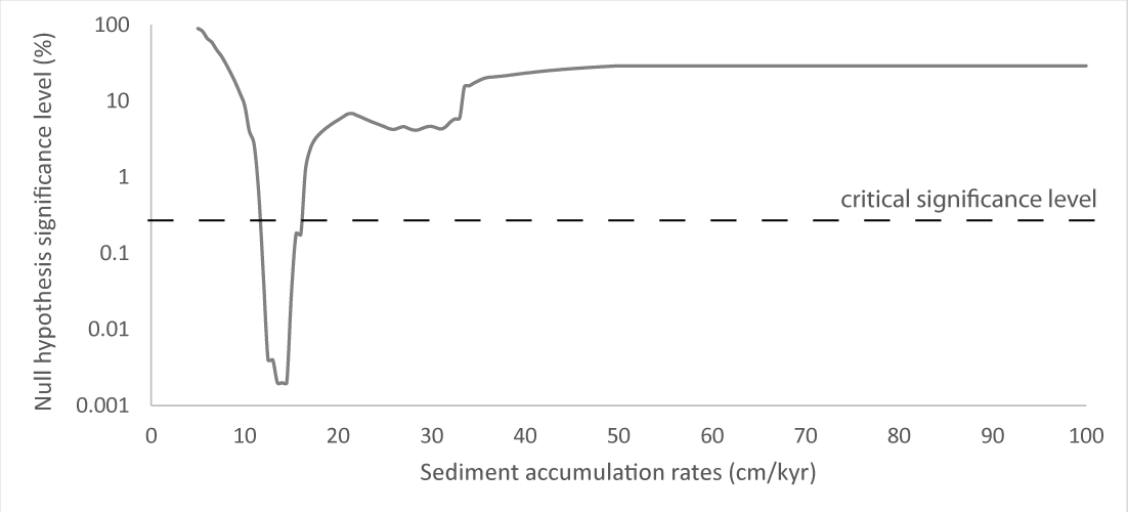

Figure 5.104 ASM results of the Guaso section. ASM analyses include a total of 6 frequencies identified from spectral analysis of the spectral gamma-ray and sandstone turbidite intensity data with a confidence level > 80%. For a list of frequencies refer to Table 5.51. The analysis used a Rayleigh number of 9.900990099 x 10^{-4} and a Nyquist frequency of 2.4 cycles/m. Orbital parameters were established at ~ 45 Ma using Berger *et al.* (1992) equations. A total of 191 SARs ranging from 5-100 cm/kyr with an increment of 0.5 cm/kyr were investigated using 100,000 Monte Carlo interactions. Critical significance levels were established at 0.52%. ASM analysis has identified significant SAR values ranging from 12-16 cm/kyr. Only 4 orbital parameters (obliquity and precession) were investigated in the ASM studies. Analysis used the ASM software developed by Meyers and Sageman (2007).

Table 5.51 Temporal period duration of significant frequencies in the Guaso section.

Frequency (cycles/m)♠	C.L. (%)	N□	Period (m)	Period duration (kyr) at different SAR				
				12.5 cm/kyr	13 cm/kyr	13.5 cm/kyr	**14 cm/kyr**	14.5 cm/kyr
0.1406	95	2	7.1	56.9	54.7	52.7	**50.8**	49.1
0.1563	99	1	6.4	51.2	49.2	47.4	**44.7**	44.1
0.1712	90	1	4.8	46.7	45	43.3	**41.7**	40.3
0.3281	95	1	3	24.4	23.4	22.6	**21.8**	21
0.3594	90	1	2.8	22.3	21.4	20.6	**19.9**	19.2
0.4219	90	1	2.4	19	18.2	17.6	**16.9**	16.3

The table shows calculated cycle duration for each significant frequency (> 90% confidence levels) at different SARs. The SAR which most closely matches the orbital periods of the Middle Eocene (~ 45 Ma) is 14 cm/kyr.

♠Frequencies present in the total-gamma, K, Th and sandstone turbidite intensity spectra with confidence levels > 90%.

□ N is the number of spectra containing that specific frequency.

Underlined are frequencies which are contained in more than 1 spectrum with at least 1 confidence level > 95%.

Estimated orbital cycles in the Middle Eocene at 45 Ma using Berger *et al*. (1992) equations are: eccentricity 123.8 and 94.8 kyr, obliquity 52.3 and 40 kyr and precession 22.6 and 18.8 kyr.

(d) Wavelet analysis

Results from the wavelet analysis include two main frequency ranges > 90% confidence levels. Figure 5.105 shows the wavelet power spectra of the sandstone turbidite intensity, K, Th and total-gamma data. The most spatially persistent frequency range is 0.14-0.17 cycles/m (1/5-1/7 m). This frequency range is significant with a confidence level > 90% in all the analysed wavelet spectra although the significant regions vary for each of them. Non-significant regions have in general an increase in power at this frequency range. The wavelet spectrum is mostly continuous throughout the records at this frequency range in the total-gamma data and Th wavelet spectra, but, in the sandstone turbidite intensity spectrum is only significant in the first

half of the records. Spectral analysis using REDFIT and ASM has associated this frequency to obliquity.

The frequency range 0.32-0.42 cycles/m (1/2-1/3 m) which has been linked to precession, is also significant in all the wavelet spectra analysed but is spatially more sporadic and discontinuous.

Figure 5.105 (next page) Wavelet analysis of the sandstone turbidite intensity, K, total-gamma and Th data in the Guaso section. (a) The wavelet power spectrum calculates spectral power at different frequencies throughout the Guaso section using sandstone turbidite intensity, K, Th and total-gamma records. Black contours mark the 10% significant regions. **(b)** The global wavelet shows the scale-averaged wavelet power across the studied frequency bands. Values to the right of the dashed line have a significance > 90% confidence level. Significant spectral peaks which have been associated with Milankovitch frequencies using REDFIT and ASM analysis have been labelled (E-eccentricity, O-obliquity, and P-precession). Analysis has used the online tool http://paos.colorado.edu.research/wavelets based on the algorithms of Torrence and Compo (1998).

Figure 5.105 Wavelet analysis of the Guaso section.

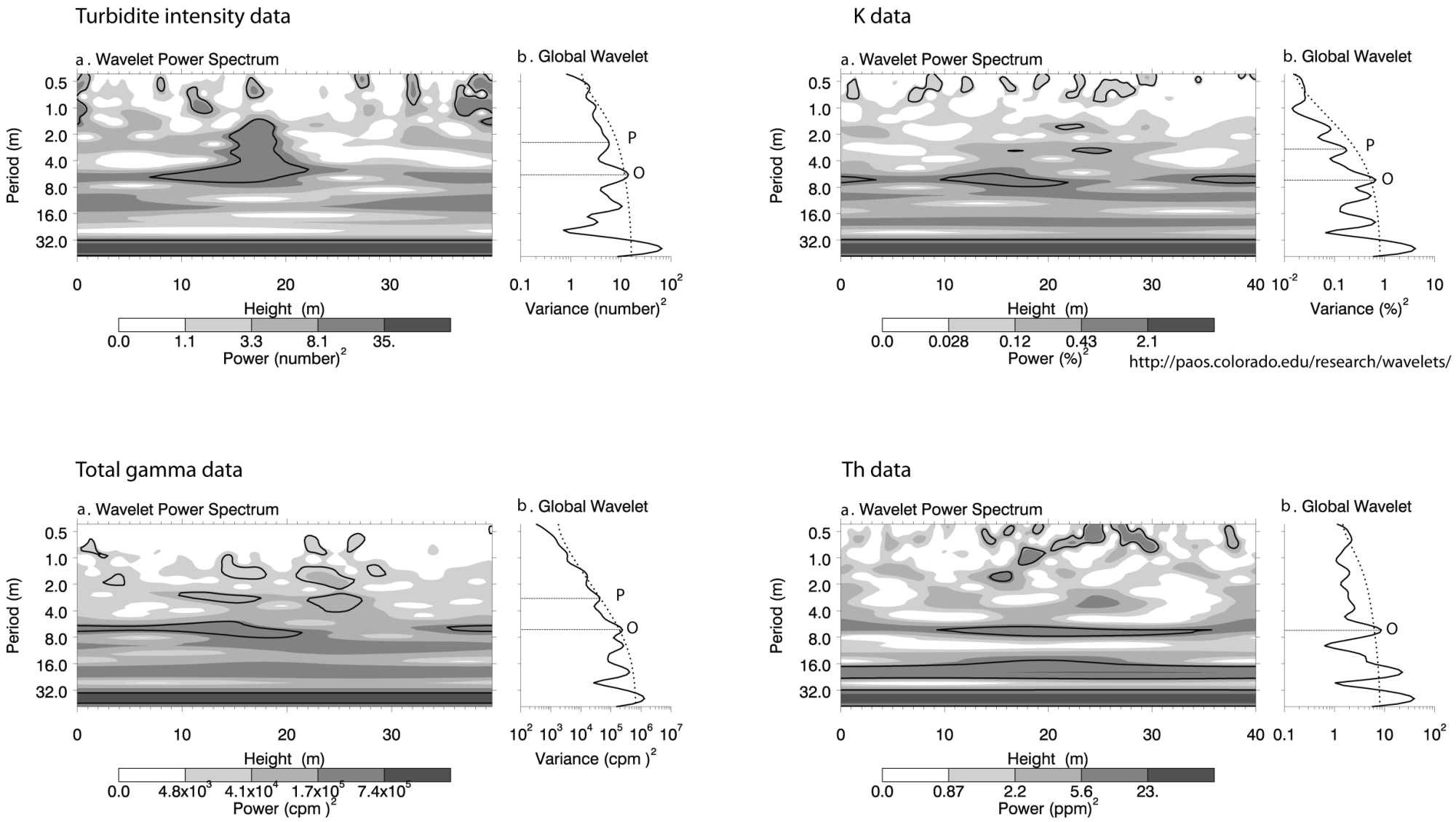

(e) Frequency-selective filtering

The frequencies 0.1563 and 0.3594 cycles/m have been filtered using a bandwidth of 0.0756 cycles/m derived from REDFIT spectral analysis (Figure 5.106). These two frequencies are present in the total-gamma records with confidence levels > 80% and 90%, respectively.

The total-gamma records filtered at a frequency of 0.1563 cycles/m (1/6 m) show well-developed high-amplitude cycles throughout the section. These cycles can be easily distinguishable looking at the total-gamma ray detrended data. This frequency has been linked to obliquity. The total-gamma records filtered at the frequency 0.3594 cycles/m (1/2 m) show well defined precession cycles throughout the records. These cycles show a good match with the total-gamma records.

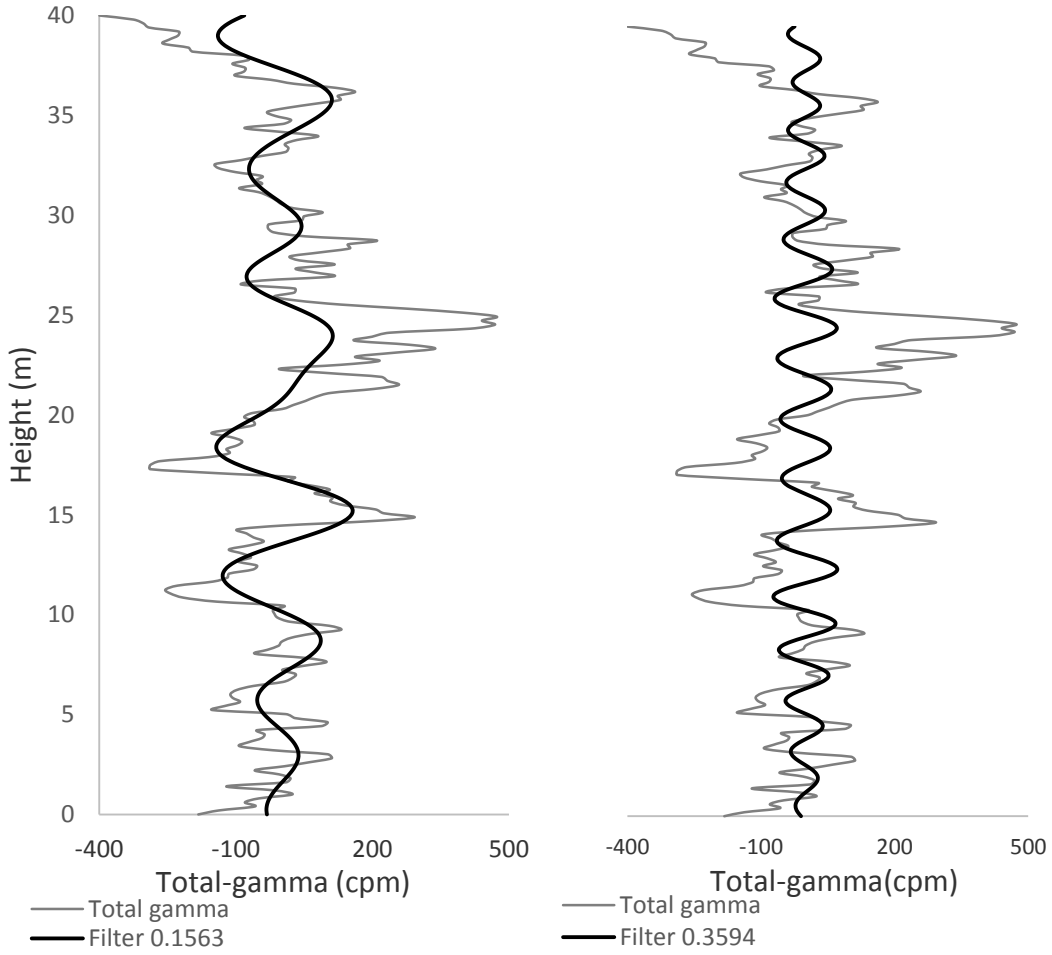

Figure 5.106 Frequency-selective filtering of the Guaso section. The total-gamma records have been interpolated and detrended prior to analysis. Filtering has been undertaken using a band-pass Gaussian filter and a bandwidth of 0.0756 cycles/m. The total-gamma records have been filtered to the frequencies 0.1563 and 0.3594 cycles/m. The frequency 0.1563 has been associated with obliquity and the frequency 0.3594 cycles/m to precession using REDFIT and ASM spectral analysis. Obliquity cycles in the Guaso section are well-developed throughout the stratigraphy and can be very easily distinguishable looking at the total-gamma ray data. There is a relatively good match between the filtered records, the total-gamma ray data with good amplitude precession cycles throughout the records The shortness of the Guaso section prevents the recognition of eccentricity cycles with confidence. Filtering has used the program Analyseries (Paillard *et al.*, 1996).

5.3.7 SAR variation across the Ainsa Basin stratigraphy

The deep-marine sediments of the Ainsa Basin record a progressive decrease in the rates of sediment accumulation (Figure 5.107). ASM studies suggest that the SARs have varied from 50 cm/kyr in the older sediments of the Arro System to ~ 13 cm/kyr in the younger sediments of the Guaso System. The fastest SARs of the Arro System coincides with a period of intense tectonic deformation and rapid basin subsidence deepening which resulted in slope instabilities and failures during the deposition of the Arro System (Millington and Clark, 1995). The system stabilised during the deposition of the Gerbe and Banastón systems and the SAR progressively decreased to ~ 37 cm/kyr. During the deposition of the Ainsa and Morillo systems the basin was incorporated into the hanging wall of the Gavarnie Thrust and undergone a transitional stage from a foredeep basin to a thrust-top basin (e.g., Muñoz *et al*., 1998; Dreyer *et al*., 1999; Fernández *et al*., 2004, 2012). Advancement of the Gavarnie Thrust caused the active growth of the Mediano, Añisclo and Boltaña anticlines and resulted in a general uplift and narrowing of the basin (e.g., Fernández *et al*., 2004, 2012; Bayliss and Pickering, 2014a, 2014b). The deposition of these systems are characterised by tectonic confinement and SARs are in the order of 25-30 cm/kyr. As the basin continued to fill the SAR reduced even further to ~ 13 cm/kyr during the deposition of the Guaso System.

5.3.8 Interfan duration in the Ainsa Basin

The interfan duration can be calculated by using the stratigraphic thicknesses of the interfan deposits and the SAR identified from ASM studies. Table 5.52 summarises the duration of each interfan succession. Interfan deposits have accumulated over time

intervals that vary greatly from 130 kyr to 779 kyr with averaged values of 364±204 kyr. The 364 kyr averaged interfan duration approximates the periodicity of the 400 kyr long eccentricity. However, the large standard deviation values suggest that there is no regular periodicity in the deposition of these interfan deposits. Figure 5.108 shows how the duration of the interfan deposits have varied throughout the stratigraphy. Older systems such as the Gerbe and Banastón are in general characterised by shorter interfan duration than the younger systems (Morillo and Guaso). The timing of the interfan deposits can be fitted with a polynomial curve (Figure 5.109a). This figure reflects how the basin has been filled in time.

This study estimates a total thickness of the interfan deposits from the Gerbe to the Guaso system of ~ 1.7 km and a total duration of 5.8 Myr (Figure 5.109). Average SARs of the interfan sediments is ~ 30 cm/kyr. This average SAR does not take into consideration the duration of the deposition of the coarse-grained sandbodies SARs which are expected to have been much higher than for the interfan deposits (Heard *et al*., 2008). SARs for the Upper Hecho Group are estimated to be at 40 cm/kyr Pickering and Bayliss (2009) and ~ 43 cm/kyr by Scotchman *et al*. (2012).

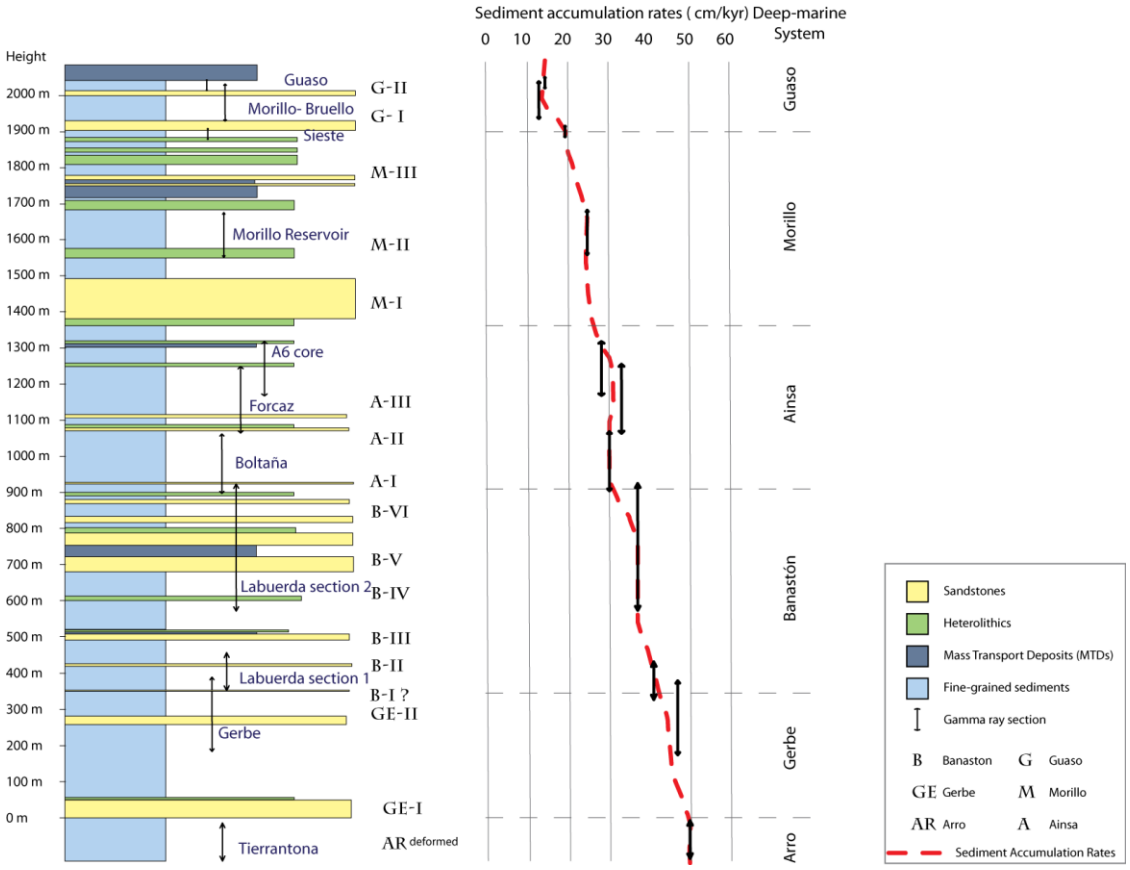

Figure 5.107 SARs across the Upper Hecho Group in the Ainsa Basin. There is a progressive decrease of the SAR from the Gerbe System ~ 47 cm/kyr to ~ 13 cm/kyr in the Guaso System.

Table 5.52 Interfan duration of the Upper Hecho Group of the Ainsa Basin.

Turbidite system	Thickness of interfan deposits	SAR♠	Estimated interfan duration	System duration
Delta-GII	27.6 m	12.5-14 cm/kyr	209±17 kyr	**Guaso 676 ±137 kyr**
GI-GII	70.5 m	12.5-19 cm/kyr	467±136 kyr	
M III –G I	124.1 m	19-25 cm/kyr	574±110 kyr	**Morillo 1912 ±119 kyr**
M II –MIII	194.7 m	25 cm/kyr	779 kyr	
M I –MII	147.8 m	25-28 cm/kyr	559±45 kyr	
A III –MI	206.5 m	28-33.5 cm/kyr	677±96 kyr	**Ainsa 1340±97 kyr**
AII-AIII	54.4 m	30-33.5 cm/kyr	172±13 kyr	
A I –AII	147.4 m	30 cm/kyr	491 kyr	
BVI-AI	77 m	30-37 cm/kyr	232±34 kyr	**Banastón 1316±62 kyr**
BV-BVI	104 m	30-37 cm/kyr	314±46 kyr	
BIV-BV	92.6 m	37 cm/kyr	250 kyr	
BIII-BIV	87 m	37-41 cm/kyr	223±16 kyr	
BII-BIII	65 m	37-41 cm/kyr	167±12 kyr	
BI-BII	57 m	41-47 cm/kyr	130±12 kyr	
GeII-BI	78.3 m	47 cm/kyr	166 kyr	**Gerbe 588±18 kyr**
GeI-GeII	204.7 m	50-47 cm/kyr	422±18 kyr	

♠SARs calculated from ASM analysis of outcrop spectral gamma-ray sections across the basin.

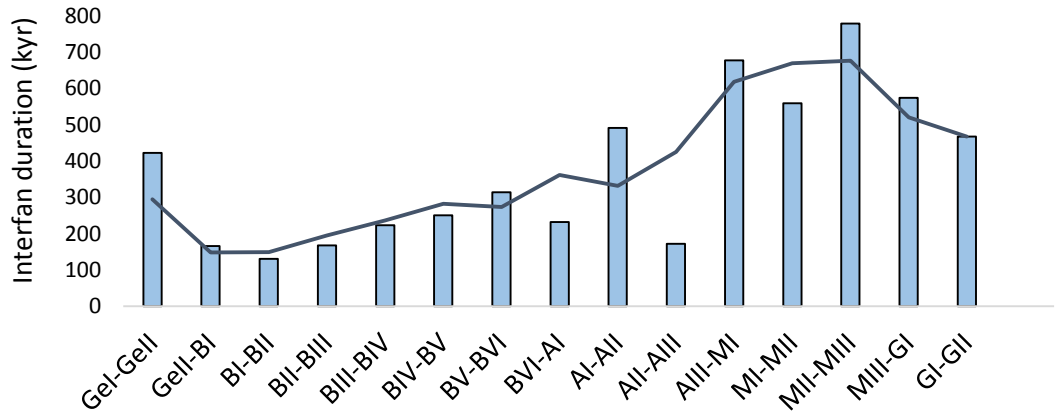

Figure 5.108 Interfan thickness duration in the Upper Hecho Group. There is a general increase in the interfan duration throughout the stratigraphy. The line is a 2-weight moving average.

a)

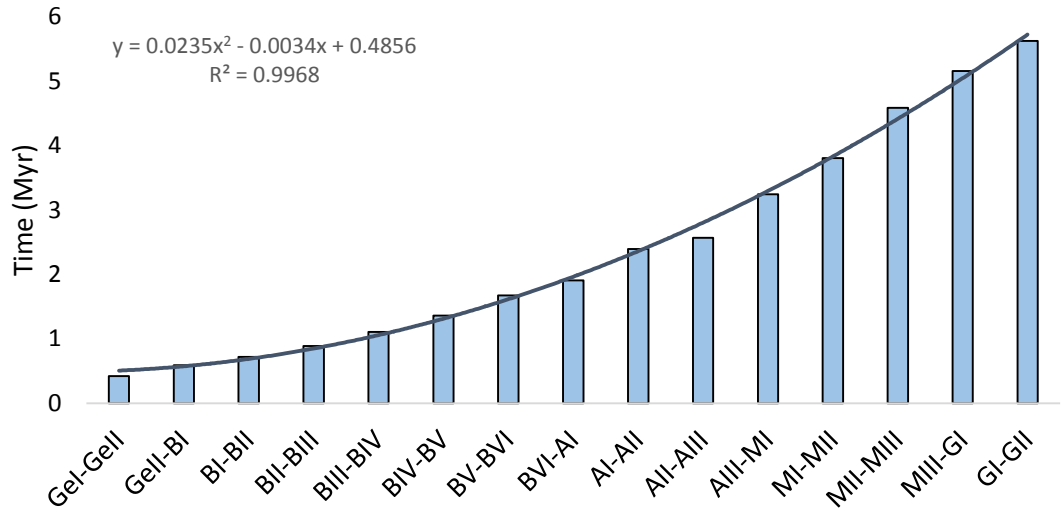

b)

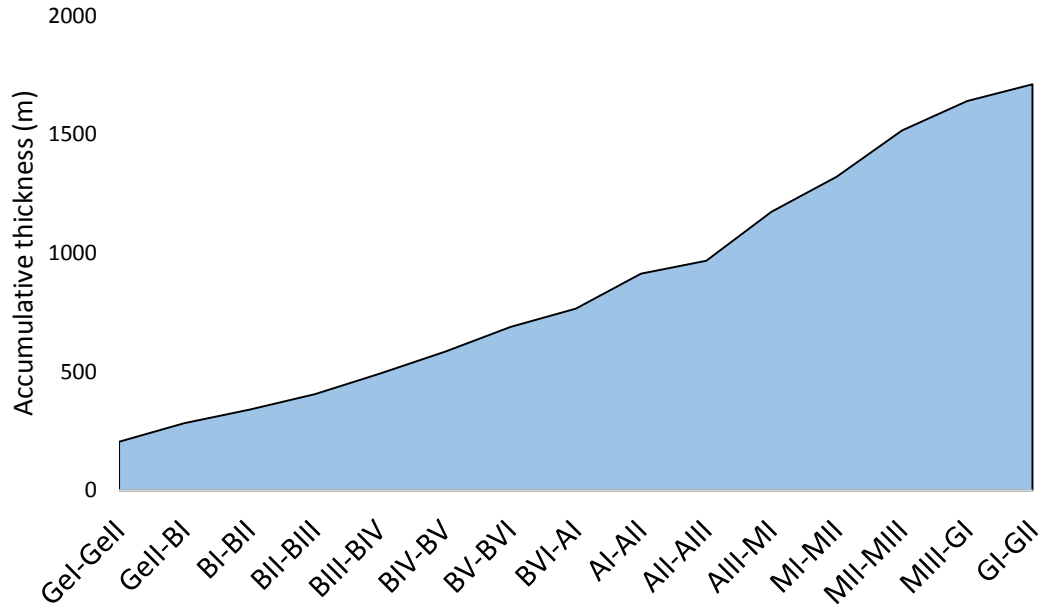

Figure 5.109 Accumulative time and thickness of the interfan successions. (a) The figure shows the accumulative time of the interfan deposits. The interfan timing across the deep-marine stratigraphy of the Ainsa Basin can be fitted to a polynomial curve. **(b)** The figure shows the accumulative thickness of the interfan successions from the Gerbe to the Guaso systems.

5.3.9 Conversion of a depth-stratigraphy to an age-stratigraphy

Orbital tuning of the gamma-ray logged sections to the eccentricity curves allows the conversion of a depth-stratigraphy to an age-stratigraphy. This conversion has only been attempted in the Gerbe, Banastón, Ainsa and the lower part of the Morillo System where there is a good chronostratigraphic control from magnetostratigraphy. An age-stratigraphy allows the estimation of the age of initiation of the Ainsa Basin deep-marine systems and of individual sandbodies. The Gerbe System is estimated to have been initiated at 47.73 Ma, the Banastón System at 46.97 Ma and the Ainsa System at 45.16 Ma.

Table 5.53 Time of initiation of the sandbodies of the Ainsa Basin.

Sandbody	Age (Ma)
Gerbe I	47.73
Gerbe II	47.18
Banastón I	46.97
Banastón II	46.7
Banastón III	46.2
Banastón IV	45.9
Banastón V	45.65
Banastón VI	45.38
Ainsa I	45.16
Ainsa II	44.83
Ainsa III	44.58

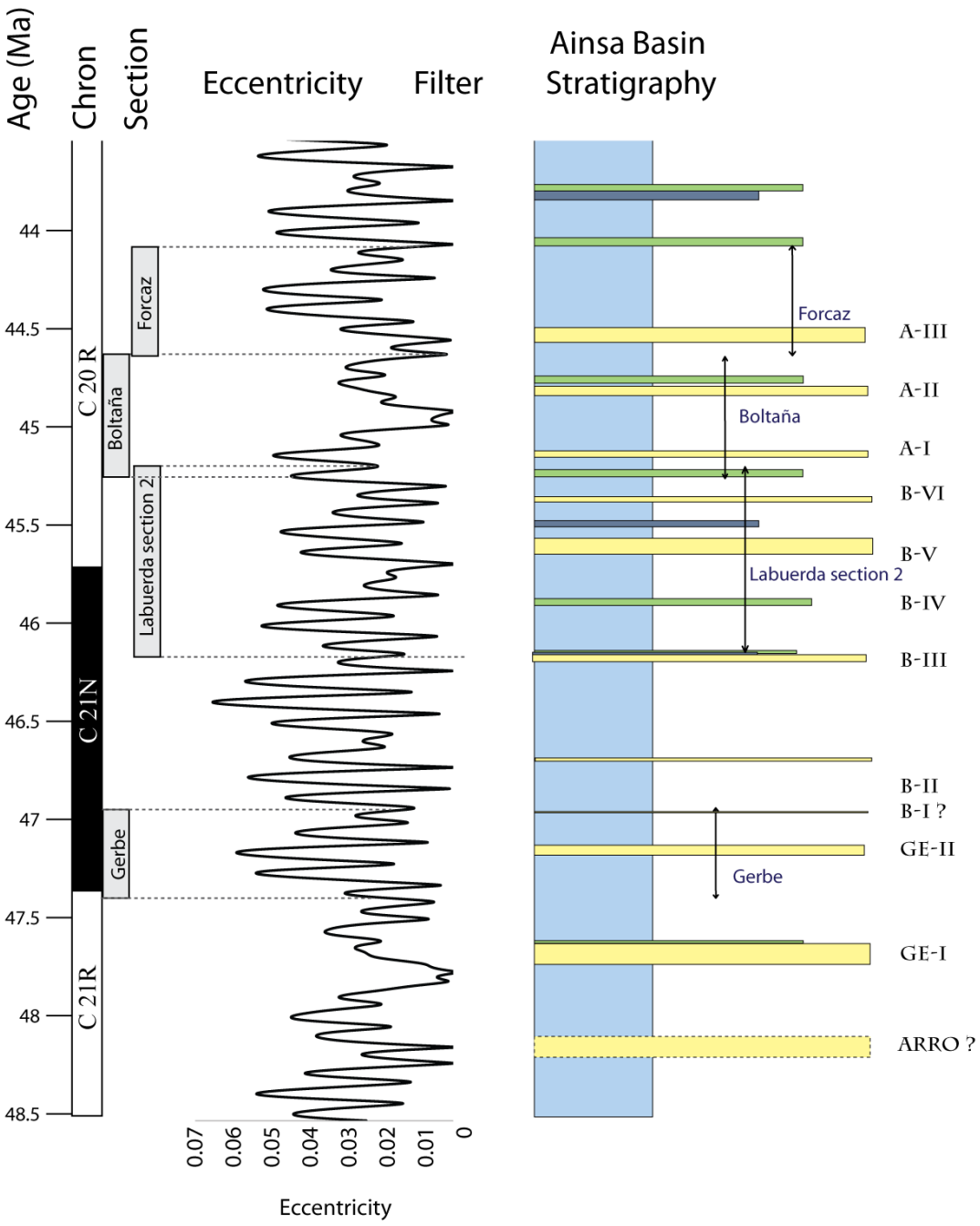

Figure 5.110 Chronostratigraphy of the Ainsa Basin. Orbital tuning of the Gerbe, Labuerda section 2, Boltaña and Forcaz sections to eccentricity curve of the Middle Eocene has allowed to transform the depth-stratigraphy to an age-stratigraphy. Eccentricity curves from the La2010a orbital solution of Laskar *et al.* (2011).

5.3.10 Conclusions

This chapter has presented sedimentological and spectral work from 10 fine-grained successions of interfan and overbank deposits located throughout most of the entire deep-marine stratigraphy of the Ainsa Basin. The Fosado and the Los Molinos systems have not been studied due to the high degree of tectonic deformation in the sediments. The location of each of the gamma-ray logged sections within the stratigraphy has been determined by detail geological mapping over large areas of the basin and by building cross-sectional profiles.

Spectral work carried out in these fine-grained successions have used a variety of cyclostratigraphic techniques to determine the presence of cyclical components within the spectral gamma-ray data collected with a portable spectrometer and sandstone turbidite intensity studies undertaken using detailed sedimentary logging. Spectral estimation methods have included REDFIT, MTM, maximum entropy and the modified periodogram. Confidence levels have been obtained after applying appropriate noise background fitting models. The association of certain frequencies to orbital parameters has been achieved by testing a large range of SAR using ASM analysis. Additional techniques to determine the spatial distribution of the cyclical components have included wavelet analysis and frequency-selective filtering.

These cyclostratigraphic techniques have demonstrated that the fine-grained successions in the Ainsa Basin have a strong climatic signal. Short sections, such as Sieste, Guaso and the Morillo-Bruello have in general lower confidence levels and noisier spectra, and the presence of Milankovitch cyclicity in these records is more difficult to prove. Eccentricity and obliquity cycles appear dominant in most of the records and precession cycles are not always present.

The Gerbe, Banastón and Ainsa systems have a good chronostratigraphic control from magnetostratigraphy (Chapter 3). Gamma-ray logged sections in these systems (Gerbe, Labuerda 2, Boltaña and Forcaz sections) have been orbitally tuned to the eccentricity curves of the La2010a orbital solution of Laskar *et al*. (2011). Using the total-gamma records filtered to the frequency identified with eccentricity, the records have been tuned using eccentricity maxima and/or minima as control points. Any polarity reversals identified have also been used as control points. Orbital tuning to the right part of the historical eccentricity curves has been achieved by establishing careful stratigraphic correlations between different gamma-ray sections and by taking into consideration SARs derived from spectral studies. Orbital tuning has resulted in a strengthening of the orbital cycles, especially the precession cycle. The resulting tuned records have good confidence levels, > 95%, and the period of the identified cycles have a similar duration to the predicted values for the orbital parameters during the Middle Eocene using Berger *et al*. (1992) equations. Tuning the records has permitted to convert a depth-stratigraphy of the Ainsa Basin to an age-stratigraphy for the lower part of the Upper Hecho Group and to establish the time of initiation of different sandbodies.

ASM analysis has permitted to calculate SAR for each of the gamma-ray logged sections. SAR appears to have decreased steadily throughout the stratigraphy. The Arro and Gerbe systems have the fastest SARs (~ 50 cm/kyr) which progressively decrease to ~ 13 cm/kyr in the Guaso System. The average SAR in the interfan deposits is ~ 30 cm/kyr.

The interfan thicknesses between the coarse-grained sandbodies can be estimated using SAR calculated from ASM studies and the thickness of the interfan successions calculated from cross-section profiles. The delivery of coarse-grained

sediments in the basin appears to have occurred at irregular intervals and it cannot be entirely explained by climatic forcing. The drivers for these coarse-grained sediments are discussed in detail in Chapter 6.

Chapter 6

Tectonic *versus* climatic controls in the delivery of sediments to the Ainsa Basin

6.1 Introduction

The deep-marine stratigraphy of the Ainsa Basin is composed of a cyclic alternation of coarse-grained sandstone packages (referred to as sandbodies and interpreted as submarine fans) and fine-grained packages of fan and interfan sediments (Van Lunsen, 1970; Mansurbeg *et al.*, 2009, Caja *et al.*, 2010). Pickering and Corregidor (2005), and Pickering and Bayliss (2009) recognised 25 coarse-grained sandbodies typically 40-70 m thick separated by hundreds of metres of thin-bedded, laminated siltstones and marlstones. These fine-grained sediments constitute both interfan and fan lateral-margin facies. The presence of these sediment packages shows a very marked variation in the sediment supply to the basin with alternating periods of coarse-grained supply being switched on and off.

The principal processes which can drive the high-frequency modulation of sediment flux to the deep-marine environment include high-frequency climatic, extra-basinal tectonics, autocyclicity and/or eustatic sea-level changes. Chapter 3 and 5 have shown that there is a strong climatic signal in the fine-grained sediments at Milankovitch periodicities. The coarse-grained sandbodies, however, do not seem to follow a regular pattern, and their initiation appears irregularly spaced (Chapter 5).

Clearly, a variety of controlling factors must have influenced the deposition of the deep-marine systems of the Ainsa Basin at different timescales.

This chapter integrates work from previous chapters and discusses the mechanism/s which may have controlled the sedimentary successions observed in the Ainsa Basin. The chapter is divided in two main sections. The first section explores different controlling factors which have driven the cyclic delivery of the fine-grained sediments and the second section discusses the possible mechanisms which may have contributed to the irregular deposition of the coarse-grained sandbodies.

6.2 Controls on the deposition of fine-grained deep-marine sediments in the Ainsa Basin

Cyclostratigraphic analysis of total-gamma, K and Th records from outcrop spectral gamma-ray data undertaken in many interfan and overbank successions throughout the entire deep-marine stratigraphy of the Upper Hecho Group in the Ainsa Basin have shown that there is a strong climatic signal in the fine-grained sediments (Chapter 5). Milankovitch short eccentricity and obliquity cycles appear dominant in most of the records with precession cycles not always being present. Time-series analysis of sandstone turbidite intensity records in these fine-grained successions yield similar frequencies than those identified from the study of spectral gamma-ray data. These interfan and overbank successions, therefore, record a high-frequency variable supply of coarse and fine-grained sediments to the deep-marine basin at Milankovitch scales.

Geochemical analysis undertaken in one of the interfan sections (Well A6 core) has helped to gain a better understanding of the cyclical associations between different

geochemical proxies in the fine-grained sediments (Chapter 4). Elemental XRF data has shown a partitioning of certain chemical elements between the sandstone turbidites and the finer fractions (siltstones and mudstones). Detrital elements such as Si, Zr and Ti are concentrated in the thin sandstone turbidites whilst the surrounding siltstones and hemipelagic unstructured mudstones are low in all these components and have a higher content of clay minerals. The detrital elements are believed to derive from fluvial sources which entered the deep-marine environment as hyperpycnal flows. Cyclostratigraphic studies of the sandstone turbidite intensity show a strong cyclicity at Milankovitch frequencies. This cyclicity is also identified in the detrital elements associated with the sandstone turbidites. The variation in the supply of sandstone turbidites has also had an effect on the delivery and preservation of terrestrial carbon which is reflected in a cyclic variation of the stable carbon isotope records. Variations in the detrital flux have also affected the degree of bioturbation which shows an inverse relationship with the intensity of the sandstone turbidite records and the precipitation of diagenetic minerals. Similarly, elements which act as proxies for oxygenation levels at the sediment interface, such as Mn, appear to have varied with the same cyclical behaviour as the sandstone turbidites.

Among the processes which can create cyclicity in the sedimentary record are high-frequency climatic cycles (linked with changes in chemical and physical weathering and erosion) and/or eustatic sea-level changes. Tectonics and autocyclicity are also considered here as they can produce semi-cyclical sedimentary processes.

6.2.1 Climate control on the deposition of the fine-grained sediments

Palaeogeographic reconstructions place the Pyrenees at ~ 35°N during the Eocene (Hay *et al*., 1999), a latitude which is known to be sensitive to astronomically-induced climate changes, with some studies inferring that orbital changes can influence annual precipitation and evaporation at such latitudes (e.g., Berger, 1978a; Kutzbach and Otto-Bliesner, 1982). An increase in the coarser sediment supply may be associated with astronomically-induced warmer and wetter periods during which chemical weathering and erosion in the source area, and discharge of eroded sediments, is increased (Schmitz, 1987; Peterson *et al*., 2000). Such processes could have acted as the principal driver on the intermittent supply of the coarser-grained sedimentary packages observed in the interfan successions of the deep-marine Ainsa Basin.

Sloan and Huber (2001) used realistic combinations of orbital parameters to model climate variability during the Eocene. Their results show that changes in insolation over precessional cycles can account for the changes in surface temperature, upwelling intensity, location and amount of continental run-off. For continental run-off, these authors calculated a 12% variance in the Pyrenees. Periods of enhanced storminess and precipitation may be linked to increase riverine run-off and higher detrital mixed and suspended load input into the deep-basin. Other studies also have shown that precessional cycles may have an important control on precipitation and river run-off (e.g., Kutzbach, 1981; Olsen, 1994; Mallinson *et al*., 2003; Tachikawa *et al*., 2011). Any changes in river run-off linked to climate change would not only affect the amount and rate of accumulation of the clastic input to the Ainsa Basin, but, would also influence the sediment chemistry through weathering patterns and grain-size distributions.

Schneider *et al*. (1997) interpreted reductions in the K/Al values to reflect enrichments of kaolinite relative to K-feldspar as a result of increased weathering intensity. They associated low K/Al ratios with warm, humid periods which resulted in the formation of kaolinite-rich sediments. Yarincik *et al*. (2000) also used the same proxy to infer changes in climate to account for differences in the amount of detrital illite and kaolinite. They argued that illite is a common weathering product of arid climates where physical weathering dominates, whilst kaolinite is a common chemical weathering product of tropical and humid climates. The K/Al ratios in sediments in the A6 core do not follow the same profile as sandstone turbidite intensity and, therefore, these ratios appear not to be associated to grain-size changes. The cyclicity observed in K/Al ratios, however, may record periodic changes from warmer and more humid conditions (with increase the chemical weathering) to drier and cooler periods with a decrease in kaolinite formation.

6.2.2 Tectonic control on the deposition of the fine-grained sediments

High-frequency tectonic pulses which mimic Milankovitch periodicities have been described in the literature (Beekman *et al*., 1995; Vakarelov *et al*., 2006), but none have been demonstrated to operate with such regularity over a 10^5 yr time frame. Tectonic processes are usually more erratic (irregular) and of variable duration. Thus, the good correlation between the predicted frequencies for Milankovitch cycles during the Eocene (Berger *et al*., 1992), also the frequencies in the geochemical proxies and spectral gamma-ray data makes it unlikely that tectonic processes were the principal driver of the sedimentary packages within the fine-grained successions.

6.2.3 Autocyclicity control on the deposition of the fine-grained sediments

Autocyclic processes in the deep-marine environment can cause cyclic arrangements of siliciclastic successions without any astronomical influence (*cf.* Lancien *et al*., 2004; Dennielou *et al*., 2006; Kane and Hodgson, 2011). The cyclic packaging identified in the fine-grained successions within the Ainsa Basin could therefore be explained entirely by autocyclic processes. However, the geochemical and mineralogical data with the presence of basin-wide dm-scale dark-coloured mudstone bands observed in the fine-grained turbidites (Sutcliffe and Pickering, 2009) suggests that extrabasinal processes were operating to influence environmental change within the basin.

6.2.4 Eustatic control on the deposition of the fine-grained sediments

The Middle Eocene, when the Ainsa Basin sediments accumulated, was a time period which witnessed a progressive cooling and deterioration of global climate and marks the transition from the warm and ice-free world of the Early Eocene (~ 55 Ma) to the icehouse conditions of the Oligocene (~ 34 Ma) (Miller *et al*., 1987; Zachos *et al*., 2001a, 2008; Coxall *et al*., 2005; Liu *et al*., 2009). Whether the change towards cooling conditions observed during the Eocene was sufficient to cause glaciation remains controversial (see Section 1.5.2). However, there are other mechanisms such as thermal expansion and groundwater and lake storage, which can cause high-frequency sea-level changes at the same frequency as glacio-eustasy, although they generally cause lower amplitude sea-level changes (Miller *et al*., 2011) (Figure 6.1).

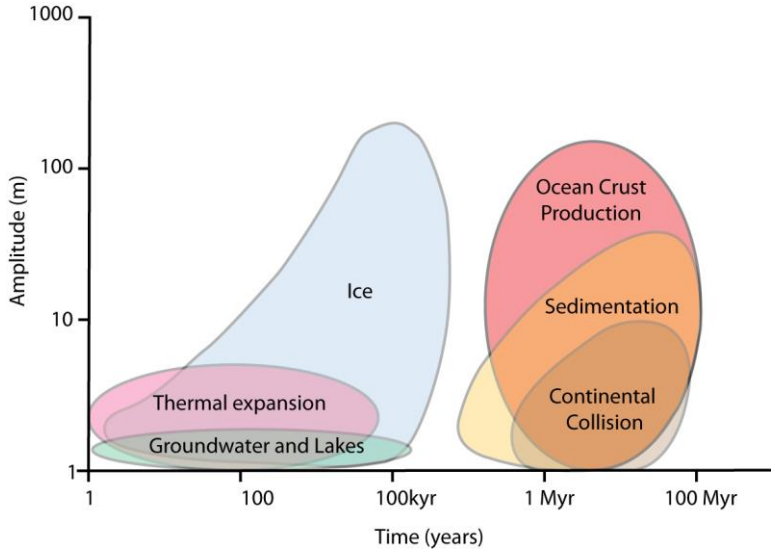

Figure 6.1 Mechanisms of sea-level change. The figure shows different mechanisms which causes changes sea-levels at a variety of amplitudes and time-scales. From Miller (2005) and Miller *et al.* (2011).

Thermal expansion and contraction of seawater causes eustatic sea-level change (Church, 1991; Mellor and Ezer, 1995; Rahmstorf, 2007). Warm climatic periods may result in a small but significant water expansion and corresponding sea-level rise, whilst colder climatic periods may be associated with lowered sea level. Thermal expansion sensitivity in long-climate model simulations has led to estimates of 0.2-0.6 m/$^{\circ}$C (Meehl *et al*., 2007). Such studies suggest that during much warmer climatic periods, for example during the Eocene, would have been associated with higher mean sea-surface temperatures when compared to the Present and, therefore, the role of thermal expansion and contraction of seawater may have resulted in significant sea-level changes. McKay *et al*. (2011) have estimated a ~ 8.5 m sea-level rise associated with thermal expansion during the last interglacial. Also, Schulz and Schäfer-Neth (1997) linked the 20 kyr sedimentary cycles during the Mesozoic greenhouse period to small-scale global sea-level fluctuations caused by thermal expansion and contraction of seawater controlled by precession cycles.

Jacobs and Sahagian (1993) argue that climate-induced changes in lake and groundwater storage with Milankovitch periodicities has the potential to produce small fluctuations in sea levels. They modelled the effects of precession on the volume storage in lake and groundwater systems and estimated that it could account for as much as 4-8 m of global sea-level change. Although it cannot be discounted changing volume of mountain glaciers as a contributory cause of global sea-level variation, the ice stored in present day mountain glaciers corresponds to ~ 0.4 m of sea-level change (Huss and Farinotti, 2012) and it is unlikely that this mechanism may have been significant during the Eocene.

Many researchers have linked changes in the geochemistry of deep-marine sediments with fluctuations in sea levels. Sageman *et al*. (2003) found that increased concentrations of heavy mineral grains containing Ti supplied by rivers and transferred to distal basin sites by sediment gravity-flows (such as turbidity currents) provide a proxy for sea-level fall and progradation of siliciclastic systems. Yarincik *et al*. (2000) also found that continental derived material with higher concentrations of Ti, Zr and Si could be linked to low sea-level stands. Periods of overall lowered sea level would have been associated with greater subaerial exposure of the continental shelf and increased delivery by reworking of marine biogenic material containing elements including Ca. High K/Al ratios are known to be associated with periods of increased detrital supply which link cold and dry periods to sea-level lows (Yarincik *et al*., 2000). In the A6 core, the cyclicity observed in elemental ratios such as K/Al, Ti/Al and Ca/Al may, therefore, record sea-level fluctuations at a Milankovitch timescale.

6.3 Depositional models for the fine-grained sediments

The variation in the coarser-grained supply, sedimentary geochemistry and cyclicity of the fine-grained successions can be explained by two alternative and equally plausible depositional models. Model A suggests that climate-triggered river floods have been the main factor controlling sandstone turbidite deposition in the deep-marine fine-grained successions of the Ainsa Basin. Model B advocates for high-frequency sea-level variations as the main controlling factor in causing a cyclical variation of coarse grained supply during the deposition of the fine-grained successions.

6.3.1 Model A: Sediment supply driven by climatic change

Periods of enhanced precipitation would have resulted in chemical and physical weathering and an increased in river run-off. High riverine discharge would have triggered high sediment flux entering the marine environment as hyperpycnal flows. Where river discharge underwent considerable density stratification, hypopycnal and hyperpycnal flows resulted (*cf.* McLeod *et al*., 1999; Kneller and Buckee, 2000). During periods of high fluvial effluent discharge, the generation of hyperpycnal and hypopycnal flows probably resulted in the deposition of sandstone turbidites and hemipelagites, whilst during periods of low river discharge, hypopycnal flows only resulted in the deposition of clay-rich hemipelagites in deep basinal sites. Sandy turbulent floods could have originated as hyperpycnal flows and carried detrital minerals such as Fe, Ti and Zr and terrestrial organic matter that also eroded and entrained material along its flow path to the shelf and down slope into the deeper basin. During periods of low riverine discharge, hyperpycnal flows would have been considerably reduced, with hypopycnal flows as the dominant process, therefore,

sedimentation consisted mainly of mudstones and siltstones. In this model, riverine run-off would have been mainly controlled by precessional cycles with the amplitude of these cycles being modulated by eccentricity.

A climatically-driven variation of sediment supply associated with high-frequency climatic changes has been observed in other studies of Eocene sections in the Pyrenees, e.g., from the Montañana Group, Tremp Basin (e.g., De Boer *et al*., 1991; Weltje *et al*., 1996; Nijman, 1998).

The rivers and deltas of the Tremp Basin are the main source of sediment supply to the Ainsa Basin. Cyclic sedimentary successions have been recognised in these fluvio-deltaic sediments (De Boer *et al.*, 1991). It is reasonable to assume that the same mechanisms that have controlled the deposition of the Tremp Basin may have had an impact on the sedimentation of the Ainsa Basin. De Boer *et al.* (1991) proposed that regular variations of sediment supply could explain the sediment packaging in these successions. Petrographic analysis and numerical-statistical modelling of sandstone compositions in these fluvio-deltaic successions by Weltje *et al.* (1996) support this interpretation. De Boer *et al.* (1991) suggested that orbitally-induced climate fluctuations of precipitation are the more obvious explanation of the observed vertical alternations. Astronomically-induced warmer and wetter periods caused an increase in the chemical weathering and erosion in the source area and resulted in an increase in the discharge of coarse-grained eroded sediments (Schmitz, 1987; Frostick and Reid, 1989; De Boer *et al.*, 1991; Peterson *et al.*, 2000), whilst during astronomical induced dry periods, the discharge of eroded sediments was suspended.

Recent work in fan-fringe and basin plain deep-marine deposits of the Western Pyrenees of a similar age as the deposits of the Ainsa Basin (Lower-Middle Eocene)

show orbitally-forced fluctuations in seasonal rainfall, riverine runoff and terrigenous input to the deep-marine environment (Payros and Martinez-Braceras, 2014). This study supports the argument that orbitally-induced climatic variations in the Pyrenees may have been the first control on coarse-grained sediment flux in the fine-grained sucessions.

6.3.2 Model B: Sediment supply driven by sea-level change

Sea-level fall and lowstand conditions may have favoured river and delta progradation to create shelf-edge deltas. The frequency and magnitude of turbidity currents are generally higher during sea-level lows because the greater subaerial exposure of the shelf causes rivers to transport their sediments directly into the heads of submarine canyons, including shelf-edge deltas (Jorry *et al*., 2008; Toucanne *et al*., 2009). Plink-Bjorklund and Steel (2004) argue that sea-level lows can facilitate the direct connection between fluvial and deeper water channels and facilitate hyperpycnal flows down the basin slope.

Sediments in the interfan and off-axis overbank deposits are generally fine-grained and thin- to very thin-bedded, even for the coarser-grained sediment packages and sea-level changes would have low-amplitude, for example those caused by thermal expansion/contraction and changes in the terrestrial hydrological cycle, e.g., lake storage/release, are sufficient to cause the variations in the coarser sediment supply observed in the fine-grained sediments.

Various studies, however, support sea-level changes in the Pyrenees during the Middle Eocene. Payros *et al*. (2009) analysed the Ypresian/Lutetian boundary interval across the Pyrenean orogen and compared it with other sections across Europe. These

authors concluded that a glacio-eustasy signal controlled the sedimentary evolution of all the sedimentary sections identified. Also, Gomez-Paccard *et al*. (2011) documented composite sequences (tens to hundreds of metres thick) in the Eocene Montserrat alluvial fan/fan-delta complex of the southeast Ebro Basin (upper Lutetian to lower Priabonian), which they interpreted as likely due to the 400 kyr long eccentricity cycles, possibly controlled by climatically induced sea-level fluctuations. The sedimentary and tectonic evolution of the Jaca and the Ainsa basins has also been explained as likely due to by global climate-controlled sea-level fluctuations (Mutti *et al*., 1985; Pickering and Corregidor, 2005; Das Gupta and Pickering, 2008, Pickering and Bayliss, 2009; Huyghe *et al*., 2012). Huyghe *et al*. (2012) described cyclic Lutetian–Bartonian carbonates of the Jaca Basin, west of the Ainsa Basin explaining them as due to high-amplitude, high-frequency (< 100 kyr) glacio-eustatic sea-level changes. These high-amplitude events resulted in an increase of erosion and river destabilisation which caused terrigenous nutrient input variations in the receiving basin.

6.4 Controls on deposition of the coarse-grained deep-marine sediments of the Ainsa Basin

The main driver on the deposition of the 25 sandbodies identified in the Ainsa Basin has been subject to recent controversy, with some researchers advocating for a tectonic origin (Mutti *et al*., 1983-84; Muñoz *et al*., 1994, 1998; Arbués *et al*., 1998; Pickering and Corregidor, 2005; Hoffman *et al*., 2009; Pyles *et al*., 2013) and others for a climatic origin (Das Gupta and Pickering, 2008; Pickering and Bayliss, 2009; Sutcliffe and Pickering, 2009).

There is, however, a general consensus that the first-order control on the creation of accommodation space in the Ainsa Basin was tectonic (Muñoz *et al*., 1994, 1998; Arbués *et al*., 1998; Fernandez *et al*., 2004, 2012; Pickering and Bayliss, 2009). Basin subsidence was driven by the advancement of thrust sheets in the Southern Pyrenean Zone causing a rapid basin deepening and transition from a shallow-marine to a deep-marine basin (Dreyer *et al*., 1999; Muñoz *et al.*, 1998, Fernández *et al.*, 2004) with depths in the order of 400-800 m (Pickering and Corregidor, 2005). The tectonic influence in the basin can be recognised in a long-term 4-5 Myr tectonic driver which caused the development of angular unconformities which can be traced from the shelf to the deep-marine environment (Muñoz *et al.*, 1998; Arbués *et al*., 1998; Remacha *et al*., 2003; Pickering and Bayliss, 2009). These unconformities divide the stratigraphy of the Ainsa Basin into two distinct successions, the older unit (Lower Hecho Group) being structurally more deformed than the overlying unit (Upper Hecho Group) (e.g., Pickering and Corregidor, 2005). Pickering and Bayliss (2009) suggest that intrabasinal tectonics controlled the deposition of the eight deep-marine systems in a process described as seesaw tectonics (Figure 6.2). This process was caused by the differential growth of the basin-bounding Mediano and Boltaña anticlines. The growth of these anticlines as thrust-propagation folds was controlled by the partitioned movement of their underlying thrusts (Pickering and Corregidor, 2005; Pickering and Bayliss, 2009). Growth of the Mediano Anticline caused a westward lateral offset stacking patterns of the sand-prone channelised fans. Subsequent growth of the Boltaña Anticline, re-located the depositional axis back towards the east. The pulsating growth of these anticlines caused successive cycles of westward and eastward movement of the systems' depositional axis. As the anticlines grew, the basin also became narrower and resulted in the depositional confinement of the submarine fans

(Pickering and Corregidor, 2005; Sutcliffe and Pickering, 2009; Bayliss and Pickering, 2014).

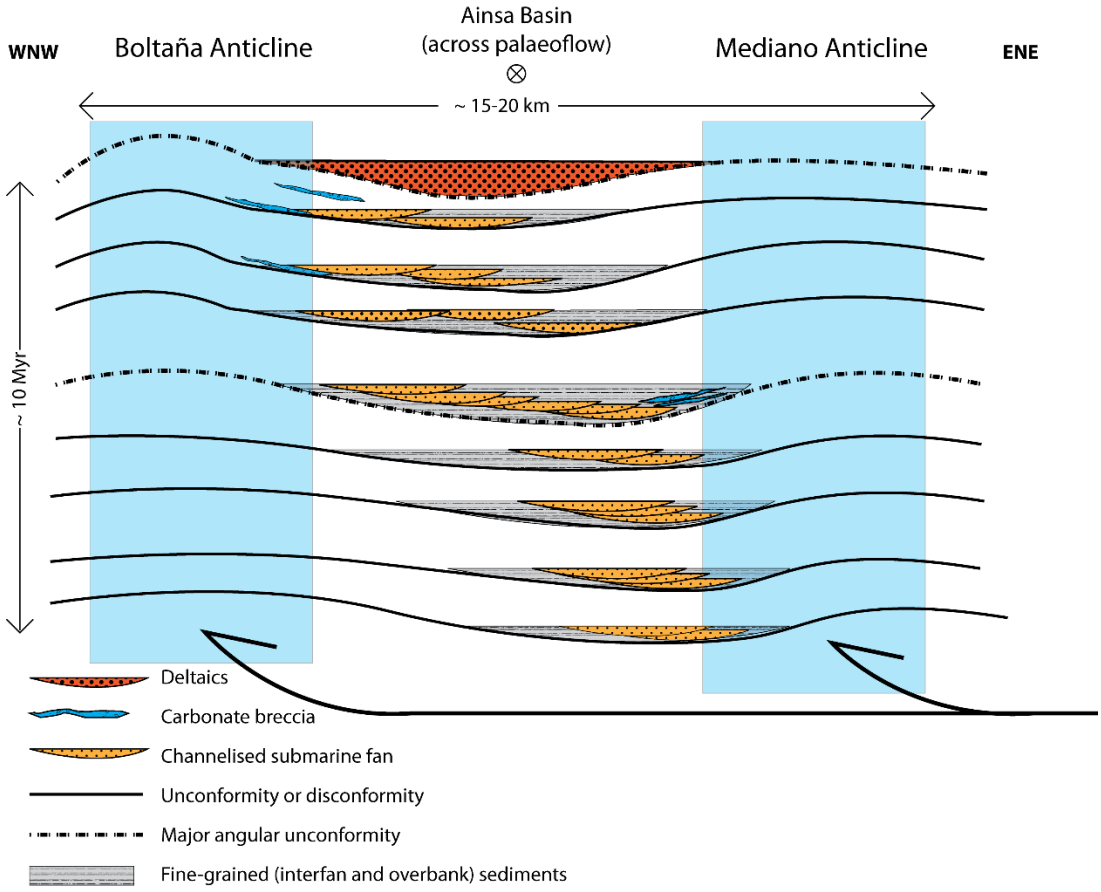

Figure 6.2 Intrabasinal tectonic control on the deposition of the Ainsa systems. The figure shows how the deposition of the 8 deep-marine systems of the Ainsa Basin has been controlled by the differential growth of the Mediano and Boltaña anticlines in a process of see-saw tectonics. Modified after Pickering and Bayliss (2009).

The submarine fan model developed by Pickering and Corregidor (2005) shows that the typical facies distribution and stratigraphy observed in the submarine fans of the Ainsa Basin can be better explained by a change in base level. An initial lowering of the sea-level could have triggered the deposition of MTDs/MTCs, triggering a lowstand fan initiation. As sea-level started to rise, sediment supply to the fan decreased and eventually resulted in fan abandonment. A change in base level in the Ainsa Basin could have been caused by basinal tectonics or by eustasy. Pickering and Corregidor (2005) have demonstrated by using foraminifera analysis that fully marine

conditions remained throughout the sedimentation of the deep marine systems of the Ainsa Basin and therefore any global changes of sea-level were reflected in the basin.

However, some studies have suggested that submarine fan initiation and MTD/MTC accumulation triggering can also result from high riverine discharge without a variation in sea levels (Ducassou *et al*., 2009). The fan development model of Pickering and Corregidor (2005) could also be explained by climatic change with periods of intense precipitation and high effluent discharge linked to fan initiation and growth.

In addition to these three allogenic factors (basin tectonics, sea-level change and climatic change), autocyclic processes can also act as possible drivers of the coarse-grained sediment to the basin. This includes, for instance, channel infill caused by the accumulation of sediment gravity-flow deposits, including sediment slide and slump material and other sediments which can plug the channel and result in channel avulsion and migration to the next adjacent topography low inter-channel area (Prins *et al.*, 2000). These four processes will be now discussed in turn.

6.4.1 Eustatic control of the deposition of the Ainsa Basin sandbodies

The most accepted dominant factor controlling deposition of turbidites and submarine-fan development in large deep-marine fan systems like the Amazon, the Mississippi, the Bengal and the Indus Fan are changes in sea-level (McHargue and Webb, 1986; Pickering *et al*., 1986a; Kolla and Coumes, 1987; Kolla and Macurda, 1988; Manley and Flood, 1988; Bouma *et al.*, 1989; Feeley *et al.*, 1990; Weimer, 1990; McHargue, 1991; Kolla and Perlmutter, 1993; Kenyon *et al.*, 1995; Weber *et al.*, 1997; von Rad and Tahir, 1997). During sea-level fall, deltas may prograde to the shelf break,

releasing large volumes of sediment on the slope or in to canyon heads, increasing sediment flux to the deep-sea (Damuth, *et al.*, 1988; Bouma *et al.*, 1989; Nelson *et al.*, 1992; Kenyon *et al.*, 1995; Normark *et al.*, 1997; Prins *et al.*, 2000; Ducassou *et al.*, 2009). The progressive exposure during low sea-level stands, typically corresponds to slope instability and MTC triggering. Thick intervals of slumps and debris flows are typically found at the base of a deep-marine fan system (Ducassou *et al.*, 2009). The new submarine channel system typically develops on top or on the side of these MTDs/MTCs (Ducassou *et al.*, 2009). During sea-level rise, deltas retrograded and delta-front sediments were deposited on the alluvial plain and the innermost part of a broadened shelf. Sediments were therefore trapped in the continental shelf, reducing the sediment supply to the deep-marine environment (Prins *et al.*, 2000). There are different global sea-level curves produced for the Middle Eocene (e.g., Haq *et al*., 1987; Miller *et al*., 2005; Komintz *et al*., 2008; Cramer *et al.*, 2009). The comparison of these global sea-level curves with the stratigraphy of the Ainsa Basin does not show any significant association since the resolution of these curves are probably too low to be compared with the basin stratigraphy (Figure 6.3). However, it can be observed that most of the curves show a general decrease in sea-levels of ~ 50 m from the Gerbe System towards the Guaso System indicating a general shallowing profile. Higher frequency sea-level variations in the order of ~ 20 m are identified in these sea-level curves.

Therefore, orbitally forced periods of sea-level lows could regulate the influx of coarse clastic sediments to the basin and result in the deposition of deep-marine sand-prone submarine fans. Pickering and Bayliss (2009) suggested that the deposition of the 25 coarse-grained sand-rich submarine fans of the Ainsa Basin was controlled by glacio-eustatic changes linked to the ~ 400 kyr Milankovitch eccentricity frequency.

Although the presence of glaciation during the Middle Eocene remains controversial, there is growing evidence that supports the presence of ephemeral ice-sheets which resulted in moderate (20-40 m) high-frequency global sea-level changes during this time period (Haq *et al.*, 1987; Miller *et al.*, 2005; Komintz *et al.*, 2008). Many studies have linked ice-sheet initiation and expansion to periods of reduced insolation during the 400 kyr eccentricity minima (Zachos *et al.*, 2001b; Pälike *et al.*, 2006a, b; Liebrand *et al.*, 2011).

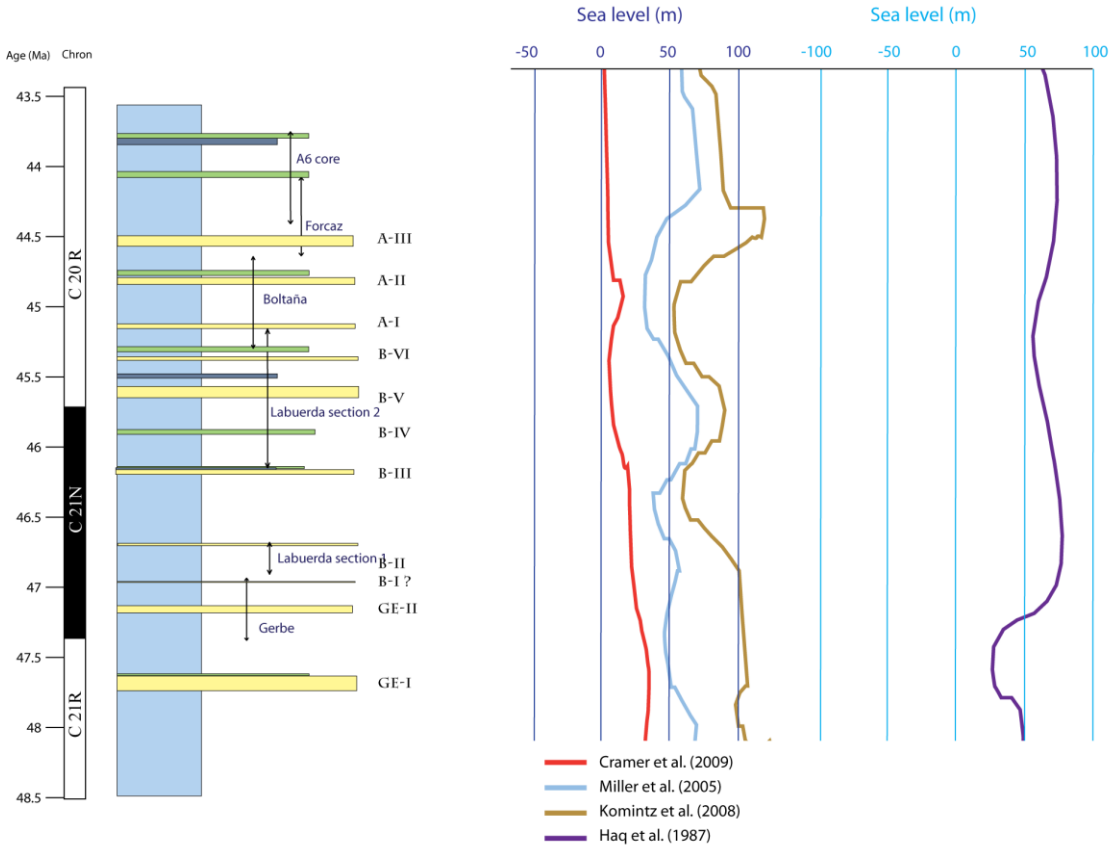

Figure 6.3 Comparison of the stratigraphy of the Ainsa Basin with global sea levels. The stratigraphy of the Ainsa Basin has been compared with global sea-level curves of Haq *et al.*, 1987; Miller *et al.*, 2005; Komintz *et al.*, 2008, and Cramer *et al.*, 2009). The Haq *et al.* (1987) global sea-level curve has been plotted separately as the amplitude of this sea-level curve based on stratigraphic records clearly differs from those estimated using other methods (e.g., backstripping).

However, results from this study suggest that the timing of deposition for each of the Ainsa deep-marine sandbodies (submarine fans) appear to have occurred at irregular intervals and therefore it cannot be entirely attributed to climatic forcing. The suggestion made by Pickering and Bayliss (2009) of a eustatic origin for the 25 sandbodies can, therefore, be rejected (*cf*. the tectonostratigraphic cycles of Pickering and Corregisor, 2005). Nevertheless, climatic forcing cannot be completely ruled out as a possible and/or contributory mechanism for the initiation of some of the submarine fans. Figure 6.4 shows the orbitally-tuned stratigraphy of the Ainsa Basin and the eccentricity curves of the La2010a orbital solution of Laskar *et al*. (2010). Periods of eccentricity minima are signalled. Some of the sandbodies including the BIII, BVI, AIII and MII and some of the heterolithic packages appear to coincide with periods of 400 kyr eccentricity minima. Although this association can be purely coincidental, this mechanism cannot be completely rejected.

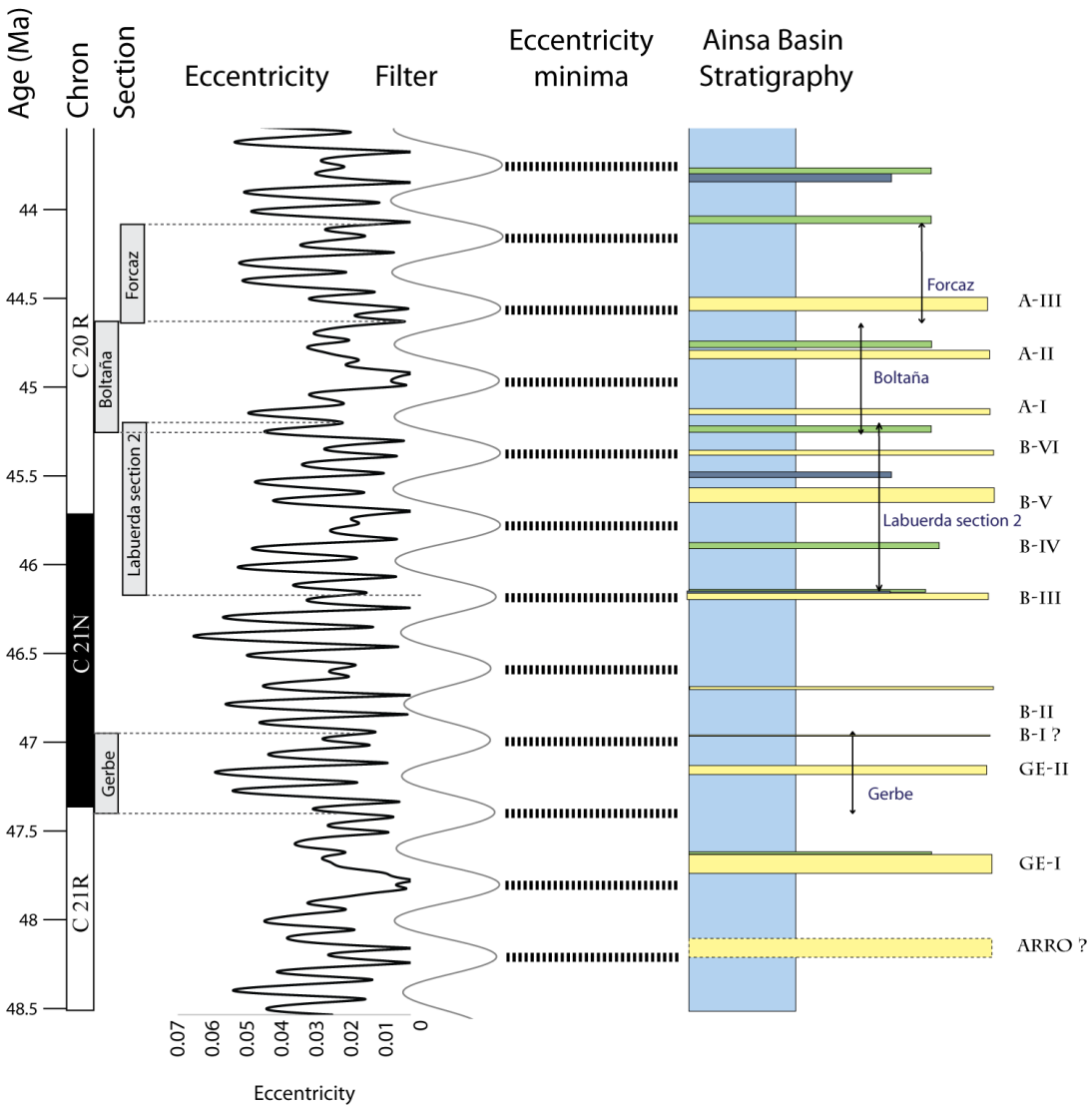

Figure 6.4 Comparison of the stratigraphy of the Ainsa Basin with eccentricity curves. The stratigraphy of the Ainsa Basin has been compared with the eccentricity curves of the La2010a orbital solution of Laskar *et al.* (2011).

6.4.2 Climatic control on the deposition of the Ainsa Basin sandbodies

Although lowstand fans are more common, some authors have found that in many submarine fans, deep-marine sediment supply was still significant during transgressions or high-sea-level stands (Piper and Normark, 1983; Kuehl *et al.*, 1989; Flood *et al.*, 1991; Kolla and Perlmutler, 1993; Weber *et al.*, 1997; Covault *et al.*, 2007; Ducassou *et al.*, 2009; Covault and Graham, 2010) and, therefore, in these cases

submarine-fan deposition continued independently of sea-level change. High fluvial discharge associated with climate change seems to have been a significant control on sediment supply in many submarine fans (Nakajima and Itaki, 2007; Covault and Graham, 2010; Covault *et al.*, 2010; Jorry *et al.*, 2011; Toucanne *et al.*, 2012). It has been proposed that periods of high fluvial discharge can result in the progradation of deltas to the shelf-edge and to the deep-marine environment (Burgess and Hovius 1998, Carvajal *et al,.* 2009). During wetter periods, an increased water discharge caused the erosion of alluvial fans and older deposits (Blum and Tornqvist, 2000) resulting in an increased of sediment flux to the shelf margin. Ducassou *et al.* (2009) found that in the Nile deep-marine system, periods of increased turbidity-current activity and the accumulation of MTDs/MTCs occurred during major flooding periods. During arid periods, fluvial discharge decreased (Blum and Tornqvist, 2000) and sediments were temporarily stored within the drainage basin (alluvial fans and fluvial deposits).

Burgess and Hovius (1998) proposed that sediment supply and not sea-level change, is the limiting factor on deep-marine sedimentation and argued that in the absence of significant sea-level fluctuations, for instance, during greenhouse conditions, fan growth can continue if rivers and deltas have sufficient sediment loads allowing sediment to be transported to the shelf edge. Milliman and Syvitski (1992) suggest that rivers in active margins are more susceptible to periodic floods and can discharge large amounts of sediments to the deep-sea even during high-stands. Basin geomorphological factors can facilitate the translation of sediment from fluvial and deltaic environments to the deep-marine with small drainage basins and the presence of narrow shelves facilitating this process (Milliman and Syvitski, 1992; Couvalt and Graham, 2010). The relatively small size (~ 30 km across) of the Ainsa Basin and the

presence of a narrow shelf typical of active margins (Milliman and Syvitski, 1992) may have facilitated that submarine fans were fed directly from the land with cycles or fan initiation and abandonment that may reflect orbitally induced climate changes (Weltje and de Boer, 1993). However, the resolution of these studies does not allow to estimate the frequency of these climatic-driven pulsating events.

Payros and Martinez-Braceras (2014) suggest that periods of enhanced seasonal rainfall, resulting in higher riverine runoff and sediment influx into the deep-marine basin were associated with precession cycles although they appear to have been enhanced during eccentricity maxima. This study could suggest that submarine fan development could follow the eccentricity cycles and have a periodicity of ~ 95 kyr, 123 kyr and 400 kyr. What seems likely is that these climatic events are likely to be more regular and periodic than the timing of fan initiation estimated from this study and therefore, it can be concluded that this mechanism is unlikely to have contributed to the deposition of the 25 submarine fans of the Ainsa Basin. Although it cannot be ruled out that some submarine fans may have been initiated by punctuated episodes of intense rainfall and flash floods which resulted in an increase of coarse-grained supply to the deep-marine environment.

6.4.3 Autocyclic control on the deposition of the Ainsa Basin sandbodies

The internal architecture of lobes and submarine fans can be controlled by intrinsic (autocyclic) factors. These factors control the redistribution of sediments within a sedimentary system and can occur independently of any external influence. Autogenic processes include channel migration and avulsion, lobe switching and lateral compensational stacking patterns (Parsons *et al*., 2002; Nicholas and Quine, 2007;

Deptuck *et al*., 2008; Prélat *et al*., 2010; Clarke *et al*., 2010). These processes occur because there is a tendency of gravity-sediment flows to occupy topographic lows and smooth topographic relief (Mutti and Sonnino, 1981; Straub *et al*., 2009; Ganti *et al*., 2011). MTDs/MTCs, for example, may cause sufficient sea-floor topography to develop which can affect the location and distribution of subsequent sand-flows by causing local ponding of deep-water sands in topographic lows forming compensational stacking patterns and channel migrations (Martinsen and Bakken, 1990; Ross *et al*., 1994; Pickering and Corregidor, 2005).

Autocyclic processes are known to produce repeating depositional cycles. Although some of these processes are intrinsic to the depositional system, they are commonly aperiodic (Cecil, 2013). The cyclic but irregular nature of autogenic processes could be a possible mechanism for the irregular timing of the coarse-grained deposition of the Ainsa Basin.

However, Pickering and Corregidor (2005) argue against an autocyclic control for the deposition of the Ainsa Basin sandbodies as the deposition and architecture of these sandbodies could not be explained by lateral switching and compensational stacking processes. The two main arguments discussed by these authors are:

(i) the westward shift of these sandbodies towards the foreland, away from the deformation front, have been attributed to the differential growth of basin bounding anticlines caused by the irregular motion of the underlying thrusts.

(ii) the switching on and off of coarse-grained sediment with thick intervals of interfan fine-grained deposits in between sandbodies imply that an external forcing must have controlled the influx of coarse-grained sediment to the basin.

Despite these arguments, autocyclic processes may still have played an important role in controlling the distribution of sediment at smaller temporal and spatial scales. Pickering and Corregidor (2005) recognised within the internal architecture of each submarine fan several cycles of erosional channel incision, sediment bypass and channel infill (backfill) which they attributed to autocyclicity.

6.4.4 Tectonic control on the deposition of the Ainsa Basin sandbodies

The irregular timing in the deposition of the 25 sandbodies could be explained by tectonic processes. Basin tectonics can steepen the depositional profile and cause relative sea-level variation of probably low to moderate amplitude (Mutti *et al*., 2003). Periods of active thrusting could result in the creation of relief in the hinterland and would therefore result in an increased supply of coarse clastic sediment, whilst, during tectonic quiescence, fine-grained deposition would dominate (De Boer *et al.*, 1991). Tectonic pulses of coarse-grained sediment have been demonstrated in Pleistocene successions (Larsen and Steel, 1978; Dunne and Hempton, 1984; Guillocheau, 2010). Different studies on tectonic modelling have shown that faulting activity can be intermittent and produce semi-cyclic sedimentation patterns at similar time-scales as climatic processes (tens of thousands of years) (Peper *et al.*, 1992; Peper and de Boer, 1995; Beekman *et al.*, 1995; Lee and Schwarcz, 1996; Nicol *et al*., 1997, 2005; Morley *et al.*, 2000; Walsh *et al*., 2002; Mouslopoulou *et al*., 2009). Many studies suggest that fault displacements accumulate at relatively uniform rates over time-periods between 20 kyr and 300 kyr whilst very high-frequency fault displacements (< 20 kyr) are highly variable (Nicol *et al*., 1997, 2005; Mouslopoulou *et al*., 2009).

The timing between the sandbodies of the Ainsa Basin has been estimated between 130 kyr and 779 kyr with an average value of 364±204 kyr. The frequencies of submarine fan initiation occur at very similar time-scales as those expected from climatic fluctuations (e.g., eccentricity 100 kyr and 400 kyr cycles) although they appear to be aperiodic. In tectonic terms, however, the timing between sandbodies seems to be relatively uniform and suggests a moderate regular tectonic activity (in the order of hundreds of kyr). The timing between sandbodies is shorter in the older systems (Gerbe and Banastón) than in the younger systems suggesting a higher frequency of fault displacement during the initial stages of basin deepening. The magnetostratigraphy study by Holl and Anastasio (1993) showed an intermittent growth of the Mediano Anticline with rapid tectonic pulses (< 1.5 Myr intervals) which have been associated with the episodic movement of the Cotiella-Montsec thrust sheet. This study has shown that a tectonic control on the sediments of the Ainsa Basin may have acted at a higher frequency in the basin than the 4-5 Myr tectonic driver identified in the formation of the tectonostratigraphic units (Muñoz *et al.*, 1998; Arbués *et al*., 1998; Remacha *et al*., 2003; Pickering and Bayliss, 2009; *cf*. Pickering and Corregidor, 2005). Holl and Anastasio (1993) identified three main rapid growth episodes of the Mediano Anticline (Figure 6.5). The first episode occurred during chron C22r and is probably linked to the initiation of the deep-marine sedimentation of the Lower Hecho Group (Fosado, Los Molinos and Arro systems) and the intense tectonic deformation which occurred in the basin with the emplacement of the Sobrarbe/Arro Fold System). The second episode of rapid growth occurred during chron C21n which this study (Chapter 3) has associated with the deposition of the Banastón System (probably during deposition of the BI-BIV sandbodies). The third rapid episode of anticline growth occurred at the top of C20r during the initiation of

the Morillo System (during deposition of the MI and MII sandbodies). These episodes of anticline growth would have resulted in relative lowering of the base level which may have triggered MTD/MTC deposition and submarine fan development. The increase in growth rates can be associated with significant episodes of tectonic shortening and strain rates in the area. Many studies have shown that an increase in the strain rates can produce faster fault recurrent intervals (Nicol *et al*., 1997, 2005; Walsh *et al*., 2002; Mouslopoulou *et al*., 2009).

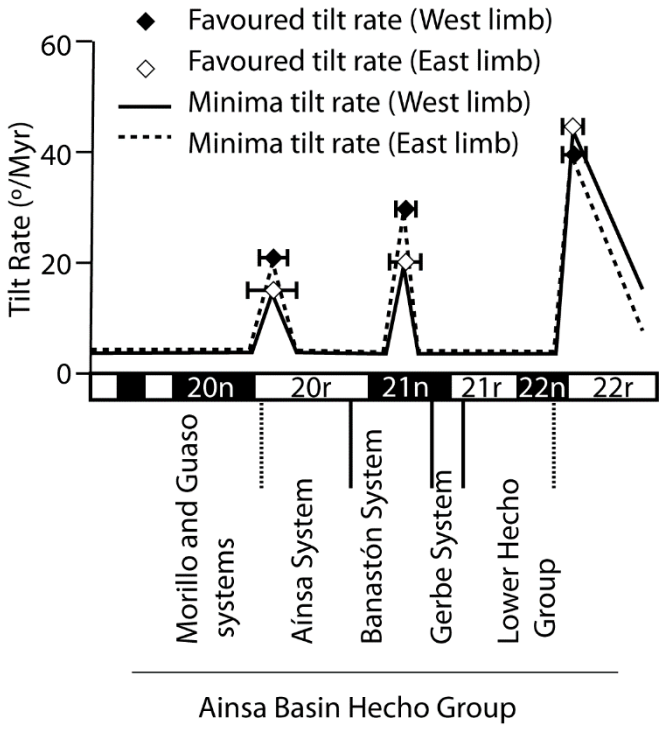

Figure 6.5 Mediano Anticline growing rates. The Mediano Anticline has undergone three main periods of rapid growing during the deposition of the Hecho Group turbidites in the Ainsa Basin. Modified after Holl and Anastasio (1993).

Clevis *et al.* (2003) used numerical modelling to study the effects of regular pulsating tectonic activity on basin drainage morphology. These authors simulated tectonic pulses of 200 kyr duration followed by periods of tectonic quiescence of the

same time duration. Their results showed a stratigraphic pattern of periodic stratigraphic alternation of prograding and retrograding alluvial fan gravels (Figure 6.6a). Periods of tectonic activity were associated with alluvial fan and coastline retreats and tectonically-quiescent periods were associated with the cessation of flexural subsidence, progradation of the alluvial fans and increased delivery of gravels to the basin. These authors suggested that coastal retreat during periods of tectonic uplift occurred because delta catchment yields were insufficient to fill the accommodation space created by flexural subsidence in response to tectonic loading (Clevis *et al*., 2003).

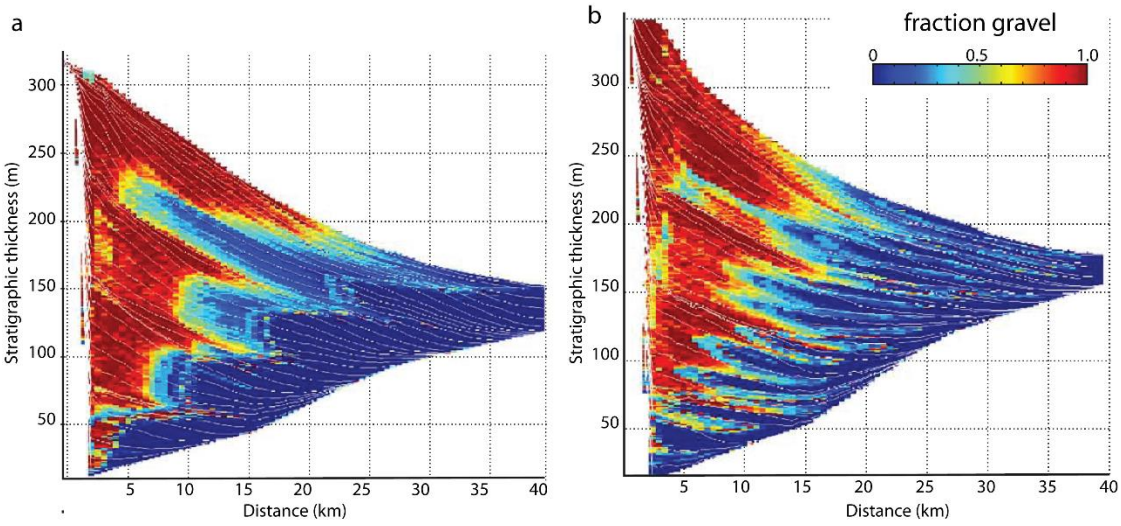

Figure 6.6 Numerical simulations of gravel delivery to basins. The figure shows the delivery of coarse-grained (gravel) material and its spatial distribution in tectonically active basins. The sections shown are perpendicular to the fault front and the axis x represents increasing distance from the fault. (**a)** Model using recurrent pulsating tectonic activity occurring with periodicities of 200 kyr followed by 200 kyr of tectonic quiescence. (**b)** Model using same tectonic variation as model (a) but with superimposed small-scaled (20m) sea-level variations at 100 kyr Milankovitch scales. Figure modified after Clevis *et al.* (2003).

The pulses of tectonic uplift recognised in the Mediano Anticline (Holl and Anastasio, 1993) could have resulted in a semi-periodic intermittent delivery of coarse-grained sediment to the Ainsa Basin. The lag-time recognised by Clevis *et al.* (2003)

between tectonic uplift and delivery of coarse-grained material in the order of tens to hundreds of thousands of years suggests that the deposition of the sandbodies are more likely to have occurred between periods of significant Mediano Anticline growth activity. The numerical model of Clevis *et al.* (2003) also shows that higher fault displacement rates reveal higher average SARs during the decrease of thrust activity. This could explain the high SARs observed during the deposition of the Arro and the Gerbe systems after the significant growth period of the Mediano Anticline during chron C22r (Figure 6.5).

In the Pyrenees, Peper and de Boer (1995) studied the Tremp-Ager Basin using a numerical model to explain the changes in the sediment supply which resulted in the deposition of cyclical sequences in the Eocene deltaic parasequences. This model suggested that both climatic forces and regular tectonic pulses could have been responsible for the cycles of coarse-grained sediments observed in the deltaics, although they lack a chronostratigraphic framework to establish the regularity of these cyclic successions.

Since the Ainsa Basin appears to have been subjected to a strong climatic influence reflected in the regular packaging of the coarser-grained turbidite packages observed during the deposition of the fine-grained successions, it is likely that this climatic influence was superimposed on the tectonic influence caused by the pulsating growth of the Mediano Anticline. Clevis *et al.* (2003) repeated the experiment shown in Figure 6.6a, but added small-scale (~ 20 m) sea-level variations controlled by 100 kyr Milankovitch eccentricity. The combination of tectonic and climatic variables resulted in a complex stratigraphic pattern (Figure 6.6b). Although major progradation events associated with the tectonic pulses could still be recognised, the tectonic signal was clearly obscured by the high-frequency climatic sea-level fluctuations. The results

of this numerical model are comparable temporally with the stratigraphic framework of the Ainsa Basin, although is more likely that the tectonic growth pulses of the Mediano Anticline were more irregular than the designed pulses of this numerical model. The initiation of the Ainsa fan systems could have resulted following major pulses of tectonic growth whilst some individual submarine fans, MTDs and smaller heterolithic packages may have been associated with small-scaled climatic variations controlled by orbital cycles. Cyclic climatic processes responsible for the sediment packaging of the fine-grained successions are likely to have been obscured by the regular activity of aperiodic tectonic processes resulting in the irregular deposition of the 25 Ainsa Basin sandbodies.

6.5 Conclusions

The interfan and overbank off-axis deposits of the Ainsa Basin contain a strong Milankovitch cyclicity. Orbital parameters most likely paced the regular delivery of the fine-grained sediment mainly by river- and delta-derived hyperpycnal turbidity currents. Two depositional models can explain the regular variation of coarser-grained supply within these fine-grained successions. High-frequency small fluctuations of global sea level which during the Eocene could result from thermal expansion/contraction of the ocean waters and/or variations groundwater storage and lake level) caused river progradation during sea-level lows and the delivery of larger amounts of detrital material to the shelf-edge. The second depositional model suggests that warm and humid periods forced by Milankovitch cycles could have resulted in increased chemical weathering and river run-off, which would have triggered a high sediment flux to the seafloor through large-volume turbidity currents.

The pacing of the coarse-grained submarine fans, however, cannot be entirely explained by climatic forces. The variable duration of each submarine fan succession cannot support the hypothesis that the 400 kyr eccentricity cycles paced the delivery of coarse-grained material to the basin. Some submarine fans coincide with periods of eccentricity minima and it is possible that some of these sandbodies may have been modulated by eustatic changes influenced by Milankovitch parameters. Similarly high sediment discharge from rivers and deltas during monsoonal pulses and flash floods driven by orbital forcing, during periods of eccentricity maxima may have contributed to the deposition of some of the sandbodies and heterolithic packages. However, this cannot explain the irregular timing of the 25 sandbodies. Autocyclic processes are likely to have caused internal reorganisation of sediment within fan architecture with many cycles of channel incision, sediment bypass and infill identified in each submarine fan succession. Although these processes alone cannot explain the sedimentary and stratigraphic architecture of the sandbodies in the basin.

The most likely mechanism which may have acted as a first control on the timing of coarse-grained delivery to the Ainsa Basin and submarine fan initiation appears to be basin tectonics. The pulsating growth activity of the Mediano Anticline is likely to have caused episodic lowering of sea level which may have triggered the influx of coarse-grained sediments and the initiation of sand-prone submarine fan development. This tectonic processes overshadowed the regular variation of sediment supply observed in the finer-grained successions. Regular activity of moderate displacement faults can explain the semi-cyclical deposition of these sandbodies.

6.6 Limitations of this study

The major limitations of this study are associated to the poor chronostratigraphic control of the younger gamma-ray sections in the Morillo and Guaso systems. Magnetostratigraphy was only undertaken across half of the total deep-marine stratigraphy sampling the Gerbe, Banastón and Ainsa systems. The age discrepancies, ~ 1 Myr, between the biostratigraphy model of Scotchman *et al*. (2014) and this study, prevents the inference of depositional ages for the younger Morillo and Guaso systems. As a consequence, orbital tuning of the younger gamma-ray sections has not been possible and the upper part of the Ainsa Basin deep-marine stratigraphy has not been converted into an age-stratigraphy model. The study of the Morillo and Guaso systems is also affected by the shortness of some of the gamma-ray sections in these systems. The Guaso and Sieste sections are only 40 m thick preventing the determination of eccentricity cycles with accuracy, which may have affected the confidence in the determination of SAR across these systems.

The use of geochemical analysis has been restricted to one of the interfan successions (Well A6) located within the Ainsa deep-marine system. The rest of the deep-marine stratigraphy has not been sampled for stable carbon isotopes or for mineralogical or elemental analysis, as a result the interpretation of different palaeo-proxies is constrained to a relatively narrow time interval.

6.7 Wider applications

This study has explored the influence of astronomical forcing on climate and on the chemistry of deep-marine sediments. High-resolution palaeo-climatic changes has

been discussed using a multi-geochemical approach. Results from this study can be used to model other modern and ancient deep-marine basins worldwide.

Results from this study can have a wide applicability to the hydrocarbon industry. Understanding the processes which have contributed to calibrate the sedimentary flux (discharge) from non-marine to marine environments can help to place the development of submarine fans in a temporal and spatial context of sedimentary basin evolution. Interpretations on the evolution of sedimentary basins are commonly based on large-scale regional seismic-reflection and kilometre-spaced well data sets which often lack the spatial resolution to understand the fine-scale architecture of submarine fan systems. An integration of seismic and outcrop studies can help to develop sequence-stratigraphic and hydrocarbon reservoir models in exploration and development areas. However, in order to establish stratigraphic and depositional comparisons of ancient basins such as the Ainsa Basin as analogues which allow us to understand sediment distribution patterns, reservoir architecture and processes of fan construction for other basins around the world, it is necessary to have a sufficiently precise chronostratigraphic framework of the depositional units within the basins.

6.8 Further work

Further research could help our understanding on the controls of sedimentary-basin evolution in the Ainsa Basin as follows:

(a) Continue the magnetostratigraphy study to the younger deep-marine stratigraphy (Morillo and Guaso systems) to establish a chronostratigraphic framework for the sediment of the Ainsa Basin and to help to refine the sediment ages at a finer scale by

orbitally tuning the successions to the orbital curves of the Eocene. A combination of magnetostratigraphic and biostratigraphic studies based on nannofossil and larger foraminifera identification across these two younger systems can help develop a more robust age-model for these younger systems.

(b) Stable carbon isotope studies undertaken in a ~ 150 m interfan succession of fine-grained sediments in the Ainsa System has recorded a dominant precession signal. Extending this study to other parts of the Ainsa Basin would be useful to identify high-resolution palaeo-environmental change and understand the variation of terrestrial and marine carbon in the deep-marine sediments. Longer stable carbon-isotope records could also be compared with isotopic records from other basins in the world to help to develop more accurate global climatic reconstructions.

(c) This study has shown that fine-grained sediments show a regular cyclicity from high-resolution SGR logging and from geochemical XRF studies. However, the spectral gamma-ray log response to the sediment and geochemical rock signatures is not well understood since it not only reflects environmental change but also accounts for outcrop geometry effects and post-depositional alteration (e.g., outcrop weathering). An integration of different analytical techniques at outcrop level such as spectral gamma-ray logging, elemental XRF and whole rock geochemistry can allow to compare log data with point elemental and mineralogical composition of discrete samples and help to understand better the forcing mechanisms responsible for the depositional cycles in the fine-grained successions.

(d) The cyclicity observed in the K/Al ratio has been explained as cyclical changes in the weathering of the sediments with important implications in climatic cycles of warm and humid periods alternating with cold and dry periods. Clay mineralogy studies can

improve our understanding on palaeo-environmental change in the basin by recognising the presence of weathering cycles of kaolinite/illite in the fine-grained sediments.

References

Abbott, S.T. and Carter, R.M. (1994) The sequence architecture of mid-Pleistocene (0.35–0.95 Ma) cyclothems from New Zealand: facies development during a period of known orbital control on sea-level cyclicity. *In*: De Boer, P.L. and Smith, D.G. (eds) Orbital Forcing and Cyclic Sequences. *International Association of Sedimentologists. Special Publication*, **19**, 367-394.

Abels, H., Lourens, L. and Gingerich, P. (2013) Terrestrial astronomical age model for Eocene Thermal Maximum 2 and H2 hyperthermal events. *Geophysical Research Abstracts*, **15**, 4379.

Abelson, M., Agnon, A. and Almogi-Labin, A. (2008) Indications for control of the Iceland plume on the Eocene-Oligocene "greenhouse-icehouse" climate transition. *Earth and Planetary Science Letters*, **265**, 33-48.

Abreu, V.S. and Baum, G. (1997) Glacio-Eustasy: a global link for sequence boundaries during the Cenozoic. *In*: Beauchamp, B. (ed) CSPG-SEPM Joint Convention. Sedimentary events and hydrocarbon systems. Program with abstracts, *Canadian Society of Petroleum Geologists*, Calgary, Canada, 17.

Abreu, V.S. and Anderson, J.B. (1998) Glacial eustasy during the Cenozoic: Sequence stratigraphic implications. *American Association of Petroleum Geoscientists Bulletin*, **82**, 1385-1400.

Agnini, C., Macrì, P., Backman, J., Brinkhuis, H., Fornaciari, E., Giusberti, L., Luciani, V., Rio, D., Sluijs, A. and Speranza, F. (2009) An early Eocene carbon cycle perturbation at ~52.5 Ma in the Southern Alps: chronology and biotic response. *Paleoceanography*, **24**, PA2209. DOI: 10.1029/2008PA001649.

Aigner, T., Schauer, M., Junghans, W.-D. and Reinhardt, L. (1995) Outcrop gamma-ray logging and its implications: examples from the German Triassic. *Sedimentary Geology*, 100, 47-61.

Allen, P. A. (1997) *Earth Surface Processes*. Hoboken, NJ: John Willey & Sons.

Amaru, M.L., Spakman, W., Villaseñor, A., Sandoval, S. and Kissling, E. (2008) A new absolute arrival time dataset for Europe. *Geophysical Journal International*, **173**, 465-472.

Arbués, P., Mellere, D., Falivene, O., Fernández, O., Muñoz, J.A., Marzo, M. and de Gilbert, J.M. (2007) Context and architecture of the Ainsa I quarry channel complex, Spain. *In*: Nilsen, T.H., Shew, R.D., Steffens, G.S. and Studlick, J.R.J. (eds) Atlas of deep-water outcrops. *AAPG Studies in Geology*, **56**, CD-ROM.

Arbués, P., Muñoz, J.A., Poblet, J., Puigdefàbregas, C. and McClay, K. (1998) Significance of submarine truncation surfaces in the sedimentary infill of the Ainsa

basin (Eocene of south-central Pyrenees, Spain). *15th International Sedimentological Congres, Alicante, Spain*, Publicaciones de la Universidad de Alicante, 145-146.

Ardèvol, L., Klimowitz, J., Malagón, J. and Nagtegaal, P.J.C. (2000) Depositional sequence response to foreland deformation in the Upper Cretaceous of the Southern Pyrenees, Spain. *American Association of Petroleum Geologists Bulletin*, **84**, 566-587.

Arostegi, J., Baceta, J.I., Pujalte, V. and Carracedo, M. (2011) Late Cretaceous-Palaeocene mid-latitude climates: inferences from clay mineralogy of continental-coastal sequences (Tremp-Graus area, southern Pyrenees, N Spain). *Clay Minerals*, **46**, 105-126.

Arrhenius, S. (1896) On the influence of carbonic acid in the air upon the temperature on the ground. *Philosophical Magazine and Journal of Science*, **41**, 237-279.

Arthur, M.A., Dean, W.E., Pollastro, R., Scholle, P.A. and Claypool, G.E. (1985) A comparative geochemical study of two transgressive pelagic limestone units, Cretaceous Western Interior basin US. In: Pratt, L. M, Kauffman, E.G. and Zelt, F.B (eds) Fine-grained deposits and biofacies of the Cretaceous western interior seaway, *Society Economic Paleontologists and Mineralogists*, Tulsa, 16-27.

Ashkenazy, Y. and Tziperman, E. (2004) Are the 41 kyr glacial oscillations a linear response to Milankovitch forcing? *Quaternary Science Reviews*, **23**, 1879-1890.

Aubry, M.P. (1992) Late Paleogene calcareous nannoplankton evolution: A tale of climatic deterioration. *In*: Prothero, D. and Berggren, W.A. (eds) *The Eocene-Oligocene Climatic and biotic changes*, Princeton, New Jersey, Princeton University Press, 272-309.

Banerjee, R., Gupta, S.M., Miura, H. and Borole, D.V. (2010) A ~400 ka supra-Milankovitch cycle in the Na, Mg, Pb, Ni, and Co records of a ferromanganese crust from the Vityaz fracture zone, central Indian ridge. *Climate of the Past Discussions*, **6**, 1311-1335.

Barker, P.F. (2001) Scotia Sea regional tectonic evolution; implications for mantle flow and palaeocirculation. *Earth Science Reviews*, **55**, 1-39.

Barlett, M.S. (1948) Smoothing periodograms from time-series with continuous spectra. *Nature*, **161**, 686-687.

Barlett, M.S. (1950) Periodogram analysis and continuous spectra. *Biometrika*, **37**, 1-16.

Barnolas, A., Samsó, J.M., Teixell, A., Tosquella, J.Y. and Zamorano, M. (1991) Evolución sedimentaria entre la cuenca de Graus-Tremp y la cuenca de Jaca-Pamplona. I Congreso del Grupo Español del Terciario, *Libro Guía de la excursión n°1*, EUMO Gràfic, Vic, 123.

Barron, E.J. (1985) Explanations of the Tertiary global cooling trend. *Palaeogeography, Palaeoclimatology, Palaeoecology*, **50**, 45-61.

Barrucand, M., Rusticucci, M. and Vargas, W. (2006) Looking for climate signals using wavelet transform: extreme temperatures in Argentina, Atlantic sea surface temperature and other related variables. *Proceedings of 8 ICSHMO*, Brazil, 1491-1499.

Bayliss, N.J. (2011) Architecture and processes of deep-marine sandbodies, Ainsa Basin, Spanish Pyrenees. University College London, PhD Thesis.

Bayliss, N.J. and Pickering, K.T. (2014a) Deep-marine structurally confined, basin-slope sandy fans: Middle Eocene Morillo System, Ainsa Basin, Spanish Pyrenees. *Earth Sciences Reviews, in press*.

Bayliss, N.J. and Pickering, K.T. (2014b) Transition from deep-marine lower-slope erosional channels to proximal basinfloor stacked channel-levée-overbank deposits, and syn-sedimentary growth structures, Middle Eocene Banastón System, Ainsa basin, Spanish Pyrenees. *Earth Sciences Reviews, in press*.

Beaumont, C., Muñoz, J.A., Hamilton, J. and Fullsack, P. (2000) Factors controlling the Alpine evolution of the central Pyrenees inferred from a comparison of observations and geodynamical models. *Journal of Geophysical Research*, **105**, 8121-8145.

Beekman, F., Bull, J.M., Cloetingh, S. and Scrutton, R.A. (1995) Crustal fault reactivation as initiator of lithospheric folding in the Central Indian Ocean. *In*: Nieuwland, D. (eds) Modem Examples in Structural Interpretation, Validation and Modelling. *Geological Society London, Special Publication*, **99**, 251-263.

Beerbower, J.R. (1964) Cyclothems and cyclic depositional mechanisms in alluvial plain sedimentation Kansas State. *Geological Survey Bulletin*, **169**, 32-42.

Beerling, D.J. and Royer, D.L. (2011) Convergent Cenozoic CO_2 history. *Nature Geosciences*, **4**, 418-420.

Bender, M.L. (2002) Orbital tuning chronology for the Vostok climate record supported by trapped gas composition. *Earth and Planetary Science Letters*, **204**, 275-289.

Bentham, P.A. and Burbank, D.W. (1996) Chronology of Eocene foreland basin evolution along the western margin of the South-Central Pyrenees. *In*: Friend, P. F. and Dabrio, C.J. (eds) *Tertiary basins of Spain, the stratigraphic record of crustal kinematics*. Cambridge University Press, Cambridge, 144-152.

Berger, A. (1977) Support for the astronomical theory of climatic change. *Nature*, **268**, 44-45.

Berger, A.L. (1978a) Long-term variations of daily insolation and Quaternary climatic changes. *Journal of the Atmospheric Sciences*, **35**, 2362-2367.

Berger, A.L. (1978b) Long-term variations of caloric insolation resulting from the Earth's orbital elements. *Quaternary Research*, **9**, 139-167.

Berger, A.L. (2001) The role of CO_2, sea-level and vegetation during the Milankovitch forced glacial-interglacial cycles. *In*: Bengtsson, L.O. and Hammer, C.U. (eds) *Geosphere-Biosphere Interactions and Climate*, Cambridge University Press, New York, 119-146.

Berger, A. Loutre, M-F. and Laskar, J. (1992) Stability of the astronomical frequencies over the Earth's history for paleoclimatic studies. *Science*, **255**, 560-566.

Berger, A. and Loutre, M-F. (1994) Precession, eccentricity, obliquity, isolation and paleoclimates. *In*: Duplessy, J.C. and Spyridakis, M.T.(eds) *Long term climatic variations Springer*, **122**, 107-151.

Berger, A. and Loutre, M.F. (2007) Milankovitch theory and palaeoclimate, *Encyclopedia of Quaternary Science*, **2**, 1017-1022.

Berger, A., Loutre, M.F. and Dehant, V. (1990a) Astronomical frequencies for pre-Quaternary palaeoclimate studies. *Terra Nova*, **1**, 474-479.

Berger, A., Gallee, H., Fichefet, T., Marsiat, I. and Tricot, C. (1990b) Testing the astronomical theory with a coupled climate-ice sheet model. *Palaeogeography, Palaeoclimatology, Palaeoecology*, **89**, 125-141.

Berger, A., Loutre, M-F. and Laskar, J. (1992) Stability of the astronomical frequencies over the Earth's history for paleoclimatic studies. *Science*, **255**, 560-566.

Berger, A., Melice, J.L, and Loutre M.F. (2005) On the origin of the 100-kyr cycles in the astronomical forcing. *Paleoceanography*, **20**, PA4019, DOI:10.1029/2005PA001173.

Berger, A., Loutre, M.F. and Mélice, J.L. (2006) Equatorial insolation: from precession harmonics to eccentricity frequencies. *Climates of the Past*, **2**, 131-136.

Berger, W.H. (2012) Milankovitch theory - hits and misses. Scripps Institution of Oceanography Technical report, *Scripps Institution of Oceanography*, UC San Diego, 1-35.

Berggren, W.A., Kent, D.V., Swisher, C.C. and Aubry, M.-P (1995) A revised Cenozoic geochronology and chronostratigraphy. *In*: Berggren, W.A., Kent, D.V., Aubry, M.-P. and Hardenbol, J. (eds) *Geochronology, time scales and global stratigraphic correlation.* SEPM (Society for Sedimentary Geology) Special Publication, **54**, 129-212.

Berner, R.A. and Westrich, J.T. (1985) Bioturbation and the early diagenesis of carbon and sulfur. *American Journal Science*, **285**, 193-206.

Berner, R.A., Lasaga, A.C. and Garrels, R.M. (1993) The carbonate-silicate geochemical cycle and its effect on atmospheric carbon dioxide over the past 100 million years. *American Journal of Science*, **283**, 641-683.

Bijl, P. K., Schouten, S., Sluijs, A., Reichart, G.-J., Zachos, J.C. and Brinkhuis, H. (2009) Early Palaeogene temperature evolution of the southwest Pacific Ocean. *Nature*, **461**, 776-779.

Billups, K., Channell, J.E.T. and Zachos, J. (2002) Late Oligocene to early Miocene geochronology and paleoceanography from the subantarctic South Atlantic. *Paleoceanography*, **17**, U39-U49.

Bjørlykke, K. and Egeberg, P.K. (1993) Quartz cementation in sedimentary basins. *American Association of Petroleum Geologists Bulletin*, **77**, 1538-1548.

Bloemsma, M.R., Zabel, M., Stuut, J.B.W., Tjallingii, R., Collins, J.A. and Weltje, G.J. (2012) Modelling the joint variability of grain size and chemical compositions in sediments. *Sedimentary Geology*, **280**, 135-148.

Blum, M.D. and Törnqvist, T.E. (2000) Fluvial responses to climate and sea-level change: a review and look forward. *Sedimentology*, **47**, 2-48.

Blum, M.D. and Straffin, E.C. (2001) Fluvial responses to external forcing: examples from the French Massif Central, the Texas Coastal Plain (USA), the Sahara of Tunisia, and the Lower Mississippi Valley (USA). *In*: Maddy, D. and Macklin, M.A. (eds) *River Basin Sedimentary Systems: Archives of Environmental Change*, Balkema Press, Rotterdam, 195-228.

Bohaty, S.M. and Zachos, J.C. (2003) Significant Southern Ocean warming event in the late middle Eocene. *Geology*, **31**, 1017-1020.

Bohaty, S.M., Zachos, J.C., Florindo, F. and Delaney, M.L. (2009) Coupled greenhouse warming and deep-sea acidification in the middle Eocene. *Paleoceanography*, **24**, PA2207. DOI: 10.1029/2008PA001676.

Bond, R.M.G. and Mc Clay, K.R. (1995) Inversion of a lower Cretaceous extensional basin, south central Pyrenees, Spain. *In*: Buchanan, J.G. and Buchanan, P.G. (eds) Basin Inversion. *Geological Society Special Publication*, **88**, 415-431.

Bouma, A.H., Coleman, J.M., Stelting, C.E. and Kohl, B. (1989) Influence of relative sea level changes on the construction of the Mississippi fan. *Geo-marine Letters*, **9**, 161-170.

Bouraoui, F., Grizzetti, B., Granlund, K., Rekolainen, S. and Bidoglio, G. (2004) Impact of climate change on the water cycle and nutrient losses in a Finnish catchment. *Climate Change*, **66**, 109-126.

Bourger, J., Zaragosi, S., Ellouz-Zimmermann, S., Ducassou, E. Prins, M.A., Garlan, T., Lanfumey, V., Jder, Schneider, J.L., Rouillard, P. and Giraudeau, J. (2010) Highstand vs. lowstand turbidite system growth in the Makran active margin: Imprints of high-frequency external controls on sediment delivery mechanisms to deep water systems. *Marine Geology*, **274**, 187-208.

Bourrouilh, R., Moen-Maurel, L., Muñoz, J. and Teixell, A. (2004) 32nd International geological congress Western Pyrenees and fold-and-thrust-belt: Geodynamics, sedimentation and plate boundary reconstruction from rifting to inversion. *Fieldtrip Guidebook- B16*. APAT, Italy.

Bown, P.R., Lees, J.A. and Young J.R. (2004) Calcareous nannoplankton evolution and diversity through time. *In*: Thierstein, H.R. and Young J.R. (eds) *Coccolithophores - From molecular processes to global impact*, Springer-Verlag, 481-508.

Boyle, E.A. (1983) Chemical accumulation variations under the Peru Current during the past 130,000 years. *Journal of Geophysical Research*, **88**, 7667-7680.

Braconnot, P. and Marti, O. (2003) Impact of precession on monsoon characteristics from coupled ocean atmosphere experiments: changes in Indian monsoon and Indian Ocean climatology. *Marine Geology*, **201**, 23-34.

Braconnot, P., Marzin, C., Grégoire, L., Mosquet, E. and Marti, O. (2008) Monsoon responses to changes in Earth's orbital parameters: comparisons between simulations of the Eemian and of the Holocene. *Climates of the Past*, **4**, 281-294.

Bradley, R.B. (2013) Palaeoclimatology: reconstructing climates of the Quaternary. Academic Press, 3rd edition, 106.

Brady, P.V. (1991) The effect of silicate weathering on global temperature and atmospheric CO_2. *Journal of Geophysical Research*, **96**, 18101-18106.

Bristow, C.S. and Williamson, B.J. (1998) Spectral gamma ray logs: core to log calibration, facies analysis and correlation problems in the Southern North Sea. *Geological Society, London, special Publications*, **136**, 1-7.

Brown, A.G. and Barber, K.E. (1985) Late Holocene sedimentary history of a small lowland catchment in central England. *Quaternary Research*, **24**, 87-102.

Browning, J.V., Miller, K.G. and Pak, D.K. (1996) Global implications of lower to Middle Eocene sequence boundaries on the New Jersey coastal plain-the icehouse cometh. *Geology*, **24**, 639-642.

Brumsack, H.J. (1986) The inorganic geochemistry of Cretaceous black shales (DSDP leg 41) in comparison to modern upwelling sediments from the Gulf of California. *In*: Summerhayes, C.P. and Shackleton, N.J. (eds) North Atlantic paleoceanography. *Geological. Society Special Publication*, **21**, 447-462.

Brunet, M.F. (1986) The influence of the evolution of the Pyrenees on adjacent basins. *Tectonophysics*, **129**, 345-354.

Buis, M.G. and Rey, J. (1975) Une évolution sédimentaire de type deltaique: le passage du Tertiare marine au Tertiare continental entre l'Ariège et le Douctouyre (Pyrénées Ariegeoises). *Bulletin de la Société d'Histoire Naturelle de Toulouse*, **111**, 80-95.

Burg, J.P. (1967) Maximum entropy spectral analysis. *37th Annual International Society of Exploration Geophysicists Meeting*, Oklahoma City, Oklahoma.

Burg, J.P. (1968) A new analysis technique for time series data. *Advance Study Institute NATO*, Enchede, Netherlands.

Burgess, C.E., Pearson, P.N., Lear, C.H., Morgans, H.E.G., Handley, L. and Pancost, R.D. (2008) Middle Eocene climate cyclicity in the southern Pacific: Implications for global ice volume. *Geology*, **36**, 651-654.

Burgess, P.M. and Hovius, N. (1998) Rates of delta progradation during highstands: Consequences for timing of deposition in deep-marine systems. *Geological Society of London*, **15**, 217-222.

Butler, R.F. (1992) Paleomagnetism: magnetic domains to geologic terranes. Blackwell Scientific Publications.

Caja, M.A., Marfil, R., García, D., Remacha, E., Morad, S., Mansurbeg, H., Amorosi, A., Martínez-Calvo, C. and Lahoz-Beltrá, R. (2010) Provenance of siliciclastic and hybrid turbiditic arenites of the Eocene Hecho Group, Spanish Pyrenees: implications for the tectonic evolution of a foreland basin. *Basin Research*, **22**, 157-180.

Calvert, S.E. and Pedersen, T.F. (1993) Geochemistry of recent oxic and anoxic marine sediments: implications for the geological record. *Marine Geology*, **113**, 67-88.

Calvert, S.E. and Pedersen, T.F. (1996) Sedimentary geochemistry of manganese; implications for the environment of formation of manganiferous black shales. *Economic Geology*, **91**, 36-47.

Cámara, P. and Klimowitz, J. (1985) Interpretación geodinámica de la vertiente centro-occidental surpirenaica (Cuencas de Jaca-Tremp). *Estudios Geológicos*, **41**, 391-404.

Campanyá, J., Ledo, J., Queralt, P., Marcuello, A., Liesa, M. and Muñoz, J.A. (2012) New geoelectrical characterisation of a continental collision zone in the West-Central

Pyrenees: Constraints from long period and broadband magnetotellurics. *Earth and Planetary Science Letters*, **333-334**, 112-121.

Cande, S.C. and Kent, D.V. (1995) Revised calibration of the geomagnetic polarity timescale for the Late Cretaceous and Cenozoic. *Journal of Geophysical Research*, **100**, 6093-6095.

Canfield, D.E. (1991) Sulfate reduction in deep-sea sediments. *American Journal of Science*, **291,** 177-188.

Capote, R., Muñoz, J.A., Simón, J.L., Liesa, C. and Arlegui, L. (2002) Alpine tectonics I: the Alpine system north of the Betic Cordillera. *In*: Gibbons, W. and Moreno, T. (eds) *The Geology of Spain*. Geological Society, London, 367-400.

Carey, A.E., Lyons, W.B. and Owen, J.S. (2005) Significance of landscape age, uplift, and weathering rates to ecosystem development. *Aquatic Geochemistry*, **11**, 215-239.

Carvajal, C., Steel, R. and Petter, A. (2009) Sediment supply: The main driver of shelf-margin growth. *Earth-Science Reviews*, **96**, 221-248

Casas, A., Kearey, P., Rivero, L. and Adam, C.R. (1997) Gravity anomaly map of the Pyrenean region and comparison of the deep geological structure of the western and eastern Pyrenees. *Earth and Planetary Science Letters*, **150**, 65-78.

Casas, A.M., Soto, R. and Martínez-Peña, M.B. (2002) Geometrical relation unconformities and subsequent folding: the Arro Folding System (Southern Pyrenees).*Comptes Rendus Geoscience*, **334**, 765-772

Cavagnetto, C. and Anadón, P. (1996) Preliminary palynological data on floristic and climate changes during the middle Eocene-early Oligocene of the eastern Ebro Basin, northeast Spain. *Review of Paleobotany and Palynology*, **92**, 281-305.

Cecil, C.B. (2013) An overview and interpretation of autocyclic and allocyclic processes and the accumulation of strata during the Pennsylvanian-Permian transition in the central Appalachian Basin, USA. *International Journal of Coal Geology*, **119**, 21-31.

Chamberlain, A.K. (1984) Surface gamma-ray logs: a correlation tool for frontier areas. *Bulletin of the American Association of Petroleum Geologists*, **68**, 1040-1043.

Choukroune, P. (1992) Tectonic evolution of the Pyrenees. *Annual review of Earth and Planetary Sciences*, **20**, 143-158.

Choukroune, P. and ECORS Team (1989) The ECORS Pyrenean deep seismic profile: reflection data and the overall structure of the orogenic belt. *Tectonics*, **8**, 23-39.

Christie-Blick, N., Mountain, G.S., and Miller, K.G. (1990) Seismic stratigraphic record of sea-level change. *In*: *Sea-level Change*. National Research Council, Washington, D.C.: National Academy Press, 116-140.

Church, J.A., Godfrey, J.S., Jackett, D.R., McDougall, T.J. (1991) A model of sea level rise caused by ocean thermal expansion. *Journal of Climate*, **4**, 438-456.

Claps, M. and Masetti, D. (1994) Milankovitch periodicities recorded in Cretaceous deep-sea sequences from the Southern Alps (Northern Italy). *In*: De Boer, P.L. and Smith, D.G. (eds) Orbital forcing and cyclic sequences, *Special Publication of the International Association of Sedimentologists*, **19**, 99-107.

Clark, J.D. and Pickering, K.T. (1996) Architectural elements and growth patterns of submarine channels: application to hydrocarbon exploration. *American Association of Petroleum Geologists Bulletin*, **80**, 194-221.

Clarke, L., Quine, T.A. and Nicholas, A. (2010) An experimental investigation of autogenic behaviour during alluvial fan evolution. *Geomorphology*, **115**, 278-285.

Clemens, S.C. and Tiedemann, R. (1997) Eccentricity forcing of Pliocene-early Pleistocene climate revealed in a marine oxygen-isotope record. *Nature*, **385**, 801-804.

Clevis, Q., de Boer, P. and Wachter, M. (2003) Numerical modelling of drainage basin evolution and three-dimensional alluvial fan stratigraphy. *Sedimentary Geology*, **163**, 85-110.

Clift, P.D. and Gaedicke, C. (2002) Accelerated mass flux to the Arabian Sea during the Middle-Late Miocene. *Geology*, **30**, 207-210.

Collinson, M.E. (1992) Vegetational and floristic changes around the Eocene/Oligocene boundary in Western and Central Europe. *In*: Prothero, D.R. and Berggren, W.A. (eds) *Eocene-Oligocene climatic and biotic evolution*, Princeton University Press, Princeton, NJ, 437-450.

Collinson, M.E. and Hooker, J.J. (2003) Paleogene vegetation of Eurasia: framework for mammalian faunas. *Deinsea,* **10**, 41-83.

Coney, P.J., Muñoz, J.A., McClay, K. and Evenchick, C.A. (1996) Syn-tectonic burial and post-tectonic exhumation of an active foreland thrust belt, southern Pyrenees, Spain. *Geological Society of London*, **153**, 9-16.

Correns, C.W. (1954) Titan in Tiefseesedimenten. *Deep Sea Research*, **1**, 78-85.

Cosgrove, M.E. (1973) The geochemistry and mineralogy of the Permian red beds of southwest England. *Chemical Geology*, **11**, 31-47.

Coulthard, T.J. and Macklin, M.G. (2001) How sensitive are river systems to climate and land-use changes? A model-based evaluation. *Journal of Quaternary Science*, **16**, 347-351.

Covault, J.A. (2011) Submarine Fans and Canyon-Channel Systems: A Review of processes, products and models. *Nature Education Knowledge*, **3** (10):4, 1-19.

Covault, J.A. and Graham, S. (2010) Submarine fans at all sea-level stands: Tectono-morphologic and climatic controls on terrigenous sediment delivery to the deep sea. *Geology*, **38**, 939-942.

Covault, J., Normark, W., Romans, B. and Graham, S. (2007). Highstand fans in the California borderland: The overlooked deep-water depositional systems. *Geology*, **35**, 783-786.

Covault, J.A., Romans, B.W., Fildani, A., McGann, M. and Graham, S.A. (2010) Rapid climatic signal propagation from source to sink in a southern California sediment-routing system. *The Journal of Geology*, **118**, 247-259.

Cowan, D.R. and Myers, K.J. (1988) Surface gamma-ray logs: a correlation tool for frontier areas: discussion. *American Association of Petroleum Geologists Bulletin*, **72**, 634-636.

Coxall, H.K. and Pearson, P.N. (2007) The Eocene–Oligocene Transition. *In*: William, M., Haywood, A.M., Gregory, F.J. and Schmidt, D.N. (eds) Deep-time perspectives on climate change: Marrying the signal from computer models and biological proxies. *The Micropaleontological Society, Special Publications*, **2**, 351-387.

Coxall, H.K., Wilson, P.A., Palike, H., Lear, C.H. and Backman, J. (2005) Rapid stepwise onset of Antarctic glaciation and deeper calcite compensation in the Pacific Ocean. *Nature*, **433**, 53-57.

Cramer, B.S., Wright, J.D., Kent, D.V. and Aubry, M.-P. (2003) Orbital climate forcing of δ13C excursions in the late Paleocene–early Eocene (chrons C24n-C25n). *Paleoceanography*, **18**, 21-1.

Cramer, B.S., Toggweiler, J.R., Wright, J.D., Katz, M.E., and Miller, K.G. (2009) Ocean overturning since the Late Cretaceous: Inferences from a new benthic foraminiferal isotope compilation. *Paleoceanography*, **24**, PA4216. DOI:10.1029/2008PA001683

Cronin, B.T., Owen, D., Hartley, A.J. and Kneller, B. (1998) Slumps, debris flows and sandy deep-water channel systems: implications for the application of sequence stratigraphy to deep water clastic sediments. *Journal of the Geological Society London*, **155**, 429-432.

Cronin, T.M. (2010) *Paleoclimates, understanding climate change past and present*, Columbia University Press, New York, 117.

Crowley, T. and Zachos, J.C. (2000) Comparison of zonal temperature profiles for past warm time periods. *In*: Huber, B.T., MacLeod, K.G. and Wing, S.L. (eds) *Warm Climates in Earth History*, Cambridge University Press, 50-76.

Cruz, F.W., Burns, S.J., Karmann, I., Sharp, W.D., Vuille, M., Cardoso, A.O., Ferrari, J.A., Silva Dias, P.L. and Vlana Jr. O. (2005) Insolation-driven changes in atmospheric circulation over the past 116,000 years in subtropical Brazil. *Nature*, **434**, 63-65.

Cuevas-Gonzalo, M.C. (1989). Sedimentary facies and sequential architecture of tide-influenced 656 alluvial deposits. An example from the middle Eocene Capella Formation, South-Central Pyrenees, Spain. PhD thesis, University of Utrecht.

Curray, J.R., Emmel, F.J. and Moore, D.G. (2002) The Bengal Fan: morphology, geometry, stratigraphy, history and processes. *Marine and Petroleum Geology*, **19**, 1191-1223.

Currie, R.G. and O'Brien, D.P. (1988) Periodic 18.6 year and cyclic 10 to 11 year signals in Northeastern United states precipitation data. *Journal of climatology*, **8**, 255-281.

D'Argenio, B.D., Fischer, A.G., Richter, G.M., Longo, G., Pelosi, N., Molisso, F. and Duarte Morias, M.L. (1998) Orbital cyclicity in the Eocene of Angola: visual and image-time-series analysis compared. *Earth and Planetary Science Letters*, **160**, 147-161.

Damuth, J.E., Flood, R.D., Kowsmann, R.O., Belderson, R.H. and Gorini, M.A. (1988) Anatomy and growth pattern of Amazon deep-sea fan as revealed by long-range side-scan sonar (GLORIA) and high-resolution seismic studies. *American Association of Petroleum Geologists Bulletin*, **72**, 885-911.

Das Gupta, K. and Pickering, K.T. (2008) Petrography and temporal changes in petrofacies of deep-marine Ainsa-Jaca basin sandstone systems, Early and Middle Eocene, Spanish Pyrenees. *Sedimentology*, **55**, 1083-1114.

Davies, R., Cartwright, J., Pike, J. and Line, C. (2001) Early Oligocene initiation of North Atlantic Deep Water formation. *Nature*, **410**, 917-920.

Davies, S.J. and Elliott, T. (1996) Spectral gamma ray characterization of high-resolution sequence stratigraphy: examples from Upper Carboniferous fluvio-deltaic systems, County Clare, Ireland. *In*: Howell, J.A. and Aitken, J.F. (eds) High-resolution sequence stratigraphy: innovations and applications. *Geological Society Special Publication*, **104**, 25-35.

Dawber, C.F. and Tripati, A.K. (2011) Constraints on glaciation in the middle Eocene (46-37Ma) from Ocean Drilling Program (ODP) Site 1209 in the tropical Pacific Ocean. *Paleoceanography*, **26**, PA 2208, DOI:10-1029/2010.

Dawber, C.F., Tripati, A.K., Gale, A.S., MacNiocaill, C. and Hesselbo, S.P. (2011) Glacioeustasy during the middle Eocene? Insights from the stratigraphy of the Hampshire basin, UK. *Palaeogeography, Palaeoclimatology, Palaeoecology*, **300**, 84-100.

De Boer, P.L. and Smith, D.G. (1994) Orbital forcing and cyclic sequences. *Special Publication of the International Association of Sedimentologists*, **19**, 1-14.

De Boer, P.L., Pragt, J.S.L. and Oost, A.P. (1991) Vertically persistent sedimentary facies boundaries along growth anticlines in the thrust-sheet-top South Pyrenean Tremp-Graus foreland basin. *Basin Research*, **3**, 63-78.

De Federico, A. (1981) La sedimentación de talud en el sector occidental de la cuenca paleógena de Aínsa. PhD Thesis. Universidad Autónoma de Barcelona, *Publicaciones de Geología*, **12**, 271-272.

DeConto, R.M. and Pollard, D. (2003) Rapid Cenozoic glaciation of Antarctica induced by declining atmospheric CO_2. *Nature*, **421**, 245-249.

Deconinck, J.-F., Hesselbo, S.P., Debuisser, N., Averbuch, O., Baudin, F. and Bessa, J. (2003) Environmental controls on clay mineralogy of an Early Jurassic mudrock (Blue Lias Formation, southern England). *International Journal of Earth Sciences*, **92**, 255-266.

Deer, W.A., Howie, R.A and Zussman, J. (1966) An introduction to the rock forming minerals: Volume 3, Sheet silicates. Longman, **3**, 270.

DeLong, K. L., Quinn, T.M., Mitchum, G.T. and Poore, R.Z. (2009) Evaluating highly resolved paleoclimate records in the frequency domain for multidecadal-scale climate variability. *Geophysical Research Letters*, **36**, L20702, doi:10.1029/2009GL.

Dennielou, B., Huchona, A., Beaudouinc, C. and Bernéa, S. (2006) Vertical grain-size variability within a turbidite levée: Autocyclicity or allocyclicity? A case study from the Rhône neofan, Gulf of Lions, Western Mediterranean. *Marine Geology*, **234**, 191-213.

Deptuck, M.E., Piper, D.J.W., Savoye, B. and Gervais, A. (2008) Dimensions and architecture of late Pleistocene submarine lobes off the northern margin of East Corsica. *Sedimentology*, **55**, 869-898.

Déramond, J., Souquet, P., Fondecave-Wallez, M.J. and Spetch, M. (1993) Relationships between thrust tectonics and sequence stratigraphy surfaces in foredeeps: model and examples from the Pyrenees (Cretaceous-Eocene, France, Spain. *In*: Williams, G.D. and Dobb, A. (eds) Tectonics and Seismic Sequence Stratigraphy. *Special Publication Geological Society London*, **71**, 193-219.

Dickens, G.R., O'Neil, J.R., Rea, D.K. and Owen, R.M. (1995) Dissociation of oceanic methane hydrate as a cause of the carbon isotope excursion at the end of the Paleocene. *Paleoceanography*, **10**, 965-971.

Diekmann, B., Kuhn, G., Gersonde, R. and Mackensen, A. (2004) Middle Eocene to Early Miocene environmental changes in the sub-Antarctic Southern Ocean: evidence from biogenic and terrigenous depositional patterns at ODP Site 1090. *Global and Planetary Change*, **40**, 295-313.

Diester-Haass, L. and Zahn, R. (1996) Eocene-Oligocene transition in the Southern Ocean: History of water mass circulation and biological productivity. *Geology*, **24**, 163-166.

Diester-Haass, L. and Zachos, J. (2003) The Eocene-Oligocene transition in the Equatorial Atlantic (ODP Site 925); paleoproductivity increase and positive delta (super 13) C excursion. *In*: Prothero, D.R., Ivany, L.C. and Nesbitt, E.A. (eds) *From greenhouse to icehouse*. Columbia University Press, New York.

Dinarés, J., McClelland, E. and Santanach, P. (1992) Contrasting rotations within thrust sheets and kinematics of thrust tectonics as derived from palaeomagnetic data: An example from the Southern Pyrenees. *In*: McClay, K.R. (ed) *Thrust tectonics*, Chapman and Hall, New York, 265-275.

Dixon, J.L. Hartshorn, A.S., Heimsath, A.M., DiBiase, R.A. and Whipple, K.X. (2012) Chemical weathering response to tectonic forcing: A soils perspective from the San Gabriel Mountains, California. *Earth and Planetary Science Letters*, **323-324**, 40-49.

Domingo, L., López-Martínez, N., Leng, M.J. and Grimes, S.T. (2009) The Paleocene-Eocene Thermal Maximum record in the organic matter of the Claret and Tendruy continental sections (South-central Pyrenees, Lleida, Spain). *Earth and Planetary Science Letters*, **281**, 226-237.

Dreyer, T., Corregidor, J., Arbués, P and Puigdefábregas, C. (1999) Architecture of the tectonically influenced Sobrarbe deltaic complex in the Ainsa Basin, northern Spain. *Sedimentary Geology*, **127**, 127-169.

Ducassou, E., Migeon, S., Mulder, T., Murat, A., Capotondi, L., Bernasconi, S.M. and Mascle, J. (2009) Evolution of the Nile deep-sea turbidite system during the Late Quaternary; influence of climate change on fan sedimentation. *Sedimentology*, **56**, 2061-2090.

Dunkley Jones, T., Bown, P.R., Pearson, N., Wade, B.S., Coxall, H.K. and Lear, C.H. (2008) Major shifts in calcareous phytoplankton assemblages through the Eocene-Oligocene transition of Tanzania and their implications for low-latitude primary production. *Paleoceanography*, **23**, PA4204, DOI:10.1029/2008PA001640.

Dunne, L.A. and Hempton, M.R. (1984) Deltaic sedimentation in the Lake Hazar pull-apart basin, southeastern Turkey. *Sedimentology*, **31**, 401-412.

Dwyer, G.S., Cronin, T.M., Baker, P.A., Raymo, M.E., Buzas, J.S. and Correge, T. (1995) North Atlantic deepwater temperature change during late Pliocene and late Quaternary climatic cycles. *Science*, **270**, 1347-1351.

Dypvik, H. and Harris, N.B. (2001) Geochemical facies analysis of fine-grained siliciclastics using Th-U, Zr-Rb and (Zr + Rb)/Sr ratios. *Chemical Geology*, **181**, 131-146.

Edgar, K.M., Wilson, P.A., Sexton, P.S. and Suganuma, Y. (2007) No extreme bipolar glaciation during the main Eocene calcite compensation shift. *Nature*, **448**, 908-911.

Ekdale, A.A. (1985) Paleoecology of the marine endobenthos. *Palaeogeography, Palaeoclimatology, Palaeoecology*, **50**, 63-81.

Ekdale, A.A. and Lewis, D.W. (1991) Trace fossils and paleoenvironmental control of ichnofacies in a late quaternary gravel and loess fan delta complex, New Zealand. *Palaeogeography, Palaeoclimatology, Palaeoecology*, **81**, 253-279.

Eldrett, J.S., Harding, I.C., Wilson, P.A., Butler, E. and Roberts, A.P. (2007) Continental ice in Greenland during the Eocene and Oligocene. *Nature*, **446**, 176-179.

Evans, N.G., Gleizes, G., LeBlanc, D. and Bouchez, J.L. (1998) Syntectonic emplacement of the Maladeta granite (Pyrenees) deduced from relationships between Hercynian deformation and contact metamorphism. *Journal of the Geological Society London*, **155**, 209-216.

Evans, R., Mory, A.J., Tait, A.M. (2007) An outcrop gamma ray study of the Tumblagooda sandstone, Western Australia. *Journal of Petroleum Science and Engineering*, **57**, 37-59.

Exon, N.F., Kennet, J.P. and Malone, M.J. (2004) Leg 189 synthesis: Cretaceous-Holocene history of the Tasmanian gateway: Cenozoic climate and oceanographic development, Sites 1168 and 1172. *In*: Exon, N.F., Kennet, J.P. and Malone, M.J. (eds) *Proceedings of the Ocean drilling Program, Scientific results*, College Station, Texas, Ocean Drilling Program, **189**, 1-37.

Fabricius, I.L., Fazladic, L.D., Steinholm, A. and Korsbech, U. (2003) The use of spectral natural gamma-ray analysis in reservoir evaluation of siliciclastic sediments: a case study from the Middle Jurassic of the Harald Field, Danish Central Graben. *Geological Survey of Denmark and Greenland Bulletin*, **1**, 349-366.

Fahl, K. and Stein, R. (1997) Modern organic carbon deposition in the Laptev Sea and the adjacent continental slope: surface water productivity versus terrigenous input. *Organic Geochemistry*, **26**, 379-390.

Fairbanks, R.G. and Matthews, R.K. (1978) The marine oxygen isotopic record in Pleistocene coral, Barbados, West Indies. *Quaternary Research*, **10**, 181-196.

Falivene, O., Arbués, P., Gardiner, A., Pickup, G., Muñoz, J.A. and Cabrera, L. (2006) Best practice stochastic facies modelling from a channel- fill turbidite sandstone analog (the Quarry outcrop, Eocene Ainsa Basin, northeast Spain). *American Association of Petroleum Geologists Bulletin*, **90**, 1003-1029.

Falivene, O., Arbués, J., Ledo, J., Benjumea, B., Muñoz, J.A., Fernández, O. and Martínez, S. (2010) Synthetic seismic models from outcrop-derived reservoir-scale three-dimensional facies models: The Eocene Ainsa turbidite system (southern Pyrenees). *American Association of Petroleum Geologists Bulletin*, **94**, 317-343.

Farge, M. (1992) Wavelet transforms and their applications to turbulence. *Annual Review of Fluid Mechanics*, **24**, 395-457.

Farrell, S.G., Williams, G.D. and Atkinson, C.D. (1987) Constraints on the age of movement of the Montsec and Cotiella thrusts, south central Pyrenees, Spain. *Journal of the Geological Society of London*, **144**, 907-914.

Feeley, M.H., Moore Jr.T.C., Loutit, T.S. and Bryant, W.R. (1990) Sequence stratigraphy of Mississippi Fan related to oxygen isotope sea level index. *American Association of Petroleum Geologists Bulletin*, **74**, 407-424.

Feng, R. and Kerrich, R. (1990) Geochemistry of fine-grained clastic sediments in the Archaean Abitibi greenstone belt, Canada: Implications for provenance and tectonic setting. *Geochimica and Cosmochimica Acta*, **54**, 1061-1081.

Fernández, O., Muñoz, J.A., Arbués, P., Falivene, O. and Marzo, M. (2004) 3-D reconstruction of geological surfaces: an example of growth strata and turbidite systems from the Ainsa basin (Pyrenees, Spain). *American Association of Petroleum Geologists Bulletin*, **88**, 1049-1068.

Fernández, O., Muñoz, J.A., Arbués, P. and Falivene, O. (2012) 3D structure and evolution of an oblique system of relaying folds: the Ainsa basin (Spanish Pyrenees). *Journal of the Geological Society London*, **169**, 545-559.

Fischer, A.G., Helbert, T.D., Napoleone, G., Premoli Silva, I. and Ripepe, R. (1991) Albian pelagic rhythms (Piobbico core). *Journal of Sedimentary Petrology*, **62**, 1146-1172.

Fisher, A.T and Underwood, M.B. (1995) Calibration of an X-ray diffraction method to determine relative mineral abundances in bulk powders using matrix singular value decomposition: a test from the Barbados accretionary complex. *In*: Shipley, T.H., Ogawa, Y. and Blum, P. (eds) *Proceedings of the Ocean Drilling Program, Initial Reports*, **156**, 29-37. Texas, College Station: Ocean Drilling Program.

Fitzgerald, P.G., Muñoz, J.A., Coney, P.J. and Baldwin, S.L. (1999) Asymmetric exhumation across the Pyrenean orogen: implications for the tectonic evolution of a collisional orogen. *Earth and Planetary Science Letters*, **173**, 157-170.

Flood, R.D., Manley, P.L., Kowsmann, R.O., Appi, C.J. and Pirmez, C. (1991) Seismic facies and late Quaternary growth of Amazon submarine fan. *In*: Weimer, P. and Link, M.H. (eds) *Seismic facies and sedimentary processes of modern and ancient submarine fans,* New York, Springer-Verlag, 415-433.

Force, E.R. (1976) Titanium contents and titanium partitioning rocks. *Geological Survey Professional Paper* 959, A1. U.S. Government Printing Office.

Foucault, A., Powichrowski, L. and Prud'homme, A. (1987) Le contrôle astronomique de la sédimentation turbiditique: example du Flysch á Helminthoides des Alpes Ligures (Italie). *Comptes Rendus de l'Académie des sciences*, Paris, **305**, 1007-1011.

Francis, J.E. (1999) Evidence from fossil plants for Antarctica paleoclimates over the past 100 million years. *Terra Antartica*, **3**, 43-52.

Frostick, L. and Reid, I. (1989) Is structure the main control of river drainage and sedimentation in rifts? *Journal of African Earth Sciences*, **8**, 165-182.

Fulthorpe, C.S. (1991) Geological controls on seismic sequence resolution. *Geology*, **19**, 61-65.

Gale, A.S., Young, J.R., Shackleton, N.J., Crowhurst, S.J. and Wray, D.S. (1999) Orbital tuning of Cenomanian marly chalk successions: towards a Milankovitch time-scale for the Late Cretaceous. *Philosophical transactions of the Royal Society of London*, **357**, 1815-1829.

Galeotti, S., Krishnan, S., Pagani, M., Lanci, L., Gaudio, A., Zachos, J.C., Monechi, S., Morelli, G. and Lourens, L. (2010) Orbital chronology of Early Eocene hyperthermals from the Contessa Road section, central Italy. *Earth and Planetary Science Letters*, **290**, 192-200.

Ganopolski, A. and Calov, R. (2011) The role of orbital forcing, carbon dioxide and regolith in 100kyr glacial cycles. *Climates of the Past*, **7**, 1415-1425.

Ganti, V., Straub, K.M., Foufoula-Georgiou, E. and Paola, C. (2011) Space-time dynamics of depositional systems: Experimental evidence and theoretical modeling of heavy-tailed statistics. *Journal of Geophysical Research*, **116**, 2156-2202. DOI:10.1029/2010JF001893.

Garrido-Megías, A. (1968) Sobre la estratigrafía de los conglomerados de Campanué (Santa Liestra) y formaciones superiors del Eoceno (extreme oriental de la Cuenca Tremp-Graus, Pirineo Central, provincial de Huesca. *Acta Geológica Hispánica*, **3**, 39-43.

Gaspar-Escribano, J.M., van Wees, J.D., ter Voorde, M., Cloetingh, S., Roca, E. and Cabrera, L. (2001) Three-dimensional flexural modelling of the Ebro Basin (NE Iberia). *Geophysical Journal International*, **145**, 349-367.

Gee, J.S. and Kent, D.V. (2007) Source of oceanic magnetic anomalies and the geomagnetic polarity time scale. *Treatise on Geophysics*, **5**, 455-507.

George, G.T. (2000) Characterisation and high resolution sequence stratigraphy of storm-dominated braid delta and shoreface sequences from the Basal Grit Group (Namurian) of the South Wales Variscan peripheral foreland basin. *Marine and Petroleum Geology*, **17**, 445-475.

Ghasemi-Nejad, E., Ardakani, E.P. and Ruffell, A. (2010) Palaeoclimate change recorded in Upper Cretaceous (Albian-Cenomanian) Kazhdumi Formation borehole spectral gamma-ray logs, South Pars gas field, Persian Gulf. *Palaeogeography, Palaeoclimatology, Palaeoecology*, **291**, 338-347.

Ghil, M., Allen, M.R., Dettinger, M.D., Ide, K., Kondrashov, D., Mann, M.E., Robertson, A.W. Saunders, A. Tian, Y. Varadi, F. and Yiou, P. (2002) Advanced spectral methods for climatic time-series. *Reviews of Geophysics*, **40**, 1-41.

Gildor, H. and Tziperman, E. (2001) A sea ice climate switch mechanism for the 100-kyr glacial cycles. *Journal of Geophysical Research*, **106**, 9117-9133.

Goldfinger, C., Nelson, C.H. and Johnson, J. (2003) Holocene earthquake records from the Cascadia subduction zone and northern San Andreas Fault based on precise dating of offshore turbidites. *Annual Reviews of Geophysics*, **31**, 555-577.

Goldfinger, C., Morey, A., Nelson, C.H., Gutierrez-Pastor, J., Johnson, J.E., Karabanov, E., Chaytor, J. and the Shipboard Scientific Party (2007) Rupture lengths and temporal history of significant earthquakes on the offshore and north coast segments of the northern San Andreas. *Earth Planetary Science Letters*, **254**, 9-27.

Goldhaber, M.B. and Kaplan, I.R. (1974) The sulfur cycle. *In*: Goldberd, E.D. (ed), *The Sea*. Wiley, New York, 604 pp.

Gómez-Paccard, M., López-Blanco, M, Costa, E., Garcés, M., Beamud, E. and Larrasoaña, J.C. (2011) Tectonic and climatic controls on the sequential arrangement of an alluvial fan/fan-delta complex (Montserrat, Eocene, Ebro basin, NE Spain). *Basin Research*, **24**, 437-455.

Grabowski, J., Schnyder, J., Sobién, K., Koptíková, L.,Krzeminski, L., Pszczó1kowski, A. and Hejnar, J. (2013) Magnetic susceptibility and spectral gamma logs in the Tithonian- Berriasian pelagic carbonates in the Tatra Mts (Western Carpathians, Poland): Palaeoenvironmental changes at the Jurassic/Cretaceous boundary. *Cretaceous Research*, **43**, 1-17.

Gradstein, F.M., Ogg, J.G., Smith, A.G., Agterberg, F.P., Bleeker, W., Cooper, R.A., Davydov, V., Gibbard, P., Hinnov, L.A., House, M.R., Lourens, L., Luterbacher, H.-P. McArthur, J., Melchin, M.J., Robb, L.J., Sadler, P.M., Shergold, J., Villeneuve, M., Wardlaw, B.R., Ali, J., Brinkhuis, H., Hilgen, F.J., Hooker, J., Howarth, R.J., Knoll, A.H., Laskar, J., Monechi, S., Powell, J., Plumb, K.A., Raffi, I., Röhl, U., Sanfilippo, A., Schmitz, B., Shackleton, N.J., Shields, G.A., Strauss, H., Van Dam, J., Veizer, J., Van Kolfschoten, T.H. and Wilson, D. (2004) *Geologic Time Scale 2004*. Cambridge University Press.

Gradstein, F.M., Ogg, J.G. and Schmitz, M. (2012) The Geological Time scale 2012. Elsevier Science & Technology Books, Amsterdam.

Graham, S.A. Romans, B.W. and Covault, J.A. (2011) Source-to-sink in the stratigraphic record: Capturing the long-term, deep-time evolution of sedimentary systems. *AGU Chapman Conference Program*, 32-33.

Greenwood, D.R. and Wing, S.L. (1995) Eocene continental climates and latitudinal temperature gradients. *Geology*, **23**, 1044-1048.

Gubbins, D. (1999) The distinction between geomagnetic excursions and reversals. *Geophysical Journal International*, **131**, F1-F4.

Guillocheau, F. (2010) Control of alluvial sedimentation at foreland-basin active margins: A case study from the northeastern Ebro basin (southeastern Pyrenees, Spain). *Journal of Sedimentary Research*, **80**, 728-749.

Gunn, P.J., Minty, B.R.S. and Milligan, P.R. (1997) The airborne gamma-ray spectrometric response over arid Australian terranes. *In*: Gubins, A.G. (ed) Proceedings of Exploration 97. *Fourth Decennial International Conference on Mineral Exploration*, 733-740.

Hall, C.A. and Bennet, V.C. (1979) Significance of lzerzolite at the Etang de Lhers, Central Pyrenees, Southern France. *Earth and Planetary Science Letters*, **45**, 349-354.

Hansen, T.A., Kelley, P.H. and Haasl, D.M. (2004) Paleoecological patterns in molluscan extinctions and recoveries: comparison of the Cretaceous-Paleogene and Eocene-Oligocene extinctions in North America. *Palaeogeography, Palaeoclimatology, Palaeoecology*, **214**, 233-242.

Haq, B.U., Hardenbol, J. and Vail, P.R. (1987) Chronology of fluctuating sea levels since the Triassic (250 million years ago to present). *Science*, **235**, 1156-1167.

Hartmann, L.D., Ockert-Bell, M.E. and Michelsen, M.L. (1992) The effect of cloud type on Earth's energy balance: Global analysis. *Journal of Climate*, **5**, 1281-1304.

Haseldonckx, P. (1972) The presence of Nypa palms in Europe: a solved problem. *Geologie en Mijnbouw*, **51**, 645-650.

Haseldonckx, P. (1973) The palynology of some Palaeogene deposits between the Rio Esera and the Rio Segre, Southern Pyrenees, Spain. *Leidse Geologische Mededelingen*, **49**, 145-165.

Hay, W.W., DeConto, R., Wold, C.N., Wilson, K.M., Voigt, S., Schulz, M., Wold-Rossby, Dullo, W.C., Ronv, A.B., Baluukhovsky, A.N. and Soeding, E. (1999) Alternative global Cretaceous paleogeography. *In*: Barrera, E. and Johnson, C. (eds) The evolution of Cretaceous ocean/climate Systems, *Geological Society of America Special Paper*, **332**, 1-47.

Hayes, J.M., Popp, B.N., Takigiku, R. and Johnson, M.W. (1989) An isotopic study of the biochemical relationships between carbonates and organic carbon in the Greenhorn Formation. *Geochimica and Cosmochimica Acta*, **53**, 2961-2972.

Hays, J.D., Imbrie, I. and Shackleton, N.J. (1976) Variations in the Earth's orbit: pacemaker of the ice ages. *Science*, **194**, 1121-1132.

Heard, T.G. (2007) Ichnology and sedimentology of deep-marine clastic systems, Middle Eocene, Ainsa-Jaca basin, Spanish Pyrenees. University College London, PhD thesis.

Heard, T. and Pickering, K.T. (2008) Trace fossils as diagnostic indicators of deep-marine environments, Middle Eocene Ainsa-Jaca basin, Spanish Pyrenees. *Sedimentology*, **55**, 809-844.

Heard, T., Pickering, K.T. and Robinson, S.A. (2008) Milankovitch forcing of bioturbation intensity in deep-marine thin-bedded siliciclastic turbidites. *Earth and Planetary Science Letters*, **272**, 130-138.

Heard, T.G., Pickering, K.T. and Clark, J.D. (2014) Ichnofabric characterization of a deep-marine clastic system: a subsurface study of the Middle Eocene Ainsa System, Spanish Pyrenees. *Sedimentology*, *in press*.

Heller, P.L. and Frost, C.D. (1988) Isotopic provenance of clastic deposits. *In*: Klein-Spehn, K.L. and Paola, C. (eds), *New perspectives in basin analysis*, 27-42. New York, Springer-Verlag.

Herbert, A.G. and Fischer, A.G. (1986) Milankovitch climatic origin of mid-Cretaceous black shale rhythms in central Italy. *Nature*, **321**, 739-743.

Herbert, T.D. (1994) Reading orbital signals distorted by sedimentation: models and examples. *In*: de Boer P.L. and Smith, D.G. (eds) Orbital forcing and cyclic sequences. *International Association of Sedimentologists, Special Publications*, **19**, 438-507.

Hilgen, F.J., Lourens, L.J., Berger, A. and Loutre, M.F. (1993) Evaluation of the astronomically calibrated time-scale for the late Pliocene and earliest Pleistocene, *Paleoceanography*, **8**, 549-565.

Hodell, H., Crowhurst, S., Skinner, L., Tzedakis, P.C., Margari, V., Channell, J.E.T., Kamenov, G., Maclachlan, S. and Rothwell, G. (2013) Response of Iberian Margin sediments to orbital and suborbital forcing over the past 420 ka. *Paleoceanography*, **28**, 185-199. DOI:10.1002/palo.20017.

Hoffman, M., Bouroullec, R., Guzofski, C., Pyles, D., Clark, J., Setiawan, P., Moody, J., Silalahi, H. and Moss-Russell, A. (2009) Constraints on the timing of growth structures in a deepwater basin: Insights from stratigraphic growth indicators and three-dimensional structural modeling, Ainsa Basin, Spanish Pyrenees: AAPG Annual Meeting. *AAPG Annual Convention*, Denver Colorado, June 7-10, 2009.

Hofmann, C.C., Mohamed, O. and Egger, H. (2011) A new terrestrial palynoflora from the Palaeocene/Eocene boundary in the northwestern Tethyan realm (St. Pankraz, Austria). *Review of Palaeobotany and Palynology*, **166**, 295-310.

Holbrook, J.M., Willis, B.J. and Bhattacharya, J. (2003) The evolution of allocyclicity and autocyclicity as sedimentary concepts. *AAPG Annual Meeting*, Salt Lake City, Utah.

Holl, J.E. and Anastasio, D.J. (1993) Paleomagnetically derived folding rates, southern Pyrenees, Spain. *Geology*, **21**, 271-274.

Hooker, J.J., Collinson, M.E. and Sille, N.P. (2004) Eocene-Oligocene mammalian faunal turnover in the Hampshire Basin, UK; calibration to the global time scale and the global major event. *Journal of the Geological Society of London*, **161**, 161-172.

Huber, M. and Nof, D. (2006) The ocean circulation in the Southern Hemisphere and its climatic impacts in the Eocene. *Palaeogeography, Palaeoclimatology, Palaeoecology*, **231**, 9-28.

Huber, M., Brinkhuis, H., Stickley, C.E., Döös, K., Sluijs, A., Warnaar, J., Schellenberg, S.A. and Williams, G.L. (2004) Eocene circulation of the Southern Ocean: Was Antarctica kept warm by subtropical waters? *Paleoceanography*, **19**, PA4026, DOI:10.1029/2004PA001014.

Humphrey, J. and Bowen, M. (1982) Environmental chemistry. *Royal Society of Chemistry*, Cambridge, **2**, 108 pp.

Hurst, A. (1990) Natural gamma-ray spectrometry in hydrocarbon-bearing sandstones from the Norwegian continental shelf. *In*: Hurst, A., Lovell, M. and Morton, A. (eds) Geological Applications of Wireline Logs. *Geology Society London Special Publication*, **48**, 211-222.

Huss, M. and Farinotti, D. (2012) Distributed ice thicknesses and volume of all glaciers around the globe. *Journal of Geophysical Research*, **117**, 1-10.

Husson, D., Thibault, N., Galbrun, B., Gardin, S., Minoletti, F., Sageman, B. and Huret, E. (2014) Lower Maastrichtian cyclostratigraphy of the Bidart section (Basque

country, SW France): A remarkable record of precessional forcing. *Palaeogeography Palaeoclimatology Palaeoecology*, **395**, 176-197.

Huyghe, D., Castelltort, S., Mouthereau, F., Serra-Kiel, J., Filleaudeau, P., Emmanuel, L., Berthier, B. and Renard, M. (2012) Large scale facies change in the middle Eocene South-Pyrenean foreland basin: The role of tectonics and prelude to Cenozoic ice-ages. *Sedimentary Geology*, **253-254**, 25-46.

Huybers, P. (2007) Glacial variability over the last 2 million years: An extended depth-derived agemodel, continuous, obliquity pacing, and the Pleistocene progression. *Quaternary Science* reviews, **26**, 37-55.

Huybers, P. (2011) Combined obliquity and precession pacing of late Pleistocene deglaciations. *Nature*, **480**, 229-232.

Huybers, P. and Wunsch, C. (2005) Obliquity pacing of the late Pleistocene glacial terminations. *Nature*, **434**, 491-494.

Huybers, P. and Aharonson, O. (2010) Orbital tuning, eccentricity, and the frequency modulation of climatic precession. *Paleocenography*, **25**, DOI: 10.1029/2010PA001952.

IAEA (2003) Guidelines for radioelement mapping using gamma ray spectrometry data, International Atomic Energy Agency, Viena, Austria, 1-179.

Imbrie, J., Berger, A., Boyle, E.A., Clemens, S.C., Duffy, A., Howard, W.R., Kukla, G., Kutzbach, J., Martinson, D.G., Mcintyre, A., Mix, A.C., Molfino, B., Morley, J.J., Peterson, L.C., Pisias, N.G., Prell, W.L., Raymo, M.E., Shackleton, N.J. and Toggweiler, J.R. (1993) On the structure and origin of major glaciation cycles 2. The 100,000-year cycle. *Paleoceanography*, **8**, 699-735.

Imbrie, J. and Imbrie, K.P. (1979) Ice Ages. Solving the mistery. *Harvard University Press*, Cambridge, Massachusets, 1-224.

Imbrie, J., Hays, J.D., Martinson, D.G., McIntyre, A., Morley, J.J., Pisias, N.G., Prell, W.L. and Shackleton, N.J. (1984) The orbital theory of Pleistocene climate: support from a revised chronology of the marine $\delta^{18}O$ record. *In*: Berger, A.L., Imbrie, J., Hays, J., Kukla, G. and Saltzman, B. (eds) *Milankovitch and climate, Part 1*. D Reidel, Hinham, MA, USA, 269-305.

Imbrie, J., Boyle, E.A., Clemens, S.C., Duffy, A., Howard, W.R., Kukla, G., Kutzbach, J., Martinson, D.G., McIntyre, A., Mix, A.C., Molfino, B., Morley, J.J., Peterson, L.C., Pisias, N.G., Prell, W.L., Raymo, M.E., Shacketon, N.J. and Toggweiler, J.R. (1992) On the structure of major glaciation cycles. *Palaeoceanography*, **7**, 701-738.

Jacobs, D.K. and Sahagian, D.L. (1993) Climate-induced fluctuations in sea level during non-glacial times. *Nature*, **361**, 710-712.

Jacobson, A.D., Blum, J.D., Chamberlain, C.P., Craw, D. and Koons, P.O. (2003) Climatic and tectonic controls on chemical weathering in the New Zealand Southern Alps. *Geochimica and Cosmochimica Acta*, **67**, 29-46.

Jammes, S., Lavier, L. and Manatschal, G. (2010) Extreme crustal thinning in the Bay of Biscay and the Western Pyrenees: from observations to modelling. *Geochemistry Geophysics Geosystems*, **11**, Q10016.

Jaramillo, C., Rueda, M.J. and Mora, G. (2006) Cenozoic plant diversity in the Neotropics. *Science*, **311**, 1893-1896.

Jerolmack, D.J. and Paola, C. (2010). Shredding of environmental signals by sediment transport. *Geophysical Research Letters*, **37**, DOI: 10.1029/2010GL044638.

Jicha, B.R., Scholl, D.W. and Rea, D.K. (2009) Circum-Pacific arc flare-ups and global cooling near the Eocene-Oligocene boundary. *Geology*, **37**, 303-306.

Johansen, K.Ø. (2014) Magnetostratigraphy of the Ainsa Basin, NE Pyrenees. MSc Thesis, Oxford University.

Johnson, L.J., Chu, C.H and Hussey, G.A. (1985) Quantitative clay mineral analysis using simultaneous linear equations. *Clays and Clay Minerals*, **33**,107-117.

Jones, B. and Manning, D.A.C. (1994) Comparison of geochemical indices used for the interpretation of paleoredox conditions in ancient mudstone. *Chemical Geology*, **111**, 111-129.

Jones, R.W., Pickering, K.T., Boudagher-Fadel, M. and Matthews, S. (2005) Preliminary observations on the micropalaeontological characterization of submarine fan/channel sub-environments, Ainsa System, south-central Pyrenees, Spain. *In*: Powell, A.J. and Riding, J.B. (eds) *Recent Developments in Applied Biostratigraphy*. The Micropalaeontological Society, London.

Jorry, S.J., Droxler, A.W., Mallarino, G., Dickens, G.R., Bentley, S.J., Beaufort, L., Peterson, L.C. and Opdyke, B.N. (2008) Bundled turbidite deposition in the central Pandora Trough (Gulf of Papua) since Last Glacial Maximum: Linking sediment nature and accumulation to sea level fluctuations a millennial timescale. *Journal of Geophysical Research*, **113**, F01S19, doi:10.1029/2006JF000649.

Jorry, S.J., Jégou, I., Emmanuel, L., Silva Jacinto, R. and Savoye, B. (2011) Turbiditic levée deposition in response to climate changes: The Var Sedimentary Ridge (Ligurian Sea). *Marine Geology*, **279**, 148-161.

Kane, I.A. and Hodgson, D.M. (2011) Sedimentological criteria to differentiate submarine channel levée subenvironments: exhumed examples from the Rosario Fm. (Upper Cretaceous) of Baja California, Mexico, and the Fort Brown Fm. (Permian), Karoo Basin, S. Africa. *Marine and Petroleum Geology*, **28**, 807-823.

Karner, D., Levine, J., Medeiros, B. and Muller, R. (2002) Constructing a stacked benthic $\delta^{18}O$ record. *Paleoceanography*, **17**, DOI: 10.1029/2001PA000667.

Katz, M.E., Miller, K.G., Wright, J.D., Wade, B.S., Browning, J.V., Cramer, B.S. and Rosenthal, Y. (2008) Stepwise transition from the Eocene greenhouse to the Oligocene icehouse. *Nature Geoscience*, **1**, 329-334.

Keller, G., MacLeod, N. and Barrera, E. (1992) Eocene-Oligocene faunal turnover in planktic foraminifera, and Antarctic glaciation. *In*: Prothero, D. and Berggren, W.A. (eds) *The Eocene-Oligocene Climatic and biotic evolution*, Princeton, New Jersey, Princeton University Press, 218-244.

Kennett, J.P. (1977) Cenozoic evolution of Antarctic glaciation, the circum-Antarctic ocean, and their impact on global palaeoceanography. *Journal of Geophysical Research*, **82**, 3843-3860.

Kennett, J.P. and Shackleton, N.J. (1976) Oxygen isotopic evidence for the development of the psychrosphere 38 Myr ago. *Nature*, **260**, 513-515.

Kennett, J.P. and Exon, N.F. (2004) Paleoceanographic evolution of the Tasmanian Seaway and its climatic implications. *In*: Exon, N.F., Kennett, J.P. and Malone, M.J. (eds) The Cenozoic Southern Ocean: Tectonics, sedimentation, and climate change between Australia and Antarctica. *Geophysical Monograph*, **151**. American Geophysical Union, 345-367.

Kenyon, N.H., Amir, A. and Cramp, A. (1995) Geometry of the younger sediment bodies of the Indus Fan. *In*: Pickering, K.T., Hiscott, R.N., Kenyon, N.H., Ricci Lucchi, F. and Smith, R.D.A. (eds) *Atlas of Deep Water Environments: Architectural Style in Turbidite Systems*, Chapman & Hall, London, 89-93.

Kerrick, D.M. and Caldeira, K. (1998) Metamorphic CO_2 degassing from orogenic belts. *Chemical Geology*, **145**, 213-232.

Killeen, P.G. (1979) Gamma-ray spectrometric methods in uranium exploration-application and interpretation. *In*: Hood, P.J. (ed) Geophysics and geochemistry in search for metallic ores. *Geological Survey of Canada, Economic Geology Report*, **31**, 163-230.

Kneller, B. and Buckee, C. (2000) The structure and fluid mechanics of turbidity currents: a review of some recent studies and their geological implications. *Sedimentology*, **47**, 62-94.

Knobloch, E., Kvaček, Z., Bůžek, C., Mai, D.H. and Batten, D.J. (1993). Evolutionary significance of floristic changes in the Northern Hemisphere during the Late Cretaceous and Palaeogene, with particular reference to Central Europe. *Review Palaeobotany Palynology*, **78**, 41-54.

Kolla, V. and Coumes, F. (1987) Morphology, internal structure, seismic stratigraphy, and sedimentation on the Indus Fan. *American Association of Petroleum Geologists Bulletin*, **71**, 650-677.

Kolla, V. and Macurda Jr., D.B. (1988) Sea-level changes and timing of turbidity-current events in deep-sea fan systems. *In*: Wilgus, C.K., Hastings, B.K., Posamentier, H., Van Wagoner, J., Ross, C.A. and Kendall, C.G.St.C. (eds) Sea-level changes: An Integrated Approach. *Society of Economic Palaeontologists and Mineralogists Special Publication*, **42**, 381-392.

Kolla, V. and Perlmutter, M.A. (1993) Timing of turbidite sedimentation on the Mississippi Fan. *American Association of Petroleum Geologists Bulletin*, **77**, 1129-1141.

Kominz, M.A. and Pekar, S.F. (2001) Oligocene eustasy from two-dimensional sequence stratigraphy backstripping. *Geological society of America Bulletin*, **113**, 291-304.

Kominz, M.A., Miller, K.G. and Browning, J.V. (1998) Long-term and short-term global Cenozoic sea-level estimates. *Geology*, **26**, 311-314.

Kominz, M.A., Borwing, J.V., Miller, K.G., Sugarman, P.J., Mizintseva, S. and Scotese, C.R. (2008) Late Cretaceous to Miocene sea-level estimates from the New Jersey and Delaware coastal plain coreholes: an error analysis. *Basin Research*, **20**, 211-226.

Kostaschuk, R., Terry, J. and Raj, R. (2002) Suspended sediment transport during tropical floods in Fiji. *Hydrological Processes*, **17**, 1149-1164.

Koulakov, I., Kaban, M.K., Tesauro, M. and Cloetingh, S. (2009) P and S velocity anomalies in the upper mantle beneath Europe from tomographic inversion of ISC data. *Geophysical Journal International*, **179**, 345-366.

Kuehl, S.A., Hariu, T.M. and Moore, W.S. (1989) Shelf sedimentation off the Ganges-Brahmaputra river system: Evidence for sediment bypassing to the Bengal fan. *Geology*, **17**, 1132-1135.

Kumar, P. and Foufoula-Georgiou, E. (1997) Wavelet analysis for geophysical application. *Reviews of Geophysics*, **35**, 385-412.

Kutzbach, E.G. and Otto-Bliesner, B.L. (1982) The sensitivity of the African-Asian monsoonal climate to orbital parameters changes for 9000 years BP in a low-resolution general circulation model. *Journal of Atmospheric Science*, **39**, 1177-1188.

Kutzbach, J.E. (1981) Monsoon climate of the early Holocene: climate experiment with the Earth's orbital parameters for 9000 years ago. *Science*, **214**, 59-61.

Labaume, P., Séguret, M. and Seyve, C. (1985) Evolution of a turbiditic foreland basin and analogy with an accretionary prism: Example of the Eocene South-Pyrenean basin. *Tectonics*, **4**, 661-685.

Labourdette, R., Cremeyrolle, P. and Remacha, E. (2008) Characterization of dynamic flow patterns in turbidite reservoirs using 3D outcrops analogues: Example of the Eocene Morillo turbidite system (south-central Pyrenees, Spain). *Marine and Petroleum Geology*, **25**, 255-270.

Lancien, P., Metivier, F., Lajeunesse, E and Cacas, M. (2004) Simulating submarine channels in flume experiments: aspects of the channel incision dynamic. *American Geophysical Union Fall Meeting, San Francisco*, Abstract #OS41D-0509.

Langmuir, Y. and Herman, J.S. (1980) The mobility of thorium in natural waters at low temperatures. *Geochimica and Cosmochimica Acta*, **44**, 1753-1766.

Larsen, V. and Steel, R.J. (1978) The sedimentary history of a debris-flow dominated Devonian alluvial fan - a study of textural inversion. *Sedimentology*, **25**, 37-59.

Laskar, J. (1994). Large scale chaos in the Solar system. *Astronomy and Astrophysics*, **287**, L9-L12.

Laskar, J., Joutel, F. and Boudin, F. (1993) Orbital, precessional, and insolation quantities for the Earth from -20Myr to +10Myr. *Astronomy and Astrophysics*, **270**, 522-533.

Laskar, J., Robutel, P., Joutel, F., Gastineau, M., Correia, A.C.M., Levrard, B. (2004) A long term numerical solution for the insolation quantities of the Earth. *Astronomy and Astrophysics*, **428**, 261-285.

Laskar, J., Fiengal, A., Gastineau, M. and Manche, H. (2011) La2010: a new orbital solution for the long-term motion of the Earth. *Astronomy and Astrophysics*, **532**, A89, 1-15. DOI: 10.1051/0004-6361/201116836.

Lau, K.,-M. and Weng, H. (1995) Climate-signal detection using wavelet transform: how to make a time-series sing. *Bulletin of the American Meteorological Society*, **76**, 2391-2402.

Laurent, R. and Cai, X. (2007). A maximum entropy method for combining AOGCMS for regional intra-year climate change assessment. *Climatic change*, **82**, 411-435.

Lawrence, K.T., Sloan, L.C. and Sewall, J.O. (2003) Terrestrial climatic response to precessional orbital forcing in the Eocene. *In*: Wing, S.L., Gingerich, Ph.D., Schmitz, B., and Thomas, E. (eds) Causes and Consequences of globally warm climates in the Early Paleogene: Boulder, CO. *Geological Society of America Special Paper*, **369**, 65-77.

Lawrence, K.T., Sosdian, S., White, H.E. and Rosenthal, Y. (2010) North Atlantic climate evolution through the Plio-Pleistocene climate transitions. *Earth and Planetary Science Letters*, **300**, 329-342.

Lawver, L.A. and Gahagan, L.M. (2003) Evolution of Cenozoic seaways in the circum-Antarctic region. *Palaeogeography, Palaeoclimatology, Palaeoecology*, **198**, 11-37.

Le Pichon, X., Bergerat, F. and Roulet, M.J. (1988) Plate kinematics and tectonics leading to the Alpine belt formation: A new analysis. *Geological Society of America, Special Paper*, **218**, 111-131.

Lear, C.H., Elderfield, H. and Wilson, P.A. (2000) Cenozoic deep-sea temperature and global ice volumes from Mg/Ca in benthic foraminiferal calcite. *Science*, **287**, 269-272.

Lear, C.H., Bailey, T.R., Pearson, P.N., Coxall, H.K. and Rosenthal, Y. (2008) Cooling and ice growth across the Eocene-Oligocene transition. *Geology*, **36**, 251-254.

Ledo, J., Pous, C., Queralt, P., Marcuello, A. and Muñoz, J.A. (2000) New geophysical constraints on the deep structure of the Pyrenees. *Geophysical Research Letters*, **27**, 1037-1040.

Lee, H.-K. and Schwarcz, H.P. (1996) Electron spin resonance plateau dating of periodicity of activity on the San Gabriel fault zone, southern California. *Geological Society of America*, **108**, 735-746.

Lee, S.-Y. and Poulsen, C.J. (2005) Tropical Pacific climate response to obliquity forcing in the Pleistocene. *Paleoceanography*, **20**, PA4010. DOI:10.1029/2005PA001161.

Leeder, M.R. (2011) Sedimentology and Sedimentary basins: from turbulence to tectonics, 2nd Edition, 784 pp. Wiley-Blackwell. ISBN: 978-1-4443-4992-4.

Leventhal, J.S. (2004) Isotopic chemistry of organic carbon in sediments from Leg 184. *In*: Prell, W.L., Wang, P., Blum, P., Rea, D.K. and Clemens, S.C. (eds) *Proceedings of the Ocean Drilling Program, Scientific Results*, **184**,1-13.

Levrard, B. and Laskar, J. (20003) Climate friction and the Earth's obliquity. *Geophysical Journal International*, **154**, 970-990.

Liebrand, D. Lourens, L.J., Hodell, D.A., de Boer, B., van de Wal, R.S.W., and Pälike, H. (2011) Antarctic ice sheet and oceanographic response to eccentricity forcing during the early Miocene. *Climates of the Past*, **7**, 869-880.

Lisiecki, L.E. (2010) Links between eccentricity forcing and the 100,000-year glacial cycle, *Nature Geoscience*, **3**, 349-352.

Lisiecki, L. and Raymo, M. (2005) A Plio-Pleistocene stack of 57 globally distributed benthic $\delta^{18}O$ records. *Paleoceanography*, **20**, 522-533.

Liu, H.S. (1992) Frequency variation of the Earth's obliquity and the 100-kyr ice-ages cycles. *Nature*, **358**, 397-399.

Liu, H.S. (1995) A new view on the driving mechanism of Milankovitch glaciation cycles. *Earth and Planetary Science letters*, **131**, 17-26.

Liu, Z., Cleaveland, L.C. and Herbert, T.D. (2008) Early onset and origin of 100-kyr cycles in Pleistocene tropical SST records. *Earth and Planetary Science Letters*, **265**, 703-715.

Liu, Z., Pagani, M., Zinniker, D., DeConto, R., Huber, M., Brinkhuis, H., Shah, S.R., Leckie, R.M. and Pearson, A. (2009) Global cooling during the Eocene - Oligocene Climate Transition. *Science*, **323**, 1187-1190.

Livermore, R., Nankivell, A., Eagles, G. and Morris, P. (2005) Paleogene opening of Drake Passage. *Earth and Planetary Science Letters*, **236**, 459-470.

Livermore, R., Hillenbrand, C.D., Meredith, M. and Eagles, G. (2007) Drake Passage and Cenozoic climate: An open and shut case? *Geochemistry. Geophysics. Geosystems*, **8**, Q01005. DOI:10.1029/2005GC001224.

Lomb, N.R. (1976) Least-squares frequency analysis of unequally spaced data. *Astrophysics and Space Science*, **39**, 447-462.

Lourens, L.J., Sluijs, A., Kroon, D., Zachos, J.C., Thomas, E., Röhl, U., Bowles, J. and Raffi, I. (2005) Astronomical pacing of late Palaeocene to early Eocene global warming events. *Nature*, **435**, 1083-1087.

Løvborg, L. and Mose, E. (1987) Counting statistics in radioelement assaying with a portable spectrometer. *Geophysics*, **52**, 555-563.

Løvborg, L., Wollenberg, H., Sørensen, P. and Hansen, J. (1971) Field determination of uranium and thorium by gamma-ray spectrometry, exemplified by measurements in the Ilímaussaq alkaline intrusion, South Greenland. *Economic Geology*, **66**, 368-384.

Löwemark, L., Chen, H.F., Yang, T.N., Kylander, M., Yu, E.F., Hsu, Y.W., Lee, T.Q., Song, S.R. and Jarvis, S. (2011) Normalising XRF-scanner data: A cautionary note on the interpretation of high-resolution records from organic-rich lakes. *Journal of Asian Earth Sciences*, **40**, 1250-1256.

Lowenstein, T.K. and Demicco, R.V. (2006) Elevated Eocene atmospheric CO_2 and its subsequent decline. *Science*, **313** (5795), 1928.

Lyons, T.W. and Berner, R.A. (1992) Carbon-sulfur-iron systematics of the uppermost deep-water sediments of the Black Sea. *Chemical Geology*, **99**, 1-27.

Macdonald, D.I.M. (1993) Controls at convergent plate margins Special Publications *In*: Frostick, L.E. and Steel, R.J. (eds) Tectonic controls and signatures in sedimentary successions. *Special publication of the International Association of Sedimentologists*, **20**, 225-257.

Mallinson, D.J., Flower, B., Hineb, A., Brooks, G. and Garza, R.M. (2003) Paleoclimate implications of high latitude precession-scale mineralogic fluctuations during early Oligocene Antarctic glaciation: the Great Australian Bight record. *Global and Planetary Change*, **39**, 257-269.

Manley, P.L. and Flood, R.D. (1988) Cyclic sediment deposition within Amazon deep-sea fan. *American Association of Petroleum Geologists Bulletin*, **72**, 912-925.

Mann, M.E. and Lees, J.M. (1996) Robust estimation of background noise and signal detection in climatic time series. *Climate Change*, **33**, 409-445.

Manners, H.R., Grimes, S.T., Sutton, P.A., Domingo, L., Leng, M.J., Twitchett, R.J., Hart, M.B., Jones, T.D., Pancost, R.D., Duller, R. and López-Martínez, N. (2013) Magnitude and profile of organic carbon isotope records from the Paleocene-Eocene Thermal Maximum: Evidence from northern Spain. *Earth and Planetary Science Letters*, **376**, 220-230.

Mansurbeg, H., Caja, M.A., Morad, S., Remacha, E., García, D., Martín-Crespo, T., El-Ghali, M.A.C. and Nystuen, J.P. (2009) Diagenetic evolution and porosity destruction of turbiditic hybrid arenites and siliciclastic sandstones of foreland basins: evidence from the Eocene Hecho group, Pyrenees, Spain. *Journal of Sedimentary Research*, **79**, 711-735.

Mantsis, D.F., Clement, A.C., Broccoli, A.J. and Erb, M.P. (2010) Climate feedbacks in response to changes in obliquity. *Journal of Climate*, **24**, 2830-2845.

Marsset, T. Droz, L., Dennielou, B. and Pichon, E. (2009) Cycles in the architecture of the Quaternary Zaire turbidite system: a possible link with climate. *In*: Kneller, B., Martinses, O.J. and McCaffrey, B. (eds) External controls on deep water depositional systems, *SEPM Special Publication*, **92**, 89-106.

Martinsen, O.J. and Bakken, B. (1990) Extensional and compressional zones in slumps and slides in the Namurian of County Clare, Ireland. *Journal of the Geological Society*, **147**, 153-164.

Marzo, M., Nijman, W. and Puigdefábregas, C. (1988) Architecture of the Castissent fluvial sheet sst, Eocene, Southern Pyrenees, Spain. *Sedimentology*, **35**, 719-738.

Maslin, M. and Mikkelsen, N. (1997) The mass-transport deposits and interglacial sediments of the Amazon Fan: age estimates and fan dynamics. *In*: Flood, R.D., Piper, D.J.W., Klaus, A. and Peterson, L.C. (eds) *Proceedings of the Ocean Drilling*

Program, Scientific Results, College Station, TX (Ocean Drilling Program), **155**, 353-366.

Maslin, M.A. and Ridgwell, A.J. (2005) Mid-Pleistocene Revolution and the 'eccentricity myth'. *Geological Society London, Special Publications*, **247**, 19-34.

McHargue, T.R. (1991) Seismic facies, processes, and evolution of Miocene inner fan channels, Indus Submarine Fan. *In*: Weimer, P. and Link, M.H. (eds) *Seismic Facies and Sedimentary Processes of Submarine Fans and Turbidite Systems*, Springer, New York, 403-413.

McHargue, T.R. and Webb, J.E. (1986) Internal geometry, seismic facies, and petroleum potential of canyons and inner fan channels of the inner Indus Submarine Fan. *American Association of Petroleum Geologists Bulletin*, **70**, 161-180.

McIver, R.D. (1975) Hydrocarbon occurrences from JOIDES Deep Sea Drilling Project. Proceedings of the Ninth Petroleum Congress (Tokyo). Applied Science Publishers, Barking, 269-280.

McKay, N.P., Overpeck, J.T. and Otto-Bliesner, B.L (2011) The role of ocean thermal expansion in Last Interglacial sea level rise. *Geophysical Research Letters*, **38**, 1-6.

McLennan, S.M., Hemming, S., McDaniel, D.K. and Hanson, G.N. (1993) Geochemical approaches to sedimentation, provenance, and tectonics. *In*: Johnsson, M.J. and Basu, A. (eds) Processes Controlling the Composition of Clastic Sediments. *Geological Society of America, Special Paper*, **284**, 21-40.

McLeod, P., Carey, S. and Sparks, S.J. (1999) Behaviour of particle-laden flows into the ocean: experimental simulation and geological implications. *Sedimentology*, **46**, 523-536.

Meehl, G.A., Stocker, T.F., Collins, W.D., Friedlingstein, P., Gaye, A.T., Gregory, J.M., Kitoh, A., Knutti, R., Murphy, J.M., Noda, A., Raper, S.C.B., Watterson, I.G., Weaver, A.J. and Zhao, Z.-C.C. (2007) Global climate projections. *In*: Solomon, S., Qin, D., Manning, M., Chen, Z., Marquis, M., Averyt, K.B., Tignor, M. and Miller, H.L. (eds), *Climate Change 2007: The Physical Science Basis: Contribution of Working Group I to the Fourth Assessment Report of the Intergovernmental Panel on Climate Change*. Cambridge University Press, Cambridge, United Kingdom and New York, USA.

Meigs, A.J. (1997) Sequential development of selected Pyrenean thrust faults. *Journal of Structural Geology*, **19**, 481-502.

Meigs, A.J. and Burbank, D.W. (1997) Growth of the South Pyrenean orogenic wedge. *Tectonics*, **16**, 239-258.

Meigs, A.J., Vergés, J. and Burbank, D.W. (1996) Ten-million-year history of a thrust sheet. *Geological Society of America Bulletin*, **108**, 1608-1625.

Mellor, G.L. and Ezer T. (1995) Sea level variations induced by heating and cooling: An evaluation of the Boussinesq approximation in ocean models. *Journal of Geophysical Research*, **100**, C10, 20565.

Merico, A., Tyrell, T. and Wilson, P.A. (2008) Eocene/Oligocene ocean deacidification linked to Antarctic glaciation by sea-level fall. *Nature*, **452**, 979-982.

Meyers, P.A. (1994) Preservation of elemental and isotopic source identification of sedimentary organic matter. *Chemical Geology*, **114**, 289-302.

Meyers, S.D., Kelly, B.G. and O'Brien, J.J. (1993) An introduction to wavelet analysis in oceanography metereology: with application to the dispersion of Yanai waves. *Monthly Weather Review*, **121**, 2858-2866.

Meyers, S.R. and Sageman, B.B. (2000) Latitude-dependent climatic response to Milankovitch orbital forcing and its expression in Cretaceous rocks of the northern hemisphere. *Summary of Investigations*, **1**, 76-81.

Meyers, S.R. and Sageman, B.B. (2007) Quantification of deep-time orbital forcing by average spectral misfit. *American Journal of Science*, **307**, 773-792.

Meyers, S.R., Sageman, B.B. and Hinnov, L.A. (2001) Integrated quantitative stratigraphy of the Cenomanian –Turonian Bridge Creek Limestone Member using evolutive harmonic analysis and stratigraphic modelling. *Journal of Sedimentary Research*, **71**, 627-643.

Mikolajewicz, U., Maier-Reimer, E. and Crowley, T.J. (1993) Effect of Drake Passage and Panamian gateways on the circulation of an ocean model. *Paleoceanography*, **8**,409-426.

Miller, K.G., Fairbanks, R.G. and Mountain, G.S. (1987) Tertiary oxygen isotope synthesis, sea level history, and continental margin erosion. *Paleoceanography*, **2**, 1-19.

Miller, K.G., Wright, J.D. and Fairbanks, R.G. (1991) Unlocking the ice house: Oligocene-Miocene oxygen isotopes, eustasy, and margin erosion. *Journal of Geophysical research*, **96**, 6829-6848.

Miller, K.G., Wright, J.D. and Browning, J. (2005) Visions of ice sheets in a greenhouse world. *Marine Geology*, **217**, 215-231.

Miller, K.G., Browning, J.V., Aubry, M-P., Wade, B.S., Katz, M.E., Kulpecz, A.A. and Wright, J.D. (2008) Eocene-Oligocene global climate and sea-level change changes: St. Stephens Quarry, Alabama. *Geological Society of America Bulletin*, **120**, 34-53.

Miller, K.G., Wright, J.D., Katz, M.E., Wade, B.S., Browning, J.V., Cramer, B.S. and Rosenthal, Y. (2009) Climate threshold at the Eocene-Oligocene transition: Antarctic

ice sheet influence on ocean circulation. *In*: Koeberl, C. and Montanari, A. (eds) The Late Eocene Earth-Hothouse, Icehouse, and Impacts. *Geological Society of America Special Paper*, **452**, 169-178.

Miller, K.G., Mountain, G.S., Wright, J.D. and Browning, J.V. (2011) A 180-million-year record of sea level and ice volume variations from continental margin and deep-sea isotopic records. *Oceanography*, **24**, 40-53.

Milliman, J.D. and Syvitski, J.P.M. (1992) Geomorphic/tectonic control of sediment discharge to the ocean: the importance of small mountainous rivers. *Journal of Geology*, **100**, 525-544.

Millington, J.J. and Clark, J.D. (1995) The Charo/Arro canyon-mouth sheet system, south-central Pyrenees, Spain: a structurally influenced zone of sediment dispersal. *Journal of Sedimentary Research*, **65**, 443-454.

Milne, A.R. and Fitzpatrick, R.W. (1977) Titanium and Zirconium minerals. *In*: Dixon, J.B. and Weed, S.B. (eds) Minerals in soil environments. Madison, WI. *Soil Science Society of America*, 1131-1205.

Minelli, N., Manzi, V. and Roveri, M. (2013) The record of the Paleocene-Eocene thermal maximum in the Ager Basin (Central Pyrenees, Spain). *Geologica Acta*, **11**, 421-441.

Minty, B. (1997) Fundamentals of airborne gamma-ray spectrometry, AGSO. *Journal of Australian Geology and Geophysics*, **17**, 39-50.

Mochales, T. (2010) Chronostratigraphy, vertical axis rotations and AMS in the Boltaña anticline (Southern Pyrenees): kinematic implications. PhD Thesis, University of Zaragoza (Spain).

Mochales, T., Casas, A.M., Pueyo, E.L. and Barnolas, A. (2012) Rotational velocity for oblique structures (Boltaña anticline, Southern Pyrenees). *Journal of Structural Geology*, **35**, 2-16.

Montigny, R., Azambre, B., Rossy, M and Thuizat, R. (1986) A study of Cretaceous magmatism and metamorphism from the Pyrenees: age and length of rotation of the Iberian Peninsula. *Tectonophysics*, **129**, 257-273.

Moodley, L., Middelburg, J.J., Herman, P.M.J., Soetaert, K, and De Lange, G.J. (2005) Oxygenation and organic-matter preservation in marine sediments: direct experimental evidence from ancient organic carbon-rich deposits. *Geology*, **33**, 889-892.

Moody, J.D., Pyles, D.R., Clark, J. and Bouroullec, R. (2012) Quantitative outcrop characterization of an analog to weakly confined submarine channel systems: Morillo 1 Member, Ainsa Basin, Spain. *American Association of Petroleum Geologists Bulletin*, **96**, 1813-1841.

Moran, K., Backman, J., Brinkhuis, H., Clemens, S.C., Cronin, T., Dickens, G.R., Eynaud, F., Gattacceca, J., Jakobsson, M., Jordan, R.W., Kaminski, M., King, J., Koc, N., Krylov, A., Martinez, N., Matthiessen, J., McInroy, D., Moore, T.C., Onodera, J., O'Regan, M., Palike, H., Rea, B., Rio, D., Sakamoto, T., Smith, D.C., Stein, R., St John, K., Suto, I., Suzuki, N., Takashashi, K., Watanabe, M., Yamamoto, M., Farrell, J., Frank, M., Kubik, P., Jokat, W. and Kristoffersen, Y. (2006) The Cenozoic paleoenvironment of the Arctic Ocean. *Nature*, **441**, 601-605.

Moreno, A., Nave, S., Kuhlmann, H., Canals, M., Targarona, J., Freudenthal, T. and Abrantes, F. (2002) Productivity response in the north Canary basin to climate changes during the last 250000 yr: a multi-proxy approach. *Earth and Planetary Science Letters*, **196**, 147-159.

Morley, C.K., Vanhauwaert, P. and De Batist, M. (2000) Evidence for high-frequency cyclic fault activity from high-resolution seismic reflection survey, Rukwa Rift, Tanzania. *Journal of the Geological Society*, **157**, 983-994.

Mosbrugger, V., Utescher, T. and Dilcher, D.L. (2005) Cenozoic continental climatic evolution of Central Europe. *Proceedings of the National Academy of Sciences*, **102**, 14964-14969.

Mouslopoulou, V., Walsh, J.J. and Nicol, A. (2009) Fault displacement rates on a range of timescales. *Earth and Planetary Science Letters*, **278**, 186-197.

Muller, R.A. and MacDonald, G.J. (1995) Glacial cycles and orbital inclination. *Nature*, **377**, 107-108.

Muller, R.A. and MacDonald, G.J. (2000) Ice ages and astronomical causes. Data, spectral analysis and mechanisms. Springer, Prxis Publishing, Chichester, UK, 19-40.

Muñoz, J.A. (1992) Evolution of a continental collision belt: ECORS-Pyrenees crustal balanced cross-section. *In*: McClay, K.R. (eds) *Thrust Tectonics*, Chapman & Hall, New York, 235-246.

Muñoz, J.A. (2002) Alpine Tectonics I, the Alpine system north of the Beltic Cordillera: The Pyrenees. *In*: Gibbons, W. and Moreno, T. (eds) Geology of Spain, *Geological Society, London*, 370-385.

Muñoz, J.A., Martínez, A. and Vergés, J. (1986) Thrust sequences in the Eastern Spanish Pyrenees. *Journal of Structural Geology*, **8**, 399-405.

Muñoz, J.A., McClay, K. and Poblet, J. (1994) Synchronous extension and contraction in frontal thrust sheets of the Spanish Pyrenees. *Geology*, **22**, 921-924.

Muñoz, J.A., Arbués, P. and Serra-Kiel, J. (1998) The Ainsa basin and the Sobrarbe oblique thrust system: Sedimentological and tectonic processes controlling slope and platform sequences deposited synchronously with a submarine emergent thrust system. *In*: Meléndez Hevia, A. and Soria, A.R. (eds) *Field Trip Guidebook of the 15th*

International Association of Sedimentologists International Congress of Sedimentology, 213-223.

Muñoz, J.A., Beamud, E., Fernández, O., Arbués, P., Dinarés-Turell, J. and Poblet, J. (2013) The Ainsa fold and thrust oblique zone of the central Pyrenees: Kinematics of a curved contractional System from paleomagnetic and structural data. *Tectonics*, **32**, 1142-1175.

Murray, R.W. and Leinen, M. (1996) Scavenged excess aluminium and its relationship to bulk titanium in biogenic sediment from the central equatorial Pacific Ocean. *Geochimica et Cosmochimica Acta*, **60**, 3869-3878.

Mutti, E. (1983/1984) The Hecho Eocene Submarine Fan System, South-Central Pyrenees, Spain. *Geo-Marine Letters*, **3**, 199-202.

Mutti, E. (1989) Alcuni problemi relativi all'applicazione dei concetti della stratigrafia sequenziale all'Eocene e al Cretacico superiore Sud Pirenaico. *Supplemento al Giornale di Geologia*, **51**, 37-53.

Mutti, E. (1992) Turbidite sandstones. AGIP Instituto de Geologia Universitá di Parma, Italy.

Mutti, E., and Sonnino, M. (1981) Compensational cycles: A diagnostic feature of turbidite sandstone lobes. *International Association of Sedimentologists*, Second European Regional Meeting, 120-123.

Mutti, E. and Normark, W.R. (1987) Comparing examples of modern and ancient turbidite systems; problems and concepts. *In*: Legget, J.K. and Zuffa, G.G. (eds) *Marine Clastic Sedimentology: Concepts and Case Studies*, London, UK, Graham and Trotman, 1-38.

Mutti, E., Luterbacher, H.P., Ferrer, J. and Rosell, J. (1972) Schema estratigrafico e lineamenti di facies del Paleogene marino della zona central subpirenaica tra Tremp (Catalogna) e Pamplona (Navarra). *Societa Geologica Italiana*, **11**, 391-416.

Mutti, E., Remacha, E., Sgavetti, M., Rosell, J., Valloni, R. and Zamorano, M. (1985) Stratigraphy and facies characteristics of the Eocene Hecho Group turbidite systems, south-central Pyrenees. *In*: Mila, M.D. and Rosell, J. (eds). *Excursion Guidebook of the 6th European Regional Meeting of International Association of Sedimentologists, Lerida*, 233-291.

Mutti, E, Séguret, M and Sgavetti, M. (1988) Sedimentation and deformation in the Tertiary sequences of the southern Pyrenees. *Fieldtrip 7 Guidebook. American Association of Petroleum Geologists, Mediterranean Basins Conference, Nice, France*, 153-157. Special Publication of the Institute of Geology of the University of Parma.

Mutti, E., R. Tinterri, G. Benevelli, D. DiBiase, and Cavanna, G. (2003) Deltaic, mixed and turbidite sedimentation of ancient foreland basins. *In*: Mutti, E., Steffens,

G.S., Pirmez, C., Orlando, M. and Roberts, D. (eds) Turbidites: models and problems. *Marine and Petroleum Geology*, **20**, 733-755.

Myers, K.J. and Wignall, P.B. (1987) Understanding Jurassic organic-rich mudrocks new concepts using gamma-ray spectrometry and palaeoecology: examples from the Kimmeridge Clay of Dorset and the Jet Rock of Yorkshire. *In*: Legget, J.K. and Zuffa, G.G. (eds) *Marine clastic sedimentology*. Graham and Trotman, London, 172-189.

Myers, K.J. and Bristow, C.S. (1989) Detailed sedimentology and gamma-ray log characteristics of a Namurian detail deltaic succession II: Gamma-ray logging. *In*: Whateley, M.K.C. and Pickering, K.T. (eds) Deltas: Sites and Traps for fossil fuels. *Geological Society, London, Special Publications*, **41**, 81-88.

Nakajima, T. and Itaki, T. (2007) Late Quaternary terrestrial climatic variability recorded in deep-sea turbidites along the Toyama Deep-Sea Channel, central Japan Sea. *Palaeogeography, Palaeoclimatology, Palaeoecology*, **247**, 162-179.

Neeman, B. (1993) Orbital tuning of paleoclimate records: A reassessment, Rep. LBNL-39572, Lawrence Berkeley Laboratory repost, Berkeley, California.

Nelson, C.H., Twichell, D.C., Schwab, W.C., Lee, H.J. and Kenyon, N.H. (1992) Upper Pleistocene turbidite sand beds and chaotic silt beds in the channelized, distal, outer-fan lobes of the Mississippi Fan. *Geology*, **20**, 693-696.

Nelson, P.A., Venditti, J.G., Dietrich, W.E., Kirchner, J.W., Ikeda, H., Iseya, F. and Sklar, L.S. (2009) Response of bed surface patchiness to reductions in sediment supply. *Journal of Geophysical Research*, **114**, F02005, DOI: 10.1029/2008JF001144.

Nicholas, A.P. and Quine, T.A. (2007). Modelling alluvial landform change in the absence of external environmental forcing. *Geology*, **35**, 527-530.

Nicol, A., Walsh, J., Watterson, J. and Underhill, J.R. (1997) Displacement rates of normal faults. *Nature*, 390, 157-159.

Nicol, A., Walsh, J.J., Manzocchi, T. and Morewood, N. (2005). Displacement rates and average earthquake recurrence intervals on normal faults. *Journal of Structural Geology*, **27**, 541-551.

Nicolo, M.J., Dickens, G.R., Hollis, C.J. and Zachos, J.C. (2007) Multiple early Eocene hyperthermals: Their sedimentary expression on the New Zealand continental margin and in the deep sea. *Geology*, **35**, 699-702.

Nijman, W. (1998) Cyclicity and basin axis shift in a piggyback basin: towards modelling of the Tremp-Ager Basin, South Pyrenees, Spain. *In*: Mascle, A., Puigdefabregas, C., Luterbacher, H.P. and Fernández, M. (eds) Cenozoic Foreland Basins of Western Europe. *Geological Society Special Publication*, **134**, 135-162.

Nittrouer, C.A., Austin, J.A., Field, M.E., Kravitz, J.H., Syvitski, J.P.M. and Wiberg, P.L (2007) Writing a Rosetta stone: insights into continental-margin sedimentary

processes and strata. *In*: Nittrouer, C., Austin, J., Field, M., Kravitz, J., Syvitski, J. and Wiberg, P. (eds), *Continental Margin Sedimentation*, 1-48. Wiley-Blackwell.

Normark, W.R., Posamentier, H. and Mutti, E. (1993) Turbidite systems: state of the art and future directions. *Reviews of Geophysics*, **31**, 91-116.

Normark, W.R., Damuth, J.E., Cramp, A., Flood, R.D., Hiscott, R.N., Kowsmann, R.O., Lopez, M., Manley, P.L., Nanayama, F., Piper, D.J.W., Pirmez, C. and Schneider, R.R. (1997) Sedimentary facies and associated depositional elements of the Amazon Fan. *In*: Flood, R.D., Piper, D.J.W., Klaus, A., Burns, S.J., Busch, W.H., Cisowski, S.M., Cramp, A., Damuth, J.E., Goni, M.A., Haberle, S.G., Hall, F.R., Hinrichs, K., Hiscott, R.N., Kowsmann, R.O., Kronen, J.D., Long, D., Lopez, M., McDaniel, D.K., Manley, P., Maslin, M.A., Mikkelsen, N., Nanayama, F., Normark, W.R., Pirmez, C., dos Santos, J.R., Schneider, R.R., Showers, W.J., Soh, W., Thibal, J. and Fox, G.L. (eds) *Proceedings of the Ocean Drilling Program, Scientific Results*, Ocean Drilling Program, College Station, **155**, 611-651.

North, C., Ruffell, P. and Boering, M. (1999) Spectral gamma-ray logging for facies discrimination in mixed fluvial–eolian successions: a cautionary tale. *American Association of Petroleum Geologists Bulletin*, **83**, 155-169.

Olsen, H. (1994) Orbital forcing on continental depositional systems: lacustrine and fluvial cyclicity in the Devonian of East Greenland. *In*: De Boer, P.L and Smith, D.G. (eds) Orbital forcing and cyclic sequences. *International Association of Sedimentologists Special Publication*, Oxford: Blackwell Scientific, **19**, 429-438.

Olsen, P.E. and Kent, D.V. (1996) Milamkovitch climate forcing in the tropics of Pangaea during the Late Triassic. *Palaeogeogrphy, Palaeoclimatology, Palaeoecology*, **122**, 1-26.

Oms, O., Dinarès-Turel, J. and Remacha, E. (2003) Magnetic stratigraphy from deep clastic turbidites: an example from the Eocene Hecho Group (southern Pyrenees). *Studia Geophysica Geodetica*, **47**, 275-288.

Osmond, J. K. and Ivanovich, M. (1992) Uranium series mobilization and surface hydrology. *In*: Ivanovich, M. and Harmon, R.S. (eds) *Uranium-Series Disequilibrium: Application to Earth Marine and Environmental Sciences*, Clarendon Press, Oxford, 259-289.

Owen, R.M. and Rea, D.K. (1985) Sea floor hydrothermal activity links climate to tectonics - the Eocene carbon dioxide greenhouse. *Science*, **227**, 166-169.

Pagani, M., Zachos, J.C., Freeman, K.H., Tipple, B. and Bohaty, S. (2005) Marked decline in atmospheric carbon dioxide concentrations during the Paleogene. *Science*, **309**, 600-603.

Pagani, M., Pedentchouk, N., Huber, M., Sluijs, A., Schouten, S., Brinkhuis, H., Sinninghe Damsté, J.S., Dickens, G.R. and the Expedition 302 Scientists (2006).

Arctic hydrology during global warming at the Palaeocene/Eocene thermal maximum. *Nature*, **442**, 671-675.

Paillard, D. and Parrenin, F. (2004) The Antarctic ice sheet and the triggering of deglaciations. *Earth Planetary Science Letters*, **227**, 263-271.

Paillard, D., Labeyrie, L. and Yiou, P. (1996) Macintosh program performs time-series analysis. *Eos, Transactions American Geophysical Union*, **77**, 379.

Pälike, H., Frazier, J., and Zachos, J. C. (2006a) Extended orbitally forced palaeoclimatic records from the Equatorial Atlantic Ceara Rise. *Quaternary Science reviews*, **25**, 3138-3149.

Pälike, H., Norris, R.D., Herrle, J.O., Wilson, P.A., Coxall, H.K., Lear, C.H., Shackleton, N.J., Tripati, A.K., and Wade, B.S. (2006b) The heartbeat of the Oligocene climate system. *Science*, **314**, 1894-1898.

Pardo-Igúzquiza, E. and Rodriguez-Tovar, F. (2006) Maximum entropy spectral analysis of climatic time series revisited: Assessing the statistical significance of estimated spectral peaks. *Journal of geophysical Research*, **111**, D10102. DOI: 10.1029/2005JD006293.

Parkinson, D.N. (1996) Gamma-ray spectrometry as a tool for stratigraphical interpretation: examples from the western European Lower Jurassic. *In*: Hesselbo, S.P. and Parkinson, D.N. (eds) Sequence Stratigraphy in British Geology. *Geological Society Special Publication*, **103**, 231-255.

Parrenin, F. and Paillard, D. (2003) Amplitude and phase of glacial cycles from a conceptual model. *Earth and Planetary Science Letters*, **214**, 243-250.

Parrenin, F. and Paillard, D. (2012) Terminations VI and VIII (∼530 and ∼720 kyr BP) tell us the importance of obliquity and precession in the triggering of deglaciations. *Climates of the Past*, **8**, 2031-2037.

Parsons, J.D., Bush, J.W.M. and Syvitski, J.P.M. (2001) Hyperpycnal plume formation from riverine outflows with small sediment concentrations. *Sedimentology*, **48**, 465-478.

Parsons, J.D., Schweller, W.J., Stelting, C.W., Southard, J.B., Lyons, W.J. and Grotzinger, J.P. (2002) A preliminary experimental study of turbidite fan deposits. *Journal of Sedimentary Research*, **72**, 619-628.

Payros, A. and Martínez-Braceras, N. (2014) Orbital forcing in turbidite accumulation during the Eocene greenhouse interval. *Sedimentology, in press*.

Payros, A., Pujalte, V. and Orue-Etxebarria, X. (1999) The South Pyrenean Eocene carbonate megabreccias revisited: new interpretation based on evidence from the Pamplona Basin. *Sedimentary Geology*, **125**, 165-194.

Payros, A., Tosquella, J., Bernaola, G., Dinares-Turell, J., Orue-Etxebarria, X. and Pujalte, V. (2009) Filling the North European Early/Middle Eocene (Ypresian/Lutetian) boundary gap: Insights from the Pyrenean continental to deep-marine record. *Palaeogeography, Palaeoclimatology, Palaeoecology*, **280**, 313-332.

Pearson, P.N., van Dongen, B.E., Nicholas, C.J., Pancost, R.D., Schouten, S., Singaro, J.M. and Wade, B.S. (2007) Stable warm tropical climate through the Eocene epoch. *Geology*, **35**, 211-214.

Pearson, P.N., McMillan, I.K., Wade, B.S., Jones, T.D., Coxall, H.K., Bown, P.R. and Lear, C.H. (2008) Extinction and environmental change across the Eocene-Oligocene boundary in Tanzania. *Geology*, **36**, 179-182.

Pearson, P.N., Foster, G.L. and Wade, B.S. (2009) Atmospheric carbon dioxide through the Eocene-Oligocene climate transition. *Nature*, **461**, 1110-1113.

Pekar, S.F., Christie-Blick, N., Kominz, M.A. and Miller, K.G. (2002) Calibration between eustatic estimates from backstripping and oxygen isotopic records for the Oligocene. *Geology*, **30**, 903-906.

Pekar, S.F., Hucks, A., Fuller, M. and Li, S. (2005) Glacioeustatic changes in the early and middle Eocene (51-42 Ma): shallow-water stratigraphy from ODP Leg 189 Site 1171 (South Tasman Rise) and deep-sea $\delta^{18}O$ records. *Geological Society of America Bulletin*, **117**, 1081-1093.

Peper, T. and De Boer, P.L. (1995) Intrabasinal thrust tectonic versus climate control on rhythmicities in the Eocene South Pyrenean Tremp-Graus foreland basin: inferences from forward modelling. *Tectonophysics*, **249**, 93-107.

Peper, T., Beekman, F. and Cloefingh, S. (1992) Consequences of thrusting and intraplate stress fluctuations for vertical motions in foreland basins and peripheral areas. *Geophysical Journal International*, **111**, 104-126.

Percival, D.B. and Walden, A.T. (1993) Spectral Analysis for physical applications. Multitaper and conventional univariate techniques. *Cambridge University Press*, Cambridge, 1-583.

Pervesler, P. and Uchman, A. (2004) Ichnofossils from the type area of the Grand Formation (Miocene, Lower Badenian) in northern Lower Austria (Molasse basin). *Geológica Carpathica*, **55**, 103-110.

Peters, S.E., Carlson, A.E., Kelly, D.C. and Glingerich, P.D. (2010) Large-scale glaciation and deglaciation of Antarctica during the Late Eocene. *Geology*, **38**, 723-726.

Peterson, L. C., Haug, G.H., Hughen, K.A. and Röhl, U. (2000) Rapid changes in the hydrologic cycle of the tropical Atlantic during the last glacial. *Science*, **290**, 1947-1951.

Phillips, J. P. and Held, I.M. (1994) The response to orbital perturbations in an atmospheric model coupled to a slab ocean. *Journal of Climate*, **7**, 767-782.

Pickering, K.T. and Corregidor, J. (2000) 3D Reservoir scale study of Eocene confined submarine fans, south central Spanish Pyrenees. *In*: Weimer, P., Slatt, R.M., Coleman, J., Rosen, N.C., Nelson, H., Bouma, A.H., Styzen, M.J., and Lawrence, D.T. (eds) Deep Water Reservoirs of the World: SEPM, Gulf Coast Section, 20th Annual Bob F. Perkins Research Conference, 776-781.

Pickering, K.T. and Corregidor, J. (2005) Mass-Transport Complexes (MTCs) and tectonic control on basin-floor submarine fans, Middle Eocene, South Spanish Pyrenees. *Journal of Sedimentary Research*, **75**, 761-783.

Pickering, K.T. and Bayliss, N.J. (2009) Deconvolving tectono-climatic signals in deep-marine siliciclastics, Eocene Ainsa basin, Spanish Pyrenees: Seesaw tectonics versus eustasy. *Geology*, **37**, 203-206.

Pickering, K.T., Coleman, J., Cremer, M., Droz, L., Kohl, B., O'Connell, S., Stow, D., Meyer-Wright, A. (1986a). A high-sinuosity, laterally-migrating submarine fan channel-levée-overbank: results from DSDP Leg 96 on the Mississippi Fan, Gulf of Mexico. *Marine and Petroleum Geology*, **3**, 3-18.

Pickering, K.T., Stow, D.A.V., Watson, M. and Hiscott, R.N. (1986b) Deep-water facies processes and models: a review and classification scheme for modern and ancient sediments. *Earth Sciences Reviews*, **23**, 75-174.

Pickering, K.T., Hiscott, R.N. and Hein, F.J. (1989) Deep marine environments: clastic sedimentation and tectonics. London: Harper-Collins (Chapman & Hall), 416 pp. ISBN 004-4452012/5511225.

Pickering, K.T., Souter, C., Oba, T., Taira, A., Schaaf, M. and Platzman, E. (1999) Glacio-eustatic control on deep-marine clastic forearc sedimentation, Pliocene-mid-Pleistocene (c. 1180-600 ka) Kazusa Group, SE Japan. *Journal of the Geological Society*, London, **156**, 125-136.

Pierau, R., Hanebuth, T.J.J., Krastel, S. and Henrich, R. (2010) Late quaternary climatic events and sea-level changes recorded by turbidite activity, Dakar Canyon, NW Africa. *Quaternary Research*, **73**, 385-392.

Pierini, C., Mizusaki, A.-M.P., Claiton, M.S. and Alves, D.B. (2002) Integrated stratigraphic and geochemical study of the Santa Maria and Caturrita formations (Triassic of the Paraná Basin), southern Brazil. *Journal of South American Earth Sciences*, **15**, 669-681.

Pillans, B., Chappell, J. and Naish, T.R. (1998) A review of the Milankovitch climatic beat: template for Plio-Pleistocene sea-level changes and sequence stratigraphy. *Sedimentary Geology*, **122**, 5-21.

Piper, D.J.W. and Normark, W.R. (1983) Turbidite depositional patterns and flow characteristics, Navy submarine fan, California Borderland. *Sedimentology*, **30**, 681-694.

Piper, D.J.W., Pirmez, C., Manley, P.L., Long, D., Flood, R.D., Normark, W.R. and Showers, W. (1997) Mass-transport deposits of the Amazon Fan. *In*: Flood, R.D., Piper, D.J.W., Klaus, A. and Peterson, L.C. (eds) *Proceedings of the Ocean Drilling Program, Scientific Results, Ocean Drilling Program*, College Station, **155**, 109-146.

Pittet, B. and Strasser, A. (1998) Long distance correlations by sequence stratigraphy and cyclostratigraphy: examples and implications (Oxfordian from the Swiss Jura, Spain and Normandy) Geologische Rundschau, **98**, 852-874.

Plink-Björklund, P. and Steel, R.J. (2004) Initiation of turbidity currents: outcrop evidence for Eocene hyperpycnal flow turbidites. *Sedimentary Geology*, **165**, 29-52.

Poblet, J., Muñoz, J.A., Travé, A. and Serra Kiel, J. (1998) Quantifying the kinematics of detachment folds using three-dimensional geometry: application to the Mediano anticline (Pyrenees, Spain). *Geological Society of America Bulletin*, **110**,111-125.

Pohl, F. and McCann, T. (2013) Architecture and depositional development of the Eocene deep-marine Morillo and Coscojuela Formation, Ainsa Basin, Spain. *Geological Journal*, **49**, 221-238.

Prélat, A., Covault, J.A., Hodgson, D.M., Fildani, A. and Flint, S.S. (2010) Intrinsic controls on the range of volumes, morphologies, and dimensions of submarine lobes. *Sedimentary Geology*, **232**, 66-76

Prell, W.L. and Kutzbach, J.E. (1992) Sensitivity of the Indian monsoon to forcing parameters and implications for its evolution. *Nature*, **360**, 647-652.

Press, W.H., Teukolsky, S.A., Vetterling, W.T. and Flannery, B.P. (1992) *Numerical recipes, the art of scientific computing*, Cambridge University Press, Cambridge, 1-963.

Prins, M.A., Postma, G., Cleveringa, J., Cramp, A. and Kenyon, N.H. (2000) Controls on terrigenous sediment supply to the Arabian Sea during the late Quaternary; the Indus Fan. *Marine Geology*, **169**, 327-349.

Prokoph, A. and Barthelmes, F. (1996) Detection of nonstationarities in geological time series: wavelet transform of chaotic and cyclic sequences. *Computers & Geosciences*, **22**, 1097-1108.

Pueyo, E.L., Pocoví, A., Millán, H. and Sussman, A.J. (2004) Map-view models for correcting and calculating shortening estimates in rotated thrust fronts using paleomagnetic data. *In*: Sussman, A.J. and Weil, A.B. (eds) Orogenic curvature: Integrating paleomagnetic and structural analyses. *Geological Society of America Special Publication*, **383**, 57-71.

Puigdefábregas, C. (1975) La sedimentacióon molásica en la cuenca de Jaca. *Pirineos*, **104**, 1-188.

Puigdefábregas, C. and Souquet, P. (1986) Tectosedimentary cycles and depositional sequences of the Mesozoic and Tertiary from the Pyrenees. *Tectonophysics*, **129**, 173-203.

Puigdefábregas, C., Muñoz, J.A and Vergés, J. (1992) Thrusting and foreland basin evolution in the Southern Pyrenees. *In*: McClay, K.R. (ed) *Thrust Tectonics*, 247-254. Chapman and Hall.

Pyles, D.R., Moody, J., Gordon, G., Hoffman, M., Moss-Russell, A., Silalahi, H., Setiawan, P., Clark, J., Bracken, B. and Guzofski, C. (2013) Using the stratigraphic record to document tectonic-geomorphologic interactions in a foreland basin settings: outcrop study of the Ainsa Basin, Spain. *American Geophysical Union, Fall Meeting 2013*.

Quigley, M.C., Sandiford, M. and Cupper, M.L. (2007) Distinguishing tectonic from climatic controls on range-front sedimentation. *Basin Research*, **19**, 491-505.

Rahl, J.M., Haines, S.H. and van der Pluijm, B.A. (2011) Links between orogenic wedge deformation and erosional exhumation: Evidence from illite age analysis of fault rock and detrital thermochronology of syn-tectonic conglomerates in the Spanish Pyrenees. *Earth and Planetary Science Letters*, **307**, 180-190.

Rahmstorf, S. (2007) A semi-empirical approach to projecting future sea-level rise. *Science*, **315**, 368-370.

Raymo, M.E. (1997) The timing of major climate terminations. *Paleoceanography*, **12**, 557-585.

Raymo, M.E. and Nisancioglu, K. (2003) The 41 kyr world: Milankovitch's other unsolved mystery. *Paleoceanography*, **18**, 1011.

Raymo, M.E., Ruddiman, W.F. and Froelich, P.N. (1988) Influence of late Cenozoic mountain building on ocean geochemical cycles. *Geology*, **16**, 649-653.

Rea, D. (1992) Delivery of Himalayan sediment to the northern Indian Ocean and its relation to global climate, sea level, uplift, and seawater strontium. *American Geophysical Union, Geophysical Monograph*, **7**, 287-402.

Rea, D.K. and Lyle, M.W. (2005) Paleogene calcite compensation depth in the eastern subtropical Pacific: Answers and questions. *Paleoceanography*, **20**, DOI: 10.1029/2004PA001064.

Reading, H.G. and Richards, M. (1994) Turbidite systems in deep-water basin margins classified by grain size and feeder system. *Bulletin of the American Association of Petroleum Geologists*, **78**, 792-822.

Remacha, E. and Fernández, L.P. (2003) High-resolution correlation patterns in the turbidite systems of the Hecho Group (South-Central Pyrenees, Spain). *Marine and Petroleum Geology*, **20**, 711-726.

Remacha, E., Oms, O. and Coello, J. (1995) The Rapitán turbidite channel and its related eastern levée-overbank deposits, Eocene Hecho group, south-central Pyrenees, Spain. *In*: Pickering, K.T., Hiscott, R.N., Kenyon, N.H., Ricci Lucchi, F. and Smith, R.D.A. (eds) Atlas of Deep Water Environments: Architectural Style in Turbidite Systems, Chapman & Hall, London, 145-149.

Remacha, E., Gual, G., Bolaño, F., Arcuri, M., Oms, O., Climent, F., Crumeyrolle, P., Fernández, L.P., Vicente, J.C. and Suárez, J. (2003) Sand-rich turbidite systems of the Hecho Group from slope to the basin plain: facies, stacking patterns, controlling factors and diagnostic features: *American Association of Petroleum Geologists, International Conference and Exhibition*, Barcelona, Spain, September 21-24. Geological Field Trip no. 12, South-Central Pyrenees.

Richter, T.O., van der Gaast, S., Koster, B., Vaars, A., Gieles, R., de Stigter, H.C., de Haas, H. and van Weering, T.C.E. (2006) The Avaatech XRF core scanner: technical description and applications to NE Atlantic sediments. *In*: Rothwell, G. (ed) New techniques in sediment core analysis. *Geological Society London Special Publication*, **267**, 39-50.

Ricken, W. (1994) Complex rhythmic sedimentation related to third order sea-level variations: Upper Cretaceous, Western Interior Basin, USA. *In*: De Boer, P.L. and Smith, D.G. (eds) Orbital forcing and cyclic sequences, *Special Publication of the International Association of Sedimentologists*, **19**, 99-107.

Rider, M.H. (1990) Gamma-ray log shape used as a facies indicator: critical analysis of an oversimplified methodology. *In*: Hurst, A., Lovell, M.A. and Morton, A.C. (eds) Geological applications of wireline logs. *Geological Society, London, Special Publications*, **48**, 27-37.

Ridwell, A.J., Watson, A.J. and Raymo, M.E. (1999) Is the spectral signature of the 100 kyr glacial cycle consistent with a Milankovitch origin? *Paleoceanography*, **14**, 437-440.

Riebe, C.S., Kirchner, J.W., Granger, D.E. and Finkel, R.C. (2001) Strong tectonic and weak climatic control of long-term chemical weathering rates. *Geology*, **29**, 511-514.

Riebe, C.S., Kirchner, J.W. and Finkel, R.C. (2004) Erosional and climatic effects on the long-term chemical weathering rates in granitic landscapes spanning diverse climate regimes. *Earth and Planetary Science Letters*. **224**, 547-562.

Robert, M. and Carter, R.M. (1998) Two models: global sea-level change and sequence stratigraphic architecture. *Sedimentary Geology*, **122**, 23-36.

Roest, W.R. and Srivastava, S.P. (1991) Kinematics of the plate boundaries between Eurasia, Iberia, and Africa in the North Atlantic from the late Cretaceous to the present. *Geology*, **19**, 613-616.

Röhl, U., Brinkhuis, H., Stickley, C.E., Fuller, M., Schellenberg, S.A., Wefer, G. and Williams, G.L. (2004) Sea level and astronomically induced environmental changes in Middle and Late Eocene sediments from the East Tasman Plateau. *Geophysical monograph*, **151**, 127-151.

Röhl, U., Westerhold, T., Monechi, S., Thomas, E., Zachos, J.C. and Donner, B. (2005) The third and final Early Eocene Thermal Maximum: characteristics, timing and mechanisms of the 'X' event, GSA *Annual Meeting 37. Geological Society of America*, Salt Lake City, USA, 264.

Röhl, U., Westerhold, T., Bralower, T.J. and Zachos, J.C. (2007) On the duration of the Paleocene-Eocene Thermal Maximum (PETM). *Geochemistry. Geophysics, Geosystems*, **8**, 1-13.

Rosenbaum, G., Lister, G.S. and Duboz, C. (2002) Relative motions of Africa, Iberia and Europe during Alpine orogeny. *Tectonophysics*, **359**, 117-129.

Rosholt, J.N. (1992) Mobilisation and weathering. *In*: Ivanovich, M. and Harmon, R.S. (eds) *Uranium-series Disequilibrium: Applications to Earth, Marine and Environmental Sciences*. Clarendon Press, Oxford, 167-178.

Ross, W.C., Halliwell, B.A., May, J.A., Watts, D.E. and Syvitski, J.P.M. (1994) Slope readjustment: a new model for the development of submarine fans and aprons. *Geology*, **22**, 511-514.

Roure, F., Choukroune, P., Berastegui, X., Muñoz, J.A., Villien, A., Matheron, P., Bareyt, M., Seguret, M., Camara, P. and Deramond, J. (1989) ECORS deep-seismic data and balanced cross sections: geometric constraints on the evolution of the Pyrenees. *Tectonics*, **8**, 41-50.

Ruffell, A. and Worden, R. (2000) Palaeoclimate analysis using spectral gamma-ray data from the Aptian (Cretaceous) of southern England and southern France. *Palaeogeography, Palaeoclimatology, Palaeoecology*, **155**, 265-283.

Ruffell, A.H., Worden, R.W. and Evans, R. (2003) Palaeoclimate controls on spectral gamma-ray radiation from sandstones. *In*: Morad, S. (ed) Clay Cements in Sandstones. *Special Publication of the International Association of Sedimentologists*, **34**, 93-108.

Rupke, N.A. and Stanley, D.J. (1974) Distinctive properties of turbiditic and hemipelagic mud layers in the Algero-Balearic basin, western Mediterranean Sea. Smithsonian *Contributions to the Earth Sciences*, **13**, 1-40.

Sageman, B.B., Murphy, A.E., Werne, J.P, Ver Straeten, C.A., Hollander, D.J. and Lyons, T.W. (2003) A tale of shales: the relative roles of production, decomposition,

and dilution in the accumulation of organic-rich strata, Middle-Upper Devonian, Appalachian basin. *Chemical Geology*, **195**, 229-273.

Salamy, K.A. and Zachos, J.C. (1999) Latest Eocene-Early Oligocene climate change and Southern Ocean fertility; inferences from sediment accumulation and stable isotope data. *Palaeogeography, Palaeoclimatology, Palaeoecology*, **145**, 61-77.

Saltzman, B. and Maasch, K.A. (1988) Carbon cycle instability as a cause of the late Pleistocene ice age oscillations: Modelling the symmetric response. *Global Biochemistry Cycle*, **2**, 177-185.

Samanta, A., Sarkar, A., Bera, M.K., Rai, J. and Rathore, S.S. (2013) Late Paleocene–early Eocene carbon isotope stratigraphy from a near-terrestrial tropical section and antiquity of Indian mammals. *Journal of Earth System Science*, **122**, 163-171.

Satterley, A.K. (1996) The interpretation of cyclic successions of the Middle and Upper Triassic of the Northern and Southern Alps. *Earth Science Reviews*, **40**, 181-207.

Satur, N., Hurst, A., Cronin, B.T., Kelling, G. and Gürbüz, K. Sand body geometry in a sand-rich, deep-water clastic system, Miocene Cingöz Formation of southern Turkey. *Marine and Petroleum Geology*, **17**, 239-252.

Saura, E. and Teixell, A. (2006) Inversion of small basins: effects on structural variations at the leading edge of the Axial Zone antiformal stack (Southern Pyrenees, Spain). *Journal of Structural Geology*, **28**, 1909-1920.

Savostin, L.A., Sibuet, J.C., Zonenshain, L.P., Le Pichon, X. and Roulet, M.J. (1986) Kinematic evolution of the Tethys belt from the Atlantic Ocean to the Pamirs since the Triassic. *Tectonophysics*, **228**, 33-55.

Scargle, J.D. (1982) Studies in astronomical time series analysis. II. Statistical aspects of spectral analysis of unevenly spaced data. *The Astrophysical Journal*, **263**, 835-853.

Scargle, J.D. (1989) Studies in astronomical time series analysis. III. Fourier transforms, autocorrelation functions, and cross-correlation functions of unevenly spaced data. *The Astrophysical Journal*, **343**, 874-887.

Scher, H.D. and Martin, E.E. (2004) Circulation in the Southern Ocean during the Paleogene inferred from neodymium isotopes. *Earth and Planetary Science Letters*, **228**, 391-405.

Scher, H.D. and Martin, E.E. (2006) Timing and climatic consequences of the opening of Drake Passage. *Science*, **312**, 428-430.

Schlager, W. (1993) Accommodation and supply - a dual control on stratigraphic sequences. *Sedimentary Geology*, **86**, 111-136.

Schmitz, B. (1987) Barium, equatorial high productivity, and the north-ward wandering of the Indian continent. *Paleoceanography*, **2**, 63-77.

Schmitz, B. and Pujalte, V. (2003) Sea-level, humidity, and land erosion records across the initial Eocene thermal maximum from a continental-marine transect in northern Spain. *Geology*, **31**, 689-692.

Schmitz, B. and Pujalte, V. (2007) Abrupt increase in seasonal extreme precipitation at the Paleocene-Eocene boundary. *Geology*, **35**, 215-218.

Schmitz, B., Pujalte, V. and Nuñez-Betelu, K. (2001). Climate and sea-level perturbations during the initial Eocene Thermal Maximum: evidence from siliciclastic units in the Basque Basin (Ermua, Zumaia and Trabakua Pass), northern Spain. *Palaeogeography, Palaeoclimatology, Palaeoecology*, **165**, 299-320.

Schneider, R.R., Price, B., Muller, P.J., Kroon, D. and Alexander, I. (1997) Monsoon related variations in Zaire (Congo) sediment load and influence of fluvial silicate supply on marine productivity in the east equatorial Atlantic during the last 200,000 years. *Paleoceanography*, **12**, 463-481.

Schnetger, B., Brumsack H.J., Schale, H., Hinrichs, J. and Dittert, L. (2000) Geochemical characteristics of deep-sea sediments from the Arabian Sea: a high resolution study. *Deep-Sea Research II*, **47**, 2735-2768.

Schnyder, J., Ruffell, A., Deconinck, J.-F. and Baudin, F. (2006) Conjunctive use of spectral gamma-ray logs and clay mineralogy in defining late Jurassic-early Cretaceous palaeoclimate change (Dorset, U.K.). *Palaeogeography, Palaeoclimatology, Palaeoecology*, **229**, 303-320.

Schulz, M. and Schäfer-Neth, C. (1997) Translating Milankovitch climate forcing into eustatic fluctuations via thermal deep water expansion: a conceptual link. *Terra Nova,* **9**, 228-231.

Schulz, M. and Stattegger, K. (1997) SPECTRUM: spectral analysis of unevenly spaced paleoclimatic time series. *Computers and Geosciences*, **23**, 929-945.

Schulz, M. and Mudelsee, M. (2002) REDFIT: estimating red-noise spectra directly from unevenly spaced paleoclimatic time-series. *Computers and Geosciences*, **28**, 421-426.

Schuster, A. (1898) On the investigation of hidden periodicities with application to a supposed 26-day period of meterological phenomenon. *Terrestrial Magnetism and Atmospheric Electricity*, **3**, 13-41.

Scotchman, J.I. (2012) Stratigraphic context and timing of sand supply to deep-marine Ainsa-Jaca basin, middle Eocene, Spanish Pyrenees: Constraints from geochemistry and sedimentology, University College London, PhD thesis.

Scotchman, J.I., Bown, P., Pickering, K.T., BouDagher-Fadel, M., Bayliss, N.J. and Robinson, S.A. (2014) A new age model for the middle Eocene deep-marine Ainsa Basin, Spanish Pyrenees. Earth Sciences Reviews, *in press*.

Séguret, M. (1972) Étude tectonique des nappes et séries décollées de la partie centrale du versant sud des Pyrénées - Caractère synsedimentaire, rôle de la compresion et de la gravité. Publications USTELA, Montpellier, *Série géologie structurale*, **2**, 155.

Serra-Kiel, J., Canudo, J.I., Dinarés, J., Molina, E., Ortiz, N., Pascual, J.O., Samso, J.M. and Tosquella, J. (1993) Cronostratigrafia de los sedimentos marinos del Terciario inferior de la Cuenca de Graus-Tremp (Zona Central Surpirenaica). *Revista de la Sociedad Geológica de España*, **7**, 273-297.

Sewall, J.O., Sloan, L.C., Huber, M. and Wing, S. (2000) Climate sensitivity to changes in land surface characteristics. *Global and Planetary Change*, **26**, 445-465.

Shackleton, N.J. and Opdyke, N.D. (1973) Oxygen isotope and palaeo-magnetic stratigraphy of equatorial Pacific core V28- 238: oxygen isotope temperatures and ice volumes in a 10^5 and 10^6 year scale. *Quaternary Research*, **3**, 39-55.

Shackleton, N.J. and Kennett, J.P. (1975) Paleotemperature history of the Cenozoic and the initiation of Antarctic glaciation: Oxygen and carbon isotope analyses in DSDP sites 277, 279 and 281. *Initial Reports of the Deep Sea Drilling Project*, **29**, 743-755.

Shackleton, N.J., Berger, A. and Peltier, W.R. (1990) An alternative astronomical calibration of the lower Pleistocene timescale based on ODP Site 677. Trans Royal Society Edinburg. *Earth Sciences*, **81**, 251-261.

Shackleton, N.J., Hagelberg, T.K. and Crowhurst, S.J. (1995) Evaluating the success of astronomical tuning: pitfalls for using coherence as a criterion for assessing pre-Pleistocenetimescales. *Paleoceanography*, **10**, 693-697.

Shimmield, G.B. and Mowbray, S.R. (1991) The inorganic geochemical record of the northwestern Arabian Sea: a history of productivity variation over the last 400 k.y. from sites 722 and 724. *In*: Prell, W.L and Niitsuma, N. (eds) *Proceedings of the Ocean Drilling Program, Scientific Results*, **117**, 409-429. Texas, College Station, Ocean Drilling Program.

Sibuet, J.-C., Srivastava, S.P. and Spakman, W. (2004) *Journal of Geophysical Research*, **109**. DOI: 10.1029/2003JB002514.

Sijp, W.P. and England, M.H. (2004) Effect of the Drake Passage through flow on global climate. *Journal of Physical Oceanography*, **34**, 1254-1266.

Šimíček, D., Bábek, O. and Leichmann, J. (2012) Outcrop gamma-ray logging of siliciclastic turbidites: Separating the detrital provenance signal from facies in the

foreland-basin turbidites of the Moravo-Silesian basin, Czech Republic. *Sedimentary Geology*, **261-262**, 50-64.

Slatt, R.M., Jordan, D.W., D'Agostino, A. and Gillespie, R.H. (1992) Outcrop gamma-ray logging to improve understanding of subsurface well log correlations. *In*: Hurst, A., Griffiths, C.M. and Worthington, P.F. (eds) Geological Applications of Wireline Logs II. *Geological Society Special Publication*, **65**, 3-19.

Slatt, R.M., Stone, C.G. and Weimer, P. (2000) Characterisation of slope and basin facies tracts, Jackfork Group, Arkansas, with applications to deepwater (turbidite) Reservoir management. *GCSSEPM Foundation 20th Annual Research conference, Deep-water Reservoirs of the world, December 3-6*, 940-980.

Sloan, L.C. (1994) Equable climates during the early Eocene: significance of regional paleogeography for North American climate. *Geology*, **22**, 881-884.

Sloan, L.C. and Huber, M. (2001) Eocene oceanic responses on orbital forcing on precessional time scales. *Paleoceanography*, **16**, 101-111.

Sloan, L.C., Walker, J.C., Moore, T.C.Jr, Rea, D.K. and Zachos, J.C. (1992) Possible methane-induced polar warming in the early Eocene. *Nature*, **357**, 320-322.

Sloss, L.L. (1963) Sequences in the cratonic interior of North America. *Geological Society of America Bulletin*, **74**, 93-114.

Slujis, A., Bowen, G.J., Brinkhuis, H., Lourens, L.J. and Thomas, E. (2007). The Palaeocene-Eocene Thermal Maximum super greenhouse: biotic and geochemical signatures, age models and mechanisms of global change. *In*: Williams, M., Haywood, A.M., Gregory, F.J. and Schmidt, D.N. (eds) Deep-time perspectives on climate change: Marrying the signal from computer models and biological proxies. *Geological Society of London*, 323-349.

Sluijs, A., Schouten, S., Donders, T.H., Schoon. P.L., Röhl, U., Reichart, G.J., Sangiorgi, F., Kim, J.H., Sinninghe Damsté, J.S. and Brinkhuis, H. (2009) Warm and wet conditions in the Arctic region during Eocene Thermal Maximum 2. *Nature Geoscience*, **2**, 777-780.

Sømme, T.O., Helland-Hansen W. and Granjeon D. (2009) Impact of eustatic amplitude variations on shelf morphology, sediment dispersal, and sequence stratigraphic interpretation: Icehouse versus greenhouse systems. *Geology*, **37**, 587-590.

Sosdian, S. and Rosenthal, Y. (2009) Deep-sea temperature and ice volume changes across the Pliocene-Pleistocene climate transitions. *Science*, **325**, 306-310.

Souquet, P. (1988) Evolución del margen noribérico en los Pirineos durante el Mesozoico. *Revista de la Sociedad Geológica de España*, **1**, 349-356.

Souriau, A., Chevrot, S. and Olivera, C. (2008) A new tomographic image of the Pyrenean lithosphere from teleseismic data. *Tectonophysics*, **460**, 206-214.

Srivastava, S.P., Roest, W.R., Kovacs, L.C., Oakey, G., Lévesque, S., Verhoef, J. and Macnab, R. (1990a) Motion of Iberia since the Late Jurassic: results from detailed aeromagnetic measurements in the Newfoundland basin. *Tectonophysics*, **184**, 229-260.

Srivastava, S.P., Schouten, H., Roest, W.R., Klitgord, K.D., Kovacs, L.C., Verhoef, J. and Macnab, R. (1990b) Iberian plate kinematics: a jumping plate boundary between Eurasia and Africa. *Nature*, **344**, 756-759.

Srivastava, S., Sibuet, J.-C., Cande, S., Roest, W.R. and Reid, I.R. (2000) Magnetic evidence for slow seafloor spreading during the formation of the Newfoundland and Iberian margins. *Earth and Planetary Science Letters*, **182**, 61-76.

St John, K. (2008) Cenozoic ice-rafting history of the central Arctic Ocean: terrigenous sands of the Lomonosov Ridge. *Paleoceanography*, **23**, 1-12.

Stap, L., Lourens, L.J., Thomas, E., Sluijs, A., Bohaty, S. and Zachos, J.C. (2010) High-resolution deep-sea carbon and oxygen isotope records of Eocene Thermal Maximum 2 and H2. *Geology*, **38**, 607-610.

Steckler, M.S. and Watts, A.B. (1978) Subsidence of the Atlantic-type continental margin off New York. *Earth and Planetary Science Letters*, **41**, 1-13.

Stein, R., ten Haven, H.L., Littke, R., Rullkötter, J. and Welte, H. (1989) Accumulation of marine and terrigenous organic carbon at upwelling site 658 and non upwelling sites 657 and 659: implications for the reconstruction of paleoenvironments in the eastern subtropical Atlantic through late Cenozoic times. *In*: Ruddiman, W., Sarnthein, M., Baldauf, J., Backmann, J., Bloemendal, J., Curry, W., Farrimond, P., Faugeres, J.C., Janecek, T.R., Katsura, Y., Manivit, H., Mazzullo, J., Mienert, J., Pokras, E.M., Raymo, M.E., Schultheiss, P.J., Steinn, R., Tauxe, L., Valet, J.P., Weaver, P. and Yasuda, H. (eds) *Proceedings of the Ocean Drilling Program, Scientific Results*, **108**, 361-385. Texas, College Station: Ocean Drilling Program.

Stickley, C.E., Brinkhuis, H., Schellenberg, S.A., Sluijs, A., Röhl, U., Fuller, M., Grauert, M., Huber, M., Warnaar, J. and Williams, G.L. (2004) Timing and nature of the deepening of the Tasmanian Gateway. *Paleoceanography*, **19**, PA4027, DOI:10.1029/2004PA001022.

Stickley, C.E., St John, K., Koc, N., Jordan, R.W. Passchier, S., Pearce, R.B. and Kearns, L.E. (2009) Evidence for middle Eocene Arctic sea ice from diatoms and ice-rafted debris. *Nature*, **460**, 376-379.

Stocchi, S. (1992) Guaso system. *In*: Mutti, E. and Davoli, G. (eds) Turbidite sandstones, Milan, Istituto di Geologia, Universita di Parma and Agip, 123-129.

Stocchi, S., Cavalli, C., and Baruffini, L. (1992) The Guaso (south-central Pyrenees), Gremiasco and Castagnola (eastern sector of Tertiary Piedmont basin) turbidite deposits: Geometry and detailed correlation pattern. *Atti Ticensi di Scienze della Terra*, **35**, 153-177.

Stow, D.A.V. and Tabrez, A.R. (1998) Hemipelagites: processes, facies and model. *In*: Stoker, M.S., Evans, D. and Cramp, A. (eds) Geological processes on continental margins. *Geological Society of London, Special Publication*, **129**, 317-337. Oxford: Blackwell Scientific.

Straub, K.M., Paola, C., Mohrig, D., Wolinski, M.A. and George, T. (2009) Compensational stacking of channelized sedimentary deposits. *Journal of Sedimentary Research*, **79**, 673-688.

Stüben, D., Kramar, U., Berner, Z.A., Meudt, M., Keller, G., Abramovich, S., Adatte, T., Hambach, U. and Stinnesbeck, W. (2003) Late Maastrichtian paleoclimatic and paleoceanographic changes inferred from Sr/Ca ratio and stable isotopes. *Palaeogeography, Palaeoclimatology, Palaeoecology*, **199**, 107-127.

Sudom, M.D. and Arnaud, R.J. ST. (1971) Use of quartz, zirconium and titanium as indices in pedological studies. *Canadian Journal of Soil Science*, **51**, 385-396.

Sutcliffe, C. and Pickering, K.T. (2009) End-signature of deep-marine basin-fill, as a structurally confined low-gradient clastic slope: The middle Eocene Guaso system, south-central Spanish Pyrenees. *Sedimentology*, **56**, 1670-1689.

Svendsen, J.B. and Hartley, N.R. (2001) Comparison between outcrop spectral gamma ray logging and whole rock geochemistry: implications for quantitative reservoir characterisation in continental sequences. *Marine and Petroleum Geology*, **18**, 657-670.

Tachikawa, K., Cartapanis, O., Vidal, L., Beaufort, L., Barlyaeva, T. and Bard, E. (2011) The precession phase of hydrological variability in the western pacific warm pool during the past 400ka. *Quaternary Science Reviews*, **30**, 3716-3727.

Tavani, S., Storti, F., Fernández, O., Muñoz, J.A. and Salvini, F. (2006) 3-D deformation pattern analysis and evolution of the Añisclo anticline, southern Pyrenees. *Journal of Structural Geology*, **28**, 695-712.

Teixell, A. (1996) The Ansó transect of the southern Pyrenees: basement and cover thrust geometries. *Journal of the Geological Society*, **153**, 301-310.

Teixell, A. (1998) Crustal structure and orogenic material budget in the west central Pyrenees. *Tectonics*, **17**, 395-406.

Tesauro, M., Kaban, M.K. and Cloetingh, S.A.P.L. (2009) A new thermal and rheological model of the European lithosphere. *Tectonophysics*, **476**, 478-495.

Thomas, D.J., Zachos, J.C. and Bralower, T.J. (2001) Deep-sea environments on a warm Earth: Latest Palaeocene-early Eocene. *In*: Huber, B.T., MacLeod, K.G. and Wing, S.L. (eds) Warm climates in Earth History, Cambridge University Press, New York, 132-160.

Thomas, D.J., Zachos, J.C., Bralower, T.J., Thomas, E. and Bohaty, S. (2002) Warming the fuel for the fire: evidence for the thermal dissociation of methane hydrate during the Paleocene-Eocene thermal maximum. *Geology*, **30**, 1067-1070.

Thompson, L.G., Davis, M.E., Mosley-Thompson, E., Lin, P.-N., Henderson, K.A. and Mashiotta, T.A. (2005) Tropical ice core records: evidence for asynchronous glaciation on Milankovitch timescales. *Journal of Quaternary Science*, **20**, 723-733.

Thomson, D.J. (1982) Spectrum estimation and harmonic analysis. *Proceedings of the IEEE, **70***, 1055-1096.

Tiedemann, R. and Franz, S.O. (1997) Deep-water circulation chemistry and terrigenous sediment supply in the equatorial Atlantic during the Pliocene, 3.3-2.6 Ma and 5-4.5 Ma. *In*: Shackleton, N.J., Curry, W.B., Richter, C. and Brawlower, T.J. (eds) *Proceedings of the Ocean Drilling Program: Scientific Results*, **154**, 299-318.

Tiedemann, R., Sarnthein, M. and Shackleton, N.J. (1994) Astronomical timescale for the Pliocene Atlantic $\delta^{18}O$ and dust flux records of Ocean Drilling Program site 659. *Paleoceanography*, **9**, 619-638.

Tjalsma, R.C. and Lohmann, G.P. (1983) Paleocene-Eocene bathyal and abyssal benthic Foraminifera from the Atlantic Ocean. *Micropaleontology Special Publications*, **4**, 1-90.

Torrence, C. and Compo, G.P. (1998) A practical guide to wavelet analysis. *Bulletin of the American Meteorological Society*, **79**, 61-78.

Torsvik, T.H., Müller, R.D., Van der Voo, R., Steinberger, B. and Gaina, C. (2008) Global plate motion frames: toward an unified model. *Reviews of geophysics*, **46**, 1-44.

Toucanne, S., Zaragosi, S., Bourillet, J.F., Gibbard, P.L., Eynaud, F., Giraudeau, J.L., Turon, M., Cremer, E., Martinez, P. and Rossignol, L. (2009) A 1.2 Ma record of glaciation and fluvial discharge from the West European Atlantic margin. *Quaternary Science Reviews*, **28**, 25-26.

Toucanne, S., Zaragosi, S., Bourillet, J.-F., Dennielou, B., Jorry, S.J., Jouet, G. and Cremer, M. (2012) External controls on turbidite sedimentation on the glacially-influenced Armorican margin (Bay of Biscay, western European margin). *Marine Geology*, **303-306**, 137-153.

Trenberth, E.K. and Caron, J.M. (2001) Estimates of meridional atmosphere and ocean heat transports. *Journal of Climate*, **14**, 3433-3443.

Tripati, A., Backman, J., Elderfield, H. and Ferretti, P. (2005) Eocene bipolar glaciation associated with global carbon cycle changes. *Nature*, **436**, 341-346.

Tripati, A.K., Eagle, R.A., Morton, A., Dowdeswell, J.A., Atkinson, K.L., Bahé, Y., Dawber, C.F., Khadun, E., Shaw, R.M.H., Shorttle, O. and Thanabalasundaram, L. (2008) Evidence for glaciation in the Northern Hemisphere back to 44 Ma from ice-rafted debris in the Greenland Sea. *Earth and Planetary Science Letters*, **265**, 112-122.

Underwood, M.B., Moore, G.F., Taira, A., Klaus, A., Wilson, M.E.J., Fergusson, C.L., Hirano, S., Steurer, J., Becker,K., Becker, L., Boeckel, B., Cragg, B., Dean, A., Henry, P., Hisamitsu, T., Hunze, S., Kastner, M., Maltman, A., Morgan, J., Murakami, Y., Saffer, D., Sanchez-Gomez, M., Screaton, E., Smith, D., Spivak, A., Tobin, H. and Ujiie, K. (2003) Sedimentary and tectonic evolution of a trench-slope basin in the Nankai subduction zone of Southwest Japan. *Journal of sedimentary Research*, **73**, 589-602.

Utescher, T. and Mosbrugger, V. (2007) Eocene vegetation patterns reconstructed from plant diversity-A global perspective. *Palaeogeography, Palaeoclimatology, Palaeoecology*, **247**, 243-271.

Vail, P.R., Mitchum Jr., R.M. and Thompson, S. (1977) Seismic stratigraphy and global changes of sea level. Part 4. Global cycles of relative changes of sea level. *American Association of Petroleum Geologists Memoir*, **26**, 83-89.

Vakarelov, B.K., Bhattacharya J.P and Nebrigic, D.D. (2006) Importance of high-frequency tectonic sequences during greenhouse times of Earth history. *Geology*, **34**, 797-800.

Van Andel, T.H. (1975) Mesozoic/Cenozoic calcite compensation depth and global distribution of calcareous sediments. *Earth and Planetary Science Letters*, **26**, 187-194.

Van Buchem, F.S.P. and McCave, I.N. (1989) Cyclic sedimentation patterns in Lower Lias mudstones of Yorkshire (GB). *Terra Nova*, **1**, 461-467.

Van Buchem, F.S.P., Melynk, D.H. and McCave, I.N. (1992) Chemical cyclicity and correlation of Lower Lias mudstones using gamma ray logs. *Journal of the Geological Society of London*, **149**, 991-1002.

Van der Voo, R. and Zijderveld, J.D.A. (1971) Renewed paleomagnetic study of the Lisbon volcanics and implications for the rotation of the Iberian Peninsula. *Journal of Geophysical Research*, **76**, 3913-3921.

Van der Voo, R. and Boessenkool, A. (1973) Permian paleomagnetic results from the Western Pyrenees delineating the plate boundary between the Iberian Peninsula and stable Europe. *Journal of Geophysical Research*, **78**, 5118-5127.

Van der Zwan, C.J. (2002) The impact of Milankovitch-scale climatic forcing on sediment supply. *Sedimentary geology*, **147**, 271-294.

Van Hesit, M.W.I.M. (2000) Quantitative analogue experimental sequence stratigraphy Faculteit Aardwetenschappen, Universiteit Utrecht. *Geologica Ultraiectina*, **198**, 1-144.

Van Lunsen, H.A. (1970) Geology of the Ara-Cinca Region, Spanish Pyrenees, Province of Huesca. PhD Thesis, Utrecht University.

Vautard, R., Yiou, P. and Ghil, M. (1992) Singular-spectrum analysis: A toolkit for short, noisy chaotic signals. *Physica D: Non-linear Phenomena*, **58**, 95-126.

Vergés, J. and Muñoz, J.A. (1990) Thrust sequences in the southern central Pyrenees. *Bulletin de la Societé Géologique de France*, **8**, 265-271.

Vergés, J. and García Senz, J.M. (2001) Mesozoic Evolution and Cenozoic Inversion of the Pyrenean Rift. *In*: Ziegler, P.A., Cavazza, W., Robertson, A.H.F. and Crasquin-Soleau, S. (eds) Peri-Tethys Memoir 6: Pery-Tethyan Rift/Wrench Basins and Passive Margins. *Mémoires Muséum National d'Histore Naturelle*, **186**, 187-212.

Vergés, J., Millán, H., Roca, E., Muñoz, J.A. and Marzo, M. (1995) Eastern Pyrenees and related foreland basins: pre-, syn- and post-collisional crystal scale cross-sections. *Marine and Petroleum Geology*, **12**, 893-915.

Vergés, J., Fernández, M. and Martínez, A. (2002) The Pyrenean orogen; pre-, syn-, and postcollisional evolution. *Journal of the Virtual Explorer*, **8**, 57-76.

Verosub, K.L. (1977) Depositional and post-depositional processes in the magnetization of sediments. *Reviews of geophysics*, **15**, 129-143.

Vielzeuf, D. and Kornprobst, J. (1983) Crustal splitting and the emplacement of Pyrenean lherzolites and granulites. *Earth Planetary and Science Letters*, **67**, 87-96.

Vimeux, F., Masson, V., Jouzel, J., Stievenard, M. and Petit, J.R. (1999) Glacial-interglacial changes in ocean surface conditions in the Southern Hemisphere. *Nature*, **398**, 410-413.

Vissers, R.L.M. (1992) Variscan extension in the Pyrenees. *Tectonics*, **11**, 1369-1384.

Vissers, R.L.M. and Meijer, P.T. (2012) Iberian plate kinematics and Alpine collision in the Pyrenees. *Earth-Science reviews*, **114**, 61-83.

Von Rad, U. and Tahir, M. (1997) Late Quaternary sedimentation on the outer Indus shelf and slope (Pakistan): evidence from high-resolution seismic data and coring. *Marine Geology*, **138**, 193-236.

Vonhof, H.B., Smit, J., Brinkhuis, H., Montanari, A. and Nederbragt, A.J. (2000) Global cooling accelerated by early late Eocene impacts? *Geology*, **28**, 687-690.

Vött, A. (2007) Relative sea level changes and regional tectonic evolution of seven coastal areas in NW Greece since the mid-Holocene. *Quaternary Sciences Reviews*, **26**, 894-919.

Wade, B.S. and Pearson, P.N. (2008) Planktonic foraminiferal turnover, diversity fluctuations and geochemical signals across the Eocene/Oligocene boundary in Tanzania. Marine *Micropaleontology*, **11**, 157-170.

Walker, M. (2005) Quatrnary dating methods. Wiley, London, pp 201.

Walker, J.C.G., Hays, P.B. and Kasting, J.F. (1981) A negative feedback mechanism for the long term stabilization of Earth's surface-temperature. *Journal of Geophysical Research. Oceans and Atmosphere*, **86**, 9776-9782.

Walsh, J.J., Nicol, A. and Childs, C. (2002) An alternative model for the growth of faults. *Journal of Structural Geology*, **24**, 1669-1675.

Wang, Y., Cheng, H., Edwards, R.L., An, Z.S., Wu, J., Shen, C.C. and Dorale, J.A. (2001) A high-resolution absolute-dated Late Pleistocene monsoon record from Hulu Cave, China. *Science*, **294**, 2345-2348.

Wang, Y., Cheng, H., Edwards, R.L., Kong, X., Shao, X., Chen, S., Wu, J, Jiang, X., Wang, X. and An, Z. (2008) Millenial- and orbital-scale changes in the Asian monsoon over the past 224,000 years. *Nature*, **451**, 1090-1093.

Waseda, A., Didyk, B.M. and Kajiwara, Y. (1995) Carbon isotope compositions of organic matter from the Chile continental margin. *In*: Behrmann, S.D., Musgrave, R.J. and Cande, S.C. (eds*), Proceedings of the Ocean Drilling Program, Scientific Results*, **141**, 299-305. Texas, College Station: Ocean Drilling Program.

Watts, A.B. and Thorne, J. (1984) Tectonics, global changes in sea level and their relationship to stratigraphical sequences at the US Atlantic continental margin. *Marine and Petroleum Geology*, **1**, 319-339.

Weber, M.E., Wiedicke, M.H., Kudrass, H.R., Hübscher, C. and Erlenkeuser, H. (1997) Active growth of the Bengal Fan during sea-level rise and highstand: *Geology*, **25**, 315-318.

Weedon, G. (1989) The detection and illustration of regular sedimentary cycles using the Walsh power spectra and filtering, with examples from the Lias of Switzerland. *Journal of the Geological Society London*, **146**, 133-144.

Weedon, G.P. (2005) Time-series analysis and cyclostratigraphy (examining stratigraphic records of environmental cycles). Cambridge University Press, 81-214.

Weedon, G.P., Shackleton, N.J. and Pearson, P.N. (1997). The Oligocene timescale and cyclostratigraphy on the Ceara Rise, western equatorian Atlantic. *Proceedings of the Ocean Drilling Program Scientific Results*, **154**, 101-104.

Weedon, G.P., Coe, A.L. and Gallois, R.W. (2004) Cyclostratigraphy, orbital tuning and inferred productivity for the type kimmeridge clay (Late Jurassic), Southern England. *Journal of the Geological Society*, **161**, 655-666.

Weimer, P. (1990) Sequence stratigraphy, facies geometries, and depositional history of the Mississippi Fan, Gulf of Mexico. *American Association of Petroleum Geologists Bulletin,* **74**, 425-453.

Welch, P.D. (1967) The use of the fast Fourier transform for the estimation of power spectra: A method based on time averaging over short, modified periodograms. *IEEE Transactions on Audio and Electroacoustics*, **15**, 70-73.

Weltje, G.J. and de Boer, P.L. (1993) Astronomically induced palaeoclimatic oscillations reflected in Pliocene turbidite deposits on Corfu (Greece): implications for the interpretation of higher order cyclicity in fossil turbidite systems. *Geology*, **21**, 307-310.

Weltje, G.J., Van Ansenwoude, S.O.K.J. and De Boer, P.L. (1996) High-frequency detrital signals in Eocene fan-delta sandstones of mixed parentage (South-Central Pyrenees, Spain): a reconstruction of chemical weathering in transit. *Journal of Sedimentary Research*, **66**, 119-131.

Wentworth, C.K. (1922) A Scale of Grade and Class Terms for Clastic Sediments. *The journal of Geology*, **30**, 377-392.

Werne, J.P., Hollander, D.J., Lyons, T.W. and Peterson, L.C. (2000) Climate-induced variations in productivity and planktonic ecosystem structure from the Younger Dryas to Holocene in the Cariaco Basin, Venezuela. *Paleoceanography*, **15**, 19-29.

Westerhold, T., Röhl, U., Pälike, H., Wilkens, R., Wilson, P.A. and Acton, G. (2013) Orbitally tuned time scale and astronomical forcing in the middle Eocene to early Oligocene, *Climate of the Past Discussions*, **9**, 6635-6682.

Westrich, J.T. and Berner, R.A. (1984) The role of sedimentary organic matter in bacterial sulphate reduction: the G model tested. *Limnology and Oceanography*, **29**, 236-249.

White, A.F. and Blum, A.E. (1995) Effects of climate on chemical weathering in watersheds. *Geochimica and Cosmochimica Acta,* **59**, 1729-1747.

Wigley, T.M.L. (1981) Climate and palaeoclimate: what can we learn about solar luminosity variations? *Solar Physics,* **74**, 435-471.

Wignall, P.B. and Myers, K.J. (1988) Interpreting benthic oxygen levels in mudrocks: a new approach. *Geology*, **16**, 452-455.

Wignall, P.B. and Twitchett, R.J. (1996) Ocean anoxia and the end-Permian mass extinction. *Science*, **272**, 1155-1158.

Williams, D.F., Thunell, R.C., Tappa, E., Domenico, R. and Raffi, I. (1988) Chronology of the Pleistocene oxygen isotope record: 0–1.88 m.y. B.P. *Palaeogeography, Palaeoclimatology, Palaeoecology*. **64**, 221-240.

Wilson, R.C.L., Manatschal, G. and Wise, S. (2001) Rifting along non-volcanic passive margins: Stratigraphic and seismic evidence from the Mesozoic successions of the Alps and western Iberia. *In*: Wilson, R.C.L., Whitmarsh, R.B., Froitzheim, N. and Taylor, B. (eds) Non-volcanic rifting of continental margins: a comparison of evidence from land and sea. *Geological Society Special Publication*, **197**, 429-452.

Wing, S.L., Alroy, J. and Hickey, L.J. (1995). Plant and mammal diversity in the Paleocene to early Eocene of the Bighorn Basin. *Palaeogeography, Palaeoclimatology, Palaeoecology*, **115**, 117-155.

Wing, S.L., Harrington, G.J., Smith, F.A., Bloch, J.I., Boyer, D.M. and Freeman, K.H. (2005) Transient floral change and rapid global warming at the Paleocene-Eocene boundary. *Science*, **310**, 993-996.

Winkler, W. and Gawenda, P. (1999) Distinguishing climatic and tectonic forcing of turbidite sedimentation, and the bearing on turbidite bed scaling: Palaeocene-Eocene of Northern Spain. *Journal of the Geological Society*, **156**, 791-800.

Wolfe, J.A. (1985) Distribution of major vegetational types during the Tertiary. *In*: Sundquist, E.T. and Broecker, W.S. (eds) The carbon cycle and atmospheric CO_2: Natural variations Archean to Present. *Geophysical Monograph*, **32**, 357-375.

Wolff, E.W., Fischer, H. and Röthlisberger, R. (2009) Glacial terminations as southern warmings without northern control. *Nature Geoscience*, **2**, 206-209.

Wu, H., Zhang, S., Feng, Q., Jiang, G., Li, H. and Yang, T (2012) Milankovitch and sub-Milankovitch cycles of the early Triassic Daye Formation, South China and their geochronological and paleoclimatic implications. *Gondwana Research*, **22**, 748-759.

Wunsch, C. (2000) On sharp spectral lines in the climate record and the millennial peak. *Paleoceanograph*y, **15**, 417-424.

Yapp, C.J. (2004) Fe (CO_3)OH in goethite from a mid-latitude North American oxisol: estimate of atmospheric CO_2 concentration in the Early Eocene "climatic optimum". *Geochimica and Cosmochimica Acta*, **68**, 935-947.

Yarincik, K.M., Murray, R.W. and Peterson, L.C. (2000) Climatically sensitive eolian and hemipelagic deposition in the Cariaco Basin, Venezuela, over the past 578,000 years: Results from Al/Ti and K/Al. *Palaeoceanography*, **15**, 210-228.

Zachos, J.C. and Kump, L.R. (2005) Carbon cycle feedbacks and the initiation of Antarctic glaciation in the earliest Oligocene. *Global and Planetary Change*, **47**, 51-66.

Zachos, J.C., Lohmann, K.C., Walker, J.C.G. and Sherwood, W.W. (1993) Abrupt climate change and transient climates during the Paleogene: A marine perspective. *The Journal of Geology*, **101**, 191-213.

Zachos, J.C., Stott, L.D. and Lohmann, K.C. (1994) Evolution of Early Cenozoic marine temperatures. *Paleoceanography*, **9**, 353-387.

Zachos, J.C., Quinn, T.M., and Salamy, K.A. (1996) High-resolution (104 years) deep-sea foraminiferal stable isotope records of the Eocene-Oligocene climate transition: *Paleoceanography*, **11**, 251-266.

Zachos, J., Pagani, M., Sloan, L., Thomas, E. and Billups, K. (2001a) Trends, rhythms, and aberrations in global climate 65 Ma to present. *Science*, **292**, 689-693.

Zachos, J.C., Shackleton, N.J., Revenaugh, J.S., Palike, H., and Flower, B.P. (2001b) Climate response to orbital forcing across the Oligocene-Miocene boundary. *Science*, **292**, 274-278.

Zachos, J.C., Rohl, U., Schellenberg, S.A., Sluijs, A., Hodell, D.A., Kelly, D.C., Thomas, E., Nicolo, M., Raffi, I., Lourens, L.J., McCarren, H. and Kroon, D. (2005) Rapid acidification of the ocean during the Paleocene–Eocene thermal maximum. *Science*, **308**, 1611-1615.

Zachos, J.C., Schouten, S., Bohaty, S., Sluijs, A., Brinkhuis, H., Gibbs, S., Bralower, T. and Quattlebaum.T. (2006) Extreme warming of mid-latitude coastal ocean during the Paleocene-Eocene Thermal Maximum: Inferences from TEX86 and Isotope Data. *Geology*, **34**,737-740.

Zachos, J.C., Dickens, G.R. and Zeebe, R.E. (2008) An early Cenozoic perspective on greenhouse warming and carbon-cycle dynamics. *Nature*, **451**, 279-283.

Zanazzi, A., Kohn, M.J., MacFadden, B.J. and Terry Jr, D.O. (2007) Large temperature drop across the Eocene-Oligocene transition in central North America. *Nature*, **445**, 639-642.

Zhang, Z.-S., Yan, Q. and Wang, H.-J. (2010) Has the Drake Passage Played an Essential Role in the Cenozoic Cooling? *Atmospheric and oceanic science letters*, **3**, 288-292.

Zidjerveld, J.D.A. (1967) The N.R.M. of the Exeter volcanic traps (Permian, Europe). *Tectonophysics*, **4**, 121-153.

APPENDICES

Table of appendices

Appendix 3	Electronic versions of the sedimentary logs	CD
Appendix 4	Magnetostratigraphy data table	CD
Appendix 5	XRF A6 core and spectral gamma-ray data documents	CD
Appendix 6	Cantalejo, B. and Pickering, K.T. (2014) Climate forcing of fine-grained deep-marine system in an active tectonic setting: Middle Eocene, Ainsa Basin, Spanish Pyrenees. *Palaeogeography, Palaeoclimatology, Palaeoecology*, **410**, 351-371.	CD

Tierrantona map **APPENDIX 1**

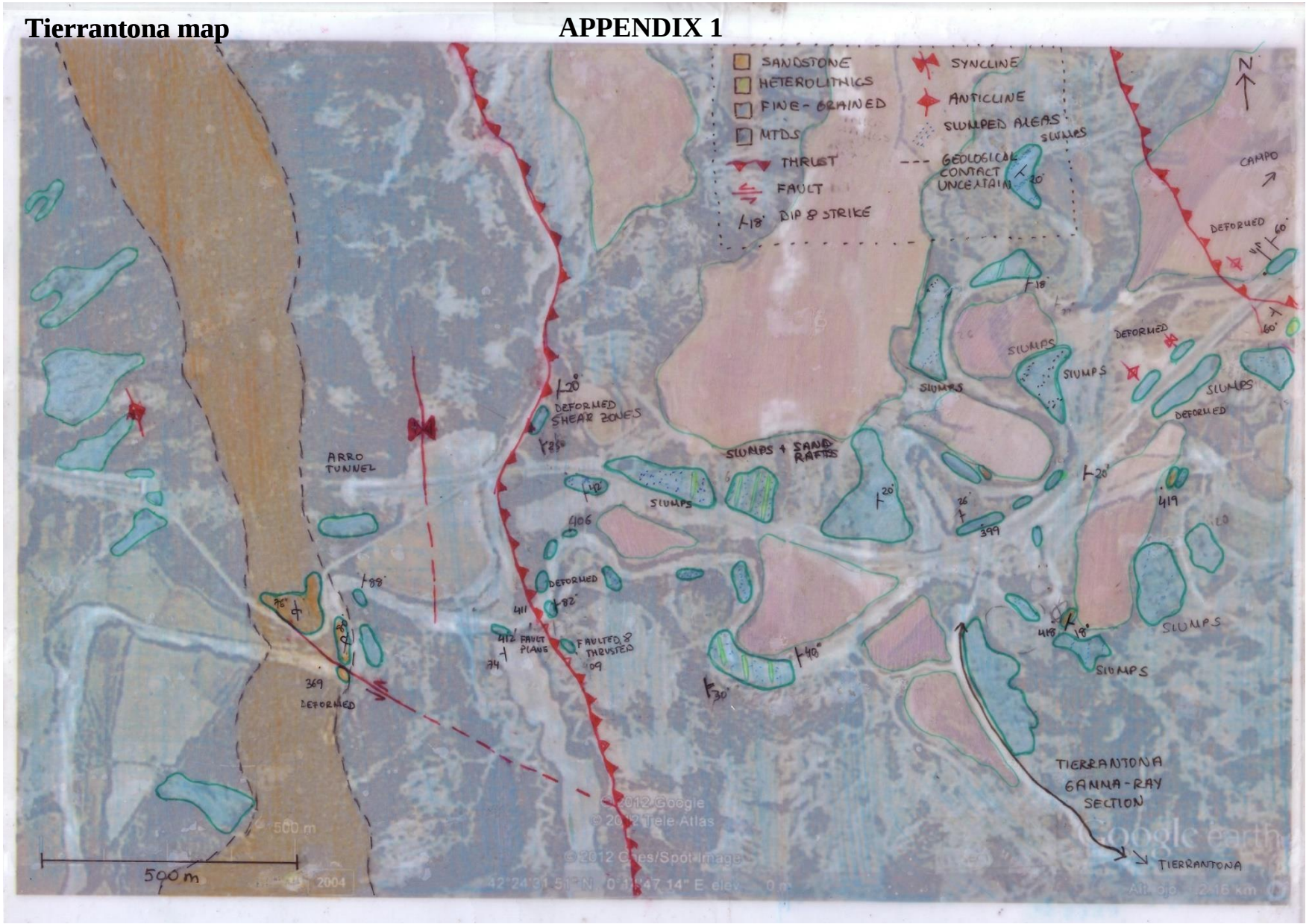

Gerbe map

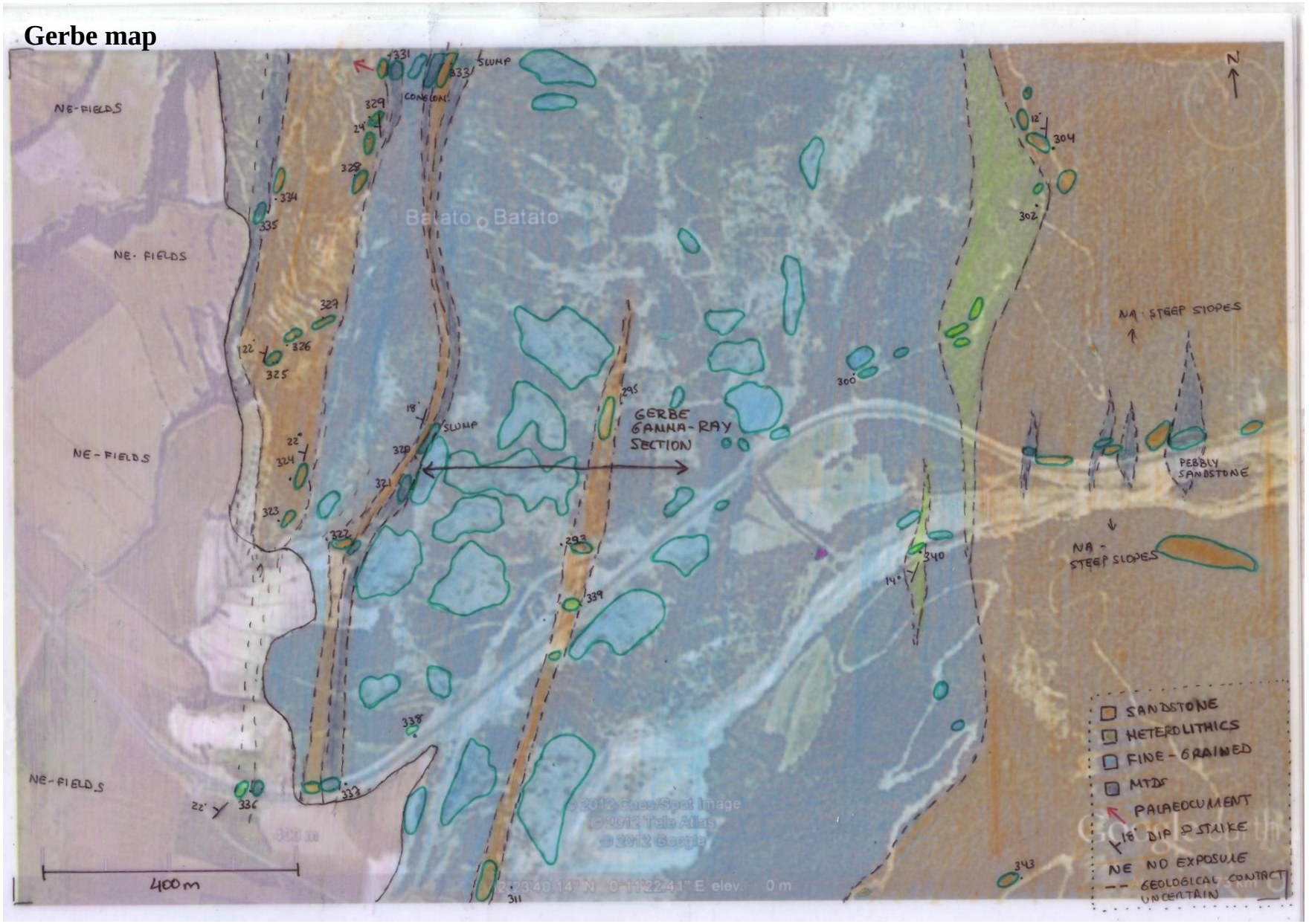
NE-FIELDS
NE- FIELDS
NE-FIELDS
NE-FIELDS
CONGLOM.
SLUMP
SLUMP
GERBE GANNA-RAY SECTION
NA - STEEP SLOPES
NA - STEEP SLOPES
PEBBLY SANDSTONE
N
400 m
SANDSTONE
HETEROLITHICS
FINE-GRAINED
MTDS
PALAEOCURRENT
DIP & STRIKE
NE NO EXPOSURE
GEOLOGICAL CONTACT UNCERTAIN

Labuerda map

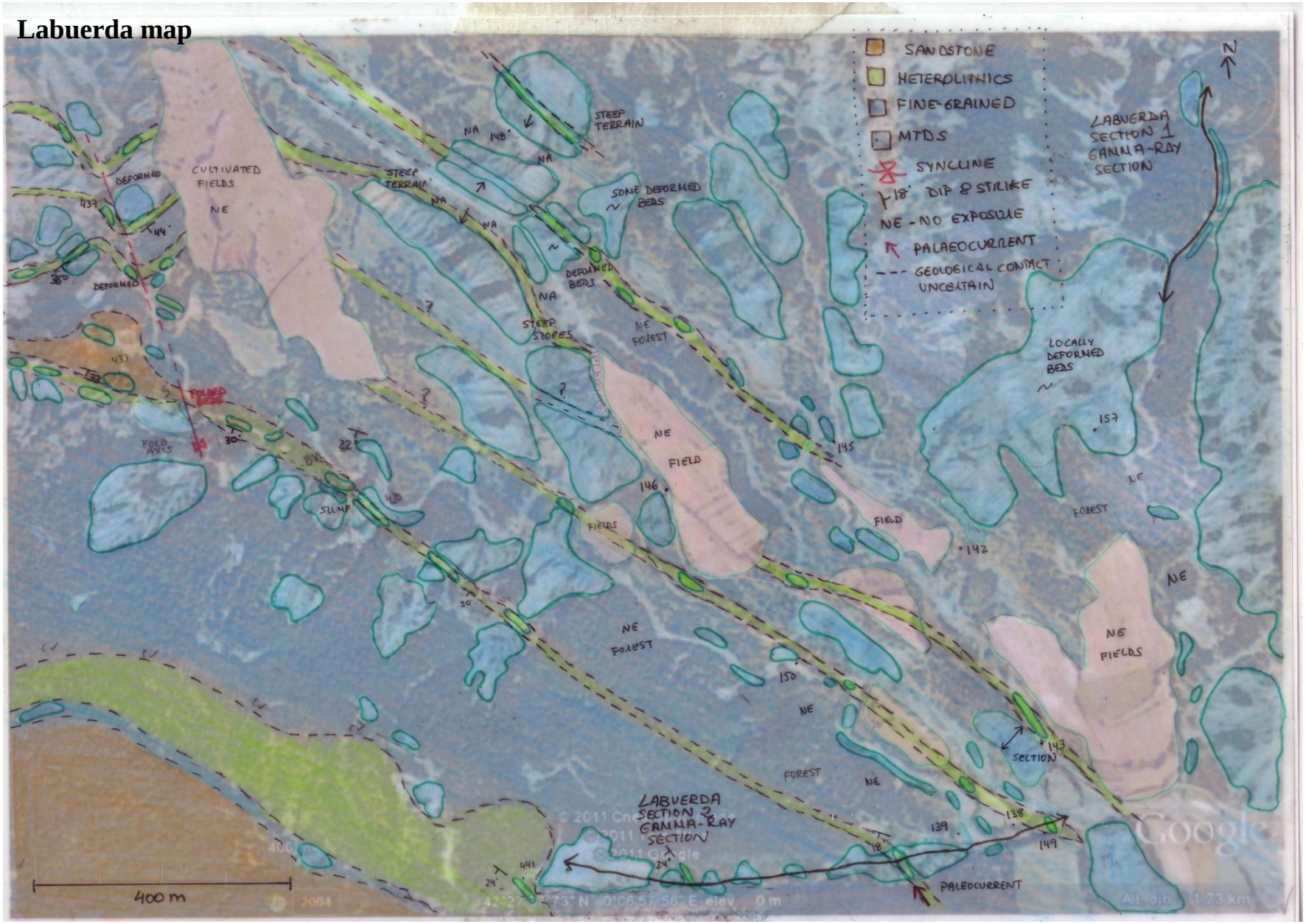

Boltaña map

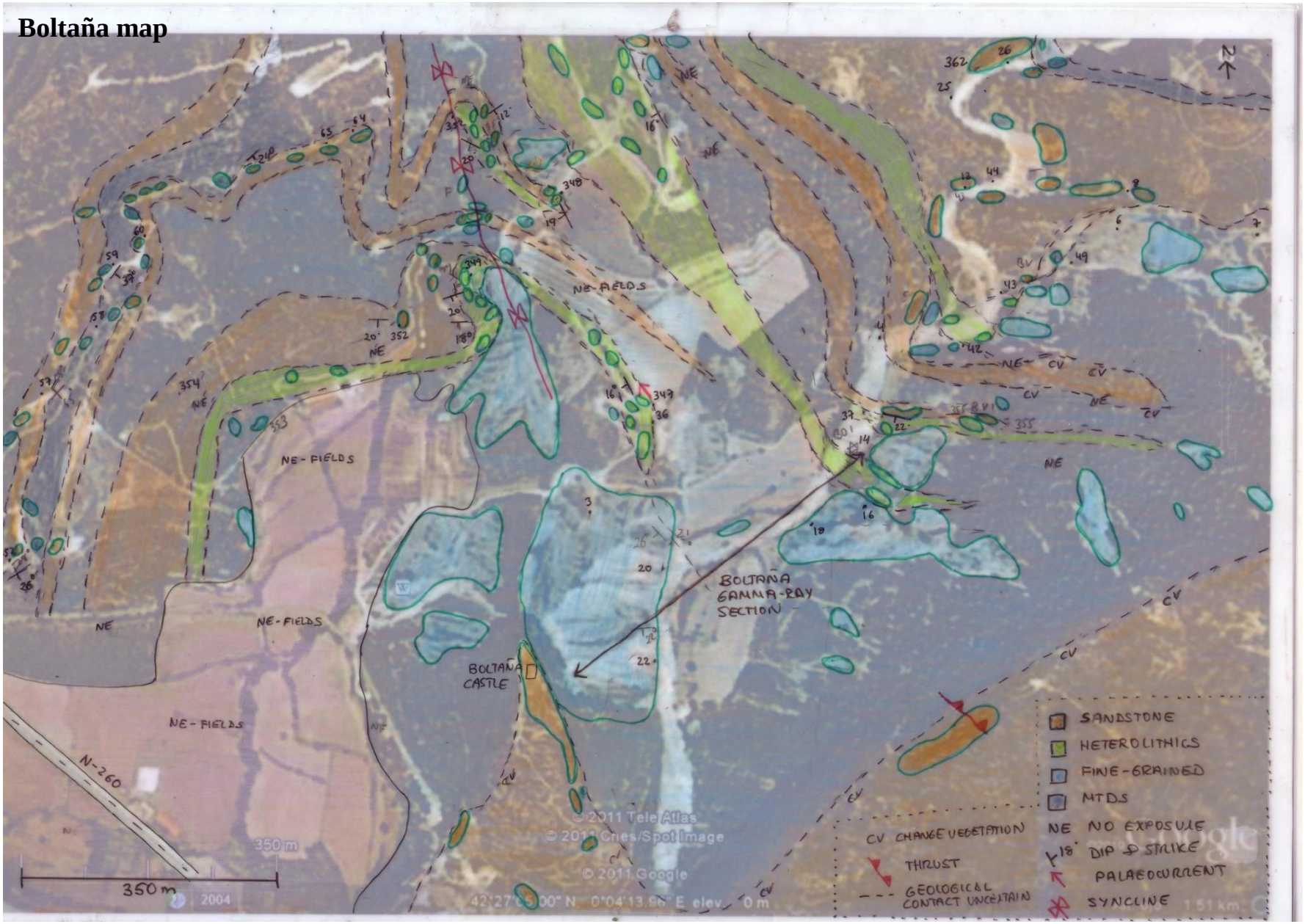
NE-FIELDS
BOLTAÑA GAMMA-RAY SECTION
BOLTAÑA CASTLE
N-260
350 m
SANDSTONE
HETEROLITHICS
FINE-GRAINED
MTDS
NE NO EXPOSURE
DIP & STRIKE
PALAEOCURRENT
SYNCLINE
CV CHANGE VEGETATION
THRUST
GEOLOGICAL CONTACT UNCERTAIN
© 2011 Tele Atlas
© 2011 Google

Forcaz map

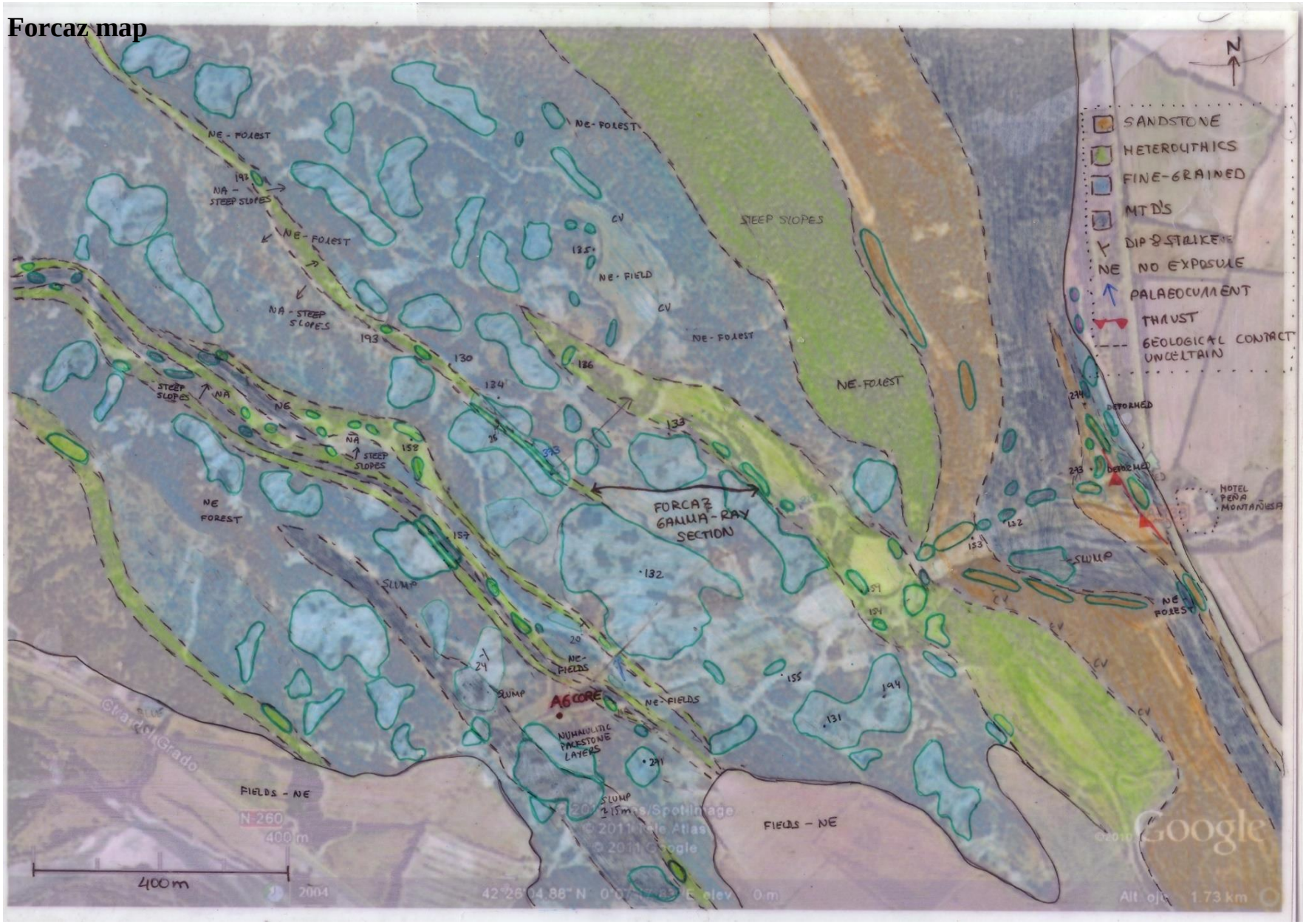
N
SANDSTONE
HETEROLITHICS
FINE-GRAINED
MTD'S
DIP & STRIKE
NE NO EXPOSURE
PALAEOCURRENT
THRUST
GEOLOGICAL CONTACT UNCERTAIN
NE-FOREST
NA - STEEP SLOPES
NE-FIELD
STEEP SLOPES
FORCAZ GAMMA-RAY SECTION
DEFORMED
HOTEL PEÑA MONTAÑESA
SLUMP
A6 CORE
NUMMULITIC PACKESTONE LAYERS
FIELDS - NE
400m
Google

Morillo map

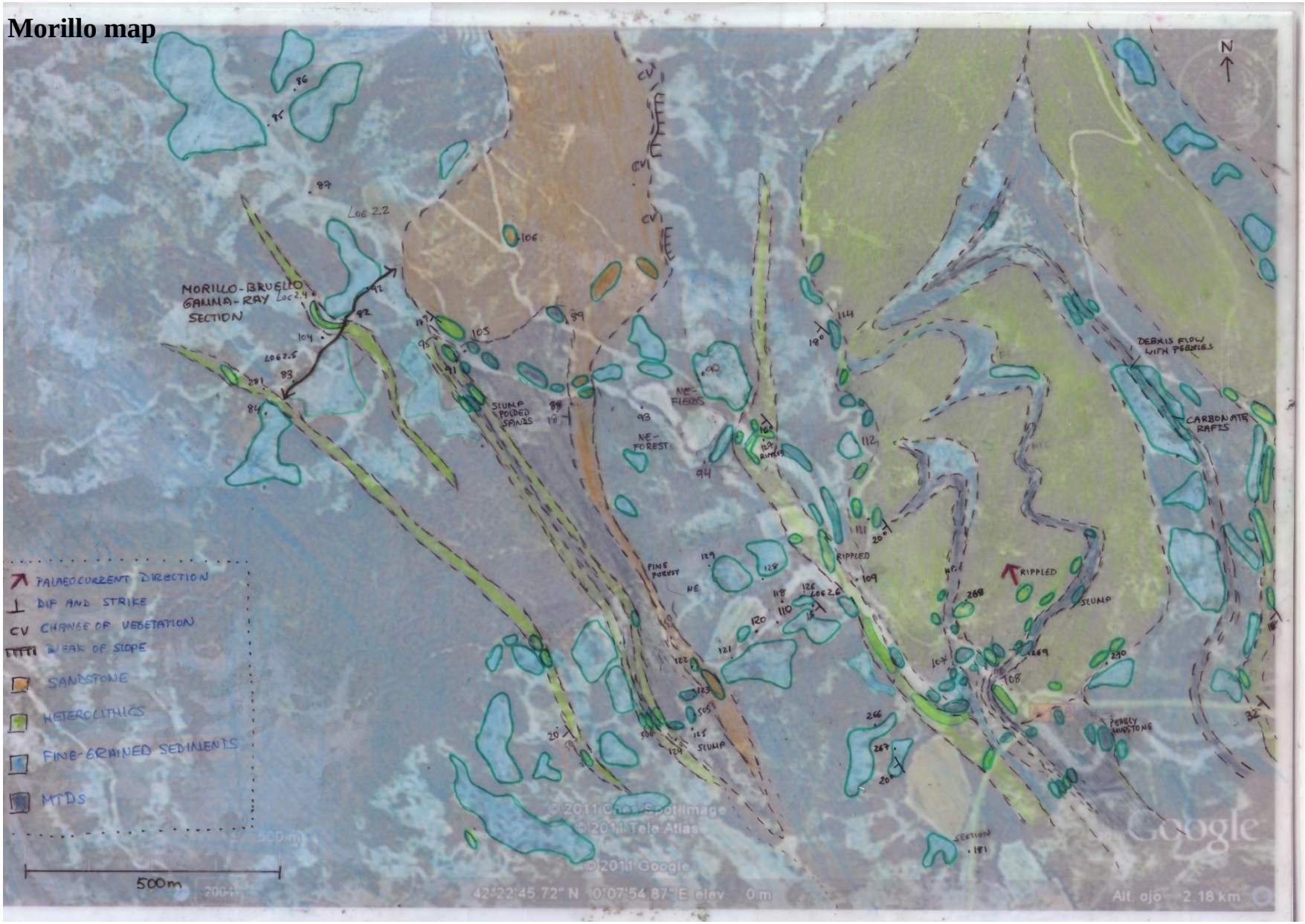
MORILLO-BRUELLO GAMMA-RAY SECTION
Log 2.2
Log 2.4
Log 2.5
Log 2.6
PALAEOCURRENT DIRECTION
DIP AND STRIKE
CV CHANGE OF VEGETATION
BREAK OF SLOPE
SANDSTONE
HETEROLITHICS
FINE-GRAINED SEDIMENTS
MTDS
500m
STUMP FOLDED SANDS
NE-FIELDS
NE-FOREST
FINE FOREST
RIPPLED
DEBRIS FLOW WITH PEBBLES
CARBONATE RAFTS
PEBBLY MUDSTONE
SECTION
N
©2011 Google
42°22'45.72" N 0°07'54.87" E elev 0 m
Alt ojo 2.18 km

Guaso map

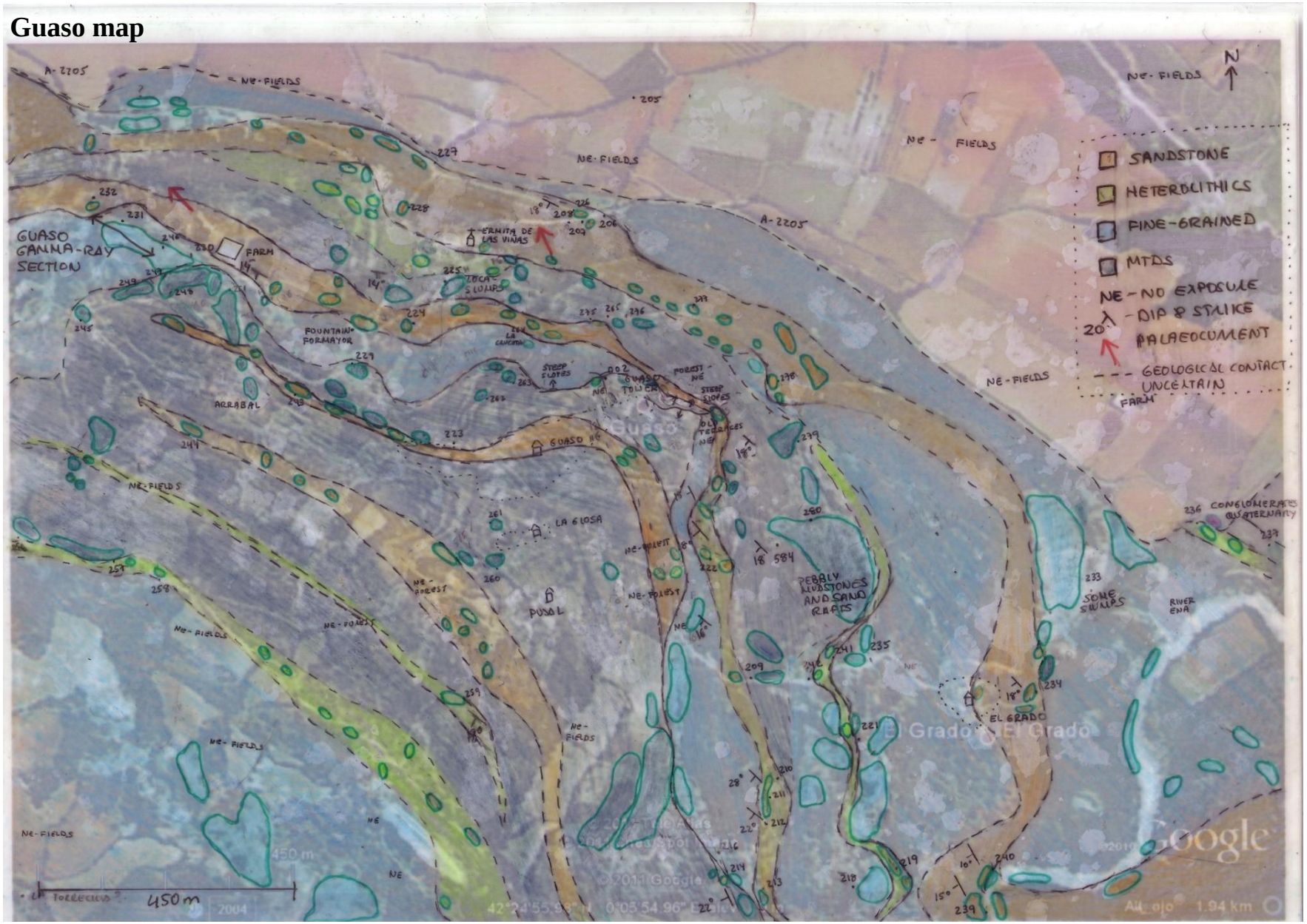
GUASO GAMMA-RAY SECTION
SANDSTONE
HETEROLITHICS
FINE-GRAINED
MTDS
NE - NO EXPOSURE
20 - DIP & STRIKE
PALAEOCURRENT
GEOLOGICAL CONTACT UNCERTAIN
NE-FIELDS
FARM
ERMITA DE LAS VIÑAS
FOUNTAIN FORMATION
ARRABAL
GUASO
LA GLOSA
PUYAL
EL GRADO
PEBBLY MUDSTONES AND SANDSTONES
CONGLOMERATES QUATERNARY
RIVER ENA
STEEP SLOPES
FOREST NE
450 m

APPENDIX 2

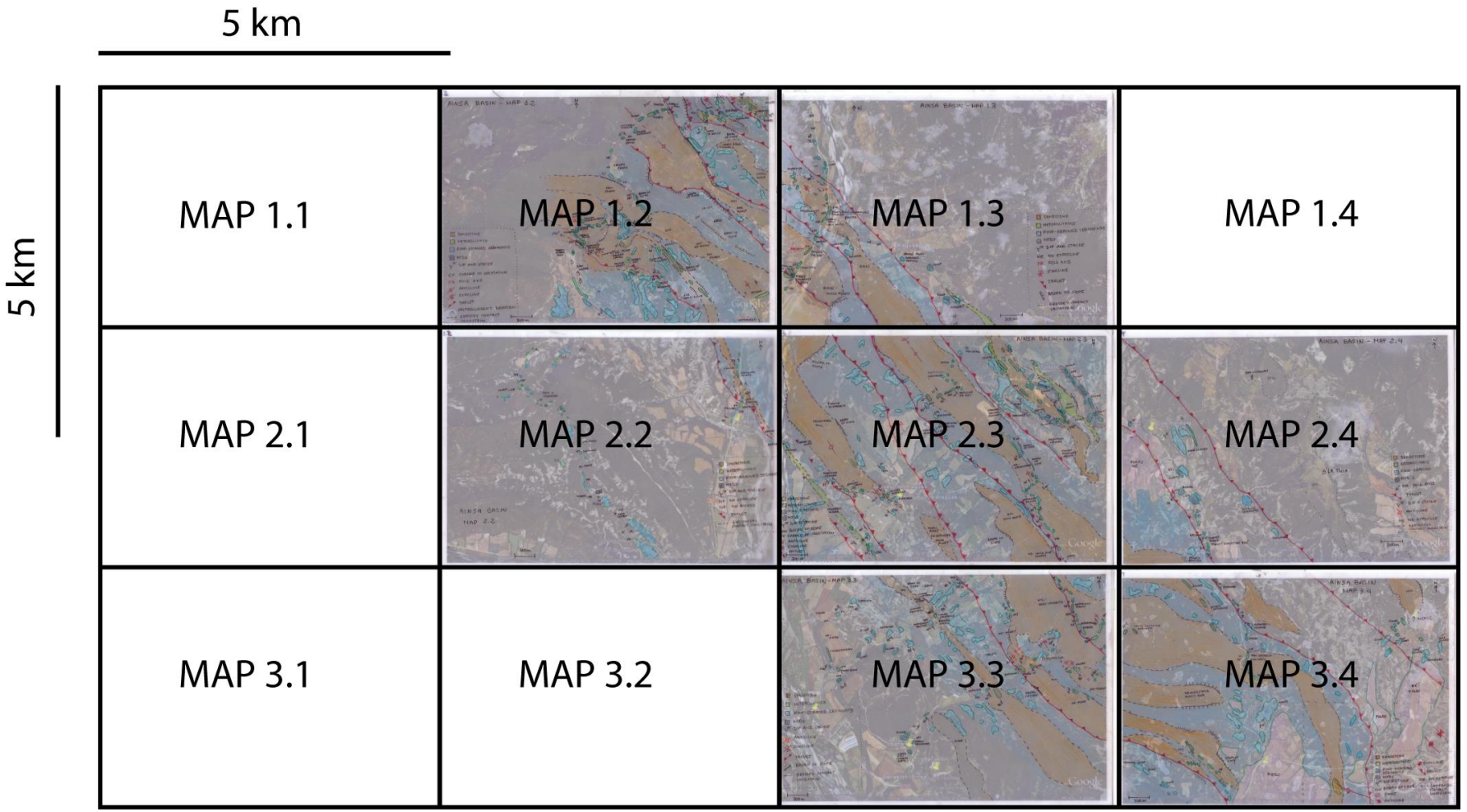
5 km
5 km
MAP 1.1
MAP 1.2
MAP 1.3
MAP 1.4
MAP 2.1
MAP 2.2
MAP 2.3
MAP 2.4
MAP 3.1
MAP 3.2
MAP 3.3
MAP 3.4

Map 1.2

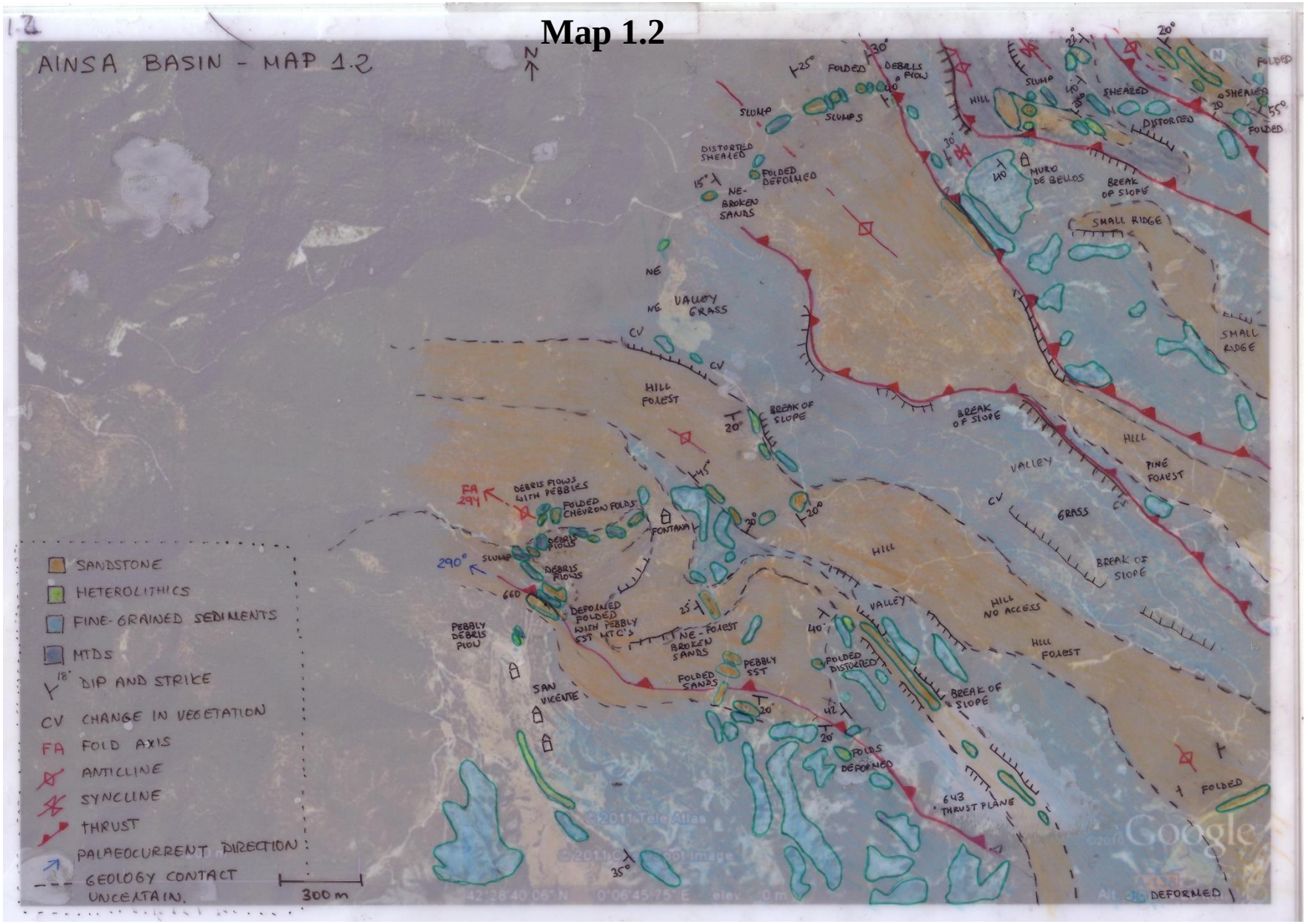
1.2
AINSA BASIN - MAP 1.2
N
SANDSTONE
HETEROLITHICS
FINE-GRAINED SEDIMENTS
MTDs
DIP AND STRIKE
CV CHANGE IN VEGETATION
FA FOLD AXIS
ANTICLINE
SYNCLINE
THRUST
PALAEOCURRENT DIRECTION
GEOLOGY CONTACT
UNCERTAIN.
300 m
SLUMP
SLUMPS
FOLDED
DEBRIS FLOW
DISTORTED SHEARED
FOLDED DEFORMED
NE-BROKEN SANDS
VALLEY GRASS
HILL FOREST
BREAK OF SLOPE
MURO DE BELLOS
SMALL RIDGE
SHEARED
DISTORTED
DEBRIS FLOWS WITH PEBBLES
FOLDED CHEVRON FOLDS
FONTANA
DEBRIS FLOWS
PEBBLY DEBRIS FLOW
DEFORMED FOLDED WITH PEBBLY SST MTC's
FOLDED SANDS
PEBBLY SST
SAN VICENTE
FOLDED DISTORTED
FOLDS DEFORMED
643 THRUST PLANE
HILL NO ACCESS
PINE FOREST
DEFORMED
©2011 TeleAtlas
Google

Map 1.3

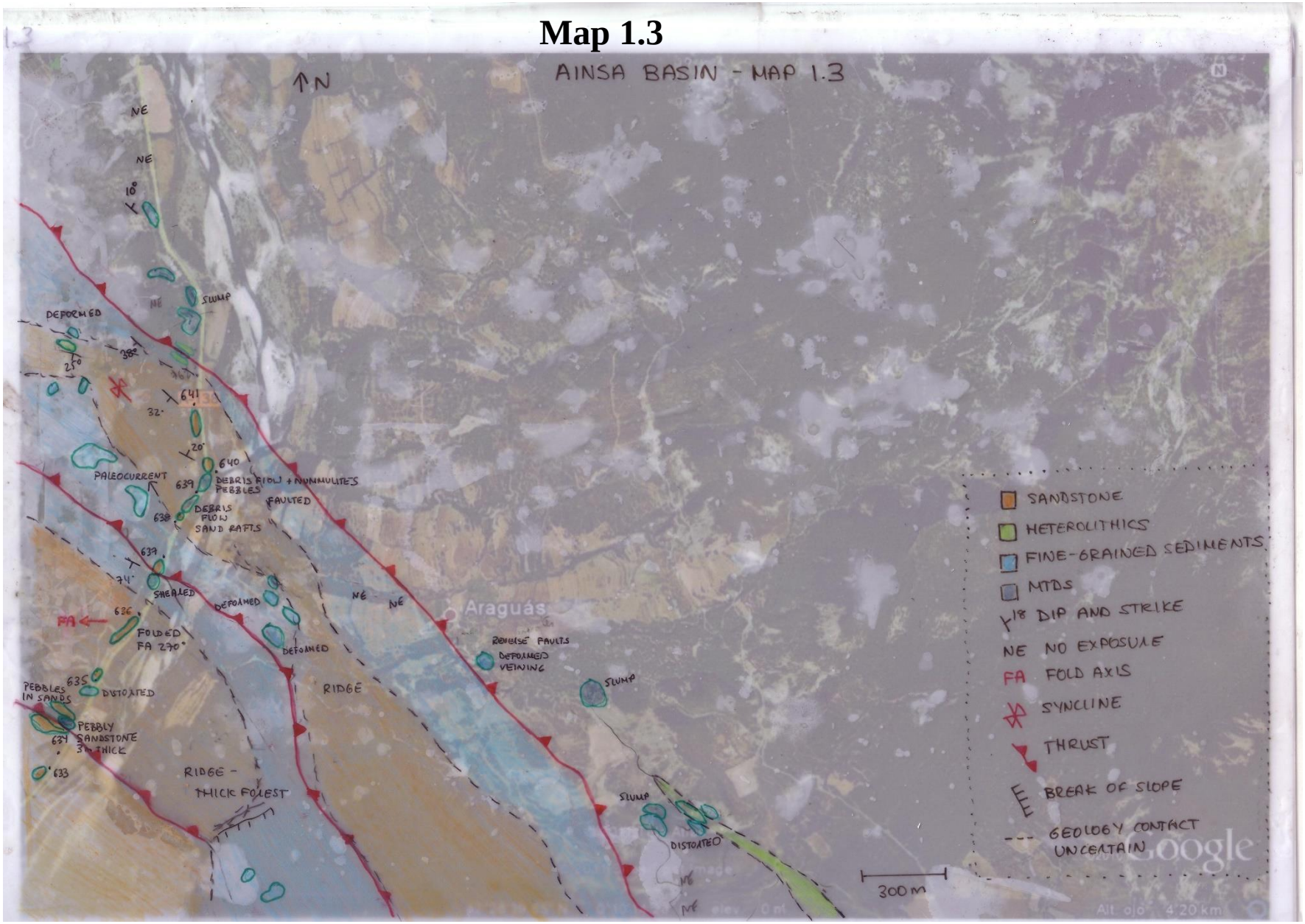
AINSA BASIN - MAP 1.3
↑N
NE
NE
10°
SLUMP
DEFORMED
25°
38°
36°
641
32°
20°
640
639
638
637
74°
636
635
634
633
PALEOCURRENT
DEBRIS FLOW + NUMMULITES PEBBLES
FAULTED
DEBRIS FLOW SAND RAFTS
SHEARED
DEFORMED
FA
FOLDED FA 270°
DEFORMED
PEBBLES IN SANDS
DISTORTED
PEBBLY SANDSTONE 3m THICK
RIDGE
RIDGE - THICK FOREST
NE
NE
Araguás
REVERSE FAULTS
DEFORMED VEINING
SLUMP
SLUMP
DISTORTED
NE
NE
300 m
SANDSTONE
HETEROLITHICS
FINE-GRAINED SEDIMENTS
MTDS
18 DIP AND STRIKE
NE NO EXPOSURE
FA FOLD AXIS
SYNCLINE
THRUST
BREAK OF SLOPE
GEOLOGY CONTACT UNCERTAIN
Google

Map 2.2

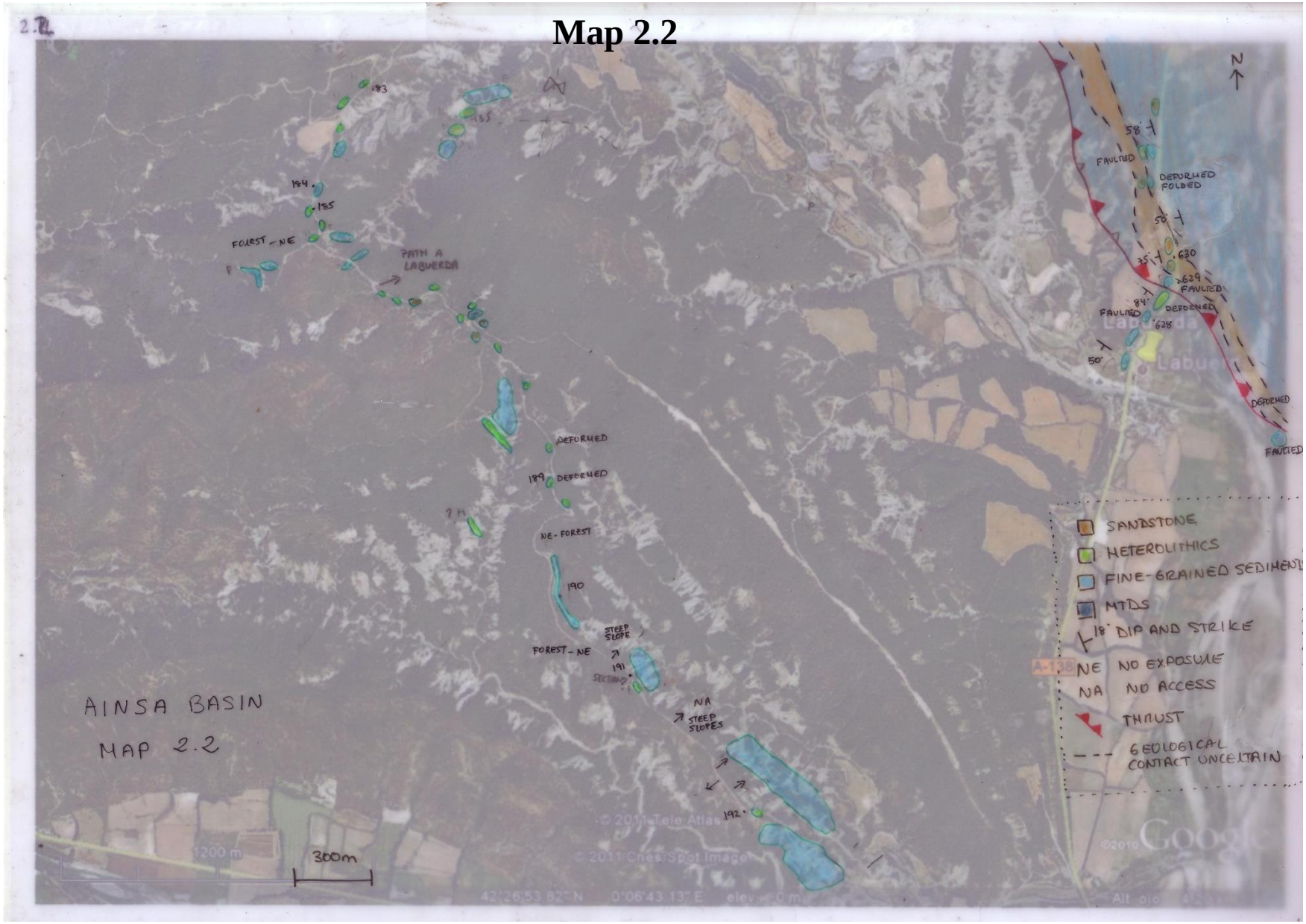
AINSA BASIN
MAP 2.2
PATH A LABUERDA
FOREST - NE
DEFORMED
189
DEFORMED
NE - FOREST
190
STEEP SLOPE
FOREST - NE
191
NA
STEEP SLOPES
192
FAULTED
DEFORMED FOLDED
FAULTED
DEFORMED
FAULTED
DEFORMED
FAULTED
SANDSTONE
HETEROLITHICS
FINE-GRAINED SEDIMENTS
MTDS
DIP AND STRIKE
NE NO EXPOSURE
NA NO ACCESS
THRUST
GEOLOGICAL CONTACT UNCERTAIN
300m

Map 2.3

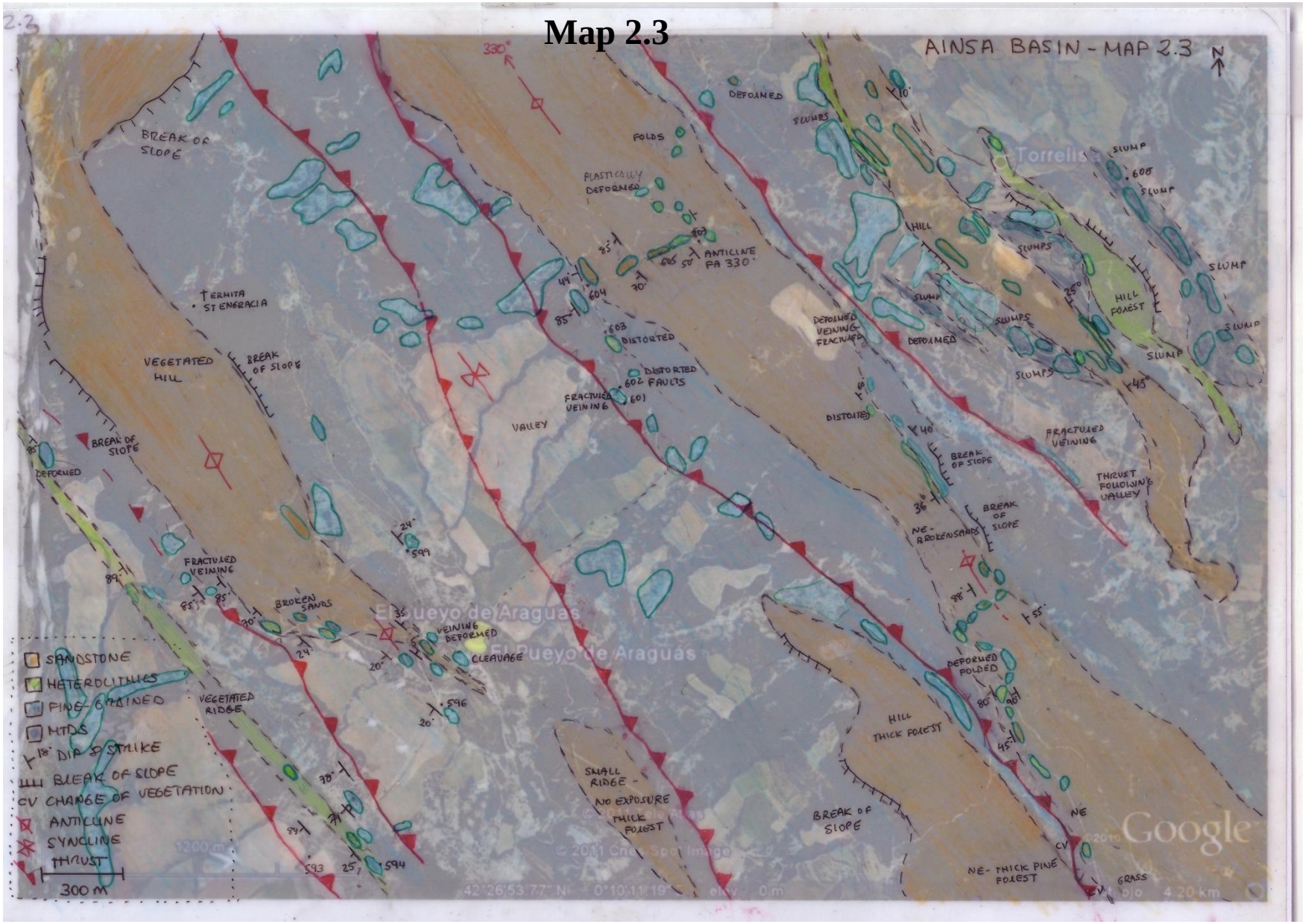
AINSA BASIN - MAP 2.3
N
330°
BREAK OF SLOPE
FOLDS
PLASTICALLY DEFORMED
DEFORMED
SLUMPS
HILL
SLUMP
HILL FOREST
ANTICLINE PA 330°
TERMITA ST ENGRACIA
VEGETATED HILL
DISTORTED
DISTORTED FAULTS
FRACTURED VEINING
VALLEY
DEFORMED VEINING FRACTURED
FRACTURED VEINING
THRUST FOLLOWING VALLEY
NE-BROKEN SANDS
BROKEN SANDS
VEINING DEFORMED
CLEAVAGE
DEFORMED FOLDED
VEGETATED RIDGE
HILL THICK FOREST
SMALL RIDGE - NO EXPOSURE THICK FOREST
NE- THICK PINE FOREST
GRASS
SANDSTONE
HETEROLITHICS
FINE-GRAINED
MUDS
DIP & STRIKE
BREAK OF SLOPE
CV CHANGE OF VEGETATION
ANTICLINE
SYNCLINE
THRUST
300 m
El Sueyo de Araguás
Google

Map 2.4

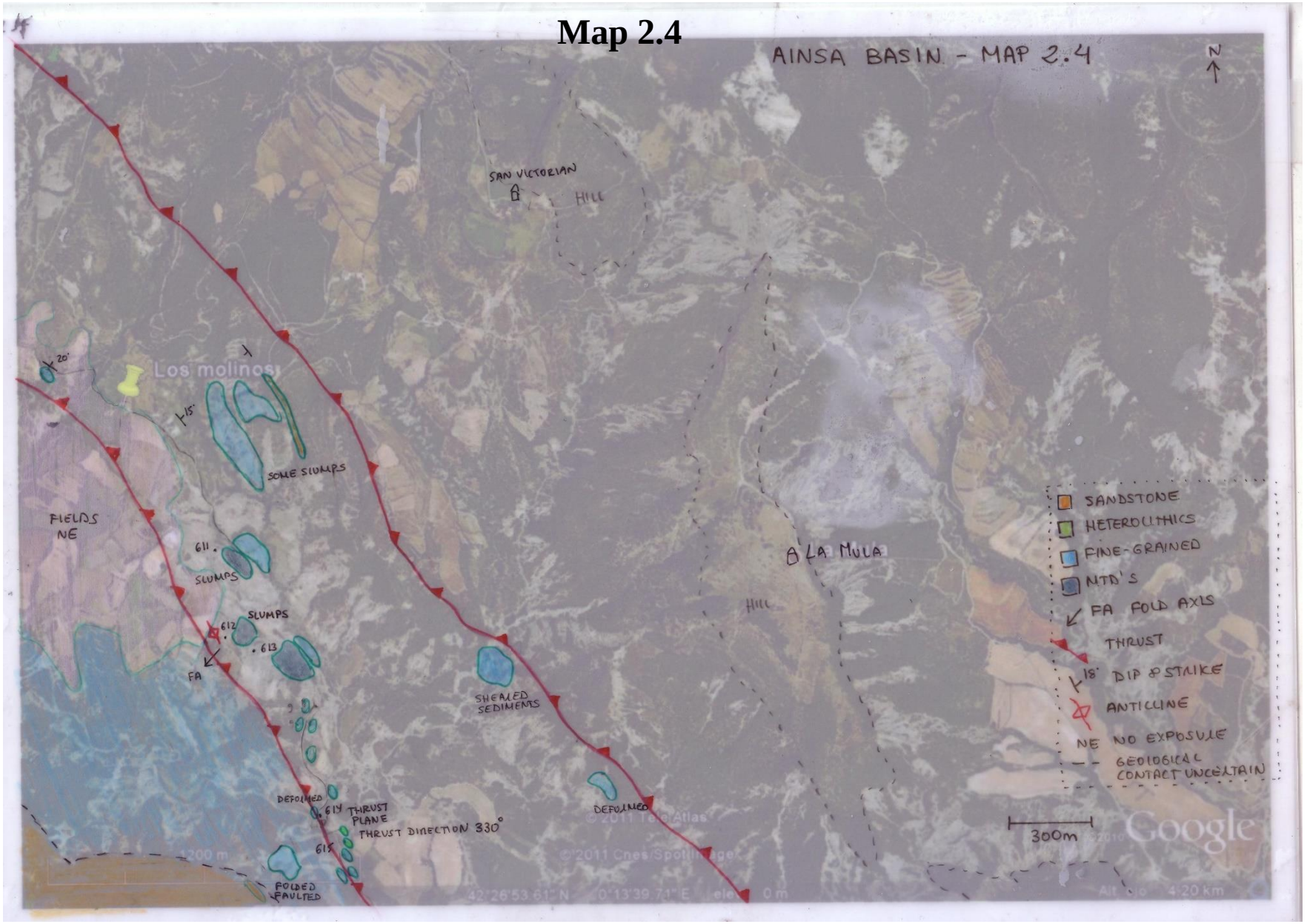
AINSA BASIN - MAP 2.4
N
SAN VICTORIAN
HILL
Los molinos
20°
15°
SOME SLUMPS
FIELDS NE
611
SLUMPS
SLUMPS
612
613
FA
SHEALED SEDIMENTS
LA MULA
HILL
DEFORMED
614 THRUST PLANE
THRUST DIRECTION 330°
615
DEFORMED
FOLDED FAULTED
SANDSTONE
HETEROLITHICS
FINE-GRAINED
NTD'S
FA FOLD AXIS
THRUST
18° DIP & STRIKE
ANTICLINE
NE NO EXPOSURE
GEOLOGICAL CONTACT UNCERTAIN
300m
Google

Map 3.3

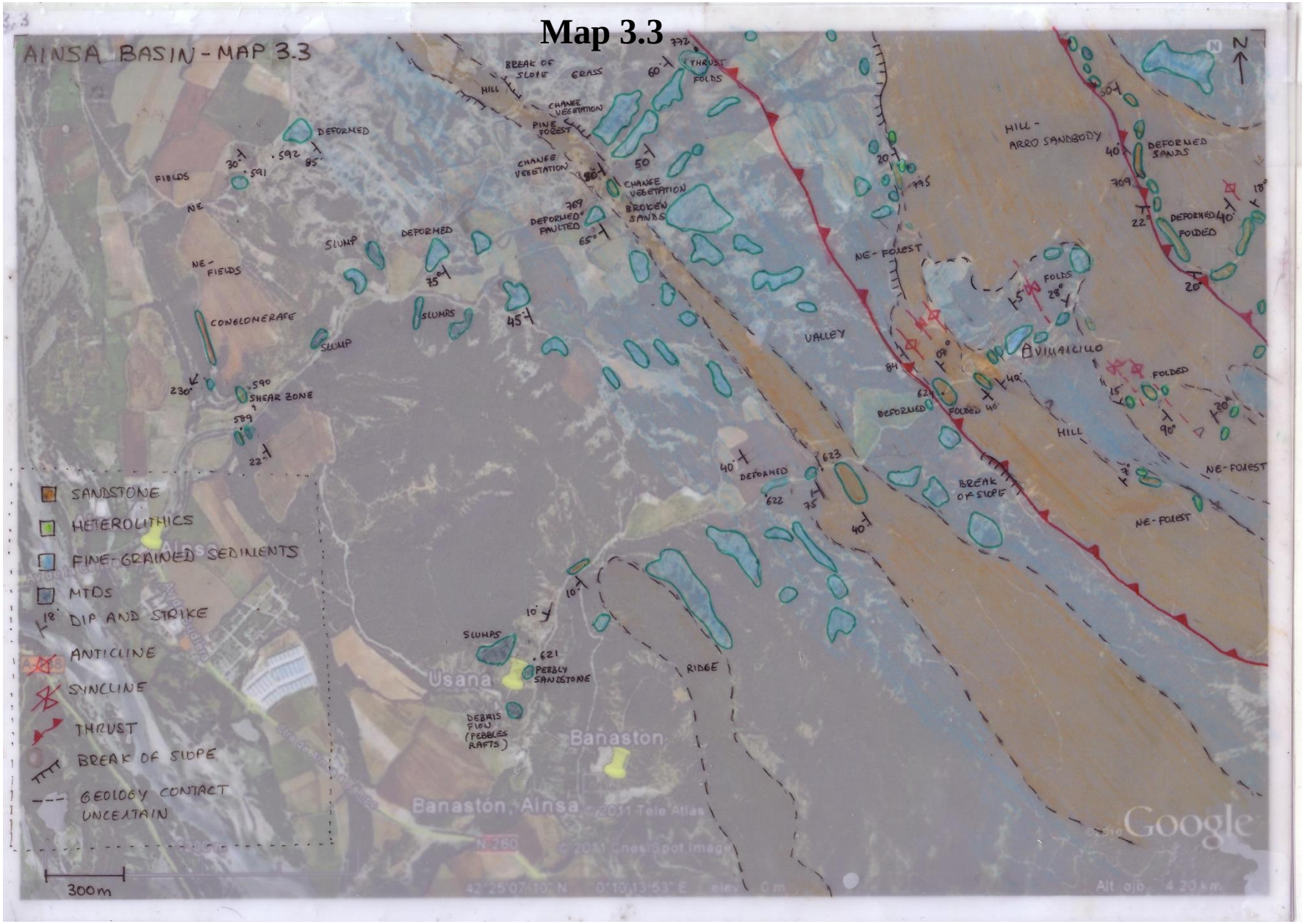
AINSA BASIN - MAP 3.3
SANDSTONE
HETEROLITHICS
FINE-GRAINED SEDIMENTS
MTDS
DIP AND STRIKE
ANTICLINE
SYNCLINE
THRUST
BREAK OF SLOPE
GEOLOGY CONTACT UNCERTAIN
300m
BREAK OF SLOPE
GRASS
HILL
THRUST FOLDS
CHANGE VEGETATION
PINE FOREST
DEFORMED
FIELDS
NE
NE-FIELDS
SLUMP
CONGLOMERATE
SHEAR ZONE
DEFORMED FAULTED
BROKEN SANDS
SLUMPS
VALLEY
NE-FOREST
HILL - ARRO SANDBODY
DEFORMED SANDS
DEFORMED FOLDED
FOLDS
VIMALCILLO
FOLDED
BREAK OF SLOPE
RIDGE
PEBBLY SANDSTONE
DEBRIS FLOW (PEBBLES RAFTS)
Usana
Banaston
Banaston, Ainsa
Google

Map 3.4

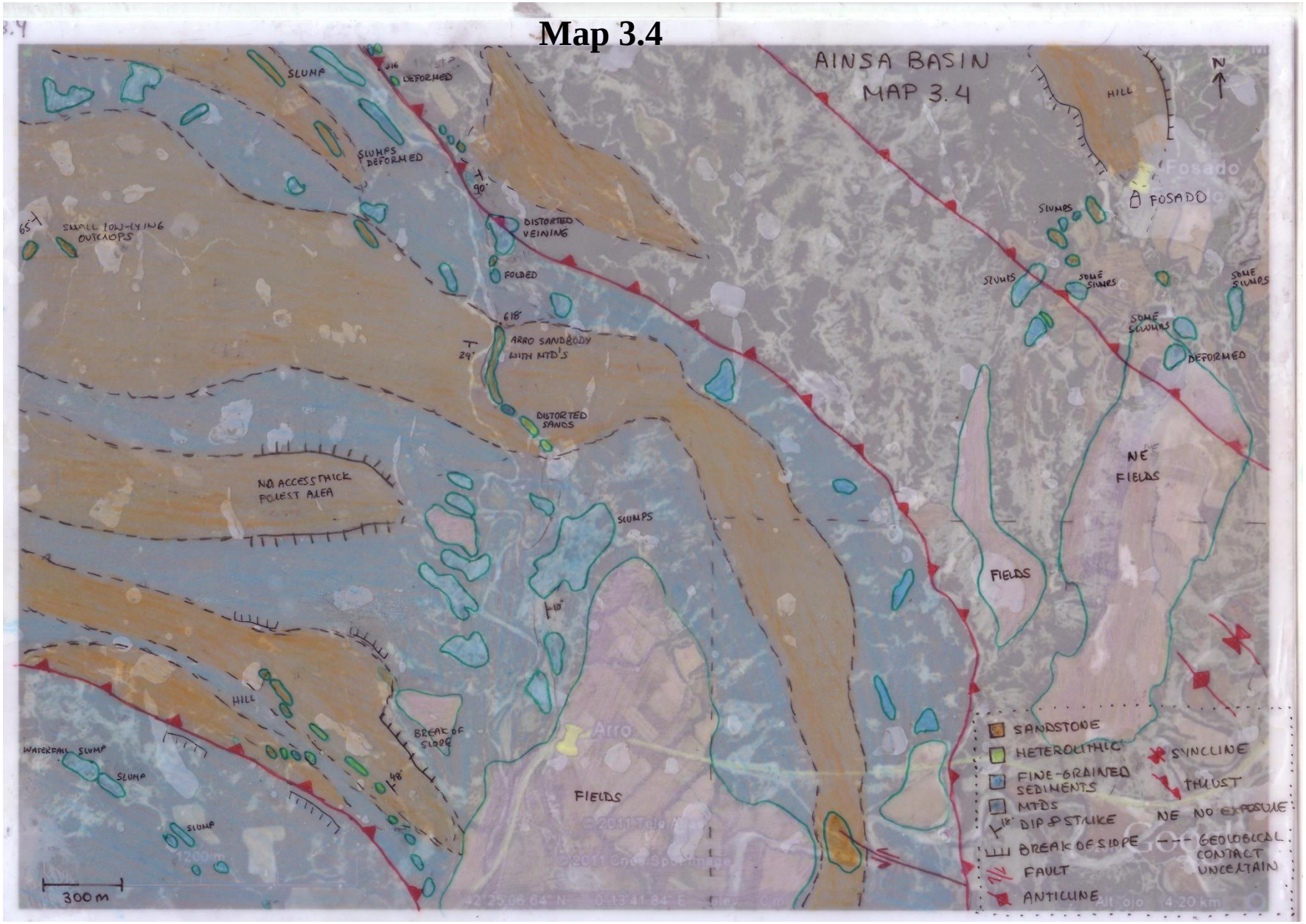
AINSA BASIN
MAP 3.4
N
SLUMP
DEFORMED
SLUMPS DEFORMED
SMALL LOW-LYING OUTCROPS
DISTORTED VEINING
FOLDED
ARRO SANDBODY WITH MTD'S
DISTORTED SANDS
NO ACCESS THICK FOREST AREA
SLUMPS
HILL
FOSADO
SLUMPS
SOME SLUMPS
SOME SLUMPS
SOME SLUMPS
DEFORMED
NE FIELDS
FIELDS
FIELDS
HILL
BREAK OF SLOPE
WATERFALL SLUMP
SLUMP
SLUMP
300 m
SANDSTONE
HETEROLITHIC
FINE-GRAINED SEDIMENTS
MTDS
DIP & STRIKE
BREAK OF SLOPE
FAULT
ANTICLINE
SYNCLINE
THRUST
NE NO EXPOSURE
GEOLOGICAL CONTACT UNCERTAIN